

Lecture Notes in Earth System Sciences

LNESS

Chi-Yuen Wang
Michael Manga

Water and Earthquakes

OPEN ACCESS

 Springer

Lecture Notes in Earth System Sciences

Series Editors

Philippe Blondel, Department of Physics, University of Bath, Bath, Avon, UK

Joachim Reitner, Göttingen, Germany

Kurt Stüwe, Graz, Austria

Martin H. Trauth, Potsdam, Brandenburg, Germany

David A. Yuen, Department of Geology and Geophysics, University of Minnesota,
Minneapolis, MN, USA

Founding Editors

G. M. Friedman, Brooklyn, USA

A. Seilacher, Tübingen, USA

The Lecture Notes in Earth System Science (LNESS) series reports on new developments in research and teaching in the entire field of earth system science: from the focused study of phenomena on the nano and micro-scales to the entire earth system including its early formation, evolution and future status. The series is thoroughly interdisciplinary presenting studies of the litho-, atmo-, hydro- and biospheres and humanities interactions with them. The series publishes: monographs on advanced topics, technical reports of high quality and broad interest and reports of workshops, expeditions and surveys, provided they are of exceptional interest and focused on a single topic. As the name implies, the submission of manuscripts based on advanced courses such as collections of lectures and tutorials, course materials for laboratory and field courses and summer schools is highly encouraged. The Lecture Notes in Earth System Science (LNESS) is now also the home of Springer Earth Sciences Open Access proceedings. Conference proceedings published in the series are free to read online under the Creative Commons License Agreement whereby the copyright of the contributions remains with the authors.

More information about this series at <http://www.springer.com/series/10529>

Chi-Yuen Wang · Michael Manga

Water and Earthquakes

 Springer

Chi-Yuen Wang
Department of Earth and Planetary Science
University of California
Berkeley, CA, USA

Michael Manga
Department of Earth and Planetary Science
University of California
Berkeley, CA, USA



ISSN 2193-8571 ISSN 2193-858X (electronic)
Lecture Notes in Earth System Sciences
ISBN 978-3-030-64307-2 ISBN 978-3-030-64308-9 (eBook)
<https://doi.org/10.1007/978-3-030-64308-9>

© The Editor(s) (if applicable) and The Author(s) 2021. This book is an open access publication.

Open Access This book is licensed under the terms of the Creative Commons Attribution 4.0 International License (<http://creativecommons.org/licenses/by/4.0/>), which permits use, sharing, adaptation, distribution and reproduction in any medium or format, as long as you give appropriate credit to the original author(s) and the source, provide a link to the Creative Commons license and indicate if changes were made.

The images or other third party material in this book are included in the book's Creative Commons license, unless indicated otherwise in a credit line to the material. If material is not included in the book's Creative Commons license and your intended use is not permitted by statutory regulation or exceeds the permitted use, you will need to obtain permission directly from the copyright holder.

The use of general descriptive names, registered names, trademarks, service marks, etc. in this publication does not imply, even in the absence of a specific statement, that such names are exempt from the relevant protective laws and regulations and therefore free for general use.

The publisher, the authors and the editors are safe to assume that the advice and information in this book are believed to be true and accurate at the date of publication. Neither the publisher nor the authors or the editors give a warranty, expressed or implied, with respect to the material contained herein or for any errors or omissions that may have been made. The publisher remains neutral with regard to jurisdictional claims in published maps and institutional affiliations.

This Springer imprint is published by the registered company Springer Nature Switzerland AG
The registered company address is: Gewerbestrasse 11, 6330 Cham, Switzerland

*We dedicate this book to John Verhoogen—a
dear colleague and admirable scientist.*

Preface

Water and earthquakes, while two seemingly separate subjects, do interact, as evidenced by the great many earthquakes during the last decade in the mid-continental USA induced by the injection of toxic wastewater co-produced from hydrocarbon extraction. This occurrence has spurred many studies on induced seismicity, which, in turn, have led to much progress in understanding the interactions between water and earthquakes beyond that presented when our first book on Earthquakes and Water was published ~10 years ago. Three new research directions and opportunities have advanced the studies of the interaction between earthquakes and water. One is an increased use of the tidal response of groundwater to quantify earthquake-induced changes in groundwater systems, which has moved the field of earthquake hydrology from a more descriptive study to a more quantitative science. Second, several drilling projects into active fault zones have provided new insights into their hydraulic and thermal properties. Third, many large earthquakes in the last decade produced a great amount of new data that have revealed some hitherto unknown and unexpected groundwater responses to earthquakes. These advances have prompted us to write the present volume that is significantly different from our first book.

Earthquakes are well known to induce a wide range of responses in surface water and groundwater. Studies of these responses in the past two decades have revealed that the permeability of the crust, the most important parameter that controls groundwater flow and transport, is a dynamic property that evolves with both time and space. The dynamic nature of crustal permeability may have fundamental implications for our understanding of groundwater flow, the transport of contaminants, the formation of minerals and ore deposits, and the security of the subsurface reservoirs. The observed phenomena also allow us to probe the interaction between hydrogeological processes and mechanical deformation in the shallow crust. Hence, they provide insight into the interactions between the water cycle, tectonics, and properties of the crust. As such, the study of earthquake hydrology also has the potential to provide a more quantitative and in-depth understanding of the nature of earthquake precursors and to evaluate whether they are in fact precursors.

Our emphasis here is on understanding the hydrological phenomena induced or modified by earthquakes and the hydrogeologic process that induce earthquakes. The boundary between the ‘hydrology of earthquakes’ and the ‘earthquake-induced

hydrological phenomena', however, can sometimes be blurred. For example, triggered earthquakes are sometimes explained by a redistribution of pore pressure following the triggering earthquake. Hence, triggered seismicity may be an example of an earthquake-induced hydrological phenomenon. The study of the latter, therefore, can be important towards a better understanding of the mechanics of at least some earthquakes.

Berkeley, USA

Chi-Yuen Wang
Michael Manga

Acknowledgements

There are many students, postdocs and colleagues we wish to thank for collaborating on research projects related to the topics reviewed in this book or participating in stimulating discussions in the class we taught called ‘Earthquake hydrology’. In particular, we thank Christian Mohr for translating a quotation from Emmanuel Kant, which is used as the introduction to Chap. 1. We thank some colleagues for reading drafts of chapters from the book and providing helpful comments; Lian Xue, Zheming Shi and Yan Zhang for reading Chap. 5, Lian Xue for reading Chap. 6, Takahiro Hosono and Steven Breen for reading Chap. 7, and Yaolin Shi for reading Chap. 8. We thank the Sonoma Ecology Center and Gaye Lub for assistance during the initial stage of our field work following the 2014 South Napa earthquake, Chung-Ho Wang for providing the water level data from Taiwan, Simon Cox for providing the liquefaction data from New Zealand, and Kyoochui Ha for providing the technical details of temperature measurement in Korea. We also wish to thank Emily Brodsky, Mai-Linh Doan, Lian Xue, Andrew Barbour, Takahiro Hosono, Simon Cox, Heiko Woith, Yaolin Shi, Zheming Shi, Yan Zhang, Xin Liao, Ai-Yu Zhu, Douglas Dreger, Shemin Ge, Tom Holzer, Matthew Weingarten, Chris Huber, Joel Rowland, Martin Saar, Max Rudolph, Noah Randolph-Flagg, Theresa Sawi, Mark Tingay, Richard Davies, Maria Brumm, Steve Breen, Marco Bonini, Zack Geballe, Weiqun Liu, Ikuro Sumita, Atsuko Namiki, Steve Ingebritsen, Shaul Hurwitz, Christian Mohr, Oliver Korup, Guang Zhai, Manoocher Shirzaei, Yeeping Chia and Chung-Ho Wang for enlightening exchanges. Susan Storch and Lee-Ping Wang helped collect the data in Fig. 9.17. Finally, we thank the National Science Foundation, the Miller Institute for Basic Research in Science, and NASA for supporting the research and synthesis in this volume.

Contents

1	Introduction	1
	References	5
2	Groundwater Flow and Transport	9
2.1	Introduction	9
2.2	Pressure, Hydraulic Head and Darcy's Law	12
2.3	Permeability of Layered Media	13
2.4	Specific Storage and Specific Yield	14
2.5	Saturated Flow	14
	2.5.1 Isothermal Flow	14
	2.5.2 Flow Through Variable Temperatures	15
2.6	Unsaturated Flow	16
2.7	Heat Transport	17
2.8	Solute Transport	19
	References	21
3	Hydro-Mechanical Coupling	23
3.1	Introduction	23
3.2	Linear Poroelasticity and Groundwater Flow	24
	3.2.1 Constitutive Relations for Isotropic Stress: Biot (1941)	26
	3.2.2 Effective Stress	27
	3.2.3 Related Poroelastic Constants	28
	3.2.4 Constitutive Relationship for Anisotropic Stress: Biot (1955)	31
	3.2.5 Poroelastic Constants	33
	3.2.6 Governing Equations for Flow in Poroelastic Media	39
	3.2.7 Uncoupling Stress or Strain from Fluid Flow	40
3.3	Consolidation	42
	3.3.1 Consolidation of Sediments in Sedimentary Basin	42
	3.3.2 Terzaghi Theory of Consolidation	43

- 3.4 Liquefaction 46
- 3.5 Rock Friction and Instability 49
 - 3.5.1 Friction and Frictional Instability 50
 - 3.5.2 The Rate-and-State Equation 55
- References 59
- 4 Earthquakes Influenced by Water 61**
 - 4.1 Introduction 61
 - 4.2 Fluids and Rock Failure 62
 - 4.3 Earthquakes Induced by Fluid Injection 64
 - 4.4 Earthquakes Induced by Fluid Extraction 67
 - 4.5 Reservoir-Induced Seismicity 69
 - 4.6 Natural Hydrological Triggering of Earthquakes 72
 - 4.7 Earthquake Triggering of Earthquakes via Hydrological Processes 73
 - 4.8 Concluding Remarks and Outlook 76
 - References 77
- 5 Response to Tides, Barometric Pressure and Seismic Waves 83**
 - 5.1 Introduction 83
 - 5.2 Tidal Potential 85
 - 5.3 Earth Tides 87
 - 5.4 Groundwater Response to Earth Tides 89
 - 5.4.1 Tidal Response of a Confined Aquifer 93
 - 5.4.2 Tidal Response of an Unconfined Aquifer with Flow to the Water Table 95
 - 5.4.3 An Example of Seasonal Change of Tidal Response 98
 - 5.4.4 Tidal Response of a Leaky Aquifer 100
 - 5.4.5 Numerical Simulation for the Tidal Response of a Leaky Aquifer 104
 - 5.4.6 Tidal Response of an Unconfined Aquifer with the Capillary Effect 114
 - 5.5 Groundwater Response to Barometric Changes 121
 - 5.5.1 Barometric Response of Aquifers and Barometric Efficiency 121
 - 5.5.2 Analytical Solution with a Half-Space Aquitard 122
 - 5.5.3 Analytical Solution with a Finite Aquitard 127
 - 5.5.4 Numerical Solution 128
 - 5.5.5 Applications 130
 - 5.6 Estimating Hydraulic Property with Tidal and Barometric Methods 131
 - 5.7 Groundwater Oscillations in Response to Seismic Waves 136
 - 5.8 Concluding Remarks 140
 - Appendices. Derivation of Equations 143
 - References 150

- 6 Groundwater Level** 155
 - 6.1 Introduction 155
 - 6.2 Observations 159
 - 6.2.1 Coseismic Step-like Changes of Groundwater Level 159
 - 6.2.2 Sustained Changes 162
 - 6.2.3 Breached Confinement 162
 - 6.3 Models and Constraints 165
 - 6.3.1 Coseismic Static Strain 165
 - 6.3.2 Undrained Consolidation and Liquefaction 167
 - 6.3.3 Enhanced Permeability 167
 - 6.3.4 Shaking Water Out of Unsaturated Soil 169
 - 6.4 Constraints 170
 - 6.4.1 Constraints from Laboratory Experiments 170
 - 6.4.2 Constraints from Field Observations 171
 - 6.4.3 Constraint from Tidal Analysis 174
 - 6.4.4 Constraints from Threshold Seismic Energy 177
 - 6.4.5 Post-seismic Recession of Groundwater Level 180
 - 6.5 Pore Pressure and Permeability of Continental Faults 184
 - 6.6 Pore Pressure and Permeability on the Ocean Floor 188
 - 6.6.1 Pore Pressure and Permeability in an Accretionary Prism 188
 - 6.6.2 Pore Pressure Changes Near an Ocean Ridge 191
 - 6.7 Concluding Remarks 193
- Appendix: Derivation of Eq. 6.13 194
- References 195

- 7 Stream Flow** 201
 - 7.1 Introduction 201
 - 7.2 Observations 203
 - 7.2.1 Measurement with Flow Meter and Tape 203
 - 7.2.2 Measurement with Stream Gauges 203
 - 7.3 Proposed Mechanisms 206
 - 7.3.1 Static Elastic Strain 207
 - 7.3.2 Consolidation and Liquefaction 209
 - 7.3.3 Water Released from Mountains 210
 - 7.3.4 Water Released from Unsaturated Soils 210
 - 7.3.5 Enhanced Permeability 212
 - 7.3.6 Enhanced Vertical Permeability 212
 - 7.4 Model Constraints 215
 - 7.4.1 Constraints from Earthquake Mechanism 215
 - 7.4.2 Constraints from Recession Analysis 216
 - 7.4.3 Constraints From Multiple Stream Gauges 222
 - 7.4.4 Constraints From the Threshold Seismic Energy 222
 - 7.4.5 Constraints from Laboratory Experiment 223

- 7.4.6 Constraints from Chemical Composition
of the Excess Flow 224
- 7.5 Streamflow Changes in Hydrothermal Areas 224
- 7.6 Concluding Remarks 228
- References 228
- 8 Groundwater Temperature 231**
 - 8.1 Introduction 231
 - 8.2 Land Measurements 232
 - 8.2.1 China 232
 - 8.2.2 Japan 236
 - 8.2.3 Korea 237
 - 8.3 Basin-Wide Changes 237
 - 8.4 Springs 241
 - 8.4.1 Cold Springs 241
 - 8.4.2 Hot Springs 242
 - 8.5 Seafloor Measurements 245
 - 8.5.1 Subduction Zones 245
 - 8.5.2 Near Oceanic Ridge 247
 - 8.6 Turbulent Mixing of Well Water 250
 - 8.7 Concluding Remarks 254
 - References 254
- 9 Groundwater and Stream Composition 257**
 - 9.1 Introduction 257
 - 9.2 Groundwater Composition 258
 - 9.2.1 Major Elements 258
 - 9.2.2 Trace Elements 267
 - 9.2.3 Stable Isotopes 272
 - 9.3 Stream Water Composition 278
 - 9.4 Need of Integrated Data to Interpret Composition Change 283
 - 9.5 Concluding Remarks 285
 - References 285
- 10 Geysers 289**
 - 10.1 Introduction 289
 - 10.1.1 Response of Geysers to Earthquakes 290
 - 10.1.2 Response of Geysers to Other Sources of Stress 293
 - 10.2 Mechanisms 294
 - 10.2.1 How Do Geysers Work? 294
 - 10.2.2 Mechanisms for Altering Eruptions 295
 - 10.3 Conclusions About Geysers 296
 - References 297

11	Liquefaction	301
11.1	Introduction	301
11.2	Sediment Consolidation and Liquefaction in Cyclic Loading	304
11.3	Liquefaction Beyond the Near Field	308
11.4	Experiment at Wildlife Liquefaction Array, California	310
11.5	Dependence of Liquefaction on Seismic Frequency	315
11.6	Concluding Remarks	318
	References	319
12	Mud Volcanoes	323
12.1	Introduction	323
12.2	Response of Mud Volcanoes to Earthquakes	325
12.3	Insights from Triggered Eruptions of Magmatic Volcanoes	327
12.4	Mechanisms	329
	12.4.1 Static or Dynamic Stresses?	329
	12.4.2 Mechanisms for Initiating Eruptions	330
12.5	The Sidoarjo (Lusi) Mud Flow	333
12.6	Effect of Earthquakes on Already-Erupting Mud Volcanoes	335
12.7	Concluding Remarks About Mud Volcanoes	336
	References	337
13	Hydrologic Precursors	343
13.1	Introduction	343
13.2	What is a Precursor?	345
13.3	Identifying Precursors	346
13.4	Examples	348
	13.4.1 China: Haicheng, 1975 and Tangshan, 1976	348
	13.4.2 Kobe, Japan, 1995	349
	13.4.3 Nankaido, Japan, 1946	349
	13.4.4 Oxygen Isotope Precursors to the 2016 Tottori Earthquake, Japan	350
	13.4.5 Kettleman Hills, California, 1985	351
	13.4.6 Chi-Chi, Taiwan, 1999	352
	13.4.7 Kamchatka	354
	13.4.8 Pyrenees, France, 1996	356
	13.4.9 Reservoir Induced Seismicity, Koyna, India	357
	13.4.10 Calistoga Geysers, California	357
	13.4.11 Iceland, 2012–2013	359
	13.4.12 Central Italy Seismic Sequence, 2016	359
	13.4.13 Precursory Changes in Spring Temperature	362
13.5	Outlook	363
	References	364

- 14 Epilogue** 369
 - 14.1 General Framework 369
 - 14.2 Future Research 374
 - References 376

- Index** 381

Chapter 1

Introduction



“... The waters that seem to have been cut off on the land of all communion with the sea, the springs, the lakes, were in extraordinary agitation in many distant lands at the same time. Most of the lakes in Switzerland, the lake at Templin in the Marches, some lakes in Norway and Sweden, took on a swirling motion that was far more tumultuous than a storm, and the air was at the same time calm. The lake at Neuchâtel, if one can rely on the news, went into hidden crevices, and the one at Meiningen did the same, but soon returned. In just these minutes, the mineral water at Töplitz in Bohemia suddenly stopped and returned to blood red. The force with which the water had drifted had widened its old course, and it got thereby a stronger inflow. The inhabitants of this city had to sing *te deum laudamus*, ... In the Kingdom of Fez in Africa, a subterranean force split a mountain and poured blood-red streams out of its mouth. At Angoulême in France, there was an underground roar, and a deep crypt opened up on the plain, holding in itself unfathomable water. At Gçmenos in Provence, a spring suddenly became muddy and turned red. The surrounding areas reported similar changes of their sources. All this happened in the same minutes as the earthquake devastated the coasts of Portugal. Every now and then in just these short times some earth tremors in far-off countries were perceived. Almost all happened close to the seacoast. At Cork in Ireland, as in Glückstadt, and at some other places lying on the seas, there were slight changes. Milan is perhaps the place that has been shaken at the furthest distance from the shore of the lake on the very same day. Just this morning at 8 o'clock Vesuvius raged at Neapolis, and was silent again the time when the shock came to Portugal. ...” von Kant (1756), translated by Christian Mohr, University of Potsdam.

For thousands of years, hydrologic changes have been documented following earthquakes. Examples include increased stream discharge, changes in groundwater level, changes in the temperature and chemical composition of groundwater, formation of new springs, disappearance of previously active springs, the liquefaction of sediments, and changes in the activities of mud volcanoes and geysers. The introductory quotation from Kant, for example, describes responses throughout Europe



Fig. 1.1 Well in Meizhou County, Guangdong, China, responding to the December 26, 2004, M 9.2 Sumatra earthquake 3200 km away, 2 days after the Sumatra earthquake. The fountain was 50–60 m high when it was first sighted 1 day after the earthquake. Picture taken by Hou Banghua, Earthquake Office of Meizhou County

to the 1755 great Lisbon earthquake. It is not unexpected that earthquakes can cause hydrologic changes because the stresses created by earthquakes can be large. What is surprising are the large amplitudes of hydrologic responses and the great distances over which these changes occur. Following the 2004 M9.2 Sumatra earthquake, for example, groundwater erupted in southern China, 3200 km away from the epicenter, and the water fountain shown in Fig. 1.1 reached a height of 50–60 m above the ground surface when it was first sighted. Because earthquakes and water interact with each other through changes in both stress and physical properties of rocks, understanding the origin of hydrological responses can provide unique insight into hydrogeologic and tectonic processes at spatial and temporal scales that otherwise could not be studied.

Earthquakes cause both static and dynamic changes of the stresses in the crust. Both types of stress change decrease with increasing distance from the earthquake, but at different rates. Figure 1.2, from Kilb et al. (2002), illustrates how static and dynamic stress change with increasing distance from the epicenter. The dynamic component of the Coulomb stress change, $\Delta CFS(t)$, as defined in the caption of Fig. 1.2, is the time-dependent change in the Coulomb failure stress resolved onto a possible failure plane. The static stress change, denoted by ΔCFS , diminishes much more rapidly with distance than the transient, dynamic change. Thus, at close distances the ratio (peak $\Delta CFS(t)$)/ ΔCFS is approximately inversely proportional to the source-receiver distance, r^{-1} , and at larger distances proportional to r^{-2} (Aki and Richards 1980). At distances up to ~ 1 ruptured fault length, the static and the peak dynamic changes are comparable in magnitude, while at distances greater than

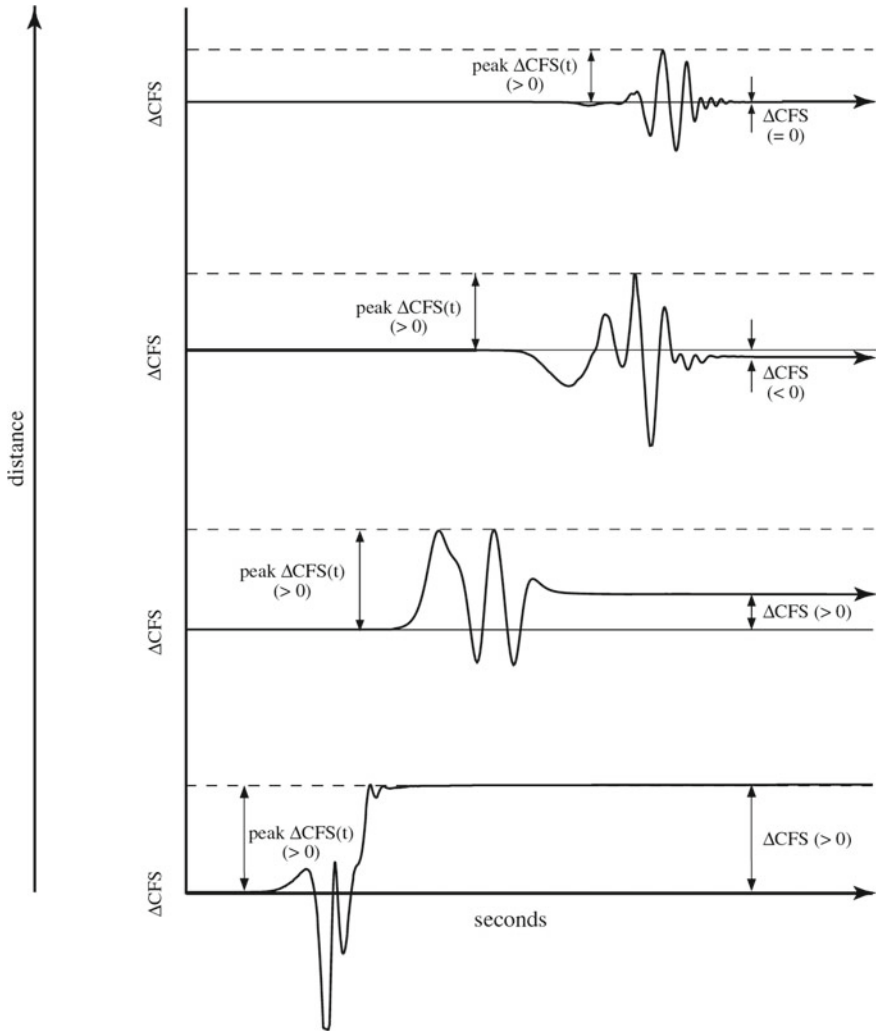


Fig. 1.2 Cartoon illustrating the peak dynamic Coulomb stress change (peak $\Delta CFS(t)$) and static Coulomb stress change (ΔCFS), and their variation with distance from the ruptured fault. $\Delta CFS(t) \equiv \Delta \tau(t) - \mu [\Delta \sigma(t) - \Delta P(t)]$, where τ is shear stress on the fault, σ is the stress normal to the fault, P is the pore pressure, and μ is the coefficient of friction. In the far field, peak dynamic stresses, $\Delta CFS(t)$, are far greater than the static change, ΔCFS , but in the near field, both are comparable in magnitude. Modified from Kilb et al. (2002)

several ruptured fault lengths, the peak dynamic change is much greater than the static change. As discussed in later chapters, the relative magnitude of the static and dynamic stresses is reflected in the hydrologic responses to earthquakes and is critical to understanding the origin of hydrological changes. We thus hereafter use the expression ‘near field’ to denote distances within about one ruptured fault

length, ‘far field’ to denote distances many times greater than the fault length, and ‘intermediate field’ for distances in between.

Besides being a matter of academic interest, the study of earthquake-induced hydrologic changes also has important implications for water resources, hydrocarbon exploration and engineered systems. For example, groundwater level changes following earthquakes can affect water supplies (Chen and Wang 2009). The abandonment of Crete during the Late Minoan period has been attributed by some to a depletion of groundwater caused by earthquake (Gorokhovich 2005). In more recent times, it is sometimes necessary to evaluate the causative role of an earthquake in insurance claims for loss of water supply (Roeloffs 1998). Furthermore, earthquake-induced increase in crustal permeability (e.g., Rojstaczer et al. 1995; Roeloffs 1998; Brodsky et al. 2003; Wang et al. 2004; Elkhoury et al. 2006; Wang and Chia 2008; Zhang et al. 2019a, b) has important implications on hydrocarbon migration and recovery on the one hand, and contaminant transport on the other. Forensic earthquake hydrology was also applied to evaluate whether an earthquake may have played causative role in the 2006 mud eruption near the Indonesian city of Sidoarjo, in eastern Java, that led to massive destruction of property and evacuation of people (Tingay et al. 2018). Groundwater level changes following earthquakes may also put some underground waste repositories at risk (Carrigan et al. 1991; O’Brien 1992; Wang et al. 2018). Earthquake-induced fluid pressure changes can induce liquefaction of the ground that causes great damage to engineered structures (e.g., Seed and Lee 1966; National Research Council 2016), affect hydrocarbon production (Beresnev and Johnson 1994), and trigger seismicity (Hill and Prejean 2007; Guglielmi et al. 2015; Craig et al. 2017). Finally, measured changes of the pore pressure in rocks and/or the chemical composition of groundwater are sometimes taken as signatures of the crustal response to tectonic deformation (e.g., Davis et al. 2006) or even as earthquake precursors (e.g., Silver and Wakita 1996).

In the last two decades, there has been a rapid increase in the number and especially the quality of quantitative data documenting hydrological changes during and following earthquakes, largely due to the implementation of modern hydrological, seismological and geodetic monitoring systems around the globe. Research results on this topic, however, have been published in various journals and various fields (geoscience, hydrology, geotechnical engineering, petroleum geology). We felt it desirable to summarize the advances made so far in a single volume, both in terms of observations as well as their analysis and interpretation. Such a volume may serve on one hand as a convenient reference for researchers active in this area, and, on the other hand, as a starting point for students interested in this topic and may thus help to advance the studies of the interactions between water and earthquakes.

This volume does not address all possible interactions between water and earthquakes. Not covered are tsunamis, for example. We also do not address how the chemical properties of water affect faults and rock failure, and address only the physical effects of water on rock properties. Further, most studies of groundwater response to earthquakes tend to focus on the responses of groundwater systems that are directly detected and measured, such as the coseismic and post-seismic changes of water level in wells, discharge in streams, and changes in water temperature and

composition. Others have considered the response of deep fluid systems, such as fluids released from metamorphic processes that occur at depths of several tens of km (e.g., Ingebritsen and Manning 2010), for which the response to earthquakes are not directly measured. In order to keep the book within a reasonable scope, we focus on processes that are directly measurable with available instruments, and are thus relatively shallow, even though deep metamorphic and magmatic processes are relevant and important for understanding both Earth's subsurface water cycle and the feedback between tectonics and fluids in the crust.

In keeping with the spirit of the series of Lecture Notes in Earth System Sciences, we prepared the chapters in the style of lecture notes; we also used some of these chapters in teaching a graduate course in the fall 2019 at the University of California, Berkeley. The basic principles for groundwater flow and transport and hydro-mechanical coupling are summarized in Chaps. 2 and 3. These chapters are provided as background for those new to the study of hydrogeology, and concepts and results from these chapters will be referred to when observations are discussed. In Chap. 4 we discuss induced seismicity, i.e., earthquakes influenced by water. In Chap. 5 we discuss the tidal and barometric responses of groundwater and how these responses can be used to monitor changes caused by earthquakes. In the later chapters we discuss separately the different types of hydrologic changes caused by earthquakes, including changes of groundwater level (Chap. 6), changes of stream flow (Chap. 7), changes of groundwater temperature (Chap. 8), changes of groundwater composition (Chap. 9), changes in geyser activity (Chap. 10), earthquake-induced liquefaction (Chap. 11), and the eruptions of mud and magmatic volcanoes (Chap. 12). We also summarize the current state of the art on detecting and interpreting hydrologic precursors before earthquakes in Chap. 13. The concepts of dynamic strain and seismic energy density are used interchangeably throughout the book. The latter is defined in Chap. 3 as the maximum seismic energy available to do work in a unit volume estimated from the earthquake magnitude and the distance from the earthquake source. It provides a convenient metric to relate and compare the different hydrologic responses and allows us to integrate and compare the various hydrologic responses in the last chapter (Chap. 14) and to provide a coherent picture for all these responses.

References

- Aki K, Richards PG (1980) Quantitative seismology. New York, W.H. Freeman and Company
- Beresnev IA, Johnson PA (1994) Elastic wave stimulation of oil production: a review of methods and results. *Geophysics* 59:1000–1017
- Brodsky EE, Roeloffs E, Woodcock D et al (2003) A mechanism for sustained groundwater pressure changes induced by distant earthquakes. *J Geophys Res* 108:2390. <https://doi.org/10.1029/2002JB002321>
- Carrigan CR, King GCP, Barr GE et al (1991) Potential for water-table excursions induced by seismic events at Yucca Mountain, Nevada. *Geology* 19:1157–1160
- Chen JS, Wang CY (2009) Rising springs along the Silk Road. *Geology* 37:243–246

- Craig TJ, Chanard K, Calais E (2017) Hydrologically-driven crustal stresses and seismicity in the New Madrid Seismic Zone. *Nat Commun* 8:1–11
- Davis EE, Becker K, Wang K et al (2006) A discrete episode of seismic and aseismic deformation of the Nankai trough subduction zone accretionary prism and incoming Philippine Sea plate. *Earth Planet Sci Lett* 242:73–84
- Elkhoury JE, Brodsky EE, Agnew DC (2006) Seismic waves increase permeability. *Nature* 411:1135–1138
- Gorokhovich Y (2005) Abandonment of Minoan palaces on Crete in relation to the earthquake induced changes in groundwater supply. *J Archaeol Sci* 32(2):217–222
- Guglielmi Y, Cappa F, Avouac JP et al (2015) Seismicity triggered by fluid injection–induced aseismic slip. *Science* 348(6240):1224–1226
- Hill DP, Prejean SG (2007) Dynamic triggering. In: Schubert G (ed) *Treatise on geophysics*, vol 4, p 257–292
- Ingebritsen SE, Manning CE (2010) Permeability of the continental crust: dynamic variations inferred from seismicity and metamorphism. *Geofluids* 10:193–205
- Kilb D, Gombert J, Bodin P (2002) Aftershock triggering by complete Coulomb stress changes. *J Geophys Res* 107(B4):2060. <https://doi.org/10.1029/2001JB000202>
- National Research Council (2016) State of the art and practice in the assessment of earthquake-induced soil liquefaction and its consequences. The National Academies Press, Washington DC. <https://doi.org/10.17226/23474>
- O'Brien GM (1992) Earthquake-induced Water-level Fluctuations at Yucca Mountain, vol 92, Nevada. US Department of the Interior, US Geological Survey
- Roeloffs EA (1998) Persistent water level changes in a well near Parkfield, California, due to local and distant earthquakes. *J Geophys Res* 103:869–889
- Rojstaczer S, Wolf S, Michel R (1995) Permeability enhancement in the shallow crust as a cause of earthquake-induced hydrological changes. *Nature* 373:237–239
- Seed HB, Lee KL (1966) Liquefaction of saturated sands during cyclic loading. *J Soil Mech Found Div* 92:105–134
- Silver PG, Wakita H (1996) A search for earthquake precursors. *Science* 273:77–78
- Tingay M, Manga M, Rudolph ML et al (2018) An alternative review of facts, coincidences and past and future studies of the Lusi eruption. *Mar Pet Geol* 95:345–361
- von Kant E (1756) *Geschichte und Naturbeschreibung der merkwürdigsten Vorfälle des Erdbebens welches an dem Ende des 1755sten Jahres einen grossen Theil der Erde erschüttert hat*, Königberg, Hartung
- Wang CY, Chia Y (2008) Mechanism of water level changes during earthquakes: near field versus intermediate field. *Geophys Res Lett* 35:L12402. <https://doi.org/10.1029/2008GL034227>
- Wang CY, Doan ML, Xue L et al (2018) Tidal response of groundwater in a leaky aquifer—application to Oklahoma. *Water Resour Res* 54:8019–8033. <https://doi.org/10.1029/2018WR022793>
- Wang CY, Wang CH, Manga M (2004) Coseismic release of water from mountains: evidence from the 1999 ($M_w=7.5$) Chi-Chi earthquake. *Geology* 32:769–772
- Zhang H, Shi Z, Wang G et al (2019) Large earthquake reshapes the groundwater flow system: Insight from the water-level response to Earth tides and atmospheric pressure in a deep well. *Water Resour Res* 55:4207–4219. <https://doi.org/10.1029/2018WR024608>
- Zhang Y, Wang CY, Fu LY et al (2019) Unexpected far-field hydrological response to a great earthquake. *Earth Planet Sci Lett* 519:202–212. <https://doi.org/10.1016/j.epsl.2019.05.007>

Open Access This chapter is licensed under the terms of the Creative Commons Attribution 4.0 International License (<http://creativecommons.org/licenses/by/4.0/>), which permits use, sharing, adaptation, distribution and reproduction in any medium or format, as long as you give appropriate credit to the original author(s) and the source, provide a link to the Creative Commons license and indicate if changes were made.

The images or other third party material in this chapter are included in the chapter's Creative Commons license, unless indicated otherwise in a credit line to the material. If material is not included in the chapter's Creative Commons license and your intended use is not permitted by statutory regulation or exceeds the permitted use, you will need to obtain permission directly from the copyright holder.



Chapter 2

Groundwater Flow and Transport



Abstract We summarize the basic principles of, and governing equations for, groundwater flow and transport. Topics covered include the concepts of pressure and hydraulic head, Darcy's law, permeability, and storage. We compare saturated and unsaturated flow. We provide an introduction to heat and solute transport.

2.1 Introduction

Many excellent texts are available on the theory and practice of groundwater flow and transport (e.g., Bear 1972; Freeze and Cherry 1979; de Marsily 1986; Fetter 2000; Ingebritsen et al. 2006). Here we summarize the essentials so that subsequent discussions have some context and theoretical underpinning.

The study of groundwater flow through porous media is important for several related disciplines, including groundwater hydrogeology, contaminant transport, reservoir engineering, chemical engineering and, more recently, earthquake hydrology. It has been an active area of research since Henry Darcy established what we now call Darcy's law based on column experiments conducted in 1855 and 1856.

An aquifer is a permeable and porous geologic formation or a fracture zone that allows significant fluid flow, thus may serve as an underground source of groundwater. More recently, aquifers have increasingly been used for the storage of wastewater coproduced from hydrocarbon exploration and nuclear energy production. An aquiclude is an impervious geologic unit that prevents the flow of water, and an aquitard is a semi-confining unit that may allow limited water flow.

Confined aquifers are aquifers that are bounded on both sides by aquitards or aquicludes. Unconfined aquifers (also called phreatic aquifers or water-table aquifers) are aquifers that are bounded on their base by aquitards or aquicludes but by a water table on the top. Leaky aquifers are aquifers that are confined only partially by an aquitard on the top and/or on the base. Most aquifers behave somewhere between the confined and unconfined endmembers. The vertical impedance to flow across the boundary of a confined aquifer is not infinite, and the response of aquifers to applied loads may depend on the time scale of the applied load. In

other words, the leakage of an aquifer may be frequency-dependent. For example, a confined aquifer may exchange flow across its boundaries at low frequencies; at the same time, an unconfined aquifer may exhibit some confined behaviors at high frequencies. Furthermore, the permeability of a groundwater system may change when stresses are applied (for example, by earthquakes), and confinement may thus be a dynamic property. For example, a confined aquifer may become leaky after an earthquake, and its permeability may or may not recover with time soon after the earthquake.

A porous geologic unit consists of a solid component and void space. The solid component forms the matrix, and the void space is referred as pores. The matrix of most unconfined aquifers consists of unconsolidated sediments with grain size from fine sand to gravel with a permeability that increases as grain size and sorting increase. Sediments with grain sizes finer than silt usually do not have permeability high enough to allow significant fluid flow. Confined aquifers may consist of either unconsolidated or consolidated sediments (sedimentary rocks). Some igneous rocks, such as fractured granites, pyroclastic deposits and lavas, may have appreciable connected pores and fractures to transmit groundwater and can make good aquifers.

For the study of groundwater as a continuum, a representative elementary volume (REV) is defined, which is sufficiently large relative to the scales of the microscopic heterogeneity (mineral grains, pores) that its averaged hydraulic properties become nearly constant from place to place, but is sufficiently small to be treated as microscopic in the continuum study. Given this definition, we may define porosity as the ratio between the volume of the void space to the bulk volume of a REV of the porous rock or sediments, i.e.,

$$\varphi = \frac{\text{volume of void space in an REV}}{\text{bulk volume of an REV}}. \quad (2.1)$$

Porosity of crustal materials may be as small as ~ 0 in some crystalline rocks and as large as $>80\%$ in some clay-rich sediments or volcanic deposits. We further differentiate between isolated and connected porosities. Only the connected porosity provides the channels for groundwater flow and is denoted as φ_e —the effective porosity. However, the term ‘porosity’ is often used to represent the effective porosity and the subscript of the symbol φ_e is often removed.

The top layer beneath the land surface is often unsaturated and the water content generally increases with depth in this layer until the rocks or sediments are fully saturated. Thus, as illustrated in Fig. 2.1, the subsurface may be vertically divided into an unsaturated zone, in which the pore space is partly filled with groundwater and partly with air, and a saturated zone, in which all the pores are filled with groundwater.

The water table is a surface above the groundwater on which the pressure is atmospheric; at equilibrium, its elevation is that of the water level in wells. The vertical position of the water table may change with time in response to precipitation, earthquakes, tides, barometric pressure, and anthropogenic processes such as irrigation.

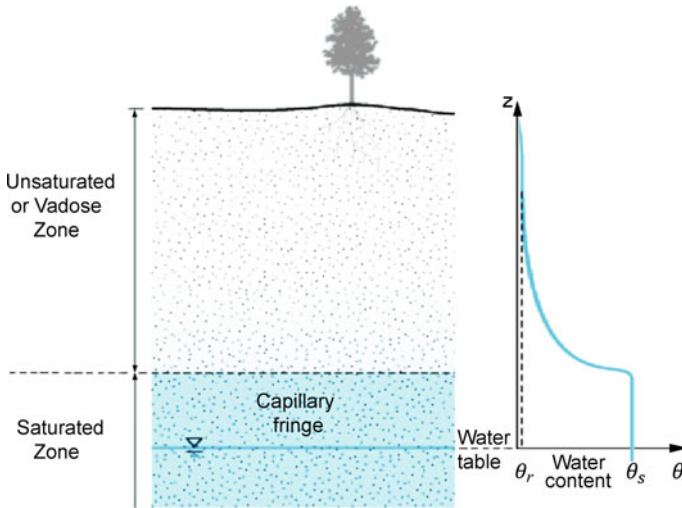


Fig. 2.1 The unsaturated zone and the saturated zone in the groundwater occurrence. θ is the water content (volume of water divided by bulk volume), θ_s is the saturated water content and θ_r is the residual water content

The unsaturated zone above the saturated zone extends to the surface. Here the capillary force between pore water and the surfaces of the solid grains acts to pull groundwater upward from the water table against gravity, forming a zone of negative pressure and variable saturation, which is also referred as the “capillary zone”. In response to the capillary force, the saturated zone actually extends a certain distance above the water table into the vadose zone, where pressure is negative. Following previous workers (e.g., Bear 1972; Gillham 1984) we refer to this saturated layer above the water table as the “capillary fringe” (Fig. 2.1).

The capillary zone may significantly affect the hydrogeologic response to earthquakes. Following the 2010 M8.8 Maule earthquake in Chile, for example, Mohr et al. (2015) reported increased stream flow in the Chilean Coast Range and proposed that the increased flow was due to the release of groundwater from the unsaturated zone. Breen et al. (2020) verified the hypothesis with a column experiment and showed that strong vibrations, such as seismic shaking, may disrupt the capillary tension to release water from unsaturated sands. The capillary zone is also known to significantly affect the response of aquifers to ocean tides (e.g., Barry et al. 1996) and solid Earth tides (Wang et al. 2019).

In most studies of groundwater, pore water is treated as fresh water with constant density and viscosity. This may change substantially in some cases in the study of the interactions between water and earthquakes. A notable example is the induced seismicity caused by the injected wastewater coproduced from hydrocarbon production. Here the high density of the injected saline water may drive deep flow and cause persistent induced earthquakes (e.g., Pollyea et al. 2019). On the other hand, in some Enhanced Geothermal Systems (EGS) developed for the recovery of geothermal

energy, the injected water may be heated by the high temperature of the crust and expand in volume, and viscosity and density may differ substantially from ambient conditions. The expansion of heated water may cause tensile fractures in rocks and induce non-double-couple earthquakes (e.g., Martínez-Garzón et al. 2017). In such cases, the density and viscosity of water change with pressure and temperature, and thus with space and time.

2.2 Pressure, Hydraulic Head and Darcy's Law

Groundwater flow is driven by both the gradient of the pressure energy and the gravitational energy (elevation), which are conveniently combined into the hydraulic head h [m] in hydrogeology:

$$h = \frac{P}{\rho_f g} + z \quad (2.2)$$

where P [Pa] is fluid pressure, g [m/s²] is gravity, ρ_f [kg/m³] is fluid density and z [m] is elevation. The first term on the right of the equation is the pressure head, the second the elevation head.

Henry Darcy established what we now call Darcy's law based on column experiments conducted in 1855 and 1856. The permeability unit darcy ($\sim 10^{-12}$ m²) is named in his honor. According to Darcy's law, the specific discharge \mathbf{q} [m/s] (volume flux per unit area) is given by

$$\mathbf{q} = -\mathbf{K} \cdot \nabla h \quad (2.3)$$

where the bold symbols indicate vector or tensor quantities. \mathbf{K} [m/s] is the hydraulic conductivity that is a second order tensor and depends on properties of both the fluid (density ρ_f and viscosity μ [Pa s]) and porous material (permeability \mathbf{k} [m²])

$$\mathbf{K} = \frac{\rho_f g \mathbf{k}}{\mu}. \quad (2.4)$$

In most groundwater studies, where water temperature is nearly uniform and thus the density and viscosity of water are nearly constant, it is often convenient to use the parameter \mathbf{K} instead of \mathbf{k} . It is also often convenient to orient the coordinate axes of a Cartesian coordinate system along the principal directions of the \mathbf{K} tensor so that the diagonal elements take the principle values K_x , K_y and K_z , and the off-diagonal elements become zero. In this case, Darcy's law (2.3) takes the following form

$$q_x = -K_x \frac{\partial h}{\partial x}, \quad (2.5a)$$

$$q_y = -K_y \frac{\partial h}{\partial y}, \quad (2.5b)$$

$$q_z = -K_z \frac{\partial h}{\partial z}. \quad (2.5c)$$

Darcy's law is found to be a good approximation at Reynolds numbers up to ~ 10 , where the Reynolds number is defined as $\rho_f v d / \mu$, d is the pore dimension and v is the speed of the fluid itself (variably called the interstitial, pore, linear, or seepage velocity), which is different from the specific discharge and can be approximated as

$$v \sim q / \varphi \quad (2.6)$$

where φ is porosity.

2.3 Permeability of Layered Media

In the previous section we showed that permeability in general is a second-order tensor. In this section we show that the average permeability of layered rocks, common in hydrogeological settings, are generally anisotropic, even if the permeability of each individual layer is isotropic. For layered rocks, the average permeabilities parallel to and normal to the bedding of the layered rocks are, respectively,

$$k_{\parallel} = \sum_i k_i \left(\frac{b_i}{b_t} \right) \quad (2.7a)$$

and

$$k_{\perp} = \left(\frac{b_t}{\sum_i b_i / k_i} \right), \quad (2.7b)$$

where k_i is the permeability of the i th layer, b_i [m] is the thickness of the i th layer, and b_t is the total thickness of the layered sediments or rocks. Equations (2.7a, b) show that the average permeability parallel to the bedding of layered rocks or sediments is dominated by the layer with the greatest transmissivity ($b_i k_i$), while the average permeability perpendicular to the bedding is dominated by the layer with the lowest value of k_i / b_i . Hence the average permeability of layered rocks is generally anisotropic even if the permeability of each individual layer is isotropic.

Permeability may also evolve with time due to ongoing geological and biogeochemical processes such as dissolution, precipitation, and the formation of clay minerals, cracks and fractures. The time scales for calcite dissolution is 10^4 – 10^5 years and for silica precipitation is weeks to years. Permeability may also change

suddenly during earthquakes, at time scales of one to tens of seconds. In addition, permeability can be scale dependent and spatially variable.

2.4 Specific Storage and Specific Yield

The specific storage S_s [m^{-1}] is the amount of water released per unit volume of a saturated confined aquifer per unit change of the hydraulic head; i.e.,

$$S_s = \frac{1}{\rho_f} \frac{\partial(\varphi\rho_f)}{\partial h}. \quad (2.8)$$

Replacing h by $P/(\rho_f g)$ and applying the chain rule, $\frac{\partial(\varphi\rho_f)}{\partial h} = \frac{\partial(\varphi\rho_f)}{\partial P} \frac{\partial P}{\partial h}$, we have

$$S_s = \rho_f g (\beta_\varphi + \varphi\beta_f) \quad (2.9)$$

where $\beta_\varphi [\text{Pa}^{-1}] = \frac{\partial\varphi}{\partial P}$ and $\beta_f [\text{Pa}^{-1}] = \frac{1}{\rho_f} \frac{\partial\rho_f}{\partial P}$ are the compressibilities of porosity and water, respectively. The storativity of a saturated confined aquifer is $S = bS_s$ where b is the thickness of the aquifer. While S_s has a dimension of [m^{-1}], S is dimensionless.

The specific yield S_y of an unconfined aquifer is similarly defined, except that here the amount of water released from a column of sediment or rock is due to a unit change of the water table instead of that of the hydraulic head. The ratio of the volume of water drained to the volume of the aquifer is the specific yield.

2.5 Saturated Flow

2.5.1 Isothermal Flow

Most studies of earthquake-induced hydrological processes consider only the uppermost crust where temperature is nearly constant; as a result, density and viscosity of pore water are also nearly constant, which considerably simplifies the differential equation that controls groundwater flow. This will be studied first.

In the absence of a fluid source, the continuity (conservation of mass) equation for fluid mass in a saturated aquifer is

$$\frac{\partial(\varphi\rho_f)}{\partial t} = -\nabla \cdot (\rho_f \mathbf{q}) + \rho_f Q, \quad (2.10)$$

where Q is a fluid source (positive) or a sink (negative) per unit volume.

Applying the chain rule $\frac{\partial(\varphi\rho_f)}{\partial t} = \frac{\partial(\varphi\rho_f)}{\partial h} \frac{\partial h}{\partial t}$, Darcy's law (2.3) and the definition of the specific storage (2.8) we obtain the differential equation for saturated flow

$$\rho_f S_s \frac{\partial h}{\partial t} = \nabla \cdot (\rho_f \mathbf{K} \nabla h) + \rho_f Q. \quad (2.11)$$

In most studies where the fluid density ρ_f is constant we have the more familiar form of the equation for saturated flow

$$S_s \frac{\partial h}{\partial t} = \nabla \cdot (\mathbf{K} \nabla h) + Q. \quad (2.12a)$$

We adopt a Cartesian coordinate system along the principle directions of \mathbf{K} . If K_x , K_y and K_z are spatially constant, Eq. (2.12a) may be expressed as

$$S_s \frac{\partial h}{\partial t} = K_x \frac{\partial^2 h}{\partial x^2} + K_y \frac{\partial^2 h}{\partial y^2} + K_z \frac{\partial^2 h}{\partial z^2} + Q. \quad (2.12b)$$

In the study of groundwater flow to wells, polar coordinates are used. Here the aquifer is usually treated as a horizontal and laterally isotropic layer, and the principal components of \mathbf{K} are thus K_r and K_z . Equation (2.12a) may then be expressed as

$$S_s \frac{\partial h}{\partial t} = K_r \left(\frac{\partial^2 h}{\partial r^2} + \frac{1}{r} \frac{\partial h}{\partial r} \right) + K_z \frac{\partial^2 h}{\partial z^2} + Q. \quad (2.12c)$$

2.5.2 Flow Through Variable Temperatures

In the cases where groundwater flows across considerable depth or occurs in geothermal areas where temperature changes along the flow paths, the assumptions made for isothermal flow break down. Here we need to 'couple' the groundwater flow equation to the heat transport equation such that the temperature dependence of the physical parameters may be calculated as a function of time and, at the same time, the effect of groundwater flow on the groundwater temperature may be calculated at the same time. Here we only consider the effect of groundwater temperature on the flow equation. Considering only the effects of temperature on fluid density and fluid viscosity, we may write the two-dimensional flow equation as follows:

$$S_s \frac{\partial h}{\partial t} = \frac{\partial}{\partial x} \left(\frac{\rho_w(T) g k_H}{\mu(T)} \frac{\partial h}{\partial x} \right) + \frac{\partial}{\partial z} \left(\frac{\rho_w(T) g k_V}{\mu(T)} \frac{\partial h}{\partial z} \right), \quad (2.13)$$

where k_H and k_V are, respectively, the horizontal and vertical permeability, ρ_w and μ are, respectively, density and viscosity of water; S_s is the specific storage defined as

$$S_s = \frac{1}{\rho_w(T)} \frac{\partial[\varphi\rho_w(T)]}{\partial h}. \quad (2.14)$$

2.6 Unsaturated Flow

Only isothermal flow is considered here. Richards (1931) showed that the basic proportionality between flow and the driving force in Darcy's law, as shown previously for saturated flow (2.3), remains true for unsaturated flow. The essential difference between the saturated and unsaturated flows is that the hydraulic conductivity \mathbf{K} for the latter is a function of the water content θ of the porous medium, defined as

$$\theta = \frac{\text{volume of water in an REV}}{\text{bulk volume of REV}}. \quad (2.15)$$

Thus, Darcy's equation for unsaturated flow has the following form (Richards 1931)

$$\mathbf{q} = -\mathbf{K}(\theta) \cdot \nabla h, \quad (2.16)$$

where h is the hydraulic head, identical to (2.2), but has a negative value owing to the capillary force and is often called suction or the 'matric potential'. $\mathbf{K}(\theta)$ is the unsaturated hydraulic conductivity tensor and is often expressed as $\mathbf{K}(\theta) = k_r(\theta)\mathbf{K}_s$ where $k_r(\theta)$ is the relative conductivity that varies between 0 and 1, and \mathbf{K}_s is the saturated hydraulic conductivity tensor.

Neglecting a fluid source, the continuity equation for fluid in unsaturated rocks is

$$\frac{\partial(\theta\rho_f)}{\partial t} = -\nabla \cdot (\rho_f\mathbf{q}). \quad (2.17)$$

If we assume the water in unsaturated flow is incompressible, (2.17) becomes

$$\frac{\partial\theta}{\partial t} = -\nabla \cdot \mathbf{q}. \quad (2.18)$$

Combining (2.16) and (2.18) we obtain the equation that governs unsaturated flow

$$C(\theta)\frac{\partial h}{\partial t} = \nabla \cdot [\mathbf{K}(\theta)\nabla h]. \quad (2.19)$$

where $C(\theta)$ [m^{-1}] is the specific water capacity defined as (Bear 1972, p 496)

$$C(\theta) = \frac{\partial \theta}{\partial h}. \quad (2.20)$$

For horizontally layered porous media, with water content θ changing only in the vertical direction, we choose a Cartesian coordinate system with the z -axis in the vertical direction and the x - and y -axes in the horizontal plane and along the principle directions. $K_z(\theta)$ thus depends on z , and $K_x(\theta)$ and $K_y(\theta)$ are spatially constant. Equation (2.19) reduces to

$$C(\theta) \frac{\partial h}{\partial t} = K_x(\theta) \frac{\partial^2 h}{\partial x^2} + K_y(\theta) \frac{\partial^2 h}{\partial y^2} + \frac{\partial}{\partial z} \left(K_z(\theta) \frac{\partial h}{\partial z} \right). \quad (2.21)$$

Similarly, for the study of groundwater flow to wells, we have,

$$C(\theta) \frac{\partial h}{\partial t} = K_r(\theta) \left(\frac{\partial^2 h}{\partial r^2} + \frac{1}{r} \frac{\partial h}{\partial r} \right) + \frac{\partial}{\partial z} \left(K_z(\theta) \frac{\partial h}{\partial z} \right). \quad (2.22)$$

Comparing Eqs. (2.21) and (2.22) with the equations for saturated flow (2.12b) and (2.12c) shows that the differences between the saturated and unsaturated flows are that the conductivity for unsaturated flow is a function of water content and that the specific storage S_s is replaced by the specific water capacity $C(\theta)$.

2.7 Heat Transport

Heat transport in groundwater systems occurs through both conduction and advection by fluid flow. The conductive transport is governed by Fourier's law

$$\mathbf{q}_h = -\mathbf{K}_h \cdot \nabla T \quad (2.23)$$

where \mathbf{q}_h [W/m^2] is the heat flux by conduction, \mathbf{K}_h [$\text{W}/(\text{m}\cdot\text{K})$] is the thermal conductivity tensor, and T [$^\circ\text{K}$] is temperature. While the hydraulic conductivity of rock varies by 16 orders of magnitude, the average thermal conductivity K_h varies by less than a factor of five. Clay, one of the least conductive materials, has $K_h = 1 \text{ W}/(\text{m}\cdot\text{K})$, while granite, a relatively good thermal conductor, has $K_h = 3 \text{ W}/(\text{m}\cdot\text{K})$. For saturated porous media, the average thermal conductivity may be estimated with

$$K_h = K_f^\varphi K_r^{1-\varphi} \quad (2.24)$$

where K_f and K_r are, respectively, the thermal conductivity of the pore fluid and the solid rock. At 25 °C, K_f is about 0.6 W/(m K) so that the thermal conductivity of saturated porous rocks is dominated by the mineralogy.

Combining Fourier's law (2.23) with the conservation law for thermal energy, we obtain the differential equation for the thermal transport of heat by conduction

$$\rho c \frac{\partial T}{\partial t} = \nabla \cdot (\mathbf{K}_h \nabla T) + Q_h, \quad (2.25)$$

where ρ [kg/m³] and c [J/(kg-K)] are, respectively, the bulk density and specific heat of the aquifer Q_h is a heat source (positive) or heat sink (negative) per unit volume. If $Q_h = 0$ and the aquifers is uniform and isotropic (i.e., constant K_h), Eq. (2.25) takes the simplified form:

$$c\rho \frac{\partial T}{\partial t} = K_h \nabla^2 T \quad (2.26)$$

The product $c\rho$ for a porous rock with porosity φ may be estimated from the arithmetic mean of the solid and fluid components of the aquifer, i.e., $c\rho = \varphi\rho_f c_f + (1 - \varphi)\rho_r c_r$, where c_f is the specific heat of the pore fluid and c_r that of the rock matrix.

Fluid flow can be effective at transporting heat. The amount of advective transport is proportional to the gradient of the thermal energy and the specific discharge. Hence heat transport in groundwater consists of both a conductive process and an advective process, and the governing equation becomes

$$[\varphi\rho_f c_f + (1 - \varphi)\rho_r c_r] \frac{\partial T}{\partial t} = K_h \nabla^2 T - \rho_f c_f \mathbf{q} \cdot \nabla T, \quad (2.27)$$

The specific discharge \mathbf{q} in the equation couples groundwater flow to heat transport. In most studies, the effect of temperature on flow is small and the 'coupling' between flow and heat transport is treated 'one-way', meaning that groundwater discharge is included in the transport equation, but the flow equation assumes an isothermal condition (2.12a).

The isothermal assumption is acceptable when the temperature of the groundwater is nearly constant. However, in situations where groundwater flows across steep geothermal gradients such as in geothermal systems, temperature may affect the density and viscosity of water, which in turn affect the velocity and direction of groundwater flow. The effect of pressure is relatively small and usually neglected. In such cases, the equation for groundwater transport becomes nonlinear and may be expressed as

$$\frac{\partial[\rho(T)c(T)T]}{\partial t} = \nabla \cdot [K_h(T)\nabla T] - \mathbf{q} \cdot \nabla[\rho_f(T)c_f(T)T], \quad (2.28)$$

where c and ρ are, respectively, the specific heat and density of the bulk sediments or rocks, K_h the thermal conductivity, and the subscript f refers to the properties of water. The bulk properties of the saturated sediments may be approximated as the linear mixture of solid grains and pore water, e.g., $K_h = \varphi K_f + (1 - \varphi)K_s$, etc., where the subscript s indicates solid grains. Here the coupling between groundwater flow and transport is ‘two-way’, meaning that the temperature affects the flow (2.13, 2.14) and the latter affects the groundwater temperature. Solution of equation (2.28) requires the simultaneous solution of groundwater flow (2.13). Numerical procedures are often required for solving the coupled nonlinear equations.

The relative significance of the advective versus the conductive heat transport may be accessed by using the following procedure. Since the magnitude of the conductive transport across a region with temperature difference ΔT is of the order of $K_h \Delta T/L^2$ and the magnitude of the advective transport is of the order of $\rho_f c_f q \Delta T/L$, where L is the linear dimension of the studied region, the relative significance of the advective versus the conductive transport is given by the ratio

$$\text{Pe} = \frac{\rho_f c_f q \Delta T/L}{K_h \Delta T/L^2} = \frac{\rho_f c_f q L}{K_h} \quad (2.29)$$

which is known as the Peclet number. If Pe is greater than 1, the advective heat transport is more important than the conductive heat transport, and vice versa.

Some other dimensionless number related to heat transport in porous flow include the Nusselt number Nu which is the ratio between the total heat transport and the conductive transport:

$$\text{Nu} = \frac{c_f \rho_f q T + \frac{K_h \Delta T}{L}}{\frac{K_h \Delta T}{L}} \quad (2.30)$$

and the Rayleigh number Ra which indicates the tendency of the pore fluid towards free convection, i.e., flow driven purely by density differences.

$$\text{Ra} = \frac{\left[\frac{k \alpha_f \rho_f g \Delta T}{\mu} \right] \rho_f c_f L}{K_h} \quad (2.31)$$

where α_f is the thermal expansivity of the pore fluid. Fluid will start to convect when Ra exceeds some critical value depending on the boundary conditions.

2.8 Solute Transport

The concentration of a solute in groundwater can be expressed either as a mass fraction or mass per unit volume. Here we use the latter, i.e., mass per unit volume, as the definition. Let C_c [kg/m^3] be the concentration of a chemical component in

the fluid. If there is a gradient in C_c , diffusion will occur, with flux \mathbf{q}_d [kg/(m²s)] given by Fick's law

$$\mathbf{q}_d = -D_w \nabla C_c, \quad (2.32)$$

where D_w [m²/s] is the coefficient of molecular diffusion in water.

In isotropic porous media, the diffusion of chemical components is impeded by the tortuous paths, in addition to the limited pore space, and the diffusion coefficient for the porous media D_m may be related to D_w by

$$D_m = \frac{\varphi_e}{\tau} D_w, \quad (2.33)$$

where φ_e is the effective porosity (i.e., pore space in which chemical components can move with flow) and τ is tortuosity (i.e., the ratio between the actual path length of the solute molecule through the porous medium from one point to another and the straight-line distance between the two points). Typical values for the diffusion coefficients for geologic media range from 10⁻¹³ to 10⁻¹¹ m²/s. Here Fick's law for diffusion is modified as

$$\mathbf{q}_d = -D_m \nabla C_c. \quad (2.34)$$

The continuity equation for solute transport is

$$\frac{\partial(\varphi_e C_c)}{\partial t} = -\nabla \cdot \mathbf{q}_d. \quad (2.35)$$

Combining (2.34) and (2.35) and assuming that φ_e is constant, we have

$$\varphi_e \frac{\partial C_c}{\partial t} = D_m \nabla^2 C_c. \quad (2.36)$$

Porous flow is another important mechanism for solute transport, and the amount of solute transport by this mechanism is proportional to the velocity of groundwater flow. Combining the diffusive solute transport (Fick's law) and the advective solute transport, we have the governing equation for solute transport with groundwater flow in a porous medium

$$\frac{\partial C_c}{\partial t} = \nabla \cdot (\mathbf{D} \cdot \nabla C_c) - \mathbf{v} \cdot \nabla C_c + Q_c, \quad (2.37)$$

where $\mathbf{D} = \mathbf{D}_m/\varphi_e$, $\mathbf{v} = \mathbf{q}/\varphi_e$ and Q_c is the rate at which mass of the solute is produced (positive) or removed (negative) per unit volume by chemical reactions.

Microscopic heterogeneities and velocity variations across pores in the porous medium cause mechanical dispersion that results in dispersion anisotropy even if the

porous medium is macroscopically isotropic. The combined effect of the mechanical dispersion and the molecular diffusion along and normal to the direction of groundwater flow may be represented in terms of the longitudinal and transverse dispersivities, α_L and α_T ,

$$D_L = \alpha_L |v| + D \quad (2.38a)$$

$$D_T = \alpha_T |v| + D \quad (2.38b)$$

where D_L and D_T , respectively, are the longitudinal and transverse hydrodynamic dispersion coefficients.

The relative significance of the advective versus the diffusive solute transport may be accessed by a procedure similar to that discussed in the last section on heat transport. Since the magnitude of the diffusive transport is of the order of $D\Delta C/L^2$ and the magnitude of the advective transport is of the order of $v\Delta C/L$, the relative significance of the advective versus the diffusive transport is given by the ratio

$$Pe = \frac{v\Delta C/L}{D\Delta C/L^2} = \frac{vL}{D}, \quad (2.39)$$

which is the Peclet number for solute transport. If Pe is greater than 1, the advective solute transport is more important than the diffusive solute transport, and vice versa.

References

- Barry DA, Barry SJ, Parlange JY (1996) Capillarity correction to periodic solutions of shallow flow approximation. *Coast Estuar Stud* 50:495–510
- Bear J (1972) *Dynamics of fluids in porous media*. Dover
- Breen S, Zhang Z, Wang CY (2020) Shaking water out of sands: an experimental study. *Water Resour Res* 55:e2020WR028153. <https://doi.org/10.1029/2020WR028153>
- de Marsily G (1986) *Quantitative hydrogeology*. Academic Press, New York
- Fetter CW (2000) *Applied hydrogeology*, 4th edn. Prentice Hall, Upper Saddle River
- Freeze RA, Cheery JA (1979) *Groundwater*. Prentice-Hall, Englewood Cliffs
- Gillham RW (1984) The capillary fringe and its effect on water-table response. *J Hydrol* 67:307–324
- Ingebritsen SE, Sanford WE, Neuzil CE (2006) *Groundwater in geologic processes*, 2nd edn. Cambridge Univ Press, New York
- Martínez-Garzón P, Kwiatek G, Bonhoff M et al (2017) Volumetric components in the earthquake source related to fluid injection and stress state. *Geophys Res Lett* 44:800–809
- Mohr CH, Manga M, Wang C, Kirchner JW, Bronstert A (2015) Shaking water out of soil. *Geology* 43:207–210
- Pollyea RM, Chapman MC, Jayne RS, Wu H (2019) High density oilfield wastewater disposal causes deeper, stronger, and more persistent earthquakes. *Nat Commun* 10:3077. <https://doi.org/10.1038/s41467-019-11029-8>
- Richards LA (1931) Capillary conduction of liquids through porous mediums. *Physics* 1(5):318–333. <https://doi.org/10.1063/1.1745010>

Wang CY, Zhu AY, Liao X et al (2019) Capillary effects on groundwater response to Earth tides. *Water Resour Res* 55. <https://doi.org/10.1029/2019WR025166>

Open Access This chapter is licensed under the terms of the Creative Commons Attribution 4.0 International License (<http://creativecommons.org/licenses/by/4.0/>), which permits use, sharing, adaptation, distribution and reproduction in any medium or format, as long as you give appropriate credit to the original author(s) and the source, provide a link to the Creative Commons license and indicate if changes were made.

The images or other third party material in this chapter are included in the chapter's Creative Commons license, unless indicated otherwise in a credit line to the material. If material is not included in the chapter's Creative Commons license and your intended use is not permitted by statutory regulation or exceeds the permitted use, you will need to obtain permission directly from the copyright holder.



Chapter 3

Hydro-Mechanical Coupling



Abstract We summarize the basic principles that couple rock deformation and fluid flow. Topics covered include linear poroelasticity, consolidation, liquefaction, rock friction, and frictional instability. Together, these are the processes that serve as a starting point for understanding how water and earthquakes influence each other.

3.1 Introduction

The linkage between the hydrogeological and the mechanical processes in Earth's crust, i.e., hydro-mechanical coupling, underpins any quantitative analysis of the interactions between water and earthquakes. It embodies a spectrum of processes, from poroelastic deformation to the fluidization of an initially solid matrix. Here we discuss three major components of this broad field essential to the themes of this book: the linear theory of poroelasticity, nonlinear deformation (including consolidation and liquefaction), and friction and the rate-and-state model.

At small deformation, the response of rocks and sediments to an applied force is linearly elastic, and stress and strain are related by Hooke's law. Analysis of the elastic deformation of porous media and its effect on porous flow, and vice versa, is the domain of poroelasticity. In this chapter we first introduce poroelasticity and provide the equations essential for interpreting many important hydrogeological processes such as the response of groundwater to tidal forces and barometric loading (Chap. 5). At relatively large deformation, the relationship between stress and strain becomes nonlinear and deformations become irreversible. Common hydrogeological examples include consolidation and liquefaction (Chap. 8). The third topic of this chapter is rock friction that is closely related to the mechanisms of earthquakes, especially induced earthquakes (Chap. 4).

3.2 Linear Poroelasticity and Groundwater Flow

Deforming a rock changes the volume of pore space, which in turn causes the pore fluid pressure to change unless the fluid has enough time to escape. Subsurface fluid pressure and strain are thus generally ‘coupled’. For this reason, water level in confined aquifers can sometimes be used as a strain-meter. An example of this coupling is the periodic fluctuations of the water level in wells in response to the strain induced by Earth’s tides.

At the same time, changing fluid pressure in the subsurface will deform the rock. Thus, the cause-and-effect between the coseismic volumetric strain and the coseismic change of water level can become complex. The theory of linear poroelasticity is often invoked to explain the interactions between rock deformation and pore pressure change.

Linear poroelasticity addresses the coupling between small deformation of the rock matrix and fluid flow within the rock and is thus at the core of the discussions in this book. Several excellent texts (e.g., Wang 2000; Cheng 2016) provide more detailed expositions of the topic. The equations developed in this section summarize concepts from Chaps. 1–4 from Wang (2000). Roeloffs (1996) provides a more brief and applied presentation.

We begin with some examples and comments to illustrate the applications of poroelastic models and illustrate some of the interesting phenomena that can be understood. Figure 3.1 shows the response of water level in a well near the coast in southern Bangladesh to the loading of ocean tides (Burgess et al. 2017). Oscillations of the water level (colored curves in Fig. 3.1b) are not synchronous with, but lag behind, the ocean tides (grey curve in Fig. 3.1b) and their amplitudes at different depths are different. These amplitude differences reflect depth-varying poroelastic properties of the Bengal aquifer system (Burgess et al. 2017).

Figure 3.2 shows the responses of water level and volumetric strain to Earth tides measured in a Plate Boundary Observatory borehole in southern California. It also shows the response of the water level to the 2010 Mw7.2 El Mayor-Cucupah earthquake (Wang and Barbour 2017). Before the earthquake, water level and volumetric strain responded to Earth tides with the expected oscillations of opposite signs (expansion is positive). During the earthquake, volumetric strain suddenly decreased while pore pressure immediately increased. That is, the coseismic increase in pore pressure was caused by a coseismic volumetric contraction. Such changes are characteristic of the undrained response of aquifers to loading, i.e., a response that occurs without flow of pore water during loading. These responses are determined by the poroelastic Skempton’s coefficient $B \equiv -(\partial P / \partial \sigma)_f$, where P is pore pressure, σ is the applied volumetric stress, and the subscript f means that the process occurs at constant water content f . This relation may be re-expressed as $\Delta p = -B \Delta \sigma = -BK_u \Delta \epsilon$, where K_u is the undrained bulk modulus and $\Delta \epsilon$ the change of volumetric strain. Based on the BK_u estimated from the pre-seismic amplitudes of the tidal responses of water level and volumetric strain, Wang and Barbour (2017) converted the coseismic

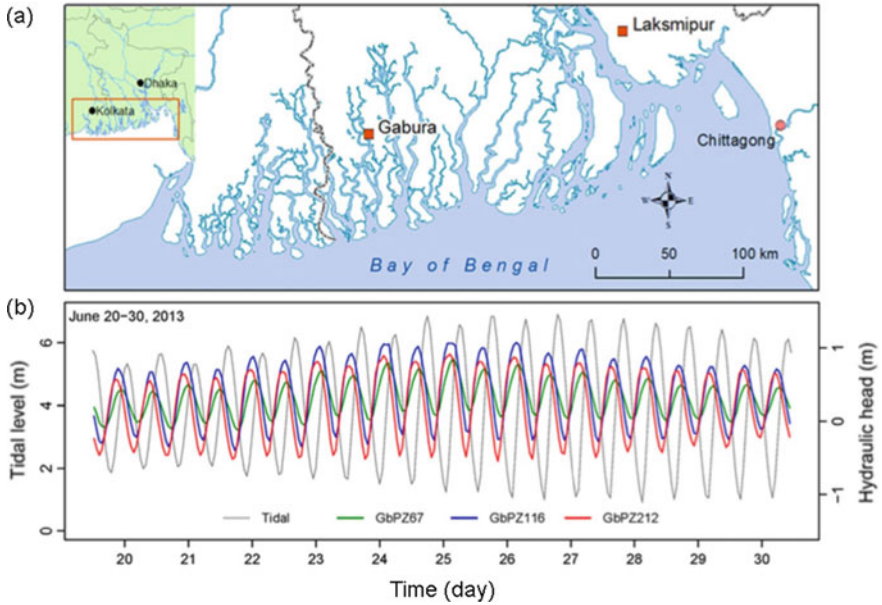


Fig. 3.1 Water level in a well at Gabura (panel a), southern Bangladesh, showing hydraulic head in a coastal aquifer in response to the loading of local ocean tides (grey curve in b) recorded at Chittagong from June 20 to June 30, 2013 (panel b). Colored curves in b correspond to different screen depths in m below the ground surface. Notice the difference in phase and amplitude, reflecting different hydrogeological properties (modified from Burgess et al. 2017)

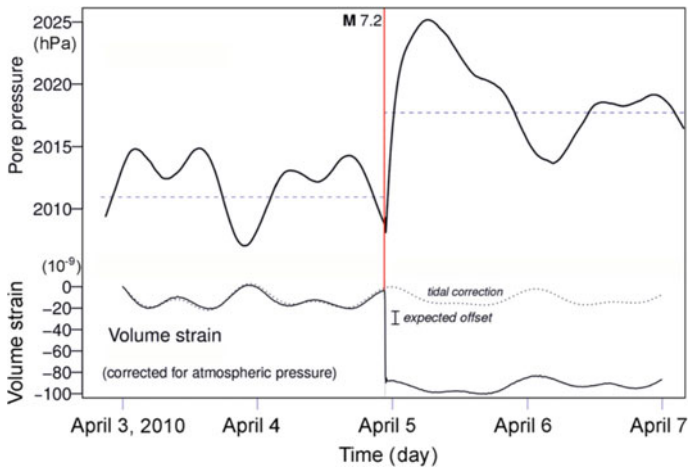


Fig. 3.2 Pore pressure and volumetric strain in Plate Boundary Observatory borehole B084 in southern California, before and after the 2010 Mw7.2 El Mayor-Cucupah earthquake in Mexico. Negative strain shows contraction (from Wang and Barbour 2017)

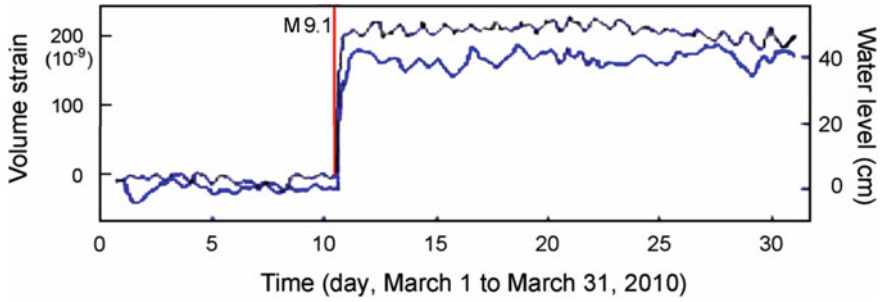


Fig. 3.3 Water level (blue, lower curve) and volumetric strain (black, upper curve) in the Fuxin well in northeastern China, before and after the 2011 Mw9.1 Tohoku earthquake, Japan (modified from Zhang et al. 2019)

change in water level to a coseismic change of volumetric strain of -61×10^{-9} , similar to the measured coseismic volumetric strain of -85×10^{-9} (Fig. 3.2).

If, on the other hand, the pressure response occurs together with flow of pore water, the process is no longer undrained. Figure 3.3 shows a case of coseismic increase of water level (lower curve) in the Fuxin well, NW China, which occurred together with a coseismic increase of volumetric strain during the 2011 Mw9.1 Tohoku earthquake, Japan (Zhang et al. 2019). The occurrence of a coseismic increase of water level together with a coseismic increase of volumetric strain suggests that the latter was caused by the coseismic increase of pore pressure, which can only be caused by the occurrence of coseismic flow. The two examples of water level responses to earthquakes illustrate how the cause-and-effect relationship between the coseismic change of volumetric strain and the coseismic change of water level may be complicated by the different boundary conditions near the well. Thus, the interpretation of coseismic changes of water level requires careful analysis and testing.

3.2.1 Constitutive Relations for Isotropic Stress: Biot (1941)

Consider a saturated and isothermal rock. Stress σ (extension positive) and pore pressure p are the independent variables; the strain ϵ and the increment of fluid content f of the rock may be expressed as

$$\epsilon = \epsilon(\sigma, p) \quad (3.1)$$

$$f = f(\sigma, p). \quad (3.2)$$

We consider first the case of an isotropic strain, for which $\epsilon = dV/V$ where V is volume. Changes in ϵ and f due to changes in σ and p are thus given by

$$d\epsilon = \left(\frac{\partial \epsilon}{\partial \sigma} \right)_p d\sigma + \left(\frac{\partial \epsilon}{\partial p} \right)_\sigma dp \quad (3.3)$$

$$df = \left(\frac{\partial f}{\partial \sigma} \right)_p d\sigma + \left(\frac{\partial f}{\partial p} \right)_\sigma dp. \quad (3.4)$$

Biot (1941) defined four parameters K , R , H and H_1 such that

$$d\epsilon = \frac{1}{K} d\sigma + \frac{1}{H} dp \quad (3.5)$$

$$df = \frac{1}{H_1} d\sigma + \frac{1}{R} dp \quad (3.6)$$

and thus

$$\frac{1}{K} = \left(\frac{\partial \epsilon}{\partial \sigma} \right)_p, \quad \frac{1}{H} = \left(\frac{\partial \epsilon}{\partial p} \right)_\sigma, \quad \frac{1}{H_1} = \left(\frac{\partial f}{\partial \sigma} \right)_p, \quad \frac{1}{R} = \left(\frac{\partial f}{\partial p} \right)_\sigma. \quad (3.7)$$

$1/K$ is the *compressibility* and K is the *bulk modulus*. Biot (1941) further assumed there is a potential density function

$$U = \frac{1}{2}(\sigma\epsilon + pf). \quad (3.8)$$

Because σ and p are independent variables, $\partial U/\partial \sigma = \epsilon/2$ and $\partial U/\partial p = f/2$; thus $\partial^2 U/\partial p \partial \sigma = \partial^2 U/\partial \sigma \partial p$ and

$$\left(\frac{\partial \epsilon}{\partial p} \right)_\sigma = \left(\frac{\partial f}{\partial \sigma} \right)_p \quad (3.9)$$

and hence

$$H = H_1. \quad (3.10)$$

3.2.2 Effective Stress

From (3.5) we have

$$d\epsilon = \frac{1}{K} \left(d\sigma + \frac{K}{H} dp \right) = \frac{1}{K} (d\sigma + \alpha dp) = \frac{1}{K} d(\sigma + \alpha p) = \frac{1}{K} d\sigma', \quad (3.11)$$

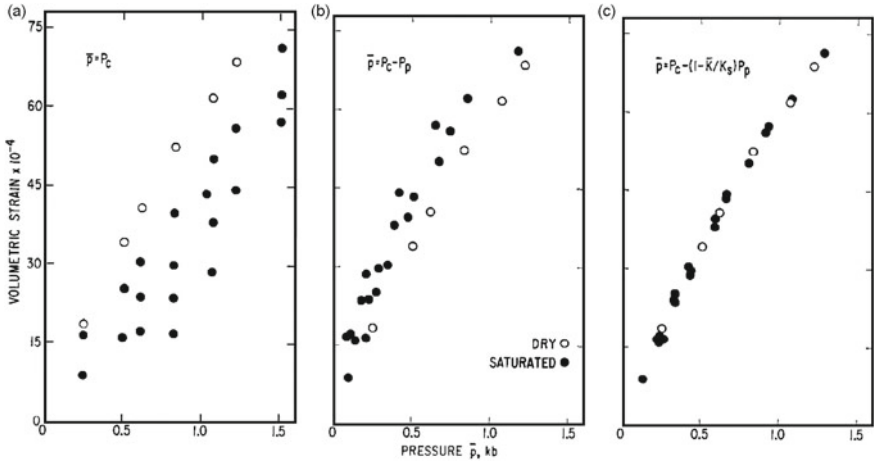


Fig. 3.4 Volumetric strain of Weber sandstone under confining pressure. **a** Strain versus confining pressure P_c . Solid circles represent data at elevated pore pressure. Open circles represent data for a dry sample in which $P = 0$. **b** Strain versus $P_c - P$, where P is pore pressure. **c** Strain versus the effective pressure $P_c - \alpha P$. Here all data overlap with the dry sample data, showing that the effective pressure produces the same change in strain as does confining pressure with $P = 0$ (from Nur and Byerlee 1971)

where α is the *Biot-Willis coefficient* (Sect. 3.2.3) and $\sigma' = \sigma + \alpha p$ is the effective stress, first proposed by Terzaghi (1925). The effective stress concept has been applied to many geological problems where pore pressure interacts with deformation. As an example, Fig. 3.4 shows laboratory measurements of the volumetric strain of Weber sandstone under controlled confining pressure and pore pressure (Nur and Byerlee 1971). It illustrates how the effective stress relation may be used to explain the volumetric deformation of rocks under confining pressure and pore pressure.

3.2.3 Related Poroelastic Constants

More commonly used poroelastic constants, such as the Skempton’s coefficient B and the Biot-Willis coefficient α , may be expressed in terms of K , H and R . The *Skempton’s coefficient* is defined as

$$B = -\left(\frac{\partial p}{\partial \sigma}\right)_f = \frac{R}{H} \tag{3.12}$$

using Eq. (3.7).

The *Biot-Willis coefficient* is defined as

$$\alpha = \frac{K}{H}. \quad (3.13)$$

We defined in the last chapter a quantity called the specific storage S_s . The specific storage at constant stress is

$$S_\sigma = \left(\frac{\partial f}{\partial p} \right)_\sigma = \frac{1}{R}. \quad (3.14)$$

The *specific storage at constant strain* $S_\epsilon = \left(\frac{\partial f}{\partial p} \right)_\epsilon$ can be derived by eliminating $d\sigma$ from Eqs. (3.5) and (3.6)

$$df = \frac{K}{H}d\epsilon + \left(\frac{1}{R} - \frac{K}{H^2} \right)dp \quad (3.15)$$

and hence

$$S_\epsilon = \left(\frac{\partial f}{\partial p} \right)_\epsilon = S_\sigma - \frac{K}{H^2} \quad (3.16)$$

and, from (3.13), (3.15) and (3.16)

$$df = \alpha d\epsilon + S_\epsilon p. \quad (3.17)$$

With the definitions of B and α , Eqs. (3.5) and (3.6) can be rewritten as

$$d\epsilon = \frac{1}{K}d\sigma + \frac{\alpha}{K}dp, \quad (3.18)$$

$$df = \frac{\alpha}{K}d\sigma + \frac{\alpha}{KB}dp. \quad (3.19)$$

Equation (3.18) is sometimes called the *Biot relation*. Equations (3.18) and (3.19) can be rearranged for stress and pressure

$$d\sigma = \left(\frac{K}{1 - \alpha B} \right) d\epsilon - \left(\frac{K}{1 - \alpha B} B \right) df \quad (3.20)$$

$$dp = - \left(\frac{K}{1 - \alpha B} B \right) d\epsilon + \left(\frac{K}{1 - \alpha B} \frac{B}{\alpha} \right) df. \quad (3.21)$$

We can define $K_u = d\sigma/d\epsilon$ for $f = 0$, and hence identify K_u as an *undrained bulk modulus* (the bulk modulus when there is no fluid gain or loss)

$$K_u = \frac{K}{1 - \alpha B}. \quad (3.22)$$

Furthermore, from (3.12), (3.13) and (3.14)

$$S_\sigma = \frac{\alpha}{KB}. \quad (3.23)$$

We can rewrite Eqs. (3.20) and (3.21) in terms of K_u

$$d\sigma = K_u d\epsilon - K_u B df \quad (3.24)$$

$$dp = -K_u B d\epsilon + \frac{K_u B}{\alpha} df. \quad (3.25)$$

This last relation (3.25) is the basis for using water wells as strain meters. If the pore pressure causes changes in the water height $dh = dp/\rho_w g$ in a well, and is an undrained response to a volumetric strain $d\epsilon$, the change of the volumetric strain and that of the water height are then related by

$$dh = \frac{1}{\rho_w g} dp|_{f=0} = -\frac{1}{\rho_w g} B d\sigma|_{f=0} = -\frac{K_u B}{\rho_w g} d\epsilon \quad (3.26)$$

As noted earlier, the validity of this undrained assumption depends on the rate of loading compared to the permeability of the formation.

From Eq. (3.25) we obtain

$$df = \alpha d\epsilon + \frac{\alpha}{K_u B} dp \quad (3.27)$$

which leads to a physical interpretation of α

$$\alpha = \left. \frac{df}{d\epsilon} \right|_{dp=0}, \quad (3.28)$$

that is, α is the ratio of the increment in fluid content to volumetric strain at constant pressure. From (3.27) we can also obtain an expression for the *constrained specific storage coefficient*

$$S_\epsilon = \left. \frac{df}{dp} \right|_{\epsilon=0} = \frac{\alpha}{K_u B} \quad (3.29)$$

and

$$\frac{S_\sigma}{S_\epsilon} = \frac{K_u}{K} = \frac{1}{1 - \alpha B}. \quad (3.30)$$

From Eq. (3.24) we obtain

$$d\epsilon = \frac{d\sigma}{K_u} + Bdf. \quad (3.31)$$

The volumetric strain ϵ is thus composed of two components: an elastic component under undrained conditions, and a second component from the transfer of fluid. Equation (3.31) provides another physical interpretation of Skempton's coefficient

$$B = \left. \frac{d\epsilon}{df} \right|_{d\sigma=0} \quad (3.32)$$

that is, B is the ratio of the increment in volumetric strain to fluid content at constant stress.

Equations (3.28) and (3.32) show that the Biot-Willis coefficient α and the Skempton coefficient B are closely related. These coefficients are often used in the study of different hydrogeological responses, as illustrated in the examples that follow. There are few direct comparisons between the volumetric strain and that estimated from the change of water level because most wells do not have the required measurements of both pore pressure and strain. At some special well-equipped wells, such as some Plate Boundary Observatory (PBO) boreholes (e.g., Barbour 2015), pore pressure measurement is collocated with the measurement of strain, allowing comprehensive characterization of the responses to tides, barometric pressure and teleseismic waves (Barbour et al. 2019).

3.2.4 Constitutive Relationship for Anisotropic Stress: Biot (1955)

Our variables are now pore pressure p , stress σ_{ij} , strain ϵ_{ij} and increment in fluid content df . The mean stress is $\sigma = \frac{1}{3}(\sigma_{xx} + \sigma_{yy} + \sigma_{zz}) = \frac{1}{3}(\sigma_1 + \sigma_2 + \sigma_3)$ and the volumetric strain is $\epsilon = \epsilon_{11} + \epsilon_{22} + \epsilon_{33}$. In principal coordinates the constitutive relations are

$$d\epsilon_1 = \frac{1}{E}d\sigma_1 - \frac{\nu}{E}d\sigma_2 - \frac{\nu}{E}d\sigma_3 + \frac{dp}{3H} \quad (3.33)$$

$$d\epsilon_2 = -\frac{\nu}{E}d\sigma_1 + \frac{1}{E}d\sigma_2 - \frac{\nu}{E}d\sigma_3 + \frac{dp}{3H} \quad (3.34)$$

$$d\epsilon_3 = -\frac{\nu}{E}d\sigma_1 - \frac{\nu}{E}d\sigma_2 + \frac{1}{E}d\sigma_3 + \frac{dp}{3H} \quad (3.35)$$

$$df = \frac{1}{H}d\sigma + \frac{1}{R}dp \text{ with } \sigma = \frac{1}{3}(\sigma_1 + \sigma_2 + \sigma_3) \quad (3.36)$$

The elastic constants E (Young's modulus) and ν (Poisson ratio) are defined for drained conditions ($dp = 0$).

In general coordinates, there are shear strains and stresses, thus seven equations since the stress and strain tensors are symmetric

$$d\epsilon_{xx} = \frac{1}{E}d\sigma_{xx} - \frac{\nu}{E}d\sigma_{yy} - \frac{\nu}{E}d\sigma_{zz} + \frac{dp}{3H} \quad (3.37)$$

$$d\epsilon_{yy} = -\frac{\nu}{E}d\sigma_{xx} + \frac{1}{E}d\sigma_{yy} - \frac{\nu}{E}d\sigma_{zz} + \frac{dp}{3H} \quad (3.38)$$

$$d\epsilon_{zz} = -\frac{\nu}{E}d\sigma_{xx} - \frac{\nu}{E}d\sigma_{yy} + \frac{1}{E}d\sigma_{zz} + \frac{dp}{3H} \quad (3.39)$$

$$d\epsilon_{xy} = \frac{1}{2G}d\sigma_{xy} \quad (3.40)$$

$$d\epsilon_{yz} = \frac{1}{2G}d\sigma_{yz} \quad (3.41)$$

$$d\epsilon_{xz} = \frac{1}{2G}d\sigma_{xz} \quad (3.42)$$

$$df = \frac{1}{H}d\sigma + \frac{1}{R}dp \quad (3.43)$$

where G is the shear modulus which can be related to E and ν via $G = E/2(1 + \nu)$.

The first 6 of these equations can be written in standard index notation

$$\epsilon_{ij} = \frac{1}{2G} \left(\sigma_{ij} - \frac{\nu}{1 + \nu} \sigma_{kk} \delta_{ij} \right) + \frac{p}{3H} \delta_{ij} \quad (3.44)$$

with $\sigma_{kk} = \frac{1}{3}(\sigma_{xx} + \sigma_{yy} + \sigma_{zz})$ and the notation d has been dropped so that the variable now indicates a change in that variable. Using $\alpha = K/H$ and $K = \frac{2(1+\nu)}{3(1-2\nu)}G$ to include the last term into the parenthesis, (3.44) becomes

$$\epsilon_{ij} = \frac{1}{2G} \left(\sigma_{ij} - \frac{\nu}{1 + \nu} \sigma_{kk} \delta_{ij} + \frac{1 - 2\nu}{1 + \nu} \alpha p \delta_{ij} \right). \quad (3.45)$$

As defined in Eq. (3.11), the effective stress $\sigma'_{ij} = \sigma_{ij} + \alpha p \delta_{ij}$, then

$$\epsilon_{ij} = \frac{1}{2G} \left(\sigma'_{ij} - \frac{\nu}{1 + \nu} \sigma'_{kk} \delta_{ij} \right). \quad (3.46)$$

Equation (3.44) can be rearranged into equivalent but useful forms

$$\sigma_{ij} = 2G \left(\epsilon_{ij} + \frac{\nu}{1-2\nu} \epsilon_{kk} \delta_{ij} \right) - \alpha p \delta_{ij} \quad (3.47)$$

$$\epsilon_{ij} = \frac{1}{2G} \left(\sigma_{ij} - \frac{\nu_u}{1+\nu_u} \sigma_{kk} \delta_{ij} \right) + \frac{B}{3} f \delta_{ij} \quad (3.48)$$

where ν_u is the *undrained Poisson ratio* and is related to ν by

$$\nu_u = \frac{3\nu + \alpha B(1-2\nu)}{3 - \alpha B(1-2\nu)}. \quad (3.49)$$

3.2.5 Poroelastic Constants

There are a number of poroelastic constants that depend on different constraints on the Representative Elementary Volume (REV).

Compressibility There are several measures of the compressibility of porous rocks depending on the constraints on the REV. Following Wang (2000) we use a thought experiment to help define the different measures of compressibility. In the thought experiment, a rock is subjected to a confining pressure p_c and an independently controlled pore pressure p . We define a differential pressure $p_d = p_c - p$ and use p_d and p as the independent variables.

If the sample is unjacketed, $p_c = p$ and hence $p_d = 0$; we may define two bulk moduli

$$\frac{1}{K'_s} = -\frac{1}{V} \left(\frac{\partial V}{\partial p} \right)_{p_d=0} \quad \text{and} \quad \frac{1}{K_\phi} = -\frac{1}{V_p} \left(\frac{\partial V_p}{\partial p} \right)_{p_d=0} \quad (3.50)$$

where V is the sample volume, V_p is the pore volume, K'_s is the *unjacketed bulk modulus*, and K_ϕ is the *unjacketed pore modulus*.

If the sample is jacketed and drained, $p = 0$, $p_c = p_d$; we may define two more bulk moduli

$$\begin{aligned} \frac{1}{K} &= -\frac{1}{V} \left(\frac{\partial V}{\partial p_c} \right)_{p=0} = -\frac{1}{V} \left(\frac{\partial V}{\partial p_d} \right)_{p=0} \quad \text{and} \\ \frac{1}{K_p} &= -\frac{1}{V_p} \left(\frac{\partial V_p}{\partial p_c} \right)_{p=0} = -\frac{1}{V_p} \left(\frac{\partial V_p}{\partial p_d} \right)_{p=0} \end{aligned} \quad (3.51)$$

where K is the *drained bulk modulus* and K_p is the *drained pore modulus*. Then

$$\frac{dV}{V} = \frac{1}{V} \left[\left(\frac{\partial V}{\partial p} \right)_{p_d=0} dp + \left(\frac{\partial V}{\partial p_d} \right)_{p=0} dp_d \right] = -\frac{1}{K'_s} dp - \frac{1}{K} dp_d \quad (3.52)$$

$$\begin{aligned} \frac{dV_p}{V_p} &= \frac{1}{V_p} \left[\left(\frac{\partial V_p}{\partial p} \right)_{p_d=0} dp + \left(\frac{\partial V_p}{\partial p_d} \right)_{p=0} dp_d \right] \\ &= -\frac{1}{K_\phi} dp - \frac{1}{K_p} dp_d. \end{aligned} \quad (3.53)$$

Taking the confining pressure as the applied stress, we may replace $d\sigma$ by $-dp_c$ and rewrite Eq. (3.5) as

$$\epsilon = \frac{dV}{V} = -\frac{1}{K} dp_c + \frac{1}{H} dp = -\frac{1}{K} dp_d - \left(\frac{1}{K} - \frac{1}{H} \right) dp. \quad (3.54)$$

Comparing (3.54) with (3.52), we obtain

$$\frac{1}{K'_s} = \frac{1}{K} - \frac{1}{H} = \frac{1}{K} (1 - \alpha), \quad \text{or} \quad \alpha = 1 - \frac{K}{K'_s}. \quad (3.55)$$

The poroelastic constant K'_s can thus be obtained from the measurable constants K and α . Similarly, the other poroelastic constants K_p and K_ϕ can all be written in terms of the measurable constants K , K_f , α , B and ϕ .

For the drained pore modulus K_p , we start from its definition (3.51). For a fully saturated medium, $\phi = V_p/V = V_f/V$. The increment of water is

$$df = \frac{dV_p - dV_f}{V} = \phi \left(\frac{dV_p}{V_p} - \frac{dV_f}{V_f} \right) = \phi \left(\frac{dV_p}{V_p} + \frac{dp}{K_f} \right). \quad (3.56)$$

where K_f is the compressibility of the fluid

$$\frac{1}{K_f} = -\frac{1}{V_f} \frac{dV_f}{dp}. \quad (3.57)$$

From (3.6) we have

$$df = \frac{1}{H} d\sigma + \frac{1}{R} dp = -\frac{1}{H} dp_c + \frac{1}{R} dp. \quad (3.58)$$

Solving (3.56) for dV_p/V_p and using (3.58) we have

$$\frac{dV_p}{V_p} = -\frac{1}{\phi H} dp_c + \left(\frac{1}{\phi R} - \frac{1}{K_f} \right) dp$$

$$= -\frac{\alpha}{\phi K} dp_c + \left(\frac{\alpha}{\phi B K} - \frac{1}{K_f} \right) dp \quad (3.59)$$

and thus

$$\frac{1}{K_\phi} = -\frac{1}{V_p} \frac{dV_p}{dp_c} \Big|_{p=0} = \frac{\alpha}{\phi K}. \quad (3.60)$$

Theunjacketed pore modulus K_ϕ can also be related to other poroelastic constants. Replacing p_c in (3.59) by $p_d + p$ we have

$$\frac{dV_p}{V_p} = -\frac{\alpha}{\phi K} dp_d + \left(\frac{\alpha}{\phi B K} - \frac{\alpha}{\phi K} - \frac{1}{K_f} \right) dp \quad (3.61)$$

and thus

$$\frac{1}{K_\phi} = -\frac{1}{V_p} \frac{dV_p}{dp} \Big|_{p_d=0} = \frac{\alpha}{\phi K} \left(1 - \frac{1}{B} \right) + \frac{1}{K_f}. \quad (3.62)$$

Storage capacity There are several measures of storage capacity of a rock depending on the constraints on the REV.

As defined earlier (3.14), the *unconstrained specific storage* S_σ is

$$S_\sigma = \frac{\partial f}{\partial p} \Big|_\sigma = \frac{1}{R} = \frac{\alpha}{KB}. \quad (3.63)$$

A micromechanical interpretation is provided by using (3.55) and (3.62) in (3.63)

$$S_\sigma = \left(\frac{1}{K} - \frac{1}{K'_s} \right) + \phi \left(\frac{1}{K_f} - \frac{1}{K_\phi} \right). \quad (3.64)$$

Also defined earlier (3.16) is the *constrained specific storage* S_ϵ

$$S_\epsilon = \frac{\partial f}{\partial p} \Big|_\epsilon = S_\sigma - \frac{K}{H^2} = S_\sigma - \frac{\alpha^2}{K} \quad (3.65)$$

S_ϵ can also be expressed in terms of G , ν and ν_u (see Detournay and Cheng 1993)

$$S_\epsilon = \frac{\alpha^2(1 - 2\nu_u)(1 - 2\nu)}{2G(\nu_u - \nu)}. \quad (3.66)$$

The *unjacketed specific storage* S_γ

$$S_\gamma = \left(\frac{\partial f}{\partial p} \right)_{p_d=0} = \phi \left(\frac{1}{K_f} - \frac{1}{K_\phi} \right). \quad (3.67)$$

The hydrogeological definition of the *uniaxial specific storage* S_s is

$$S_s = \rho_f g \left(\frac{\partial f}{\partial p} \right)_{\sigma_{zz}, \epsilon_{xx} = \epsilon_{yy} = 0} \quad (3.68)$$

where z is the vertical direction, and x and y are two horizontal directions. Hence it is the volume of water released per unit volume per unit decline in hydraulic head while maintaining zero lateral strain and constant vertical stress.

The constraints $\epsilon_{xx} = \epsilon_{yy} = 0$ and $\sigma_{zz} = 0$ can be used in Eq. (3.45) to obtain σ_{xx} and σ_{yy} which can be summed to obtain

$$\sigma_{kk} = -4\eta p \quad (3.69)$$

where

$$\eta = \alpha \frac{1 - 2\nu}{2(1 - \nu)}. \quad (3.70)$$

Thus the change in the mean stress is a scalar multiple of the change in pore pressure.

Substituting (3.69) and (3.63) into (3.19) and using $S = \frac{S_s}{\rho_f g}$, we have the storage coefficient

$$S = S_\sigma \left(1 - \frac{4\eta B}{3} \right). \quad (3.71)$$

It can also be shown that

$$S_\sigma \geq S \geq S_\epsilon. \quad (3.72)$$

The different storage coefficients illustrate the significance of boundary conditions on the REV for poroelastic behavior.

With so many different storage coefficients it may be useful to estimate their difference in practical applications. Here we examine the difference between $S = S_s/\rho_f g$ and S_σ . From (3.71) and the definition of η (3.70) we have $S/S_\sigma = 1 - \frac{2(1-2\nu)}{3(1-\nu)}\alpha B$. Assuming $\alpha B \sim 0.5$ and $\nu \sim 0.25$ for most rocks with experimental data, we have $S/S_\sigma \approx 0.8$. Hence, in practice, the differences among different specific storages may be small in comparison with the usually large uncertainties in this parameter.

Poroelastic expansion coefficient One of the Biot (1941) parameters, the *poroelastic expansion coefficient*, is, from (3.11) and (3.55),

$$\frac{1}{H} = \left(\frac{\partial \epsilon}{\partial p} \right)_{\sigma} = \frac{\alpha}{K} = \frac{1}{K} - \frac{1}{K'_s}. \quad (3.73)$$

The poroelastic expansion coefficient is thus the difference between the bulk compressibility and the unjacketed compressibility.

If there is no horizontal strain, i.e., $\epsilon_{xx} = \epsilon_{yy} = 0$, we may derive the vertical stress from (3.47) as

$$\sigma_{zz}|_{\epsilon_{xx}=\epsilon_{yy}=0} = \frac{2G(1-\nu)}{1-2\nu} \epsilon_{zz} - \alpha p = K_v \epsilon_{zz} - \alpha p, \quad (3.74)$$

where

$$K_v = \frac{2G(1-\nu)}{1-2\nu} \quad (3.75)$$

is the *vertical incompressibility*. Rearranging for the strain

$$\epsilon_{zz} = \frac{1}{K_v} \sigma_{zz}|_{\epsilon_{xx}=\epsilon_{yy}=0} + \frac{\alpha}{K_v} p. \quad (3.76)$$

Thus, for constant vertical stress, the volumetric strain is proportional to the pore pressure change, and the constant of proportionality

$$c_m = \alpha / K_v, \quad (3.77)$$

is known as the *Geertsma uniaxial expansion coefficient* (and can be shown to equal η/G).

Coefficients of undrained pore pressure buildup Skempton's coefficient $B = -\left(\frac{\partial p}{\partial \sigma}\right)_{f=0}$ can also be expressed in terms of compressibilities. Using $K_u = K/(1-\alpha B)$ and $\alpha = 1 - K/K'_s$, we have

$$B = \frac{1 - K/K_u}{1 - K/K'_s}. \quad (3.78)$$

Using (3.62) and $\alpha = 1 - K/K'_s$, we also have

$$B = \frac{1/K - 1/K'_s}{1/K - 1/K'_s + \phi(1/K_f - 1/K_\phi)}. \quad (3.79)$$

Finally, B can also be written in terms of Poisson ratios

$$B = \frac{3(\nu_u - \nu)}{\alpha(1 + \nu_u)(1 - 2\nu)}. \quad (3.80)$$

Returning to the case with no horizontal strains, we can define a uniaxial undrained loading efficient as

$$\gamma = - \left(\frac{\partial p}{\partial \sigma_{zz}} \right)_{\epsilon_{xx}=\epsilon_{yy}=0, f=0}. \quad (3.81)$$

From the constitutive law (3.43) with $\epsilon_{xx} = \epsilon_{yy} = 0$ and $f = 0$, we have

$$\sigma_{xx}|_{\epsilon_{xx}=\epsilon_{yy}=f=0} = \sigma_{yy}|_{\epsilon_{xx}=\epsilon_{yy}=0, f=0} = \frac{\nu_u}{1 - \nu_u} \sigma_{zz}. \quad (3.82)$$

Since $\sigma = \frac{1}{3}(\sigma_{xx} + \sigma_{yy} + \sigma_{zz}) = \frac{1}{3} \frac{1+\nu_u}{1-\nu_u} \sigma_{zz}$ and $B = - \left(\frac{\partial P}{\partial \sigma} \right)_f$

$$\gamma = - \left(\frac{\partial P}{\partial \sigma_{zz}} \right)_{\epsilon_{xx}=\epsilon_{yy}=f=0} = - \left(\frac{\partial P}{\partial \sigma} \right)_f \left(\frac{\partial \sigma}{\partial \sigma_{zz}} \right)_{\epsilon_{xx}=\epsilon_{yy}=f=0} = \frac{B}{3} \frac{1 + \nu_u}{1 - \nu_u} \quad (3.83)$$

The *tidal efficiency TE* can be defined as the water level change in a well divided by the water level change in the ocean. The uniaxial strain condition is often assumed for aquifers close to a shoreline; thus $TE = \gamma$.

γ can also be expressed in terms of other poroelastic constants, e.g.,

$$\gamma = \frac{\alpha}{K_v S}. \quad (3.84)$$

If we further assume $1/K'_s = 1/K_\phi = 0$, then

$$S = \frac{1}{K_v} + \phi \frac{1}{K_f}. \quad (3.85)$$

Combining (3.84) and (3.85) we have

$$TE = \gamma = \frac{1/K_v}{(1/K_v) + (\phi/K_f)} = \frac{K_f}{K_f + \phi K_v}. \quad (3.86)$$

Since ϕ and K_f can be measured, this equation may be used to estimate the vertical incompressibility (K_v) of aquifers beneath the ocean and near the shoreline from measurement of γ or TE.

Another surface source of loading is variation in atmospheric pressure. The *barometric efficiency* is defined as the ratio between the change in water level dh in a well to the change in atmospheric pressure dp_{atm} converted to an equivalent head $dp_{atm}/\rho_f g$, i.e.,

$$BE = -\rho_f g dh/dP_a. \quad (3.87)$$

where P_a is the barometric pressure, and the negative sign is included to make BE positive. The atmospheric pressure exerts a load both on the surface of the Earth and the water surface in the well. The former causes water level to rise by an amount $\gamma dP_a/\rho_f g$ and the latter for the level to drop by $dP_a/\rho_f g$. Thus $dh = (\gamma - 1)dP_a/\rho_f g$, and

$$BE = 1 - \gamma. \quad (3.88)$$

This relation is only for purely confined aquifers under undrained condition where the BE is a constant. Assume $1/K'_s = 1/K_\phi = 0$, we may have

$$BE = \frac{\phi K_v}{K_f + \phi K_v}. \quad (3.89)$$

Since K_f is known, independent measures of both TE and BE yield estimates of the aquifer porosity (ϕ) and the vertical incompressibility (K_v). For semi-confined aquifers (i.e., leaky aquifers), the barometric efficiency is no longer a constant but depends on frequency, i.e., $BE(\omega)$ and is sometimes denoted as the 'barometric response function' (e.g., Rojstaczer et al., 1988) to distinguish from the constant barometric efficiency for purely confined aquifers. Determination of $BE(\omega)$ and its hydrogeological applications are discussed in Chap. 5.

3.2.6 Governing Equations for Flow in Poroelastic Media

Coupling between elastic deformation and fluid flow occurs between the equation for fluid flow (assumed to be Darcy's law) and conservation of mass. We begin with the continuity equation for fluid

$$\frac{\partial f}{\partial t} = -\nabla \cdot \mathbf{q} + Q, \quad (3.90)$$

where \mathbf{q} is the specific discharge vector and Q is the fluid source per unit volume per unit time.

Substituting Darcy's law into the conservation of mass equation yields

$$\frac{\partial f}{\partial t} = \frac{k}{\mu} \nabla^2 p + Q, \quad (3.91)$$

where k is permeability (assumed constant in space) and μ the fluid viscosity. Assuming uniaxial strain and constant vertical stress, then $f = Sp$ (Eq. 3.68), which when used in Eq. (3.90) leads to the standard flow equation in hydrogeology

$$S \frac{\partial p}{\partial t} = \frac{k}{\mu} \nabla^2 p + Q. \quad (3.92)$$

The assumption of uniaxial strain and constant vertical stress are not satisfied in 2D and 3D flows in general because the flow distorts the strain field. A more general flow equation can be obtained by replacing (3.27) in (3.91), leading to

$$\frac{\alpha}{KB} \left[\frac{B}{3} \frac{\partial \sigma_{kk}}{\partial t} + \frac{\partial p}{\partial t} \right] = \frac{k}{\mu} \nabla^2 p + Q, \quad (3.93)$$

where the first term on the left, the time derivative of the mean stress, is equivalent mathematically to a fluid source.

Since $S_\sigma = \alpha/KB$ (Eq. 3.63), then

$$S_\sigma \left[\frac{B}{3} \frac{\partial \sigma_{kk}}{\partial t} + \frac{\partial p}{\partial t} \right] = \frac{k}{\mu} \nabla^2 p + Q. \quad (3.94)$$

Using the relations $\sigma_{kk}/3 = K\epsilon - \alpha p$ and $S_\epsilon = (1 - \alpha B)S_\sigma$, Eq. (3.94) may be transformed to

$$\alpha \frac{\partial \epsilon_{kk}}{\partial t} + S_\epsilon \frac{\partial p}{\partial t} = \frac{k}{\mu} \nabla^2 p + Q, \quad (3.95)$$

in which fluid flow is coupled to the time variation of volumetric strain that acts mathematically as a fluid source.

These PDEs are inhomogeneous even when there are no explicit fluid sources Q . Simplification to a homogeneous diffusion equation needs to be justified throughout the region of interest.

3.2.7 Uncoupling Stress or Strain from Fluid Flow

Uncoupling in poroelasticity means that the mechanical term in the fluid flow equation is omitted. The uncoupling is one-way in that the pore-pressure field does affect stress and strain, but the changes in stress and strain do not affect fluid flow. In such cases, the transient flow equation can be solved independently and the resulting fluid pressure field then be inserted into the elastostatic equation and solved separately.

Uncoupling of the mechanical term in the fluid flow equation occurs in several classes of poroelastic problems. An important class is irrotational displacement in an infinite or semi-infinite domain without a body force, and includes deformation under barometric loading and deformation affected by groundwater flow between a well and aquifer. To illustrate how the uncoupling occurs in an irrotational displacement field, we insert the constitutive relation (3.47) into the force balance equation $\frac{\partial \sigma_{ij}}{\partial x_i} = 0$

to obtain the mechanical equilibrium equation (Wang 2000, Eq. 4.18)

$$G\nabla^2 u_i + \frac{G}{1-2\nu} \frac{\partial \epsilon}{\partial x_i} = \alpha \frac{\partial p}{\partial x_i}. \quad (3.96)$$

x_i For irrotational displacement fields, $\partial/\partial = \partial/\partial$, where is the displacement component in the direction; thus

$$G\nabla^2 \epsilon_{ii} + \frac{G}{1-2\nu} \frac{\partial^2 \epsilon}{\partial x_i^2} = \alpha \frac{\partial^2 p}{\partial x_i^2}, \quad (3.97)$$

Summing the three equations of (3.97) for $i = 1, 2$ and 3 , we arrive at, with (3.75)

$$\nabla^2 \left(\epsilon - \frac{\alpha}{K_v} P \right) = 0. \quad (3.98)$$

In the absence of a body force, equation (3.98) reduces to

$$\frac{\partial^2 w}{\partial z^2} = \frac{\alpha}{K_v} \frac{\partial P}{\partial z}. \quad (3.99)$$

For irrotational displacement fields, $\partial u_i/\partial x_j = \partial u_j/\partial x_i$, where u_i is the displacement component in the x_i direction; thus

$$\nabla^2 u_i = \frac{\partial^2 u_i}{\partial x_1^2} + \frac{\partial^2 u_i}{\partial x_2^2} + \frac{\partial^2 u_i}{\partial x_3^2} = \frac{\partial}{\partial x_i} \left(\frac{\partial u_1}{\partial x_1} + \frac{\partial u_2}{\partial x_2} + \frac{\partial u_3}{\partial x_3} \right) = \frac{\partial \epsilon}{\partial x_i}. \quad (3.100)$$

Equation (3.100) allows us to rewrite Eq. (3.99) as

$$\frac{\partial \epsilon_z}{\partial z} = \frac{\alpha}{K_v} \frac{\partial P}{\partial z}. \quad (3.101)$$

Integrating Eq. (3.101) yields

$$\epsilon_z = \frac{\alpha}{K_v} P + g(t), \quad (3.102)$$

where $g(t)$ is a ‘constant’ of integration that may be a function of t . Given the boundary conditions that ϵ_z and P must vanish at infinity, the function $g(t)$ must also vanish. Combining (3.102) with the constitutive relation in Eq. (3.18) leads to

$$\sigma_{kk} = -4\eta P. \quad (3.103)$$

Substituting (3.103) into Eq. (3.94) and using $S = S_\sigma(1 - 4\eta B/3)$ yields the decoupled flow equation

$$S \frac{\partial P}{\partial t} = \frac{k}{\mu} \nabla^2 P + Q. \quad (3.104)$$

Therefore, for an irrotational displacement field in an unbounded or semi-infinite space in the absence of body force, the flow equation is decoupled from stress or strain. These results are applied in the following section on the study of soil consolidation.

3.3 Consolidation

The relationships between stress and strain at sufficiently large deformation become nonlinear and the corresponding analysis may become complicated except in simplified cases. Thus we provide in this section mostly a qualitative description of a hydro-mechanical geologic process, i.e., the consolidation of sediments, which is ubiquitous on Earth's surface, especially in sedimentary basins, in which the hydrological responses to earthquakes have been abundantly documented. As illustrated in the cartoon of Fig. 3.5, earthquake shaking may be strong enough to break the grain-to-grain contact in unconsolidated sediments and cause the transfer of load from the solid matrix to the pore fluids; given time, the pressurized pore fluids may be expelled and the sediments may consolidate under gravity.

3.3.1 Consolidation of Sediments in Sedimentary Basin

Consolidation is the process of compaction of sediments owing to the effects of gravity under drained conditions, when enough time is available for pore fluids to

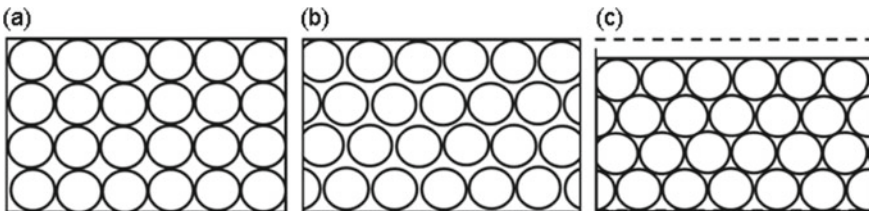


Fig. 3.5 Idealized schematic of pore-pressure change in soils during earthquakes. **a** Before an earthquake, individual soil grains are held in place by frictional or adhesive contact forces, creating a solid soil structure with water filling the spaces between the grains. Note the grain-to-grain contact. **b** After seismic shaking, particle rearrange with no change in volume (e.g., a lateral shift of a half diameter of every other row of particles in the figure), causing the particles to lose contact and go into suspension, and increased pore pressure as gravity load is transferred from the soil skeleton to the pore water. **c** As water flows out of the soil, pore pressure decreases, the soil particles settle into a denser configuration (National Academy of Sciences, Engineering and Medicine 2016)

move to the surface. Observations show that the porosity of sediments in sedimentary basins decreases with depth. Athy's law (Athy 1930), one of the several widely used empirical relations to describe the decrease of sediment porosity with depth (or increasing effective pressure), has the form

$$\varphi = \varphi_o e^{-bP'}, \quad (3.105)$$

where φ_o is the porosity at zero effective pressure, b is an empirical parameter, and P' is the effective pressure. Athy's law was based on field measurements, where additional processes such as chemical precipitation or pressure solution, in addition to consolidation, may have occurred to change the distribution of porosity with depth.

For porosities commonly encountered in sedimentary basins (0.2–0.5), b ranges from 10^{-7} to 10^{-8} Pa $^{-1}$ for shale and from 10^{-8} to 10^{-9} Pa $^{-1}$ for sandstone. It should be noted that in sedimentary basins, consolidation may not be the only process that changes sediment porosity. For example, the distribution of porosity may also be significantly affected by non-mechanical processes such as chemical precipitation and dissolution, and mineral transformations.

3.3.2 Terzaghi Theory of Consolidation

Terzaghi (1925) first analyzed the processes of soil consolidation with the effective stress relation. The discussion below follows the presentation in Wang (2000, Sect. 6.5). In Terzaghi's model, a constant stress $-\sigma_o$ is applied on the surface ($z = 0$) of a column of saturated soil of height L at time equal to 0. The piston applying the load is permeable such that the top boundary is drained. If the wall of the container is rigid, the deformation is uniaxial. As discussed in Sect. 3.2.7, the flow equation under uniaxial, poroelastic deformation is decoupled from stress or strain. We assume here that this decoupling may be extended to finite deformation. Thus the homogeneous diffusion equation (Eq. (3.104) with $D \equiv k/\mu S$ and $Q = 0$) applies

$$\frac{\partial P}{\partial t} - D \frac{\partial^2 P}{\partial z^2} = 0, \quad (3.106)$$

where D is the uniaxial hydraulic diffusivity.

The surface load produces an instantaneous undrained response

$$P_o = \gamma \sigma_o, \quad (3.107)$$

where γ is the loading efficiency (Eq. 3.81). Following the step deformation at $t = 0$, the sample consolidates gradually as water flows out of the top boundary. The boundary conditions are:

$$\sigma_{zz} = -\sigma_o, \tag{3.108}$$

$$w(L, t) = 0, \tag{3.109}$$

$$P(0, t) = 0, \tag{3.110}$$

$$\left. \frac{\partial P}{\partial z} \right|_{z=L} = 0. \tag{3.111}$$

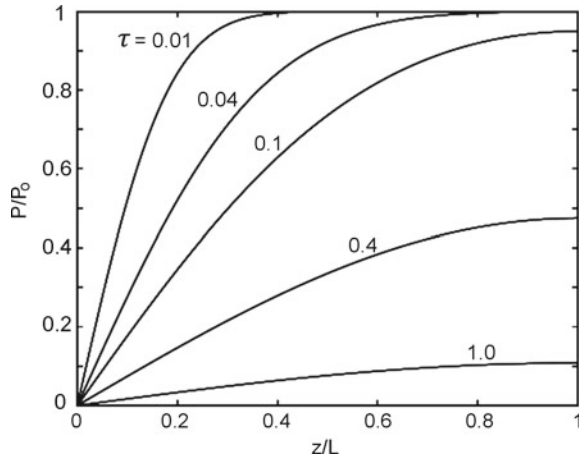
The solution for the pore pressure in this boundary value problem is the same as that for the temperature in a classical heat conduction problem (Carslaw and Jaeger 1959, p. 96) and is

$$P(z, t) = \frac{4\gamma\sigma_o}{\pi} \sum_{m=0}^{\infty} \frac{1}{2m+1} \times \exp\left[\frac{-(2m+1)^2\pi^2 Dt}{4L^2} \right] \sin\left[\frac{(2m+1)\pi z}{2L} \right] \tag{3.112}$$

The calculated pore pressure, normalized by the initial pressure P_o , is plotted in Fig. 3.6 against z/L at several values of the dimensionless time $\tau = Dt/L^2$. Initially, the decline in pore pressure is confined to the top region near the drained boundary. At large τ , $P(z, \infty) = 0$.

The instantaneous mechanical response is the undrained poroelastic response and may be obtained from the uniaxial constitutive relation (3.75)

Fig. 3.6 Evolution of normalized pore pressure in a column of sediments of height L under a vertical load on the surface, suddenly applied at $t = 0$ (from Wang, 2000). The successive contours are for dimensionless time $\tau = ct/L^2$



$$K_v \equiv \frac{\delta\sigma_{zz}}{\delta\epsilon_{zz}} \Big|_{\epsilon_{xx}=\epsilon_{yy}=f=0} = \frac{2G(1-\nu)}{1-2\nu}. \quad (3.113)$$

Integrating (3.113) we have

$$\sigma_{zz} \Big|_{\epsilon_{xx}=\epsilon_{yy}=0} = \frac{2G(1-\nu_u)}{1-2\nu_u} \epsilon_{zz}. \quad (3.114)$$

Thus,

$$\frac{dw}{dz} \equiv \epsilon_{zz} \Big|_{f=\epsilon_{xx}=\epsilon_{yy}=0} = \frac{1-2\nu_u}{2G(1-\nu_u)} \sigma_o = \frac{1}{K_v^{(u)}} \sigma_o. \quad (3.115)$$

Integrating Eq. (3.115) from L to z with the boundary condition $w = 0$ at $z = L$, we have

$$w(z, 0^+) = \frac{\sigma_o(L-z)}{K_v^{(u)}} \quad (3.116)$$

Thus, the initial displacement at the surface ($z = 0$) is

$$w_o \equiv w(0, 0^+) = \frac{\sigma_o L}{K_v^{(u)}}. \quad (3.117)$$

The time-dependent displacement $\Delta w(z, t)$ during the drainage phase may be calculated from the pore pressure,

$$\Delta P(z, t) = P(z, t) - P_o. \quad (3.118)$$

where $P(z, t)$ is given in Eq. (3.112) and P_o is given in Eq. (3.107). Utilizing (3.102) by replacing P in this equation by ΔP in Eq. (3.118) and integrating $\partial w / \partial z = \epsilon_z$ with the resulting series solution for w from $z = L$ (where $\Delta w = 0$ hence $g = 0$) to $z = 0$, we obtain (Wang 2000, Eq. 6.41)

$$\Delta w(0, t) = \frac{\alpha\gamma\sigma_o L}{K_v} \left\{ 1 - \frac{8}{\pi^2} \sum_{m=0}^{\infty} \frac{1}{(2m+1)^2} \exp\left[\frac{-(2m+1)^2 \pi^2 Dt}{4L^2} \right] \right\} \quad (3.119)$$

where, as defined earlier, α and K_v are the Biot-Willis coefficient and the vertical compressibility, respectively.

The series solution (3.119) varies from 0 at $t = 0$ to $\frac{\alpha\gamma\sigma_o L}{K_v}$ at $t = \infty$, and is plotted against $\log(Dt/L^2)$ in Fig. 3.7. The total surface displacement is

$$w(0, t) = \frac{\sigma_o L}{K_v^{(u)}} + \frac{\alpha\gamma\sigma_o L}{K_v}. \quad (3.120)$$

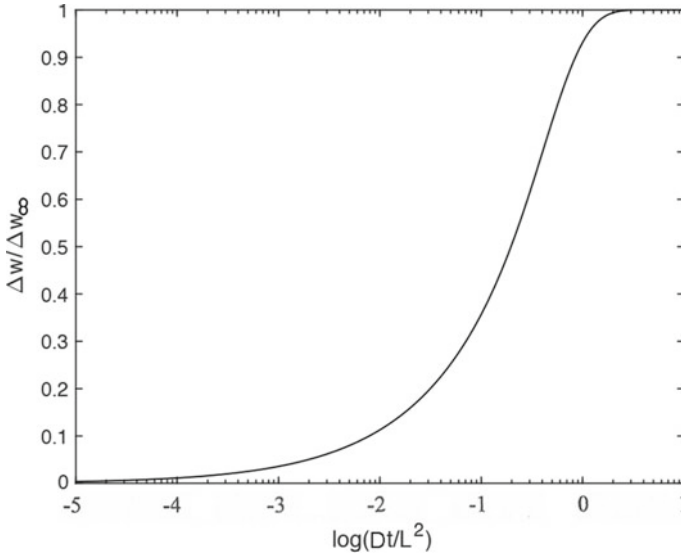


Fig. 3.7 Surface displacement change of a column of saturated soil of height L during the drainage phase, following a step loading at the surface (3.119), normalized with $\Delta w(0, \infty) = \alpha \gamma \sigma_o L / K_v$ and plotted against $\log(Dt/L^2)$ (from the authors)

The poroelastic parameters in the above model are assumed constant to simplify integration. In reality, these parameters are not constant at finite deformation. On the other hand, the solutions so obtained do provide some insight into the consequence of sediment consolidation and an order-of-magnitude estimate of the settlement of a sedimentary layer under consolidation.

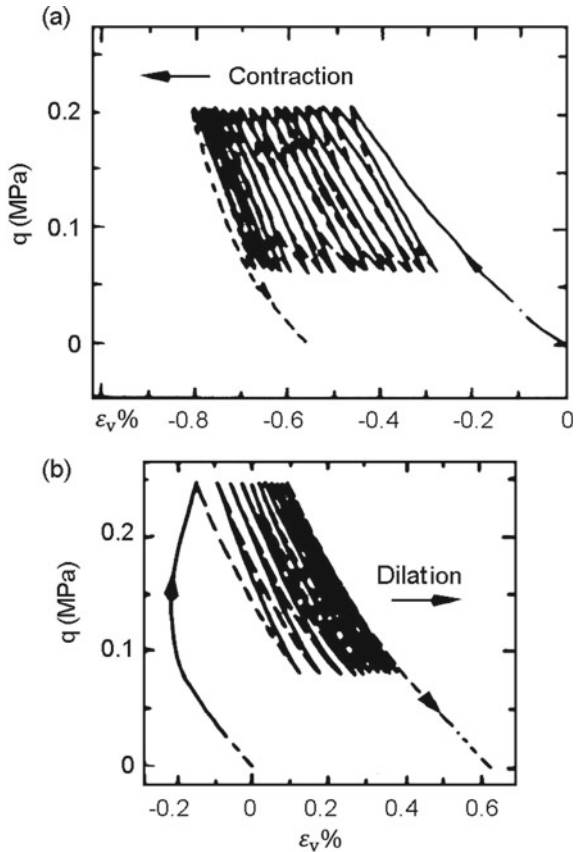
3.4 Liquefaction

In the previous section we showed that deformation of sediments in sedimentary basins due to consolidation is a function of time and that, in response to instantaneous loading, pore pressure in these sediments increases. Here we review a particular time-dependent deformation of sediments, which occurs when saturated sediments are subjected to cyclic loading such as that generated by earthquakes. This phenomenon became widely studied in the earthquake engineering communities after the great 1960 M9.2 Alaska earthquake that caused widespread liquefaction and property damage. Many laboratory and field measurements have been performed on saturated sediments to simulate the response of sedimentary basins and soils to seismic shaking. These experiments demonstrate that, as seismic waves propagate through saturated sediments, pore pressure increases. Pore pressure increases because sediments consolidate under cyclic deformation, during which part of the load on the

solid matrix is transferred to the pore fluids (e.g., Figure 3.5). If there is little time for pore pressure to dissipate, pore pressure may continue to rise under ongoing shaking. If the rising pore pressure stays below the overburden pressure, the effective pressure will remain positive, and the sediments will remain solid. Pore pressure will eventually dissipate and sediments will consolidate. On the other hand, if the rising pore pressure reaches the magnitude of the overburden pressure during seismic shaking, the overburden is supported entirely by the pore pressure and the sediments will lose strength and become fluid-like—a phenomenon known as liquefaction.

Figure 3.8 shows the deformation of porous sediments under cyclic loading in a drained condition (Luong 1980). If the shear stress is below a characteristic threshold, cyclic shearing causes the volume of the sheared sample to decrease (Fig. 3.8a). On the other hand, at shear stress above the threshold, cyclic shearing causes the volume of the sheared sample to increase (Fig. 3.8b). The transition between the two responses, where no contraction or dilatancy occurs, corresponds to a ‘critical state’ in soil mechanics (Wang et al. 2001; National Academies

Fig. 3.8 Deviatoric stress versus volumetric strain for two sand samples of the same constitution. **a** Shearing at a maximum deviatoric stress ‘ q ’ of 0.2 MPa. Note that the volumetric strain decreases with increasing number of stress cycles and the sample contracts under cyclic shearing. **b** Shearing at a maximum deviatoric stress of 0.25 MPa. Note that the volumetric strain increases with increasing number of stress cycles and the sample dilates under cyclic shearing. (from Luong 1980)



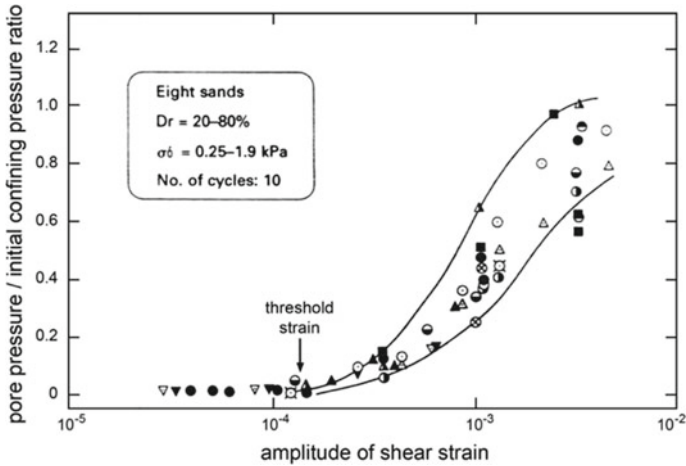


Fig. 3.9 Experimental results for pore-pressure generation in eight different sands with dry density from 20 to 80% of the mineral density, under initial confining pressure from 0.25 to 1.9 kPa, and 10 cycles of uniform loading. Note that, for sands with such diverse densities and confining pressures, pore-pressure buildup begins at a threshold strain of 10^{-4} (From Vucetic 1994)

of Science, Engineering and Medicine 2016) where volume stays unchanged during deformation.

Note that the case in Fig. 3.8a is normally reported because experiments are normally performed at shear stresses below that required to cause shear-induced dilatation. Using a wide variety of saturated sediments under a wide range of confining pressures, Dobry et al. (1982), Vucetic (1994) and Hsu and Vucetic (2004) showed that pore pressure begins to increase when sediments are sheared above a strain amplitude of 10^{-4} (Fig. 3.9), defining a threshold strain amplitude for the initiation of sediment consolidation.

Seed and Lee (1966) showed how deformation and pore pressure changed in two sand specimens under cyclic shearing at constant stress amplitude of ± 50 kPa (Fig. 3.10). Note that the loose sand failed at the 9th stress cycle, while the dense sand withstood hundreds of stress cycles without complete failure. In the loose sand experiment, the axial strain was small during the first eight cycles, but increased significantly afterwards. The large strains during 9th stress cycle suggest that the sample was failing. The loss in rigidity, and thus the occurrence of liquefaction, is marked by the drastic increase in shear strain at the 10th cycle of the experiment.

Experiments performed at constant strain amplitude are complimentary to those performed at constant stress amplitude (Fig. 3.11). Note that pore pressure starts to increase from the first strain cycle and continues to increase while the stress amplitude continues to decline, suggesting that the sample is weakening. Stress amplitude is reduced to zero (i.e., sample liquefies) when pore pressure becomes equal to the confining pressure.

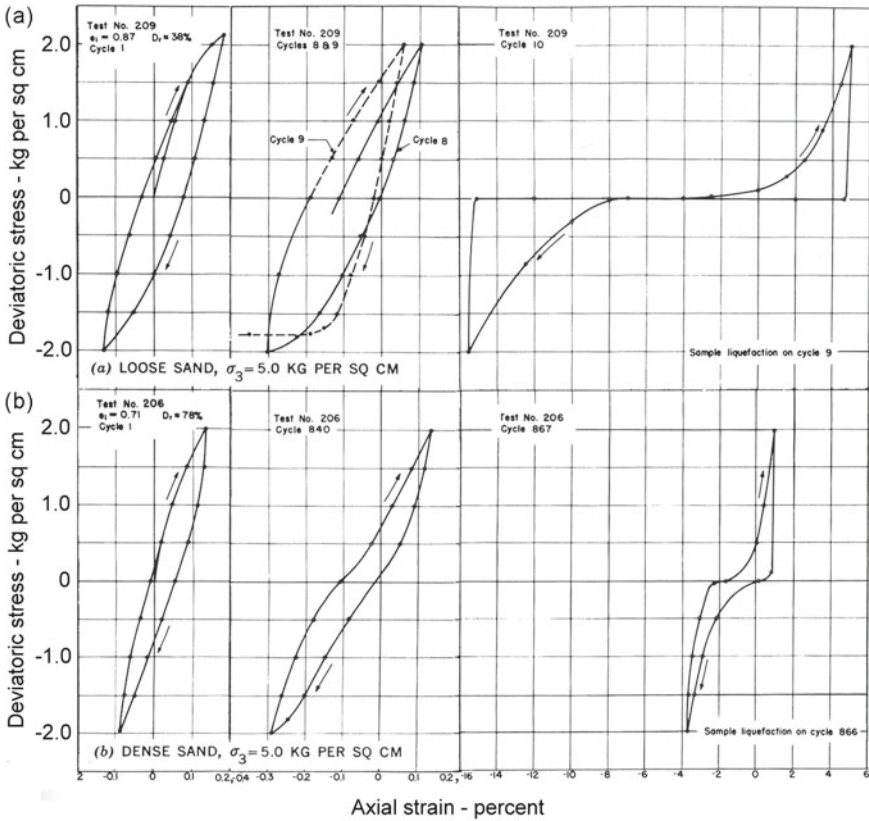


Fig. 3.10 Experimental stress-strain relations for **a** loose sand and **b** dense sand under cyclic shear stress of constant stress amplitude of 2 kg per cm² (0.2 MPa). The loose sand, at a dry density of 38% of the mineral density, showed relatively small deformation during the first eight cycles but failed at the 9th stress cycle. The dense sand at a dry density of 78%, on the other hand, did not fail for hundreds of stress cycles (from Seed and Lee 1966)

3.5 Rock Friction and Instability

Earth’s shallow crust is permeated by fractures; frictional sliding and instability on these fractures are important processes controlling crustal deformation and the occurrence of shallow earthquakes. Because intact rocks usually have poor permeability, fractures may also control crustal permeability. Some fractures are ‘opened’ for fluid flow, while others may be clogged by precipitates and/or colloidal particles. Thus rock friction and instability can involve multiple interacting hydro-mechanical processes.

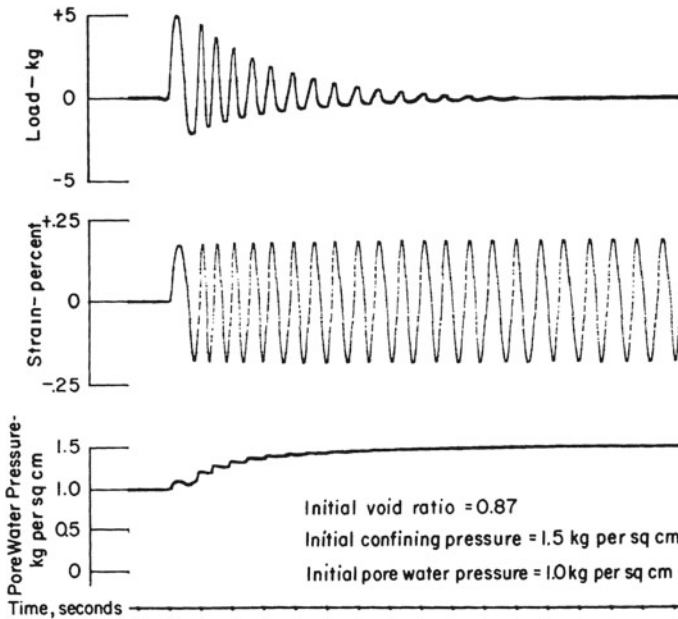


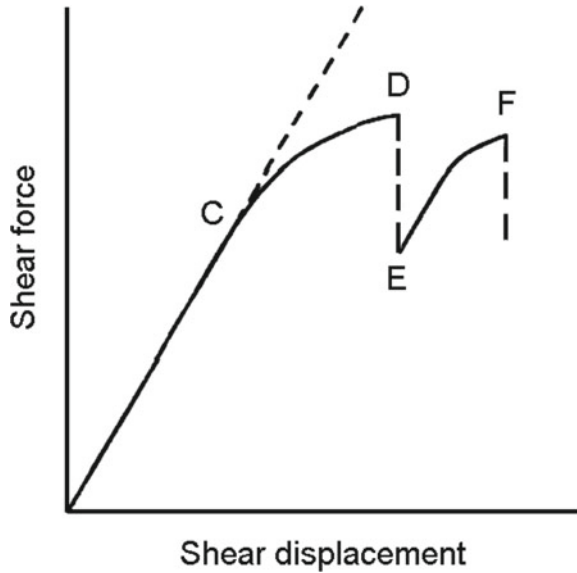
Fig. 3.11 Experimental results showing pore-pressure generation and mechanical weakening of a saturated sand specimen subjected to cyclic shearing at constant strain amplitude of $\pm 0.2\%$. The sediment specimen had an initial void ratio of 87% and was subjected to a confining pressure of 0.15 MPa and an initial pore pressure of 0.1 MPa. Note that the axial stress is reduced to zero when pore pressure becomes equal to the confining pressure (from Seed and Lee 1966)

3.5.1 Friction and Frictional Instability

Rock masses containing joints or fractures may be mechanically stable if the shear stresses on these surfaces are smaller than the frictional resistance. If the shear stress on one of the surfaces reaches the frictional resistance, the rocks on the two sides of the surface may slip past each other. If sliding occurs abruptly, the accumulated shear stress and strain are suddenly released. The sudden change in the state of stress and strain may give rise to an earthquake that is characterized by crustal vibrations and the emission of seismic waves. The time-dependent evolution of stress accumulation, development of instability, release of the crustal stress and strain, and the eventual recovery of the state of stress, is known as the elastic rebound theory for earthquakes (Reid 1911). The shear strength of the fault is linearly related to the normal stress and the friction coefficient by the well-known Coulomb effective friction law, which is discussed later in this section. Complications arise from the dependence of the friction coefficient on the slip velocity, which leads to slip instability and fault rupture, and is discussed in Sect. 3.5.2.

Brace and Byerlee (1966) proposed that instability in frictional sliding is the mechanism for earthquakes. Since then, a large amount of work has been done to

Fig. 3.12 Schematic diagram of shear force versus shear displacement in a frictional sliding experiment. At shear force below point C, the relation is linear and deformation is elastic. Stable sliding occurs between points C and D (stick). At point D, instability occurs and shear force suddenly releases (slip). Equilibrium re-establishes at point E. The stick-slip process repeats between points E and F (modified from Byerlee 1978)



understand friction in rocks and its instability. The schematic diagram in Fig. 3.12 plots the shear force on a sliding surface against shear displacement at a constant normal force. At small shear force (below point C on the curve), shear force is linearly proportional to displacement and deformation is elastic. Stable sliding occurs between points C and D, and displacement increases nonlinearly with shear force. At point D, instability occurs with a sudden release of shear force and little displacement. The system reaches a new equilibrium at point E at a lower shear force. Stable sliding commences again when shear force is once more increased until the second unstable release of shear force occurs at point F. The sequence of stable sliding followed by instability may repeat with continued deformation, and is commonly referred to as the stick-slip process.

Experimental observation shows that the shear stress at which unstable sliding occurs is related to the normal stress by the Coulomb failure criterion

$$\tau = c - \mu\sigma = c + \mu|\sigma|, \tag{3.121}$$

where τ is the applied shear stress at which unstable sliding occurs, σ is the normal stress (extension positive), μ the friction coefficient, and c the cohesion strength across the surface. Here we use the absolute magnitude of the normal stress $|\sigma|$ in Eq. (3.121), rather than $-\sigma$, in order to retain the sign convention in rock mechanics experiments where data are presented with compression taken to be positive.

Figure 3.13 shows the experimental data for τ versus σ on rock surfaces (Byerlee 1978) measured at elevated normal stress. The slope of the curve given by the experimental data defines the friction coefficient μ . At normal stress above ~ 100 MPa,

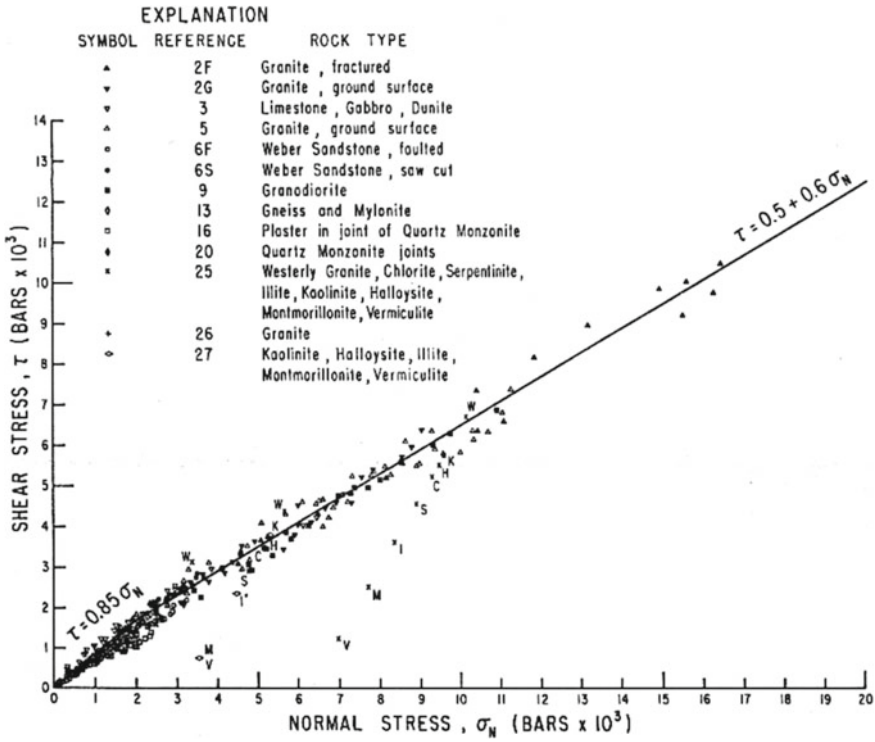


Fig. 3.13 Shear stress plotted as a function of normal stress at the maximum friction for a variety of rock types (from Byerlee 1978)

μ is ~ 0.6 for most rocks, although it may be much lower if the sliding surface is covered with clay minerals such as montmorillonite and vermiculite. At high normal stresses, such as those on faults at seismogenic depths, c is relatively small and is often neglected.

When the sliding surface is subjected to pore pressure, its frictional properties change significantly. Byerlee and Brace (1972) showed that, when fluids are present, it is not the normal stress that is important but the effective normal stress, as defined in Eq. (3.11). In other words, the failure criterion (3.121) should be replaced by

$$\tau = c + \mu(|\sigma| - \alpha P). \tag{3.122}$$

The relation between the state of stress on a surface and the failure criterion may be illustrated by the schematic diagram in Fig. 3.14. The state of stress on any surface in a rock may be represented by a point (τ, σ) on the Mohr circle (Fig. 3.14) where the angle θ is the angle between the surface and the direction of the maximum principle stress, and the failure criterion is represented by the straight line, i.e., equation (3.121). The surface is stable if this point falls below the failure criterion, but is unstable if

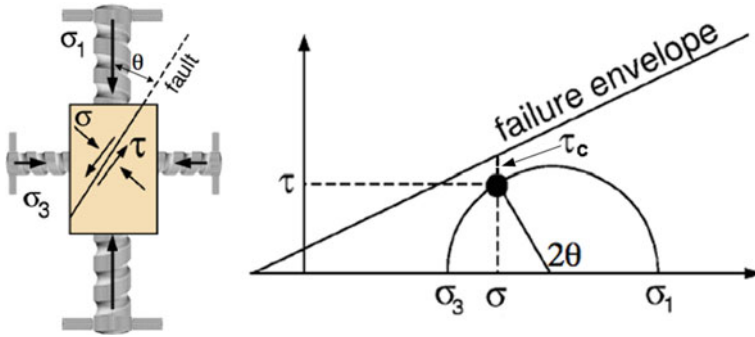


Fig. 3.14 Left: Definition of normal and shear stresses on a sliding surface inclined at angle θ with respect to σ_1 . Right: Graphic representation of the magnitude of normal and shear stresses as a function of the angle θ compared with the magnitude of shear resistance ($\tau + \tau_c$) (modified from Wang and Manga 2010)

it touches the failure criterion. It is convenient to define the difference between the shear stress on a surface and the frictional resistance on this surface as τ_c (Fig. 3.14), i.e.,

$$\tau_c = \tau - [c + \mu(|\sigma| - \alpha P)]. \tag{3.123}$$

When the shear stress τ acting on a surface (fault) equals the shear resistance (sum of cohesion and the product of the absolute magnitude of the effective normal stress and the friction coefficient), τ_c becomes zero and failure occurs. Failure may be brought about in different ways; Fig. 3.15 shows that failure may be induced by increasing the absolute magnitude of the maximum principle stress (Fig. 3.15a), by

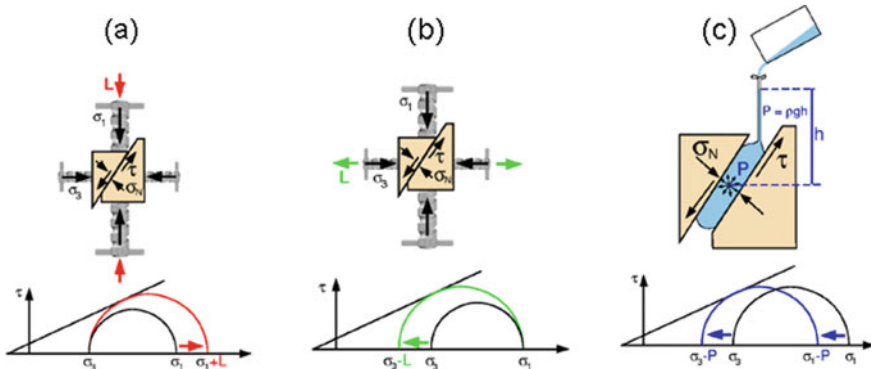


Fig. 3.15 Three ways to induce failure on a fault by causing the Mohr circle to move to the failure criterion: **a** increasing the absolute magnitude of the maximum principle stress, **b** decreasing the absolute magnitude of the minimum principle stress, and **c** increasing the pore pressure on the fault (modified from Wang and Manga 2010)

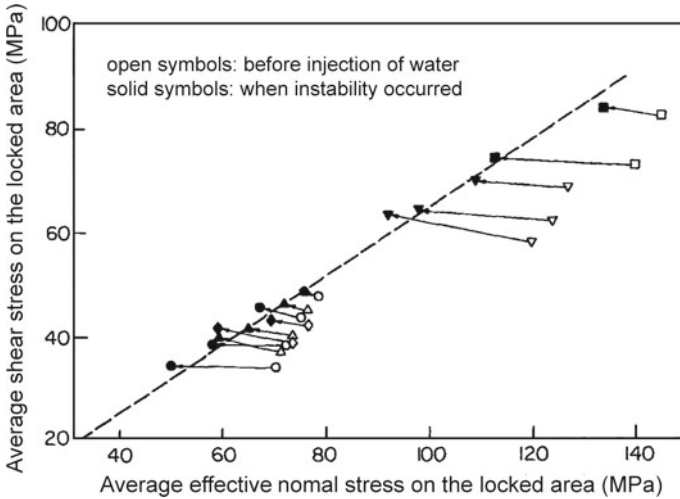


Fig. 3.16 Average shear stress and the absolute magnitude of the normal stress on a laboratory fault (sawcut) in granite. Symbols of different shapes represent results of different experiments. Open symbols: stress condition on locked area before injection of water or just after the preceding stick-slip event. Solid symbols: stress condition just prior to moment of unstable stick-slip. Each arrow connecting two states of stress (open symbol and solid symbol) shows the change of stress conditions that led to instability, or rupture of the sliding surface. Dashed line: failure criterion for frictional sliding (from Shi and Wang 1985)

decreasing the absolute magnitude of the minimum principle stress (Fig. 3.15b), or by increasing the pore pressure on the fault (Fig. 3.15c).

These concepts were successfully tested in laboratory experiments. Figure 3.16 shows the results of an experiment of frictional sliding on a laboratory fault in granite. Many sets of experiments were carried out. Each open symbol shows the initial average shear stress and the absolute magnitude of the normal stress on the fault in an experiment when the fault was stable. Pressurized water was then injected into the fault to raise pore pressure. As a result, the absolute magnitude of the effective normal stress on the fault was reduced, as indicated by an arrow. Unstable sliding occurred when pore pressure was raised so high that the absolute magnitude of the average effective normal stress was reduced to the position of the solid symbols. The dashed line shows the failure criterion for frictional sliding. The assemblage of solid symbols falls along the failure criterion, confirming the concept illustrated in Fig. 3.15c that instability on faults is controlled by the effective normal stress, rather than by the normal stress itself.

3.5.2 The Rate-and-State Equation

While Brace and Byerlee (1966) proposed instability in frictional sliding as a mechanism for earthquakes, they did not address the transition from stable sliding to instability with the sudden release of shear stress. Dieterich (1994) bridged this gap with the rate-and-state equation, which is based on the experimental finding (Dieterich 1979) that the friction between two surfaces is not a constant but rather depends on the velocity of their relative displacement (Fig. 3.17). Dieterich (1994) assumed a spring-slider model to represent the nucleation of a single source and reformulated the frictional criterion as

$$\tau(t) - k\delta(t) = \sigma \left[\mu_o + A \log\left(\frac{v}{v_o}\right) + B \log\left(\theta(t) \frac{v_o}{d_c}\right) \right] \tag{3.124}$$

where $\tau(t)$ is the applied shear stress, $\delta(t)$ the frictional slip, σ the effective normal stress, v the slip velocity ($d\delta/dt$), v_o is a reference velocity, μ_o is a reference frictional coefficient corresponding to v_o , k the effective stiffness of the source patch, assumed constant, $-k\delta(t)$ the shear stress relaxed by slip, A and B are constitutive parameters relating friction to changes in slip speed and state, respectively, $\theta(t)$ is a state variable in the fault constitutive formulation, and is a characteristic slip distance over which fault state evolves.

Ruina's (1983) formulated the so-called aging law for the evolution of the state variable θ

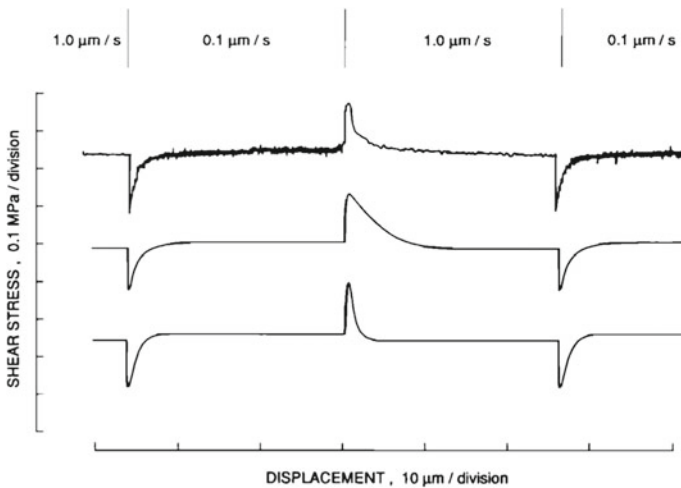


Fig. 3.17 Shear stress on the sliding surface versus displacement in which the loading velocity is stepped by one decade. The normal stress is held constant at 5 MPa. The top curve is data. The lower two curves are simulations with different rate-and-state equations (from Linker and Dieterich 1992)

$$\dot{\theta} = 1 - \frac{\theta}{d_c} \dot{\delta} - \frac{\alpha \theta}{B \sigma} \dot{\sigma}, \quad (3.125)$$

where α is a parameter to account for the effect of the normal stress. Using this relation, Dieterich (1994) derived his rate-state equation

$$R = \frac{r}{\gamma \dot{\tau}_r}, \quad (3.126)$$

and

$$\dot{\gamma} = \frac{1}{A \sigma} \left[1 - \gamma \left(\dot{\tau} + \left(\frac{\tau}{\sigma} - \alpha \right) \dot{\sigma} \right) \right], \quad (3.127)$$

where R is the rate of seismicity, r is the background rate of seismicity, $\dot{\tau}_r$ is the background shear stressing rate and γ is a state variable.

The above relation may be tested against field seismicity data, but the state variable γ is difficult to estimate. Segall and Lu (2015) eliminated the state variable γ between the two equations to obtain a single equation for R

$$\frac{dR}{dt} = \frac{R}{t_a} \left(\frac{\dot{\tau}}{\dot{\tau}_r} - \frac{R}{r} \right), \quad (3.128)$$

where $t_a = \frac{A \sigma_o}{\dot{\tau}_r}$ is a characteristic decay time. This equation was used in recent studies of the seismicity in the mid-continental USA induced by the injection into deep aquifers large amounts of wastewater coproduced from the extraction of hydrocarbons (Segall and Lu 2015; Zhai et al. 2019), a subject discussed in Chap. 4. The slight difference between the above equation and Segall and Lu's Eq. (12) is to keep the definition of $R = dN/dt$, i.e., the rate of seismicity, instead of the rate of seismicity relative to the background rate.

Heimisson and Segall (2018) revisited and re-derived the rate-state equation. They omitted the 1 in Eq. (3.125) by assuming that the seismogenic source is 'well above the steady state' and then integrated the equation to obtain

$$\theta(t) = \theta_o e^{F(t)}, \quad (3.129)$$

where

$$F(t) = - \left[\frac{\delta(t)}{d_c} + \frac{\alpha}{B} \log \left(\frac{\sigma(t)}{\sigma_o} \right) \right]. \quad (3.130)$$

Inserting Eq. (3.129) and (3.130) into (3.124) they obtained

$$\frac{\tau(t) - k\delta(t)}{\sigma} = \mu_o + A \log\left(\frac{v}{v_o}\right) - B \left[\frac{\delta}{d_c} + \frac{\alpha}{B} \log\left(\frac{\sigma(t)}{\sigma_o}\right) + \log\left(\frac{v_o}{d_c} \theta_o\right) \right] \quad (3.131)$$

which may be solved for δ and v (Heimisson and Segall 2018)

$$\delta = -\frac{A}{H} \log\left(1 - \frac{Hv_o}{A} \int_o^t K(t') dt'\right), \quad (3.132)$$

$$v = \frac{v_o K(t)}{1 - \frac{Hv_o}{A} \int_o^t K(t') dt'}, \quad (3.133)$$

where

$$H = \frac{B}{d_c} - \frac{k}{\sigma_o}, \quad (3.134)$$

$$K(t) = \exp\left(\frac{\tau(t)}{A\sigma(t)} - \frac{\tau_o}{A\sigma_o}\right) \left(\frac{\sigma(t)}{\sigma_o}\right)^{\alpha/A}, \quad (3.135)$$

v_o is the sliding velocity at time $t = 0$ (taken to be the same as the background velocity) and τ_o and σ_o are the background shear stress and normal stress.

Instability occurs when the slip velocity v becomes singular; i.e., when the denominator on the right side of Eq. (3.133) vanishes,

$$\int_o^{t_{inst}} K(t') dt' = \frac{A}{Hv_o}, \quad (3.136)$$

where t_{inst} is the time to instability. Solving this equation at constant effective normal stress σ_o and shear stressing rate $\dot{\tau}_r$, i.e., $K(t) = \exp(\dot{\tau}_r t / A\sigma_o)$, Heimisson and Segall (2018) obtained for the single spring-slider system

$$t_{inst} = \frac{A\sigma_o}{\dot{\tau}_r} \log\left(1 + \frac{\dot{\tau}_r}{Hv_o\sigma_o}\right). \quad (3.137)$$

For a population of background seismic sources that fail at constant rate r , the time to instability of the N th source is N/r , and Eq. (3.136) may be rewritten as, assuming that N can take non-integer values,

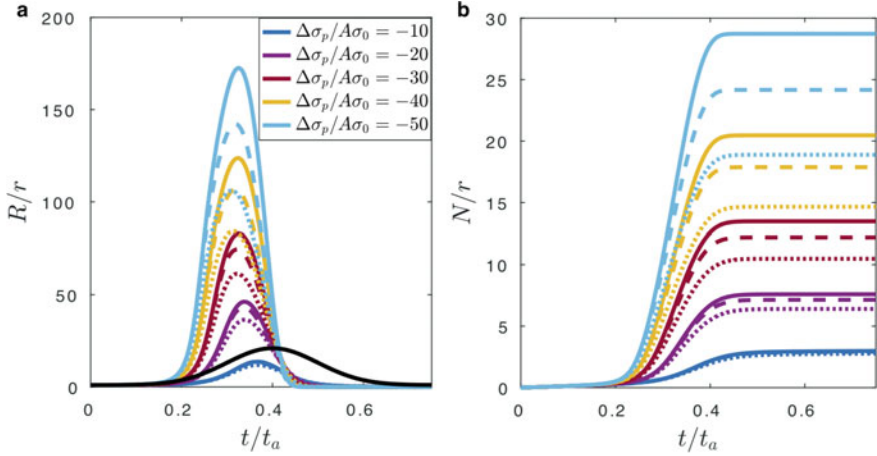


Fig. 3.18 **a** Comparison of the predicted seismicity rate by Dieterich's (1994) rate-and-state equation (dashed lines) with the Coulomb stress approximation (dotted lines), and with the prediction by the formulation by Heimisson and Segall (2018) (solid lines). Black line indicates the shape of the Gaussian normal stress perturbation and $\Delta\sigma_p$ is the peak stress of the Gaussian perturbation. **b** Same as for (a), but showing the cumulative number of events (from Heimisson and Segall 2018)

$$\int_0^{N/r} \exp\left(\frac{\dot{\tau}_r t'}{A\sigma_o}\right) dt' = \left(\frac{A}{Hv_o}\right)_N, \quad (3.138)$$

which gives the value A/Hv_o for the N th source in a population of sources that fail at constant rate r under background conditions. Inserting (3.138) in Eq. (3.136) we have

$$\int_0^{t_{inst}} K(t') dt' = \int_0^{N/r} \exp\left(\frac{\dot{\tau}_r t'}{A\sigma_o}\right) dt'. \quad (3.139)$$

From this equation Heimisson and Segall (2018) derived the cumulative number of events N

$$\frac{N}{r} = t_a \log\left(1 + \frac{1}{t_a} \int_0^t K(t') dt'\right). \quad (3.140)$$

From $R = dN/dt$, the seismicity rate R is

$$\frac{R}{r} = \frac{K(t)}{1 + \frac{1}{t_a} \int_0^t K(t') dt'}. \quad (3.141)$$

Figure 3.18 compares the seismicity rate and the cumulative number of events predicted by Heimisson and Segall (2018) and those by Dieterich (1994). The two sets of predictions are similar except at large changes in the normal stress.

The rate-and-state equation has been central in the recent discussions of induced seismicity (e.g., Segall and Lu 2015; Zhai et al. 2019) as discussed in Chap. 4.

References

- Athy LF (1930) Density, porosity, and compaction of sedimentary rocks. *Am Asso Petrol Geol Bull* 14:1–24
- Barbour AJ (2015) Pore pressure sensitivities to dynamic strains: observations in active tectonic regions. *J Geophys Res* 120:5863–5883
- Barbour AJ, Xue L, Roeloffs E, Rubinstein JL (2019) Leakage and increasing fluid pressure detected in Oklahoma’s wastewater disposal reservoir. *J Geophys Res* 124:2896–2919
- Biot MA (1941) General theory of three dimensional consolidation. *J Appl Phys* 12:155–164
- Biot MA (1955) Theory of elasticity and consolidation for a porous anisotropic solid. *J Appl Phys* 26:182–185. <http://dx.doi.org/10.1063/1.1721956>
- Brace WF, Byerlee JD (1966) Stick-slip as a mechanism for earthquakes. *Science* 153:990–992
- Burgess WG, Shamsudduha M, Taylor RG et al (2017) Terrestrial water load and groundwater fluctuation in the Bengal Basin. *Sci Rep* 7:3872. <https://doi.org/10.1038/s41598-017-04159-w>
- Byerlee JD (1978) Friction of rocks. *Pure Appl Geophys* 116:615–626
- Byerlee JD, Brace WF (1972) Fault stability and pore pressure. *Bull Seismol Soc Am* 62:657–660
- Carslaw HS, Jaeger JC (1959) *Conduction of heat in solids*. Clarendon Press, Oxford
- Cheng AHD (2016) *Poroelasticity*. Springer
- Detournay E, Cheng AHD (1993) Fundamentals of poroelasticity. In: Hudson JA (ed) *Comprehensive rock engineering: principles, practice and projects*, vol 2. Pergamon Press
- Dieterich JH (1979) Modeling of rock friction, 1, experimental results and constitutive equations. *J Geophys Res* 84:2161–2168
- Dieterich JH (1994) A constitutive law for rate of earthquake production and its application to earthquake clustering. *J Geophys Res* 99:2601–2618. <https://doi.org/10.1029/93JB02581>
- Dobry R, Ladd RS, Yokel FY, Chung RM, Powell D (1982) Prediction of pore water pressure buildup during earthquakes and liquefaction of sands during earthquakes by the cyclic strain method, vol 138. National Bureau of Standards
- Heimisson ER, Segall P (2018) Constitutive law for earthquake production based on rate-and-state friction: Dieterich 1994 revisited. *J Geophys Res Solid Earth* 123:4141–4156
- Hsu CC, Vucetic M (2004) Volumetric threshold shear strain for cyclic settlement. *J Geotech Geoenviron Eng* 130:58–70
- Linker MF, Dieterich JH (1992) Effects of variable normal stress on rock friction: observations and constitutive equations. *J Geophys Res* 97:4923–4940
- Luong MP (1980) Stress-strain aspects of cohesionless soils under cyclic and transient loading. In: Pande GN, Zienkiewicz OC (eds) *Proceedings of the international symposium on soils under cyclic and transient loading*. AA Balkema, Rotterdam, Netherlands, pp 315–324
- National Academy of Sciences, Engineering and Medicine (2016) *State of the art and practice in the assessment of earthquake-induced soil liquefaction and its consequences*. The National Academies Press, Washington, DC. <https://doi.org/10.17226/23474>
- Nur A, Byerlee JD (1971) An exact effective stress law for elastic deformation of rock with fluids. *J Geophys Res* 76:6414–6419
- Reid HF (1911) *The mechanics of the earthquake*. Volume II of *The California Earthquake of April 18, 1906*. Carnegie Institution of Washington, DC
- Roeloffs E (1996) Poroelastic techniques in the study of earthquake-related hydrologic phenomena. *Adv Geophys* 37:135–195
- Ruina A (1983) Slip instability and state variable friction laws. *J Geophys Res* 88:10359–10370

- Seed HB, Lee KL (1966) Liquefaction of saturated sands during cyclic loading. *J Soil Mech Found Div* 92:105–134
- Segall P, Lu S (2015) Injection-induced seismicity: Poroelastic and earthquake nucleation effects. *J Geophys Res Solid Earth* 120:5082–5103. <https://doi.org/10.1002/2015JB012060>
- Shi XJ, Wang CY (1985) Instability on a weakening fault. *Pure Appl Geophys* 122:478–491
- Terzaghi K (1925) *Erdbaummechanik*. Franz Deuticke, Vienna
- Vucetic M (1994) Cyclic threshold of shear strains in soils. *J Geotech Eng* 120:2208–2228
- Wang HF (2000) *Theory of linear poroelasticity*. Princeton University Press, Princeton, NJ
- Wang CY, Cheng LH, Chin CV et al (2001) Coseismic hydrologic response of an alluvial fan to the 1999 Chi-Chi earthquake, Taiwan. *Geology* 29:831–834
- Wang CY, Barbour AJ (2017) Influence of pore pressure change on coseismic volumetric strain. *Earth Planet Sci Lett* 47:152–159. <https://doi.org/10.1016/j.epsl.2017.07.034>
- Wang CY, Manga M (2010) *Earthquakes and water*. Springer
- Zhai G, Shirzaei M, Manga M et al (2019) Pore pressure diffusion, enhanced by poroelastic stresses, controls induced seismicity in Oklahoma. *Proc Natl Acad Sci* 116:16228–16233. <https://doi.org/10.1073/pnas.1819225116>
- Zhang Y, Wang CY, Fu LY et al (2019) Unexpected far-field hydrological response to a great earthquake. *Earth Planet Sci Lett* 519:202–212. <https://doi.org/10.1016/j.epsl.2019.05.007>

Open Access This chapter is licensed under the terms of the Creative Commons Attribution 4.0 International License (<http://creativecommons.org/licenses/by/4.0/>), which permits use, sharing, adaptation, distribution and reproduction in any medium or format, as long as you give appropriate credit to the original author(s) and the source, provide a link to the Creative Commons license and indicate if changes were made.

The images or other third party material in this chapter are included in the chapter's Creative Commons license, unless indicated otherwise in a credit line to the material. If material is not included in the chapter's Creative Commons license and your intended use is not permitted by statutory regulation or exceeds the permitted use, you will need to obtain permission directly from the copyright holder.



Chapter 4

Earthquakes Influenced by Water



Abstract Injecting fluids in the crust, or their extraction, changes pore pressure and poroelastic stresses. Both pressure and stress changes can promote seismicity and, hence, the seismic events are called induced earthquakes. The filling of reservoirs on Earth's surface can also induce earthquakes from some combination of surface loading and pore pressure changes. Attribution of any given earthquake to human activities, however, is not always straightforward. There remains debate about what controls the magnitude of induced earthquakes, the relative importance of pore pressure changes and poroelastic stresses, and how to best manage injection and extraction to minimize seismicity. As the scale and distribution of subsurface engineering expand globally, we should expect more and larger induced earthquakes in the future.

4.1 Introduction

Hydro-mechanical coupling (Chap. 3) connects changes in pore pressure to changes in stress. Changes in stress can also promote rock failure and motion on pre-existing faults and fractures. Changes in pore pressure can thus cause earthquakes. In the past decades our manipulation of the subsurface by injecting and extracting fluids has led to a dramatic increase in the number and magnitude of human-caused earthquakes. A particularly striking example is the rapid increase in seismicity in the tectonically stable mid-continent of the USA (Fig. 4.1) including the magnitude 5.8 Pawnee earthquake, Oklahoma in 2016. This increase is acknowledged to be the result of injecting co-produced brines that are extracted during hydrocarbon recovery (Ellsworth 2013) and the flowback of the injected fluids (EPA 2011). In this chapter we thus discuss several ways in which hydrology influences seismicity.

The expressions “induced” and “triggered” are sometimes used interchangeably. Here we use the definition that an “induced earthquake” is one caused by human activity that alters stresses in the crust. A “triggered earthquake” is one caused by natural stress changes, either static or dynamic. In practice, the distinction can be difficult to make because the mechanisms through which water influences seismicity are not always straightforward to quantify.

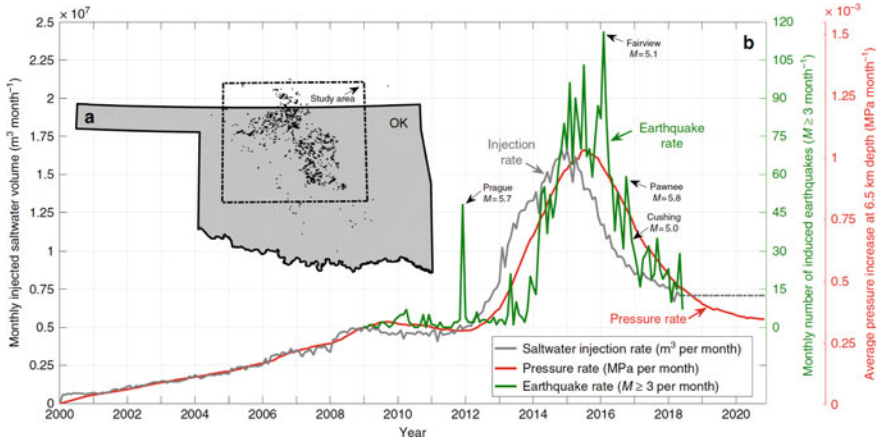


Fig. 4.1 Induced seismicity and injection in Oklahoma (OK), USA. **a** Map showing the spatial distribution of events. **b** Time series of earthquakes with magnitude greater than or equal to 3, injection rate, and modeled rate of pressure increase. From Langenbruch et al. (2018)

Davis and Frolich (1993) proposed a straightforward approach for deciding whether an earthquake was induced by fluid injection (Table 4.1). They assess the past history of seismicity, temporal and spatial relationships, as well as features of the injection. The end result is a score that expresses the confidence in ascribing earthquakes to injection. Foulger et al. (2018) created a database of induced earthquakes, summarized in a 77-page paper with 119 figures. Beyond identifying likely induced earthquakes, they note several additional challenges in constructing this database and hence summarizing observations: incomplete or ambiguous reporting, lack of operation data, multiple subsurface disturbances, limitations imposed by minimal seismic monitoring, and inaccuracies in earthquake locations.

4.2 Fluids and Rock Failure

The basis for fluids influencing friction and fault motion is summarized in Sect. 3.5. Here rock failure does not mean the failure of intact rocks but frictional motion on existing fractures or faults. Motion initiates when the shear stress τ on an existing surface exceeds the Coulomb failure criterion (Eq. 3.121)

$$\tau = c + \mu(|\sigma| - \alpha P). \quad (4.1)$$

where σ is the normal stress on this fracture or fault (extension positive), μ the friction coefficient that may be a function of slip rate and state, c the cohesion strength across the surface, P the pore pressure, and α the Biot-Willis coefficient.

Table 4.1 A set of questions to assess whether earthquakes are induced (from Davis and Frolich 1993)

Question	Earthquake clearly not induced	Earthquakes clearly induced	I Denver, Colorado	II Painesville, Ohio
<i>Background seismicity</i>				
1. Are these events the first known earthquakes of this character in the regions?	NO	YES	YES	NO
<i>Temporal correlation</i>				
2. Is there a clear correlation between injection and seismicity?	NO	YES	YES	NO
<i>Spatial correlation</i>				
3a Are epicenters near wells (within 5 km)?	NO	YES	YES	YES?
3b Do some earthquakes occur at or near injection depths?	NO	YES	YES	YES?
3c If not, are there known geologic structures that may channel flow to sites of earthquakes?	NO	YES	NO?	NO?
<i>Injection practices</i>				
4a Are changes in fluid pressure at well bottoms sufficient to encourage seismicity?	NO	YES	YES	YES
4b Are changes in fluid pressure at hypocentral locations sufficient to encourage seismicity?	NO	YES	YES	NO?
Total "YES" answers	0	7	6	3

This so-called Mohr-Coulomb law and the concept of effective stress do not capture the effects of viscous deformation or dilatation that depend on deformation rate and history—processes that can have a non-trivial effect on earthquake nucleation and rupture. It is nevertheless useful for illustrating how and why fluids can have a significant influence on earthquakes. Equation (4.1) shows that earthquakes can be induced by increasing the shear stress, reducing the normal stresses clamping faults shut, or increasing fluid pressure (or some combination).

The transition from stable to unstable sliding depends on the properties and slip history of the surfaces, captured with the rate-and-state friction models described in Chap. 3.5.2. These processes also depend on stressing rate. Rate-and-state models are useful for studying induced seismicity because they connect changes in stress and pressure to changes in seismicity.

4.3 Earthquakes Induced by Fluid Injection

There are both natural and engineering processes that can raise pore pressures and hence influence seismicity. Here we focus on the engineered examples because the sources of fluids are constrained in both space and time. The growth of case studies and literature on injection-induced earthquakes has paralleled the rapid increase in the number and size of induced earthquakes (Keranen and Weingarten 2018).

The first well-studied example of human-induced earthquakes caused by an increase of pore pressure occurred at the Rocky Mountain Arsenal, Colorado, USA. Here, a magnitude 5.5 earthquake likely occurred in response to fluid injection at a depth of 3.6 km (Evans 1966). Continued and controlled monitoring established a relationship between injection and seismicity: Fig. 4.2 from Healy et al. (1968) shows the history of fluid injected and occurrence of earthquakes. Here, seismicity persisted after injection ended, reflecting the continued diffusion of high pore pressures away from the injection site (Healy et al. 1968; Hsieh and Bredehoeft 1981).

Pore pressure diffusion allows stress changes to spread over time, inducing earthquakes several tens of km from wells (Keranen et al. 2014) to distances approaching 100 km (Peterie et al. 2018; Zhai et al. 2020). Strains produced by pore pressure changes can also create poroelastic stresses that further extend the spatial reach of pressure changes (Goebel and Brodsky 2018) and may promote or decrease seismicity depending on fault orientation (e.g., Segall and Lu 2015). Aseismic creep may also accompany fluid injection (e.g., Guglielmi et al. 2015; McGarr and Barbour 2018; Cappa et al. 2019) and hence stressing rate may influence seismicity through rate-and-state friction. Lab experiments have documented a dependence of fault behavior on pressurization rate, with creep favored by slow pressure changes and stick-slip episodes for high pressurization rates (Wang et al. 2019).

To compute seismicity rates from pore pressure and stress changes, some authors use the rate-and-state friction models described in Sect. 3.5.2 (e.g., Dieterich 1994; Segall and Lu 2015; Zhai et al. 2019). Figure 4.3 shows computed changes in stressing rate from changes in pore pressure and poroelastic stresses, and how the changes

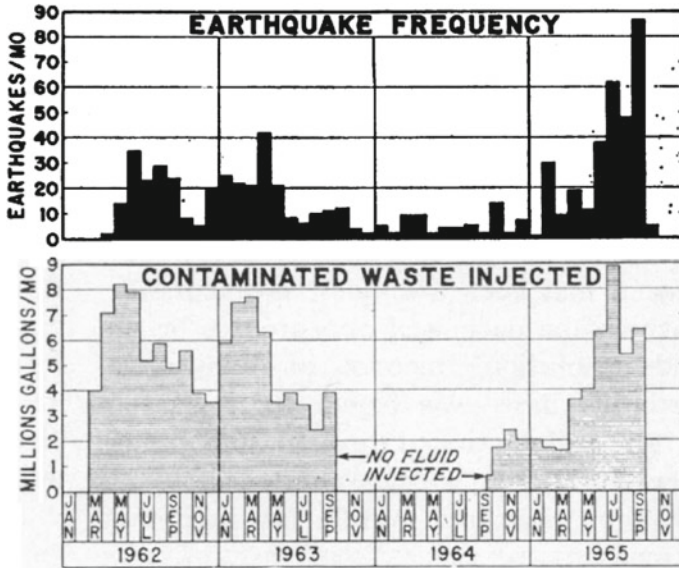


Fig. 4.2 Number of earthquakes recorded at the Rocky Mountain Arsenal waste injection site (top) and volume of fluid injected (bottom). From Healy et al. (1968)

contribute to a computed seismicity rate. These models involve parameters that are not necessarily known a priori, such as the background seismicity rate and background stress. In some cases, it may be possible to use induced seismicity to constrain some of those unknown parameters (e.g., Zhai et al. 2020). Other approaches to forecast seismicity have been introduced. For example, Langenbruch and Zoback (2016) connect the seismicity rate to the volume injected and a seismogenic index that captures the number of, and stress state on, existing faults; Langenbruch et al. (2018) allow the productivity of earthquakes to also scale with the square of the rate of pressure change. Since in both models the effects of a decrease in pressure are not captured (pressure rate squared is always positive), a different model must be introduced when pressure is no longer increasing.

To convert seismicity rate to earthquake magnitude, a Gutenberg-Richter scaling is normally used

$$\log_{10} N = a - bM \tag{4.2}$$

where N is the number of earthquakes with magnitude greater than M , and a and b are constants that may vary from region to region. In general b is close to 1. Deviation of observations from this logarithmic scaling at low magnitudes is generally assumed to reflect the incompleteness of the earthquake catalog because small events are difficult to detect. A topic of active debate and discussion is the maximum size of induced earthquakes, and whether it scales with the volume injected (McGarr 2014) or the

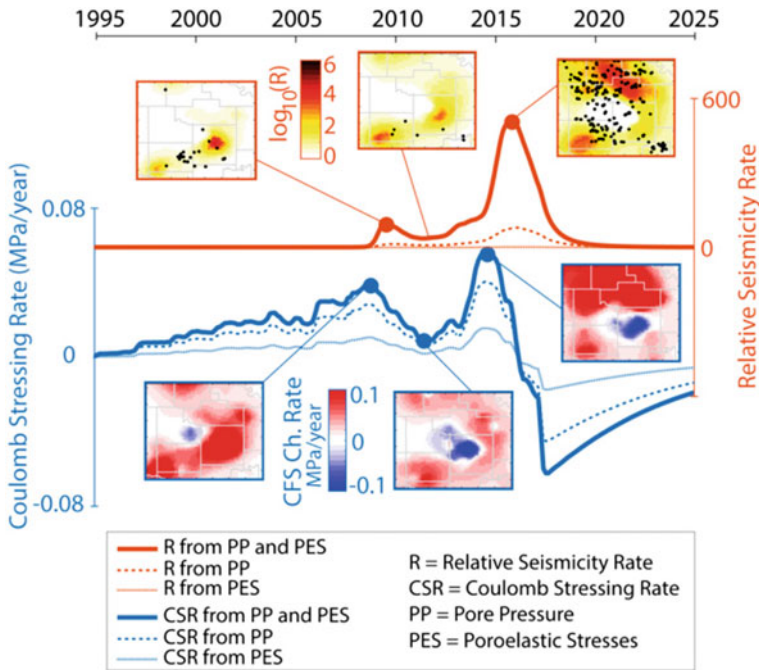


Fig. 4.3 Evolution of stressing rate and modeled seismicity rate from injection in central Oklahoma. Curves show average values within the region and the maps show the spatial distribution. Black dots in the maps are the locations of earthquakes in the time period between successive maps, or since 1995 for the first map. Simulation curves show the effects of pore pressure changes (PP), poroelastic stresses (PES), or both combined. From Zhai et al. (2019)

largest possible earthquake in a region (van der Elst et al. 2016)—that is, is size controlled by injection parameters or tectonics?

An increase in seismicity, and indeed some of the largest earthquakes, sometimes occurs following a shut in or reduction of injection (e.g., Chang et al. 2018). This can arise from the rapid change in stress before pore pressure can decrease. This effect in hydrogeology is sometimes called the Noodbergum effect: a quick and short term rise in water level in wells near a well from which water is pumped. This reverse and paradoxical response is an example of a poroelastic effect that arises because elastic stresses are transmitted much faster than pore pressure changes. The effect is named after the location in the Netherlands where it was documented and explained (Verruijt 1969). The operational implication is that tapering of injection reduction may reduce the seismicity rate (e.g., Segall and Lu 2015).

The most compelling seismic evidence for seismicity induced by fluid injection is a space and time pattern consistent with pore pressure diffusion, with the distance of induced seismicity from the well increasing with the square root of time. These patterns are sometimes seen (e.g., Tadokoro et al. 2000; Shapiro et al. 2006) at least for a subset of events (Goebel and Brodsky 2018). The migration rate of seismicity

provides constraints on fault zone or aquifer hydraulic diffusivity (hence permeability) and, when combined with the known pressure at the injection sites, the state of stress on the fault.

It is worth highlighting additional geological factors that may contribute to induced seismicity and fault reactivation: fault orientation, the hydraulic connectivity between injection formations and the seismogenic faults in basement rocks, and the state of stress on those faults (Kolawole et al. 2019). The spatial variations of induced events, their isolation to narrow fault planes, the vast range of earthquake productivity between basins, highlight the importance of subsurface heterogeneity and geological setting and history (Keranen and Weingarten 2018).

Another example of rock failure caused by high pore pressure is hydraulic fracturing. Here, pore pressure is increased to the point that tensile failure occurs. Hydraulic fracture is induced intentionally to increase the permeability of oil and gas bearing units to enhance recovery, the process colloquially called “fracking”. It is the now widespread use of hydraulic fracturing to extract non-conventional hydrocarbons that has led to the massive increase in wastewater injection that in turn induces earthquakes. While the goal of hydraulic fracturing is to break rock (many small earthquakes), earthquakes with magnitude greater than 3 have been attributed to hydraulic fracturing (e.g., Atkinson et al. 2016).

Geothermal systems are another setting where injection induced earthquakes are common. Figure 4.4 shows one example of the relationship between injected volume and seismicity at the Geysers, California, the largest geothermal facility globally (Hartlin et al. 2019). Here, temperature changes may play an additional role in creating stresses through thermal contraction (e.g., Segall and Fitzgerald 1998; Majer et al. 2007). Rock failure is often induced in geothermal settings to create or enhance permeability to enable production and create an Enhanced Geothermal Systems (EGS). Rather than being called “fracking”, this process is called “stimulation”. In general, EGS earthquakes are small. However, in 2017 a magnitude 5.5 earthquake near Pohang, South Korea injured many people and caused extensive damage and has been attributed to injection at a geothermal facility (Grigoli et al. 2018; Kim et al. 2018).

In summary, observations, theory and lab experiments show that pore pressure changes, poroelastic stresses, and stressing rate all contribute to injection induced seismicity. In geothermal systems, temperature changes also matter. A combination of geological conditions and operational parameters (injection pressure, rate and history) thus control induced seismicity.

4.4 Earthquakes Induced by Fluid Extraction

The concept of effective stress makes it straightforward to understand how injection (i.e., pressure increases) can induce earthquakes. The opposite case, fluid extraction, can also induce earthquakes, even though pore pressure reduction acts to stabilize faults. The best and most widespread documented examples are associated with

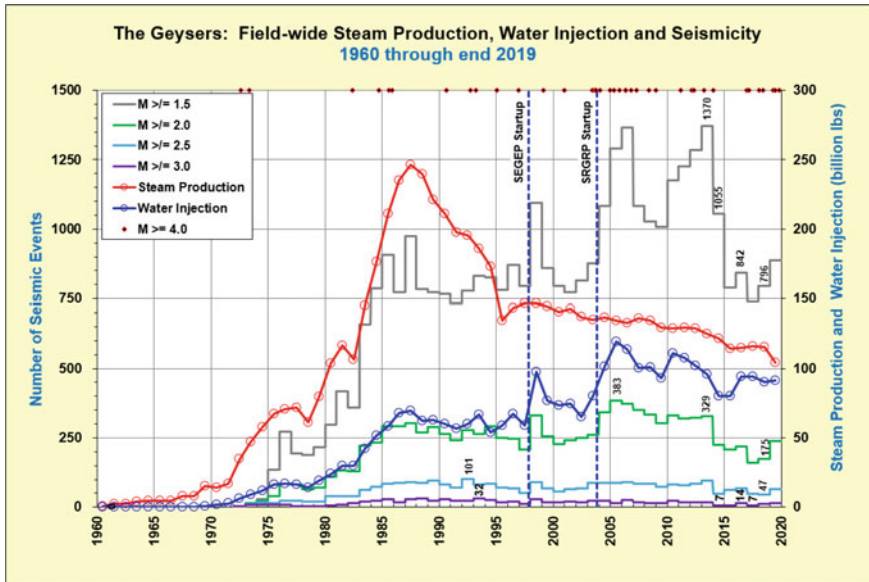


Fig. 4.4 Number of seismic events and history of steam production and water injection at the Geysers, California. The red symbols show when magnitude 4 or greater earthquakes occurred. The decrease in 2015 is partly due to instrument loss in a fire. 2016 values are projected. Figure provided by Craig Hartline

the extraction of oil and gas (e.g., Segall et al. 1994; Gomberg and Wolf 1999; Zoback and Zinke 2002). There are also a few examples of earthquakes attributed to groundwater extraction (e.g., Gonzalez et al. 2012; Wetzler et al. 2019). The much smaller number of examples connected to groundwater extraction (compared with hydrocarbon extraction), despite being volumetrically so much greater, may reflect the shallower depths from which water is extracted and that earthquakes tend to nucleate at depths of at least several kilometers.

There are a couple of processes by which extraction can cause earthquakes, illustrated schematically in Fig. 4.5. Segall (1989) shows how poroelastic deformation will increase the magnitude of deviatoric stresses away from the region from which fluid is extracted and where there are no changes in pore-fluid content. The focal mechanisms of seismic events should be diagnostic of whether they are possibly induced, with details depending on the orientation of pre-existing structures and elastic properties. A second mechanism to create seismicity is the differential rock compaction that may build up stresses (Candela et al. 2018). For each process, knowing the location, orientation, and stress state of faults can play a role in mitigating seismic hazard.

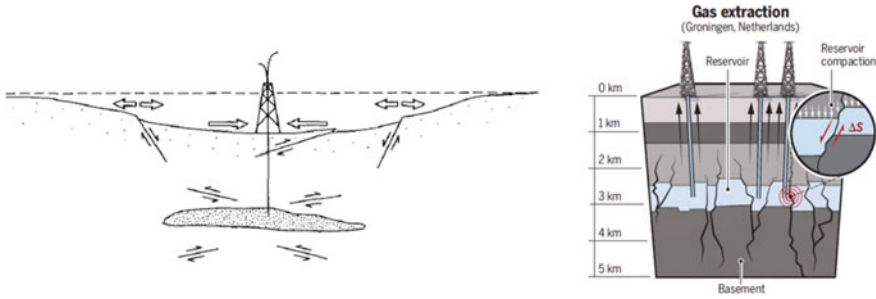


Fig. 4.5 Schematic illustration of processes that can induce earthquakes by fluid extraction. **a** Extraction from the stippled region contracts the reservoir producing stresses in the surroundings (from Segall 1989). **b** Extraction of fluids compresses reservoirs and differential stresses can increase shear stress (from Goebel et al. 2019)

4.5 Reservoir-Induced Seismicity

The filling of surface reservoirs with water also causes earthquakes. This so-called “reservoir-induced” seismicity has been documented ever since large reservoirs were constructed. The first well studied example accompanied the impoundment of the Colorado River, USA by the Hoover Dam to form Lake Mead (Carder 1945). Figure 4.6 shows that as water level rose, the number of earthquakes increased with a very large number early on. This topic is reviewed in more detail in a number of books (e.g., Gupta 1992) and review papers (e.g., Simpson 1976; Gupta 2002).

Earthquakes associated with reservoirs are not confined only to tectonically active regions, hence the reason it is usually called “induced” seismicity. Gupta (2002) in contrast notes that the stresses caused by reservoir loading are of order 0.1 MPa, much smaller than earthquake stress drops and hence that these events are better classified as “triggered”. Regardless, earthquakes near reservoirs appear to be ubiquitous.

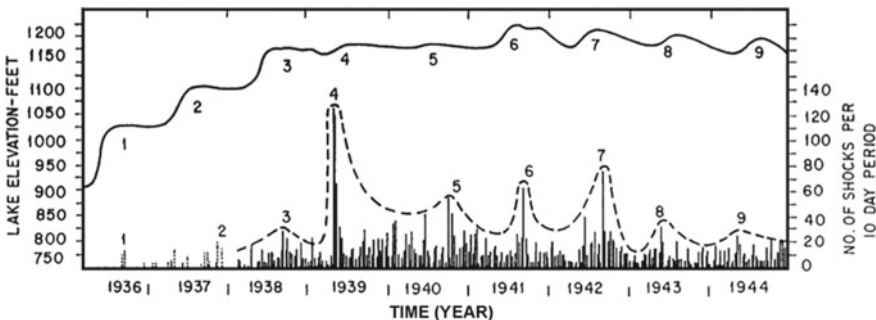


Fig. 4.6 Lake Mead water level and the local seismicity. The rises in water levels and the corresponding bursts of seismic activity are numbered. General trend of tremor-frequency variation is shown by dotted lines (after Carder 1945)

Seismicity associated with reservoirs has been documented at passive margins in the United States and South America and within stable cratons in Canada and Africa. Foulger et al. (2018) include 24 different reservoirs with associated earthquakes of magnitude >5 , large enough to cause damage. The Kariba dam between Zambia and Zimbabwe induced a M 6.2 event 5 years after impounding began (Gough and Gough 1970). A M 6.3 event in 1967 in Western India was induced by water impoundment behind the Koyna dam (Gupta and Rastogi 1976). In some cases, the seismicity peaks soon after filling and decays (e.g., Figure 4.7), suggesting that preexisting tectonic stresses were relieved. In the Koyna region, seismicity has been decreasing over the 50 years since the largest earthquake (Gupta 2018).

There are three ways in which filling a reservoir can induce earthquakes. First, the weight of the water can increase both elastic stresses and pore fluid pressure in response to the change in elastic stress—a poroelastic response. In this case, the orientation of faults and the background stress field will determine where and how faults get reactivated (e.g., Roeloffs 1988). Groundwater pore pressure should also rise as water seeps out of the reservoir and fluids migrate. The most distinctive signature of this second case would be a migration in space and time of the earthquakes away from the reservoir, consistent with pore pressure diffusion, i.e., the distance of the induced earthquakes from the reservoir increasing with the square root of time. This type of migration has been documented at some reservoirs (Talwani and Acree 1985; Tao et al. 2015). Third, induced seismicity may be modulated by the loading

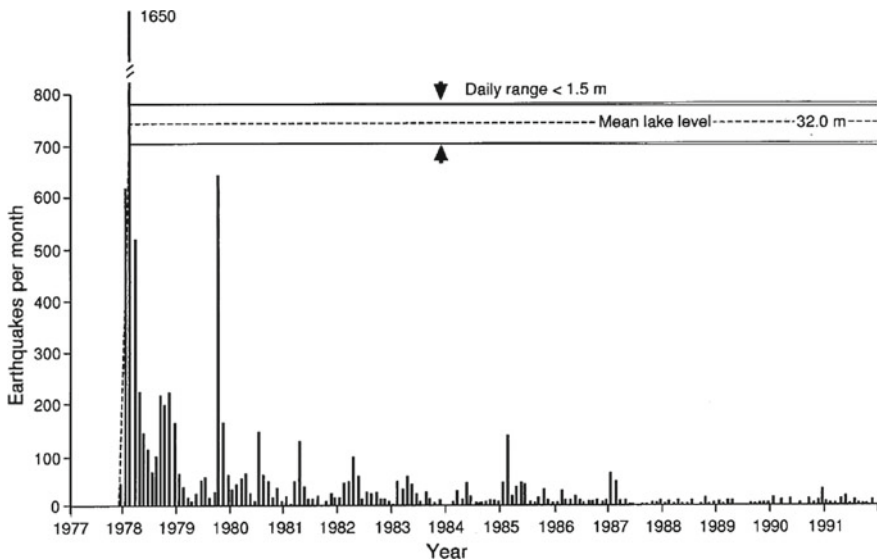


Fig. 4.7 Water level in the Monticello Reservoir, South Carolina, USA (dashed line) and the number of monthly earthquakes (histogram). Note that the peak seismicity rate reaches 1650 in one month. Seismicity returned towards background levels over a decade. From Talwani (1997)

rate, through the physics in rate-and-state friction. Annual modulation of reservoir-induced seismicity in the Koyna region appears to be influenced by loading and unloading rate as well as water level heights (Gupta 2018).

The largest proposed reservoir-induced earthquake is the May 2008 magnitude 7.9 Wenchuan earthquake (Klose 2012). Ge et al. (2009), using a two-dimensional model, suggested that it was the combination of pore pressure diffusion and surface loading that promoted slip (Fig. 4.8). This conclusion is sensitive to the assumed dip of the fault and three-dimensional effects and the proposal that the Wenchuan earthquake was induced has been contested (Deng et al. 2010; Zhou and Deng 2011; Tao et al. 2015). Tao et al. (2015) note that an expanding pattern of microseismicity likely documents the effects of pore pressure diffusion, favoring direct or indirect poroelastic triggering of seismic events that ended with the large earthquake. The case of the Wenchuan earthquake highlights the challenge in identifying induced earthquakes (Table 4.1).

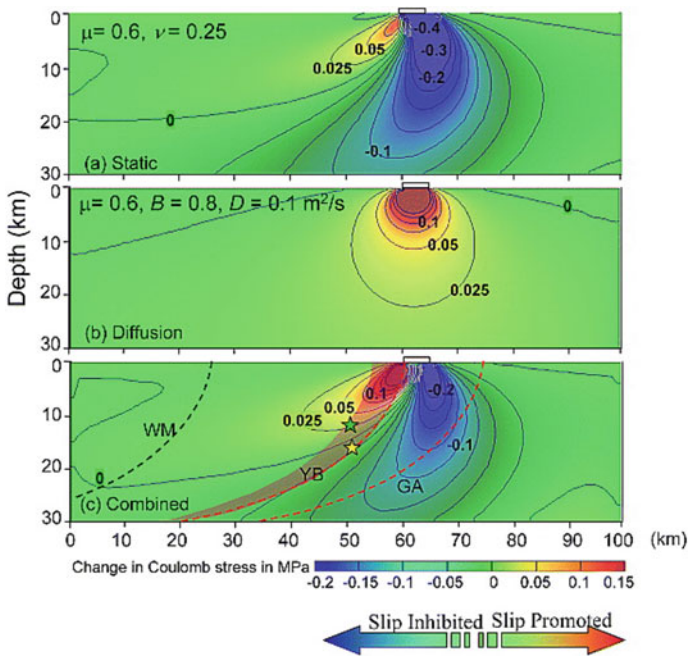


Fig. 4.8 Modeled change in Coulomb stress from reservoir filling **a**, pore pressure diffusion **b**, and the combined effects **c**. The two stars show inferred epicenter locations for the 2008 magnitude 7.9 Wenchuan earthquake. From Ge et al. (2009)

4.6 Natural Hydrological Triggering of Earthquakes

With insights gained from the engineered occurrences of hydrologically mediated earthquakes, we turn to possible examples of earthquakes triggered by natural hydrological and hydrogeological processes. Here, establishing a connection is more difficult because the magnitudes of the pressure and stress changes are usually smaller. However, their study is potentially more rewarding as they may provide unique insight into interactions between hydrogeological and tectonic processes.

Identifying seasonality in seismicity may be indicative of a hydrological influence on earthquakes. This influence could either be in the form of increased stress from the surface load of water or snow, or by changes in pore pressure that accompany groundwater recharge. The distinctive signature of the latter, as with reservoir-induced seismicity, is a time lag between the hydrological loading (groundwater recharge) and seismicity.

Seasonal variations of seismicity, while not ubiquitous, have been identified in regions with strong seasonality of recharge (e.g., Wolf et al. 1997; Bollinger et al. 2007; Johnson et al. 2017, 2020). For example, Heki (2003) identified a seasonal modulation of seismicity in Japan that he attributed to the loading of the surface by snow. Others have attributed seasonal variations of seismicity to groundwater recharge (e.g., Saar and Manga 2003; Christiansen et al. 2007; Montgomery-Brown et al. 2019). A correlation between precipitation and earthquakes (e.g., Roth et al. 1992; Jimenez and Garcia-Fernandez 2000; Hainzl et al. 2006; Kraft et al. 2006; Husen et al. 2007) supports the idea that pore pressure changes caused by recharge can influence seismicity. Over longer time scales, extended droughts and wet periods can also modulate seismicity (e.g., Hammond et al. 2019)

As with reservoir-induced earthquakes, surface loading, loading rate, and pore pressure changes can influence seismicity. In some cases, the loading appears to explain seasonal variations (e.g., Johnson et al. 2017; Craig et al. 2017; D'Agostino et al. 2018). Sometimes the seasonal variations are best correlated with stressing rate changes (Bettinelli et al. 2008) as expected from rate-and-state friction models for perpetual oscillatory loading (Heimisson and Avouac 2020). In other cases, the time lag between recharge and seismicity supports an origin from pore pressure diffusion (e.g., Saar and Manga 2003; Montgomery-Brown et al. 2019; Johnson et al. 2020). Figure 4.9 shows an example at the edge of Long Valley caldera, California. Here there are large seasonal variations in precipitation, with precipitation being dominated by snow, and recharge occurring as springtime snow melt. Downward migration of seismicity is apparent, and seismicity is ~37 times greater during spring snowmelt than the driest period (Montgomery-Brown et al. 2019). At regional scales, changes in hydrological loading, loading rate, and pore pressure changes may all contribute to seasonal variations in seismicity (Ueda and Kato 2019).

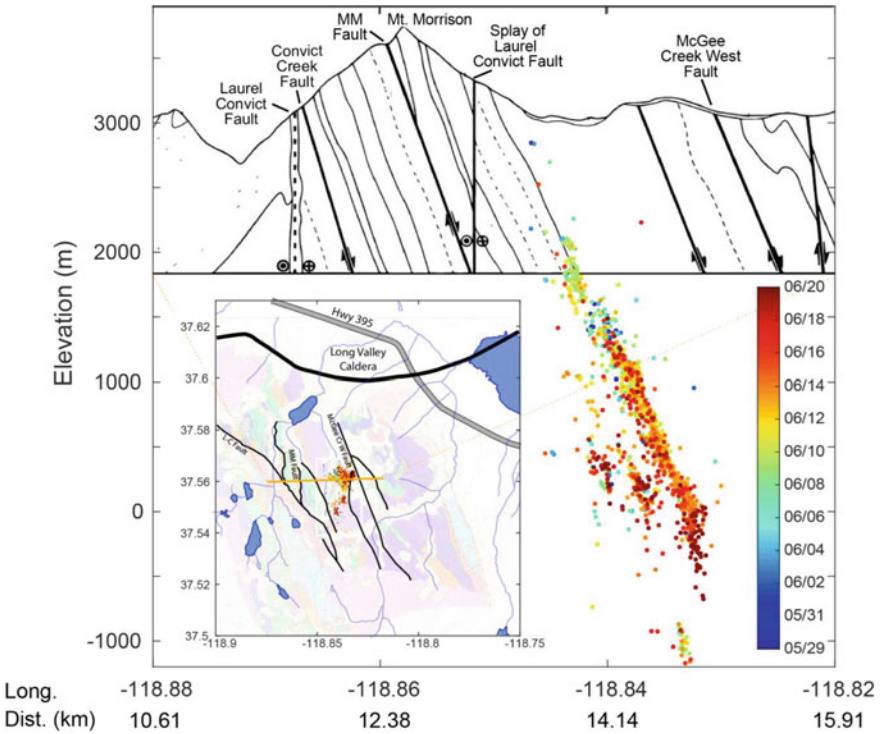


Fig. 4.9 Possible snowmelt triggered earthquakes at the edge of Long Valley caldera, California. Detected and relocated seismicity between May 28 and June 21, 2017 plotted on a geological cross-section. Color indicates date and shows downward migration over time. From Montgomery-Brown et al. (2019)

4.7 Earthquake Triggering of Earthquakes via Hydrological Processes

The stresses generated by earthquakes influence the occurrence of additional earthquakes. Many reviews have addressed such connections, including the role of (a) the coseismic static stress changes (e.g., Stein 1999; King and Deves 2015), (b) dynamic stresses associated with the passage of seismic waves (e.g., Kilb et al. 2000; Prejean and Hill 2018), and (c) the postseismic relaxation of stresses (Freed 2005). Here we focus exclusively on mechanisms and processes in which water may play a direct role.

In the near-field and intermediate-field, volumetric strains that accompany earthquakes will change pore pressure (e.g., Fig. 3.2). Stress changes resulting from post-seismic pore pressure diffusion have been invoked to explain aftershocks (e.g., Nur

and Booker 1972; Bosl and Nur 2002) and similar seismic sequences (Noir et al. 1997; Antonioli et al. 2005; Miller et al. 2004).

In the far-field, fluid flow and poroelastic pressure changes caused by static stress changes are negligible. Triggering of earthquakes in the far-field is thus dominated by dynamic stresses. Examples include seismicity 1250 km away from the M 7.3 Landers earthquake in 1992 (Hill et al. 1993); 1400 km away from the M 8.1 Tokachi-oki earthquake in 2003 (Miyazawa and Mori 2005); 11,000 km away from the M 8.0 Sumatra earthquake in 2004 (West et al. 2005); triggered events after the M 9.0 Tohoku-Oki earthquake in 2011 occurred in the USA, Russia, China, Ecuador and Mexico (Gonzalez-Huizar et al. 2012); a M 8.6 east Indian Ocean earthquake triggered aftershocks globally (Pollitz et al. 2012). Distant triggering is sometimes coincident with the passage of the seismic waves, usually the surface waves that have the greatest amplitudes at these distances. Both Love and Rayleigh waves appear to trigger earthquakes (Velasco et al. 2008). Moreover, triggered events are sometimes even correlated with a particular phase of the waves. As shown in Fig. 4.10 from West et al. (2005), triggered events occur during the maximum horizontal extension associated with the waves. Remote, triggered seismicity need not only be confined to the period of shaking and can sometimes continue for days or longer (e.g., Hill et al. 1993; Li et al. 2019).

Dynamic triggering may be ubiquitous, independent of tectonic environment (Velasco et al. 2008). However, dynamic triggering is most common in regions undergoing tectonic extension, where faults transition between locked and creeping, where human perturbations are large (van der Elst et al. 2013), and in geothermal and volcanic settings (Aiken and Peng 2014).

The underlying mechanisms of dynamic triggering are not known (Brodsky and van der Elst 2014). Because dynamic strains are small in the far-field and there is no net elastic strain after the passage of the seismic waves, triggering likely requires a mechanism to translate small and periodic strains into lasting change. Larger dynamic stresses do trigger larger earthquakes (Aiken et al. 2018). One mechanism could be by accelerating creep from rate-and-state friction. If rocks are damaged and close to failure, strain oscillations can lead to nonlinear elastic behavior leading to compaction or dilation and hence change stresses (Shalev et al. 2016). Another mechanism could be changes in pore pressure or permeability (which in turn allows pore pressure to change). The mechanisms discussed in other chapters for explaining the response of streams, groundwater level, geysers and mud volcanoes to earthquakes have also been invoked to explain dynamic triggering of earthquakes: nucleation of new bubbles (Crews and Cooper 2014), advective overpressure as bubbles shaken loose by seismic waves carry high pressure to more shallow depths (Linde et al. 1994), and breaching hydrologic barriers (Brodsky et al. 2003). Changes in permeability would explain observed delays in remote triggering (Parson et al. 2017). In contrast, however, West et al. (2005) conclude that their observations (shown in Fig. 4.10) can be simply explained by failure on normal faults caused by the shear stresses generated by the

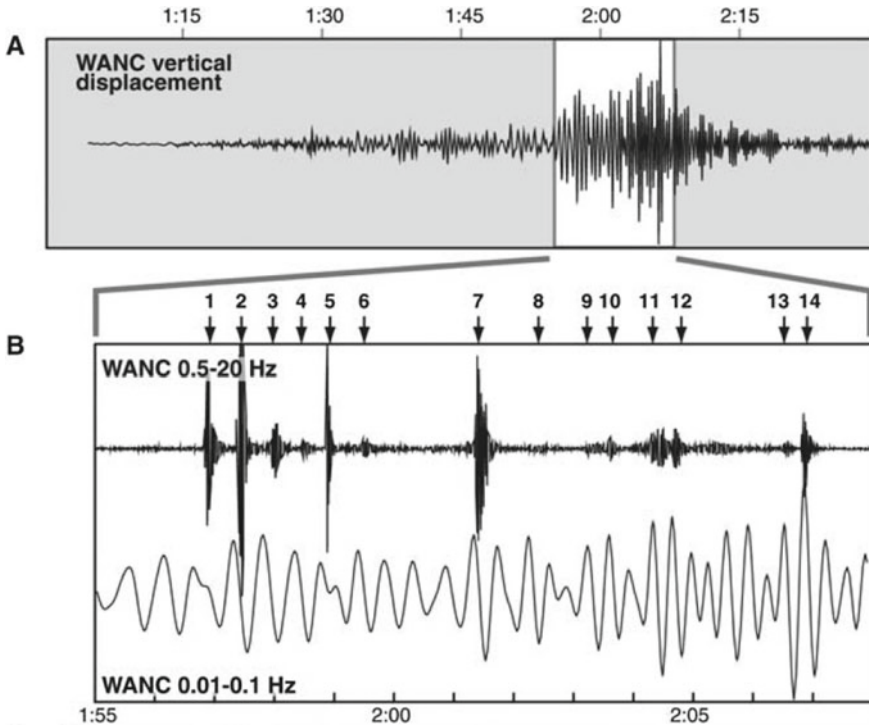


Fig. 4.10 Example of small, local earthquakes triggered in Alaska during the passage of teleseismic waves from the 26 December, 2004 Sumatra earthquake. **a** Vertical displacement with scale in hours and minutes. **b** Expanded view of surface waves filtered from 0.5 to 20 Hz and 0.01 to 0.1 Hz. The long period signals are from the Sumatra earthquake. The high frequency ground motion reveals the local triggered earthquakes. Modified from West et al. (2005)

seismic waves. Fluids only need play a role by making the pore pressure high enough that the small dynamic stresses can cause failure.

Identifying whether fluids play any role in causing aftershocks, seismic sequences, or far-field triggering is difficult to confirm observationally because pore pressure measurements are not available. At best, model simulations can be compared with the distribution of earthquakes in space and time, and plausibility can be assessed if the needed parameters are reasonable. New approaches for detecting small triggered earthquakes, such as machine learning, may at least help to improve the observational record (Tang et al. 2020).

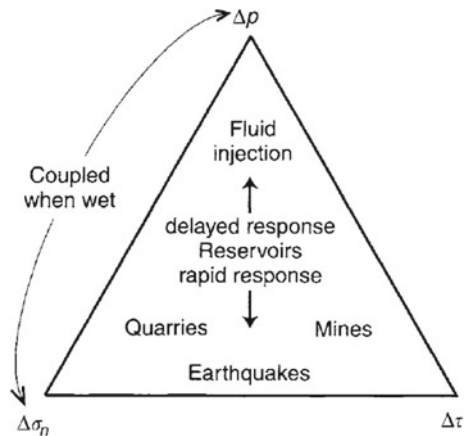
4.8 Concluding Remarks and Outlook

The theory of poroelasticity (Chap. 3) provides an explanation for how changes in fluid pressure and stress can influence seismicity. Coupled with models for how stress changes influence seismicity, in principle it is possible to forecast induced seismicity. However, there are many idealizations in these physical models and unknown parameters and properties that limit forecasts and hence our ability to identify whether and how earthquakes were induced. Figure 4.11 summarizes how stress and pressure perturbations influence induced seismicity.

There remain many open questions about human induced earthquakes. Why do some areas, for example California and North Dakota, seem to have few induced earthquakes? Is it just a matter of time? In Oklahoma, for example, it has been argued that there is a critical time for aquifers to be pressurized to the point that earthquakes can be induced. Or, is the hydrogeology such that pore pressure and poroelastic stress changes are not able to reach critical values? Can we identify signatures of induced earthquakes that are different from those that would otherwise have occurred? Progress, as briefly reviewed, has been made in forecasting induced earthquakes from hydromechanical models. But, is the subsurface too heterogeneous and with too many unknowns, that a useful forecast cannot be made prior to injection? With mitigation in mind, what measurements should be acquired prior to injection?

The rapid increase in the number of induced earthquakes around the world and their increasing magnitude are trends we should expect to continue. The scale of engineering projects has increased, hence their ability to change stresses in the subsurface. Figure 4.12 from Foulger et al. (2018) shows their compilation of the magnitude of induced earthquakes and the magnitude of the disturbance, characterized by the mass of fluid involved. Some of the included events may be controversial, but regardless, there is a pattern of increasing maximum earthquake size with magnitude of disturbance. Some of these proposed induced earthquakes are large enough to cause disasters depending on location. If carbon capture and sequestration expand

Fig. 4.11 Schematic illustration of the mechanisms that influence seismicity from perturbations in stress and the time scales over which responses will be seen. Reservoirs (in the middle) influence pore pressure, normal stress and shear stress. From McGarr et al. (2002)



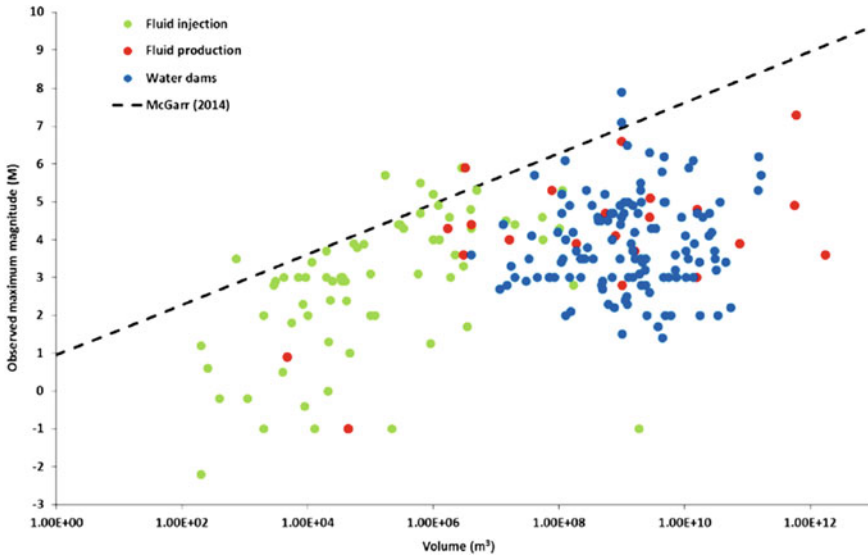


Fig. 4.12 Maximum earthquake magnitude as a function of the volume of fluid added, removed or accumulated in reservoirs. The dashed line is a proposed maximum size from McGarr (2014). From Foulger et al. (2018)

to become a climate-change solution, we can also expect new large-scale changes in subsurface stress. The public finds induced earthquakes less acceptable than natural ones, however, even if the earthquakes are a byproduct of climate change mitigation (McComas et al. 2016). The hope is that a better quantitative understanding of how earthquakes are induced can inspire management practices and inform decisions about where and how to inject and extract fluids.

References

- Aiken C, Peng Z (2014) Dynamic triggering of microearthquakes in three geothermal/volcanic regions of California. *J Geophys Res Solid Earth* 119:6992–7009
- Aiken C, Meng X, Hardebeck J (2018) Testing for the ‘predictability’ of dynamically triggered earthquakes in the Geysers geothermal field. *Earth Planet Sci Lett* 486:129–140
- Atkinson GM, Eaton DW, Ghofrani H et al (2016) Hydraulic fracturing and seismicity in the western Canada sedimentary basin. *Seismol Res Lett* 87:631–647
- Antonoli A, Piccinini D, Chiaraluca L, Cocco M (2005) Fluid flow and seismicity pattern: evidence from the 1997 Umbria-Marche (central Italy) seismic sequence. *Geophys Res Lett* 32:L10311. <https://doi.org/10.1029/2004GL022256>
- Bettinelli P, Avouac JP, Flouzat M et al (2008) Seasonal variations of seismicity and geodetic strain in the Himalaya induced by surface hydrology. *Earth Planet Sci Lett* 266(3–4):332–344
- Bollinger L, Perrier F, Avouac JP et al (2007) Seasonal modulation of seismicity in the Himalaya of Nepal. *Geophys Res Lett* 34:L08304. <https://doi.org/10.1029/2006GL029192>

- Bosl WJ, Nur A (2002) Aftershocks and pore fluid diffusion following the 1992 Landers earthquake. *J Geophys Res Solid Earth* 107(B12):2366. <https://doi.org/10.1029/2001JB000155>
- Brodsky EE, van der Elst NJ (2014) The uses of dynamic earthquake triggering. *Annu Rev Earth Planet Sci* 42:317–339
- Brodsky EE, Roeloffs E, Woodcock D et al (2003) A mechanism for sustained groundwater pressure changes induced by distant earthquakes. *J Geophys Res Solid Earth* 108(B8):2390. <https://doi.org/10.1029/2002JB002321>
- Candela T, Wassing B, Ter Heege J et al (2018) How earthquakes are induced. *Science* 360(6389):598–600
- Cappa F, Scuderi MM, Collettini C et al (2019) Stabilization of fault slip by fluid injection in the laboratory and in situ. *Sci Adv* 5:eau4065. <https://doi.org/10.1126/sciadv.aau4065>
- Carder DS (1945) Seismic investigations in the Boulder Dam area, 1940–1944, and the influence of reservoir loading on local earthquake activity. *Bull Seismol Soc Am* 35(4):175–192
- Christiansen LB, Hurwitz S, Ingebritsen SE (2007) Annual modulation of seismicity along the San Andreas Fault near Parkfield, CA. *Geophys Res Lett* 34(4):L04306. <https://doi.org/10.1029/2006GL028634>
- Chang KW, Yoon H, Martinez MJ (2018) Seismicity rate surge on faults after shut-in: poroelastic response to fluid injection. *Bull Seismol Soc Am* 108(4):1889–1904
- Craig TJ, Chanard K, Calais E (2017) Hydrologically-driven crustal stresses and seismicity in the new madrid seismic zone. *Nat Commun* 8(1):1–11
- Crews JB, Cooper CA (2014) Experimental evidence for seismically initiated gas bubble nucleation and growth in groundwater as a mechanism for coseismic borehole water level rise and remotely triggered seismicity. *J Geophys Res Solid Earth* 119(9):7079–7091
- D'Agostino N, Silverii F, Amoroso O et al (2018) Crustal deformation and seismicity modulated by groundwater recharge of karst aquifers. *Geophys Res Lett* 45(22):12–253
- Davis SD, Frohlich C (1993) Did (or will) fluid injection cause earthquakes?—criteria for a rational assessment. *Seismol Res Lett* 64(3–4):207–224
- Deng K, Zhou S, Wang R et al (2010) Evidence that the 2008 M_w 7.9 Wenchuan earthquake could not have been induced by the Zippingpu Reservoir. *Bull Seismol Soc Am* 100(5B):2805–2814
- Dieterich JH (1994) A constitutive law for rate of earthquake production and its application to earthquake clustering. *J Geophys Res* 99:2601–2618. <https://doi.org/10.1029/93JB02581>
- Ellsworth WL (2013) Injection-induced earthquakes. *Science* 341(6142):1225–942
- EPA (2011) Proceedings of the technical workshops for the hydraulic fracturing study: water resources management, EPA 600/R-11/048
- Evans DM (1966) The Denver area earthquakes and the Rocky Mountain Arsenal disposal well. *Mt Geol* 3:23–26
- Foulger GR, Wilson MP, Gluyas JG et al (2018) Global review of human-induced earthquakes. *Earth Sci Rev* 178:438–514
- Freed AM (2005) Earthquake triggering by static, dynamic, and postseismic stress transfer. *Ann Rev Earth Planet Sci* 33:335–367
- Ge S, Liu M, Lu N et al (2009) Did the Zippingpu reservoir trigger the 2008 Wenchuan earthquake? *Geophys Res Lett* 36:L20315. <https://doi.org/10.1029/2009GL040349>
- Goebel TH, Brodsky EE (2018) The spatial footprint of injection wells in a global compilation of induced earthquake sequences. *Science* 361(6405):899–904
- Goebel TH, Rosson Z, Brodsky EE et al (2019) Aftershock deficiency of induced earthquake sequences during rapid mitigation efforts in Oklahoma. *Earth Planet Sci Lett* 522:135–143
- Gomberg J, Wolf L (1999) Possible cause for an improbable earthquake: the 1997 M_w 4.9 southern Alabama earthquake and hydrocarbon recovery. *Geology* 27:367–37
- González PJ, Tiampo KF, Palano M et al (2012) The 2011 Lorca earthquake slip distribution controlled by groundwater crustal unloading. *Nat Geosci* 5(11):821–825
- Gonzalez-Huizar H, Velasco AA, Peng Z, Castro RR (2012) Remote triggered seismicity caused by the 2011, M_w 9.0 Tohoku-Oki, Japan earthquake. *Geophys Res Lett* 39(10):L10302. <https://doi.org/10.1029/2012gl051015>

- Gough DI, Gough WI (1970) Load-induced earthquakes at Lake Kariba—II. *Geophys J Int* 21(1):79–101
- Grigoli F, Cesca S, Rinaldi AP et al (2018) The November 2017 Mw 5.5 Pohang earthquake: a possible case of induced seismicity in South Korea. *Science* 360:1003–1006
- Guglielmi Y, Cappa F, Avouac JP et al (2015) Seismicity triggered by fluid injection—induced aseismic slip. *Science* 348(6240):1224–1226
- Gupta HK (1992) Reservoir induced earthquakes. Elsevier
- Gupta HK (2018) Reservoir triggered seismicity (RTS) at Koyna, India, over the Past 50 Yrs. *Bull Seismol Soc Am* 108(5B):2907–2918
- Gupta HK (2002) A review of recent studies of triggered earthquakes by artificial water reservoirs with special emphasis on earthquakes in Koyna, India. *Earth Sci Rev* 58(3–4):279–310
- Gupta HK, Rastogi BK (1976) Dams and earthquakes. Elsevier, Amsterdam, p 229
- Hainzl S, Kraft T, Wassermann J et al (2006) Evidence for rainfall-triggered earthquake activity. *Geophys Res Lett* 33(19):L19303. <https://doi.org/10.1029/2006gl027642>
- Hammond WC, Kreemer C, Zaliapin I, Blewitt G (2019) Drought-triggered magmatic inflation, crustal strain, and seismicity near the long Valley Caldera, Central Walker Lane. *J Geophys Res Solid Earth* 124(6):6072–6091
- Hartline C, Walters M, Wright M, Rawal C, Garcia J, Farison J (2019) The Northwest Geysers enhanced geothermal system demonstration project, the Geysers, California (No. DE-FC36-08G018201). Geysers Power Company, LLC
- Healy JH, Rubey WW, Griggs DT et al (1968) The Denver earthquakes. *Science* 161(3848):1301–1310
- Heki K (2003) Snow load and seasonal variation of earthquake occurrence in Japan. *Earth Planet Sci Lett* 207(1–4):159–164
- Heimisson ER, Avouac J (2020) Analytical prediction of seismicity rate due to tides and other oscillating stress. *EarthArXiv*. <https://doi.org/10.31223/osf.io/duvq2>
- Hill DP, Reasenber PA, Michael A et al (1993) Seismicity remotely triggered by the magnitude 7.3 Landers, California, earthquake. *Science* 260(5114):1617–1623
- Husen S, Bachmann C, Giardini D (2007) Locally triggered seismicity in the central Swiss Alps following the large rainfall event of August 2005. *Geophys J Int* 171(3):1126–1134
- Hsieh PA, Bredehoeft JD (1981) A reservoir analysis of the Denver earthquakes: a case of induced seismicity. *J Geophys Res Solid Earth* 86(B2):903–920
- Jiménez MJ, García-Fernández M (2000) Occurrence of shallow earthquakes following periods of intense rainfall in Tenerife, Canary Islands. *J Volcanol Geoth Res* 103(1–4):463–468
- Johnson CW, Fu Y, Bürgmann R (2017) Seasonal water storage, stress modulation, and California seismicity. *Science* 356(6343):1161–1164
- Johnson CW, Fu Y, Bürgmann R (2020) Hydrospheric modulation of stress and seismicity on shallow faults in southern Alaska. *Earth Planet Sci Lett* 530:115904. <https://doi.org/10.1016/j.epsl.2019.1115904>
- Keranen KM, Weingarten M, Abers GA et al (2014) Sharp increase in central Oklahoma seismicity since 2008 induced by massive wastewater injection. *Science* 345(6195):448–451
- Keranen KM, Weingarten M (2018) Induced seismicity. *Ann Rev Earth Planet Sci* 46:149–174
- Kilb D, Gomberg J, Bodin P (2000) Triggering of earthquake aftershocks by dynamic stresses. *Nature* 408(6812):570–574
- Kim KH, Ree JH, Kim Y et al. (2018) Assessing whether the 2017 Mw 5.4 Pohang earthquake in South Korea was an induced event. *Science* 360(6392):1007–1009
- King GCP, Devès MH (2015) Fault interaction, earthquake stress changes, and the evolution of seismicity. In: *Treatise of Geophysics*, 2nd ed. Elsevier
- Klose CD (2012) Evidence for anthropogenic surface loading as trigger mechanism of the 2008 Wenchuan earthquake. *Environ Earth Sci* 66(5):1439–1447
- Kolawole F, Johnston CS, Morgan CB et al (2019) The susceptibility of Oklahoma’s basement to seismic reactivation. *Nat Geosci* 12(10):839–844

- Kraft T, Wassermann J, Schmedes E et al (2006) Meteorological triggering of earthquake swarms at Mt. Hochstaufen, SE-Germany. *Tectonophysics* 424(3–4):245–258
- Langenbruch C, Zoback MD (2016) How will induced seismicity in Oklahoma respond to decreased saltwater injection rates? *Sci Adv* 2(11):e1601542
- Langenbruch C, Weingarten M, Zoback MD (2018) Physics-based forecasting of man-made earthquake hazards in Oklahoma and Kansas. *Nat Commun* 9(1):1–10
- Li T, Gu YJ, Wang Z et al (2019) Spatiotemporal variations in crustal seismic anisotropy surrounding induced earthquakes near Fox Creek, Alberta. *Geophys Res Lett* 46(10):5180–5189
- Linde AT, Sacks IS, Johnston MJ, Hill DP, Bilham RG (1994) Increased pressure from rising bubbles as a mechanism for remotely triggered seismicity. *Nature* 371(6496):408–410
- Majer EL, Baria R, Stark M et al (2007) Induced seismicity associated with enhanced geothermal systems. *Geothermics* 36(3):185–222
- McComas KA, Lu H, Keranen KM et al (2016) Public perceptions and acceptance of induced earthquakes related to energy development. *Energ Pol* 99:27–32
- McGarr A, Simpson D, Seeber L (2002) Case histories of induced and triggered seismicity. *Int Handb Earthquake Eng Seismol* 81(A):647–664
- McGarr A (2014) Maximum magnitude earthquakes induced by fluid injection. *J Geophys Res Solid Earth* 119(2):1008–1019
- McGarr A, Barbour AJ (2018) Injection-induced moment release can also be aseismic. *Geophys Res Lett* 45(11):5344–5351
- Miller SA, Collettini C, Chiaraluce L et al (2004) Aftershocks driven by a high-pressure CO₂ source at depth. *Nature* 427(6976):724–727
- Miyazawa M, Mori J (2005) Detection of triggered deep low-frequency events from the 2003 Tokachi-oki earthquake. *Geophys Res Lett* 32(10):L10307. <https://doi.org/10.1029/2005gl022539>
- Montgomery-Brown EK, Shelly DR, Hsieh PA (2019) Snowmelt-triggered earthquake swarms at the margin of Long Valley Caldera, California. *Geophys Res Lett* 46(7):3698–3705
- Noir J, Jacques E, Bekri S et al (1997) Fluid flow triggered migration of events in the 1989 Dobi earthquake sequence of Central Afar. *Geophys Res Lett* 24(18):2335–2338
- Nur A, Booker JR (1972) Aftershocks caused by pore fluid flow? *Science* 175(4024):885–887
- Parsons T, Malagnini L, Akinci A (2017) Nucleation speed limit on remote fluid-induced earthquakes. *Sci Adv* 3(8):e1700660
- Peterie SL, Miller RD, Intfen JW et al (2018) Earthquakes in Kansas induced by extremely far-field pressure diffusion. *Geophys Res Lett* 45(3):1395–1401
- Pollitz FF, Stein RS, Sevilgen V (2012) The 11 April 2012 east Indian Ocean earthquake triggered large aftershocks worldwide. *Nature* 490(7419):250–253
- Prejean SG, Hill DP (2018) The influence of tectonic environment on dynamic earthquake triggering: a review and case study on Alaskan volcanoes. *Tectonophysics* 745:293–304
- Roeloffs EA (1988) Fault stability changes induced beneath a reservoir with cyclic variations in water level. *J Geophys Res Solid Earth* 93(B3):2107–2124
- Roth P, Pavoni N, Deichmann N (1992) Seismotectonics of the eastern Swiss Alps and evidence for precipitation-induced variations of seismic activity. *Tectonophysics* 207(1–2):183–197
- Saar MO, Manga M (2003) Seismicity induced by seasonal groundwater recharge at Mt. Hood, Oregon. *Earth Planet Sci Lett* 214(3–4):605–618
- Segall P (1989) Earthquakes triggered by fluid extraction. *Geology* 17(10):942–946
- Segall P, Fitzgerald SD (1998) A note on induced stress changes in hydrocarbon and geothermal reservoirs. *Tectonophysics* 289(1–3):117–128
- Segall P, Lu S (2015) Injection-induced seismicity: poroelastic and earthquake nucleation effects. *J Geophys Res Solid Earth* 120(7):5082–5103
- Segall P, Grasso JR, Mossop A (1994) Poroelastic stressing and induced seismicity near the Lacq gas field, southwestern France. *J Geophys Res Solid Earth* 99(B8):15423–15438
- Shalev E, Kurzon I, Doan ML et al (2016) Sustained water-level changes caused by damage and compaction induced by teleseismic earthquakes. *J Geophys Res Solid Earth* 121(7):4943–4954

- Shapiro SA, Kummerow J, Dinske C et al (2006) Fluid induced seismicity guided by a continental fault: injection experiment of 2004/2005 at the German Deep Drilling Site (KTB). *Geophys Res Lett* 33(1):L01309. <https://doi.org/10.1029/2005gl024659>
- Simpson DW (1976) Seismicity changes associated with reservoir loading. *Eng Geol* 10(2–4):123–150
- Stein RS (1999) The role of stress transfer in earthquake occurrence. *Nature* 402(6762):605–609
- Tadokoro K, Ando M, Nishigami KY (2000) Induced earthquakes accompanying the water injection experiment at the Nojima fault zone, Japan: seismicity and its migration. *J Geophys Res Solid Earth* 105(B3):6089–6104
- Talwani P (1997) On the nature of reservoir-induced seismicity. *Pure Appl Geophys* 150(3–4):473–492
- Talwani P, Acree S (1985) Pore pressure diffusion and the mechanism of reservoir-induced seismicity. In: *Earthquake prediction*. Birkhäuser, Basel, pp 947–965
- Tang V, Seetharaman P, Chao K et al (2020) Automating the detection of dynamically triggered earthquakes via a deep metric learning algorithm. *Seismol Res Lett*. <https://doi.org/10.1785/0220190165>
- Tao W, Masterlark T, Shen ZK (2015) Impoundment of the Zipingpu reservoir and triggering of the 2008 Mw 7.9 Wenchuan earthquake, China. *J Geophys Res Solid Earth* 120(10):7033–7047
- Ueda T, Kato A (2019) Seasonal variations in Crustal Seismicity in San-in District, Southwest Japan. *Geophys Res Lett* 46(6):3172–3179
- Van der Elst NJ, Savage HM, Keranen KM et al (2013) Enhanced remote earthquake triggering at fluid-injection sites in the midwestern United States. *Science* 341(6142):164–167
- Van der Elst NJ, Page MT, Weiser DA (2016) Induced earthquake magnitudes are as large as (statistically) expected. *J Geophys Res Solid Earth* 121(6):4575–4590
- Velasco AA, Hernandez S, Parsons T et al (2008) Global ubiquity of dynamic earthquake triggering. *Nat Geosci* 1(6):375–379
- Verruijt A (1969) An interface problem with a source and a sink in the heavy fluid. *J Hydrol* 8(2):197–206
- Wang L, Kwiatek G, Rybacki E (2019) Laboratory study on fluid-induced fault slip behavior: the role of fluid pressurization rate. *Geophys Res Lett* 47:e2019GL086627. <https://doi.org/10.1029/2019gl086627>
- West M, Sánchez JJ, McNutt SR (2005) Periodically triggered seismicity at Mount Wrangell, Alaska, after the Sumatra earthquake. *Science* 308(5725):1144–1146
- Wetzler N, Shalev E, Göbel T et al (2019) Earthquake swarms triggered by groundwater extraction near the Dead Sea Fault. *Geophys Res Lett* 46(14):8056–8063
- Wolf LW, Rowe CA, Horner RB (1997) Periodic seismicity near Mt. Ogden on the Alaska-British Columbia border: a case for hydrologically triggered earthquakes? *Bull Seismol Soc Am* 87(6):1473–1483
- Zhai G, Shirzaei M, Manga M et al (2019) Pore-pressure diffusion, enhanced by poroelastic stresses, controls induced seismicity in Oklahoma. *Proc Natl Acad Sci* 116(33):16228–16233
- Zhai G, Shirzaei M, Manga M (2020) Elevated seismic hazard in Kansas due to high volume injections in Oklahoma. *Geophys Res Lett* 47:e2019GL085705. <https://doi.org/10.1029/2019gl085705>
- Zhou S, Deng K (2011) Reply to “Comment on ‘Evidence that the 2008 Mw 7.9 Wenchuan earthquake could not have been induced by the Zipingpu reservoir’ by Kai Deng, Shiyong Zhou, Rui Wang, Russell Robinson, Cuiping Zhao, and Wanzheng Cheng” by Shemin Ge. *Bull Seismol Soc Am* 101(6):3119–3120
- Zoback MD, Zinke J C (2002) Production-induced normal faulting in the Valhall and Ekofisk oil fields. In: *The mechanism of induced seismicity*. Birkhäuser, Basel, pp 403–420

Open Access This chapter is licensed under the terms of the Creative Commons Attribution 4.0 International License (<http://creativecommons.org/licenses/by/4.0/>), which permits use, sharing, adaptation, distribution and reproduction in any medium or format, as long as you give appropriate credit to the original author(s) and the source, provide a link to the Creative Commons license and indicate if changes were made.

The images or other third party material in this chapter are included in the chapter's Creative Commons license, unless indicated otherwise in a credit line to the material. If material is not included in the chapter's Creative Commons license and your intended use is not permitted by statutory regulation or exceeds the permitted use, you will need to obtain permission directly from the copyright holder.



Chapter 5

Response to Tides, Barometric Pressure and Seismic Waves



On the shores of the Bætis (now the Guadalquivir River, Spain), there is a town where the wells become lower when the tide rises, and fill again when it ebbs; while at other times they remain stationary. The same thing occurs in one well in the town of Hispalis (now Seville, Spain), while there is nothing peculiar in the other wells.

Pliny the Elder, *Natural History*, Chapter 100, translation of Bostock 1855).

Abstract Groundwater responses to Earth tides and barometric pressure have long been reported and increasingly used in hydrogeology to advance our understanding of groundwater systems. The response of groundwater to seismic waves has also been used in recent years to study the interaction between earthquakes and fluids in the crust. These methods have gained popularity for monitoring groundwater systems because they are both effective and economical. This chapter reviews the response of groundwater system to Earth tides, barometric pressure, and seismic waves as a continuum of poroelastic responses to oscillatory forcing across a broad range of frequency.

5.1 Introduction

Pliny the Elder (AD 23–79) may be the first to report that the water level in a coastal well responds to the rise and fall of ocean tides. The basic principle of tidal and barometric effects on groundwater may be illustrated by using Fig. 5.1. Barometric pressure, ocean tides and the Earth's solid tides cause poroelastic deformation of the aquifer, inducing changes of pore pressure and groundwater flow between aquifers and wells. Such changes of water level in wells may be measured, analyzed and interpreted to reveal the hidden information on the hydraulic properties of the aquifer and their changes.

In the past few decades a great amount of work has been done to use the tidal response of aquifers to estimate the hydraulic properties of groundwater systems

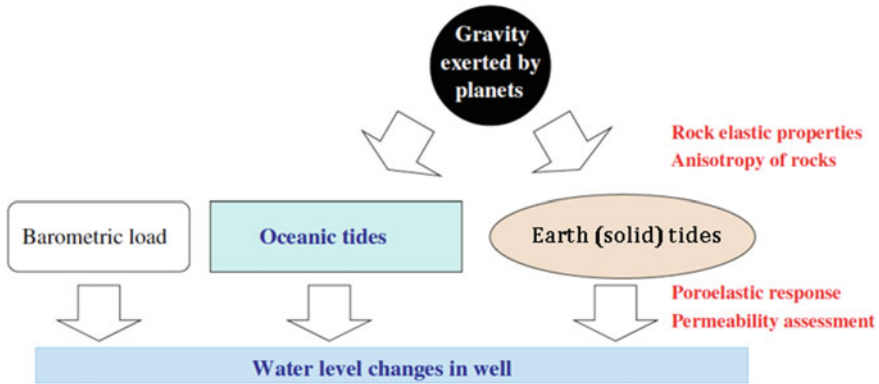


Fig. 5.1 Poroelastic response of solid Earth to tidal, barometric and other types of disturbances and water level changes in wells (modified from Doan et al. 2006)

(e.g., Hsieh et al., 1987; Roeloffs, 1996) and to compare these properties before and after earthquakes in order to quantify earthquake effects (e.g., Elkhoury et al. 2006; Xue et al. 2013; Yan et al. 2014). In addition, the tidal response of aquifers was also found to be particularly sensitive to subsurface disturbances such as mining (Shi et al. 2020). The ocean tides, though much bigger in amplitude than the solid tides (Earth tides) along the coast, are complicated because they depend sensitively on the local bathymetry and the configuration of the coast. The Earth tides, on the other hand, are much better characterized and are therefore more useful in the study of the groundwater system. In the following three sections we introduce the principles of tides, the tide-induced deformation of the solid Earth, i.e., the Earth tides, the response of groundwater to the Earth tides, and the models that are used to interpret the tidal responses of water level.

Groundwater level also responds to changes of the barometric pressure, and the study of this response can provide important insight to the hydraulic properties of both the aquifer and the aquitard (e.g., Jacob 1940; Rojstaczer 1988; Olding et al. 2015). A welcoming development is a joint analysis of the tidal and the barometric responses in some recent studies to evaluate earthquake effects on groundwater systems (Barbour et al. 2019; Zhang-Shi et al. 2019; Zhang-Wang et al. 2019). We review in a separate section the principles of the barometric response of the water level in wells and the existing applications to earthquake hydrology.

At the high-frequency end of the continuum is the response of groundwater to seismic waves. It has been known for a long time that groundwater responds to seismic waves (e.g., Byerly and Blanchard 1935). Some recent efforts have made use of this response to estimate aquifer properties (Barbour et al. 2019; Shih 2009; Sun et al. 2019, 2020), based on a model developed by Cooper et al. (1965). Such efforts may provide useful understanding on the dependence of aquifer properties on the frequency of the forcing mechanisms. We review in another separate section

the principles of water-level response to seismic waves and the model used in its interpretation and application to earthquake hydrology.

Finally, fractures in the shallow crust may significantly affect the response of water level to tides, barometric pressure, and seismic waves. This aspect has not received adequate attention.

5.2 Tidal Potential

The tidal acceleration due to the gravitational attraction of a planet with center P and mass M , at a point N on the surface of the Earth with center at O , is

$$g = GM \left(\frac{\vec{PN}}{PN^3} - \frac{\vec{PO}}{PO^3} \right). \tag{5.1}$$

Given the notations in Fig. 5.2, we may express the tidal potential W at a point N on Earth's surface due to the planet P with mass M as

$$W = \frac{GM}{s}, \tag{5.2}$$

where M is the mass of the planet. Expressing $1/s$ in terms of a , R and α , we have

$$\begin{aligned} \frac{1}{s} &= \frac{1}{(a^2 + R^2 - 2aR \cos \alpha)^{1/2}} = \frac{1}{R} \left[1 - 2 \frac{a}{R} \cos \alpha + \left(\frac{a}{R} \right)^2 \right]^{-1/2} \\ &= \frac{1}{R} \left[1 + \left(\frac{a}{R} \right) \cos \alpha + \left(\frac{a}{R} \right)^2 \frac{3 \cos^2 \alpha - 1}{2} + \left(\frac{a}{R} \right)^3 \frac{5 \cos^3 \alpha - 3 \cos \alpha}{2} + \dots \right] \end{aligned}$$

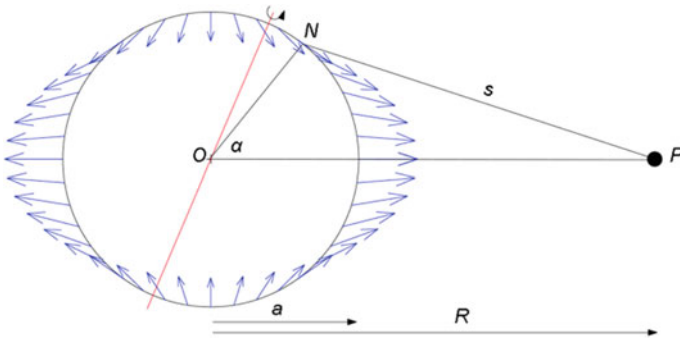


Fig. 5.2 Tidal displacement (exaggerated) of the equipotential surface on Earth's surface due to planet P

$$= \frac{1}{R} \left[1 + \sum_1^{\infty} \left(\frac{a}{R} \right)^n P_n(\cos \alpha) \right], \quad (5.3)$$

where $P_n(\cos \alpha)$ are the Legendre polynomials of order n .

Hence the gravitational potential W may be expressed as

$$W = \frac{GM}{R} \left[1 + \sum_1^{\infty} \left(\frac{a}{R} \right)^n P_n(\cos \alpha) \right]. \quad (5.4)$$

The first term is a constant and does not give rise to a force. The second term gives rise to the attraction at the centers, i.e., $GM \left(\frac{\vec{PO}}{PO^3} \right)$. Thus, the tidal potential consists of the remaining terms. Furthermore, since the ratio a/R is small, $(a/R)^n$ decreases rapidly with n , only the term with $n = 2$ is usually considered in the studies of Earth tides, and we may express the tidal potential approximately as

$$W_2 = \frac{GM}{R} \left(\frac{a}{R} \right)^2 \frac{3 \cos^2 \alpha - 1}{2}. \quad (5.5)$$

Finally, expressing $\cos \alpha$ in terms of the latitudes and longitudes of the observation point (λ_N, ϕ_N) and of the planet (λ_P, ϕ_P) and ωt , where ω is the angular frequency of Earth's rotation, we have (e.g., Doan et al. 2006)

$$W_2 = \frac{GMa^2}{R^3} \left\{ \begin{array}{l} \frac{1}{32} [\cos^2 \lambda_N \cos^2 \lambda_P \cos(2\omega t - 2\phi_P)] \\ + \frac{3}{8} [\sin(2\lambda_N) \sin(2\lambda_P) \cos(\omega t - \phi_P)] \\ + \frac{1}{32} [3 \cos(2\lambda_N - 1)][3 \cos(2\lambda_P - 1)] \end{array} \right\}. \quad (5.6)$$

The first term inside the parenthesis is the semi-diurnal tide that produces the two symmetrical bulges in Fig. 5.2; the second term is the diurnal tide due to the inclination of the orbit of the planet (Moon) to the equator; the third term is independent of the rotation of the Earth and is thus a constant.

In reality, the potential is more complicated due to the facts that the Earth's orbit about the Sun and the Moon's orbit about the Earth are both elliptical rather than circular, the Moon's orbital plane does not align with Earth's equator and the Earth's rotation is not aligned with the ecliptic. There are thus numerous tides (see Fig. 5.3), but most of these tides are too small to be clearly recorded in water level data and thus are not used in groundwater studies. The solar tides are affected by thermally induced changes in the atmospheric pressure, which are difficult to correct. As a consequence, the most often used tides for hydrological studies are the semi-diurnal lunar tide M_2 and the diurnal lunar tide O_1 .

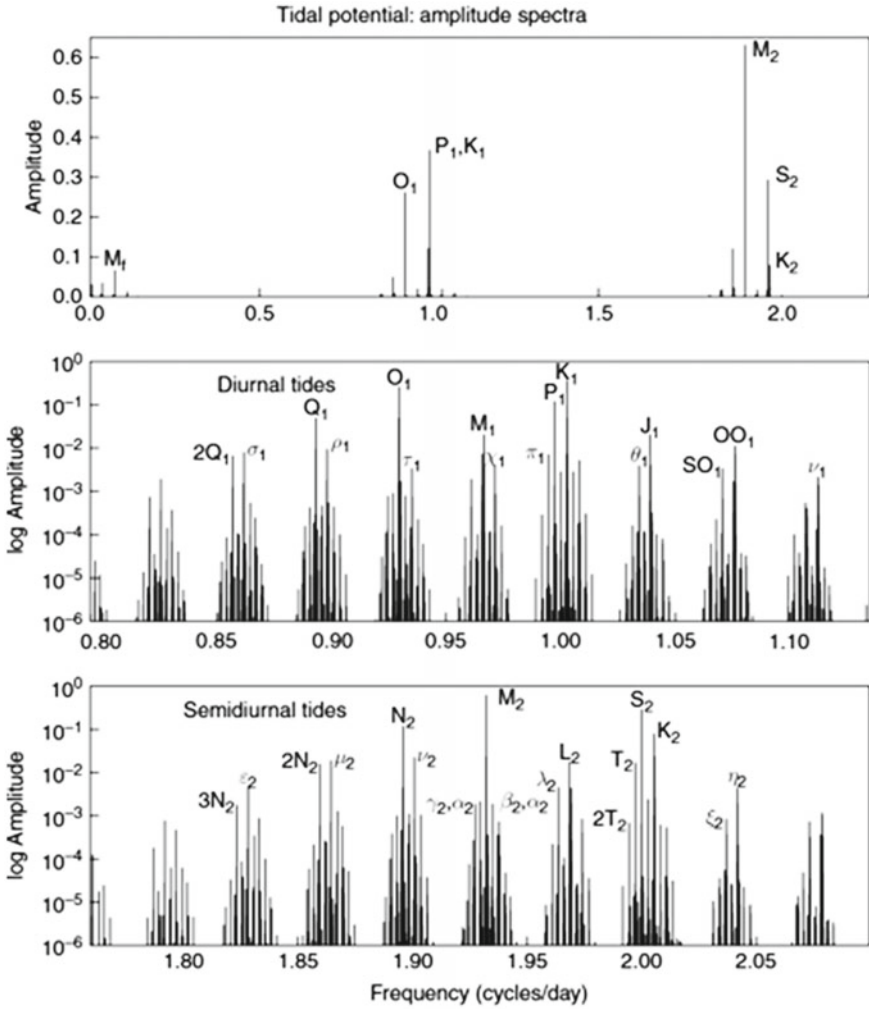


Fig. 5.3 Spectrum of the tidal potential on Earth’s surface shown as the amplitudes of the tidal harmonics (from Agnew 2007). The larger harmonics are shown in the top diagram and the diurnal and the semi-diurnal harmonics in the lower two diagrams

5.3 Earth Tides

Figure 5.4 shows an example of the Earth tides in Oklahoma recorded by a three-component, broadband seismometer. Because of the long periods of the Earth tides, the tidal deformations occur at mechanical equilibrium, i.e., there is no acceleration. The ground velocity in the records (Fig. 5.4) may be integrated with time to yield the surface displacements that, in turn, may be used to calculate the tidal strain at

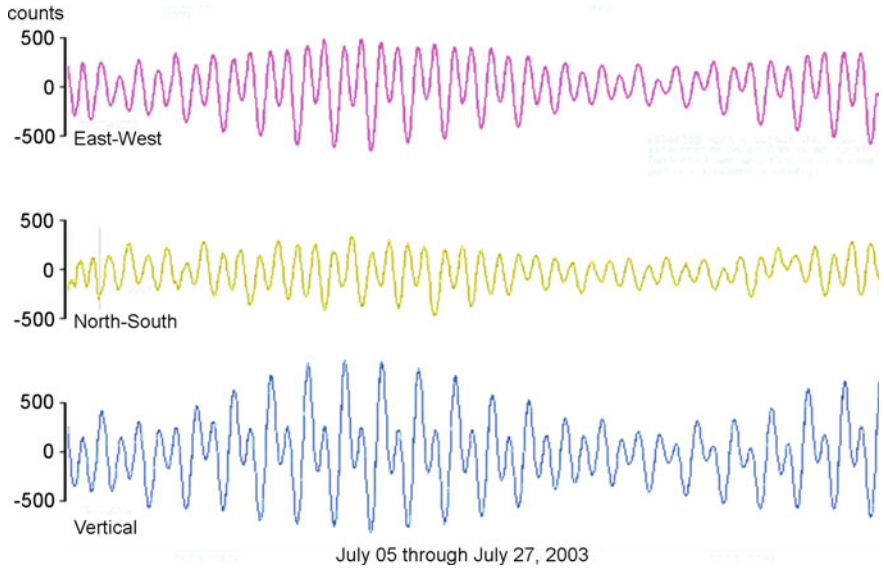


Fig. 5.4 Earth tides recorded by a three-component, broadband seismometer in a 840 m deep well in Leonard, Oklahoma (Oklahoma Geological Survey Observatory)

this location (Eqs. 5.8 and 5.9). GPS measurements have also been used to measure tidal displacements at many stations.

Love (1911) associated the tidal displacement to the tidal potential by the following relations:

$$u_r = \sum_n \frac{h_n}{g} W_n \tag{5.7a}$$

$$u_\theta = \sum_n \frac{l_n}{g} \frac{\partial W_n}{\partial \theta} \tag{5.7b}$$

$$u_\phi = \sum_n \frac{l_n}{g} \frac{1}{\sin \theta} \frac{\partial W_n}{\partial \phi} \tag{5.7c}$$

where h_n is the Love number, l_n is the Shida number, and (r, θ, ϕ) are the spherical coordinates of the point of interest.

From the tidal displacements, the tidal strains may be evaluated from the tidal potential:

$$\epsilon_{rr} = \frac{\partial u_r}{\partial r} = \sum_n \frac{h_n}{ga} \frac{\partial W_n}{\partial r} \tag{5.8a}$$

Table 5.1 Love numbers calculated from several Earth models (from Doan et al. 2006)

Software	h_2	l_2	k_2
Wilhelm et al. (1997, p. 46)	0.6033	0.0838	0.2980
PREM	0.6032	0.0839	0.2990
Gutenberg-Bullen	0.6114	0.0832	0.3040
MT80W (MOLODENSKY model)	0.6206	0.0904	
ETGTAB/ETERNA	0.6165	0.0840	0.3068
PIASD	0.6114	0.0832	0.304
BAYTAP	0.606	0.0840	0.299

$$\epsilon_{\theta\theta} = \frac{u_r}{r} + \frac{1}{r} \frac{\partial u_\theta}{\partial \theta} = \sum_n \frac{1}{ga} \left(h_n W_n + l_n \frac{\partial^2 W_n}{\partial \theta^2} \right) \quad (5.8b)$$

$$\begin{aligned} \epsilon_{\phi\phi} &= \frac{u_r}{r} + \frac{u_\theta \cot \theta}{r} + \frac{1}{r} \frac{\partial u_\phi}{\partial \phi} \\ &= \sum_n \frac{1}{ga} \left(h_n W_n + l_n \cot \theta \frac{\partial W_n}{\partial \theta} + \frac{l_n}{\sin \theta} \frac{\partial^2 W_n}{\partial \phi^2} \right) \end{aligned} \quad (5.8c)$$

The areal tidal strain (ϵ_a) and the volumetric tidal strain (ϵ_v) may then be calculated

$$\epsilon_a = \epsilon_{\theta\theta} + \epsilon_{\phi\phi} = \sum_n \frac{2h_n - n(n+1)l_n}{g} \frac{W_n}{a} \quad (5.9a)$$

$$\epsilon_v \cong \frac{1-2\nu}{1-\nu} \epsilon_a = \frac{1-2\nu}{1-\nu} \sum_n \frac{2h_n - n(n+1)l_n}{g} \frac{W_n}{a}. \quad (5.9b)$$

The approximation in Eq. (5.9b) is valid near the Earth's surface. The Love numbers may be calculated from Earth models. Table 5.1 shows the Love numbers ($n = 2$) calculated from different Earth models.

The tidal strains may be measured with strain gauges. They may also be calculated theoretically from Earth models, as shown in Fig. 5.5. In practice, strain measurements are often unavailable near the well site and theoretical tides are calculated and used as the reference for the tidal response.

5.4 Groundwater Response to Earth Tides

Wells (or boreholes) are hydrogeologists' 'telescopes' to study the properties of groundwater systems. Thus the analysis of the response of groundwater level in wells to various kinds of forcing has been a time-honored topic of groundwater research and is an important and effective tool for the study of the hydraulic properties of aquifers.

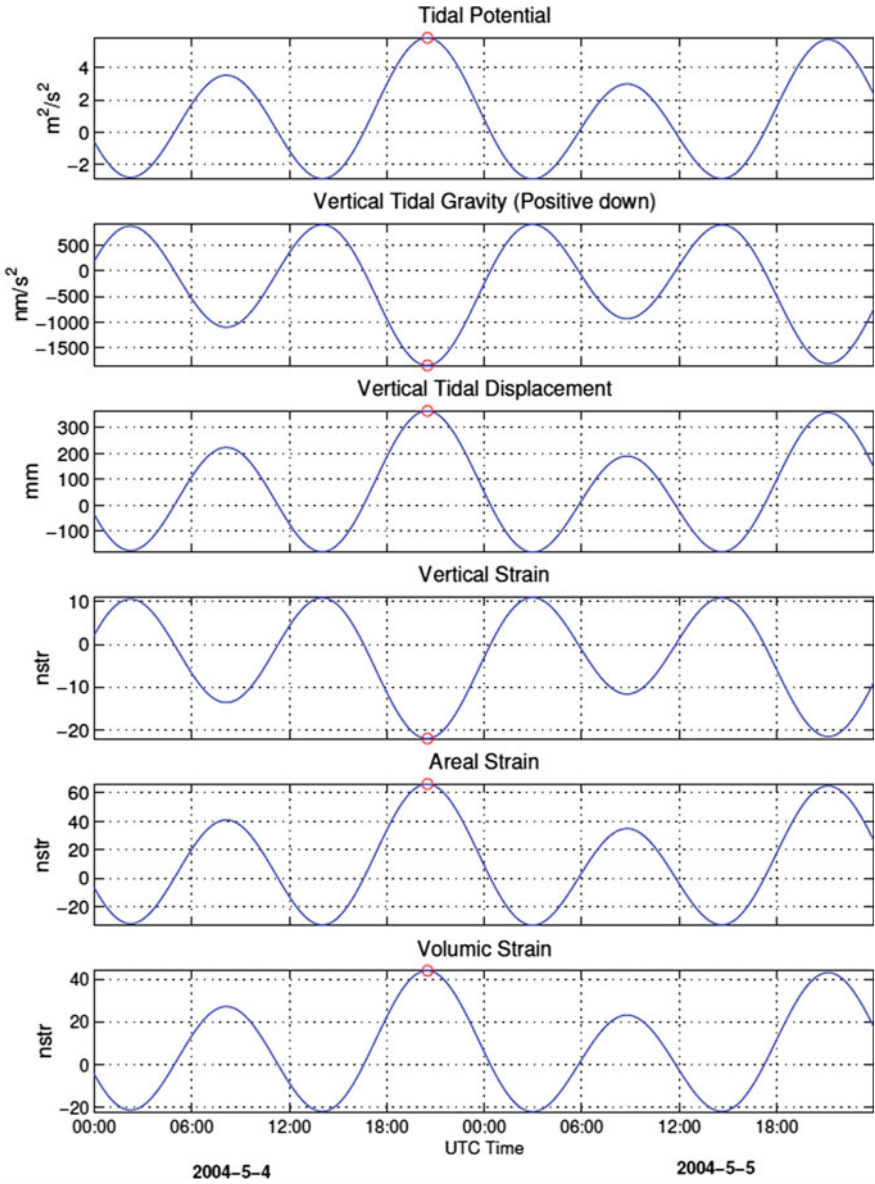


Fig. 5.5 Theoretical Earth tides predicted by ETGTAB software for the lunar eclipse of May 4, 2004, 20:30 UT, northeast of Madagascar (from Doan et al. 2006)

The most often used technique is the so-called ‘well test’ where the water level in a well is artificially changed and the subsequent time-dependent recovery of water level measured in the well or in nearby wells is interpreted to estimate the hydraulic properties of the affected aquifer. For the study of the interactions between earthquakes and groundwater, however, one often needs to compare the responses before and after the earthquake, and well tests become impractical because continuous well tests are too laborious and expensive. In comparison, the analyses of the response of groundwater level to natural forcing, such as tides and barometric pressure, are much more economical for continuously monitoring the hydraulic properties of aquifers and have gained increasing attention in hydrogeologic studies, particularly in the study of groundwater response to large earthquakes (e.g., Ingebritsen and Manga 2019).

The volumetric tidal strain causes oscillations of pore pressure in aquifers and water level in wells (e.g., Fig. 5.6). The tidal signals are often small in comparison with water-level changes due to seasonal recharge, ocean tides and groundwater extraction and need to be isolated from the water level time series by applying some standard technique such as Fourier analysis. The flow of groundwater between the aquifer and a well or a boundary causes a difference between the phase of the water level and that of the tidal strain, referred to as the phase shift and in the amplitude of the water level compared to that of the equivalent pore pressure produced by the Earth tide; the ratio between the two amplitudes is referred to as the amplitude ratio. Since direct measurement of the tidal strains near the studied well is often not available, the theoretical tidal strain at the well location is often used as the reference in calculating the phase shift and amplitude ratio of the tidal response. However, tidal strains are known to be significantly affected by local geologic heterogeneity, topographic irregularity and underground cavities (Beaumont and Berger, 1975; Harrison, 1974); hence this assumption constitutes an uncertainty in most studies, especially when some small differences in phase shift are of concern, as discussed later in this chapter.

Interpretation of the tidal oscillations in water levels requires an understanding of the flow of groundwater from aquifers to wells. Traditional interpretations treated aquifers either as perfectly confined (Hsieh et al., 1987) or perfectly unconfined (Roeloffs 1996; Wang 2000; Doan et al. 2006). Most aquifers, however, are neither perfectly confined nor perfectly unconfined, but are between these two end members. A leaky aquifer model (Wang et al. 2018; Zhu and Wang 2020) is therefore more appropriate for such interpretation. In addition, the water table of an unconfined aquifer is usually overlain by an unsaturated zone. The interfacial tension between air, water and solid grains in the unsaturated zone may cause groundwater to rise and form a layer of negative pore pressure, i.e., a capillary zone, above the water table, which may significantly affect the tidal response of some unconfined aquifers (Wang et al. 2019). These different models are discussed in the following sub-sections in the sequence of their historical development.

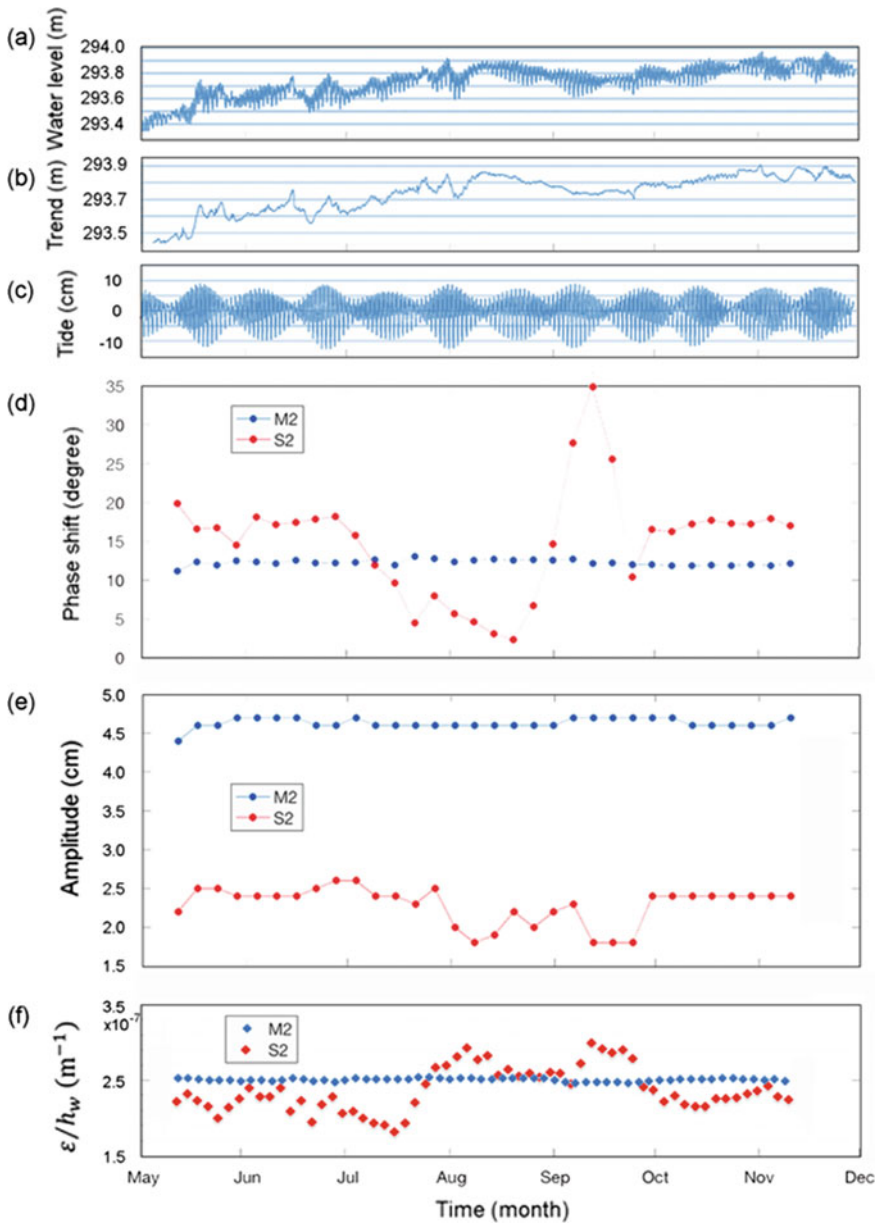


Fig. 5.6 Time series of **a** raw data for water level above the mean sea level in the USGS Oklahoma deep monitoring well, **b** drift that was removed, **c** remaining tides in water level used in the analysis, **d** phase shift of water level response to the M_2 and S_2 tides referenced to the local tidal volumetric strain, **e** amplitude of water level response to the M_2 and S_2 tides, and **f** response of $\epsilon_o/h_{w,o}$ to the M_2 and S_2 tides, where ϵ_o is the amplitude of the volumetric strain converted from surface strain computed in Baytap08, and $h_{w,o}$ is the amplitude of water level changes (modified from Wang et al. 2018)

5.4.1 Tidal Response of a Confined Aquifer

The following discussion parallels that in Hsieh et al. (1987) but with fewer special functions to simplify the expressions. Consider a horizontal, laterally extensive aquifer of thickness b , confined at its top and base, and open to a vertical well. The differential equation of groundwater flow in the aquifer may be expressed in cylindrical coordinates

$$T \left[\frac{\partial^2 h}{\partial r^2} + \frac{1}{r} \frac{\partial h}{\partial r} \right] = S \frac{\partial h}{\partial t} + Qb, \tag{5.10}$$

where h is the hydraulic head in the aquifer above a common reference (Fig. 5.7), r is the radial distance from the axis of the well, $T = Kb$ and $S = S_s b$ are the transmissivity and storativity of the aquifer, respectively, and Q is the source of groundwater per unit volume (Eq. 2.12c). The aquitard is assumed to be perfectly impervious, i.e., $K' = 0$.

Roeloffs (1996) pointed out that differential Eq. (5.10) does not consider aquifer deformation, even though deformation may occur in response to pore pressure changes. The equation, however, is valid under conditions of constant vertical stress and zero strain in the two orthogonal directions (Sect. 3.2.6), which are approximately met for areally extensive aquifers near the Earth’s surface under tidal loading.

The solid tides cause volumetric strains in the aquifer, which change the hydraulic head and induce cyclic flows of groundwater between the aquifer and well. Representing the tidal-induced head as a source term and taking compression to be positive,

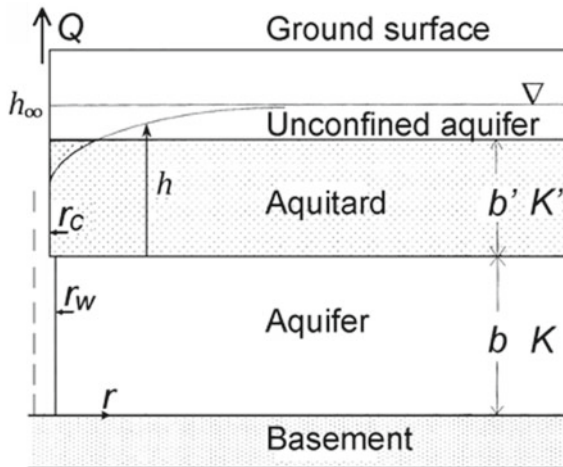


Fig. 5.7 Idealized open well drilled into a confined aquifer. If $K' = 0$, the aquifer is perfectly confined, as assumed in Hsieh et al. (1989). If $K' > 0$, groundwater may leak in and out of the aquifer through the aquitard, as assumed in Wang et al. (2018)

i.e., $Q = -S_s \frac{BK_u}{\rho g} \frac{\partial \epsilon}{\partial t}$, the flow equation becomes

$$T \left[\frac{\partial^2 h}{\partial r^2} + \frac{1}{r} \frac{\partial h}{\partial r} \right] = S \left(\frac{\partial h}{\partial t} - \frac{BK_u}{\rho g} \frac{\partial \epsilon}{\partial t} \right). \quad (5.11)$$

The symbol ϵ in the last term of Eq. (5.11) is the tidal volumetric strain of the aquifer, B is the Skempton's coefficient, $B = (\partial P / \partial \sigma)_f$, and K_u is the undrained bulk modulus of the aquifer, defined as

$$K_u = (\partial \sigma / \partial \epsilon)_f, \quad (5.12)$$

where P is pore pressure, σ the mean stress, and the subscript f denotes constant fluid content, i.e., an undrained condition. Considering only the tidal driven water-level oscillations, h in Eq. (5.11) represents the change of hydraulic head due to the tidal strain.

The boundary conditions for the problem are

$$h(r, t) = h_\infty(t) \text{ at } r = \infty, \quad (5.13)$$

$$h(r, t) = h_w(t) = r_w \text{ and,} \quad (5.14)$$

$$2\pi r_w T (\partial h / \partial r)_{r=r_w} = \pi r_c^2 (\partial h_w / \partial t), \quad (5.15)$$

where $h_w = h_{w,o} e^{i\omega t}$ is the periodically changing water level in the well, with complex amplitude $h_{w,o}$, $h_\infty(t)$ is the pressure-equivalent water level in the aquifer at $r = \infty$, $\omega [s^{-1}] = 2\pi/\tau$ is the angular frequency, τ is the period of the tidal oscillation, r_w is the radius of the screened portion of the well, and r_c [m] is the inner radius of well casing in which water level fluctuates with tides.

The solution to the boundary value problem is derived in Appendix 5.1 (see also Hsieh et al. 1987) and may be expressed in terms of a well factor ξ , i.e.,

$$h_{w,o} = \frac{1}{\xi} \left(\frac{BK_u \epsilon_o}{\rho g} \right) = \frac{1}{\xi} h_{\infty,o} \quad (5.16)$$

where

$$\xi = 1 + \left(\frac{r_c}{r_w} \right)^2 \frac{i\omega r_w}{2T\beta} \frac{K_0(\beta r_w)}{K_1(\beta r_w)}, \quad (5.17)$$

$h_{\infty,o}$ is the amplitude of h_∞ , K_0 and K_1 are modified Bessel functions of the second kind of zeroth and first order, respectively, and

$$\beta = \left(\frac{i\omega S}{T} \right)^{1/2} \quad (5.18)$$

The tidal response of a confined aquifer thus depends on the aquifer's poroelastic properties, B and K_u , its hydraulic properties, T and S , the tidal frequency ω , and the well geometry, r_w and r_c . From (5.16) we may calculate the amplitude ratio A and the phase shift η of the tidal response as

$$A = |h_{w,o}/h_{\infty,o}| = \left| \frac{1}{\xi} \right|, \quad (5.19a)$$

and

$$\eta = \arg[h_{w,o}/h_{\infty,o}] = \arg \left[\frac{1}{\xi} \right], \quad (5.19b)$$

where $\arg(z)$ is the argument of the complex number z .

The well-bore storage produces a slight delay in the water-level response, thus a negative phase shift, as shown in Fig. 5.8. Given the measured phase shift and amplitude ratio of the tidal response of the water level, we may estimate T and S of the aquifer.

Figure 5.8a shows that the phase shift of a confined aquifer is largely negative due to the finite well bore storage. At large transmissivity, however, the phase shift approaches zero and the amplitude ratio approaches one. Thus, at sufficiently large transmissivity, the tidal response in the well perfectly matches that in the aquifer and is no longer sensitive to transmissivity. Given a typical well radius of a few cm and the period of the M_2 tide, this occurs at $T \geq 10^{-4} \text{ m}^2/\text{s}$.

5.4.2 Tidal Response of an Unconfined Aquifer with Flow to the Water Table

The tidal response of unconfined aquifers is traditionally treated with the boundary condition of free flow to the water table (Fig. 5.9). In Sect. 5.4.4 we will discuss the effect of capillary tension above the water table on the tidal response of unconfined aquifers.

The traditional governing differential equation for groundwater flow in an unconfined aquifer is

$$K \frac{\partial^2 h}{\partial z^2} = S_s \left(\frac{\partial h}{\partial t} - \frac{BK_u}{\rho g} \frac{\partial \epsilon}{\partial t} \right), \quad (5.20a)$$

where the parameters are the same as defined in the last section. Introducing the hydraulic diffusivity $D = K/S_s$, Eq. (5.20a) is simplified as

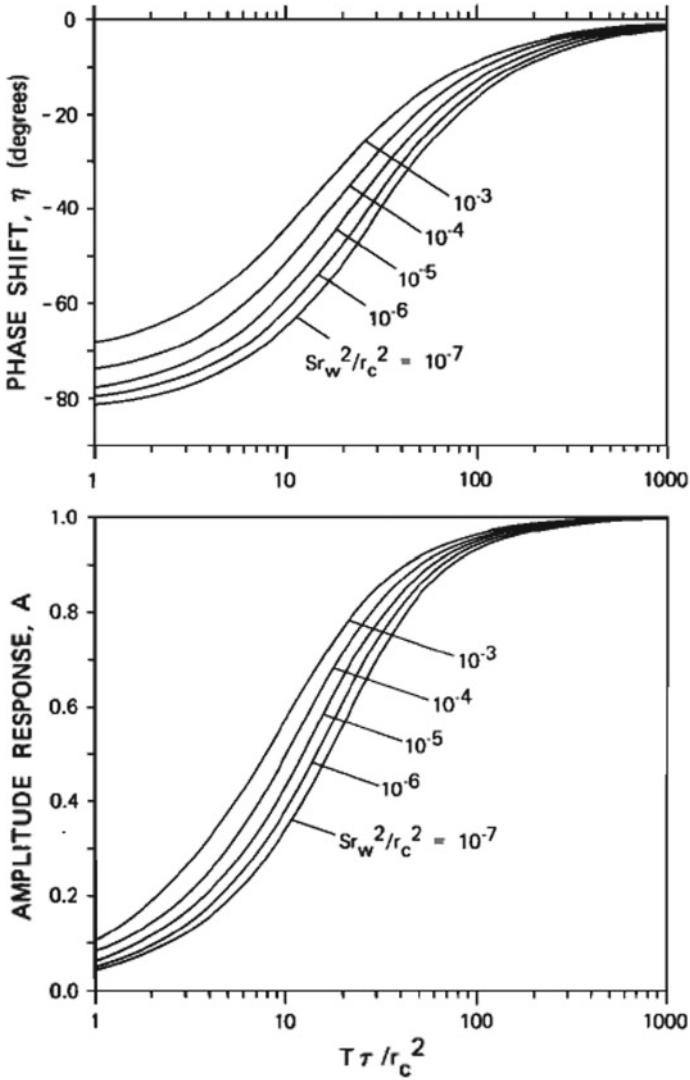


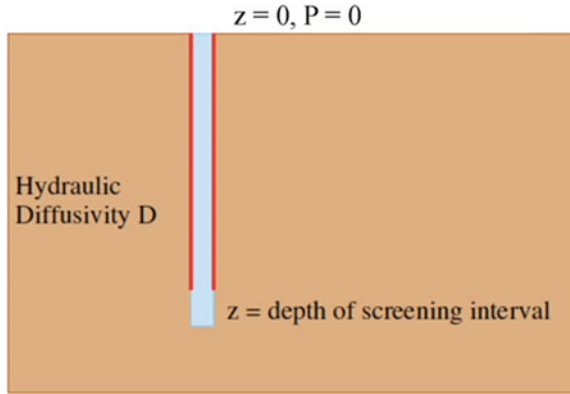
Fig. 5.8 Predicted phase shift and amplitude ratio of the tidal response of a confined aquifer (from Hsieh et al. 1987)

$$D \frac{\partial^2 h}{\partial z^2} = \frac{\partial h}{\partial t} - \frac{BK_u}{\rho g} \frac{\partial \epsilon}{\partial t}. \tag{5.20b}$$

If the water table is at the surface, the boundary condition at the surface is

$$h(z = 0) = 0. \tag{5.21}$$

Fig. 5.9 Well in an unconfined aquifer with free flow to the water table at the surface (from Doan et al. 2006)



Often the unconfined aquifer is approximated by a half space and the boundary condition at the base is

$$h(z \rightarrow \infty) = \frac{BK_u}{\rho g} \epsilon. \tag{5.22}$$

The general solution is

$$h_o = \frac{BK_u}{\rho g} \epsilon_o (1 + D_1 e^{(1+i)z/\delta} + D_2 e^{-(1+i)z/\delta}), \tag{5.23}$$

where $\delta \equiv \sqrt{2D/\omega}$. The boundary conditions (5.22) and (5.23) assert that $D_1 = 0$ and $D_2 = -1$. The solution is thus

$$h_o = \frac{BK_u}{\rho g} \epsilon_o (1 - e^{-(1+i)z/\delta}). \tag{5.24}$$

When the finite thickness of the aquifer is considered, a no-flow boundary condition is assigned at the base ($z = L$),

$$\left. \frac{\partial h}{\partial z} \right|_{z=L} = 0. \tag{5.25}$$

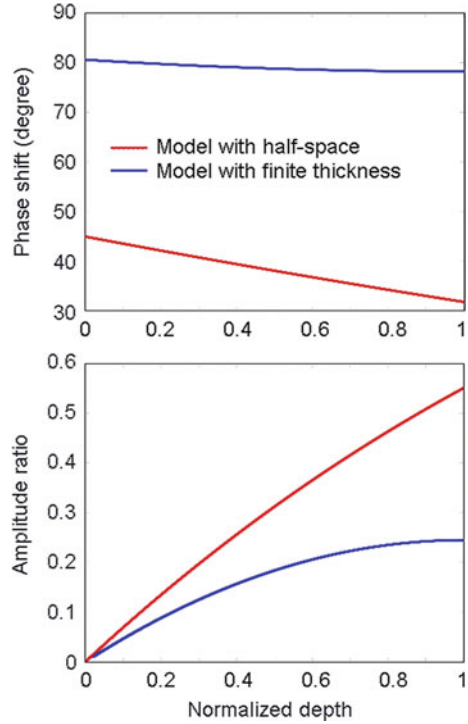
The solution becomes (Detournay and Cheng 1993)

$$h_o = \frac{BK_u}{\rho g} \epsilon_o [1 + \tanh \lambda \sinh(\lambda z/L) - \cosh(\lambda z/L)], \tag{5.26}$$

where $\lambda \equiv L\sqrt{i\omega/D}$.

Figure 5.10 compares the solutions for the tidal response of an unconfined aquifer with the half-space approximation and that with an assumed thickness of

Fig. 5.10 Comparison between the half-space model for an unconfined aquifer and the finite layer model with an assumed thickness of $L = \sqrt{D/2\omega}$ (author’s figure)



$L = \sqrt{D/2\omega}$. For z/L between 0 and 1, the phase shift for a half-space model declines from 45 to $\sim 30^\circ$, while that for a finite layer model declines gently from slightly above 80 degrees to slightly below 80° .

The phase shift for the unconfined aquifer model is positive, in contrast to that for the confined aquifer model. The explanation for the positive phase shift of an unconfined aquifer has been a point of debate. Allègre et al. (2016) explained: “The apparent phase leads are due to the constant pressure boundary condition at the water table that makes the driving force effective the tidal strain rate, which is phase shifted from the dilatational strain.” However, under identical boundary conditions to those in the confined aquifer model (Eqs. 5.14–5.16), the leaky aquifer model also predicts positive phase shift at significant leakage (Fig. 5.13; Wang et al. 2018). We examine this point further at the end of Sect. 5.4.4.

5.4.3 An Example of Seasonal Change of Tidal Response

Most existing studies of the tidal response of an unconfined aquifer use the traditional unconfined aquifer model (without considering the capillary effect) to interpret the observed positive phase shift. An unusual case occurs in SW China where the positive

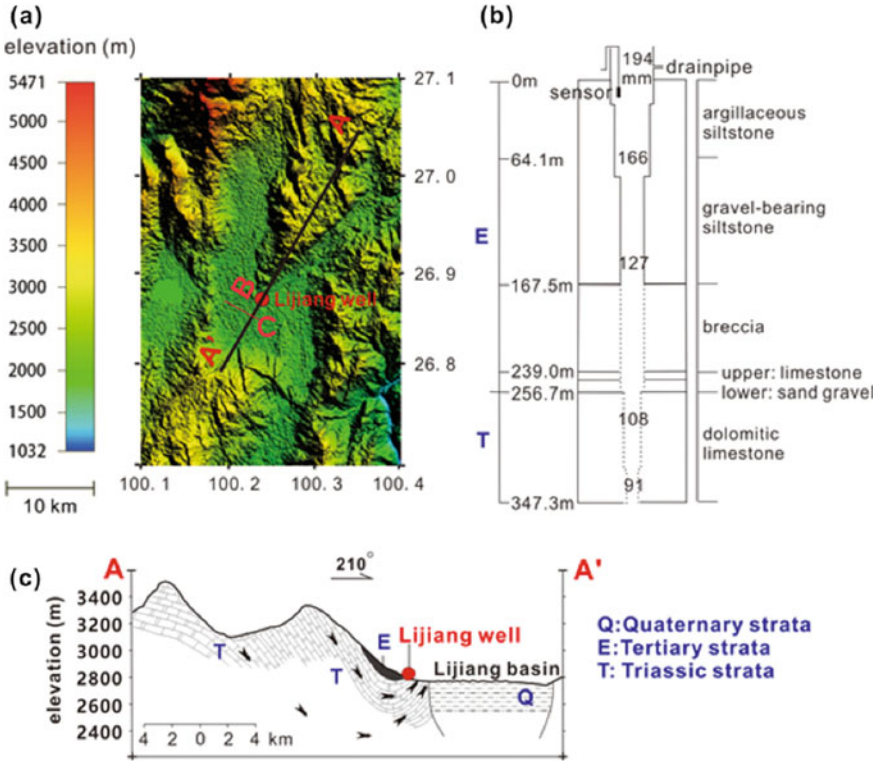


Fig. 5.11 **a** The hydrogeology and the location of the observation well (Lijiang well). **b** Simplified diagram of the Lijiang well. Numbers in the well show the inner diameters of the well in mm; numbers on the side show depth beneath the surface. Dashed lines show the open section of the well. **c** Sketch of the hydrogeologic cross-section of the groundwater recharge and discharge of the aquifer open to the Lijiang well (from Liao and Wang 2018)

phase shift of the tidal response of water level in a well changes with season (Fig. 5.11) and was interpreted with the traditional model (Liao and Wang 2018) and also with the capillary model (Wang et al. 2019). We use this case as an example to first illustrate the interpretation with the traditional model and then compare this interpretation with that with a different model that includes the capillary effect in Sect. 5.4.5.

Figure 5.12a shows a 10 year record of the water level response to the M_2 tide in the Lijiang well. The record shows large swings of the tidal responses with season, with large increases of the phase shift and corresponding decreases of the amplitude during the local rainy season (June–October). Figure 5.12b shows a 10-year composite plot of the phase shift and amplitude versus water level. It shows that the upward swing of the phase shift and the downward swing of the amplitude occur at the time when the groundwater level rises to the surface. The data points with water level above the surface correspond to overflow of the well and are not included in the analysis. Liao and Wang (2018) interpreted the seasonal variation of the tidal response with

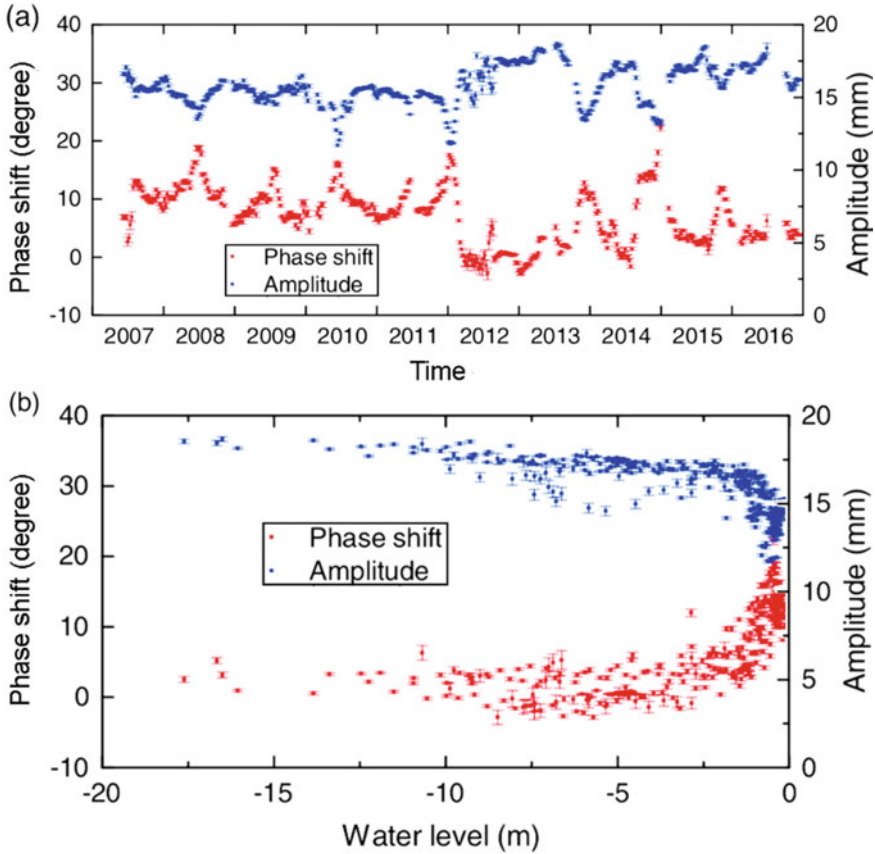


Fig. 5.12 **a** Time series of the amplitude and phase shift of the tidal response of water level in the Lijiang well to the local M_2 (theoretical) tide, plotted with error bars. The root-mean-square errors, on average, are $\sim 0.3^\circ$ for phase shift and ~ 0.2 mm for amplitude. **b** Composite of 10 years of amplitude and phase shift of the water level response to the M_2 tide plotted as functions of water level. Water level was referenced to the drainage pipe (Fig. 5.11b) 0.4 m above ground. Each point in the plot represents an averaged value over a 30-day period. Positive phase shift indicates local phase advance (from Liao and Wang 2018)

Eq. (5.24)—the unconfined aquifer model—suggesting a seasonal six-fold increase of permeability during the rainy season. The data may also be interpreted with the capillary model, as discussed in Sect. 5.4.5.

5.4.4 Tidal Response of a Leaky Aquifer

As noted earlier, most aquifers are neither completely confined nor completely unconfined, but somewhere between the two end conditions. The vertical impedance to flow

across a confining layer (aquitard) is not infinite but depends on the thickness of the layer and the time scale of the applied load. At low frequencies, a confining layer may exchange flow across its boundaries; but at high frequencies, it may exhibit confining behavior. Thus it may be more appropriate to treat groundwater systems as a leaky system with a broad spectrum of different degrees of aquifer leakage.

In addition, earthquakes may breach the confinement of aquifers and cause leakage from an initially confined aquifer, as discussed in Sect. 6.8. The analysis of the tidal response of leaky aquifers may thus be useful for quantitative assessment of the effect of an earthquake on the confinement of a groundwater system.

In this section we discuss the analytical solution for the tidal response of a simplified leaky aquifer. Hantush and Jacob (1955) provided the first differential equation for a horizontal and laterally extensive aquifer confined by a semi-confining aquitard, assuming that the flow through it is vertical. With these simplifications they derived the flow equation for a leaky aquifer (Hantush and Jacob 1955):

$$T \left[\frac{\partial^2 h}{\partial r^2} + \frac{1}{r} \frac{\partial h}{\partial r} \right] - \frac{K'}{b'} h = S \frac{\partial h}{\partial t}, \quad (5.27)$$

where h is the hydraulic head in the aquifer above a common reference (Fig. 5.7), r is the radial distance from the studied well, T and S , respectively, are the transmissivity and storativity of the aquifer, K' is the vertical hydraulic conductivity of the aquitard and b' is its thickness (Fig. 5.7). Here the aquifer leakage per unit area q_1 is approximated by a sink proportional to the product of the average hydraulic gradient and the conductivity across the aquitard, i.e.,

$$q_1 = -K' \frac{h}{b'}. \quad (5.28)$$

and the ratio K'/b' is referred as the leakage factor. The model by Hantush and Jacob has been extensively used and extended in well tests. Here we discuss the tidal response of groundwater in a leaky aquifer. Adding a source term in Eq. (5.27) to represent the driving tidal strain we have (Wang et al. 2018):

$$T \left[\frac{\partial^2 h}{\partial r^2} + \frac{1}{r} \frac{\partial h}{\partial r} \right] - \frac{K'}{b'} h = S \left(\frac{\partial h}{\partial t} - \frac{BK_u}{\rho g} \frac{\partial \epsilon}{\partial t} \right). \quad (5.29)$$

where ϵ is the oscillating tidal volumetric strain of the aquifer (compression is taken to be positive), and B and K_u , respectively, are the Skempton's coefficient and the undrained bulk modulus of the aquifer.

The boundary conditions for the horizontal flow of groundwater between the aquifer and the well are identical to those for a confined aquifer, i.e.,

$$h(r, t) = h_\infty(t) \text{ at } r = \infty, \quad (5.30)$$

$$h(r, t) = h_w(t) \text{ at } r = r_w, \text{ and} \quad (5.31)$$

$$2\pi r_w T (\partial h / \partial r)_{r=r_w} = \pi r_c^2 (\partial h_w / \partial t) \quad (5.32)$$

where r_w is the radius of the screened portion of the well, r_c is the inner radius of well casing in which water level fluctuates with tides, $h_w = h'_{w,o} e^{i\omega t}$ is the periodic water level in the well, with complex amplitude $h'_{w,o}$, $\omega = 2\pi/\tau$ is the angular frequency, and τ is the period of tidal oscillation.

The solution for the boundary value problem, (5.29)–(5.32), is obtained by first deriving the response away from the well, h_∞ , and then considering the effect of the well on aquifer response by using a flux condition at the well that accounts for wellbore storage.

The hydraulic head away from the well may be evaluated by replacing h by h_∞ in (5.29)

$$-\frac{K'}{b'} h_\infty = S \frac{\partial h_\infty}{\partial t} - \frac{SBK_u}{\rho g} \frac{\partial \epsilon}{\partial t}. \quad (5.33)$$

Since h_∞ and ϵ are both periodic with the same frequency ω we have the relation between their complex amplitudes $h'_{\infty,o}$ and ϵ_o

$$h'_{\infty,o} = \frac{i\omega S}{i\omega S + K'/b'} \left(\frac{BK_u \epsilon_o}{\rho g} \right). \quad (5.34)$$

It is notable that leakage causes both the amplitude and the phase shift of $h'_{\infty,o}$ to deviate from that of a perfectly confined aquifer and that $h'_{\infty,o}$ becomes identical to that of a perfectly confined aquifer when $K' = 0$.

The rest of the derivation of the solution is given in Appendix 5.2 (see also Wang et al. 2018); the solution may be expressed in terms of a modified well factor ξ' , i.e.,

$$h_{w,o} = \frac{i\omega S}{(i\omega S + K'/b')\xi'} \left(\frac{BK_u \epsilon_o}{\rho g} \right) = \frac{1}{\xi'} h'_{\infty,o}, \quad (5.35)$$

where

$$\xi' = 1 + \left(\frac{r_c}{r_w} \right)^2 \frac{i\omega r_w K_o(\beta' r_w)}{2T\beta' K_1(\beta' r_w)}, \quad (5.36)$$

and

$$\beta' = \left(\frac{K'}{Tb'} + \frac{i\omega S}{T} \right)^{1/2}. \quad (5.37)$$

Here the primed parameters $h'_{\infty,o}$, ξ' and β' are used to distinguish them from those parameters for the perfectly confined aquifer in Eqs. (5.16)–(5.18).

The amplitude ratio and the phase shift of the tidal response are, respectively,

$$A = \left| h_{w,o} / \left(\frac{BK_u \epsilon_o}{\rho g} \right) \right|, \quad (5.38a)$$

$$\eta = \arg \left[h_{w,o} / \left(\frac{BK_u \epsilon_o}{\rho g} \right) \right]. \quad (5.38b)$$

The difference between these expressions (5.38) and those for a confined aquifer (5.19) reflects the fact that, for a leaky aquifer, the tidal response away from the well may no longer be useful as a reference because this response now depends on the unknown aquifer storativity (S) and the aquitard leakage (K') (5.34). The solution (5.35) has three independent parameters, T and S for the aquifer and K'/b' for the aquitard. The material property BK_u is an additional unknown but is eliminated in the expressions for A and η . The parameters T , S and K'/b' may be estimated from the measured phase shifts and amplitude ratios of the diurnal tide and the semidiurnal tide. In the case where T and S of the aquifer are known from independent measurements, the model may be used to estimate the leakage of the aquitard.

Figure 5.13 plots the phase shift and the amplitude ratio of the tidal response against K'/b' for assumed values of T and S . At $T > 10^{-4} \text{ m}^2/\text{s}$ and given S , the curves for different T collapse onto a single curve (red markers in Fig. 5.13); in other words, at such high T the tidal response is no longer sensitive to the changes of T . On the other hand, the phase shift for a given pair of T and S may change with K'/b' from a confined response at low leakage over a transition to an unconfined response at high leakage. At relatively small leakage the phase shift may be negative but becomes positive at increasing K'/b' . Thus the traditional criterion that a positive phase shift signifies an unconfined aquifer and a negative phase shift identifies an confined aquifer (e.g., Hsieh et al. 1987; Doan et al. 2006) may fail where the aquitard has finite conductivity.

We end this sub-section with a brief comment on the difference between the tidal response of a leaky aquifer and that of a confined aquifer. Since the two models have identical boundary conditions, the difference between the predicted tidal responses must originate from the difference between the two controlling equations, i.e., the introduction of K'/b' in Eq. 5.29. For the convenience of discussion, we re-express the solution for phase shift (5.38b), together with (5.35), as $\eta = \arg \{ i\omega S / (i\omega S + K'/b') \} / \xi'$, $= \arg \{ i / (i + [K'/b'] / \omega S) \} / \xi'$. Since the argument of a product is the sum of the arguments of its factors, the phase shift of the tidal response of a leaky aquifer is the sum of the phase shifts of $i / (i + [K'/b'] / \omega S)$ and that of $1/\xi'$. Plotting the former as a function of $[K'/b'] / \omega S$ in Fig. 5.14, we see that the phase shift of $i / (i + [K'/b'] / \omega S)$ is nearly zero when $[K'/b'] / \omega S \ll 1$ (i.e., small leakage) but increases to $+\pi/2$ when $[K'/b'] / \omega S \gg 1$ (i.e., large leakage). In other words, when $K'/b' \ll \omega S$, the phase shift of a leaky aquifer is primarily controlled by borehole storage, similar to that for a confined aquifer, and the flow may be predominantly horizontal; on the other hand,

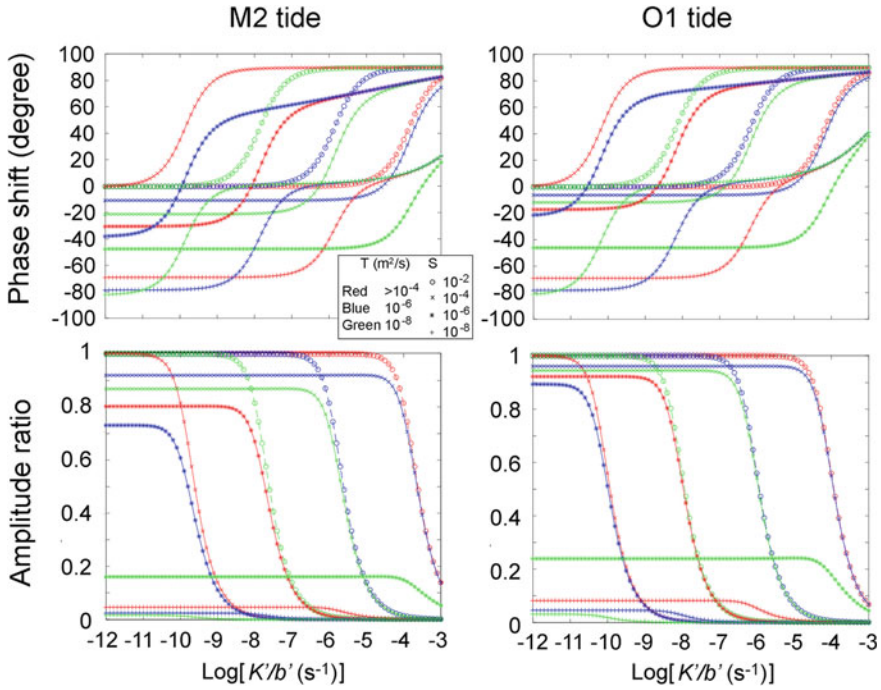


Fig. 5.13 **a** Phase shift of water level response to the M₂ tidal strain predicted by the leaky aquifer model, plotted against the logarithm of the specific leakage K'/b' for assigned values of T and S and $r_c = r_w = 10$ cm. **b** Amplitude ratio of water level response to that converted from the M₂ tidal volumetric strain, plotted against the logarithm of K'/b' for assigned values of T and S . **c** Phase shift of water level response to the O₁ tidal strain, plotted against the logarithm of the specific leakage K'/b' for assigned values of T and S and $r_c = r_w = 10$ cm. **d** Logarithm of the amplitude ratio of water level response to that converted from the O₁ tidal volumetric strain, plotted against the logarithm of K'/b' for assigned values of T and S

when $K'/b' \gg \omega S$, the phase shift of a leaky aquifer is primarily controlled by the free surface, similar to that for an unconfined aquifer, and the flow may be predominantly vertical. In the transition between these two end conditions where K'/b' is of the same magnitude as ωS , the flow may be neither predominantly horizontal nor predominantly vertical.

5.4.5 Numerical Simulation for the Tidal Response of a Leaky Aquifer

The above analytical model made several approximations to simplify the analysis. First, the leakage is treated as a volumetric sink in the aquifer. In reality, the aquifer is part of a system with multiple layers and the leakage occurs across the boundary

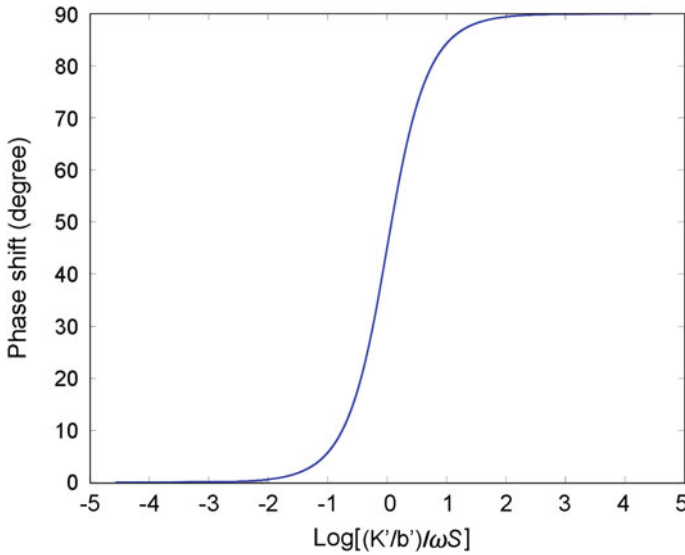


Fig. 5.14 Phase shift of $i/(i+[K'/b']/\omega S)$ plotted against $[K'/b']/\omega S$

between the aquifer and the aquitard. Thus, the approximation is acceptable only if the aquifer is relatively thin. Second, the analytical model neglects the storage and assumes a linear head profile in the aquitard, implying that the hydraulic head in the aquitard is always in a steady state, which may fail for aquitards with relatively low conductivity and large thickness with time-dependent boundary conditions (Neuman and Witherspoon 1969; Witherspoon and Freeze 1972; Feng and Zhan 2015). Third, it assumes that the flow in the aquitard is always vertical, which occurs only if the vertical hydraulic conductivity of the aquifer is large compared with that of the aquitard. Last, the analytical model assumes that the basement leakage is negligible. Most large induced earthquakes, however, occur in the basement (e.g., Schoenball and Ellsworth 2017), suggesting that some of the injected fluids must have entered the basement (e.g., Barbour et al. 2017). It is thus desirable to understand how basement leakage may affect the tidal response of an aquifer. In order to remove these simplifications and to quantify their influence on the predictions of the tidal response, Zhu and Wang (2020) revisited the tidal response of a leaky aquifer with 2D finite-element numerical simulations. Below we briefly describe the numerical approach and show how it may be used to simulate the tidal response of a multi-layered, leaky groundwater system.

The numerical model consists of a horizontal aquifer on top of a potentially leaky basement. The aquifer is overlain by a semi-confining aquitard that in turn is overlain by an unconfined aquifer (Fig. 5.15). In this model, the aquifer and the aquitard can both accommodate groundwater flow in the horizontal and the vertical directions. Also, the aquitard and the basement are assumed to have finite transmissivity and

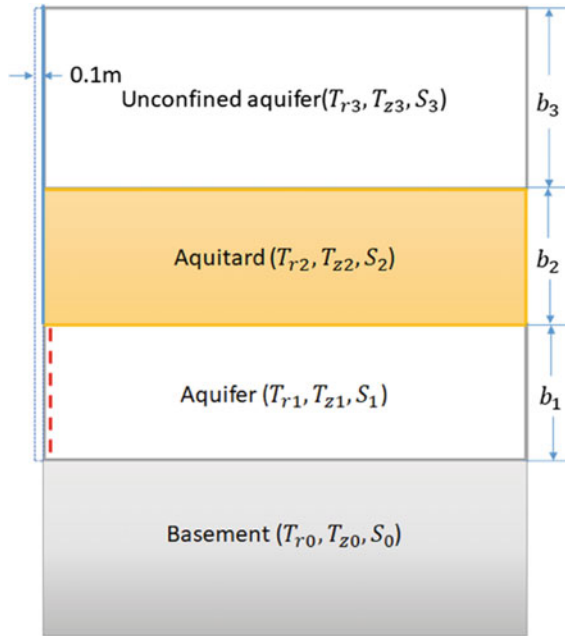


Fig. 5.15 Schematic drawing of a multi-layered groundwater system used in the numerical simulation. The vertical dashed line on the left is the position of the well axis and the radius of the well is 0.1 m; the thicknesses of the aquifer, the aquitard and the topmost unconfined aquifer are, b_1 , b_2 , and b_3 , respectively. The transmissivity and storativity of the layers are denoted by, respectively, (T_1, S_1) , (T_2, S_2) and (T_3, S_3) where $T_i = b_i K_{ri}$ and $S_i = b_i S_{si}$. The transmissivity and storativity of the basement (T_0, S_0) are assumed to be zero except where the effect of basement leakage is specifically discussed (from Zhu and Wang 2020)

storativity. The topmost unconfined aquifer is assumed to have high vertical hydraulic conductivity and is thus characterized by a hydrostatic head.

Groundwater flow in such a multi-layered system driven by the Earth tides may be simulated by solving the following differential equation:

$$K_{ri} \left[\frac{\partial^2 h_i}{\partial r^2} + \frac{1}{r} \frac{\partial h_i}{\partial r} \right] + K_{zi} \frac{\partial^2 h_i}{\partial z^2} = S_{si} \left(\frac{\partial h_i}{\partial t} - \frac{B_i K_{ui}}{\rho g} \frac{\partial \epsilon}{\partial t} \right), \quad (5.39)$$

under the boundary conditions

$$2\pi r_b T_1 \frac{\partial h_1(r, t)}{\partial r} - \pi r_c^2 \frac{\partial h_1(r, t)}{\partial t} = 0 \quad (5.40)$$

where h_i [m] is the hydraulic head in the i th layer, r [m] the radial distance from the axis of the well, K_{ri} and K_{zi} , respectively, the hydraulic conductivities in the radial and vertical directions of the i th layer, S_{si} the specific storage of the i th layer, with the subscript 1 denotes the aquifer layer, ϵ is the tidal volumetric strain, B_i and

K_{ui} , respectively, are the Skempton's coefficient and the undrained bulk modulus of the i th layer, and ρ and g , respectively, the density of water and the gravitational acceleration. K_{ri} and K_{zi} , respectively, are related to the horizontal and vertical permeabilities k_{ri} and k_{zi} of the i th layer by $K_{ri} = k_{ri}\rho g/\mu$ and $K_{zi} = k_{zi}\rho g/\mu$, respectively, μ the viscosity of water, b_i the thickness of the i th layer, r_b is the radius of the opened section of the well and r_c is the radius of the cased section of the well. Finally, a boundary condition of $p = 0$ (1 atm) is assigned on the surface ($z = 0$) and a no-flow conditions on the cased section of the well, on the right boundary ($r \rightarrow \infty$) of the model, and at the base ($z \rightarrow \infty$) of the model.

It is noticeable that leakage of groundwater across the boundary between the aquifer and the aquitard is permitted in this model, eliminating the use of a source in Eq. (5.39) to represent the leakage of the aquifer. For the lack of experimental data, B_i and K_{ui} are assumed uniform in all layers. The basement beneath the aquifer is assumed to be impervious in most simulations, except where the effect of basement leakage is specifically examined.

Zhu and Wang (2020) used a commercially available finite element code, COMSOL, to investigate the questions stated at the beginning of this sub-section.

The simulation with different aquifer thickness and hydraulic conductivity show good agreement between the analytical model and the numerical solution when the parameter $\alpha = (K_{z1}/b_1)/(K_{z2}/b_2)$ is greater or equal to 5 for the ranges of studied aquitard leakage factor K_{z2}/b_2 , K_{r1} and S_1 (Fig. 5.16), where the subscript 1 denotes the parameters of the aquifer and the subscript 2 denotes the parameters of the aquitard. At $\alpha < 5$, however, the simulated results depart progressively from the analytic solutions and lie further to the right (greater K_{z2}/b_2) of the analytical model for given values of T_{r1} and S_1 .

Another assumption in the analytical leaky aquifer model (Hantush and Jacob 1955; Wang et al. 2018) is that the semi-confining aquitard has negligible storativity. As noted earlier, this assumption is equivalent to assuming that the aquitard goes immediately into a steady state, which is valid only if the time constant for the hydraulic equilibrium across the aquitard is short in comparison with the period of the tidal forcing. The occurrence of aquitard storage significantly increases the time constant for the hydraulic equilibrium across the aquitard and renders the assumption invalid if the aquitard has relatively low conductivity and large thickness (Neuman and Witherspoon 1969; Witherspoon and Freeze 1972; Feng and Zhan 2015). Figure 5.17 compares results simulated with $S_2/S_1 = 0, 1, 10$ and 100, respectively, for $K_{r1} = 10^{-5}$ m/s and $\alpha = 10$. Good agreement between the simulated results and the analytical solution occurs when $S_2/S_1 = 0$. But when S_2/S_1 is significantly greater than 0, the departure of the simulated results from the analytical solution increases with increasing aquitard storativity at a given aquitard leakage K_{z2}/b_2 . Another interesting feature is that the simulated peak amplitude ratio may exceed 1 and the magnitude of this excess becomes greater with increasing aquitard storativity. Similar increases of the amplitude ratio were reported before and interpreted to be due to the poroelastic coupling between pore pressure and deformation (Detournay and Cheng 1993; Hsieh and Cooley 1995; Wang 2000).

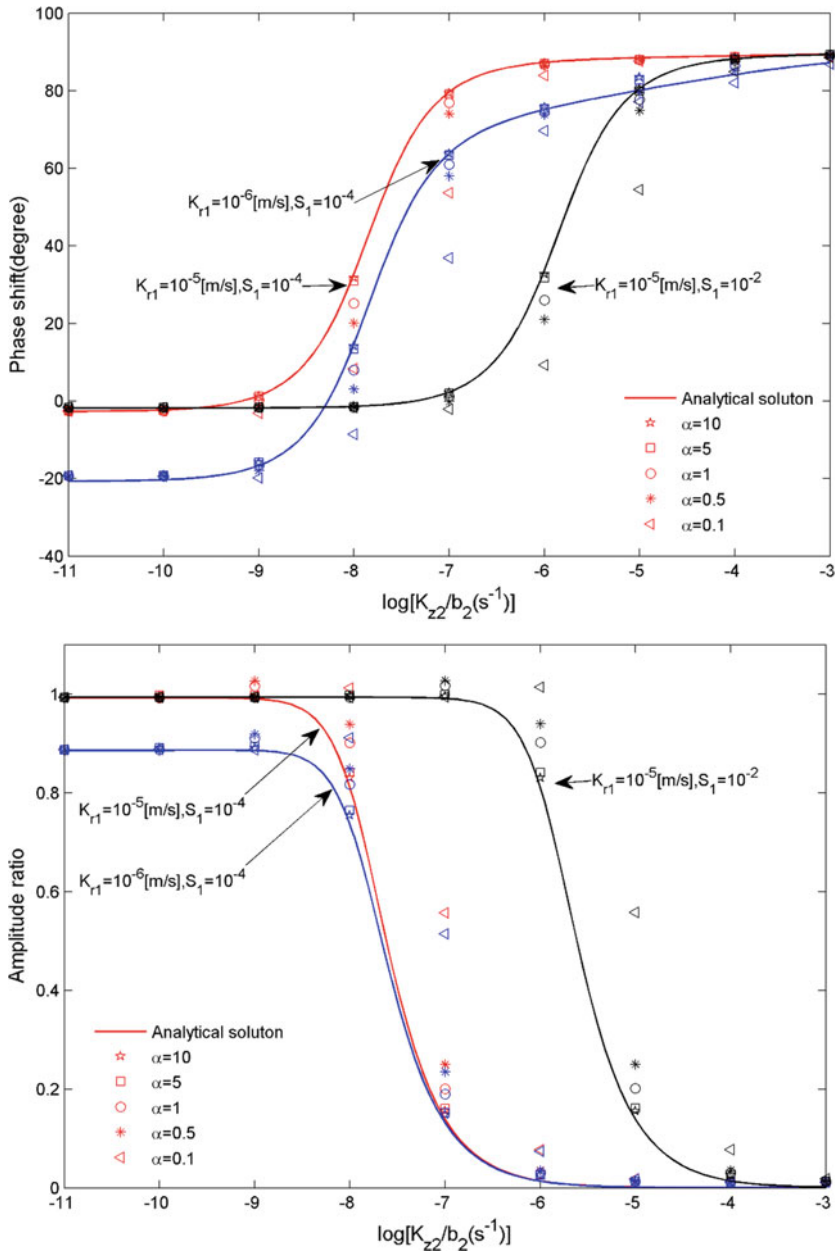


Fig. 5.16 Comparison between the numerically simulated water level response to the M_2 tide at different values of α and specific aquifer transmissivity (T_1) and storativity (S_1) (symbols) and the analytical solutions (curves; Wang et al. 2018). **a** Phase shift and **b** amplitude ratio plotted against aquitard leakage factor K_{z2}/b_2 (from Zhu and Wang 2020)

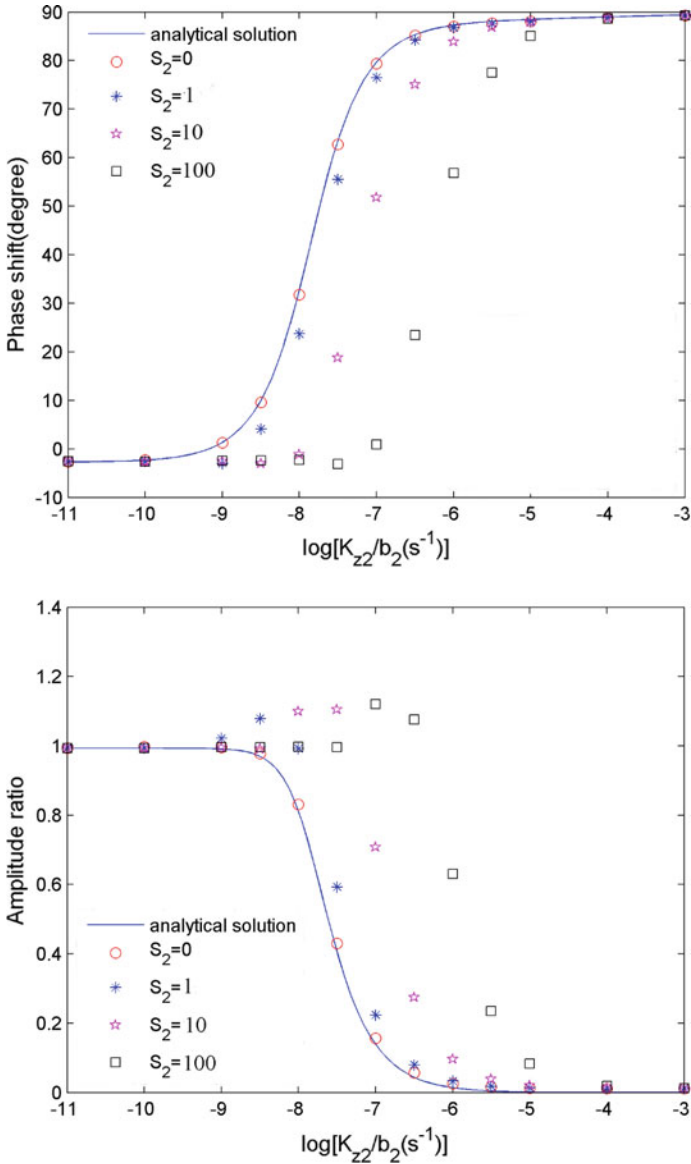


Fig. 5.17 Comparison between the numerically simulated water level response to the M_2 tide at different aquitard storativity (S_2) (symbols) and the analytical solutions (curves; Wang et al. 2018). **a** Phase shift and **b** amplitude ratio plotted against aquitard leakage factor K_{z2}/b_2 (from Zhu and Wang 2020)

Zhu and Wang (2020) also examined the effect of basement leakage. Previous studies suggested that the basement diffusivity may be as high as $1 \text{ m}^2/\text{s}$ in order to explain the induced seismicity (Barbour et al. 2017), but the effect of basement leakage on the response to Earth tides has not been investigated. Figure 5.18 shows that the effect of basement leakage on tidal response may be neglected only if the basement conductivity is below 10^{-7} m/s . At greater basement conductivity, basement leakage may cause significant decrease in phase shift and increase in amplitude ratio. Thus the omission of basement leakage from the interpretation of tidal response of water level in wells may also lead to significant underestimates of the aquifer leakage.

Finally, Zhu and Wang (2020) used their numerical procedure to simulate the tidal response in a U.S. Geological Survey monitoring well in Oklahoma (Fig. 5.19), which opens at a depth of 900 m to the carbonate Arbuckle aquifer that has been used for the injection of wastewaters co-produced from hydrocarbon exploration. Figure 5.20 shows the well construction and the lithology of the wall rocks of the well. The aquifer lies on the top of a crystalline basement and is overlain by an

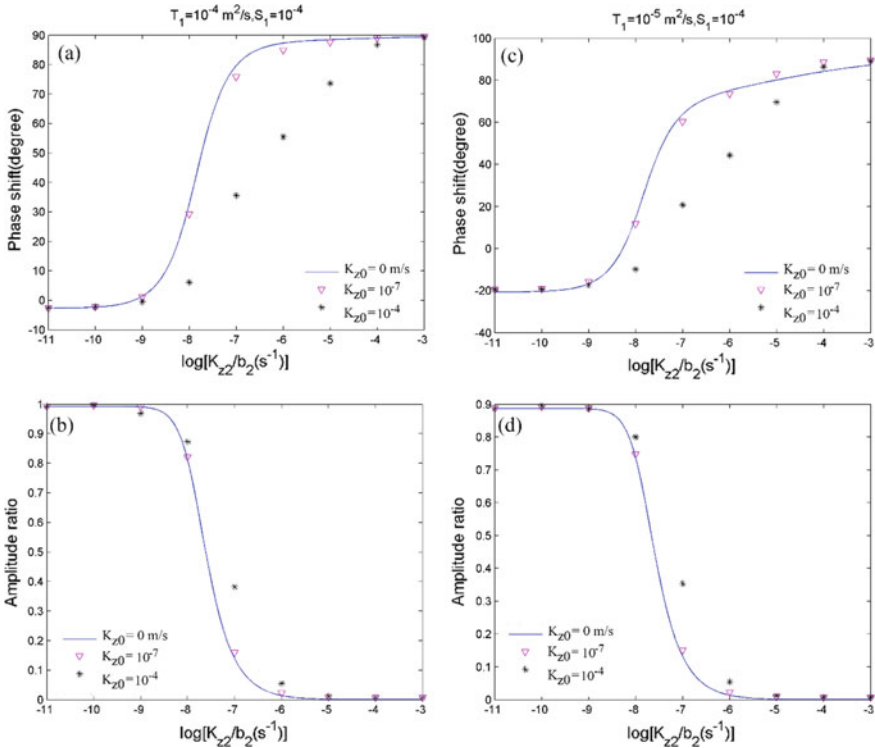


Fig. 5.18 Comparison between the numerically simulated (symbols) water level response to the M_2 tide at different basement leakage (K_{z0}) and aquifer transmissivity (T_1) and the analytical solutions (curves; Wang et al. 2018). **a, c** Phase shift and **b, d** amplitude ratio, plotted against aquitard leakage factor K_{zz}/b_2 (from Zhu and Wang 2020)

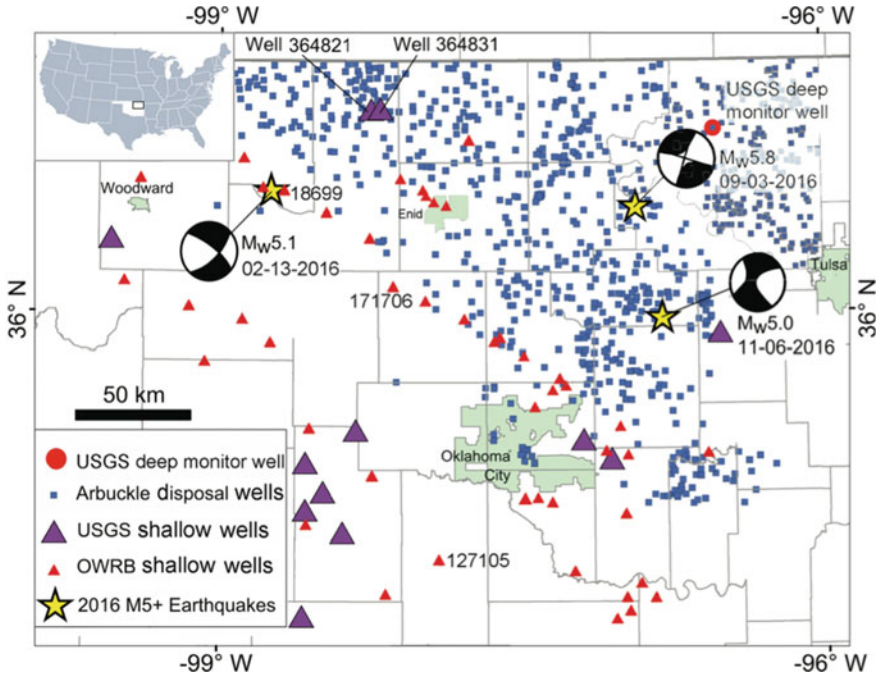


Fig. 5.19 The location of the USGS Oklahoma Deep Well (red circle in the upper right corner of figure). The epicenters of three 2016 $M \geq 5$ earthquakes are shown as yellow stars. The locations of water wells and injection wells, respectively, are shown by triangles and blue dots (from Wang et al. 2018)

aquitard consisting of a sequence of layered rocks with a basal shale; the aquitard in turn is overlain by a layer of unconsolidated sediments.

Figure 5.21 shows the time series of water level in the USGS Oklahoma Deep Well in 2017, the tides in water level and the phase shift, and amplitude of water level response to the M_2 and S_2 tides referenced to the local theoretical tidal volumetric strain. The response shows a positive phase shift of $\sim 12.5^\circ$ to the M_2 tide (Wang et al. 2018). Barbour et al. (2019) also studied the tidal response of water level in the same well (Fig. 5.21); their analysis shows a similar positive phase shift of the response to the M_2 tide. Hence both studies suggest that the Arbuckle aquifer may be leaking.

Table 5.2 lists the hydraulic properties of the Arbuckle aquifer and the geometry of the USGS Oklahoma Deep Well. Figure 5.22 shows the simulated phase shift for the M_2 tide plotted against $\log(K_{z2}/b_2)$ with the ratio of aquitard storativity specified as $S_2/S_1 = 0, 1$ and 10 , respectively. The horizontal line, showing the phase shift of 12.5° for the tidal response of the Arbuckle aquifer to the M_2 tide in the USGS well (Wang et al. 2018; Barbour et al. 2019), intersects the model curves at $K_{z2}/b_2 \sim 10^{-8.1}, \sim 10^{-7.5}$ and $\sim 10^{-6.6} [s^{-1}]$, respectively. Given the thickness of the aquitard of 277 m, the corresponding average vertical conductivity of the aquitard

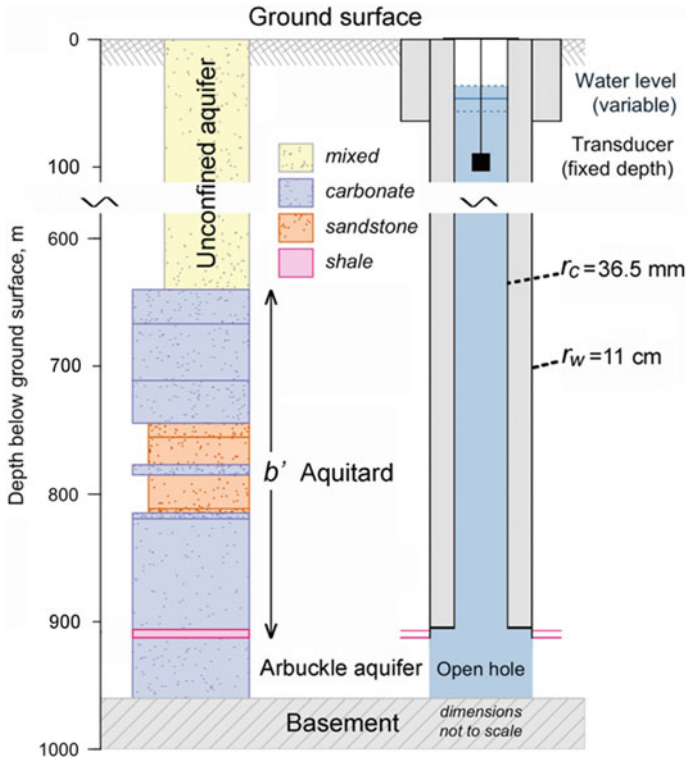


Fig. 5.20 Well construction of, and the lithology in, the USGS Oklahoma Deep Well (from Wang et al. 2018)

are, respectively, $K_{z2} = 2 \times 10^{-6}$, 9×10^{-6} and 7×10^{-5} m/s, similar to that for aquifers.

No direct measurement is available for the basement conductivity in Oklahoma. Simulating induced seismicity in Oklahoma, Langenbruch et al. (2018) estimate a basement permeability of 2×10^{-15} m² and Barbour et al. (2017) suggest a basement diffusivity that decreases from 1 m²/s at the top of the basement to 0.002 m²/s at a depth of 8 km. Here we assume two uniform basement conductivities of 10^{-8} and 10^{-4} m/s between the top of the basement and a depth of 8 km. The simulated results, plotted against the aquitard leakage factor K_{z2}/b_2 in Fig. 5.7b, intersect the horizontal black line of 12.5° phase shift at $K_{z2}/b_2 = 10^{-8.1}$ to $10^{-7.75}$ s⁻¹. Given the thickness of the aquitard of 277 m, the corresponding average vertical conductivity of the aquitard is $K_{z2} = 2 \times 10^{-6}$ and 5.4×10^{-6} m/s, respectively, as high as those of the aquifer.

In order to understand the origin of the leakage, we note that the aquitard above the Arbuckle aquifer at this location consists of a sequence of horizontally layered rocks with a total thickness of 277 m. The average vertical hydraulic conductivity of

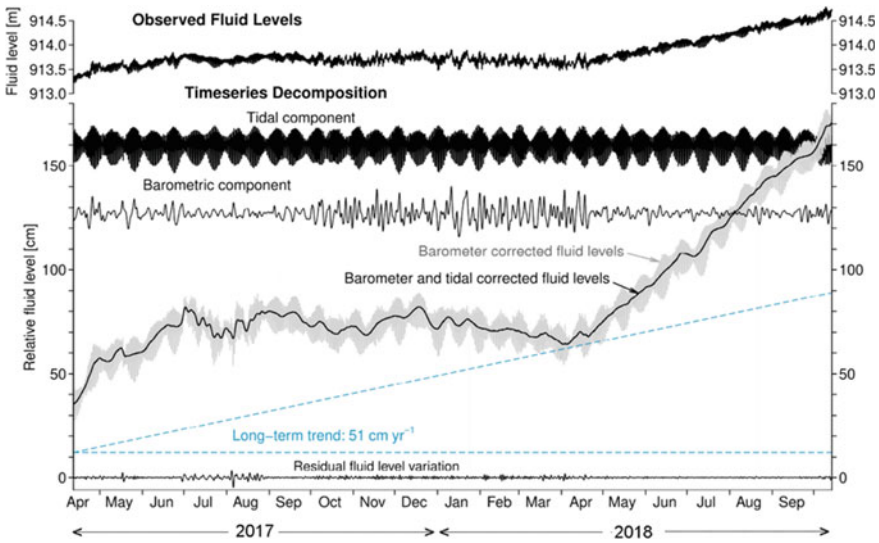


Fig. 5.21 Observed fluid level (top) from 2017 to 2018, and its decomposition into a tidal response, a barometric response, and a long-term trend (dashed line). Notice the rapid increase of water level in the well. Positive change indicates pressure increase in the Arbuckle (modified from Barbour et al. 2019)

the aquitard is therefore $b_1 / \sum_i (b_i / K_i)$ (Chap. 2), where the subscript i denotes the i th layer in the sequence and b_1 denotes the total thickness of the layers. This relation suggests that the average vertical conductivity of the aquitard is controlled by the layer with the lowest conductivity. Table 5.3 lists the thickness of each individual layer in the aquitard and its representative hydraulic conductivity assigned according to the lithology of the layer. The calculated average vertical hydraulic conductivity of the hypothetical aquitard is $\sim 5 \times 10^{-12}$ m/s that is many orders of magnitude lower than that estimated from tidal analysis (10^{-8} – 10^{-7} m/s). This average vertical conductivity is controlled by the 6-m-thick intact shale at the base of the aquitard and, in order to raise the estimation to the same order as that from tidal analysis, this basal ‘shale’ needs to have a vertical conductivity many orders of magnitude greater than that of intact shale. Wang et al (2018) thus concluded that the basal shale above the Arbuckle aquifer near the USGS Oklahoma Deep Well (Fig. 5.20) was fractured and is leaking. In other words, the ‘aquitard’ may not be confining at all at this location. On the other hand, the tidal response does not provide information on the earthquake effects on the aquifer leakage because the USGS well was installed after the occurrence of the four large ($M_w f \geq 5$) earthquakes in 2016. Given the fast rise of fluid level in this well (Fig. 5.21) and in many Arbuckle wells (Ansari et al. 2019), the Arbuckle may need to be carefully monitored in order to safeguard the overlying freshwater reservoirs and the surface environment from the hundreds of millions of barrels of wastewater injected into this aquifer.

Table 5.2 Parameters of the USGS Oklahoma deep well and the hydrogeological parameters used in the numerical simulation

Parameters	Symbol	Values	References
Well location and elevation		36.7269 N, 96.5317 W 340.16 m above sea level	USGS website ^a
Well depth		960 m beneath surface	Wang et al. (2018)
Well radius	r_w	11 cm	Wang et al. (2018)
Casing radius	r_c	3.65 cm	Wang et al. (2018)
Thickness of aquitard	b'	277 m	Wang et al. (2018)
Thickness of aquifer	b	48 m	Wang et al. (2018)
Permeability	k	2×10^{-14} to 3×10^{-12} m^2	Morgan and Murray (2015)
Transmissivity ^b	T	9.6×10^{-6} to 1.4×10^{-3} m^2/s	Calculated from k
Hydraulic conductivity	K	1.9×10^{-7} to 2.8×10^{-5} m/s	Calculated from T
Specific storage ^c	S_s	5.4×10^{-6} to 5.6×10^{-5} m^{-1}	Rahi and Halihan, (2009)
Storativity ^d	S	2.6×10^{-4} to 2.7×10^{-3}	Calculated from S_s

Modified from Wang et al. (2018)

^a https://waterdata.usgs.gov/nwis/uv/?site_no=364337096315401

^bTransmissivity is calculated from permeability using the relationship $T = b(\rho g k / \mu)$, where ρ and μ are, respectively, the density and viscosity of pore fluid in the Arbuckle aquifer. As explained in the text, groundwater in the Arbuckle aquifer near the USGS well is similar to freshwater; thus we take $\rho = 1000 \text{ kg/m}^3$ and $\mu = 0.001 \text{ Pa s}$ in the calculation of T from k

^cThe difference between the values listed here and those in Wang et al. (2018) is due to an error in this reference in converting the unit from cm^{-1} to m^{-1}

^dStorativity S is calculated from specific storage S_s (Rahi and Halihan 2009) using the relationship $S = bS_s$

5.4.6 Tidal Response of an Unconfined Aquifer with the Capillary Effect

As noted earlier, the traditional unconfined aquifer model discussed in Sect. 5.4.2 has been used for more than thirty years to interpret the positive phase shift of the groundwater response to Earth tides (e.g., Roeloffs 1996; Allègre et al. 2016; Liao and Wang 2018). But, if the water table is below the ground surface as in most cases, there is an unsaturated zone above the water table and the capillary tension between water and the solid surfaces of sediment grains may pull the pore water up against gravity to create a zone of negative (capillary) pressure. Several studies have documented that the capillary zone may have significant effects on the water table behavior. Meyboom (1967) observed that the rise in the water table during precipitation is frequently much greater in magnitude than would be predicted from the amount of precipitation and the specific yield of the aquifer. Gillham (1984) showed that the

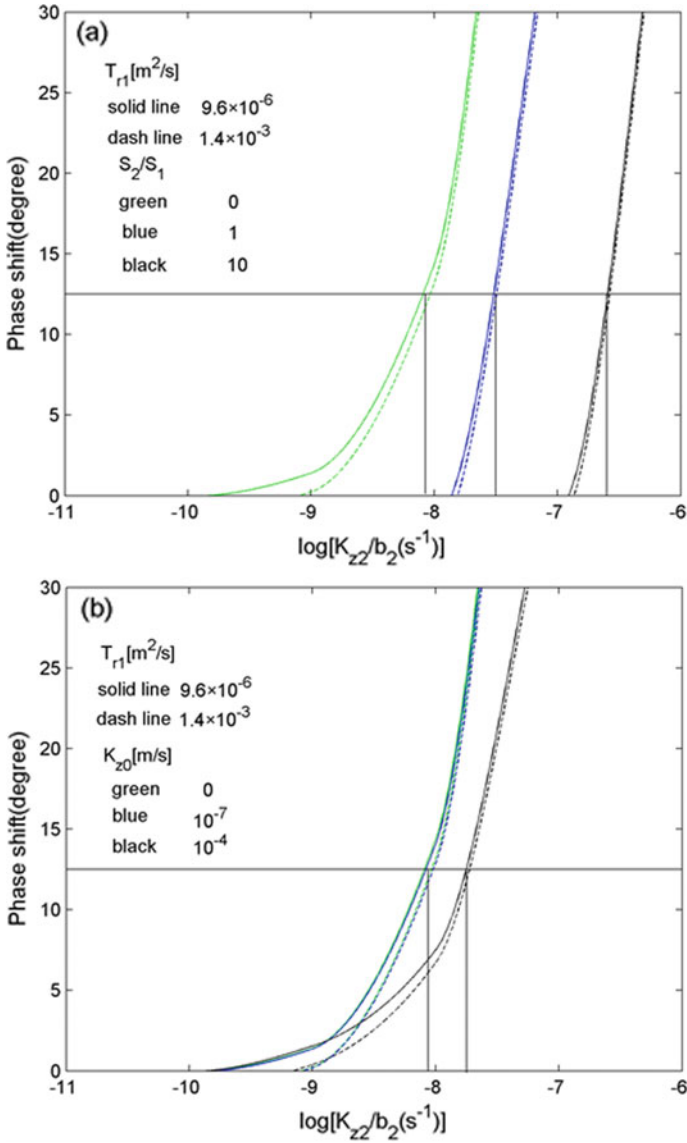


Fig. 5.22 Simulated phase shift against aquitard leakage factor K_{z2}/b_2 . **a** Without considering the basement leakage, the Arbuckle aquifer at three specified aquitard storativities of $S_2/S_1 = 0$ (red), 1 (blue) and 10 (black) and two different aquifer radial transmissivity (T_{r1}). **b** Effect of the basement leakage simulated with $S_2/S_1 = 0$ and two different aquifer transmissivities (T_{r1}). Horizontal black line shows phase shift of 12.5° of the response to the M_2 tide of the water level in the USGS Deep Well, Oklahoma (from Zhu and Wang 2020)

Table 5.3 Thickness and assumed permeability of rocks in calculating the harmonic mean of vertical permeability of a hypothetical, hydraulically intact aquitard

Rock layer	Thickness (m)	Vertical hydraulic conductivity (m/s)	References
Carbonate	106	10^{-6}	Morgan and Murray (2015)
Sandstone	31	10^{-8}	Wang (2000)
Carbonate	9	10^{-6}	Morgan and Murray (2015)
Sandstone	28	10^{-8}	Wang (2000)
Carbonate	92	10^{-6}	Morgan and Murray (2015)
Shale	6	10^{-13}	Wang (2000) (Piere shale)

addition of a small amount of water can lead to an immediate and large rise in the water table if the saturated zone of the capillary zone extends to ground surface. Turner and Nielsen (1997) measured pore pressure beneath ocean beaches in the surf zone and found that pore pressure oscillates at amplitudes much greater than that due directly to the change of surface pressure during the swash; they attributed this fluctuation of pressure to the appearance and disappearance of menisci at the sand surface during the swash. For the response to oscillatory forces, Barry et al. (1996) suggested a criterion that the capillary fringe may significantly affect the water table oscillations if the ratio $K/(\omega b) \ll 1$, where K is the hydraulic conductivity, b the effective thickness of the capillary fringe, and ω the angular frequency of the water-level oscillation. Applying this criterion to the present study, with $K \sim 10^{-6}$ m/s and $b \sim 1.6$ m for a silt aquifer (Fetter 1999), $K/(\omega b) \sim 0.006$ for the angular frequency of the M_2 tide ($\omega \sim 1.4 \times 10^{-4} \text{ s}^{-1}$). Thus, the criterion by Barry et al. (1996) suggests that the capillary fringe in a silt aquifer would significantly affect the water table response to the M_2 tide. For a sand aquifer, on the other hand, with $b \sim 0.17$ m (Fetter 1999) and $K \sim 10^{-4}$ m/s, we have $K/(\omega b) \sim 6$; thus the same criterion suggests that the capillary effect in a sand aquifer may be marginal on the water table response to Earth tides. Wang et al. (2019) showed numerically that the capillary tension may have a significant influence on the tidal response of fine grained unconfined aquifers. Here we review capillary effects and discuss their potential impact.

The basic equations for continuity of pore water in the unsaturated zone was derived in Sect. 2.6 but is relisted below for completeness,

$$\frac{\partial \theta}{\partial t} = -\nabla \cdot \mathbf{q} \quad (5.41)$$

where θ is the water content in a unit volume of variably saturated media and \mathbf{q} the vector of specific discharge. For flow in the vertical direction we have

$$q_z = -K(\theta) \left(\frac{\partial h_p}{\partial z} + 1 \right) \quad (5.42)$$

where $K(\theta) = k_r K_s$ is the unsaturated vertical hydraulic conductivity, k_r is the relative conductivity and K_s the saturated vertical hydraulic conductivity, h_p is the pressure head that equals to $p/\rho g$, ρ the density of groundwater, g the gravitational acceleration, and z the elevation above a vertical reference.

In the absence of fluid sources, the water content θ in an isotropic, partially saturated poroelastic medium is a function of the volumetric stress σ and pore pressure p ; the change of water content may thus be expressed as

$$d\theta = S_\sigma(\theta)[-B(\theta)d\sigma + dp], \quad (5.43)$$

where $S_\sigma(\theta) \equiv (\partial\theta/\partial p)_\sigma$ is the ‘unconstrained’ storage, $B(\theta)$ is the Skempton’s coefficient, and compression is considered positive to be consistent with the sign convention in the previous sections. In view that the differences among the storages defined under different boundary conditions (discussed in Chap. 3) are small, we follow Bear (1972) to express the storage as $(C(\theta) + S_e S_s)/\rho g$ to include both the saturated and unsaturated media, where $C(\theta) = \partial\theta/\partial h_p$ is the specific moisture capacity, S_s is the specific storage for saturated media, S_e is the effective saturation defined as

$$S_e = (\theta - \theta_r)/(\theta_s - \theta_r), \quad (5.44)$$

where θ_r and θ_s are, respectively, the residual and the saturated water content. Thus (5.43) may be rewritten as

$$d\theta = (C(\theta) + S_e S_s)(-B(\theta)d\sigma + dp)/\rho g. \quad (5.45)$$

Combining Eqs. (5.41), (5.42) and (5.45), we obtain

$$\frac{\partial}{\partial z} \left[K(\theta) \left(\frac{\partial h_p}{\partial z} + 1 \right) \right] = (C(\theta) + S_e S_s) \left(-\frac{B(\theta)}{\rho g} \frac{\partial \sigma}{\partial t} + \frac{\partial h_p}{\partial t} \right). \quad (5.46)$$

Finally, given $\sigma = K_u \epsilon$, Eq. (5.38) may be expressed as

$$\frac{\partial}{\partial z} \left[K(\theta) \left(\frac{\partial h_p}{\partial z} + 1 \right) \right] = (C(\theta) + S_e S_s) \left(-\frac{B(\theta) K_u}{\rho g} \frac{\partial \epsilon}{\partial t} + \frac{\partial h_p}{\partial t} \right). \quad (5.47)$$

Under saturated conditions, $C(\theta) = 0$, $S_e = 1$, $B(\theta) = B$, and $K(\theta) = K_s$, and Eq. (5.47) reduces to the traditional equation for the tidal effect on saturated flow in unconfined aquifers (5.20a).

For simulation, Wang et al. (2019) assumed a column of uniform sediment extending from the ground surface to infinite depth (Fig. 5.23), where an unsaturated zone lies above a water table at a depth b . For boundary conditions, Wang et al. (2019) assigned a no-flow boundary condition at infinite depth, i.e.,

$$q = 0 \text{ at } z = \infty, \quad (5.48)$$

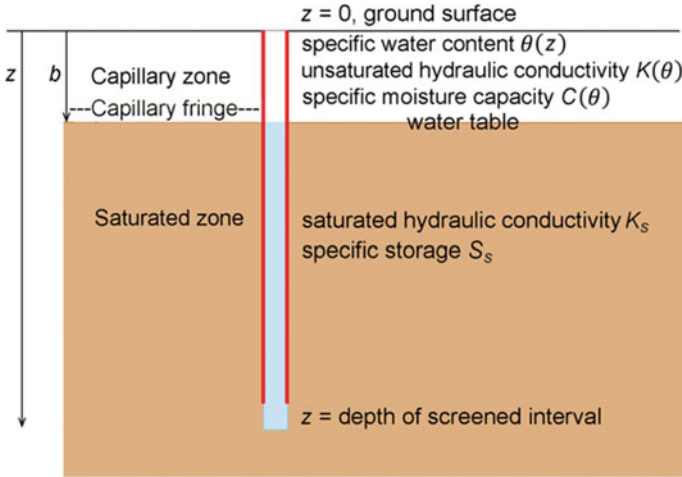


Fig. 5.23 Well in an unconfined aquifer with the water table below the surface (from Wang et al. 2019)

and a mixed boundary condition is assigned at the ground surface, i.e.,

$$q = -k_r K_s h_p / b \text{ at } z = 0, \quad (5.49)$$

which is a type of boundary condition used in numerical simulation of problems where the boundary condition depends on the solution, such as seepage-face formation, evapotranspiration and rainfall infiltration. It has the advantage that it adjusts to the dynamic changes of boundary conditions automatically without additional checks. For the present case, the water table oscillates due to seasonal and tidal forcing. When the depth of the water table is greater than the thickness of the capillary fringe, $S_e(z = 0) \rightarrow 0$ and $k_r(z = 0) \rightarrow 0$, and (5.49) is a no-flow condition. On the other hand, when the water table reaches the ground surface, i.e., $b = 0$, $k_r K_s / b = K_s / b \rightarrow \infty$, and (5.49) becomes a free-flow condition.

A large amount of experimental measurements has been accumulated for the hydraulic properties of unsaturated sediments and several empirical relations have been developed to fit the experimental data, including the van Genuchten-Mualem relation between the effective saturation $S_e(\theta)$ and the capillary pressure head h (van Genuchten 1980)

$$S_e(\theta) = [1 + (\alpha h)^n]^{-m}, \quad (5.50)$$

the van Genuchten-Mualem relation for the relative conductivity $k_r(\theta)$ (Mualem 1976)

$$k_r(\theta) = S_e^l \left[1 - \left(1 - S_e^{\frac{1}{m}} \right)^m \right]^2, \quad (5.51)$$

and the van Genuchten relation for the specific moisture capacity $C(\theta)$ (van Genuchten 1980)

$$C(\theta) = \frac{\alpha m}{1 - m} (\theta_s - \theta_r) S_e^{\frac{1}{m}} \left(1 - S_e^{\frac{1}{m}}\right)^m, \tag{5.52}$$

where α, l, m and n are fitting parameters in the empirical relations for fitting experimental data for unsaturated sediments.

Wang et al. (2019) assumed a constant Skempton coefficient in the unsaturated zone because there is no experimental data for the dependence of B on θ . Furthermore, the change of pore pressure occurs mostly in the saturated zone that is also volumetrically larger than the unsaturated zone; thus, the change of B with θ in the unsaturated zone should have a minimal effect on the tidal response of the water level. Because the system of equations is nonlinear and difficult to solve with analytical methods, a finite element numerical procedure is used. Figure 5.24 shows the simulated hydraulic head at different depths in response to the M_2 tide, with an average water table depth at 0.5 m.

Figure 5.25 shows the amplitude ratio and phase shift to the M_2 tide for (a) a silt aquifer and (b) a sand aquifer, with the average water table set at different depths, plotted against the dimensionless depth z/δ , where $\delta = \sqrt{2D/\omega}$, D is the hydraulic diffusivity and ω is the angular frequency of the M_2 tide. The difference in the tidal

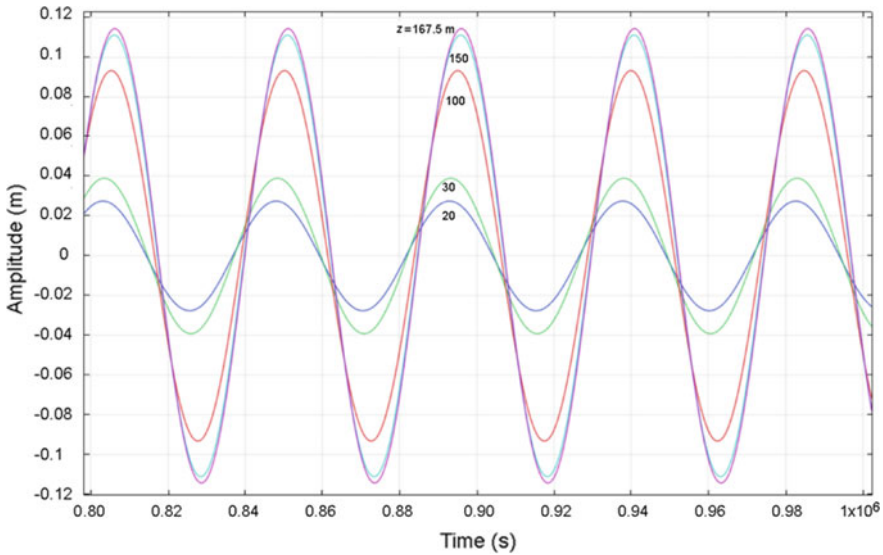


Fig. 5.24 Simulated water level oscillations in a silt aquifer in response to the M_2 tide when the average water table depth is 0.5 m. Numbers on the curves mark the depth of the screened interval of the well (from Wang et al. 2019)

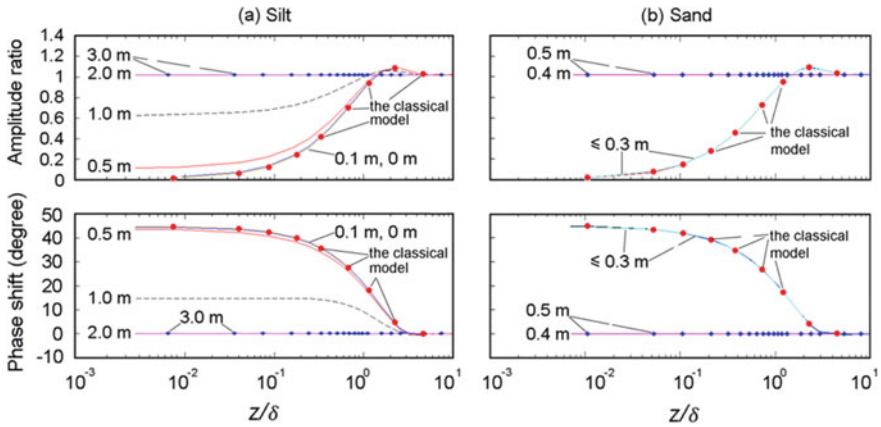


Fig. 5.25 Simulated amplitude ratio and phase shift of the tidal response of pressure head in unconfined aquifers composed of **a** silt and **b** sand, plotted against the normalized depth of the water table z/δ (see text for definition of δ). Numbers next to each curve show the average water table depth in the simulation. Red solid circles denote the predicted response for the traditional model of unconfined aquifers (from Wang et al. 2019)

response between a silt aquifer and a sand aquifer may be explained by the different thickness of their capillary fringes (where k_r decreases from 1 to ~ 0) together with their different conductivities, as explained earlier. Figure 5.26 shows the significant difference between the capillary fringe in a silt aquifer and that in a sand aquifer. Furthermore, the high conductivity and thin capillary fringe would lower the effect of the capillary fringe in a sand aquifer on its tidal response (Barry et al. 1996), as discussed earlier.

Based on the capillary model for an unconfined aquifer, Wang et al. (2019) simulated the tidal response with the seasonal change of water level documented in the Lijiang well that opens to a fine-grained carbonate aquifer (Liao and Wang 2018). Results of their simulation (stars in Fig. 5.27) show excellent agreement with observation (dots in Fig. 5.27). Thus, the seasonal change of the tidal response of water level in this well may simply be due to the capillary zone above the water table and its seasonal removal when the water table rises to the surface during rainy seasons. More studies of the capillary effect on the tidal response of groundwater are definitely needed to further demonstrate this effect.

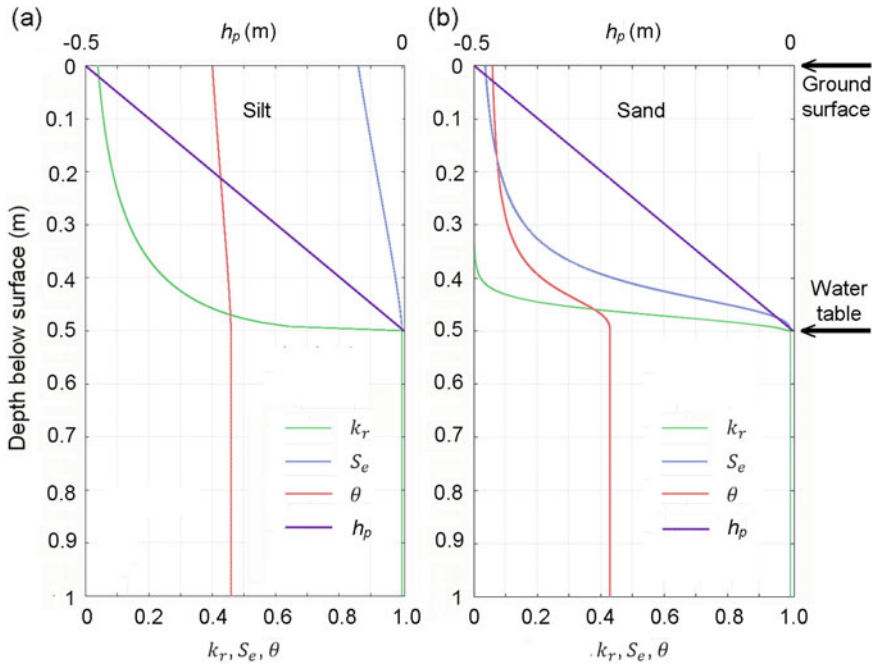


Fig. 5.26 Relative hydraulic conductivity, relative saturation, water content and pressure head in **a** a silt aquifer and **b** a sand aquifer above and below the water table, with the average water table depth set at 0.5 m (based on van Gneuchten 1980)

5.5 Groundwater Response to Barometric Changes

5.5.1 Barometric Response of Aquifers and Barometric Efficiency

The barometric pressure on Earth’s surface is due to the weight of the atmosphere per unit area. This load is balanced both by the stresses in the solid matrix and by the pressure in the pore water. A change in the barometric pressure causes changes in both the stress in the solid matrix and the pressure in the pore fluid. Thus, in response to an increase of the barometric pressure, the increase of water pressure inside an open well that penetrates a confined aquifer will be greater than the increase of pore pressure in the surrounding formations and will thus force the well water to flow into the aquifer until an equilibrium is reached between the water pressure in the well and the pore pressure in the aquifer. The response of water level in an open well (Fig. 5.28) is thus opposite in sign from that of the barometric change, i.e., water level decreases with increases in the barometric pressure, and vice versa (Fig. 5.29). Jacob (1940)

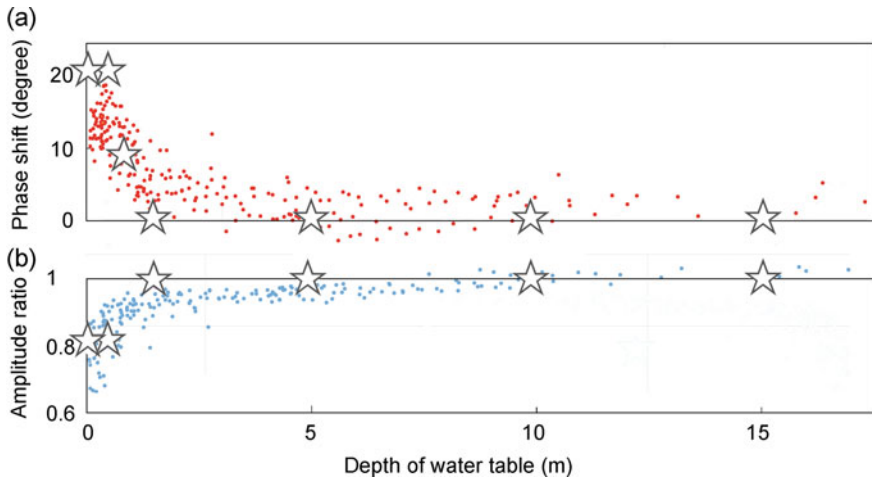


Fig. 5.27 Observed **a** phase shift (red dots) and **b** amplitude ratio (blue dots) of the tidal response to the M_2 tide in the Lijiang well plotted against the water table depth (from Liao and Wang 2018). Simulated phase shift and amplitude ratio with the hydraulic parameters listed in the last column of Table 4.3 are plotted as stars. Notice that the phase shift is close to 0 and the amplitude ratio close to 1 when the water level depth is more than 2 m, but phase shift increases while amplitude ratio decreases when the water table becomes shallower than 2 m below the ground surface (from Wang et al. 2019)

defined the ratio between the water level change in the well and the barometric change (expressed in water height) as the barometric efficiency, BE (Sect. 3.2.5; Eq. 3.87), with typical values between 0.25 and 0.75 (Bear 1972) which is a measure of the aquifer compressibility. The time-delay between the water-level response and the barometric change, as discussed in a later subsection, contains information about the diffusivity of both the aquifer and the aquitard (the semi-confining layer).

Quantitative analysis of the barometric response began with Jacob (1940) and has since been broadly applied to estimate the hydraulic properties of aquifers and aquitards (e.g., Rojstaczer 1988; Evans et al. 1991; Odling et al. 2015). It has also been used to study earthquake effects on groundwater systems (Zhang-Shi et al. 2019a, Zhang-Wang et al. 2019).

5.5.2 Analytical Solution with a Half-Space Aquitard

If the aquifer is perfectly confined and has high lateral transmissivity, the response of water level in a well to a change of barometric pressure is nearly instantaneous and linearly proportional to the barometric change. However, most aquifers are not perfectly confined and a confining layer may allow flow across its boundaries. Under such conditions, the barometric efficiency would depend on the frequency of the applied load, and is denoted by $BE(\omega)$. Analysis of this dependency may reveal how

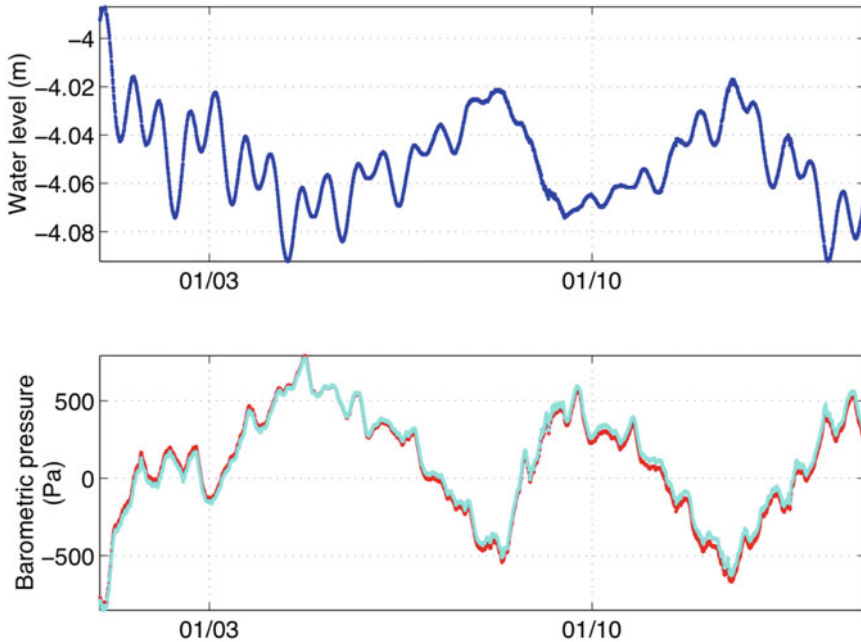


Fig. 5.28 Water level recorded in well CIB of the Pinon Flat Observatory and barometric pressure on site during the first 15 days of 1999 (modified from Doan et al. 2006)

the vertical hydraulic conductivity of the aquitard and the horizontal transmissivity of the aquifer depend on frequency and has been the subject of discussion in several papers (e.g., Rojstaczer 1988; Hussein et al. 2013; Odling et al. 2015). In the following we first review the analytical model of Rojstaczer (1988), which is often cited in barometric studies. We will then review an improved model and some numerical analyses by Olding et al. (2015). These models allow estimates of the pneumatic diffusivity of the unsaturated zone, the vertical hydraulic diffusivity of the semi-confining layer, and the lateral permeability of the aquifer, with errors due to the simplifications of the models. Comparison among the models will be made to provide some understanding of the probable errors in these estimates.

Rojstaczer (1988) derived an analytical model for interpreting the response of a semi-confined aquifer to changes of the barometric pressure. To simplify the analysis, he assumed that the barometric response may be treated by three individual but connected one-dimensional problems—a vertical pneumatic flow in the unsaturated zone of the aquitard (between the surface and the water table), a vertical groundwater flow in the saturated zone of the aquitard (between the water table and the base of the aquitard), and a radial flow between the aquifer and the well, connected by conditions of continuity across their boundaries, as described next (Rojstaczer 1988).

The amplitude of the change in water level in a well is affected by the atmospheric load, the far field pore pressure (in terms of the equivalent water level), and the

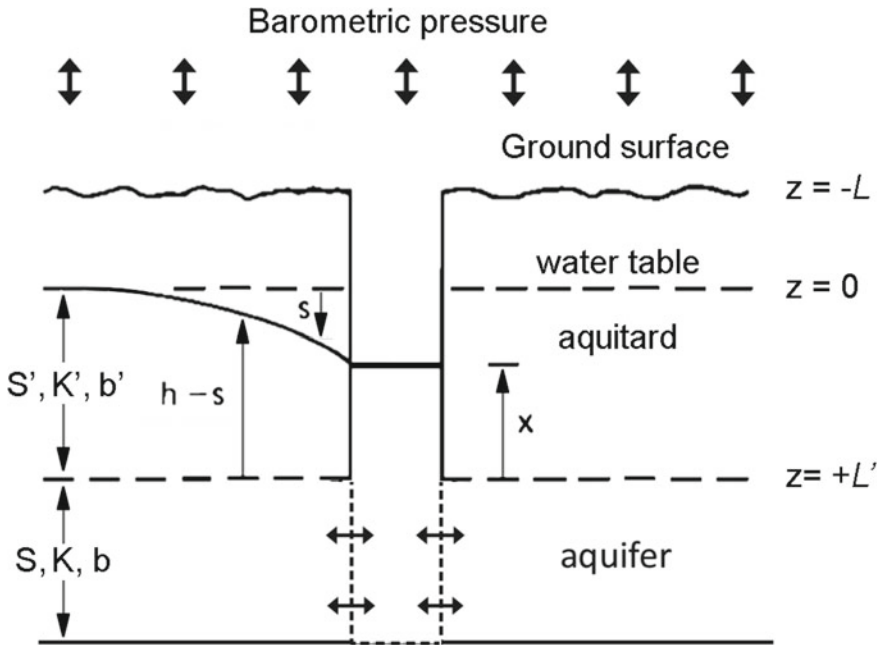


Fig. 5.29 Schematic diagram showing an aquifer and a semi-confining layer (aquitard), borehole and groundwater flow in response to changing barometric pressure (modified from Odling et al. 2015)

drawdown at the well. Thus the response of the water level in wells may be described in the frequency domain as

$$x_o = -\frac{A}{\rho g} + \frac{P_o}{\rho g} - s_o, \tag{5.53}$$

where A is the amplitude of the atmospheric load, P_o is the amplitude of the far field pore pressure in the aquifer, and s_o is the amplitude of the drawdown at the well. The periodic flow of air in the unsaturated aquitard between the surface and the water table is governed by the differential equation

$$D_a \frac{\partial^2 P_a}{\partial z^2} = \frac{\partial P_a}{\partial t}, \tag{5.54}$$

where the the barometric pressure P_a is subjected to the following boundary condition

$$P_a(\pm L, t) = A \cos(\omega t). \tag{5.55}$$

$z = -L$ is taken to be the Earth's surface above the groundwater table ($z = 0$), A is the amplitude of the barometric oscillations at the surface, D_a is the pneumatic

diffusivity in the unsaturated layer, assumed constant, and the condition at $z = L$ is a design to ensure no flow of air across the groundwater table. The solution for air-pressure at the water table ($z = 0$) is (Rojstaczer 1988)

$$P_a = A(M + iN)\exp(i\omega t) \quad (5.56)$$

where

$$M = \frac{2\cosh(\sqrt{R_a})\cos(\sqrt{R_a})}{\cosh(2\sqrt{R_a}) + \cos(2\sqrt{R_a})}, \quad (5.57)$$

$$N = \frac{2\sinh(\sqrt{R_a})\sin(\sqrt{R_a})}{\cosh(2\sqrt{R_a}) + \cos(2\sqrt{R_a})}, \quad (5.58)$$

and

$$R_a = L^2\omega/2D_a. \quad (5.59)$$

For the vertical groundwater flow in the saturated aquitard, the controlling differential equation is

$$D' \frac{\partial^2 P}{\partial z^2} = \frac{\partial P}{\partial t} + A\omega\gamma \sin \omega t, \quad (5.60)$$

where P is the excess pore pressure in the saturated aquitard (above hydrostatic pressure), D' is the hydraulic diffusivity of the aquitard, and γ is the loading efficiency defined as $1 - \text{BE}$. The upper boundary condition is equal to the barometric pressure at the water table (5.56), i.e.,

$$P(0, t) = P_a = A(M + iN)\exp(i\omega t). \quad (5.61)$$

Rojstaczer (1988) simplified the problem by assuming that the vertical flow occurs in a half space so that the lower boundary condition becomes

$$P(\infty, t) = A\gamma\exp(i\omega t). \quad (5.62)$$

Under these boundary conditions, the solution of (5.60) at the base of the aquitard ($z = L'$) is

$$P(z = L', t) = A \left[\gamma + (M + iN - \gamma)\exp\left(-(1 + i)\sqrt{R'}\right) \right] \exp(i\omega t) \quad (5.63)$$

where

$$R' = L'^2\omega/2D'. \quad (5.64)$$

Finally, assuming that the aquifer has negligible loading efficiency, i.e., $\gamma \sim 0$, and that the aquitard has negligible storage, we may express the controlling differential equation for the radial flow between the borehole and the aquifer with a semi-confining aquitard as (Hantush and Jacob 1955)

$$T \left(\frac{\partial^2 s}{\partial r^2} + \frac{1}{r} \frac{\partial s}{\partial r} \right) - \frac{K' s}{L'} = S \frac{\partial s}{\partial t}, \quad (5.65)$$

where the small letter s is the draw down near the well, T and the capital letter S are the transmissivity and storativity of the aquifer, respectively, and K' and L' are the hydraulic conductivity and the thickness of the semi-confining aquitard, respectively.

The boundary conditions are

$$s(\infty, t) = 0, \text{ at } r \rightarrow \infty, \quad (5.66)$$

and

$$\lim_{r \rightarrow 0} \frac{T \partial s}{\partial r} = \frac{\omega r_w^2 x_o}{2r_c T} \sin \omega t \quad (5.67)$$

where r_w is the radius of the cased section of the well where water level is measured, r_c is the radius of the screen section of the well, and x_o is the amplitude of the water level fluctuation in the well casing produced by the volumetric discharge of the aquifer. Subjected to these conditions, (5.65) may be solved to yield the drawdown in the well (Rojstaczer 1988)

$$s_w = \frac{i}{2} W x_o K_o \left\{ [W^2 (S^2 + q^{-2})]^{1/4} \exp \left[\frac{i}{2} \tan^{-1}(qS) \right] \right\} \exp(i\omega t) \quad (5.68)$$

where K_o is the modified Bessel function of the second kind of order zero, W is a dimensionless frequency defined as

$$W = \omega r_w^2 / T, \quad (5.69)$$

and

$$q = L' \omega / K'. \quad (5.70)$$

The barometric efficiency and the phase shift of the response are then expressed by

$$\text{BE}(\omega) = |x_o \rho g / A|, \quad (5.71a)$$

and

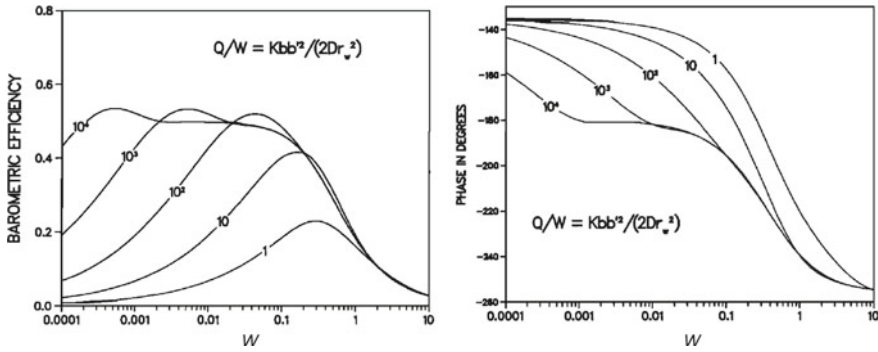


Fig. 5.30 Modeled barometric efficiency (left) and phase (right) of the response of a well to barometric pressure as a function of the dimensionless frequency W . Assumed values are $S = S' = 10^{-4}$ and $BE = 0.5$. Numbers on the curves represent the value of $Kbb^2/(2Dr_w^2)$, another dimensionless quantity (Rojstaczer 1988)

$$\eta(\omega) = \arg(x_o \rho g / A), \tag{5.71b}$$

where x_o is evaluated with (5.53), P_o from $P(z = L') \exp(-i\omega t)$ (5.63) and s_o from $s_w \exp(-i\omega t)$ (5.68). Rojstaczer (1988) evaluated and plotted the barometric efficiency and the phase shift as a function of the dimensionless frequency W (Fig. 5.30).

5.5.3 Analytical Solution with a Finite Aquitard

The model of Rojstaczer (1988) simplifies the solution with that for a half-space aquitard. Odling et al. (2015) presented the solution with an aquitard of finite thickness, which we present in Appendix 5.3. This solution is analogous to that for heat conduction in a solid of two layers with different thermal conductivities, subjected to a periodic surface condition (Carslaw and Jaeger 1959, 3.7). The solution for the pressure at the base of the aquitard (Appendix 5.3) is

$$P(z = L', t) = A \left[\gamma + (M + iN - \gamma) \left(E' - F' \frac{GE' + HG'}{GF' + HH'} \right) \right] \exp(i\omega t) \tag{5.72}$$

where M and N are defined in (5.57–5.58), and

$$E' = \cosh \left[(1 + i)\sqrt{R'} \right], \tag{5.73a}$$

$$F' = \frac{L'}{K'} \frac{\sinh\left[(1+i)\sqrt{R'}\right]}{\left[(1+i)\sqrt{R'}\right]}, \quad (5.73b)$$

$$G' = -\frac{K'}{L'} \left[(1+i)\sqrt{R'}\right] \sinh\left[(1+i)\sqrt{R'}\right], \quad (5.73c)$$

$$H' = E', \quad (5.73d)$$

L' , K' and D' are, respectively, the thickness, hydraulic conductivity and diffusivity of the saturated aquitard. The parameters E , F , G and H for the aquifer are defined similarly but with L' , K' , D' and R' replaced by L , K , D and R , respectively, and R is given by

$$R = L^2\omega/2D. \quad (5.74)$$

Here we replaced A , B , C , and D in Carslaw and Jaeger with E , F , G , and H in order to avoid the possible confusion with the parameters A and D defined earlier. We also follow the earlier use of parameters with a prime for the aquitard parameters and those without a prime for the aquifer parameters.

Since the aquifer in the model is one-dimensional and horizontal (5.65), the pressure at the base of the aquitard (5.72) is identical to that in the aquifer. Thus P_o in (5.53) is given by

$$P_o = \frac{P(z = L', t)}{\exp(i\omega t)} = A \left[\gamma + (M + iN - \gamma) \left(E' - F' \frac{GE' + HG'}{GF' + HH'} \right) \right] \quad (5.75)$$

The predicted results of the two analytical models, i.e., that for a half-space aquitard (Rojstaczer 1988) and that for a finite aquitard (Odling et al. 2015), based upon identical parameters (Odling et al. 2015, Table 1), are plotted and compared in Fig. 5.31. It shows that, at low frequencies (< 0.1 cpd), the half-space model predicts a phase shift tens of degrees smaller than that predicted by the finite-aquitard model.

5.5.4 Numerical Solution

Odling et al. (2015) carried out a suite of numerical simulations of the barometric effect on water level in wells using the software MODFLOW 2000. The model consists of an aquitard of 20 m in thickness with hydraulic conductivity and specific storage typical of glacial sediments overlying an aquifer of 10 m in thickness with hydraulic conductivity and specific storage typical of fractured chalk (Table 5.4). Odling et al. (2015) assumed that the unsaturated zone of the aquitard has a minor influence on the barometric response of the aquifer and excluded it in the numerical

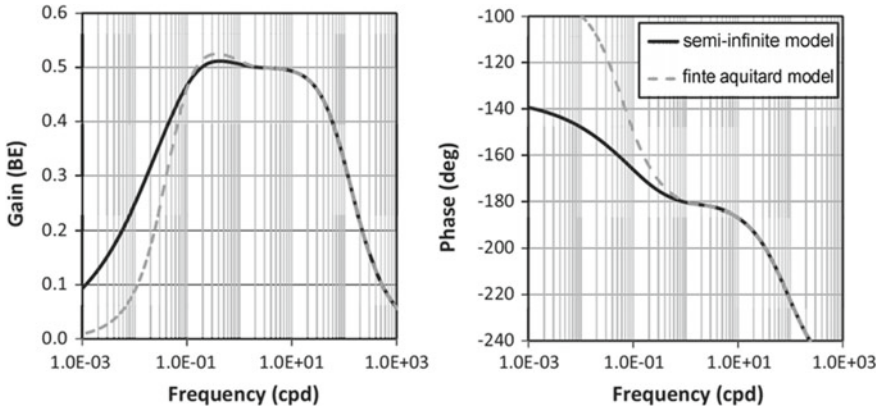


Fig. 5.31 Comparison between the half-space model of (Rojstaczer, 1988) (solid black curve) with the finite-aquitard model (dashed grey curve) (from Odling et al. 2015)

Table 5.4 Layer properties assumed in the numerical simulations

Material	K (m/d)	S_s (m^{-1})	D (m^2/d)
Confining layer A	1.57×10^{-3}	1.57×10^{-3}	1
Confining layer B	9.53×10^{-3}	9.53×10^{-4}	10
Confining layer C	3.35×10^{-2}	6.71×10^{-4}	50
Aquifer	1	2.76×10^{-6}	3.6×10^5
Heterogeneity	1	1.0×10^{-4}	1.0×10^4

simulation. The radius of the boreholes in the numerical simulations is assumed to be infinitely small, i.e., the influence on the barometric response of a finite borehole radius is not modeled, which affects the responses only at relatively high frequencies (Hussein et al. 2013). Finally, the numerical model does not include the influence of the elastic properties of the solid aquifer matrix, so that changes in barometric pressure are transmitted entirely to the pore waters. Thus, the result corresponds to the case of an aquifer with static barometric efficiency (BE) equal to 1, which scales the gain of the barometric response by a factor of BE but leaves the phase unaffected (Odling et al. 2015).

Figure 5.32 compares the numerical results with that predicted by the finite-aquitard model. The results are in general agreement at aquitard hydraulic diffusivities lower than $100 \text{ m}^2/d$, with the numerical results lying slightly towards higher frequencies. With increasing diffusivity, the peak gains from the numerical results become progressively lower than those predicted by the analytical model and, at diffusivities of 10^3 and $10^4 \text{ m}^2/d$, all phases from the numerical results lie well towards lower frequencies. This comparison led Odling et al. (2015) to suggest that the finite-aquitard model may provide reasonable predictions for the barometric response if the aquitard (confining layer) hydraulic diffusivity is $100 \text{ m}^2/d$ or below.

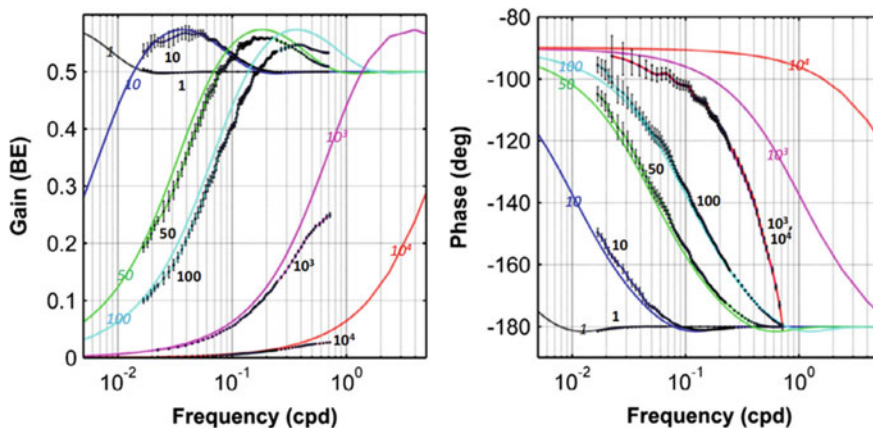


Fig. 5.32 Comparison between the finite-aquitard model (colored solid curves) and numerical simulations (black curves with one standard deviation error bars) as a function of frequency. Curves are labeled with the aquitard hydraulic diffusivity (m^2/d) (from Odling et al. 2015)

5.5.5 Applications

Odling et al. (2015) applied the numerical simulation to examine the barometric response in three open monitoring boreholes in the semi-confined Chalk Aquifer of East Yorkshire, NE England. It is a semi-confined fractured chalk aquifer of Quaternary age, confined by an aquitard of highly heterogeneous sands, gravels, clay rich till and alluvium. The Chalk Aquifer is the UK's principal aquifer and the Yorkshire area is intensely farmed; thus the aquifer is particularly vulnerable to nitrate contamination from agricultural fertilizers. Time series of borehole water levels and barometric pressure were recorded at 15 min intervals over periods of 294 to 800 days, and the barometric response of the water level in the three monitoring boreholes was determined over the frequency range 0.015–2 cpd (Fig. 5.33).

The best-fit analytical barometric response curves for the Benningholme borehole yield an estimate of $\text{BE} = 0.49$ and a confining layer hydraulic diffusivity of $10 \text{ m}^2/\text{d}$, typical of clay rich sediments. The estimated BE is similar to the value calculated from the known compressibility and matrix porosity for the Chalk Aquifer matrix in this region, suggesting that the analytical model may provide realistic predictions. On the other hand, the barometric response for the boreholes at Thornholme Moor and Bracey Bridge both show lower gain than that for the Benningholme borehole (Fig. 5.33). The fit of the analytical model to the barometric response for Thornholme Moor yields an estimate of hydraulic diffusivity ($310 \text{ m}^2/\text{d}$) typical of silt-rich alluvium and $\text{BE} = 0.39$, the latter being lower than that estimated for the Benningholme borehole. The fit of the analytical model to the barometric response for the borehole at Bracey Bridge is much poorer and gives a very low estimate of BE (0) and a very high hydraulic diffusivity ($20,000 \text{ m}^2/\text{d}$), typical of sands. Odling et al. (2015) interpret the very high value of hydraulic diffusivity and the poor fit by the analytical model

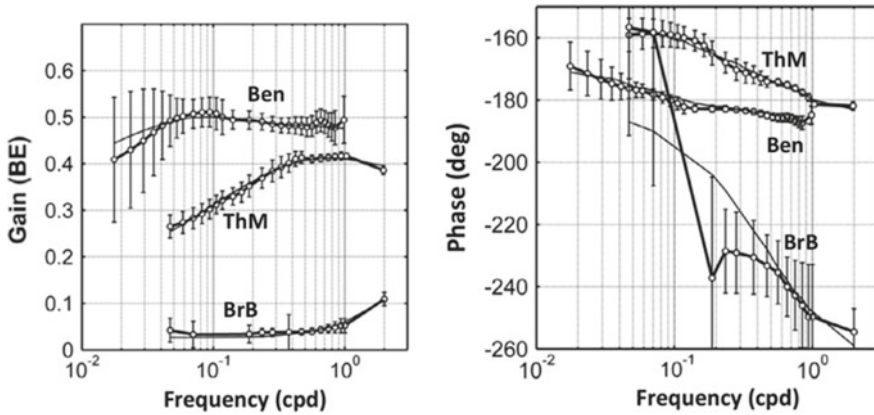


Fig. 5.33 Barometric responses estimated from water-level records in three boreholes in the Chalk Aquifer of East Yorkshire, NE England. The thick curves are the best numerical fit to the data; the thin curves are the best analytical fit to the data (from Odling et al. 2015)

as suggesting that this borehole may lie close to a fully penetrating heterogeneity with high diffusivity.

5.6 Estimating Hydraulic Property with Tidal and Barometric Methods

A recent development in earthquake hydrology is the joint analysis of the tidal and barometric responses of water levels in wells to understand earthquake effects on groundwater systems. Since this development is in its initial stage, a comparison between different studies may be useful to reveal the different approaches in such applications.

Two independent studies (Zhang-Shi et al. 2019; Zhang-Wang et al. 2019) analyzed the tidal and the barometric responses of water level in a deep (2600 m) well, Zuojiazhuang (ZJZ), in northern China (Fig. 5.34), before and after the 2011 Mw9.1 Tohoku earthquake. The well is screened between depths of 2079 and 2600 m and is open to an aquifer of Late-Precambrian carbonate rocks. The aquifer is overlain by an aquitard consisting of >2 km of younger volcanic rocks and breccia, tuff, sandstone and mudstone.

Zhang-Wang et al. (2019) analyzed the tidal response of water level in the well and calculated the barometric efficiency and the phase shift of the water-level response to barometric pressure before and after the 2011 Tohoku earthquake. Figure 5.35 shows that the earthquake caused significant changes in the tidal response by increasing the phase shift from -40° to $\sim 0^\circ$ and the amplitude ratio from ~ 0.7 to 1. Moreover, these changes stayed nearly constant from 2011 to 2015 until the well was refurbished.

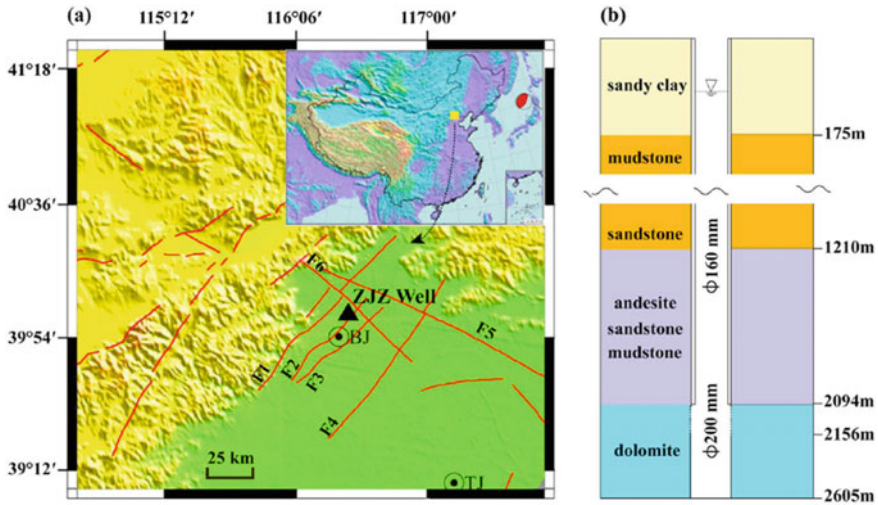


Fig. 5.34 **a** Location of the Zuojiashuang Well and the epicenter of the 2011 Tohoku earthquake. **b** Simplified lithological profile of the borehole. (F1 is the Huangzhuang-Gaolying fault, F2 is the Shunyi-Qianmen-Liangxiang fault, F3 is the Nanyuan-Tongxian fault, F4 is the Xiandian fault, F5 is the Changping-Fengnan fault, and F6 is the Nankou-Sunhe fault) (from Zhang-Shi et al. 2019)

Some post-seismic phase shifts are slightly above zero, but it is difficult to ascertain their physical significance because the analysis used the theoretical tidal strain as the reference, which may differ appreciably from the actual local strain due to the effects of local topography and subsurface heterogeneities (e.g., Beaumont and Berger 1975).

Zhang-Wang et al. (2019) noted two possible interpretations of the coseismic change of the tidal response; it could either be due to a coseismic increase of the horizontal transmissivity above $10^{-4} \text{ m}^2/\text{s}$ or due to an increase of the vertical diffusivity of $\lesssim 0.03 \text{ m}^2/\text{s}$. In order to assess which interpretation is correct, they evaluated the barometric efficiency and the phase shift of the water-level response. At frequencies up to 0.8 cpd, the barometric efficiency (Fig. 5.36a) and phase shift (Fig. 5.36b) were nearly constant at 0.6 and 0, respectively, before and after the Tohoku earthquake. At higher frequencies, the results are no longer reliable because the coherence between the two timeseries deteriorated. Zhang-Wang et al. (2019) suggested that these results are evidence that the aquifer was confined both before and after the Tohoku earthquake and thus preferred the interpretation that the coseismic increase of phase shift was due to a large increase in the horizontal permeability during the Tohoku earthquake, rather than due to an increase of the vertical permeability. Using a confined aquifer model (Hsieh et al. 1987) they interpreted the observed tidal response of water level in the ZJZ well to be due to an order of magnitude coseismic increase in the horizontal permeability and a small decrease of the specific storage.

Zhang-Shi et al. (2019) analyzed the tidal response in the same Zuojiashuang well and also found a coseismic increase of the phase shift of the water level to the M_2

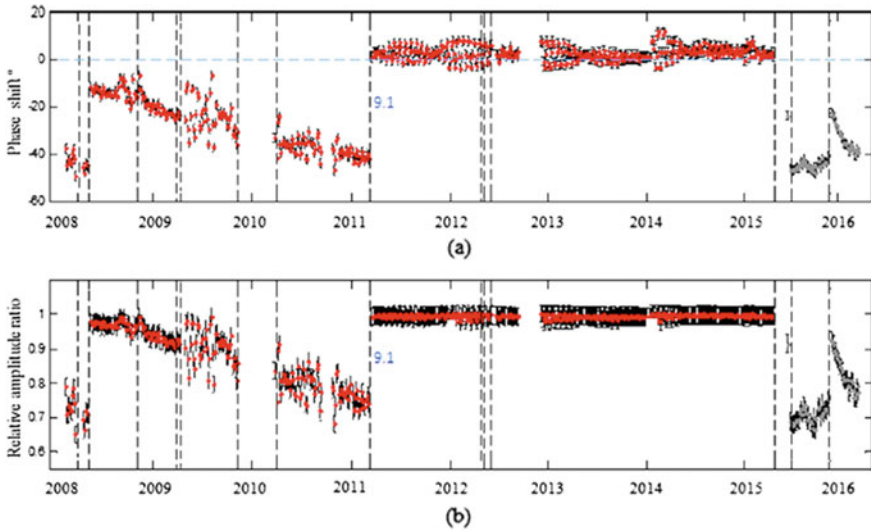


Fig. 5.35 Phase shift and amplitude ratio of the tidal response to the M2 tide in the ZJZ well. Notice that the amplitude stayed nearly constant following the 2011 Mw9.1 Tohoku earthquake. The discontinuities in the times series in year 2015 were due to well cleaning and renovation; later data were not included in the analysis (from Zhang-Wang et al. 2019)

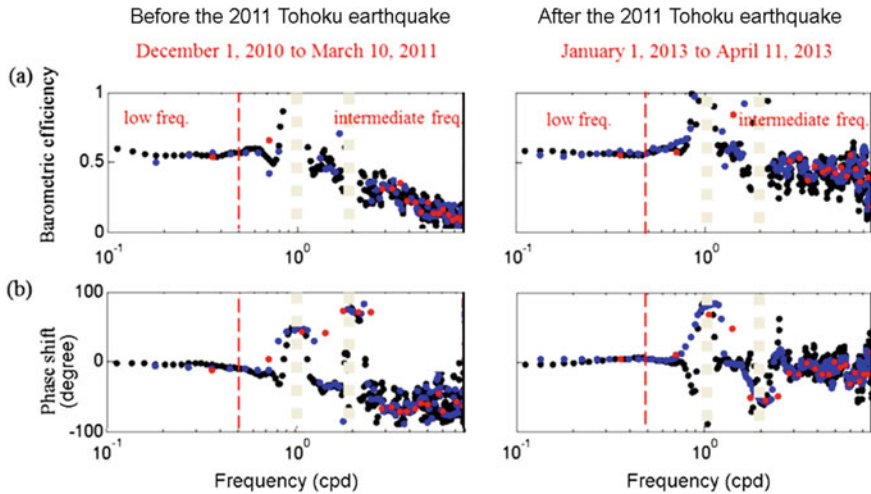


Fig. 5.36 **a** Barometric efficiency and **b** phase shift before (left) and after (right) the Tohoku earthquake, plotted against frequency between 0.1 to 8 cpd in the ZJZ well. Negative phase shifts indicate that the water-level response lags behind the change of atmospheric pressure. The water level data and the atmospheric pressure data were split into spans of $2N$ samples with $N = 16$ (black dots), 14 (blue dots) and 12 (red dots) (modified from Zhang-Wang et al. 2019)

tide during the Tohoku earthquake, from a pre-seismic -40° to a post-seismic $\sim 2^\circ$. They calculated the wavelet power spectra (WPS) for the barometric pressure and water level and the wavelet coherences (WTC) among water level, tidal volumetric strain and the barometric pressure (Fig. 5.37). They showed that the water-level WPS was enhanced after the Tohoku earthquake and the WTC between water level and the barometric pressure expanded in scope.

Zhang-Shi et al. (2019) used data 4 months before and 1 year after the 2011 Tohoku earthquake to calculate the barometric response transfer function. The barometric response, shown as circles with normalized standard errors in Fig. 5.38, shows a nearly constant gain of 0.55 before and after the earthquake over the observed frequency band (Fig. 5.38a) and a phase shift slightly less than -180° before the earthquake but slightly greater than -180° after the earthquake and (Fig. 5.38b). Fitting the data with Rojstaczer's (1988) barometric response model (5.71) they obtained the best fitting curves before and after the earthquake and estimated a six-fold increase in the horizontal permeability and a two-fold increase in the vertical

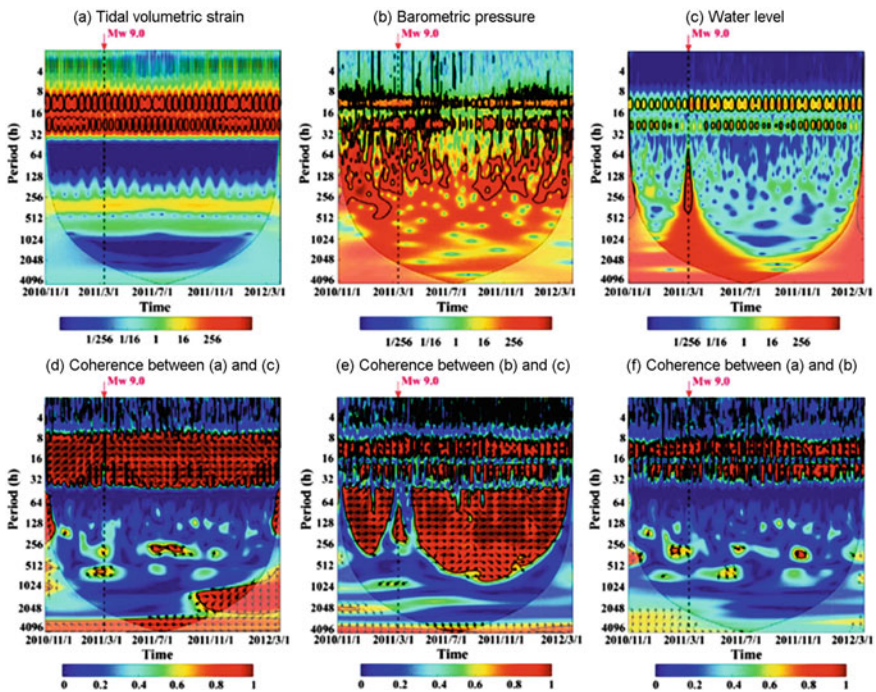
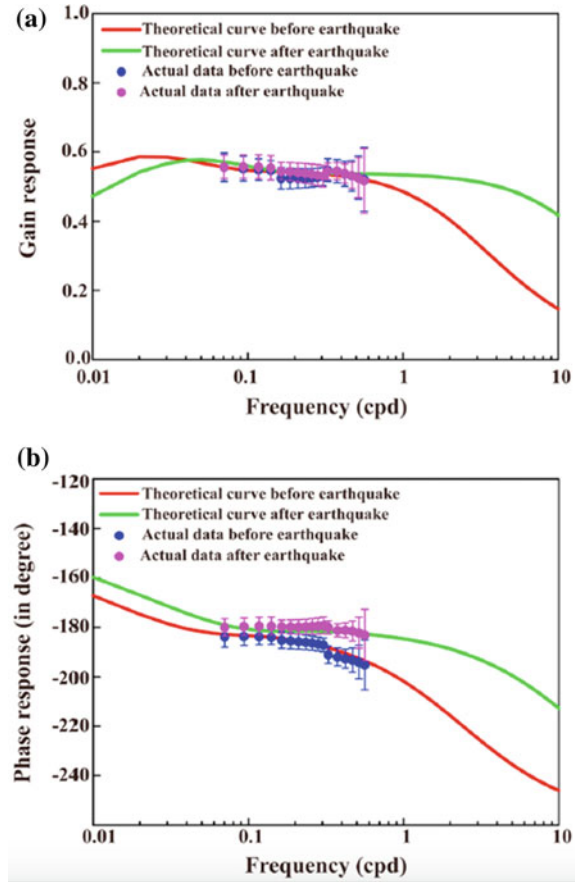


Fig. 5.37 a, b, c, respectively, wavelet power spectra of the tidal volumetric strain, the barometric pressure, and the water level. d, e, f, respectively, wavelet coherence between water level and tidal volumetric strain, between water level and barometric pressure, and between barometric pressure and tidal volumetric strain. The arrows indicate the relative phase relationship: in-phase pointing right, antiphase pointing left, and phase-leading by 90° pointing straight down (from Zhang-Shi-Shi et al. 2019)

Fig. 5.38 Barometric response function together with the Rojstaczer (1988) model before and after the earthquake. **a** Gain response, and **b** phase response (from Zhang-Shi et al. 2019)



permeability. Finally, they confirm their results for the post-seismic increase of the vertical permeability with a model of the tidal response of a leaky aquifer (Wang et al. 2018), given the aquifer transmissivity and storativity estimated from the barometric response before and after the earthquake.

It is reassuring that the two independent analyses of the tidal and barometric data from the same well have yielded nearly identical responses. The different interpretations between these studies clearly show that despite nearly identical responses there is much room for different interpretations. While Zhang-Wang et al. (2019) interpreted the small post-seismic positive phase shift as the uncertainties introduced in using the theoretical tides in the analysis, Zhang-Shi et al. (2019) interpreted the same positive phase shift as an indication of post-seismic vertical leakage. Obviously, more data and better analysis are required to resolve these ambiguities.

5.7 Groundwater Oscillations in Response to Seismic Waves

Several types of groundwater responses occur during earthquakes. Here we discuss the oscillatory response that is more closely related to the tidal and barometric responses; the other types of responses are discussed in the next chapter. Water level oscillations recorded in wells during earthquakes have long been documented and have been referred to as ‘hydroseismogram’ (e.g., Byerly and Blanchard 1935). During the 1964 M9.2 Alaska earthquake, water level oscillations with amplitudes as large as 6 m were recorded in Florida, thousands of kilometers away from the epicenter. Figure 5.39a shows a hydroseismograms in a well in Grants Pass, Oregon, during the 2002 M 7.9 Denali earthquake, Alaska, 3100 km away (Brodsky et al. 2003). Also shown (Fig. 5.39b) is the vertical component of ground velocity recorded on a broad-band seismometer adjacent to the well. Little change of water level occurred until the Rayleigh waves arrived and the oscillations of the hydroseismogram correlate well with that in the Rayleigh waves. After the seismic vibrations stopped, a ‘permanent’ change of water level of 12 cm was revealed.

Another way to show water level responses to different types of seismic waves is by plotting the occurrence time of water level response against the epicentral distance of the responding well, together with the travel time curves of the different types of seismic waves from the source. Figure 5.39c shows such a diagram for the groundwater responses on the Chinese mainland to the Tohoku earthquake (Yan et al. 2014). It clearly shows that the predominant water level responses were triggered by the surface waves rather than the body waves. Water-level oscillations in response to the passage of S-waves and Love waves were also reported (e.g., Wang et al., 2009), but the magnitude of these are much smaller than those responding to Rayleigh waves.

We briefly derive the volumetric strain associated with the Rayleigh waves. Let the x_1 and x_2 axes of a Cartesian coordinate system lie in the horizontal plane and orient respectively in the radial and transverse directions of wave propagation. The x_3 axis is in the vertical direction. The volumetric strain from the Rayleigh waves is related to the radial displacement (u_1) and the vertical displacement (u_3) according to

$$\theta = \left| \frac{\partial u_1}{\partial x_1} + \frac{\partial u_3}{\partial x_3} \right|. \quad (5.76)$$

The full solutions for u_1 and u_3 may be found in standard seismology textbooks (e.g., Aki and Richards 2009; Stein and Wysession 2003). A simplified expression was given by Lay and Wallace (1995) for material with a Poisson’s ratio of 0.25:

$$u_1 = -A'k \sin(\omega t - kx_1) [e^{-0.85kx_3} - 0.58e^{-0.39kx_3}], \quad (5.77)$$

$$u_3 = -A'k \cos(\omega t - kx_1) [0.85e^{-0.85kx_3} - 1.47e^{-0.39kx_3}]. \quad (5.78)$$

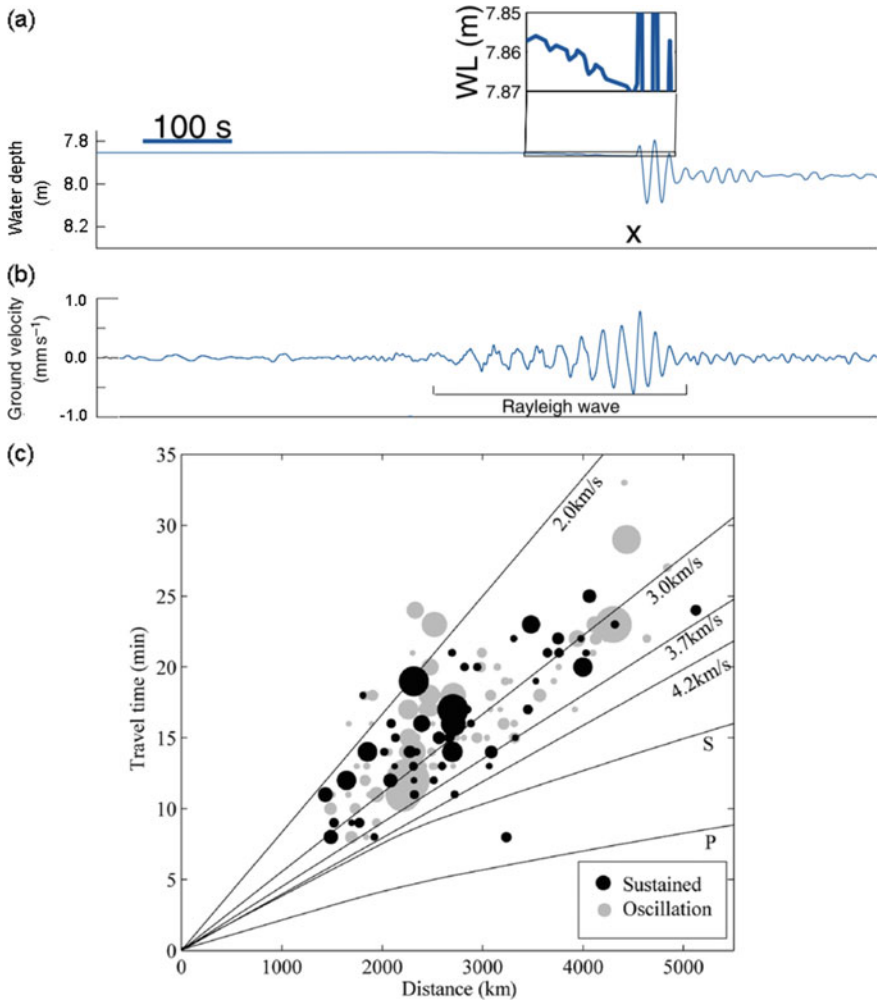


Fig. 5.39 **a** Water level measured by a float in a well in northern California for the 1999 Mw7.4 Oaxaca earthquake, with tides, barometric effects and linear trend removed. Inset shows magnified view of water level record before the onset of large oscillations. **b** Vertical ground velocity recorded at a nearby seismic station (YBH) (from Brodsky et al. 2003). **c** Relationship between travel time (deduced from the beginning of the well response) and well-epicentral distance. The solid lines are travel time curves for P and S body-wave phases (from IASP91 travel times model), as well as for surface waves with velocities of 2.0, 3.0, 3.7 and 4.2 km s⁻¹. The size of the circles is proportional to the relative amplitude of the induced water level changes (from Yan et al. 2014)

where A' is the amplitude, $k = \omega/c$ is the wave number, ω is the angular frequency and c the phase velocity of the Rayleigh waves. Inserting (5.77) and (5.78) into (5.76) we have

$$\theta = A'k^2 \cos(\omega t - kx_1) [-1.72e^{0.85kx_3} + 1.15e^{0.39kx_3}]. \quad (5.79)$$

Near the ground surface, $x_3 \approx 0$ and (5.79) reduces to,

$$\theta = -0.57A'k^2 \cos(\omega t - kx_1). \quad (5.80)$$

In practice, the volumetric strain may simply be obtained from the vertical displacement of the Rayleigh waves on the seismogram because, near the surface, (5.78) reduces to

$$u_3 = 0.62A'k \cos(\omega t - kx_1). \quad (5.81)$$

Combining (5.80) and (5.81), we obtain (Shih 2009)

$$\theta = -0.92ku_3 = \theta_o \cos(\omega t - kx_1). \quad (5.82)$$

where $\theta_o = -0.92k(u_3)_o$ and $(u_3)_o$ is the amplitude of the vertical displacement of the Rayleigh waves.

Sun et al. (2018, 2019) interpreted the water-level oscillations in response to seismic waves to estimate the aquifer parameters based on Cooper's model (1965) which shows that the amplitude ratio and the phase shift of water-level oscillations response to Rayleigh waves have the following expressions for the amplitude ratio and the phase shift of the response

$$A = |h_{w,o}/h_{\infty,o}| = \left\{ \left[1 - \frac{\pi r_w^2}{T\tau} \text{Kei}(\alpha_w) - \frac{4\pi^2 H_e}{\tau^2 g} \right]^2 + \left[\frac{\pi r_w^2}{T\tau} \text{Ker}(\alpha_w) \right]^2 \right\}^{-\frac{1}{2}}, \quad (5.83)$$

$$\eta = \arg[h_{w,o}/h_{\infty,o}] = \arg \left[\frac{2\beta\omega_w\omega}{\omega^2 - \omega_w^2} \right], \quad (5.84)$$

where $h_{w,o}$ is the amplitude of the water-level oscillations in the well during an earthquake, $h_{\infty,o}$ is the amplitude of the volumetric strain equivalent water level away from the well, which may be calculated from the vertical component of the Rayleigh waves on the seismogram according to (6.7), and

$$\alpha_w = r_w \left(\frac{\omega S}{T} \right)^{\frac{1}{2}}, \quad (5.85)$$

$$\beta = \frac{r_w^2 g}{4\omega_w T H_e} \text{Ker}(\alpha_w), \tag{5.86}$$

$$\omega_w = \sqrt{\frac{g}{H_e} \left[1 - \frac{r_w^2 \omega}{2T} \text{Kei}(\alpha_w) \right]}, \tag{5.87}$$

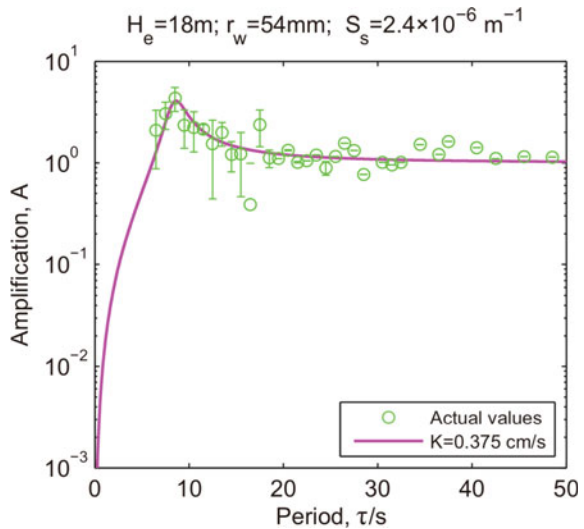
$$H_e = H + 3d/8, \tag{5.88}$$

where r_w is the radius of the well, T and S , respectively, are the transmissivity and storativity of the aquifer, K_u is the undrained bulk modulus of the aquifer, $\omega = 2\pi/\tau$ the seismic wave frequency, Kei and Ker, respectively, are the imaginary and real parts of the zeroth-order Kelvin function, H is the height of the water column in the well casing and d is the thickness of the screened aquifer.

Sun et al. (2018) analyzed the water-level response in a well (X10) near Urumqi, Xinjiang, to the 2016 Mw7.8 Solomon Island earthquake. Using the water level data from the well and the seismogram from a nearby seismic station, Sun et al. (2018) calculated the amplification of the water level $A = |h_{w,o}/h_{\infty,o}|$ as a function of frequency and plotted the results in Fig. 5.40. Fitting their result with Cooper’s model they estimated the hydraulic conductivity of the aquifer to be 3.75×10^{-3} m/s, which is several orders of magnitude greater than that estimated from the interpretation of the tidal response, as discussed below.

Using the same method, Sun et al. (2019) compared the responses of water level in the same well (X10) to another earthquake (Hutubi, Mw6.0, 104 km from the well) that occurred ~12 h earlier than the Solomon Island earthquake. The authors found that the permeability increase following the Mw7.8 Solomon Island earthquake was much greater than that induced by the Mw6.0 Hutubi earthquake, even though the

Fig. 5.40 Amplification of water level response in Well X10 in Xingjiang, China, to the Rayleigh waves from the 2016 Mw7.8 Solomon Island earthquake, plotted against wave periods. Circles represent the water level response and solid line represent the model fit with an assumed hydraulic conductivity of 3.75×10^{-3} m/s. Values on top of the graph show other parameters used in the model (from Sun et al. 2018)



latter had a seismic energy density ~ 3 orders of magnitude greater on account of its closer distance. The authors attributed this difference to a stress or strain memory from the first earthquake.

Sun et al. (2020) further compared the periodic responses for four analytical models as functions of the loading frequency (Fig. 5.41). They noticed that the transmissivity estimated from interpreting the response to seismic waves with the model by Cooper et al. (1965) is several orders of magnitude greater than that from interpreting the tidal response with the model by Wang et al. (2018) and that from interpreting the barometric response with the model of Rojstaczer (1988) (Table 5.5). They attributed these differences to factors such as spatial scale effects in the hydraulic parameter estimation, applicability of the estimation models under different conditions, and frequency of the periodic loadings. More research is needed to understand these differences.

Barbour et al. (2019) also analyzed the response of water level in the USGS deep well in Oklahoma to Rayleigh waves from several distant earthquakes. They showed that at periods below 60 to 70 s there is a frequency-dependent response similar to the theoretical prediction of a confined reservoir (Cooper et al., 1965); at longer periods, however, the response does not converge to the prediction of a confined aquifer model (e.g., Hsieh et al. 1987) but shows amplification and phase advance, which supports the occurrence of vertical flow (leakage).

5.8 Concluding Remarks

As noted in the Introduction, the analysis of the response of groundwater level to natural forcing, such as tides and barometric pressure, is an economical and effective means for continuous monitoring of hydraulic properties of aquifers. This approach has gained increasing attention among hydrogeologists, particularly in the community that studies of the groundwater response to earthquakes. The method has also been shown to be particularly effective in detecting the leakage and confinement of aquifers, which has become an important problem for the protection of shallow groundwater resources against possible leakage of hazardous wastewaters that have been increasingly injected into underground aquifers. The new development of using the response of groundwater to Rayleigh waves to estimate aquifer properties has the potential to enhance our understanding on the dependence of aquifer properties on the frequency of the applied forcing and deserves further study.

Finally, we list in Table 5.5 some estimates of permeability from the interpretations of the responses to tidal, barometric pressure and seismic waves. These are to be viewed as examples for comparison, rather than a comprehensive compilation.

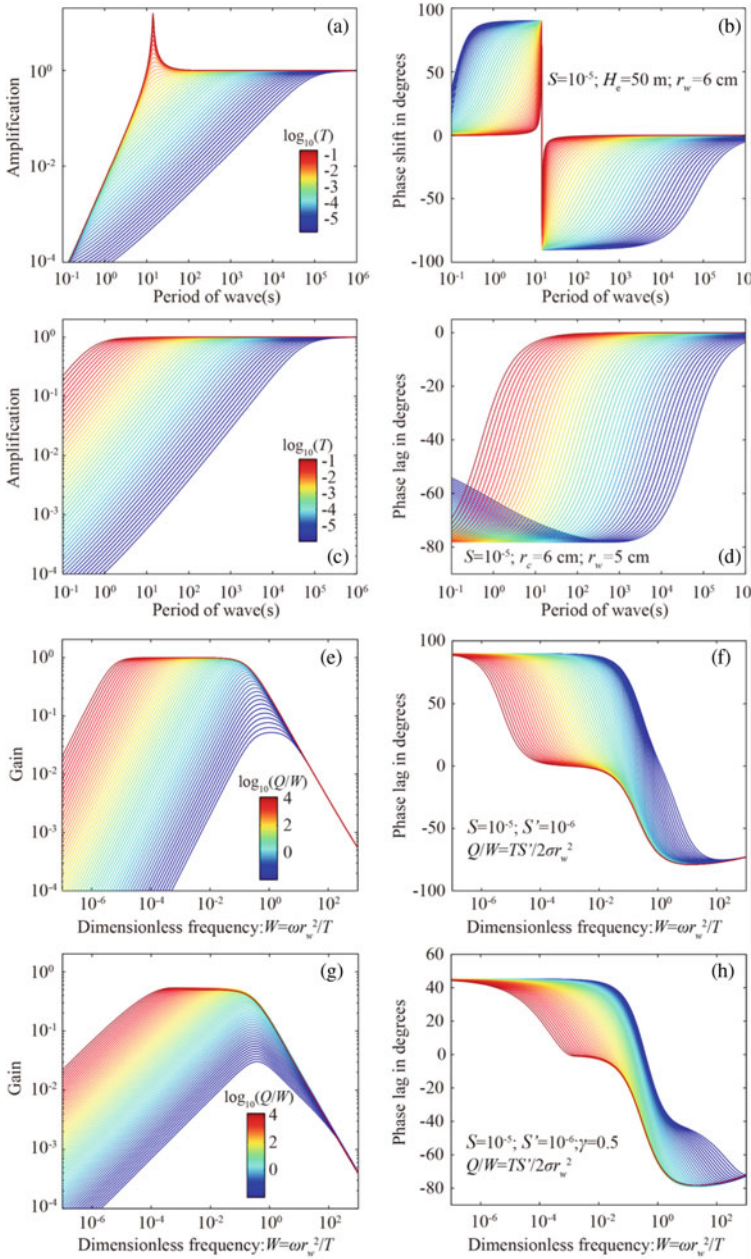


Fig. 5.41 Amplification factor and phase lag of water level response to periodic loading. K and K' in the figures are the hydraulic conductivity of the aquifer and aquitard, respectively; d and b are the thickness of the aquifer and aquitard, respectively. **a, b** Cooper's model, **c, d** Hsieh's model, **e-f** Wang's model, where $T = Kd$ and $\sigma = K'/b'$, and **g, h** Rojstaczer's model

Table 5.5 Permeability (m^2) estimated from interpreting water-level responses to tidal, barometric and seismic forcing

Methods			Locations	References
Tidal	Barometric	Seismic waves		
8×10^{-15} ($S = 10^{-4}$) ^b 2×10^{-14} ($S = 10^{-6}$)			Parkfield, CA	Hsieh et al. (1987)
1×10^{-15} (before) ^d 6×10^{-15} (after)			Pin ò n Flat Obs., S. California	Elkhoury et al. (2006)
10^{-16} (after)			Wenchuan rupture zone, China	Xue et al. (2013)
10^{-16} (before) 5×10^{-15} (after)			E. China	Yan et al. (2014)
2.4×10^{-15} (before) 7.8×10^{-15} (after)			21 km from Wenchuan rupture, China	Liao et al. (2015)
3×10^{-14} to 3×10^{-13}			S. California	Allègre et al. (2016)
2.3×10^{-14} ^a 2.2×10^{-15} ^b			31 ^a m and 548 ^b m from the San Andreas fault	Xue et al. (2016)
2×10^{-14} to 1.2×10^{-13}			Yunan, SW China	Liao and Wang (2018)
5×10^{-16} (before) 1×10^{-14} (after)			Beijing, China	Zhang-Wang et al. (2019)
6.9×10^{-16} (before) 1.4×10^{-15} (after)	7.2×10^{-16} (before) 4.0×10^{-15} (after)		Beijing, China	Zhang-Shi et al. (2019)
	2×10^{-13} ($S' = 0$) ^c 7×10^{-12} ($S' = 10^{-2}$) ^c		USGS Deep Oklahoma well	Zhu and Wang (2020)
		3 to 5×10^{-11} 7 to 25×10^{-11}	X10 well, Urumqi, China	Sun et al. (2018) Sun et al. (2019)
1.6 to 10.5×10^{-9e}	6.1×10^{-8e}	1.7×10^{-4e}	Jingle well, Shanxi, China	Sun et al. (2020)

^aBlank space means that no data are available

^b S is the assumed storativity of the aquifer

^c S' is the assumed storativity of the aquitard

^d(Before) and (after) refer to values estimated before and after a specific earthquake, respectively

^ePermeability converted from measured transmissivity and assumed aquifer thickness of 100 m

Appendices. Derivation of Equations

Appendix 5.1 Solution for a Confined Aquifer

We use complex numbers to facilitate the derivation of a solution. We first derive the response away from the well, h_∞ , and then consider the effect of the well on aquifer response from wellbore storage. Let the disturbance in water level due to the well be expressed as

$$\Delta h(r, t) = h(r, t) - h_\infty(t) \tag{A5.1}$$

where $h_\infty(t)$ [m] is the hydraulic head away from the well, which is a function of time only and may be evaluated by replacing h by h_∞ in Eq. (5.12):

$$0 = S \frac{\partial h_\infty}{\partial t} - \frac{SBK_u}{\rho g} \frac{\partial \epsilon}{\partial t}. \tag{A5.2}$$

Since h_∞ and ϵ are both periodic with the same frequency ω we have

$$h_{\infty,o} = \left(\frac{BK_u \epsilon_o}{\rho g} \right). \tag{A5.3}$$

where $h_{\infty,o}$ is the complex amplitude of h_∞ and ϵ_o the amplitude of ϵ .

Replacing h by $\Delta h + h_\infty$ in Eqs. (5.14)–(5.16) and using Eq. (5.18) we have

$$T \left[\frac{\partial^2 \Delta h}{\partial r^2} + \frac{1}{r} \frac{\partial \Delta h}{\partial r} \right] = S \frac{\partial \Delta h}{\partial t}. \tag{A5.4}$$

Since the stationary periodic solution of equation (A5.4) has the form $\Delta h = \Delta h_o(r)e^{i\omega t}$, it can be reduced to an ordinary differential equation

$$T \left[\frac{d^2 \Delta h_o}{dr^2} + \frac{1}{r} \frac{d \Delta h_o}{dr} \right] = i\omega S \Delta h_o, \tag{A5.5}$$

with the boundary conditions

$$\Delta h_o(r \rightarrow \infty) = 0, \tag{A5.6}$$

$$\Delta h_o(r = r_w) = h_{w,o} - h_{\infty,o} = h_{w,o} - \left(\frac{BK_u \epsilon_o}{\rho g} \right), \tag{A5.7}$$

$$2\pi r_w T \left. \frac{d \Delta h_o}{dr} \right|_{r=r_w} = i\omega \pi r_c^2 h_{w,o}. \tag{A5.8}$$

The solution to equation (A5.5) is $\Delta h_o = C_I I_0(\beta r) + C_K K_0(\beta r)$, where I_0 and K_0 are, respectively, the modified Bessel functions of the first and second kind and the zeroth order, and

$$\beta = \left(\frac{i\omega S}{T} \right)^{1/2}. \quad (\text{A5.9})$$

Given that $I_0(r)$ goes to infinity at large r , the boundary condition (Eq. A6) requires that $C_I = 0$; thus $\Delta h_o = C_K K_0(\beta r)$. Solving for C_K with equation (A5.8) and recalling that $\frac{dK_0(r)}{dr} = -K_1(r)$, where K_1 is the modified Bessel function of the second kind and the first order, we have

$$C_K = -\frac{i\omega r_c^2 h_{w,o}}{2T\beta r_w K_1(\beta r)}. \quad (\text{A5.10})$$

Thus,

$$\Delta h_o = -\frac{i\omega r_c^2 h_{w,o} K_0(\beta r)}{2T\beta r_w K_1(\beta r)}. \quad (\text{A5.11})$$

Inserting equation (A5.11) into equation (A5.7) we obtain the solution,

$$h_{w,o} = \frac{1}{\xi} \left(\frac{BK_u \epsilon_o}{\rho g} \right), \quad (\text{A5.12})$$

where

$$\xi = 1 + \left(\frac{r_c}{r_w} \right)^2 \frac{i\omega r_w K_0(\beta r_w)}{2T\beta K_1(\beta r_w)}. \quad (\text{A5.13})$$

Appendix 5.2 Solution for a Leaky Aquifer

Replacing h by $\Delta h + h_\infty$ in Eqs. (5.28)–(5.31) and using Eq. (5.34) we have

$$T \left[\frac{\partial^2 \Delta h}{\partial r^2} + \frac{1}{r} \frac{\partial \Delta h}{\partial r} \right] - \frac{K'}{b'} \Delta h = S \frac{\partial \Delta h}{\partial t} \quad (\text{A5.14})$$

which may be reduced to an ordinary differential equation

$$T \left[\frac{d^2 \Delta h_o}{dr^2} + \frac{1}{r} \frac{d \Delta h_o}{dr} \right] - \frac{K'}{b'} \Delta h_o = i\omega S \Delta h_o, \quad (\text{A5.15})$$

with the boundary conditions

$$\Delta h_o(r \rightarrow \infty) = 0, \quad (\text{A5.16})$$

$$\Delta h_o(r = r_w) = h_{w,o} - h_{\infty,o} = h_{w,o} - \frac{i\omega S}{i\omega S + K'/b'} \left(\frac{BK_u \epsilon_o}{\rho g} \right), \quad (\text{A5.17})$$

$$2\pi r_w T \left. \frac{d\Delta h_o}{dr} \right|_{r=r_w} = i\omega \pi r_c^2 h_{w,o}. \quad (\text{A5.18})$$

The solution to Eq. (A5.18) is $\Delta h_o = C_I I_o(\beta'r) + C_K K_o(\beta'r)$, where

$$\beta' = \left(\frac{K'}{Tb'} + \frac{i\omega S}{T} \right)^{1/2}. \quad (\text{A5.19})$$

The boundary condition (Eq. A5.19) requires that $C_I = 0$ and the boundary condition (A5.17) leads to

$$C_K = -\frac{i\omega r_c^2 h_{w,o}}{2T\beta r_w K_1(\beta'r)}, \quad (\text{A5.20})$$

and

$$\Delta h_o = -\frac{i\omega r_c^2 h_{w,o} K_o(\beta'r)}{2T\beta r_w K_1(\beta'r)}. \quad (\text{A5.21})$$

Inserting equation (A5.21) into equation (A5.17) we obtain the solution as

$$h_{w,o} = \frac{i\omega S}{(i\omega S + K'/b')\xi'} \left(\frac{BK_u \epsilon_o}{\rho g} \right) = \frac{1}{\xi'} h'_{\infty,o}, \quad (\text{A5.22})$$

where

$$\xi' = 1 + \left(\frac{r_c}{r_w} \right)^2 \frac{i\omega r_w}{2T\beta'} \frac{K_o(\beta'r_w)}{K_1(\beta'r_w)}. \quad (\text{A5.23})$$

Appendix 5.3 Barometric Response with Finite Aquitard

In order to apply the existing solution in Carlslaw and Jaeger (1959, 3.7) to the present study of vertical flow of groundwater in an aquitard of finite thickness, we need to substitute P in (5.60) by

$$P^* \equiv P - A\gamma \cos \omega t \quad (\text{A5.24})$$

and re-express Eq. (5.60) as

$$D' \frac{\partial^2 P^*}{\partial z^2} = \frac{\partial P^*}{\partial t}. \quad (\text{A5.25})$$

Following Carslaw and Jaeger (1959), the time factor $\exp(i\omega t)$ is omitted from the derivation, but is included at the end. We replace A , B , C , and D in Carslaw and Jaeger by E , F , G , and H to avoid the possible confusion with the parameters A for the amplitude of barometric oscillations and D for diffusion, as defined earlier. In using this solution, there is also a need to employ the subscripts t and b to denote the top and bottom of each layer and a prime to denote the aquitard pressure to distinguish it from the aquifer pressure without a prime. Since $P_t^* = P_b^{*'} and $q_t^* = q_b^{*'}$, we have$

$$\begin{pmatrix} P_b^* \\ q_b^* \end{pmatrix} = \begin{pmatrix} E & F \\ G & H \end{pmatrix} \begin{pmatrix} P_t^* \\ q_t^* \end{pmatrix} = \begin{pmatrix} E & F \\ G & H \end{pmatrix} \begin{pmatrix} P_b^{*'} \\ q_b^{*'} \end{pmatrix} \quad (\text{A5.26})$$

$$= \begin{pmatrix} E & F \\ G & H \end{pmatrix} \cdot \begin{pmatrix} E' & F' \\ G' & H' \end{pmatrix} \cdot \begin{pmatrix} P_t^{*'} \\ q_t^{*'} \end{pmatrix} \quad (\text{A5.27})$$

$$= \begin{pmatrix} EE' + FG' & EF' + FH' \\ GE' + HG' & GF' + HH' \end{pmatrix} \cdot \begin{pmatrix} P_t^{*'} \\ q_t^{*'} \end{pmatrix}, \quad (\text{A5.28})$$

where

$$E = \cosh[(1+i)\sqrt{R}], \quad (\text{A5.29})$$

$$F = \frac{L}{K} \frac{\sinh[(1+i)\sqrt{R}]}{[(1+i)\sqrt{R}]}, \quad (\text{A5.30})$$

$$G = -\frac{K}{L} [(1+i)\sqrt{R}] \sinh[(1+i)\sqrt{R}], \quad (\text{A5.31})$$

$$H = E, \quad (\text{A5.32})$$

$$R = L^2 \omega / 2D, \quad (\text{A5.33})$$

and L , K and D are, respectively, the thickness, hydraulic conductivity and diffusivity of the aquifer. The parameters E' , F' , G' and H' for the aquitard are defined similarly but with L , K , D and R replaced by L' , K' , D' and R' , respectively.

A no-flow condition is assumed at the base of the aquifer, hence

$$q_b = 0 = \left[(GE' + HG')P_t^{*'} + (GF' + HH')q_t^{*'} \right].$$

Thus

$$q_t^{*'} = -\frac{GE' + HG'}{GF' + HH'}P_t^{*'} \tag{A5.34}$$

From (A5.26) and (A5.34) we have

$$\begin{aligned} P_b^{*'} &= E'P_t^{*'} + F'q_t^{*'} \\ &= \left(E' - F'\frac{GE' + HG'}{GF' + HH'} \right) P_t^{*'} \end{aligned} \tag{A5.35}$$

By virtue of (A5.24) we replace $P_b^{*'}$ by $P_b' - A\gamma\exp(i\omega t)$ and $P_t^{*'}$ by $P_t' - A\gamma\exp(i\omega t)$ in (A5.34) and obtain

$$P_b' - A\gamma\exp(i\omega t) = \left(E' - F'\frac{GE' + HG'}{GF' + HH'} \right) \left[P_t' - A\gamma\exp(i\omega t) \right] \tag{A5.36}$$

Since $P_b' = P$ (aquifer pressure) and

$$P_t' = P_a = A(M + iN)\exp(i\omega t), \tag{A5.37}$$

we have the pressure in the aquifer

$$P = A \left[\gamma + (M + iN - \gamma) \left(E' - F'\frac{GE' + HG'}{GF' + HH'} \right) \right] \exp(i\omega t) \tag{A5.38}$$

Appendix 5.4 Effect of Fractures on Groundwater Response

The tidal and barometric response of groundwater in fractures has not received adequate attention. Existing models (Hanson and Owen 1982; Bower 1983) consider only the tidal response of groundwater in a single highly conductive, planar fracture, that intersects the well. The models are constructed for the purpose of finding the orientation of the conductive fractures from the tidal response of water level in wells. Both Hanson and Owen (1982) and Bower (1982) develop mathematical solutions for the problem. The results of Hanson and Owen (1983), as summarized by Barbour et al. (2019), are given below.

Consider a saturated planar fracture with a normal denoted by $\hat{n} = (\cos\alpha_1, \cos\alpha_2, \cos\alpha_3)$, where α_1 , α_2 , and α_3 are the angles between \hat{n} and the east, north, and up directions, respectively. The response of the pressure in the fracture to a time-varying

tidal strain tensor $\mathbf{e}(t)$ is

$$p(t) = -C\hat{\mathbf{n}}\mathbf{e}(t)\hat{\mathbf{n}}^T, \quad (\text{A5.39})$$

where C is a proportional constant that depends on the compliances of the fracture, wall rock, and fluid. The pressure response to a constituent of the tidal strain of frequency ω_k may be expressed in the frequency domain as

$$\tilde{p}(\omega_k)\exp(i\omega t) = -C\hat{\mathbf{n}}\tilde{\mathbf{e}}(\omega_k)\hat{\mathbf{n}}^T\exp(i\omega t). \quad (\text{A5.40})$$

Expressing the tidal strain tensor in its geographical components

$$\tilde{\mathbf{e}}(\omega_k) = \begin{bmatrix} \tilde{e}_{\lambda\lambda}(\omega_k) & \frac{1}{2}\tilde{e}_{\lambda\theta}(\omega_k) & 0 \\ \frac{1}{2}\tilde{e}_{\lambda\theta}(\omega_k) & \tilde{e}_{\theta\theta}(\omega_k) & 0 \\ 0 & 0 & \tilde{e}_{zz}(\omega_k) \end{bmatrix}, \quad (\text{A5.41})$$

where λ is longitude (positive east), θ is latitude (positive north) and z is vertical, and inserting Eq. (5.91) into Eq. (5.90), we relate the tidal response of pressure in fracture to the fracture orientation, the compliance constant C , and the tidal strain

$$\begin{aligned} \tilde{p}(\omega_k) &= \frac{C}{1-\nu}v[\tilde{e}_{\lambda\lambda}(\omega_k) + \tilde{e}_{\theta\theta}(\omega_k)] \\ &\quad - \frac{C}{1-\nu}[\tilde{e}_{\lambda\lambda}(\omega_k) + \nu\tilde{e}_{\theta\theta}(\omega_k)]\cos^2\alpha_1 \\ &\quad - \frac{C}{1-\nu}[\tilde{e}_{\theta\theta}(\omega_k) + \nu\tilde{e}_{\lambda\lambda}(\omega_k)]\cos^2\alpha_2 \\ &\quad - C\tilde{e}_{\lambda\theta}(\omega_k)\cos\alpha_1\cos\alpha_2 \end{aligned} \quad (\text{A5.42})$$

where we have used the following relationships to simply the expression:

$$\cos^2\alpha_1 + \cos^2\alpha_2 + \cos^2\alpha_3 = 1,$$

where $\tilde{e}_{zz} = -\nu(\tilde{e}_{\lambda\lambda} + \tilde{e}_{\theta\theta})/(1-\nu)$, and is valid near the Earth's surface.

Neglecting the effect of ocean tides, $\tilde{e}_{\lambda\lambda}(\omega_k)$ and $\tilde{e}_{\theta\theta}(\omega_k)$ are in phase with the tidal potential and $\tilde{e}_{\lambda\theta}(\omega_k)$ leads (diurnal constituents) or lags (semidiurnal constituents) the tidal potential by 90° . Denoting the phase of the tidal potential as ϕ_k , we have

$$\arg[\tilde{e}_{\theta\theta}(\omega_k)] = \arg[\tilde{e}_{\lambda\lambda}(\omega_k)] = \phi_k,$$

$$\phi_k - \arg[\tilde{e}_{\lambda\theta}(\omega_k)] = \mp\pi/2.$$

Equation (A5.42) becomes

$$\begin{aligned}
 \tilde{p}(\omega_k) &= \frac{C}{1-\nu} \nu [|\tilde{e}_{\lambda\lambda}(\omega_k)| + |\tilde{e}_{\theta\theta}(\omega_k)|] \exp(i\phi_k) \\
 &\quad - \frac{C}{1-\nu} [|\tilde{e}_{\lambda\lambda}(\omega_k)| + \nu |\tilde{e}_{\theta\theta}(\omega_k)|] \exp(i\phi_k) \cos^2 \alpha_1 \\
 &\quad - \frac{C}{1-\nu} [|\tilde{e}_{\theta\theta}(\omega_k)| + \nu |\tilde{e}_{\lambda\lambda}(\omega_k)|] \exp(i\phi_k) \cos^2 \alpha_2 \\
 &\quad \mp i C |\tilde{e}_{\lambda\theta}(\omega_k)| \exp(i\phi_k) \cos \alpha_1 \cos \alpha_2
 \end{aligned} \tag{A5.43}$$

where the $-$ sign is for diurnal tides and the $+$ sign is for semidiurnal tides.

The first three terms on the right side of Eq. (A5.43) are real, while the last term is imaginary. If the measured pressure response is now referenced to the tidal potential, we have

$$\begin{aligned}
 \text{Re}[\tilde{p}(\omega_k) \exp(-i\phi_k)] &= \frac{C}{1-\nu} \nu [|\tilde{e}_{\lambda\lambda}(\omega_k)| + |\tilde{e}_{\theta\theta}(\omega_k)|] \\
 &\quad - \frac{C}{1-\nu} [|\tilde{e}_{\lambda\lambda}(\omega_k)| + \nu |\tilde{e}_{\theta\theta}(\omega_k)|] \cos^2 \alpha_1 \\
 &\quad - \frac{C}{1-\nu} [|\tilde{e}_{\theta\theta}(\omega_k)| + \nu |\tilde{e}_{\lambda\lambda}(\omega_k)|] \cos^2 \alpha_2
 \end{aligned} \tag{A5.44a}$$

and

$$\text{Im}[\tilde{p}(\omega_k) \exp(-i\phi_k)] = \mp i C |\tilde{e}_{\lambda\theta}(\omega_k)| \cos \alpha_1 \cos \alpha_2. \tag{A5.44b}$$

Hanson and Owen (1982) inferred fracture orientation from three parameters of the fluid level tidal response: the phases of a diurnal tide and a semidiurnal tide, and the ratio of the amplitudes of these two constituents. The dependence on fracture compliance is avoided by using the ratio of the amplitudes of the M_2 and O_1 tides. The phase of the pressure change relative to the tidal potential is given by

$$\begin{aligned}
 \arg[\tilde{p}(\omega_k) \exp(-i\phi_k)] &= \tan^{-1} \\
 &\quad \times \left(\frac{\mp (1-\nu) |\tilde{e}_{\lambda\theta}(\omega_k)| \cos \alpha_1 \cos \alpha_2}{\nu [|\tilde{e}_{\lambda\lambda}(\omega_k)| + |\tilde{e}_{\theta\theta}(\omega_k)|] - [|\tilde{e}_{\lambda\lambda}(\omega_k)| + \nu |\tilde{e}_{\theta\theta}(\omega_k)|] \cos^2 \alpha_1 - [|\tilde{e}_{\theta\theta}(\omega_k)| + \nu |\tilde{e}_{\lambda\lambda}(\omega_k)|] \cos^2 \alpha_2} \right)
 \end{aligned} \tag{A5.45}$$

where the $-$ is used for diurnal tides and the $+$ is used for semidiurnal tides, and the ratio of the amplitudes of the M_2 and O_1 tides is given by

$$\frac{|\tilde{p}(\omega_k)|}{|\tilde{p}(\omega_j)|} = \left[\frac{\text{Re}[\tilde{p}(\omega_k)]^2 + \text{Im}[\tilde{p}(\omega_k)]^2}{\text{Re}[\tilde{p}(\omega_j)]^2 + \text{Im}[\tilde{p}(\omega_j)]^2} \right]^{\frac{1}{2}}. \tag{A5.46}$$

Hanson and Owen (1982) noted that, according to Eq. (5.95), a fracture with NW strike ($\cos \alpha_1 \cos \alpha_2 > 0$) and a fracture with NE strike ($\cos \alpha_1 \cos \alpha_2 < 0$) exhibit phase shifts of opposite sign with respect to the potential for a given tide. For a given

fracture, the diurnal and semidiurnal tides exhibit phase shifts of opposite sign with respect to the tidal potential.

Barbour et al. (2019) applied the same approach to show that the fracture model may not explain the tidal response of water level in the Arbuckle aquifer, as determined from the water level documented in the USGS Deep Well in Oklahoma.

References

- Agnew DC (2007) Earth tides. In *Treatise on geophysics* 3:163–195
- Aki K, Richards PG (2009) *Quantitative seismology*, 2nd edn. University Science Books, Mill Valley
- Allègre V, Brodsky EE, Xue L et al (2016) Using earth-tide induced water pressure changes to measure in situ permeability: a comparison with long-term pumping tests. *Water Resour Res* 52:3113–3126. <https://doi.org/10.1002/2015WR017346>
- Ansari E, Bidgoli TS, Hollenbach A (2019) Accelerated fill-up of the Arbuckle Group aquifer and links to U.S. midcontinent seismicity. *J Geophys Res Solid Earth* 124:2670–2683. <https://doi.org/10.1029/2018JB016926>
- Barbour AJ, Norbeck JH, Rubinstein JL (2017) The effects of varying injection rates in Osage County, Oklahoma, on the 2016 Mw 5.8 Pawnee earthquake. *Seismol Res Lett* 88:1040–1053. <https://doi.org/10.1785/0220170003>
- Barbour AJ, Xue L, Roeloffs E et al (2019) Leakage and increasing fluid pressure detected in Oklahoma's wastewater disposal reservoir. *J Geophys Res Solid Earth* 124:2896–2919. <https://doi.org/10.1029/2019JB017327>
- Barry DA, Barry SJ, Parlange J-Y (1996) Capillarity correction to periodic solutions of shallow flow approximation. *Coast Estuar Stud* 50:495–510
- Beaumont C, Berger J (1975) An analysis of tidal strain observations from the United States of America: I. The laterally homogeneous tide. *Bull Seismol Soc Am* 65(6):1613–1629
- Bear J (1972) *Dynamics of fluids in porous media*. Dover, New York
- Bostock J (1855) *The natural history*. Pliny the Elder, Taylor and Francis, Red Lion Court, Fleet Street, London
- Bower DR (1983) Bedrock fracture parameters from the interpretation of well tides. *J Geophys Res* 88:5025–5035
- Brodsky EE, Roeloffs E, Woodcock D et al (2003) A mechanism for sustained groundwater pressure changes induced by distant earthquakes. *J Geophys Res* 108:2390. <https://doi.org/10.1029/2002JB002321>
- Byerly P, Blanchard FG (1935) Well gauges as seismographs. *Nature* 135:303–304
- Carlsaw HS, Jaeger JC (1959) *Conduction of heat in solids*, 2nd edn. Clarendon Press, Oxford, UK
- Cooper HH, Bredehoeft JD, Papadopoulos IS et al (1965) The response of well-aquifer system to seismic waves. *J Geophys Res* 70(16):3915–3926
- Detournay E, Cheng AHD (1993) *Fundamentals of poroelasticity*, Vol. II of comprehensive rock engineering: principles, practice & projects, pp 113–171. Pergamon Press
- Doan ML, Brodsky EE, Prioul R et al (2006) *Tidal analysis of borehole pressure: a tutorial*, Schlumberger-Doll Research Report, Cambridge, Mass
- Elkhoury JE, Brodsky EE, Agnew DC (2006) Seismic waves increase permeability. *Nature* 441(7097):1135–1138
- Ellsworth WL (2013) Injection-induced earthquakes. *Science* 341(6142). <https://doi.org/10.1126/science.1225942>
- Evans K, Beavan J, Simpson D (1991) Estimating aquifer parameters from analysis of forced fluctuations in well level: An example from the Nubian formation near Aswan, Egypt I. Hydrogeological background and large-scale permeability estimates. *J Geophys Res* 96:12127–12137

- Feng Q, Zhan H (2015) On the aquitard–aquifer interface flow and the drawdown sensitivity with a partially penetrating pumping well in an anisotropic leaky confined aquifer. *J Hydrol* 521:74–83
- Fetter CW (1999) *Contaminant hydrogeology*. Prentice Hall, Upper Saddle River, NJ
- Gillham RW (1984) The capillary fringe and its effect on water-table response. *J Hydrol* 67(1–4):307–324. [https://doi.org/10.1016/0022-1694\(84\)90248-8](https://doi.org/10.1016/0022-1694(84)90248-8)
- Hanson JM, Owen LB (1982) Fracture orientation analysis by the solid Earth tidal strain method. Society Petroleum Engineers AIME Paper, SPE11070. <https://doi.org/10.2118/11070-MS>
- Hantush MS, Jacob CE (1955) Non-steady Green's functions for an infinite strip of leaky aquifers. *Trans Am Geophys Union* 36(1):101–112. <https://doi.org/10.1029/TR036i001p00101>
- Harrison JC (1974) Cavity and topography effects on the measurement of tilt and strain, EOS. *Trans Am Geophys Union* 56:1151
- Hsieh P, Bredehoeft J, Farr J (1987) Determination of aquifer permeability from earthtide analysis. *Water Resour Res* 23:1824–1832
- Hsieh PA, Cooley RL (1995) Comment on 'Horizontal aquifer movement in a Theis-Thiem confined system' by Donald C. Helm. *Water Resour Res* 31(12):3107–3111
- Hussein ME, Odling NE, Clark RA (2013) Borehole water level response to barometric pressure as an indicator of aquifer vulnerability. *Water Resour Res* 49(10):7102–7119
- Ingebritsen SE, Manga M (2019) Earthquake hydrogeology. *Water Resour Res* 55:5212–5216. <https://doi.org/10.1029/2019wr025341>
- Jacob CE (1940) The flow of water in an elastic artesian aquifer. *EOS Trans AGU* 21:574–586
- Langenbruch C, Zoback MD (2016) How will induced seismicity in Oklahoma respond to decreased saltwater injection rates? *Sci Adv* 2(11):e1601542. <https://doi.org/10.1126/sciadv.1601542>
- Langenbruch C, Weingarten M, Zoback MD (2018) Physics-based forecasting of man-made earthquake hazards in Oklahoma and Kansas. *Nat Commun* 9:2946. <https://doi.org/10.1038/s41467-018-06167-4>
- Lay and Wallace (1995) *Modern Global Seismology*, San Diego: Academic Press, 521
- Liao X, Wang CY, Liu CP (2015) Disruption of groundwater systems by earthquakes. *Geophys Res Lett* 42(22):9758–9763
- Liao X, Wang CY (2018) Seasonal permeability change of the shallow crust inferred from deep well monitoring. *Geophys Res Lett* 45:11130–11136. <https://doi.org/10.1029/2018gl080161>
- Love AEH (1911) *Some problems of geodynamics*. Cambridge University Press, Cambridge
- Meyboom P (1967) Groundwater studies in the Assiniboine River drainage basin, Part II. Hydrologic characteristics of phreatophytic vegetation in south-central Saskatchewan. *Bull Geol Surv Canada* 139:18–23
- Morgan BC, Murray KE (2015) Characterizing small-scale permeability of the Arbuckle Group, Oklahoma. Open File Report OF2–2015, 1–12. National Archives and Records Administration, 1989
- Mualem Y (1976) A new model for predicting the hydraulic conductivity of unsaturated porous media. *Water Resour Res* 12:513–522
- Neuman SP, Witherspoon PA (1969) Applicability of current theories of flow in leaky aquifers. *Water Resour Res* 5(4):817–829
- Odling NE, Serrano RP, Hussein MEA et al (2015) Detecting the vulnerability of groundwater in semi-confined aquifers using barometric response functions. *J Hydrol* 520:143–156
- Rahi K, Halihan T (2009) Estimating selected hydraulic parameters of the Arbuckle-Simpson aquifer from the analysis of naturally-induced stresses, Report, Oklahoma Water Resource Board 31
- Roeloffs EA (1996) Poroelastic techniques in the study of earthquake-related hydrologic phenomena. *Adv Geophys* 37:135–195
- Rojstaczer S (1988) Determination of fluid flow properties from the response of water levels in wells to atmospheric loading. *Water Resour Res* 24(11):1927–1938. <https://doi.org/10.1029/WR024i011p01927>
- Schoenball M, Ellsworth WL (2017) Waveform-relocated earthquake catalog for Oklahoma and southern Kansas illuminates the Regional Fault Network. *Seismol Res Lett* 88(5):1252–1258. <https://doi.org/10.1785/0220170083>

- Shi Z, Hu X, Wang CY (2020) Hydro-mechanical coupling in the shallow crust—Insight from groundwater level and satellite radar imagery in a mining area, *J Hydro*, <https://doi.org/10.1016/j.jhydrol.2020.125649>
- Shih DCF (2009) Storage in confined aquifer: spectral analysis of ground-water responses to seismic Rayleigh waves. *J Hydrol* 374:83–91
- Stein S, Wysession M (2003) An introduction to seismology, earthquakes, and earth structure. Blackwell, New York
- Sun X, Xiang Y, Shi Z (2018) Estimating the hydraulic parameters of a confined aquifer based on the response of groundwater levels to seismic Rayleigh waves. *Geophys J Int* 213:919–930
- Sun X, Xiang Y, Shi Z (2019) Changes in permeability caused by two consecutive earthquakes—insights from the responses of a well-aquifer system to seismic waves. *Geophys Res Lett* 46:10367–10374. <https://doi.org/10.1029/2019GL084704>
- Sun X, Shi Z, Xiang Y (2020) Frequency dependence of in-situ transmissivity estimation of well-aquifer systems from periodic loadings, *Water Resources Research* (in press)
- Turner IL, Nielsen P (1997) Rapid water table fluctuations within the beach face: Implications for swash zone sediment mobility? *Coast Eng* 32(1):45–59. [https://doi.org/10.1016/S0378-3839\(97\)00015-X](https://doi.org/10.1016/S0378-3839(97)00015-X)
- Van Genuchten MT (1980) A closed-form equation for predicting the hydraulic conductivity of unsaturated soils I. *Soil Sci Soc Am J* 44:892–898
- Wang CY, Chia Y, Wang PL et al (2009) Role of S waves and Love waves in coseismic permeability enhancement. *Geophys Res Lett* 36: <https://doi.org/10.1029/2009GL037330>
- Wang CY, Doan ML, Xue L et al (2018) Tidal response of groundwater in a leaky aquifer—Application to Oklahoma. *Water Resour Res* 54:8019–8033. <https://doi.org/10.1029/2018WR022793>
- Wang CY, Zhu AY, Liao X et al (2019) Capillary effects on groundwater response to Earth tides. *Water Resour Res* 55:6886–6895. <https://doi.org/10.1029/2019WR025166>
- Wang HF (2000) Theory of linear poroelasticity with applications to geomechanics and hydrogeology. Princeton University Press, New Jersey
- Witherspoon PA, Freeze RA (1972) The role of aquitards in multiple aquifer systems. *Geotimes* 17(4):22–24
- Xue L, Li HB, Brodsky EE et al (2013) Continuous permeability measurements record healing inside the Wenchuan earthquake fault zone. *Science* 340:1555–1559
- Xue L, Brodsky EE, Erskine J et al (2016) A permeability and compliance contrast measured hydrogeologically on the San Andreas Fault. *Geochem Geophys Geosyst* 17:858–871. <https://doi.org/10.1002/2015GC006167>
- Yan R, Woith H, Wang R (2014) Groundwater level changes induced by the 2011 Tohoku earthquake in China mainland. *Geophys J Int* 199:533–548. <https://doi.org/10.1093/gji/ggu196>
- Zhang Y, Wang CY, Fu LY et al (2019a) Unexpected far-field hydrological response to a great earthquake. *Earth Planetary Sci Lett* 519:202–212. <https://doi.org/10.1016/j.epsl.2019.05.007>
- Zhang H, Shi Z, Wang G et al (2019b) Large earthquake reshapes the groundwater flow system: insight from the water-level response to Earth tides and atmospheric pressure in a deep well. *Water Resour Res* 55:4207–4219. <https://doi.org/10.1029/2018WR024608>
- Zhu AY, Wang CY (2020) Response of leaky aquifers to earth tides—interpreted with numerical simulation. *J Hydrol* 581:124458. <https://doi.org/10.1016/j.jhydrol.2019.124458>

Open Access This chapter is licensed under the terms of the Creative Commons Attribution 4.0 International License (<http://creativecommons.org/licenses/by/4.0/>), which permits use, sharing, adaptation, distribution and reproduction in any medium or format, as long as you give appropriate credit to the original author(s) and the source, provide a link to the Creative Commons license and indicate if changes were made.

The images or other third party material in this chapter are included in the chapter's Creative Commons license, unless indicated otherwise in a credit line to the material. If material is not included in the chapter's Creative Commons license and your intended use is not permitted by statutory regulation or exceeds the permitted use, you will need to obtain permission directly from the copyright holder.



Chapter 6

Groundwater Level



Abstract Groundwater level has long been known to respond to earthquakes; several types of response have been documented. Advances in the last decade were made largely through the studies of water-level response to Earth tides and barometric pressure. These studies have demonstrated that the hydraulic properties of groundwater systems are dynamic and change with time in response to disturbances such as earthquakes. This approach has been applied to estimate the permeability of several drilled active fault zones, to identify leakage from deep aquifers used for the storage of hazardous wastewater, and to reveal the potential importance of soil water and capillary tension in the unsaturated zone. Enhanced permeability is the most cited mechanism for the sustained changes of groundwater level in the intermediate and far fields, while undrained consolidation remains the most cited mechanism for the step-like coseismic changes in the near field. A new mechanism has emerged that suggests that coseismic release of pore water from unsaturated soils may also cause step-like increases of water level. Laboratory experiments show that both the undrained consolidation and the release of water from unsaturated zone may occur to explain the step-like water-level changes in the near field.

6.1 Introduction

Coseismic changes of groundwater level have been documented since the time of antiquity (e.g., Institute of Geophysics—CAS 1976). Since the late twentieth century, instrumental records of groundwater level have become widely available and advanced our understanding of earthquake-induced groundwater changes (e.g., Waller et al. 1965; Wakita 1975; Whitehead et al. 1984; Rojstaczer and Wolf 1992; Quilty and Roeloffs 1997; Roeloffs 1998; Wang et al. 2001; Chia et al. 2001; Brodsky et al. 2003; Matsumoto et al. 2003; Montgomery and Manga 2003; Sato et al. 2004; Kitagawa et al. 2006; Sil and Freymueller 2006; Wang and Chia 2008; Mohr et al. 2015, 2017; Xue et al. 2013, 2016; Yan et al. 2014; Wang et al. 2016, 2018; Zhang et al. 2017; Liao and Wang 2018; Barbour et al. 2017, 2019; Zhang et al. 2019a, b; Zhu and Wang 2020). Furthermore, a broad range of coseismic responses of water

level to earthquakes have been discovered. The oscillatory response of water level was discussed in the last section of Chap. 5. Here we focus on the non-oscillatory responses (Fig. 6.1). The rise time of a non-oscillatory response ranges from ‘step-like’ to several days or even weeks. However, whether a coseismic change appears ‘step-like’ or ‘gradual’ depends on the time resolution of the recording system. For example, a ‘step-like’ change recorded at a rate of every hour may appear ‘gradual’ if recorded every minute or second. Here we qualitatively define a coseismic signal as step-like if the coseismic change between the last data point before the earthquake and the first data point after the earthquake is the predominant change in the data record (Fig. 6.1a, b), and as ‘sustained’ if the coseismic change is part of a continuous trend (Fig. 6.1c, d).

Earthquakes produce static and dynamic strains in the crust. Static strains are permanent crustal deformations produced by fault slip, and dynamic strains are oscillatory crustal deformations caused by the passage of seismic waves. Both can produce compression and extension in the crust and thus change pore pressure. Local hydraulic gradients force groundwater to flow through pores and fractures, to mobilize fine particles and to change permeability, storage and compressibility (e.g., Brodsky et al. 2003).

As noted in the previous chapter, measurements of the groundwater level response are made in wells. Two general approaches have been followed to study the water-level responses to earthquakes. First is to analyze the response of water level in a

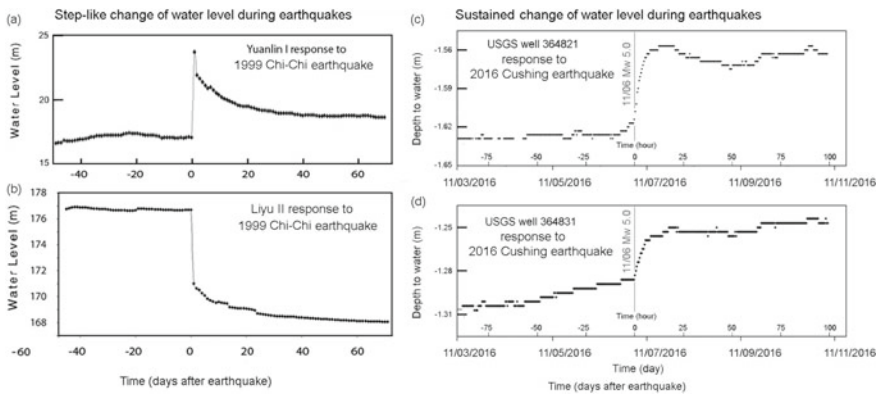


Fig. 6.1 **a** Step-like, positive water-level change in the Yuanlin I well during the 1999 Mw7.5 Chi-Chi earthquake. The well is ~ 25 km from the hypocenter, thus in the near field, and ~ 13 km from the surface rupture of the causative fault. The step-like coseismic water-level increase is $+6.55$ m. **b** Step-like, negative water-level change in the Liyu II well during the 1999 Mw7.5 Chi-Chi earthquake in Taiwan. The well is ~ 20 km from the hypocenter, thus in the near field, but is only ~ 5 km from the surface rupture of the causative fault. The step-like coseismic water-level decrease is -5.94 m. **c** Sustained change of water level in USGS well 364,821 during the 6 November Mw 5.0 Cushing earthquake. Note that the coseismic change of water level was gradual, instead of step-like, and the post-seismic water level was sustained, instead of decaying exponentially with time. **d** Sustained change of water level in USGS well 364,831 during the 6 November Mw 5.0 Cushing earthquake (modified from Wang et al. 2001, 2017)

single well to many earthquakes. Second is to compare and contrast the response of water levels in many wells in a region to a specific earthquake. The advantage of the first approach is that the well itself is often carefully calibrated, thus the various non-seismic influences on the groundwater-level records can often be eliminated and very small changes in the groundwater level may be detected at great distances from the earthquake (e.g., Roeloffs 1998). Furthermore, since the geology of the well site likely does not change between different earthquakes, the complications introduced from geological and hydrological heterogeneities at different well sites—a problem for the use of multiple wells—are eliminated and the groundwater records can often be used to effectively discriminate different models of the causal mechanisms of groundwater-level changes.

By using many wells in a region to study the groundwater response to a particular earthquake, it is possible to examine the regional pattern of the coseismic responses and thus the influence of geological and hydrogeological properties. For example, after the 2016 Mw7.0 Kumamoto earthquake, Japan, a dense network of monitoring wells in central Kyushu, Japan, captured dramatic spatiotemporal changes in groundwater levels (Fig. 6.2; Hosono et al. 2019). Water-level dropped over an area of 160 km² along crustal ruptures immediately after the main shock (within 35 min) in both confined and unconfined aquifers. A maximum drop of ~5 m was documented in a confined aquifer. Water level in the unconfined aquifer largely recovered within 45 days toward the background level (Fig. 6.2e). Water level in the confined aquifer continued to rise and reached ~5 m higher than that before the earthquake, one-year after the earthquake (Fig. 6.2h).

We may also note that currently two types of wells have been used in studying groundwater responses. Most data for studying groundwater responses to earthquakes have been collected from groundwater wells installed in unconsolidated sediments. On the other hand, a large number of wells, including those for monitoring earthquakes in China and those for oil exploration in the USA, have been installed in consolidated rocks, which have been increasingly used to study groundwater response to earthquakes. The lithologic contrast between these two types of wells may cause significant differences in their response to earthquakes. For instance, some mechanisms for groundwater response to earthquakes, such as undrained consolidation and liquefaction, may not occur in consolidated rocks. On the other hand, other mechanisms, such as enhanced permeability, may occur in both consolidated and unconsolidated rocks. Hence lithological differences among different wells need to be accounted for when comparing observations from different areas and for understanding the groundwater response to earthquakes.

As discussed in earlier chapters, studies of induced seismicity in the mid-continental U.S.A. since 2009 significantly advanced our understanding of the relationship between water injection and earthquakes (Chap. 4) and studies of the tidal and barometric responses of groundwater level (Chap. 5) have significantly improved our understanding of earthquake hydrology. In this chapter, we focus on the effects of natural earthquakes on the changes of groundwater level. We first discuss the relevant observations, followed by a discussion on the proposed hypotheses and relevant

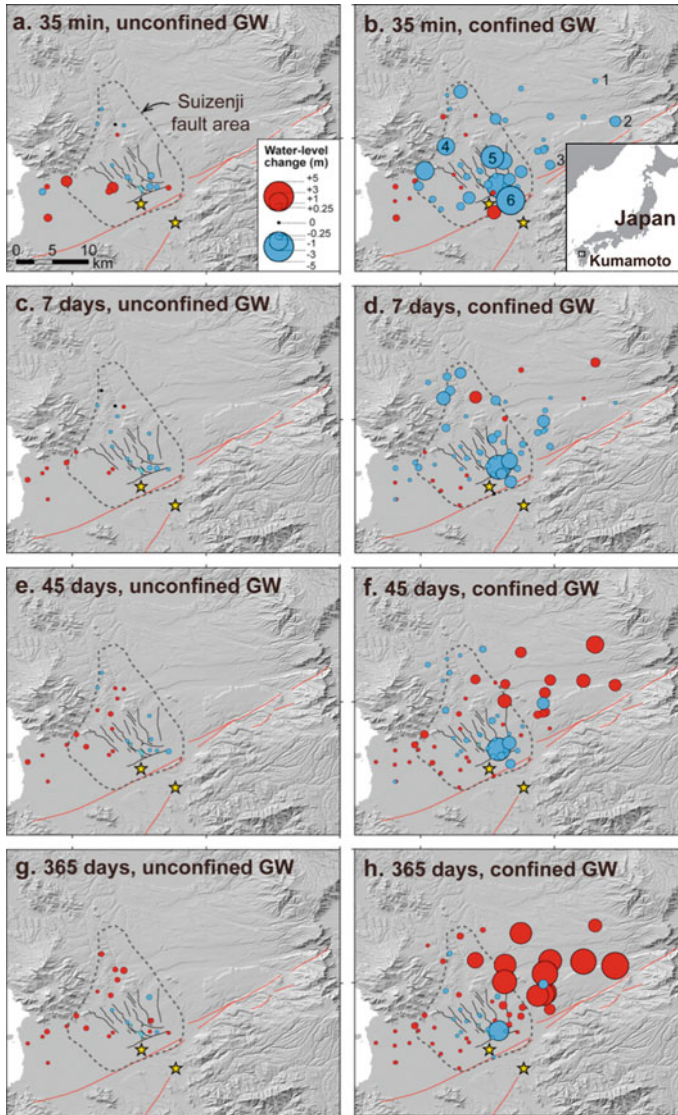


Fig. 6.2 Spatiotemporal changes of water levels following the 2016 Mw7.0 Kumamoto earthquake in Japan. The western rim of the Aso Mountain is visible on the upper right of each diagram. (a to h) Relative water level changes comparing water levels before the Kumamoto earthquake sequence at 35 min, 7 days, 45 days, and 365 days after the main shock for unconfined and confined aquifers. The area enclosed by a dashed curve shows the region affected by extensive faults. Earthquake epicenters and fault systems are marked by stars and red lines, respectively. Numbers 1–10 in (g) refer to wells discussed in Chap. 8, Fig. 8.3 (from Honoso et al. 2019)

constraints. We end the chapter with two short sections on estimating the hydraulic properties of continental fault zones and in the oceanic crust.

6.2 Observations

Based on the records from a single well in central California, Roeloffs (1998) showed three categories of groundwater-level response. In the near field, groundwater level shows step-like increases (Fig. 6.1a). In the intermediate field, groundwater-level changes are more gradual and can persist for days or weeks (Fig. 6.1c, d). At even greater distances (the far field), transient oscillations of the water-level occur (Fig. 5.39).

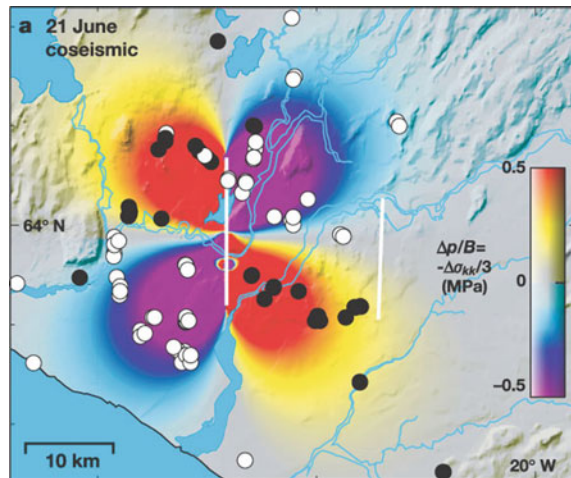
Based on the data from a network of monitoring wells in central Taiwan responding to the 1999 Chi-Chi earthquake, Wang et al. (2001) showed abrupt decreases of groundwater level in the immediate vicinity (<10 km) of the ruptured fault—(Fig. 6.1b) that were followed by either an exponential increase or an exponential decrease with time. Other examples of using large networks of wells to examine the response of groundwater level to earthquakes include the study by Yan et al. (2014) on the response of groundwater level on the Chinese mainland to the 2011 M9.0 Tohoku earthquake, Japan, and the study of by Hosono et al. (2019) on groundwater level changes in Japan after the 2016 Kumamoto earthquake (Fig. 6.2).

6.2.1 Coseismic Step-like Changes of Groundwater Level

In the near field, i.e., the area around the hypocenter within a distance of ~ 1 ruptured fault length, groundwater level often shows step-like changes during earthquakes (Wakita 1975; Quilty and Roeloffs 1997; Chia et al. 2001; Wang et al. 2001) and changes in excess of 10 m in amplitude are not uncommon. In some cases (e.g., Jonsson et al. 2003; Akita and Matsumoto 2004), coseismic changes of water level in wells show a characteristic pattern of positive and negative changes correlated with the coseismic static change of volumetric strain (Fig. 6.3). For this reason, the coseismic static change of volumetric strain has often been taken as the mechanism for coseismic step-like water-level changes.

However, such correlation was not found in other cases with distributed wells (e.g., Wang et al. 2001; Yan et al. 2014; Mohr et al. 2017; Hosono et al. 2019). For example, a dense network of monitoring wells was installed on an alluvial fan (the Choshui River fan) near the epicenter of the 1999 Mw7.6 Chi-Chi earthquake in Taiwan (Fig. 6.4) prior to the earthquake. About 200 wells captured the groundwater level changes during and after the earthquake. Water levels in these wells are recorded by digital piezometers and are logged at 1 h intervals. Some wells are equipped with data loggers operating up to 1 Hz. Piezometer readings in the well are converted to groundwater level with an accuracy of 1 cm. The resolution of the reading, on

Fig. 6.3 Calculated pore-pressure change based on the calculated coseismic volumetric strain and theory of poroelasticity (color map) and observed coseismic water-level changes (circles) following a 2000 M 6.5 strike-slip earthquake in Iceland. Black and white circles indicate water-level increases and decreases, respectively. The white line shows the mapped surface rupture (from Jonsson et al. 2003)



the other hand, is finer by an order of magnitude. In addition, several rain gauges installed around the fan provide continuous records of precipitation in the area. The close proximity to a large earthquake and the dense network of hydrological stations made this dataset one of the most comprehensive and systematic to study the spatial distribution of the hydrologic response in the near field. For the sake of better interpreting the observations, a brief summary of the subsurface hydrogeology of the Choshui River alluvial fan is needed. Figure 6.4d shows a simplified hydrogeological cross-section across the alluvial fan. It shows that the fan consists of subhorizontal layers of unconsolidated Holocene and Pleistocene sediments. Three distinct aquifers may be distinguished: Aquifer I, the topmost aquifer, is partly confined and partly unconfined, while aquifers II and III are confined. To the east of the alluvial fan is the Western Foothills of the Taiwan fold-and-thrust belt, which consists of pervasively faulted and fractured Pleistocene sedimentary rocks.

The step-like coseismic rise of groundwater level, such as that shown in Fig. 6.1a, was commonly observed on the Choshui River fan during the Chi-Chi earthquake (Wang et al. 2001; Chia et al. 2001). Figure 6.4 shows the coseismic changes in groundwater level in the three aquifers in the Choshui River fan during the Chi-Chi earthquake. In the uppermost partially confined aquifer (Fig. 6.4a), the coseismic changes are generally small except in an area on the northeastern edge of the alluvial fan where positive changes occurred. This area of positive water-level change is closely associated with the occurrence of liquefaction on the fan during the Chi-Chi earthquake (Chap. 10). The distribution of coseismic changes of water level in the two lower confined aquifers (Fig. 6.4b, c), on the other hand, showed coseismic groundwater level changes that are not associated with the occurrence of liquefaction on the surface. Instead, the water-level rise in these aquifers showed an increase with distance away from the ruptured fault, reaching a maximum at distances of 20–30 km from the fault, and then decreased at greater distances (Chia et al. 2001; Wang et al. 2001).

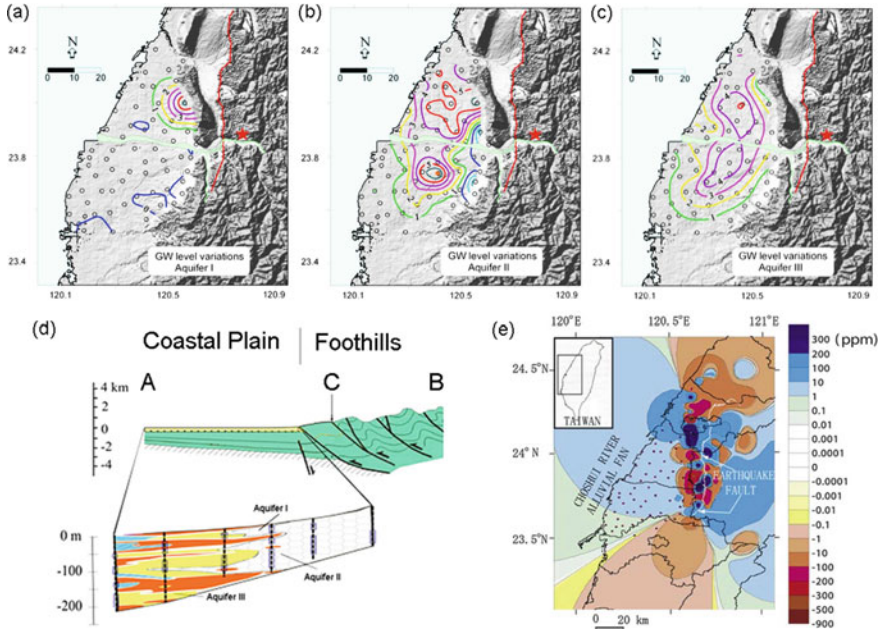


Fig. 6.4 Distribution of observed coseismic changes in groundwater level (**a**, **b**, **c**) and calculated volumetric strain (**d**) in the Choshui River fan during the Chi-Chi earthquake. **a** Contours (m) of groundwater-level change in the uppermost aquifer (Aquifer I). **b** Contours of groundwater-level changes in a confined aquifer (Aquifer II). **c** Contours of groundwater-level changes in a lower confined aquifer (Aquifer III). Groundwater monitoring stations are shown in open circles, epicenter of Chi-Chi earthquake in star, and the ruptured fault in discontinuous red traces. (from Wang et al. 2004). **d** Simplified hydrogeological cross-section along the cross-section marked by AB in Fig. 7.4, showing the Choshui River fan and the fold-and-thrust Foothills. The surface trace of the ruptured Chelungpu fault is marked by the letter C. The enlarged inset shows three aquifers in the Choshui River alluvial fan. Massive gravel beds (marked with greyish oblate ellipsoids) occur in proximal area; away from proximal area, gravel beds decrease in thickness, while coarse sands (highlighted yellow) and fine sands (highlighted blue) increase in proportion and interfinger with gravel beds; further away, silty sands and silty clays (highlighted brown) increase in proportion and eventually dominate the distal margin of fan. Three aquifers can be identified from top (Aquifer I) to bottom (Aquifer III). Dashed vertical lines show boreholes. Numbers on vertical axes give elevation relative to the mean sea-level. (from Wang et al. 2005) **(e)** Distribution of coseismic volumetric strain changes calculated from a dislocation model for the Chi-Chi earthquake. Positive and negative values indicate dilatation and contraction, respectively. Black dots are the locations of observation wells (from Koizumi et al. 2004)

Lowered groundwater levels were also reported in the vicinity of ruptured faults, including near the ruptured fault in the 1999 Mw7.5 Chi-Chi earthquake in Taiwan (Fig. 6.1c, d, Wang et al. 2001), or in areas of tectonic extension, such as the valley floor cut by extensional faults after the 2016 Mw7.0 Kumamoto earthquake in Japan (Fig. 6.2b, Hosono et al. 2019). In the second case, significant drawdown of groundwater over an area of 160 km² along crustal ruptures and ~10⁶ m³ of surface water disappeared within 35 min after the main shock. The Duoqing Co lake, located in

a rift valley in southern Tibet with an average surface area of 57 km², dried up suddenly following a nearby M3.7 earthquake in 2016. Geologic examination of the dry lake floor showed numerous tensional fractures oriented subparallel to the general direction of the rift valley (Wu et al. 2018).

6.2.2 Sustained Changes

Sustained groundwater-level changes are characterized by a gradual onset and can last for days or weeks (Fig. 6.1c, d). They are normally documented in the intermediate field of an earthquake, defined here as a distance from an earthquake source greater than 1 ruptured fault length but within a radius of 10 ruptured fault lengths. Although these changes are probably also common in the near field, their relatively small amplitude (<1 m) makes them easily obscured by the step-like changes of relatively large amplitude at such distances (see Sect. 6.2.1). Thus, they are clearly revealed only in the intermediate field where the abrupt changes become sufficiently small or absent.

Roeloffs (1998) showed that the water level changes in a well (BV) in California showed gradual responses to earthquakes and may take a few days to a few weeks to reach their peak. Furthermore, the coseismic change does not exponentially decay to the pre-seismic state (Fig. 6.1c, d). Based on observations Roeloffs (1998) showed that the occurrences of such changes are bounded by an empirical relation $M = -3.91 + 1.82 \log r$, where M is earthquake magnitude and r the maximum epicentral distance in meters for a specific M , beyond which water level response is not expected. Different relations were proposed by King et al. (1999) and Matsumoto et al. (2003) to describe the threshold distance for other data sets. The differences among these relations most likely reflect the relatively small number of the data used in the analyses and/or the different geology among the well sites where the data were documented, or both. Wang and Manga (2010) collected published data for the coseismic water-level changes (Roeloffs 1998; King et al. 1999; Roeloffs et al. 2003; Brodsky et al. 2003; Matsumoto et al. 2003; Sato et al. 2004; Kitagawa et al. 2006; Sil and Freymueller 2006) and referred to it as the 'global dataset' (Fig. 6.5). Weingarten and Ge (2014), using 24 years of data documented at Devils Hole, Nevada, significantly expanded the 'global dataset' (Fig. 6.5); new data from Sun et al. (2018) and Zhang et al. (2019b) are added to this compilation .

6.2.3 Breached Confinement

Taiwan is a north-south elongated island arc formed by the oblique collision between the Luzon volcanic arc on the Philippine Sea plate and the continental margin of China beginning in the late Cenozoic (Teng 1990). The Choshui River Alluvial Fan (Fig. 6.4) is part of the Coastal Plain that lies along the central western coast of the island and

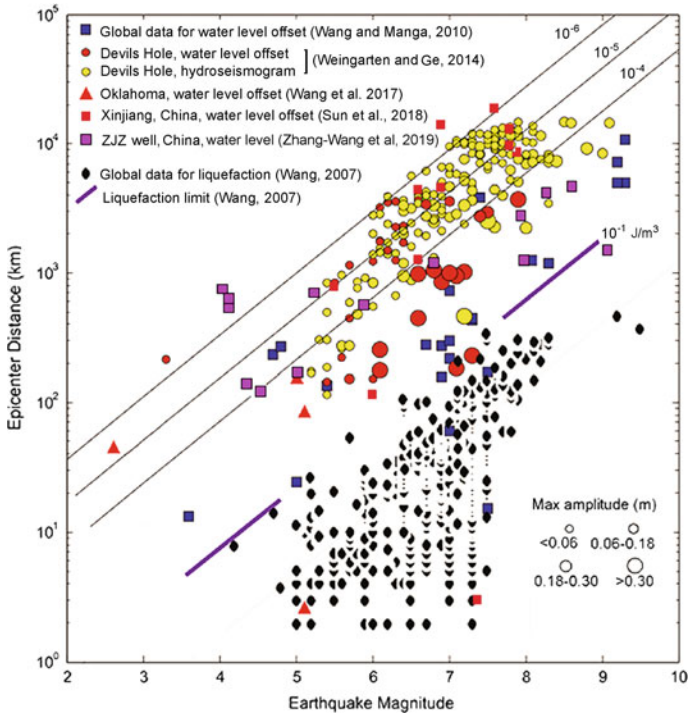


Fig. 6.5 Global coseismic occurrences of groundwater level change and liquefaction plotted on a diagram of logarithm of epicentral distance ($\log r$) versus earthquake magnitude (M). Also plotted are the contours of constant seismic energy density, based on Eq. (6.10). The thick purple line, associated with a seismic energy density of 0.1 J/m^3 , marks the upper bound of the occurrence of liquefaction and is known as the liquefaction limit (see also Chap. 10) (modified from Zhang et al. 2019)

is covered by unconsolidated sediments of Neogene and Quaternary age, floored by a faulted basement (Fig. 6.4d). The Western Foothills that lie immediately to the east of the Coastal Plain, on the other hand, is a fold-and-thrust belt of consolidated sedimentary rocks (Fig. 6.4d; Ho 1988). The 1999 Chi-Chi ($M_w = 7.5$) earthquake, the largest to hit Taiwan in the last century, ruptured the Western Foothills along a ~80 km fault on the east of the Choshui River fan (Fig. 6.4a–c).

Wang et al. (2007) showed that the 1999 Chi-Chi earthquake breached the confinement of some aquifers in the Choshui River alluvial fan (Fig. 6.4d) near the epicenter. Monitoring stations with clustered wells installed on this alluvial fan (Fig. 6.4a–c) revealed distinct water levels in different aquifers at the same station before the earthquake (Fig. 6.6) showing that good confinement was present. After the earthquakes (marked by $t = 0$), however, some stations showed converged water levels in different aquifers to the same level and stayed converged for one to several days, before they

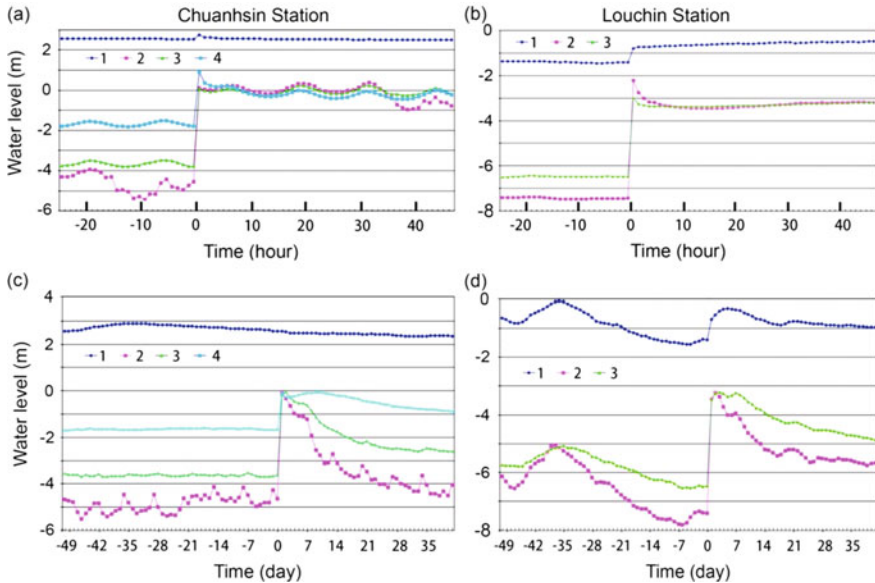


Fig. 6.6 Water levels at two stations with clustered wells before and after the Chi-Chi earthquake. Water level is referenced to the mean sea level, with positive values above sea level and negative values below sea level. **a** Hourly data for water level in four wells at the Chuanhsin Station documented by piezometers located, respectively, at depths of 8 m (aquifer 1), 111 m (aquifer 2), 181 m (aquifer 3), and 245 m (aquifer 4). Time of the earthquake is marked by $t = 0$. The wells are open to aquifers separated by aquitards 40–50 m thick. **b** Hourly data for water level in three wells at the Louchin Station documented by piezometers located, respectively, at depths of 12 m (aquifer 1), 110 m (aquifer 2), and 199 m (aquifer 3). Time of earthquake is marked by $t = 0$. The wells are open to aquifers separated by an aquitard ~60 m thick. Notice that the water levels at each station were distinct before the Chi-Chi earthquake, but converged rapidly to the same level after the earthquake. **c, d** Daily average of water levels at the same two stations (from Wang et al. 2016)

gradually diverged and returned to the pre-seismic levels. Such convergence of water levels is unlikely to have occurred by chance, because the probability for the earthquake to generate pore pressure changes in different aquifers that reach the same level, and stay at the same level for an extended time, is extremely small. It is more likely that the earthquake created or opened hydraulically conductive paths (e.g., cracks) that allowed pore pressures in the different aquifers to communicate and to equilibrate. The different amount of time for water levels at different stations to reach equilibrium may reflect the uneven distribution of the hydraulically conductive paths created by the earthquake.

The suggestion that the confinement of the aquifer was breached during the Chi-Chi earthquake was further demonstrated by using the change of the tidal response of the aquifer before and after the earthquake (Wang et al. 2016), as further explained in Sect. 6.4.3. Loss of confinement may commonly occur, even for deeply buried aquifers such as the Arbuckle aquifer in Oklahoma, as discussed in Chap. 5 (see also Wang et al. 2018).

6.3 Models and Constraints

Many hypotheses have been proposed to explain the observed water level changes during earthquakes. In this section we briefly describe in separate sub-sections the frequently invoked hypotheses, which include coseismic static strain, undrained consolidation and liquefaction, enhanced permeability, and shaking water out of the unsaturated zone.

6.3.1 Coseismic Static Strain

The coseismic static strain model (Wakita 1975) proposes that coseismic changes of volumetric strain cause the coseismic changes of groundwater level; it thus predicts water-level rises in areas of coseismic contraction and falls in areas of coseismic dilation. In support of this hypothesis, several authors reported a correlation between the distribution of coseismic groundwater level changes after some earthquakes and the calculated coseismic changes of static strain from a dislocation model in support of this hypothesis (e.g., Wakita 1975; Igarashi and Wakita 1991; Roeloffs 1996; Quilty and Roeloffs 1997; Ge and Stover 2000; Jonsson et al. 2003; Akita and Matsumoto 2004). As an example, Fig. 6.3 shows the spatial correlation in the pattern of groundwater level changes observed following a 2000 M 6.5 strike-slip earthquake in Iceland and that calculated from a dislocation model (Jonsson et al. 2003).

The correlation between the observed pattern of coseismic water-level change and that calculated from a dislocation model, however, was not found in some areas with a dense distribution of monitoring wells were installed and the coseismic groundwater level changes were documented; these include the responses to the 1999 Mw7.6 Chi-Chi earthquake in western Taiwan (Chia et al. 2001; Wang et al. 2001), to the Darfield earthquake sequence in eastern New Zealand (Rutter et al. 2016), to the 2010 Maule earthquake in Chile (Mohr et al. 2017), and to the 2016 Mw7.0 Kumamoto earthquake in southern Japan (Hosono et al. 2019). Figure 6.4a, b, c show that the coseismic changes of water level in western Taiwan during the 1999 Mw 7.6 Chi-Chi earthquake were mostly positive in three aquifers. This pattern of the coseismic changes of water level is opposite to that expected from the static strain hypothesis because the thrust mechanism of the Chi-Chi earthquake predicts a positive change (extension) of coseismic strain in front of the ruptured thrust fault, and thus predicts a coseismic decrease of water level over the Choshui River fan (Wang et al. 2001). This argument was further supported by the result of a numerical simulation by Koizumi et al. (2004) (Fig. 6.4e), in contradiction to the prediction of the coseismic strain hypothesis.

Wang and Barbour (2017) showed that most measured coseismic volumetric strains differ substantially from the predicted strains based on the static dislocation model, sometimes with opposite signs. The disagreement suggests that some

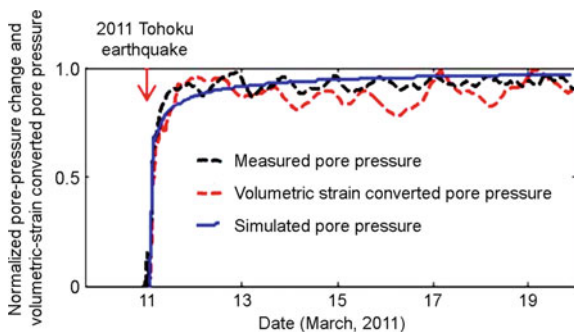


Fig. 6.7 Time histories of the measured normalized volumetric strain (black), volumetric strain converted from the measured pore pressure (red), and volumetric strain converted from calculated pore pressure based on the Roeloffs (1998) model of diffusion from a localized coseismic source (blue) during the Tohoku earthquake with an assumed hydraulic diffusivity of $10^{-3} \text{ m}^2/\text{s}$ (modified from Zhang et al. 2017)

processes affecting the coseismic volumetric strain are missing from the dislocation model. Roeloffs (1998) also found that some sustained changes of water level in wells have opposite signs to that expected from the static volumetric strain, and that the groundwater level always rises in some wells but falls in other wells, regardless of the locations or focal mechanisms of the earthquakes, in contradiction to the static strain model. Kitagawa et al. (2006) showed that only half of the measured coseismic strains and water level changes in Japan during the 2004 M9 Sumatra earthquake, more than 5000 km away, were consistent with the static strain hypothesis. Finally, the static strains at such large distances are too small to explain many of the observed water-level responses (e.g., Igarashi and Wakita 1991; Itaba and Koizumi 2007; Wang and Barbour 2017).

Figure 6.7 shows the water level and volumetric strain in the Fuxin well, NW China, during the 2011 Mw9.1 Tohoku earthquake, Japan, which was >1500 km from the well. At such a large epicentral distance, the static elastic strain due to the earthquake rupture is negligible and cannot produce any measurable coseismic change of pore pressure. However, significant changes of both pore pressure and volumetric strain occurred in this well and, furthermore, the observed coseismic increase of pore pressure (Fig. 6.7, black dashed curve) is in the opposite direction from that expected from the hypothesis that the observed volumetric strain was the causal mechanism (Fig. 6.7, red dashed curve, converted to the equivalent water level, extension positive). Zhang et al (2017) suggested that, instead, the increase of volumetric strain was caused by a coseismic increase of pore pressure. They converted the volumetric strain to pore pressure and compared the measured time-series of pore pressure with the predicted pore pressure from the model of pressure diffusion from a local coseismic source (Roeloff 1998). The good agreement among the three curves (Fig. 6.7, blue curve) supports the hypothesis that the coseismic increase

of volumetric strain was due to increased pore pressure produced by earthquake-enhanced permeability and diffusion between the well and a pre-existing, local crustal heterogeneity in pore pressure.

6.3.2 *Undrained Consolidation and Liquefaction*

The undrained consolidation and liquefaction model was based on the results of a great number of laboratory experiments in the past four decades by geotechnical engineers to study earthquake-induced liquefaction (e.g., Seed and Lee 1966; Dobry et al. 1982; Vucetic 1994; Hsu and Vucetic 2004) and was used to explain the coseismic increase of groundwater level following the Chi-Chi earthquake (Wang et al. 2001). These experiments show that loose sediments consolidate under cyclic shear stress, which causes pore-pressure to increase, the effective stress to decrease, and eventually liquefaction of sediments. Examples of the experimental results are shown in Chap. 3 (Figs. 3.8 and 3.10–3.12). More discussions are given in Chap. 11.

After the Chi-Chi earthquake, an interesting correspondence was found between the area of liquefaction occurrence (Fig. 3.10) and the occurrence of coseismic increase of water level in the topmost aquifer (Fig. 6.4a; Wang et al. 2006). Also interesting is the absence of an association between liquefaction occurrence and water-level increase in the lower aquifers (Fig. 6.4b, c). Such association between liquefaction occurrence with pore-pressure increases in the topmost aquifer and the lack of association with pore pressure change in the lower aquifers supports the common assumption in earthquake engineering that liquefaction occurs mostly in the upper 15 m of sediments.

6.3.3 *Enhanced Permeability*

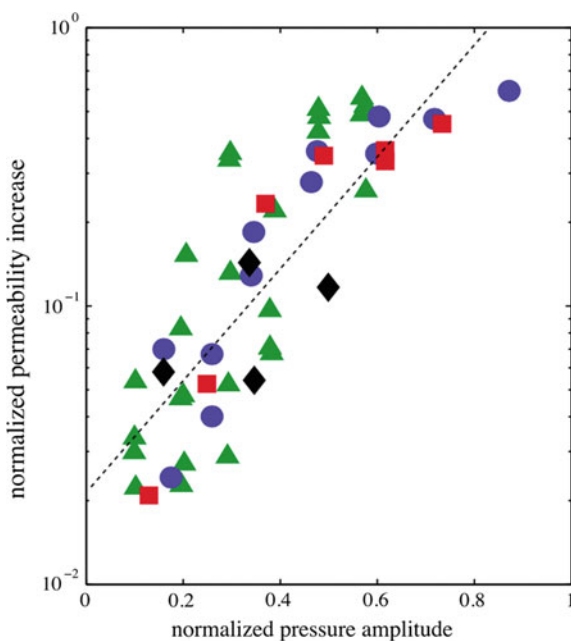
Permeability controls groundwater flow; thus, any change of permeability would lead to changes in groundwater flow and groundwater level if the hydraulic gradient is fixed. One model of seismically enhanced permeability assumes that seismic shaking increases the mobility of colloidal particles and air bubbles and removes them from flow channels such as microcracks and pore throats, which may increase the permeability of rocks and sediments (e.g., Mogi et al. 1989; Roeloffs 1998; Brodsky et al. 2003; Roberts and Abdel-Fattah 2009; Manga et al. 2012).

Another model assumes that permeability may change due to poroelastic opening and closing of micro-fractures in response to the transient pore pressure (Faoro et al. 2012). If the external stress remains constant, the aperture of a fracture would change in response to transient pore pressure in the fracture, and the evolving permeability would scale with the change in aperture Δb as $k/k_o = (1 + \Delta b/b_o)^3$, where b_o is the initial width of the aperture.

Brodsky et al. (2003) found that the water level recorded in a well in Southern Oregon did not respond significantly to the first 10 cycles of the ~ 20 s Rayleigh waves from the 1999 Mw7.4 Oaxaca earthquake, but responded with large amplifications to the Rayleigh waves that arrived later (Fig. 5.39a). These observations are more consistent with mobilization of trapped colloidal particles or air bubbles, which are progressively mobilized by the oscillatory pressure beyond some threshold, rather than with poroelastic opening or closing of fractures (Manga et al. 2012). The common observation of increased turbidity in wells after earthquakes (e.g., Sneed et al. 2003) is also consistent with the model of mobilization of colloidal particles in pores and fractures of aquifers by earthquakes.

Elkhoury et al. (2011) used Berea sandstone samples fractured in a triaxial deformation apparatus to investigate the influence of pore pressure oscillations on permeability. A servo-control system was applied at the inlet and outlet to establish pore pressures. After the fluid flow reached a steady state, sinusoidal oscillations of pore pressure, with 20 s periods, were applied at the inlet while keeping the outlet pressure constant. The application of the pore pressure oscillation leads to an immediate increase of permeability, with magnitude increasing exponentially with the amplitude of the pressure oscillations (Fig. 6.8). Following the dynamic oscillations, permeability recovered as the inverse square root of time. This recovery demonstrates that the observed flow rate change was due to changes of permeability, but not to the change of poroelastic storage (Elkhoury et al. 2011). It also led the authors to favor the mechanism of clogging and unclogging of the fracture flow paths. Additional experiments were performed on samples fractured outside the apparatus and

Fig. 6.8 Permeability changes in sandstone samples measured in laboratory as a function of imposed pore pressure oscillation amplitude. Permeability changes are normalized by permeability before the oscillations; pressure amplitudes are normalized by the pore pressure difference driving the flow. Different symbols and colors correspond to different rock samples (modified from Elkhoury et al. 2011)



then re-assembled for the flow through experiments. In these instances no change in permeability was observed after stimulation.

Roberts (4) studied the influence of axial stress oscillations on permeability in intact sandstone cores. After steady state had been reached, continuous dynamic stressing with frequency of 50 Hz and amplitude of 0.3 MPa was applied, resulting in no observable effects on permeability. The amplitude of the continuous stress cycling was increased to 0.6 MPa; after which permeability increased 15%. A further increase in the amplitude of stress cycling to 0.9 MPa added another 5% increase in permeability. Permeability returned to the original value after the stress oscillations terminated.

Liu and Manga (2009) performed similar experiments on fractured sandstone samples saturated with de-ionized water. Permeability was first measured with steady flow, followed by transient stresses by oscillating the axial displacement to achieve strain amplitudes of 10^{-4} at frequencies from 0.3 to 2.5 Hz. In general, permeability decreased after each set of oscillations. Additional experiments were performed with natural silt particles injected into the fractures. Fractures with added silt showed the largest decrease in permeability in response to the oscillatory stresses. No recovery of permeability was documented within ~10 min of the stimulation.

Collectively, these experiments show that rock permeability does change with oscillatory stresses and pore pressure. The observed differences in these experiments may be due to differences in the sample preparation, in the type of applied stresses (oscillation of pore pressure or axial strain/stress), and in the differences in the applied oscillation frequency (Manga et al. 2012). Also noticeable is that the transient strains in all these experiments are at least an order of magnitude greater than those that cause permeability to change in natural systems ($\sim 10^{-6}$).

6.3.4 Shaking Water Out of Unsaturated Soil

Mohr et al. (2015) observed that the stream flows in some headwater catchments in the Chilean Coast Range increased following the 2010 Mw8.8 Maule (Chile) earthquake. They attributed this increase to the release of water from the unsaturated soil to recharge the local groundwater. This observation will be discussed further in the next chapter on stream flow. The proposed mechanism of water lease from the unsaturated zone is tested in a recent laboratory study (Breen et al., 2020) and is discussed in the next section.

6.4 Constraints

6.4.1 Constraints from Laboratory Experiments

Both the mechanism of water release from the unsaturated zone (Mohr et al. 2015; Sect. 6.3.4) and that of undrained consolidation (Wang et al. 2001; 6.3.2) predict step-like increases of pore pressure in the affected aquifer. Breen et al. (2020) used laboratory experiments to test and distinguish between these mechanisms. The experiments were designed to study the response of unconsolidated sediments during “seismic” shaking and were carried out in a sand column (Fig. 6.9a) subjected to

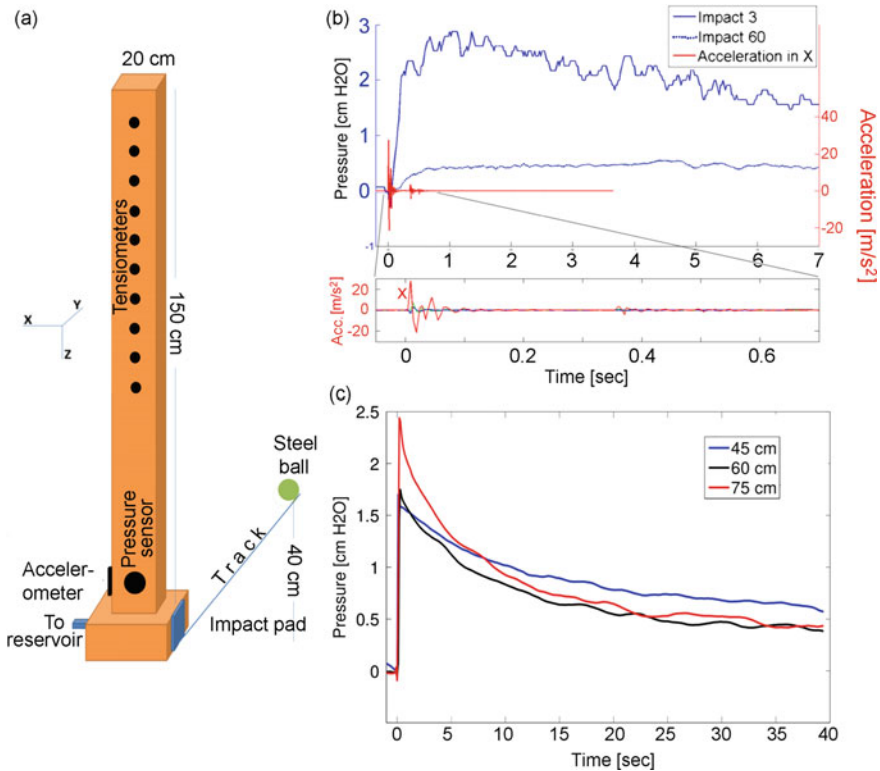


Fig. 6.9 a Schematic drawing of the sand column in the experiment. b Pore pressure relative to hydrostatic in the experiments with the water level above the sand surface. The solid blue line shows the pore pressure during the third impact, and the dotted blue line shows the pore pressure after the last (60th) impact. Time is relative to impact. Note that the duration of the pressure increase far exceeds the duration of shaking (acceleration). c Measured pore pressure in three sets of experiment with an unsaturated zone above the water table. In each experiment, the water level was set at a distinct height above the base of the sand column, as shown in the figure legend. Time of impact is marked by $t = 0$ (from Breen et al. 2020)

“seismic” shaking of controlled energy. In one set of experiments, the water level was set above the sand surface; thus, there was no capillary effect. All the experiments showed that, under “seismic” shaking, pore pressure suddenly increased with a rise time of ~ 1 s, and then declined slowly with time (Fig. 6.9b). Since there was no capillary effect, the increase of pore pressure must be due to the in situ volumetric contraction of the sediment matrix, confirming the undrained consolidation hypothesis. If the water level was set below the sand surface, leaving a thick unsaturated zone above the water table, pore pressure also suddenly increased with shaking, and then declined exponentially with time (Fig. 6.9c). Breen et al. (2020) attributed the rise to the disruption of capillary tension, which caused pore pressure to suddenly increase, supporting the hypothesis that capillary forces were altered. The rise time of pore pressure in the experiments with the unsaturated zone is much shorter (< 0.1 s) than that in the experiments with the undrained consolidation mechanism. Hence, in principle, these two mechanisms can be distinguished from their different rise times. However, most field experiments have so far been carried out at a recording rate much lower than 1 Hz, and hence do not have the time resolution to distinguish between the two mechanisms. For this reason, both mechanisms are acceptable for the moment to explain the coseismic step-like water-level changes.

6.4.2 Constraints from Field Observations

Direct association of field-scale observations to a specific mechanism is challenging because the subsurface cannot be easily monitored at the scales required for making such connections (Manga et al. 2012). On the other hand, indirect inferences may be drawn from field observations and laboratory experiments to provide useful constraints on the various mechanisms.

Wang and Chia (2008) showed in Fig. 6.10a that, for a global dataset, the sign and magnitude of sustained coseismic water level changes were randomly distributed with the epicentral distance. The enhanced permeability model requires connection of the well to a nearby source (or sink) that can occur either up-gradient or down-gradient of the well; thus, either positive or negative change of water-level may be expected. If a sufficiently large number of observations is available, the enhanced permeability model would predict a statistically random occurrence in the sign and the magnitude of the water-level changes, consistent with the global data presented in Fig. 6.10a.

Figure 6.10b shows the data from a dense network of monitoring wells in central Taiwan near the epicenter of the 1999 Mw7.6 Chi-Chi earthquake (Fig. 6.4). The data provides a nearly continuous sequence of the changes of sign and amplitude of water-level from the vicinity of the ruptured fault to a distance of 160 km.

In the immediate neighborhood of the ruptured fault during the Chi-Chi earthquake, marked by the downward arrow, large decreases of groundwater level occurred. This was attributed to downward flow through dilatant fractures formed during strong seismic vibrations (Chap. 3, Sect. 3.4). Similarly, large decreases of

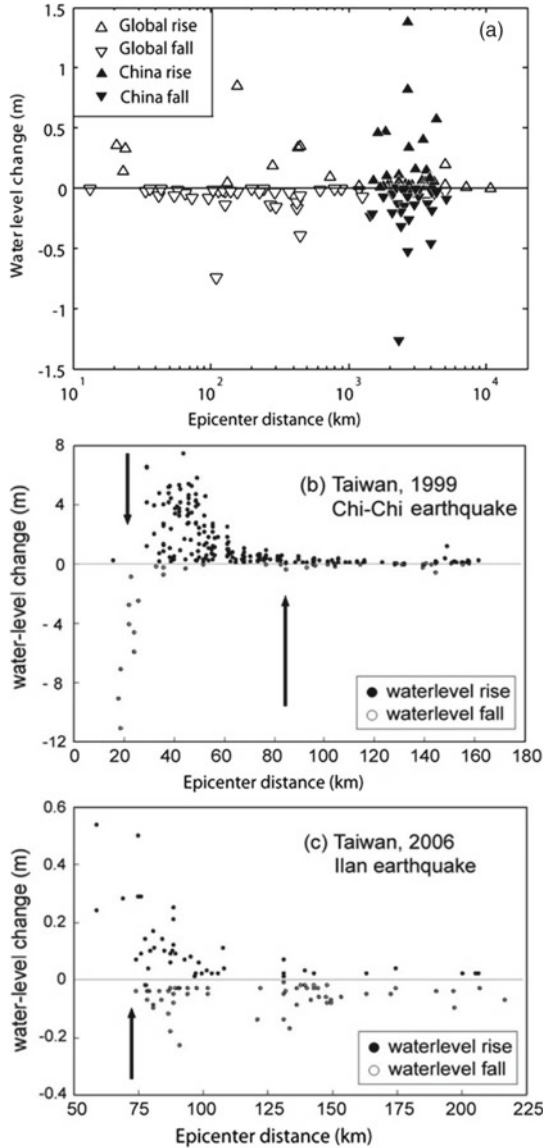


Fig. 6.10 Amplitude and sign of water-level changes during earthquakes plotted as a function of the epicentral distance. **a** Water-level changes in a global dataset (Wang and Chia 2008) updated with responses to the 2011 Tohoku earthquake in wells on the Chinese mainland (Yan et al. 2014). **b** Water-level changes during the 1999 Chi-Chi earthquake. The upward-pointing arrow shows the distance equal to one ruptured fault length. The downward-pointing arrow shows the location of the ruptured fault. Note that nine wells near the downward-pointing arrow documented abrupt decreases of water level as illustrated in Fig. 6.1b. These wells are all located within 5 km of the surface rupture of the causative fault. **c** Water-level changes during the 2006 Hengchun earthquake. The upward-pointing arrow shows the distance equal to one ruptured fault length. Note that at distances beyond one ruptured fault length, the sign of water-level changes is random (from Wang and Chia 2008)

groundwater level were also reported near the ruptured faults during the 1989 Mw6.9 Loma Prieta earthquake, California (Rojstaczer and Wolf 1992; Rojstaczer et al. 1995) and during the 1995 Mw6.9 Kobe earthquake, Japan (Tokunaga 1999).

At epicentral distances further from the ruptured fault but still within one ruptured fault length (~85 km) during the Chi-Chi earthquake, the groundwater-level changes were predominantly positive (Fig. 6.10b), consistent with the undrained consolidation hypothesis. At epicentral distances greater than one ruptured fault length, marked by the upward arrow, the signs of the water level changes become random and the magnitude of the changes became relatively small.

Figure 6.10c shows the water-level changes in a large number of monitoring wells in southern Taiwan, documented during the 2006 Hengchun earthquake off the southern coast of Taiwan. Most wells were at distances beyond one ruptured fault length, marked by the upward arrow, and showed random distribution of signs, with both positive and negative changes at further distances, consistent with the enhanced permeability model. A few wells at closer distances show positive changes, consistent with the occurrence of undrained consolidation.

Overall, the observations from wells installed in unconsolidated sediments are consistent with the model that the dominant mechanism for the coseismic change of groundwater level in the near field is undrained consolidation of saturated sediments and/or release of water from the unsaturated zone. In the intermediate and far fields, the dominant mechanism may be earthquake-enhanced permeability. These mechanisms provide simple explanation for why the water-level changes are step-like in the near field, but are more gradual and sustained in the intermediate and far fields. Furthermore, in the intermediate and far fields, since the same source (or sink) and the same passageway may be activated during different earthquakes, some wells may show consistently positive or consistently negative water-level changes during different earthquakes (e.g., Roeloffs 1998; Matsumoto et al. 2003).

Finally, we note that enhanced permeability may occur both in the near field and in the intermediate field. In the near field, the change of groundwater level due to undrained dilatation or consolidation may be so large that the sustained groundwater level changes, which are usually of smaller amplitude (<1 m), are obscured. Sustained changes can thus be clearly detected only in the intermediate and far fields where undrained consolidation is no longer important (Wang and Chia 2008). We also note that the post-seismic recovery of the enhanced permeability would proceed with re-clogging of the passageways by various hydrological and geochemical processes that take time. Thus, the model predicts a gradual recovery of the water level, in contrast to the exponential recovery that characterizes pressure diffusion following the step-like increases of water level in the near field.

6.4.3 Constraint from Tidal Analysis

The tidal response of groundwater was discussed in Chap. 5. Here we discuss the application of this response to the study of the interaction between water and earthquakes. Elkhoury et al. (2006) first applied this method to study earthquake-induced changes in groundwater systems by analyzing 20 years of water-level response using data from two wells in southern California. They found repeated step-like changes in phase at the time of earthquakes (Fig. 6.11), each followed by a gradual recovery of the phase to the pre-earthquake values. They also noted that all earthquakes produce decreases in the phase lag, implying an increase in aquifer permeability (Hsieh et al. 1987), regardless of the sign of the earthquake-induced static strain at the well sites, which shows that the change in permeability was not caused by the coseismic static strain. They further showed that the amount of increase in permeability appears to be linearly proportional to the magnitude of the peak ground velocity (PGV) of ground shaking, with a maximum increase of a factor of 2–6 (Fig. 6.12).

Since the study by Elkhoury et al. (2006), the tidal method has been widely applied to study earthquake effects on groundwater systems. These studies have revealed that earthquakes can not only enhance aquifer permeability but also breach the confinement between aquifers and the surface. Wang et al. (2016) analyzed the tidal response of groundwater level in two wells discussed in Sect. 6.2.3 (the Chuanhsin station); their results before and after the Chi-Chi earthquake are plotted in Fig. 6.13a, b on amplitude versus phase shift diagrams. On such a diagram, data points before the Chi-Chi earthquake (blue dots) in each well show a trend consistent with that of a confined aquifer model (dotted lines). After the earthquake, however, data points (red dots) deviate significantly from that of a confined aquifer. Each data point represents a 3-day average of the tidal response. The arrows in both diagrams connect

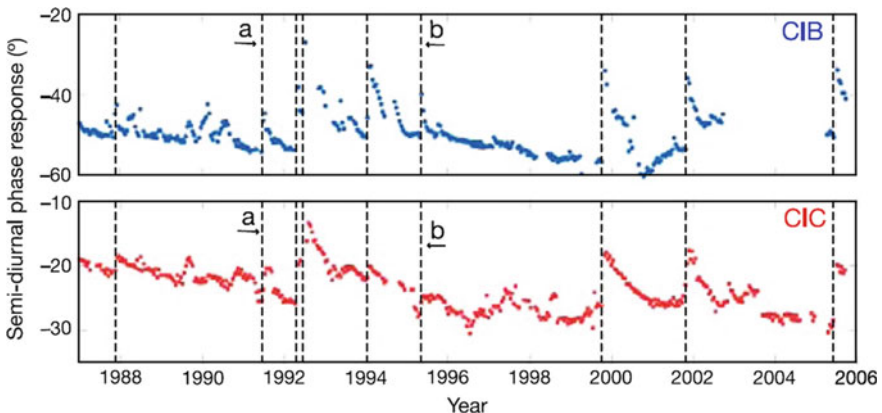
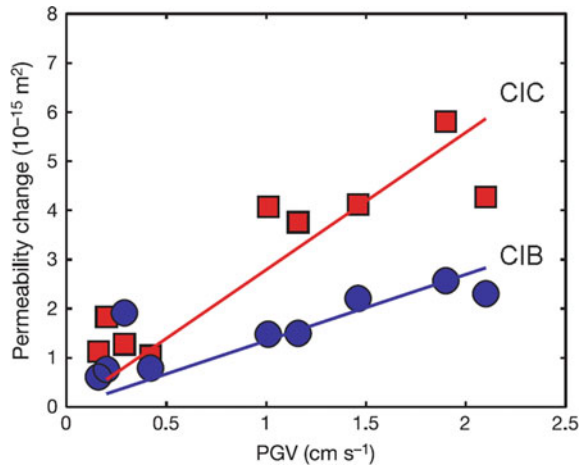


Fig. 6.11 Phase of the semi-diurnal tides for the water levels in two wells in southern California relative to the tidal strain. Transient changes of the phase are clearly evident at the time of earthquakes, as shown by the vertical lines (from Elkhoury et al. 2006)

Fig. 6.12 Increased permeability of the aquifers at the two wells plotted against the peak ground velocity (PGV) of ground motion during earthquakes. The maximum increases correspond to a factor of 5–6 increase in aquifer permeability (from Elkhoury et al. 2006)



the last tidal data before the Chi-Chi earthquake to the first data after the earthquake; these also deviate significantly from the trend defining a confined aquifer (dashed lines). The numbers attached to the data points show the number of days since the Chi-Chi earthquake. Thus, after the earthquake, the tidal response in each well exhibits a time-dependent excursion from the trend defining a confined aquifer, and the excursions in the two wells are closely similar, suggesting that the two aquifers behaved hydraulically the same after the earthquake. In other words, the two aquifers were effectively connected by hydraulically conductive fractures after the earthquake and they behaved hydraulically in the same way. The excursions in both wells terminated ~60 days after the earthquake after which the tidal responses fall back onto the trend for a confined aquifer, as indicated by the dotted lines. Note also that the duration of the excursion of the tidal response in each well from that of a confined aquifer lasted ~60 days, an order of magnitude longer than the duration suggested by the change of groundwater level in Fig. 6.6a, c. This difference suggests a greater sensitivity of the tidal response to the occurrence of aquifer leakage. Quantitative interpretation of the tidal response, however, was not made for the present case because the data for ocean tides off western Taiwan, which load on the aquifers and cause the groundwater to oscillate, was not measured before or after the Chi-Chi earthquake.

Numerous other applications of the tidal method have been made to study earthquake-affected aquifer properties including evaluating the permeability of the ruptured fault in the 2008 Mw7.9 Wenchuan earthquake (Xue et al. 2013; Sect. 6.5), the long-term or irreversible changes of aquifer permeability after the Wenchuan and the 2011 Mw9.0 Tohoku earthquakes (Liao et al. 2015; Zhang et al. 2019b; Fig. 5.37), the leaking of the Arbuckle aquifer in Oklahoma, a target for a great amount of wastewater disposal produced by hydrocarbon extraction (Wang et al. 2018; Zhu and Wang 2020; Sect. 5.4.3), and capillary effects on the tidal response of unconfined aquifers (Wang et al. 2019; Sect. 5.4.4).

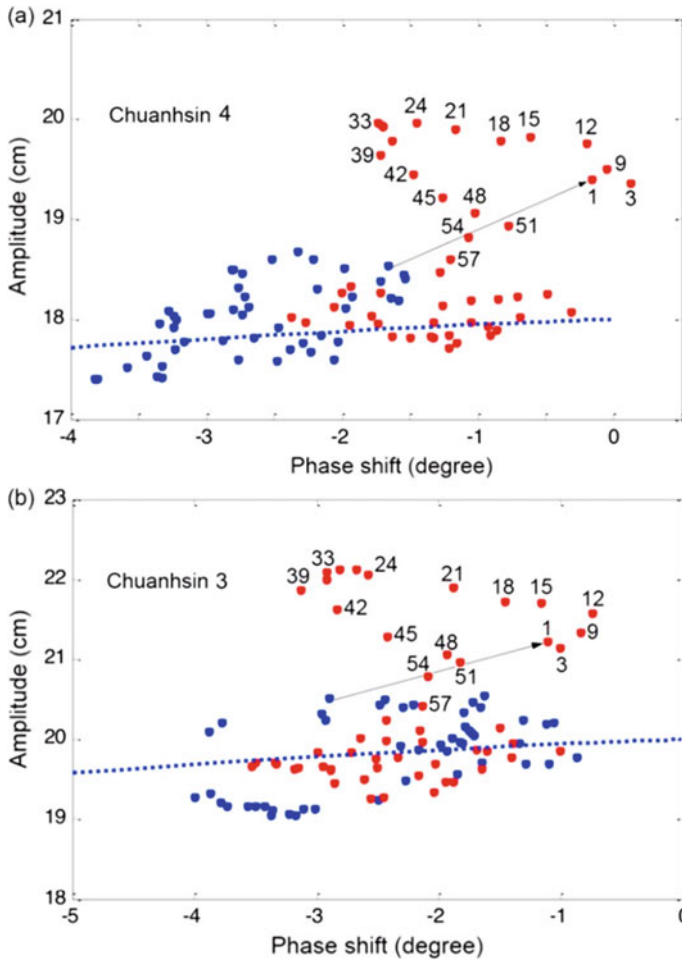


Fig. 6.13 Amplitude versus phase shift for water-level response to the M_2 tide in two wells at the Chuanhsin Station. In each well, each point represents the phase shift and amplitude calculated for a data window. Data points in both wells before the earthquake are shown by blue dots and after the earthquake by red dots. Before the earthquake the data fall along a trend for a confined aquifer model (dashed line) (Hsieh et al. 1987). During the earthquake, the coseismic changes in both wells are given by the arrows that connect the last pre-seismic data point to the first post-seismic data point. Data points during the first 60 days after the earthquake are numbered in sequence to show the time-dependent evolution. Both the arrows and the post-seismic data points during the first ~60 days deviate significantly from the trend defining a confined aquifer (dashed line). Numbering refers to the number of days after the earthquake (from Wang et al. 2016)

6.4.4 Constraints from Threshold Seismic Energy

In the past four decades earthquake engineers have performed numerous laboratory experiments to study consolidation and liquefaction of saturated sediments under cyclic shearing (e.g., National Research Council 1985, 2016; Ishihara 1996). The results of these experiments show that, when sediments are subjected to cyclic shearing, they begin to consolidate if the shear strain magnitude exceeds a threshold of $\sim 10^{-4}$ (Fig. 3.9; Dobry et al. 1982; Vucetic 1994). Since deformation during earthquakes is undrained, pore pressure increases when the shear strain exceeds 10^{-4} and the effective stress decreases. This would eventually lead to liquefaction if deformation continues. Wang et al. (2001) suggested that undrained consolidation explains the coseismic water-level rises on the Choshui River fan during the Chi-Chi earthquake. If the amplitude of shear deformation exceeds some critical threshold, however, cracks and fractures may form and cause pore pressure to decrease (Luong 1980), which may explain the water-level drop immediately adjacent to the ruptured fault during the Chi-Chi earthquake (Wang et al. 2001).

The geotechnical laboratory data may be used to calculate the amount of dissipated energy required to cause undrained consolidation; the magnitude of this energy may then be compared with the seismic wave energy in the field at different epicentral distances to constrain the mechanism. In cyclic loading, the dissipated energy density required to initiate undrained consolidation in saturated sediments may be estimated from the experimental time histories of shear stress τ and shear strain γ by performing the following integration:

$$e_d(t) = \int_0^t \tau d\gamma, \quad (6.1)$$

where the integration extends from the beginning of the cyclic loading to the onset of pore-pressure increase. Since both the shear strain and the dissipation are small and the stress and strain relation is nearly linear in this case, we may express the cyclic experimental stress and strain in the form $\tau = \tau_o \sin\theta$ and $\gamma = \gamma_o \sin(\theta + \varphi)$, respectively, where τ_o and γ_o are the corresponding amplitudes, and φ is the phase angle between stress and strain. Integrating Eq. (6.1) we obtain, for small φ ,

$$e_d = \frac{N\pi}{2} \tau_o \gamma_o \sin \varphi \approx \frac{N\pi}{2} \mu \gamma_o^2 \varphi \quad (6.2)$$

where $N \sim 10$ is the usual number of cycles adopted in experimental studies, μ is the shear modulus measured at strain amplitude of 10^{-4} and φ is also known as the damping ratio (Ishihara 1996).

Table 6.1 lists some experimental data for the shear modulus and the damping ratio of sands and gravels collected from different sources, prepared with different procedures, and subjected to different confining pressures. These experimental data are used with Eq. (6.2) to calculate the dissipated energy density e_d required to initiate

Table 6.1 Shear moduli and damping ratios of sediments, determined under laboratory conditions and cyclically sheared to strain amplitude (γ_o) of 10^{-4}

Samples	Shear modulus (MPa)	Damping ratio	Dissipated energy (J/m^3)
Undisturbed Fujisawa sand	100	0.07	1
Disturbed Fujisawa sand	40	0.02	0.1
Undisturbed Tokyo gravel, at a confining pressure of 300 kPa	300	0.04	2
Undisturbed Tokyo gravel, at a confining pressure of 500 kPa	600	0.05	5
Reconstituted Tokyo gravel, at a confining pressure of 300 kPa	200	0.07	2
Reconstituted Tokyo gravel, at a confining pressure of 500 kPa	400	0.08	5

Dissipated energy density is calculated using Eq. (6.2) with $N = 10$. Experimental values for the shear modulus and the damping ratio were extracted from figures on p. 143 and 145 in Ishihara (1996)

undrained consolidation of the sediments. The calculated dissipated energy density required to initiate undrained consolidation, e_d , range from ~ 0.1 to $\sim 5 \text{ J/m}^3$. The broad range of energy density required to initiate undrained consolidation highlights that different sediments have different sensitivity to cyclic loading and that the sediments were subjected to different confining pressures during the measurements (e.g., Ishihara 1996). Irrespective of the limited laboratory experiments, the existing data suggests that a threshold energy density of 0.1 J/m^3 may be taken as the threshold e_d to initiate undrained consolidation in saturated sands.

Wang et al. (2006) argued that the observed bounds on the epicentral distance for a hydrologic response to earthquakes may reflect the threshold seismic energy required to initiate the hydrologic response. Here we first derive an empirical relation among the seismic energy density, epicentral distance, and earthquake magnitude; we then use this relation to associate the threshold energy density to epicentral distance and earthquake magnitude. Using $\sim 30,000$ strong-motion records for southern California earthquakes, Cua (2004) showed that the peak ground velocity (PGV) for sediment sites attenuates with the epicentral distance as

$$\text{PGV} \sim A/r^{1.5} \quad (6.3)$$

where A is an empirical parameter for southern California. The seismic energy density e at a site during ground shaking may be evaluated from the time histories of particle velocity of the ground motion as recorded by strong-motion seismometers (Lay and Wallace 1995):

$$e(r) = \frac{1}{2} \sum_i \frac{\rho}{T_i} \int v_i(t)^2 dt, \quad (6.4)$$

where the summation is taken over all the relevant modes of the ground vibrations, ρ is density, and T_i and v_i are, respectively, the period and the velocity of the i th mode. Since most energy in the ground motion resides in the peak ground velocity, Wang et al. (2006) simplifies (6.4) to

$$e(r) \sim \text{PGV}^2 \quad (6.5)$$

and showed that this relation is consistent with ground motion records in California. It follows from Eqs. (6.3) and (6.5) that the seismic energy density declines with the epicentral distance according to

$$e(r) \sim A/r^3. \quad (6.6)$$

Note that this relation does not include the effect of source dimension or rupture directivity that may become important for the distribution of seismic energy, and thus can only be taken as a first-order point-source approximation. The constant A in (6.6) may be evaluated by noting that the total seismic energy of an earthquake from a point source is related to the energy density by

$$E = \frac{4\pi}{3} r^3 e(r). \quad (6.7)$$

Thus, at $r = 1$ m we have

$$E \sim \frac{4\pi}{3} A. \quad (6.8)$$

Inserting this A into Eq. (6.6) we have

$$e(r) = \left(\frac{3E}{4\pi} \right) r^{-3} \quad (6.9)$$

Replacing E in Eq. (6.9) by the Båth's empirical relation $\log E = 5.24 + 1.44 M$ (Båth 1966, Eq. 11.9), where the unit of energy is converted to Joule, we obtain a relation among e , r and M (Wang 2007)

$$\log_{10} e = -3 \log_{10} r + 1.44M - 4.62, \quad (6.10)$$

where r is in km. Equation (6.10) shows that contours of constant seismic energy density e plot as straight lines on a diagram of $\log r$ versus M (Fig. 6.5). Note that this relation is entirely empirical and is based on the field data from southern California and is thus strictly valid only for southern California. This relation is expected to show significant differences from region to region. However, due to the lack of sufficient seismic data in different regions, the southern California attenuation relation has often been applied to other regions without validation.

Figure 6.5 shows that the coseismic change of groundwater level may occur at a threshold seismic energy density as low as 10^{-6} J/m^3 , many orders of magnitude lower than the threshold seismic energy density of 0.1 J/m^3 required for the initiation of undrained consolidation of saturated sand and the occurrence of liquefaction under laboratory condition (Ishihara 1996). Thus, there are large differences in the minimum energy required to initiate different earthquake-induced hydrological responses. Regardless of whether the mechanism for hydrological responses is directly connected to seismic energy density, these differences imply very different sensitivities to transient stresses. While part of this difference may be due to incomplete data and different geological conditions, some data sets, such as those for groundwater level and liquefaction, are large and the differences in the threshold seismic energy density should be robust. These differences also indicate that during earthquakes there may be more than one mechanism at work and responsible for the observed hydrological responses.

Hazirbaba and Rathje (2004) measured the threshold strain required to initiate undrained consolidation in the laboratory and showed that it is the same as that in the field. Wang and Chia (2008) showed that this threshold agrees well with the field-observed liquefaction limit but is many orders of magnitude greater than that required for the coseismic changes of groundwater level (see also Fig. 6.5). Thus, assuming that the laboratory data may be compared with field observations, other mechanisms must be evoked to explain the coseismic occurrence of groundwater level change beyond the near field.

The threshold energy for triggering hydrological responses may depend on the type of seismic wave. Wang et al. (2006) observed that liquefaction documented during underground explosions is characterized by a threshold energy two orders of magnitude greater than that for liquefaction during earthquakes, even though a similar attenuation relation exists between ground-motion energy density and distance. They interpret the observation to be consistent with the understanding that the seismic energy generated by explosion occurs mostly in compression, with much less shear energy than that in natural earthquakes of equivalent magnitude, and shearing is more effective than compression in triggering liquefaction.

6.4.5 Post-seismic Recession of Groundwater Level

The coseismic disturbances of the groundwater level in the near field are often followed by an exponential decline of the water level towards an equilibrium state

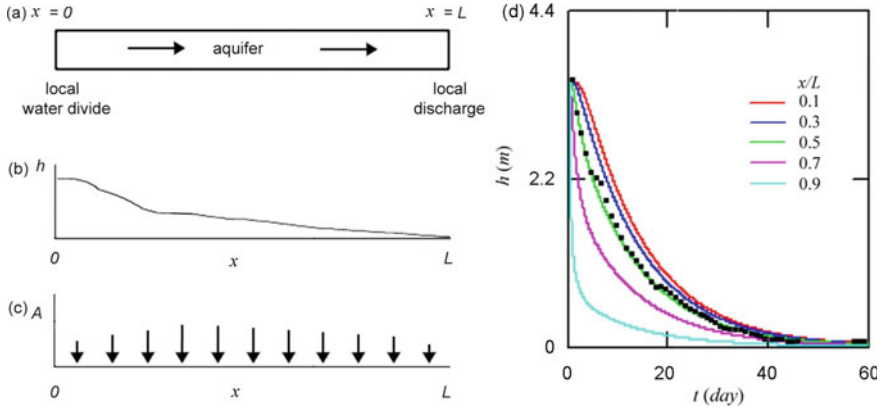


Fig. 6.14 **a** Schematic drawing of model geometry, with water divide at $x = 0$ and local discharge at $x = L$. **b** Schematic drawing of hydraulic head, with zero head gradient at the local water divide and zero head at the local discharge. **c** Schematic drawing of coseismic vertical recharge A to the aquifer. **d** Time-history of post-seismic groundwater level documented at Yuanlin I well (Wang et al. 2001). Black dots show data points. Colored curves are model predictions with several values of x/L (see text for explanation). Excellent fit between data and curve occurs for $x/L = 0.5$ (modified from Wang et al. 2004)

(Fig. 6.1a, b). This post-seismic recession of water level contains information about aquifer properties immediately after the earthquake (Wang et al. 2001), that may provide useful constraints on the proposed mechanisms. We discuss here the post-seismic recession and how to extract information about the aquifer properties from post-seismic recession data.

Using an analytical model (Fig. 6.14), Wang et al. (2004) simulated the post-seismic water level recession often observed in water wells in the near field. The model assumes a subhorizontal aquifer with length much greater than its thickness, and may thus be approximated by a one-dimensional model extending from a local groundwater divide ($x = 0$) to a local discharge or recharge area ($x = L$). The time-dependent change of the hydraulic head h is controlled by the governing flow equation (Chap. 2):

$$S_s \frac{\partial h}{\partial t} = K \frac{\partial^2 h}{\partial x^2} + A \tag{6.11}$$

where K is the horizontal hydraulic conductivity, S_s is the specific storage, and $A(x, t)$ is the rate of water released per unit volume (Fig. 6.14c) from the coseismic consolidation in the saturated zone or water released from the unsaturated zone due to the disruption of the capillary force during seismic shaking, or a coseismic sink of water due to earthquake-induced porosity or fractures. Even though this model may appear highly simplified, many studies have demonstrated that the procedure is useful for characterizing the catchment-scale response of hydrological systems to earthquakes (e.g., Roeloffs 1998; Manga 2001; Manga et al. 2003; Brodsky et al.

2003; Montgomery et al. 2003; Manga et al. 2016; Wang et al. 2017; Mohr et al 2017).

Taking the background head as the reference, the initial condition before the earthquake is $h = 0$ at $t = 0$. For boundary conditions, a no-flow boundary condition is applied at the local water divide (i.e., $\partial h/\partial x = 0$ at $x = 0$) and $h = 0$ at the local discharge ($x = L$). Since the time duration for the coseismic release of water is very much shorter than the time duration for the post-seismic recession of groundwater level, we may consider that the coseismic release of water occurs instantaneously; i.e.,

$$A(x, t) = A_o(x)\delta(t = 0). \quad (6.12)$$

The solution for this problem is (derivation is given in the Appendix)

$$h(x, t) = \frac{1}{LS_s} \sum_{n=1}^{\infty} \cos \frac{n\pi x}{2L} \exp\left[-\frac{Dn^2\pi^2 t}{4L^2}\right] \int_{-L}^L Q_o(x') \cos \frac{n\pi x'}{2L} dx' \quad (6.13)$$

where L is the length of the aquifer, $D \equiv K/S_s$ and $Q_o(x)$ is the integration of (6.12) with time and is a function of x only. The terms in (6.13) decrease rapidly with increasing n and time; thus Eq. (6.13) is dominated by the first term ($n = 1$) of the series expansion for sufficiently long times after the earthquake, i.e.,

$$h(x, t) \approx \frac{1}{LS_s} \cos \frac{\pi x}{2L} \exp\left[-\frac{D\pi^2}{4L^2} t\right] \int_{-L}^L Q_o(x') \cos \frac{\pi x'}{2L} dx'. \quad (6.14)$$

Differentiating Eq. (6.14) with respect to time we have

$$\frac{\partial \log h}{\partial t} \approx -\frac{\pi^2 D}{4L^2} \equiv -b \equiv -\frac{1}{\tau}. \quad (6.15)$$

We use the letter b here to denote the post-seismic recession of groundwater level to distinguish it from the post-seismic recession of stream discharge c in Chap. 7.

Notice that Eq. (6.15) is independent of the location of measurement; hence τ (or its inverse, $b = 1/\tau$, the recession constant), thus D/L^2 , of a responding well may be determined from the field measurement of water level versus time during the post-seismic recession. Various environmental factors such as barometric pressure, precipitation, tides, and human activities such as the withdrawal or injection of groundwater, may affect the temporal groundwater-level record, which are not considered in this formulation. Such environmental disturbances thus need to be corrected before the water level records may be used for estimating the characteristic time or the recession constant of an aquifer.

Table 6.2 lists the values for b , τ and the square of the correlation coefficient, R^2 , determined from least square fitting of the data for the postseismic recession

Table 6.2 Values for the post-seismic recession constant, b , the characteristic time, τ , and the square of the correlation coefficient, R^2 , determined by least square fitting of the data for several aquifers on the Choshui River alluvial fan, documented at several monitoring stations after the 1999 Chi-Chi earthquake (from Wang et al. 2004)

		Aquifer I	Aquifer II	Aquifer III	R^2
Chiulung	b (s^{-1}) τ (s)			4.0×10^{-7} 2.5×10^6	0.99
Hsihu	b (s^{-1}) τ (s)			3.6×10^{-7} 2.8×10^6	0.99
Huatang	b (s^{-1}) τ (s)		3.8×10^{-7} 2.6×10^6		0.99
Kuoshen	b (s^{-1}) τ (s)		9.7×10^{-7} 1.0×10^6		0.98
Yuanlin	b (s^{-1}) τ (s)	8.8×10^{-7} 1.1×10^6	9.3×10^{-7} 1.1×10^6		1.00
Chukou	b (s^{-1}) τ (s)	1.7×10^{-6} 5.9×10^5	2.0×10^{-6} 5.0×10^5		0.98
Liyu	b (s^{-1}) τ (s)	4.4×10^{-7} 2.2×10^6	6.0×10^{-7} 1.7×10^6		0.99
Hsichou	b (s^{-1}) τ (s)		1.0×10^{-5} 1.0×10^5		0.92
Chushan	b (s^{-1}) τ (s)	1.4×10^{-5} 0.7×10^5			0.99
Hsinguang	b (s^{-1}) τ (s)	1.0×10^{-5} 1.0×10^5			0.99
Pingting	b (s^{-1}) τ (s)	1.4×10^{-5} 0.7×10^5			0.98

documented at several monitoring stations on the Choshui River alluvial fan after the 1999 Chi-Chi earthquake. It shows that the characteristic time for the postseismic dissipation of the hydraulic head is about 3×10^6 s for most aquifers. But the last three stations (Chushan, Hsinguang and Pingting) show characteristic times an order-of-magnitude shorter, i.e., $\sim 10^5$ s. These wells are all located close to the ruptured Chelungpu fault and the smaller characteristic times may reflect a relatively high post-seismic hydraulic diffusivity (D), a relatively small post-seismic characteristic length (L), or both, at these stations.

Given the characteristic time τ in Table 6.2 determined from the recession analysis and a specific storage of $10^{-4} m^{-1}$ from well tests (Tyan et al. 1996), we may compare the model prediction with the post-seismic time history of the groundwater level change. As an example, we compare in Fig. 6.14d the post-seismic time history of the groundwater level change at the well Yuanlin I against the model predictions (Eq. 6.14) for different values of x/L . A constant value of $Q_o = 3.4 \times 10^{-4} m^3/m^3$ was used to match the amplitude of h at $t = 0$. The curve for $x/L = 0.5$ shows an excellent fit to the field data (Fig. 6.14d), suggesting that the Yuanlin station may be

situated roughly at the mid-point of an aquifer between a local groundwater divide and the local discharge location.

The transmissivity (T) and the storativity (S) of the aquifers determined from well tests on the Choshui River fans (Lee and Wu 1996; Kester and Ouyang 1996; Tyan et al. 1996), yielded an average diffusivity $D = T/S \sim 10 \text{ m}^2/\text{s}$. Combining this D with an average value of $\tau \sim 10^6 \text{ s}$ (Table 6.2) and Eq. (6.15), we obtain $L \sim 5000 \text{ m}$ for the confined aquifers. It is interesting to note that this characteristic length for the confined aquifers is considerably shorter than that shown on the geologic cross-sections reconstructed from the hydrological well logs (Water Resource Bureau 1999). This difference might be expected because the actual geologic structure of aquifers in the alluvial fan may be more complex than that as shown on an idealized geologic cross-section.

A simple picture of the plumbing system in the Choshui River fan immediately after the Chi-Chi earthquake emerged from the analysis for post-seismic data. The stepwise rise of groundwater level, as documented by most wells in the unconsolidated sediments of the Choshui River fan, was dissipated by groundwater flow through subhorizontal aquifers with a typical length of 5 km. Aquifers with stepwise decreases of groundwater level, as documented by wells drilled at relatively high elevation near the ruptured fault, were mostly recharged locally by surface runoff, but may also discharge to aquifers at lower hydraulic potential after the earthquake. The aquifers that facilitated this discharge also have a characteristic length of $\sim 5 \text{ km}$, similar to that of the aquifers that facilitated the dissipation of the stepwise rise in the alluvial fan, hinting that similar aquifers in the Choshui River Alluvial fan may be involved in the post-seismic recovery to equilibrium.

6.5 Pore Pressure and Permeability of Continental Faults

Permeability in fault zones controls fluid flow and hence the in situ effective stress and seismic hazard, and is thus a time-honored topic of research. Earlier discussions were mostly based on inferences from geological and geophysical structures and the material properties of fault zones (e.g., Aydin and Johnson 1978; Wang 1984; Wang et al. 1978, 1986; Chester and Logan 1986; Scholz 1990; Sibson 1996; Caine et al. 1996; Schulz and Evans 2000; Bense et al. 2013). These studies converged to a basic model that fault zones consist of a narrow low-permeability, clay-rich core surrounded by a broad zone of highly fractured and damaged rocks (the ‘damage zone’). This model suggests that fault zones are hydrologically anisotropic and may serve as an effective hydraulic conduit for flow along the fault but is an effective barrier for flow across the fault (e.g., Scibek et al. 2016). More recently, instrumental measurements have provided quantitative in situ information about the hydraulic properties of fault zones (e.g., Zoback et al. 2010; Xue et al. 2013, 2016; Brixel et al. 2020a, b). Here we focus on the latter developments.

Drilling into active fault zones has been undertaken in several settings, with a central objective to determine the fault zone properties and pore pressure; these include the Nojima Fault Zone Probe in Japan (Kitagawa et al. 1999), the Chelungpu Fault Drilling Project in Taiwan (Wu et al. 2007), the San Andreas fault near Parkfield in central California (SAFOD; Zoback et al. 2010), and the Wenchuan Fault Scientific Drilling Project in China (Li et al. 2013).

The SAFOD project is probably the best documented and reported in the English language (e.g., Zoback et al. 2010). Drilling was initially vertical on the SW side of the San Andreas fault to a depth of 1.5 km, and then steered 60° from vertical to intersect the active fault zone. After passing through a variety of wall rocks with different lithology, drilling passed through a damage zone ~200 m wide and encountered three actively slipping, clay-rich gouge zones, each 2–3 m wide. From the pore-pressure measurements, Zoback et al. (2010) concluded that the active fault core showed no evidence of high pore pressure. Wang (2011) showed, however, that the very low permeability of the fault core material ($<10^{-20}$ m²; Morrow et al. 2014) implies that the amount of time available during drilling may be much too short for pore pressure to reach equilibrium and thus the measured pore pressure may not represent the equilibrium values.

While it may be difficult to show that the measured pore pressure deep in active faults is at equilibrium, several measurements of fault zone permeability have been made based on the analysis of the tidal response of pore pressure on faults. For example, Xue et al (2013) analyzed the tidal response of groundwater deep in the active fault that ruptured during the 2008 Wenshan earthquake in China. Xue et al. (2016) also monitored the tidal response of pore pressure in the vicinity of the San Andreas fault. Here we discuss the former study as an example.

After the 2008 Mw7.9 Wenchuan earthquake (Fig. 6.15a) in Sichuan, China, a drilling project drilled a series of boreholes that penetrated the main rupture zone at a depth of ~1.2 km (Li et al. 2013). Figure 6.15b shows that the borehole intersects a major slip zone at depths >600 m. Pore pressure in the borehole was monitored from January 2010 to August 2011 with a sampling interval of 2 min and a resolution of 6 mm (Fig. 6.16a). Xue et al. (2013) showed that the tidal response of groundwater in the penetrated fault zone had a phase shift from -20 to -30° and an amplitude response from 5.5×10^{-7} to 6.3×10^{-7} m⁻¹. The authors interpreted the negative phase lag as suggesting that the fault zone aquifer was confined and inverted the phase and amplitude responses with the analytical solution of Hsieh et al. (1987) for a confined, isotropic, homogeneous and laterally extensive aquifer. They obtained an average transmissivity of 5×10^{-6} m²s⁻¹ (Fig. 6.16b) and an average storage coefficient of $S = 2.2 \times 10^{-4}$ (Fig. 6.16c). The transmissivity may be converted to an average permeability of $k = 1.4 \times 10^{-15}$ m² by using the identity $k = \mu T / \rho g d$, where $d = 400$ m is the thickness of the fault zone aquifer. The use of the entire open interval of the borehole for the fault zone may have led to an estimated permeability that represents a lower bound on the fault zone permeability (Xue et al. 2013).

The inverted permeability for the ruptured fault measured during the Wenchuan drilling project shows a continuous decline during most of the study period and discontinuous increases during far-field earthquakes (Fig. 6.16b). The continuous

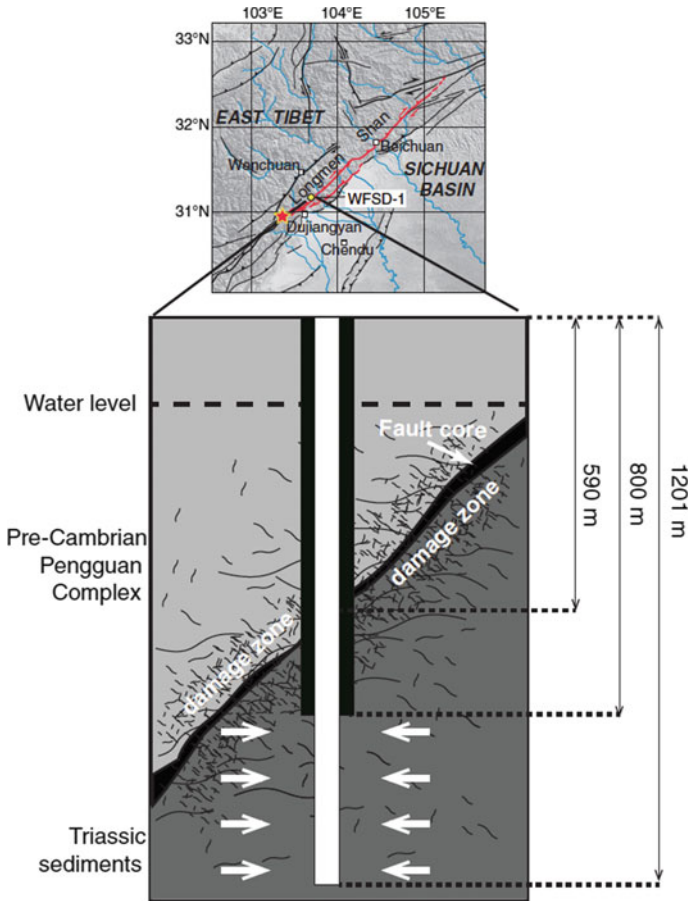


Fig. 6.15 a Location map of the studied WFS-1 site. Red lines in the inset indicate the main rupture zone; the red star is the epicenter of the Wenchuan earthquake. In the sketch b the black line is the fault core, which is surrounded by the damage zone. The borehole is 1201 m deep, and 800–1201 m is the open interval where water can flow into the hole from the formation (white arrows). The fault that was most likely active during the Wenchuan earthquake is the major lithological boundary between the Precambrian complex and the Triassic sediments at 590 m (from Xue et al. 2013)

decline of permeability was interpreted to represent post-seismic healing of the fractures generated by the Wenchuan earthquake (Xue et al. 2013) that was interrupted intermittently by seismic waves from remote earthquakes.

The permeability of the Chelungpu fault that ruptured in the 1999 Chi-Chi earthquake was also determined in a drilling project (10^{-18} – 10^{-16} m²; Doan et al. 2006). The experiment was designed to determine the permeability along the ruptured fault, with cross-hole pumping experiments between two boreholes, separated by ~40 m, drilled across the ruptured fault (Fig. 6.17). Because the flow during the pump tests

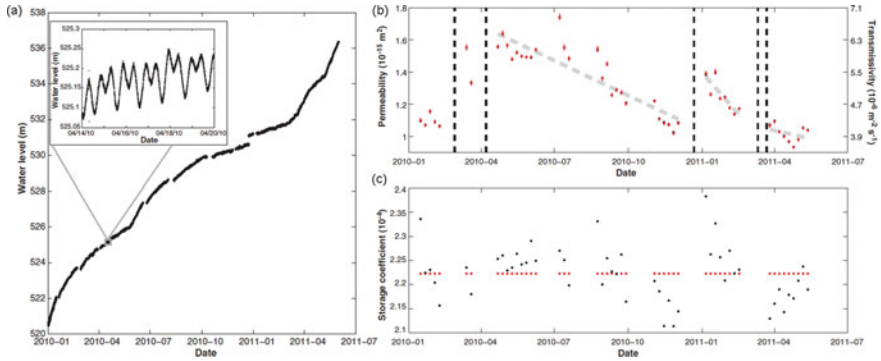
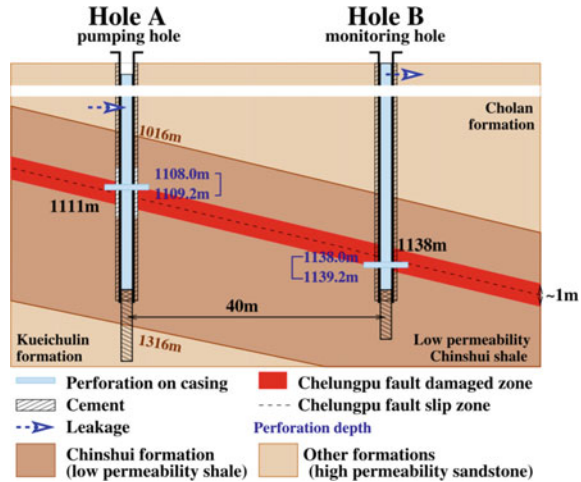


Fig. 6.16 **a** Water levels from the borehole recorded from 1 January 2010 to 6 August 2011. The oscillations in the inset are generated by Earth tides. The precision of the water level measurement is 6 mm. The measured ‘water level’ is the height of water above the pressure transducer. **b** Permeability and transmissivity and **c** storage coefficient. Values were inverted from the phase and amplitude of each 29.6-day segment based on the analytical model of Hsieh et al. (1987). The black dots denote unconstrained inversion; the red dots are the results of inversion with the storage coefficient fixed to a single value. Because the two separate inversions have identical results for transmissivity, the red dots cover the black dots in (b). The vertical dashed lines show the time of the selected teleseismic events, which correspond to sudden increases in permeability. The best-fit linear trends between each set of permeability increases are shown as light gray dashed lines (from Xue et al. 2013)

would preferentially move along the high permeability damage zone along the fault, rather than along the low permeability fault core, the permeability so measured would represent that of the damage zone. This may explain the large difference between the permeability of the recovered fault cores from the SAFOD project (Morrow et al. 2014) and the in situ permeabilities from the two drilling projects. The difference between the permeabilities determined in the two in situ experiments is relatively small, and may be due to the different methods used in the two field experiments, the different fault zone lithologies in the two field sites (a damaged zone in a clay-rich Quaternary shale of the Chelungpu drilling site versus the damaged zone in a consolidated Triassic sedimentary sequence in the Wenchuan drilling site), and the different spatial scales involved in the two measurements (e.g., Ingebritsen et al. 2006; Kinoshita and Saffer 2018).

Detailed measurement of fault permeability based on boreholes drilled into granitic rocks from an underground rock laboratory in the Swiss Alps (e.g., Brixel et al. 2020a, b) showed that the permeability of fault zones in these rocks may fall sharply from 10^{-13} to 10^{-21} m² within 1–5 m from the fault. These studies suggest that fault permeability may be strongly anisotropic and the flow patterns near faults may be complex. At the same time, we should note that the thicknesses of these faults are orders of magnitudes smaller than those of the major faults, such as those in the San Andreas fault zone in central California and the Wenchuan fault zone in China. As a result, the physical properties and architecture of the faults may also be fundamentally different.

Fig. 6.17 Cross-hole experiment along the ruptured Chelungpu fault (red) in the 1999 Chi-Chi earthquake (from Doan et al. 2006)



6.6 Pore Pressure and Permeability on the Ocean Floor

Research into pore pressure within the oceanic crust began in the late last century (e.g., Davis et al. 2001, 2006, 2009; Vinas 2013; Akmal 2013; Hornbach and Manga 2014; Kinoshita et al. 2018), largely as a part of the Ocean Drilling Program (ODP). Here we review two representative studies in different tectonic settings, first in a subduction zone (Kinoshita et al. 2018), and next near an oceanic spreading ridge (Davis et al. 2001).

6.6.1 Pore Pressure and Permeability in an Accretionary Prism

The example of pore pressure and permeability measurements in accretionary prisms comes from the Nankai Trough (Fig. 6.18; Kinoshita et al. 2018), offshore of SW Honshu, Japan. A splay fault was penetrated by the C0010 borehole to a depth of 407 m beneath the seafloor; pore pressure was monitored for 5.3 years, and showed a sequence of small changes during earthquakes with implications for the poroelastic properties of the fault.

Kinoshita et al. (2018) measured pore pressure in the fault zone and the oceanic tidal loading on the seafloor. The two sets of measurements show no phase lag (Fig. 6.19a) and are linearly correlated with a mean loading efficiency (slope of pore pressure versus load, Eq. 3.81) of ~ 0.74 (Fig. 6.19b). The lack of a phase delay between the pore pressure response and the reference loading implies a high hydraulic diffusivity of the aquifer connecting the formation to the borehole and allows the authors to set a lower bound of $6.4 \times 10^{-13} \text{ m}^2$ on the fault zone permeability that

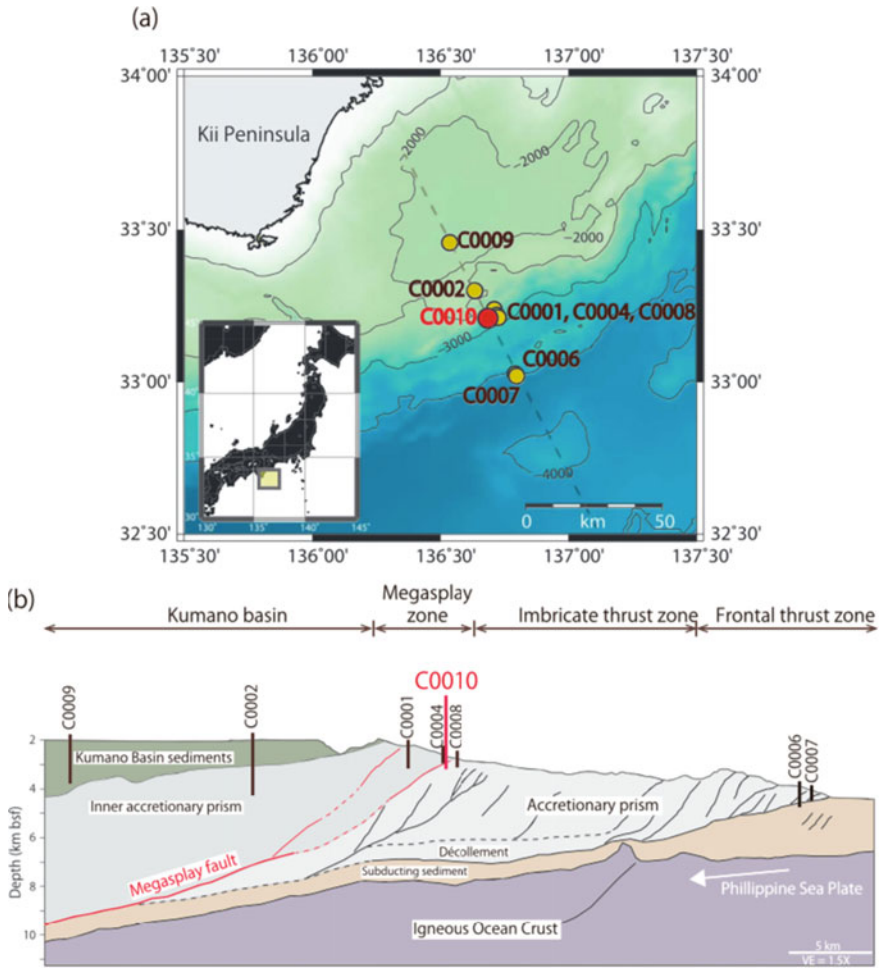


Fig. 6.18 Location of drillsites in the Nankai Trough Seismogenic Zone Experiment (Kinoshita et al. 2018). **a** Map of the drilling sites (circles). The borehole installed at Site C0010 is shown by the red circle, which penetrates a shallow fault at 407 m below seafloor. **b** Schematic image of the cross section along the dashed line in (a); red vertical line shows the location of the C0010 borehole (from Kinoshita et al. 2018)

is broadly consistent with reported fault zone permeabilities from other subduction zones (e.g., Fisher and Zwart 1997; Screaton et al. 2000; Saffer 2015). The measured loading efficiency implies a formation compressibility ~ 10 times smaller than that measured on the retrieved core sample. Kinoshita et al. (2018) interpreted this lower loading efficiency to imply a small amount of dissolved gas in the interstitial fluids.

Figure 6.19a shows that the measured pressure was dominated by oceanic tidal signals. The latter were removed by using the model of loading efficiency, i.e., $P_{\text{corr}} = P_{\text{form}} - \gamma P_{\text{ref}}$, where γ is the loading efficiency (Sect. 3.2.5), and the subscripts for

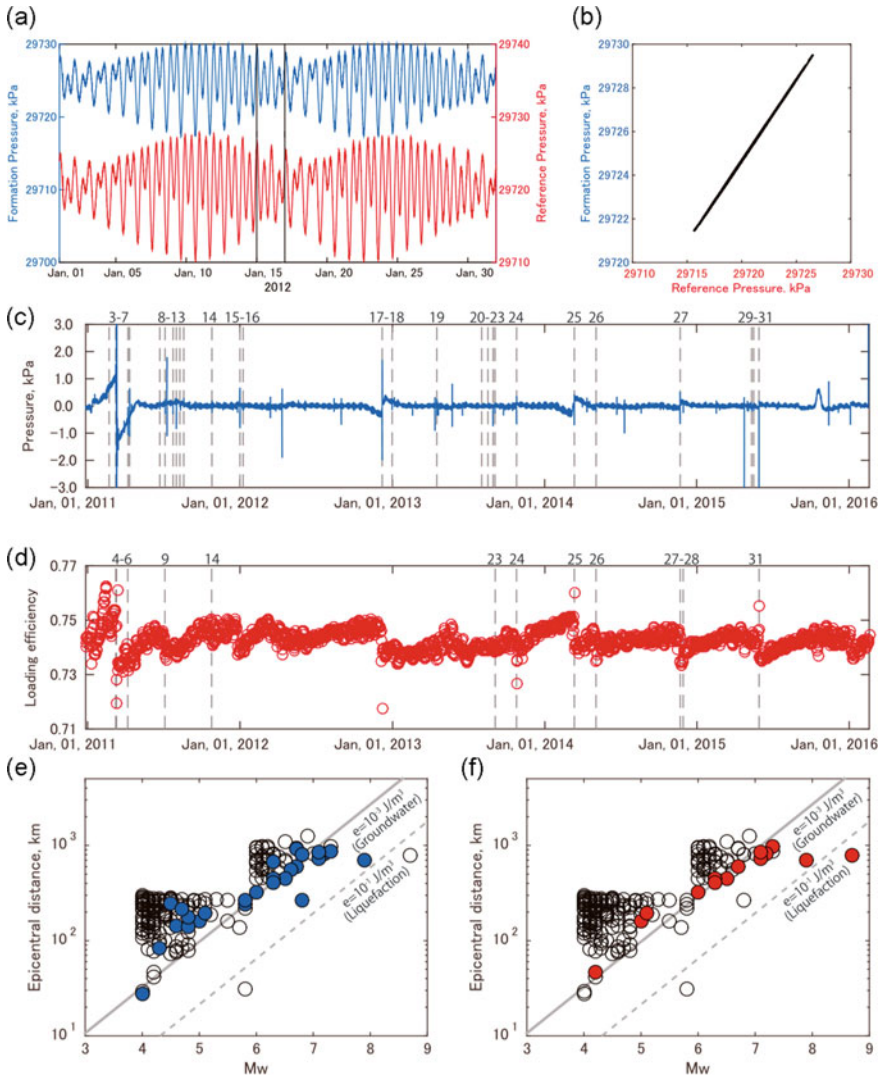


Fig. 6.19 **a** and **b** Time series of pore pressure and loading efficiency measured in the fault zone at Site C0010. Vertical lines mark the time of earthquakes that produced detectable changes of pore pressure and loading efficiency. **c** and **d** Coseismic changes of pore pressure and loading efficiency at Site C0010 plotted on diagrams of earthquake magnitude versus the epicentral distance, together with the seismic energy density relation determined on land (Wang 2007). The blue and red circles show events that produced coseismic changes in pore pressure and loading efficiency, respectively. The open circles show events that did not produce detectable coseismic changes. The gray solid and dashed lines represent the contours for constant seismic energy densities of 10^{-3} and 10^{-1} J/m^3 , respectively (modified from Kinoshita et al. 2018)

pressure (P) refer, respectively to the corrected pressure, the formation pressure and the reference pressure on the seafloor. The time series of the corrected pore pressure (Fig. 6.19c) and of the loading efficiency (Fig. 6.19d) are both affected by numerous coseismic changes during the studied period, marked by the vertical lines in the figure. While most of the changes show coseismic increases of pore pressure and decreases of the loading efficiency, the largest of these changes during the March 2011 Tohoku earthquake showed coseismic decreases of both pore pressure and loading efficiency. Also noticeable is that most postseismic recoveries of the loading efficiency have longer recovery time than the post-seismic recovery of pore pressure, suggesting different recovery mechanisms. Kinoshita et al. (2018) suggested that the coseismic decreases of loading efficiency were due to the exsolution of the dissolved gas in the pore fluid in response to dynamic shaking. Because the compressibility of free gas is much larger than that of dissolved gas, this phenomenon would produce coseismic decreases in loading efficiency. At the same time, the redissolution of this gas back into the pore water takes time, resulting in protracted recovery of the loading efficiency. The authors also supported the suggested mechanism by the volume of gas in the recovered pore fluid.

On a diagram of earthquake magnitude versus epicentral distance, the coseismic changes of pore pressure (Fig. 6.19e) and loading efficiency (Fig. 6.19f) follow a systematic linear trend similar to that defined by land-based observations of hydrological response to earthquakes (Wang 2007) and are bounded by a seismic energy density of $\sim 10^{-3} \text{ J/m}^3$. This result suggests that the coseismic responses of pore pressure beneath the seafloor may involve similar mechanisms as those on land.

Pore pressure in accretionary prisms also change during slow seismic events in which slip occurs over weeks to months. Figure 6.20 shows the occurrences of several pore pressure transients in the accretionary prism of the Nankai Trough over a period of six years from 2011 to 2016 in two boreholes (C0100 and C0002) separated by 11 km in the dip direction (Araki et al. 2017). Increases or decreases of pore pressure and occurred during slow seismic events, but the largest two changes occurred right after the Tohoku (March, 2011) and the 2016 Kumamoto (April, 2016) earthquakes, respectively, and showed decreases of pore pressure in both boreholes.

6.6.2 Pore Pressure Changes Near an Ocean Ridge

Davis et al. (2001) investigated pore pressure near the actively spreading Juan de Fuca oceanic ridge (Fig. 6.21a) during an earthquake swarm that began on June 8, 1999. The earthquake swarm lasted more than two months (Fig. 6.21e) and caused pore-pressure transients (Fig. 6.21d) in several boreholes of the Ocean Drilling Program on the eastern flank of the ridge, 25–100 km from the epicenter (Fig. 6.21b). Also recorded are the pore-pressure responses to the tidal loading of the seafloor (Fig. 6.21c). The transient responses to the first earthquake are characterized by a

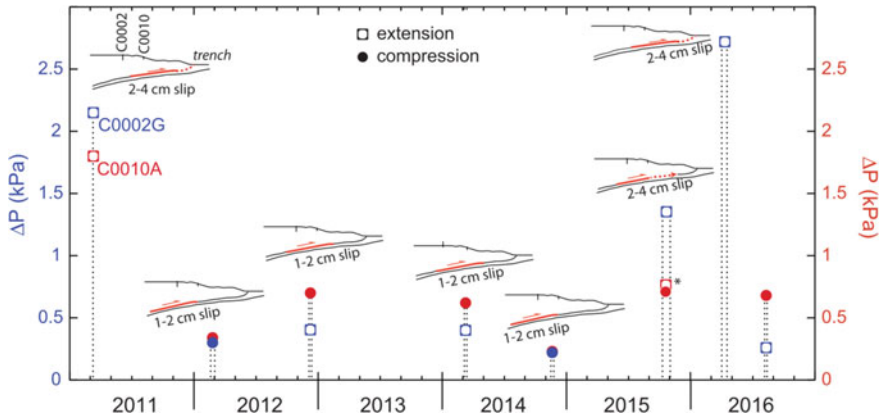


Fig. 6.20 Summary of pore pressure changes measured in boreholes C0010 (red) and C0002 (blue) (see Fig. 6.17 for locations). Solid circles show pore pressure increases, and open squares show pore pressure decreases. The red lines and arrows in the schematic cross-sections show the location, the amount and the direction of slip that are required to interpret the pore pressure measured in both boreholes assuming a dislocation model (modified from Araki et al. 2017)

rapid coseismic rise in pressure, followed by a continuing slower rise to a peak, and then a much slower decay (Fig. 6.21d), similar to the sustained groundwater responses on land described in Sect. 6.4. As noted by Davis et al. (2001), the pore-pressure transients occurred only during the first earthquake, but not during the latter earthquakes (vertical lines in Fig. 6.21e), even though several of the latter shocks were of greater magnitude than the first one. Davis et al. (2001) accounted for the differences among the pore-pressure responses by suggesting that the pore-pressure change was associated with a much larger tectonic event at the spreading center, most of which occurred aseismically; thus the earthquake was merely the seismic expression of a much larger tectonic event, not the cause of the pore-pressure transients.

Here we offer an alternative interpretation of the non-responsiveness of pore pressure to the latter earthquakes. According to the enhanced permeability model, the first earthquake opened some permeable pathways between the ODP site and local high-pressure sources, which caused the observed increase in pore pressure at the borehole. In order for the second earthquake to cause a second transient increase in pore pressure, sufficient time must pass between the two earthquakes to allow the fluid pathways to seal and the high-pressure sources to re-pressurize. According to this alternative hypothesis, there may simply be insufficient time between the first and the subsequent earthquakes during the two-month span to allow the permeable channels to re-seal and the local sources to re-pressurize. Hence, after the first pore pressure transient induced by the first earthquake, no further pore-pressure transients were possible during the remaining time span of the swarm.

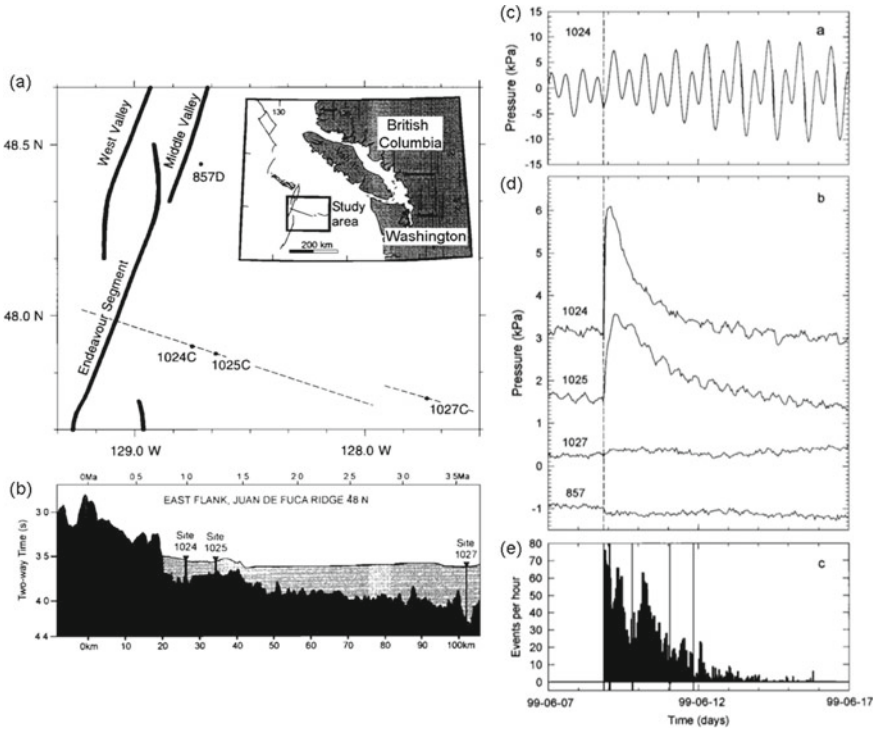


Fig. 6.21 **a** Location map of study area near the Juan de Fuca spreading ridge (thick lines). **b** Cross section of the primary lithology (basement: black; sediment cover: grey) at each of well site. **c** Raw formation pressure record from ODP Site 1024C at the time of the June 1999 earthquake swarm along the Endeavour ridge segment, showing strong tidal signals in response to the loading of the ocean tides. **d** Pore-pressure records from this site and several other ODP Sites after the removal of the responses to tidal, barometric, and oceanic loading. **e** Histogram of the number of events detected; vertical lines show earthquakes recorded at onshore seismic stations (from Davis et al. 2001)

6.7 Concluding Remarks

It is reassuring that some earlier findings on the groundwater response to earthquakes have largely stood the test of time and more observations. The coseismic response of water level in wells in the near field is dominated by step-like changes, while in the intermediate and far fields sustained changes and groundwater oscillations dominate. Enhanced permeability remains a plausible explanation for the sustained changes of groundwater level during earthquakes. Undrained consolidation remains the most cited explanation for the step-like coseismic changes, but a new mechanism has emerged that suggests that earthquakes may release pore water from unsaturated soils to cause step-like increases of water level in the near field. Laboratory experiments have verified that both mechanisms may explain the step-like coseismic changes. The

minimum seismic energy density for coseismic changes of groundwater level has been extended from 10^{-4}J/m^3 down to 10^{-6}J/m^3 .

New advances in the last decade in understanding the groundwater response to earthquakes were made mostly by using the groundwater response to tidal and barometric forcing to monitor changes in hydrogeological properties. These studies have demonstrated that the hydraulic properties of groundwater systems are dynamic and may change with time in response to disturbances by natural and induced earthquakes. These methods have been applied broadly, including to estimate the permeability of several drilled active fault zones, to identify leakage from deep aquifers used for the storage of hazardous wastewater, and to reveal the potential importance of soil water and capillary tension in the unsaturated zone. On the other hand, it should be noted that the tidal and barometric responses of water level in wells represent local responses and, when applied in a regional context, they need to be considered with hydrogeological investigations and information from deep drilling.

Appendix: Derivation of Eq. 6.13

The governing differential equation is

$$S_s \frac{\partial h}{\partial t} = K \frac{\partial^2 h}{\partial x^2} + A. \quad (6.11)$$

Taking the background head as the reference, the initial condition before the earthquake is $h = 0$ at $t = 0$. A no-flow boundary condition is applied at the local water divide (i.e., $\partial h/\partial x = 0$ at $x = 0$) and $h = 0$ at the local discharge ($x = L$). If A is a function of x only, the solution is given by (Carslaw and Jaeger, 1959, p. 132):

$$h(x, t) = \frac{4L}{\pi^2 K} \sum_{n=1}^{\infty} \frac{1}{n^2} \left[1 - \exp\left(-\frac{Dn^2\pi^2 t}{4L^2}\right) \right] \times \cos \frac{n\pi x}{2L} \int_{-L}^L A(x) \cos \frac{n\pi x'}{2L} dx' \quad (A6.1)$$

For the present problem, however, A is a function of both x and t . In this case, we apply the Duhamel's principle (Carslaw and Jaeger 1959, p. 32) to (A6.1) to obtain

$$h(x, t) = \frac{1}{LS_s} \sum_{n=1}^{\infty} \cos \frac{n\pi x}{2L} \times \int_{-L}^L \int_0^t \exp\left(-\frac{Dn^2\pi^2(t-\lambda)}{4L^2}\right) A(x, \lambda) \cos \frac{n\pi x'}{2L} d\lambda dx' \quad (A6.2)$$

Since the coseismic release of water takes much less time than that for the post-seismic recession of groundwater level, we assume that the coseismic release of water occurs instantaneously; i.e., $A(x, t) = A_o(x)\delta(t = 0)$, where $\delta(t = 0)$ equals to 1 when $t = 0$ and equals to 0 when $t > 0$. Eq. A6.2 then reduces to Eq. 6.13.

References

- Akita F, Matsumoto N (2004) Hydrological responses induced by the Tokachi-oki earthquake in 2003 at hot spring well in Hokkaido Japan. *Geophys Res Lett* 31:L16603. <https://doi.org/10.1029/2004GL020433>
- Akmal, PNE (2013) Determination of the Permeability of the south chamorro seamount in mariana forearc crust using pressure response to tidal loading method. Open Access Theses 449. https://scholarlyrepository.miami.edu/oa_theses/449
- Araki E, Saffer DM, Kopf AJ et al (2017) Recurring and triggered slow-slip events near the trench at the Nankai Trough subduction megathrust. *Science* 356:1157–1160
- Aydin A, Johnson AM (1978) Development of faults as zones of deformation bands and as slip surfaces in sandstone. *Pure Appl Geophys* 116:931–942
- Barbour AJ, Norbeck JH, Rubinstein JL (2017) The effects of varying injection rates in Osage County, Oklahoma, on the 2016 Mw 5.8 Pawnee earthquake. *Seismol Res Lett* 88:1040–1053. <https://doi.org/10.1785/0220170003>
- Barbour AJ, Xue L, Roeloffs E et al (2019) Leakage and increasing fluid pressure detected in Oklahoma's wastewater disposal reservoir. *J Geophys Res Solid Earth* 124:2896–2919. <https://doi.org/10.1029/2019JB017327>
- Båth M (1966) Earthquake energy and magnitude. *Phys Chem Earth* 7:115–165
- Bense VF, Gleeson T, Loveless SE et al (2013) Fault zone hydrogeology. *Earth Sci Rev* 127:171–192
- Breen S, Zhang Z, Wang CY (2020) Shaking water out of sands: an experimental study. *Water Resour Res* 56: e2020WR028153
- Brixel B, Klepikova M, Jalali MR et al (2020) Tracking fluid flow in shallow crustal fault zones: 1. Insights from single-hole permeability estimates. *J Geophys Res Solid Earth* 125: e2019JB018200. <https://doi.org/10.1029/2019JB018200>
- Brixel B, Klepikova M, Lei Q et al (2020) Tracking fluid flow in shallow crustal fault zones: 2. Insights from cross-hole forced flow experiments in damage zones. *J Geophys Res Solid Earth* 125: e2019JB019108. <https://doi.org/10.1029/2019jb019108>
- Brodsky EE, Roeloffs E, Woodcock D et al (2003) A mechanism for sustained groundwater pressure changes induced by distant earthquakes. *J Geophys Res* 108:2390. <https://doi.org/10.1029/2002JB002321>
- Caine JS, Evans JP, Forster CB (1996) Fault zone architecture and permeability structure. *Geology* 24:1025–1028
- Carlsaw HS, Jaeger JC (1959) *Conduction of Heat in Solids*, 2nd edn. Clarendon Press, Oxford, UK
- Chester FM, Logan JM (1986) Implications for mechanical properties of brittle faults from observations of the Punchbowl fault zone, California. *Pure Appl Geophys* 124:80–106
- Chia YP, Wang YS, Wu HP et al (2001) Changes of groundwater level due to the 1999 Chi-Chi earthquake in the Choshui River fan in Taiwan. *Bull Seism Soc Am* 91:1062–1068
- Cua GB (2004) Creating the virtual seismologist: developments in ground motion characterization and seismic early warning. Ph.D. Dissertation, Caltech@ @
- Davis EE, Wang K, Thomson RE et al (2001) An episode of seafloor spreading and associated plate deformation inferred from crustal fluid pressure transients. *J Geophys Res* 106:21953–21963

- Davis EE, Becker K, Wang K et al (2006) A discrete episode of seismic and aseismic deformation of the Nankai trough subduction zone accretionary prism and incoming Philippine Sea plate. *Earth Planet Sci Lett* 242:73–84
- Davis EE, Becker K, Wang K et al (2009) Co-seismic and post-seismic pore-fluid pressure changes in the Philippine Sea plate and Nankai décollement in response to a seismogenic strain event off Kii Peninsula Japan. *Earth Planets Space* 61(6):649–657. <https://doi.org/10.1186/BF03353174>
- Doan ML, Brodsky EE, Kano Y et al (2006) In situ measurement of the hydraulic diffusivity of the active Chelungpu Fault Taiwan. *Geophys Res Lett* 33(16):L16316. <https://doi.org/10.1029/2006GL026889>
- Dobry R, Ladd RS, Yokel FY et al (1982) Prediction of pore water pressure buildup and liquefaction of sands during earthquakes by the cyclic strain method. National Bureau of Standards Building Science Series 138: National Bureau of Standards and Technology, Gaithersburg Md, p 150
- Elkhoury JE, Brodsky EE, Agnew DC (2006) Seismic waves increase permeability. *Nature* 411:1135–1138
- Elkhoury JE, Niemeijer A, Brodsky EE et al (2011) Laboratory observations of permeability enhancement by fluid pressure oscillation of in-situ fractured rock. *J Geophys Res* 116:B02311. <https://doi.org/10.1029/2010JB007759>
- Fisher AT, Zwart G (1997) Packer experiments along the décollement of the Barbados accretionary complex: measurements of in situ permeability. *Proc Ocean Drill Program Sci Res* 156:199–218
- Faoro I, Elsworth D, Marone C (2012) Permeability evolution during dynamic stressing of dual permeability media. *J Geophys Res Solid Earth* 117(B1):B01310. <https://doi.org/10.1029/2001JB008635>
- Ge S, Stover SC (2000) Hydrodynamic response to strike- and dip-slip faulting in a half space. *J Geophys Res* 105:25513–25524. <https://doi.org/10.1029/2000JB900233>
- Hazirbaba K, Rathje EM (2004) A comparison between in situ and laboratory measurements of pore water pressure generation. In: 13th World conference on earthquake engineering, paper 1220, Vancouver
- Hornbach MJ, Manga M (2014) The ability of rock physics models to infer marine in situ pore pressure. *Geochem Geophys Geosyst* 15(12):4769–4780
- Hosono T, Yamada C, Shibata T et al (2019) Coseismic groundwater drawdown along crustal ruptures during the 2016 M_w 7.0 Kumamoto earthquake. *Water Resour Res* 55:5891–5903. <https://doi.org/10.1029/2019WR024871>
- Hsieh P, Bredehoeft J, Farr J (1987) Determination of aquifer permeability from earthtide analysis. *Water Resour Res* 23:1824–1832
- Hsu CC, Vucetic M (2004) Volumetric threshold shear strain for cyclic settlement. *J Geotech Geoenviron Eng* 130:58–70
- Institute of Geophysics–CAS (China Earthquake Administration) (1976) *China Earthquake Catalog*, 500 p, Washington, DC: Center for Chinese Research Materials (in Chinese)
- Igarashi G, Wakita H (1991) Tidal responses and earthquake-related changes in the water level of deep wells. *J Geophys Res* 96:4269–4278
- Ishihara K (1996) *Soil behavior in earthquake geotechnics*. Clarendon Press, Oxford, p 350
- Itaba S, Koizumi N (2007) Earthquake-related changes in groundwater levels at the Dogo hot springs, Japan. *Pure Appl Geophys* 164:2397–2410
- Jonsson S, Segall P, Pedersen R et al (2003) Postearthquake ground movements correlated to pore-pressure transients. *Nature* 424:179–183
- Ho CS (1988) *An introduction to the geology of Taiwan*, Central Geological Survey, 192 p
- Ingebritsen SE, Sanford WE, Neuzil CE (2006) *Groundwater in geologic processes*, 2nd edn. Cambridge Univ Press, New York
- Kester LC, Ouyang S (1996) A first investigation of the groundwater and its equilibrium in the Yunlin district. In: Conference on groundwater and hydrology of the choshui river alluvial fan, Taiwan, Water Resources Bureau, 181–206 (in Chinese)
- King CY, Azuma S, Igarashi G et al (1999) Earthquake-related water-level changes at 16 closely clustered wells in Tono, central Japan. *J Geophys Res* 104:13073–13082

- Kinoshita C, Saffer D, Kopf A et al (2018) Changes in physical properties of the Nankai trough megasplay fault induced by earthquakes, detected by continuous pressure monitoring. *J Geophys Res Solid Earth* 123:1072–1088. <https://doi.org/10.1002/2017jb014924>
- Kinoshita C, Saffer D (2018) In situ permeability and scale dependence of an active accretionary prism determined from cross-borehole experiments. *Geophys Res Lett* 45. <https://doi.org/10.1029/2018gl078304>
- Kitagawa Y, Koizumi N, Notsu K et al (1999) Water injection experiment and discharge at the Nojima fault in Awaji Island, Japan. *Geophys Res Lett* 26:3173–3176
- Kitagawa Y, Koizumi N, Takahashi M et al (2006) Changes in water levels or pressures associated with the 2004 earthquake off the west coast of northern Sumatra (M9.0). *Earth Planets Space* 58:173–179
- Koizumi N, Lai WC, Kitagawa Y et al (2004) Comment on “Coseismic hydrological changes associated with dislocation of the September 21, 1999 Chichi earthquake, Taiwan” by Min Lee et al. *Geophys Res Lett* 31: L13603. <https://doi.org/10.1029/2004gl019897>
- Lay T, Wallace TC (1995) *Modern global seismology*. Academic Press, San Diego
- Lee CS, Wu CL (1996) Pumping tests of the Choshuichi alluvial fan. In: Conference on groundwater and hydrology of the choshui river alluvial fan, Taiwan, Water Resources Bureau, 165–179. (in Chinese)
- Li H, Wang H, Xu Z et al (2013) Characteristics of the fault-related rocks, fault zones and the principal slip zone in the wenchuan earthquake fault scientific drilling project Hole-1 (WFSD-1). *Tectonophysics* 584:23–42
- Liao X Wang CY (2018) Seasonal permeability change of the shallow crust inferred from deep well monitoring. *Geophys Res Lett* 45(11):11–130, 136. <https://doi.org/10.1029/2018gl080161>
- Liao X, Wang CY, Liu CP (2015) Disruption of groundwater systems by earthquakes. *Geophys Res Lett* 42(22):9758–9763
- Liu W, Manga M (2009) Changes in permeability caused by dynamic stresses in fractured sandstone. *Geophys Res Lett* 36:L20307. <https://doi.org/10.1029/2009GL039852>
- Luong MP (1980) Stress-strain aspects of cohesionless soils under cyclic and transient loading. In: Pande GN, Zienkiewicz OC (eds). *Proc. Intern. Symp. Soils under Cyclic and Transient Loading*, A.A. Balkema, Rotterdam, Netherlands, pp 315–324
- Manga M (2001) Origin of postseismic streamflow changes inferred from baseflow recession and magnitude-distance relation. *Geophys Res Lett* 28:2133–2136
- Manga M, Brodsky EE, Boone M (2003) Response of streamflow to multiple earthquakes and implications for the origin of postseismic discharge changes. *Geophys Res Lett* 30:1214. <https://doi.org/10.1029/2002GL016618>
- Manga M, Beresnev I, Brodsky EE et al (2012) Changes in permeability caused by transient stresses: Field observations, experiments, and mechanics. *Rev Geophys* 50:RG2004. <https://doi.org/10.1029/2011RG000382>
- Manga M, Wang CY, Shirzaei M (2016) Increased stream discharge after the 3 September 2016 Mw 5.8 Pawnee Oklahoma earthquake. *Geophys Res Lett* 43:11588–11594. <https://doi.org/10.1002/2016GL071268>
- Matsumoto N, Kitagawa G, Roeloffs EA (2003) Hydrological response to earthquakes in the Haibara well, central Japan - I. Water level changes revealed using state space decomposition of atmospheric pressure, rainfall and tidal responses. *Geophys J Int* 155:885–898
- Mogi K, Mochizuki H, Kurokawa Y (1989) Temperature changes in an artesian spring at Usami in the Izu Peninsula (Japan) and their relation to earthquakes. *Tectonophysics* 159:95–108
- Montgomery DR, Greenberg HM, Smith DT (2003) Streamflow response to the Nisqually earthquake. *Earth Plane. Sci Lett* 209:19–28
- Mohr CH, Manga M, Wang CY et al (2015) Shaking water out of soil. *Geology* 43:207–210. <https://doi.org/10.1130/G36261.1>
- Mohr CH, Manga M, Wang CY, Korup O (2017) Regional changes in streamflow after a megathrust earthquake. *Earth Planet Sci Lett* 458:418–428. <https://doi.org/10.1016/j.epsl.2016.11.013>

- Montgomery DR, Manga M (2003) Streamflow and water well responses to earthquakes. *Science* 300:2047–2049
- Morrow, CA Lockner DA, Moore DE, Hickman S (2014) Deep permeability of the san andreas fault from san andreas fault observatory at depth (SAFOD) core samples. *J Structural Geology* 64: 99–114
- National Research Council (1985) Liquefaction of soils during earthquakes. National Academy Press, Washington, DC
- National Research Council (2016) State of art and practice in the assessment of earthquake-induced soil liquefaction and its consequences. National Academy Press, Washington, DC
- Quilty E, Roeloffs E (1997) Water level changes in response to the December 20, 1994, M4.7 earthquake near Parkfield California. *Bull Seismol Soc Am* 87:310–317
- Roberts PM (2005) Laboratory observations of altered porous fluid flow behavior in Berea sandstone induced by low-frequency dynamic stress stimulation. *Acoust Phys* 51:140–148. <https://doi.org/10.1134/1.2133962>
- Roberts PM, Abdel-Fattah AI (2009) Seismic stress stimulation mobilizes colloids trapped in a porous rock. *Earth Planet Sci Lett* 284:538–543. <https://doi.org/10.1016/j.epsl.2009.05.017>
- Roeloffs EA (1996) Poroelastic methods in the study of earthquake-related hydrologic phenomena. In: Dmowska R (ed) *Advances in geophysics*. Academic Press, San Diego
- Roeloffs EA (1998) Persistent water level changes in a well near Parkfield, California, due to local and distant earthquakes. *J Geophys Res* 103:869–889
- Roeloffs EA, Sneed M, Galloway DL et al (2003) Water-level changes induced by local and distant earthquakes at long valley caldera, California. *J Volcanol Geotherm Res* 127:269–303
- Rojstaczer S, Wolf S (1992) Permeability changes associated with large earthquakes: an example from Loma Prieta, California, 10/17/89 earthquake. *Geology* 20:211–214
- Rojstaczer S, Wolf S, Michel R (1995) Permeability enhancement in the shallow crust as a cause of earthquake-induced hydrological changes. *Nature* 373:237–239
- Rutter HK, Cox SC, Ward NFD et al (2016) Aquifer permeability change caused by a near-field earthquake, Canterbury, New Zealand. *Water Resour Res* 52:8861–8878. <https://doi.org/10.1002/2015WR018524>
- Saffer DM (2015) The permeability of active subduction plate boundary faults. *Geofluids* 15:193–215. <https://doi.org/10.1111/gfl.12103>
- Sato T, Matsumoto N, Kitagawa Y et al (2004) Changes in water level associated with the 2003 Tokachi-oki earthquake. *Earth Planets Space* 56:395–400
- Scholz CH (1990) *The mechanics of earthquakes and faulting*. Cambridge University Press, Cambridge UK
- Schulz SE, Evans JP (2000) Mesoscopic structure of the Punchbowl Fault, Southern California and the geologic and geophysical structure of active strike-slip faults. *J Struct Geol* 22(7):913–930
- Scibek J, Gleeson T, McKenzie JM (2016) The biases and trends in fault zone hydrogeology conceptual models: global compilation and categorical data analysis. *Geofluids* 16(4):782–798
- Screaton E, Carson B, Davis E et al (2000) Permeability of a decollement zone: results from a two-well experiment in the Barbados accretionary complex. *J Geophys Res* 105(B9):21403–21410
- Seed HB, Lee KL (1966) Liquefaction of saturated sands during cyclic loading. *J Soil Mech Found Div* 92:105–134
- Sibson RH (1996) Structural permeability of fluid-driven fault-fracture meshes. *J Struct Geol* 18(8):1031–1042. [https://doi.org/10.1016/0191-8141\(96\)00032-6](https://doi.org/10.1016/0191-8141(96)00032-6)
- Sil S, Freymueller JT (2006) Well water level changes in Fairbanks, Alaska, due to the great Sumatra-Andaman earthquake. *Earth Planets Space* 58:181–184
- Sneed M, Galloway DL, Cunningham (2003) Earthquakes-rattling the Earth's plumbing system. U.S. Geological Survey, Fact Sheet 096-03
- Sun X, Xiang Y, Shi Z (2018) Estimating the hydraulic parameters of a confined aquifer based on the response of groundwater levels to seismic Rayleigh waves. *Geophys J Int* 213: 919-930
- Teng LS (1990) Geotectonic evolution of late Cenozoic arc-continent collision in Taiwan. *Tectonophysics* 183:57–76

- Tokunaga T (1999) Modeling of earthquake-induced hydrological changes and possible permeability enhancement due to the 17 January 1995 Kobe earthquake, Japan. *J Hydrol* 223:221–229
- Tyan CL, Chang YM, Lin WK et al (1996) The brief in production to the groundwater hydrology of Choshui River Alluvial fan. In: Conference on groundwater and hydrology of the choshui river alluvial fan, Taiwan, water resources bureau, pp 207–221. (in Chinese)
- Vinas KA (2013) Mariana forearc crust CORK pressure data: observations and implications. Open Access Theses 436. https://scholarlyrepository.miami.edu/oa_theses/436
- Vucetic M (1994) Cyclic threshold of shear strains in soils. *J Geotech Eng* 120:2208–2228
- Wakita H (1975) Water wells as possible indicators of tectonic strain. *Science* 189:553–555
- Waller RM, Thomas HE, Vorhis RC (1965) Effects of the good friday earthquake on water supplies. *J Am Water Wrok Assoc* 57:123–131
- Wang CY, Lin W, Wu FT (1978) Constitution of the san andreas fault zone at depth. *Geophys Res Lett* 5:741–744
- Wang CY, Fong R, Yao Z et al (1986) Gravity anomaly and density structure of the San Andreas fault zone. *Pure appl Geophys* 124:127–140
- Wang CY, Cheng LH, Chin CV et al (2001) Coseismic hydrologic response of an alluvial fan to the 1999 Chi-Chi earthquake, Taiwan. *Geology* 29:831–834
- Wang CY, Wang CH, Kuo CY (2004) Temporal change in groundwater level following the 1999 M_w 7.5 Chi-Chi earthquake, Taiwan. *Geofluids* 4:210–220
- Wang CY, Wong A, Dreger DS et al (2006) Liquefaction limit during earthquakes and underground explosions—implications on ground-motion attenuation. *Bull Seis Soc Am* 96:355–363
- Wang CY (1984) On the constitution of the San Andreas fault. *J Geophys Res* 89:5858–5866. <https://doi.org/10.1029/JB089iB07p05858>
- Wang CY (2007) Liquefaction beyond the near field. *Seism Res Lett* 78:512–517
- Wang CY (2011) High pore pressure, or its absence, in the San Andreas fault. *Geology* 39:1047–1050
- Wang CY, Chia Y (2008) Mechanism of water-level changes during earthquakes near field versus intermediate field. *Geophys Res Lett* 35:L12402. <https://doi.org/10.1029/2008GL034227>
- Wang CY, Manga M (2010) *Earthquakes and Water*. Springer, Berlin
- Wang CY, Liao X, Wang LP et al (2016) Large earthquakes create vertical permeability by breaching aquitards. *Water Resour Res* 52:5923–5937. <https://doi.org/10.1002/2016WR018893>
- Wang CY, Barbour AJ (2017) Influence of pore pressure change on coseismic volumetric strain. *Earth Planet Sci Lett* 475:152–159
- Wang CY, Manga M, Shirzaei M et al (2017) Induced seismicity in Oklahoma affects shallow groundwater. *Seismol Res Lett* 88:956–962
- Wang CY, Doan ML, Xue L et al (2018) Tidal response of groundwater in a leaky aquifer—application to Oklahoma. *Water Resour Res* 54:8019–8033. <https://doi.org/10.1029/2018WR022793>
- Wang C-H, Wang C-Y, Kuo C-H, Chen W-F (2005) Some isotopic and hydrological changes associated with the 1999 Chi-Chi earthquake, Taiwan. *The Island Arc* 14: 37–54
- Wang CY, Zhu AY, Liao X et al (2019) Capillary effects on groundwater response to earth tides. *Water Resour Res* 55:6886–6895. <https://doi.org/10.1029/2019WR025166>
- Water Resource Bureau (1999) Summary report of groundwater monitoring network plan in Taiwan, phase I, hydrogeology of Choshui River Alluvial Fan. Water Resource Bureau, Ministry of Economic Affairs, Taipei, Taiwan (in Chinese), 240 pp
- Weingarten M, Ge S (2014) Insights into water level response to seismic waves: A 24 year high-fidelity record of global seismicity at Devils Hole. *Geophys Res Lett* 41:74–80. <https://doi.org/10.1002/2013GL058418>
- Whitehead RL, Harper RW, Sisco HG (1984) Hydrologic changes associated with the October 28, 1993. Idaho earthquake. *Pure Appl Geophys* 122:280–293
- Wu HY, Ma GF, Zoback M et al (2007) Stress orientation of Taiwan chelungpu-fault drilling project (TCDP) hole-A as observed from geophysical logs. *Geophys Res Lett* 34:L01303. <https://doi.org/10.1029/2006gl028050>

- Wu Z, Ha G, Zhao G et al (2018) Tectonic analysis on abnormal dried up of Duoqing Co Lake of southern section of Yadong-Gulu rift in South Tibet during April, 2016. *Earth Sci* 43:243–255. <https://doi.org/10.3799/dqkx.2018.204>
- Xue L, Li HB, Brodsky EE et al (2013) Continuous permeability measurements record healing inside the Wenchuan earthquake fault zone. *Science* 340:1555–1559
- Xue L, Brodsky EE, Erskine J et al (2016) A permeability and compliance contrast measured hydrologically on the San Andreas fault. *Geochem Geophys Geosyst* 17:858–871. <https://doi.org/10.1002/2015GC006167>
- Yan R, Woith H, Wang R (2014) Groundwater level changes induced by the 2011 Tohoku earthquake in China mainland. *Geophys J Int* 199:533–548
- Zhang H, Shi Z, Wang G et al (2019a) Large earthquake reshapes the groundwater flow system: Insight from the water-level response to Earth tides and atmospheric pressure in a deep well. *Water Resour Res* 55:4207–4219. <https://doi.org/10.1029/2018WR024608>
- Zhang Y, Wang CY, Fu LY, Rui Y, Chen X (2017) Mechanism of the coseismic change of volumetric strain in the far field of earthquakes. *Bulletin Seismol Soc Am* 107:475–481. <https://doi.org/10.1785/0120160253>
- Zhang Y, Wang CY, Fu LY et al (2019b) Unexpected far-field hydrological response to a great earthquake. *Earth Planet Sci Lett* 519:202–212
- Zhu AY, Wang CY (2020) Response of leaky aquifers to earth tides—interpreted with numerical simulation. *J Hydrol* 581:124458. <https://doi.org/10.1016/j.jhydrol.2019.124458>
- Zoback MD, Hickman S, Ellsworth W (2010) Scientific drilling into the San Andreas fault zone. *Eos, Trans Am Geophys Union* 91:197–204. <https://doi.org/10.1029/2010EO220001>

Open Access This chapter is licensed under the terms of the Creative Commons Attribution 4.0 International License (<http://creativecommons.org/licenses/by/4.0/>), which permits use, sharing, adaptation, distribution and reproduction in any medium or format, as long as you give appropriate credit to the original author(s) and the source, provide a link to the Creative Commons license and indicate if changes were made.

The images or other third party material in this chapter are included in the chapter's Creative Commons license, unless indicated otherwise in a credit line to the material. If material is not included in the chapter's Creative Commons license and your intended use is not permitted by statutory regulation or exceeds the permitted use, you will need to obtain permission directly from the copyright holder.



Chapter 7

Stream Flow



The earth is shaken in various ways, and wonderful effects are produced; ... sometimes great masses of earth are heaped up, and rivers forced out, sometimes even flame and hot springs, and at others the course of rivers is turned. (Pliny the Elder, Natural History, Chap. 82)

Abstract Changes in stream discharge after earthquakes are among the most interesting hydrologic responses because they are visible at Earth's surface and can be dramatic. Here we focus on changes that persist for extended periods but have no obvious source. Such increases have been documented for a long time but their origins are still under debate. We first review some general characteristics of streamflow responses to earthquakes; we then discuss several mechanisms that have been proposed to explain these responses and the source of the extra water. The different hypotheses imply different crustal processes and different water–rock interactions during the earthquake cycle. In most instances, these hypotheses are under-constrained. We suggest that multiple mechanisms may be activated by an earthquake.

7.1 Introduction

It has been known for millennia that earthquakes can induce a variety of hydrological responses. The introductory quotation from Pliny (ca. AD 77–79) describes new flows that appeared after earthquakes almost 2000 years ago. Other examples include the damming of valleys by landslides and rockfalls to form lakes and decrease downstream discharge, creation of waterfalls by the earthquake faulting, and increases of discharge in regions of high relief caused by the avalanche of large quantities of

Electronic supplementary material The online version of this chapter (https://doi.org/10.1007/978-3-030-64308-9_7) contains supplementary material, which is available to authorized users.

snow to lower elevations that increases the supply of melt water. In addition, changes in stream discharge after earthquakes are among the most interesting hydrologic responses partly because they can be directly observed and may be large enough to be visually compelling. Fig. 7.1 shows the destruction of the famed waterfall in Jiuzhaigou, western China, after the 2017 Mw7.0 Jiuzhaigou earthquake, which recovered a few months later.

Such changes only redistribute the surface discharge budget, with excess and deficit flows compensating each other. More interesting and less well understood is a type of discharge change that follows earthquakes and persists for an extended period (commonly several weeks to months) but has no obvious source. Such increases of streamflow are more than curiosities because understanding their origin can provide insight into the interactions between hydrogeologic and tectonic processes at spatial and temporal scales that are otherwise difficult to study. These changes have been quantitatively documented for a long time. For example, extensive networks of stream gauges in the western United States were established by the US Geological Survey



Fig. 7.1 Jiuzhaigou waterfall, China, before (top) and after (bottom) the 2017 M7 Jiuzhaigou earthquake. (from <https://www.sohu.com>)

(USGS) in the early twentieth century, and long and continuous gauging measurements have been collected. Such USGS data, along with measurements made globally, record streamflow changes following earthquakes. In the following sections, we first discuss some general characteristics of streamflow responses to earthquakes that have a subsurface origin. We then discuss several mechanisms that have been proposed to explain these responses and the source of the extra water. Following this, we discuss the available observational constraints on these hypotheses and how different models perform when tested against constraints. Finally, we discuss the occurrence of streamflow responses in special geologic settings, such as that in geothermal areas.

7.2 Observations

7.2.1 *Measurement with Flow Meter and Tape*

Most creeks are too small to have a permanent stream gauge installed to measure their discharge. The discharge of these creeks is more often determined manually by using measuring tapes and flow-meters (Fig. 7.2). The cross-section of the creek is subdivided into several subsections and the discharge across each subsection is determined by measuring its average depth and the depth averaged flow velocity (e.g., Fetter 2001). The discharge across each subsection is then calculated; the total discharge of the stream is then the sum of the discharges across all the sub-sections.

After the 2014 Mw6.0 South Napa earthquake, which occurred during a prolonged drought in California when most creeks in central California were nearly dry, many creeks within about 50 km of the epicenter (Fig. 7.3a) showed increased discharge by a factor of more than an order of magnitude (Fig. 7.3b, d, e). Except Sonoma Creek where discharge was measured automatically by a USGS stream gauge (Fig. 7.3b), the discharge in all the other creeks (Fig. 7.3d, e) was measured manually (Wang and Manga 2015).

7.2.2 *Measurement with Stream Gauges*

Many streams with appreciable discharge are monitored with stream gauges. For example, within the USA, at stream gauges maintained by the US Geological Survey, the elevation of the water surface (stage) at a given location is monitored and converted to discharge using a stage-discharge rating curve constructed for that section (e.g., Fetter 2001). The data are collected at 15-min interval and relayed to USGS offices via satellite and are available for viewing within minutes of arrival.

As far as can be determined from the stream-gauge records (e.g., Fig. 7.3b), the onset of streamflow changes can be coseismic. The change can, however, continue

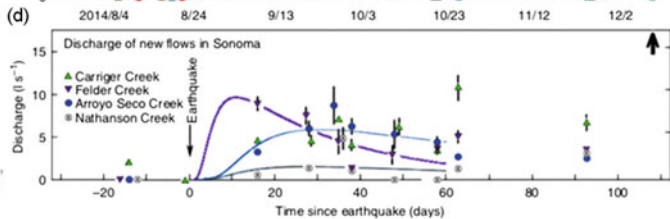
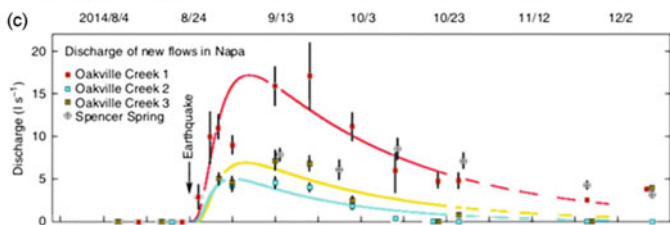
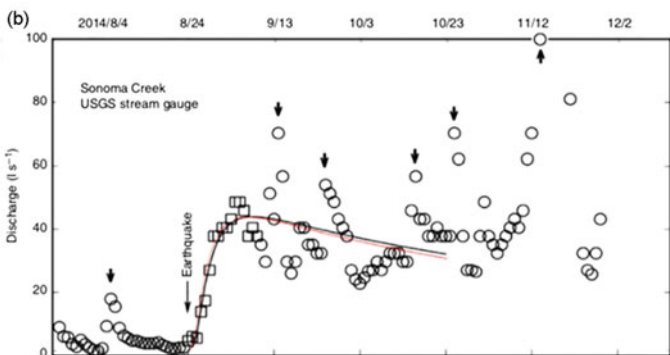
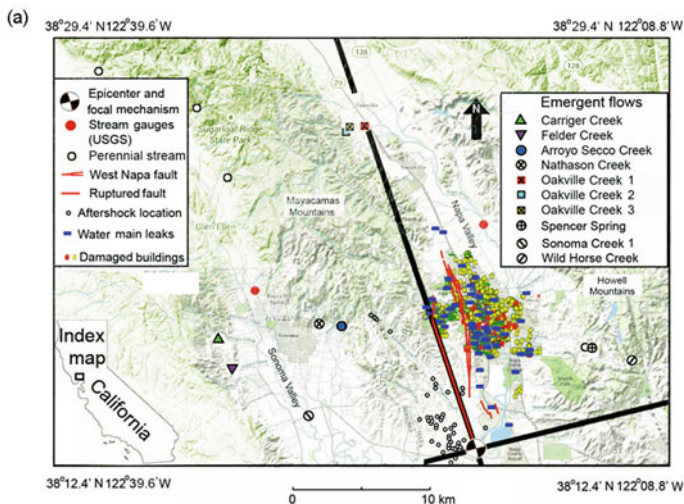


Fig. 7.2 Measuring discharge by using a flow meter and tape. Two hydrologists from the Sonoma Ecology Center measure the discharge in a small stream in the Sonoma County, California

for a few days or weeks to reach a maximum, and then gradually declines to reach the pre-earthquake level after several months. Also noticeable in Fig. 7.3 are the sudden increases in streamflow in response to precipitation. Precipitation can easily obscure the earthquake-induced streamflow response when it occurs at the time of an earthquake and makes the analysis of the latter difficult or impossible.

The majority of coseismic streamflow responses documented this way show increased discharge (e.g., Rojstaczer and Wolf 1992; Muir-Wood and King 1993; Rojstaczer et al. 1995; Sato et al. 2000; Montgomery et al. 2003; Wang et al. 2004a; Wang and Manga 2015; Mohr et al. 2015, 2017). But coseismic decrease of stream discharge has also been reported. An interesting example is the response of the Shira River to the 2016 Mw7.0 Kumamoto earthquake in Japan, documented by three stream gauges (see Fig. 7.4a for gauge locations; Hosono et al. 2019). The uppermost gauge, Gauge A (Fig. 7.4b), documented a coseismic increase of stream discharge, which was followed by a second larger increase ~ 10 h later, while the lower Gauges B and C (Fig. c and d) both showed coseismic decreases of discharge, followed by large increases ~ 10 h later. Ichiiyanagi et al. (2020) estimated from these records that an amount of approximately $900,000 \text{ m}^3$ of river water was lost between Gauge A and Gauge C in a 12-h period, consistent with the estimate of Hosono et al. (2019) from the change of groundwater level in the area (Chap. 6).

Koizumi et al. (2019) studied the stream discharge in central Kyushu at eight monitored stations (Fig. 7.5a) before and immediately after the 2016 Kumamoto



◀**Fig. 7.3** **a** Map showing sampling locations of the streams and a spring (Spencer Spring) that increased flow after the 2014 Mw6.0 South Napa earthquake, monitored sites on the perennial streams, and the USGS stream gauges. Red lines show the West Napa fault zone; thick red line shows the ruptured fault. The focal mechanism of the earthquake, shown by a ‘beach ball’ symbol, divides the surrounding region into quadrants of static compression and dilatation, bounded approximately by the thick black lines on the map. Areas extending from the white sections of the ‘beach ball’ are in static dilatation; areas extending from the black sections are in static compression. Notice that while the Sonoma Valley is located in a compressional regime, the Napa Valley is located in a tensional regime. **b** Daily averaged discharge of Sonoma Creek documented by a USGS gauge at Agua Caliente before and after the South Napa earthquake, showing changes in stream discharge after the South Napa earthquake. Measurement errors are similar to the size of symbols. Short duration increases of discharge, indicated by thick arrows, were due to precipitation both inside and outside of the studied area, and do not necessarily correspond to the precipitation in the valley. **c**. Thin arrow shows the time of the earthquake. Curves show simulated stream discharge based on the model of coseismic vertical recharge (Sect. 7.4.2). Two simulations were made for the Sonoma Creek discharge; the first simulation (black line) is based on data for the first 17 days after the earthquake (open squares) to exclude the first incursion of precipitation and the second simulation (red line) is based on all data before significant precipitation in the valley (60 days after the earthquake). The similarity between the two simulated results and data suggests robustness of the model. **d** Discharges as a function of time in streams and Spencer Spring in Napa County. Discharges in different streams and spring are shown by different colored symbols; measurement errors are shown as error bars except where the error bars are smaller than the symbols. Symbols in brackets show conditions reported by local residents and one discharge data converted from early depth measurements, with depth-to-discharge conversion calibrated during subsequent surveys. Colored curves show simulated stream discharge based on 60 days of data after the earthquake using the coseismic vertical recharge model (Sect. 7.4.2); dashed curves show extrapolations from the simulated discharges. Measurement at Spencer Spring started 21 days after the earthquake and was not simulated. **e** Discharges and simulated discharges as a function of time in new streams in Sonoma County. Upward arrow indicates that measured discharges were off scale (modified from Wang and Manga 2015)

earthquake. They showed that, while some rivers exhibited coseismic increase of discharge (Fig. 7.5b), most increases occurred during heavy rainfall that can obscure a coseismic increase.

7.3 Proposed Mechanisms

In the absence of recent precipitation or snowmelt, an increase in stream discharge implies either an increase of the hydraulic gradient created by a new source, or an increase of the hydraulic conductivity of the aquifer along the flow path, or both, see Eq. (2.3). Several mechanisms have been proposed to explain the changes in stream-flow following earthquakes, which may be generally separated into ‘new source’ and the ‘enhanced conductivity’ categories. Mechanisms involving new sources include: (1) the expulsion of deep crustal fluids resulting from coseismic elastic strain (e.g., Muir-Wood and King 1993), (2) coseismic consolidation and liquefaction of shallow sediments (Wang et al. 2001; Manga et al. 2003), (3) coseismic release of water from mountains (Fleeger et al. 1999; Wang et al. 2004a), and (4) shaking water out

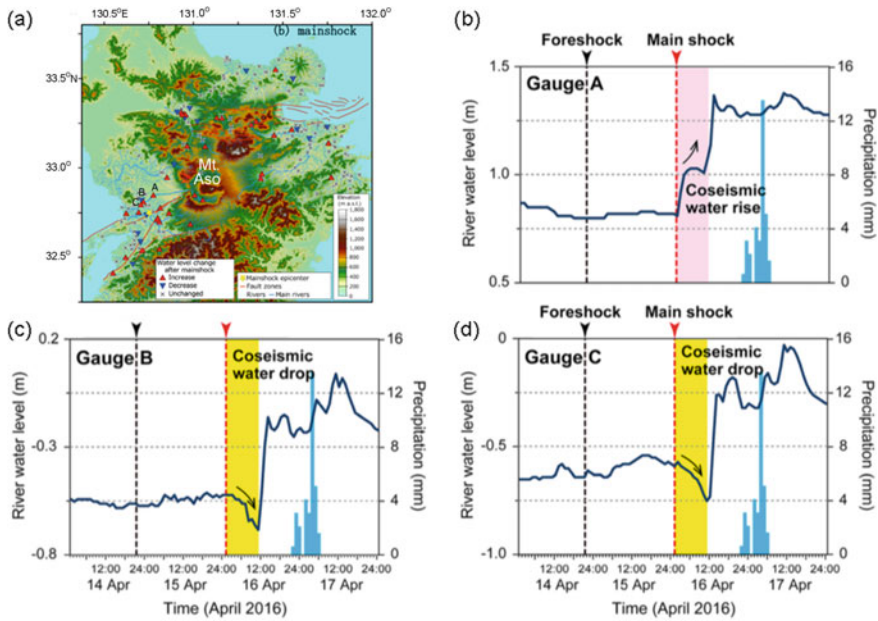


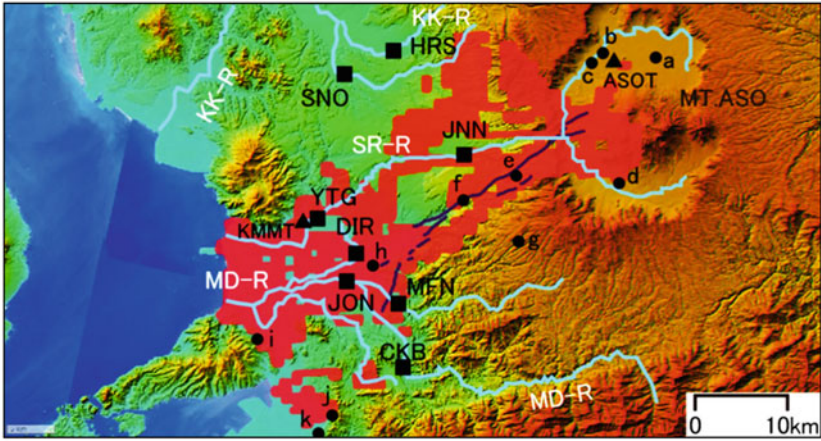
Fig. 7.4 a Map of area around Central Kyushu showing the epicenter of the 2016 Kumamoto earthquake (yellow star), stream gauge locations (triangles) and pre-existing active faults (red lines). Red triangles show gauges with coseismic increases of stream discharge and blue triangles show gauges with coseismic decreases (modified from Ichiyanagi et al. 2020). b–d Time series of relative river water level at gauges A, B and C (locations shown in panel a). Hourly records of precipitation within the catchment area are shown with the bar graphs (modified from Hosono et al. 2019). Notice that Gauge A showed a coseismic increase with the main shock, while Gauges B and C showed coseismic decreases; all were followed by a large increase ~10 h later. The foreshock did not cause significant coseismic change of water level (from Honoso et al. 2019)

of unsaturated soil (Mohr et al. 2015). Mechanisms involving enhanced hydraulic conductivity: (1) the enhancement of the horizontal permeability (Rojstaczer et al. 1995), and (2) the enhancement of the vertical permeability (Wang et al. 2004a). Differences between these different hypotheses are nontrivial because they imply different hydrologic processes during and after earthquakes, and have implications for the nature of groundwater flow paths. In the following we summarize the basic elements of the hypotheses and discuss some implications and problems of each. We then evaluate the proposed hypotheses with the existing data.

7.3.1 Static Elastic Strain

Muir-Wood and King (1993) applied the coseismic elastic strain model proposed by Wakita (1975) to explain the increased stream discharge after the 1959 M7.5

(a)



(b)

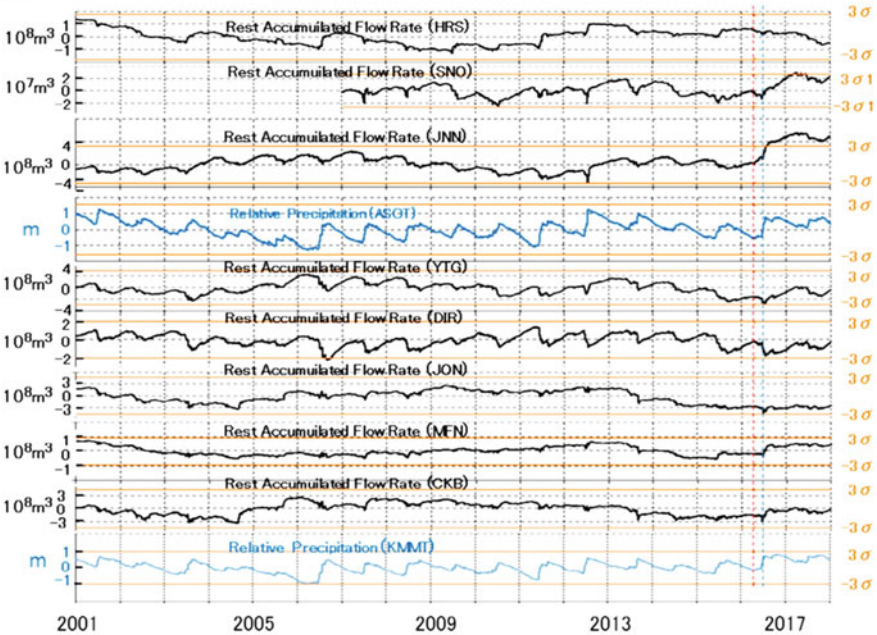


Fig. 7.5 **a** Map of central Kyushu showing locations of streamflow stations (black squares), studied springs (black circle), weather stations (black triangles), major rivers (light blue) and ruptured fault (dark blue). Red areas indicate strong ground motion during the Kumamoto earthquake. **b** Temporal changes in the accumulated flow rate (after the removal of the effect of the average accumulated precipitation) and relative precipitation from 2001 to 2017. σ is the standard deviation from 2001 to 2015. Vertical red and blue broken lines indicate, respectively, the occurrence of the main shock of the 2016 Kumamoto earthquake and of the heavy rainfall 2 months after (modified from Koizumi et al. 2019)

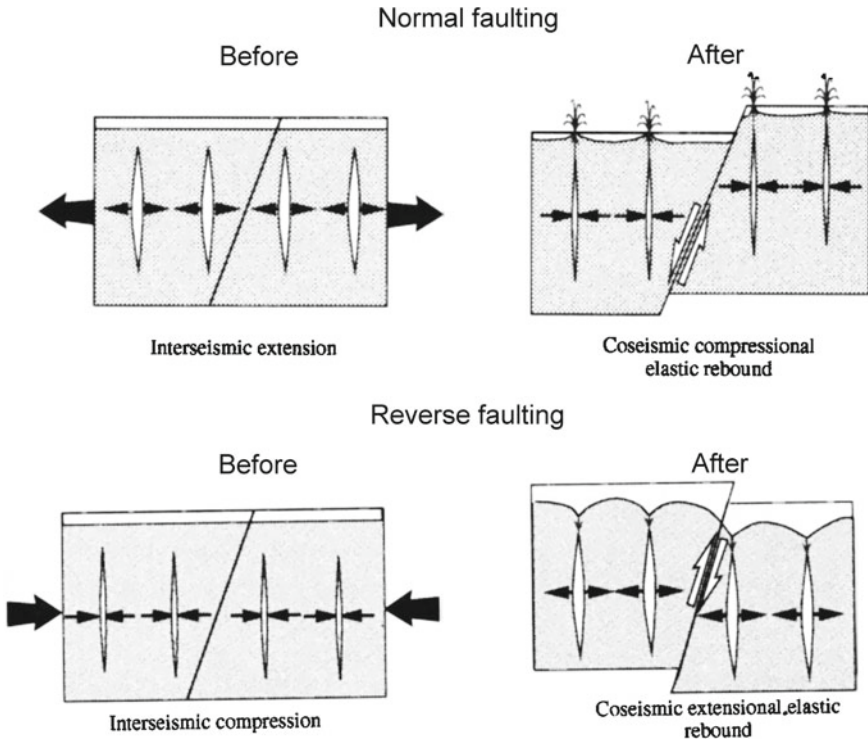


Fig. 7.6 Simplified model for the interseismic accumulation and coseismic release of strain in extensional and compressional tectonic environments. For extensional faulting, the interseismic period is associated with crack opening and increase of effective porosity. At the time of the earthquake, cracks close and water is expelled. For compressional faulting, the interseismic period is associated with crack closure and the expulsion of water. At the time of the earthquake, cracks will open and water will be drawn in. In the case of normal faulting, water can be expelled to the surface at the time of an earthquake and thus immediately affect river flow (shown schematically as surface fountains). For reverse faulting, cracks must be filled from the water table, a slower process that may not be observed in river flow rates (from Muir-Wood and King 1993)

Hebgen Lake earthquake and the 1983 M7.3 Borah Peak earthquake. They argued that changes in the static elastic strain in the crust produced by earthquake faulting cause rocks to dilate or contract and thus saturated cracks in rocks to open or close, resulting in a decrease or increase in the groundwater discharge into streams (Fig. 7.6).

7.3.2 Consolidation and Liquefaction

Consolidation of loose, saturated sediments may expel pore water in a ‘drained’ process if sufficient time is available (Sect. 3.3; Fig. 3.5). During an earthquake, the amount of time available is too short for the pore water to drain; thus, the process

is ‘undrained’ (Sect. 3.4). As numerous field observations and laboratory experiments have shown (Sect. 11.2), undrained consolidation of saturated loose sediments causes pore pressure to increase and eventually the sediments can liquefy. Wang et al. (2001) suggested that the coseismic undrained consolidation of the loose sediments on the Choshui River flood plain during the Chi-Chi earthquake caused the coseismic increase of water level (Fig. 6.2a). Manga et al. (2003) suggested that coseismic liquefaction of loose sediments on floodplains may provide the water for the increases in stream discharge following earthquakes. The occurrence of liquefaction in areas that experienced increased stream flow is suggestive, but direct evidence that associates liquefaction to the increased discharge has not been found (Montgomery and Manga 2003).

7.3.3 *Water Released from Mountains*

Within hours after the 1998 M5.2 Pymatuning earthquake in northwestern Pennsylvania, local residents reported that many wells on a local ridge becoming dry, while other wells in the valleys started to flow. Fleeger et al. (1999) reported the observed changes in groundwater level and suggested that the earthquake increased the vertical hydraulic conductivity of shales beneath the ridge, allowing groundwater to drain from the hilltops. They also used numerical modeling to show that an increase of the vertical permeability by 10–60 times from the pre-seismic values would be needed to reproduce the earthquake effects on groundwater beneath the ridge (Fig. 7.7).

After the 1999 Mw7.6 Chi-Chi earthquake in Taiwan, several stream systems showed coseismic increases in stream discharge, many wells in the foothills above the thrust fault experienced a significant decline in water level, and a tunnel beneath the foothills experienced sudden downpours right after the earthquake (Lin 2000; Yan 2001). Field mapping after the Chi-Chi earthquake also showed numerous new fractures in the hanging wall of the thrust fault (Angelier et al. 2000; Lee et al. 2000, 2002). Wang et al. (2004a) attributed these hydrologic events to the coseismic release of groundwater from mountains through subvertical fractures, which recharges aquifers in the valley, that in turn recharge the local streams. They further provided an analytical model of vertical recharge by groundwater from mountains to simulate the observed changes (Fig. 7.11). More discussion of this model is provided in Sect. 7.4.2.

After the 2016 Mw7.0 Kumamoto earthquake in Japan, several authors (e.g., Hosono et al. 2019; Ichiyanagi et al. 2020; Kagabu et al. 2020) showed that their data are consistent with the model of coseismic release of groundwater from the nearby caldera rim mountains.

7.3.4 *Water Released from Unsaturated Soils*

Following the 2010 M8.8 Maule earthquake, Mohr et al. (2015) reported increased streamflow in the Chilean coastal range (Fig. 7.8) and proposed that water was

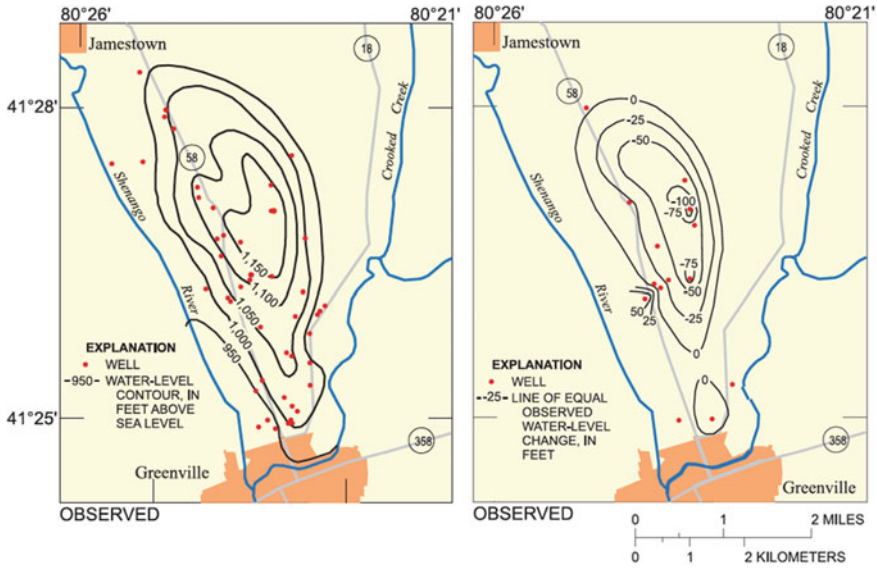


Fig. 7.7 Groundwater levels (in feet) over a ridge near Greenville, Pennsylvania, before (left) the 1998 M5.2 Pymatuning earthquake, and changes of groundwater level after the earthquake (right). Contours were reconstructed from values estimated from historical measurements and reports from homeowners and drillers (modified from Fleegeer et al. 1999)

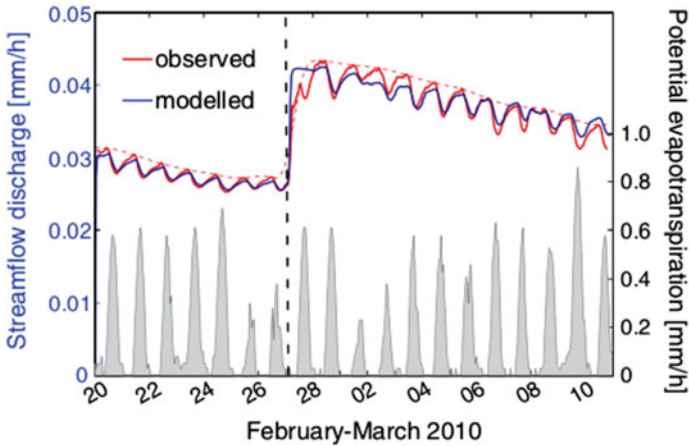


Fig. 7.8 Observed (red line) and modeled (blue line) streamflow in a catchment in the Chilean Coastal Range for periods before and after the Maule earthquake. Gray bars show potential evapotranspiration rates (in mm/h). Dashed red line indicates maximum streamflow rates assuming negligible nightly evapotranspiration. Vertical dashed black line shows time of the Maule earthquake (from Mohr et al. 2015)

released from unsaturated soils. In this model the aquifer is recharged by the coseismically released water from the unsaturated zone. The observed and the simulated discharge, subjected to evapotranspiration, show good agreement (Fig. 7.8).

Mohr et al. (2015) estimated that a threshold seismic energy density of 10^2 J/m^3 is required, which is three orders of magnitude greater than the threshold seismic energy density to initiate undrained consolidation (see Sect. 7.4.6). Thus, the mechanism of releasing pore water from the unsaturated zone may be significant only in the near field.

7.3.5 Enhanced Permeability

Following the 1989 M6.9 Loma Prieta earthquake in central California, sudden increases of stream discharge occurred in nearby drainage basins. Rojstaczer and Wolf (1992) and Rojstaczer et al. (1995) proposed that the increased stream discharge was due to coseismic enhancement of the hydraulic diffusivity of the aquifer, with flow governed by

$$\frac{\partial h}{\partial t} = D \frac{\partial^2 h}{\partial x^2}, \quad (7.1)$$

where h is the hydraulic head, D is the horizontal hydraulic diffusivity of the aquifer, x is the horizontal position, L is the length of the aquifer, and t is time. By using this equation, Rojstaczer et al. (1995) has assumed the horizontal diffusivity and its change to explain the increase of stream discharge.

Similar models were applied to the 1995 Kobe earthquake in Japan to explain observed hydrological changes (Tokunaga 1999; Sato et al. 2000). The model of enhanced permeability was also invoked to explain the increased electrical conductivity of water discharged after an earthquake (Charmoille et al. 2005) and to explain the coseismic increases of phase shifts in the water-level response to tidal strain in southern California (Elkhoury et al. 2006).

7.3.6 Enhanced Vertical Permeability

A lively debate ensued about the enhanced permeability model after the finding of Manga (2001) that no significant change of the baseflow recession occurred after the 1989 Loma Prieta earthquake and other earthquakes. We discuss this finding after a brief introduction to the concept of baseflow recession. The discharge of streams following recharge, known as baseflow recession, often shows an approximately linear relationship between the logarithm of the stream discharge (Q) and time, i.e.,

$$\log Q = a - ct \quad (7.2)$$

where a and c are the empirical constants for the linear fit, and t is the time since recharge. A minus sign is placed in front of c , known as the baseflow recession constant, so that c itself is positive; its inverse, i.e., $\tau \equiv 1/c$, is the characteristic time of the stream response to the recharge. As shown in Sect. 7.4.2, the recession constant (c) is related to the hydraulic diffusivity (D) and the characteristic length of the aquifer (L) by

$$c \approx -\frac{\pi^2 D}{4L^2}. \tag{7.3}$$

Manga (2001) analyzed the hydrographs of a number of streams, including some that responded to the 1989 Mw6.9 Loma Prieta earthquake (Fig. 7.9a). Figure 7.9b plots the recession constant c determined from the hydrographs as a function of time; no significant change in baseflow recession was found before and after the earthquake, even though discharge increased by an order of magnitude after the earthquake. Given that the length of the aquifer is not likely to change during an earthquake and the

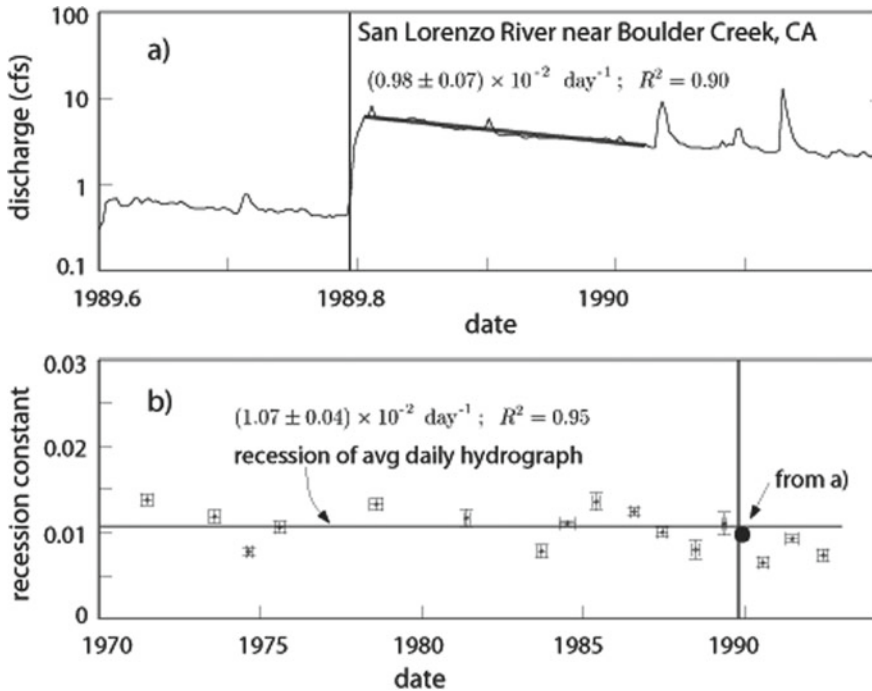


Fig. 7.9 **a** Hydrograph of the San Lorenzo River, CA, showing postseismic response to the 1989 Mw6.9 Loma Prieta earthquake. The vertical line indicates the time of the earthquake. The postseismic period of baseflow recession is shown by the bold sloping line. **b** The baseflow recession constant for periods of baseflow before and after the earthquake shows that even though discharge increased by an order of magnitude there was no significant change in baseflow recession. Figure made with US Geological Survey stream gauge data (from Manga 2001)

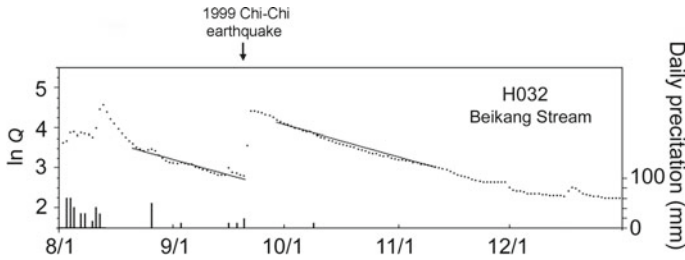


Fig. 7.10 Stream discharge (logarithm of Q , in m^3/s , daily averages) documented by stream gauge H032, located on a stream in the mountains (see Fig. 7.13 for gauge location). Note the surge in discharge right after the 1999 Chi-Chi earthquake as indicated by the downward pointed arrow. Precipitation within the study area is shown with the bar graphs. Notice that there was little precipitation many months after the Chi-Chi earthquake. Straight lines are the best fits to the baseflow recessions before and after the Chi-Chi earthquake and show similar slopes (modified from Wang et al. 2004a)

similarity in the recession constants before and after the earthquake, the finding of no significant change in baseflow recession after the earthquake (Manga 2001) implies that the horizontal diffusivity was not significantly enhanced by the earthquake, in contradiction to the conclusion of Rojstaczer et al. (1995).

Similar observations were made later. For example, after the 1999 Chi-Chi earthquake (Wang et al. 2004a), the hydrograph of a stream in the foothills of western central Taiwan (gauge H032, see Fig. 7.13 for location) shows nearly identical recession as that before the earthquake (Fig. 7.10).

After the 2010 Mw8.8 Maule earthquake in Chile, Mohr et al. (2017) analyzed the baseflow recession of eighty streams that experienced increased discharge. Their result (Fig. 7.11) again showed no clear change of baseflow recession after the earthquake and thus does not support the hypothesis of a seismic enhanced horizontal permeability as the mechanism for the observed streamflow anomalies.

Wang et al. (2004a) resolved this apparent dilemma by invoking hydraulic anisotropy; they suggested that the Chi-Chi earthquake enhanced the *vertical* permeability in the nearby mountains that allowed coseismic release of water to recharge the aquifer (Sect. 7.3.1) without significantly affecting the baseflow recession, since the latter is controlled by the horizontal permeability (Eq. 7.3). Based on this conceptual model Wang et al. (2004a) proposed an analytical model (Sect. 7.4.2) and used it to simulate the post-seismic stream discharge in Taiwan after the 1999 Chi-Chi earthquake (e.g., Fig. 7.15). This model has since been applied to simulate the increased streamflow after other earthquakes, such as that after the 2014 South Napa earthquake in central California (Wang and Manga 2015) and that after the 2016 M5.8 Pawnee earthquake in Oklahoma (Manga et al. 2016). The mechanism of enhanced vertical permeability also received direct support from the study of water level changes and tidal response after the 1999 Chi-Chi earthquake in several clustered wells on an alluvial fan near the epicenter (Wang 2007; Wang et al. 2016).

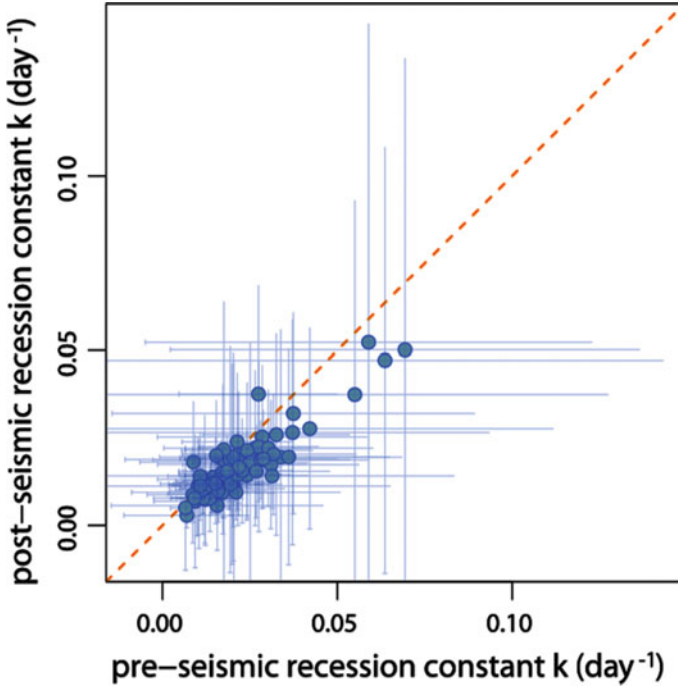


Fig. 7.11 The recession constants after the Maule earthquake plotted against the calculated recession constants before the earthquake, as daily values (m^3/day) over one year each for catchments with observed streamflow response. Error bars are $\pm 1\sigma$ of daily recession constants (from Mohr et al. 2017)

7.4 Model Constraints

7.4.1 Constraints from Earthquake Mechanism

Manga et al. (2003) took advantage of the long record of stream discharge data in the United States collected by the USGS, together with the relatively high rate of seismicity in southern California, to characterize the response of Sespe Creek, California, to several earthquakes (streamflow records go back to 1928). Figure 7.12 shows the location of the stream together with the epicenters and the focal mechanisms of several large earthquakes. Manga et al. (2003) found that the streamflow in the Sespe Creek basin always increased regardless of whether the earthquake-induced static strain in the basin was contraction or expansion. This finding rules out the static strain hypothesis as a viable mechanism for the coseismic increases of streamflow, at least for this basin.

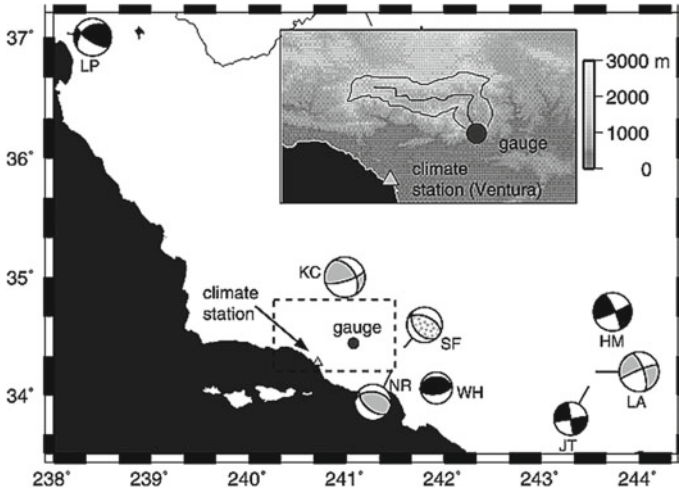


Fig. 7.12 Map showing the Sespe Creek basin in southern California and the location of stream gauge, together with the epicenters and focal mechanisms of several large earthquakes (grey—streamflow increase, grey dots—possible increase, black—no change). Inset shows the region in the dashed box (from Manga et al. 2003)

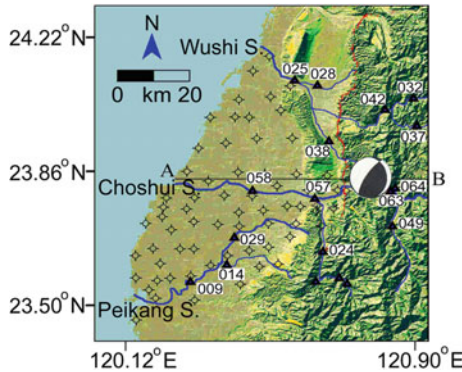


Fig. 7.13 Map shows the three stream systems and stream gauges (in black triangles, each labeled by its gauge number) near the epicenter of the Chi-Chi earthquake. Choshui alluvial fan is on west side and the foothills are on east side. Open circles with crosses show well locations. Stream systems are labeled as Choshui S. for Choshui Stream, etc. Tributaries are not labeled. AB marks the location of hydrogeologic cross-section shown in Fig. 6.4d (modified from Wang et al. 2004a)

7.4.2 Constraints from Recession Analysis

The post-seismic baseflow recession of a stream not only contains information about the hydraulic properties of the aquifers immediately after an earthquake, but can also be used to estimate the amount of extra water released by an earthquake. In this

section we show, with an example, how these parameters may be estimated from streamflow data.

Seventeen stream gauges were installed on three stream systems near the Chi-Chi earthquake epicenter (Fig. 7.13). During and after the Chi-Chi earthquake, many of these gauges registered large increases in stream discharge (Water Resource Bureau 2000; Wang et al. 2004a) and are used here as examples to illustrate how to analyze the postseismic recession and to estimate of the amount of streamflow increase.

The values for c and τ for a number of streams are obtained by fitting the stream hydrographs with Eq. 7.2. The results are listed in Table 7.1. Although these values are entirely empirical, they are closely related to the geometry and the physical properties of the aquifer that recharges the stream.

Since the aquifers are approximately horizontal with a length scale much greater than their thickness, Wang et al. (2004a) approximated them with a one-dimensional aquifer that extends from a local water divide (at $x = 0$) to a local discharge (at $x = L$), as shown in Fig. 7.14b. High-angle fractures formed during the earthquake facilitate the coseismic release of water from mountains (Fig. 7.14a, d) to recharge the aquifer below, which in turn recharges the local stream.

The baseflow recession in this case is determined by the time-dependent discharge of the aquifer at $x = L$. This may be determined by solving the groundwater flow equation under appropriate boundary and initial conditions,

$$S_s \frac{\partial h}{\partial t} = K \frac{\partial^2 h}{\partial x^2} + A(x, t) \tag{7.4}$$

where S_s and K are, respectively, the specific storage and the hydraulic conductivity of the aquifer, and are related to D (diffusivity) in Eq. 7.1 by $D = K/S_s$. Wang et al. (2004a) assumed that the enhanced vertical permeability is high such that the rate of vertical recharge to the aquifer per unit volume, i.e., $A(x, t)$ in Eq. 7.3, occurs coseismically, i.e., $A(x, t) = Q_o(x)$ at $t = 0$. Even though this model is highly simplified, several studies (e.g., Roeloffs 1998; Manga 2001; Manga et al. 2003, 2016; Brodsky et al. 2003; Wang et al. 2004a; Wang and Manga 2015) have demonstrated that such approximations are useful for characterizing the catchment-scale response

Table 7.1 Recession constant c and characteristic time τ from recession analysis of some stream gauge data after the Chi-Chi earthquake

Streams	Stream gauges	$c(s^{-1})$	$\tau(s)$
<i>Wushi system</i>			
Wushi	H025	5.2×10^{-7}	1.9×10^6
Beikang	H032	5.0×10^{-7}	2.0×10^6
Nankang	H037	5.0×10^{-7}	2.0×10^6
Wushi	H042	4.7×10^{-7}	2.1×10^6
<i>Choshui system</i>			
Choshui	H057	3.5×10^{-7}	2.9×10^6
Choshui	H058	6.7×10^{-7}	1.5×10^6
Choshui	H063	5.0×10^{-7}	2.0×10^6

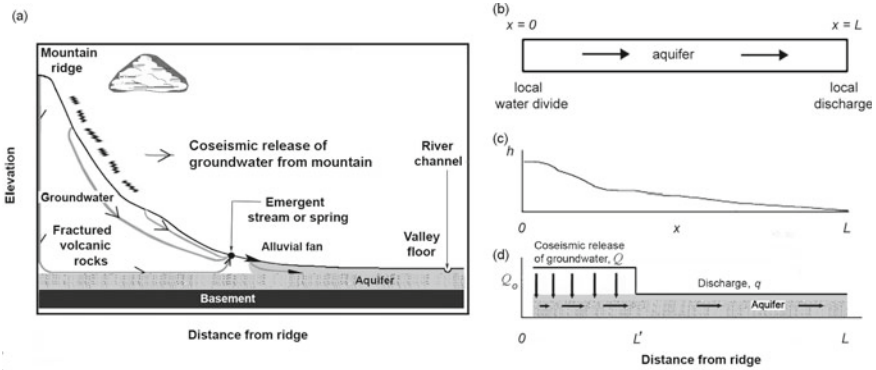


Fig. 7.14 Conceptual model for the coseismic release of groundwater from mountains. **a** Cartoon showing coseismic groundwater release from mountains to recharge an underlying aquifer (modified from Wang and Manga 2015). **b** The model aquifer between a local water divide located at $x = 0$ and a local discharge located at $x = L$. **c** The boundary conditions: the gradient of the groundwater head (i.e., dh/dx) is zero at the local water divide ($x = 0$), and $h = 0$ at the local discharge ($x = L$). **d** The initial condition: recharge to the aquifer at $t = 0$ is Q_0 for $x \leq L'$ and zero for $x > L'$ (modified from Wang et al. 2004a)

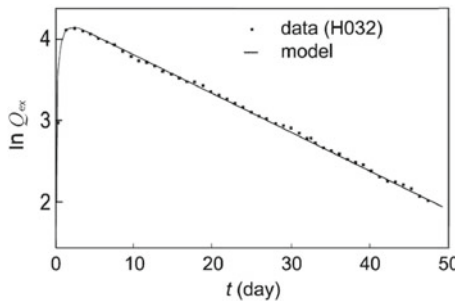


Fig. 7.15 Logarithm of the post-seismic excess discharge in m^3/s (dots) plotted against time after the Chi-Chi earthquake at stream gauge H032 adjusted to a reference of $q_{ex} = 0$ before the earthquake, compared with the predicted excess post-seismic discharge (curve) using the model of coseismic vertical recharge (from Wang et al. 2004a)

of hydrological systems to earthquakes. Equation (7.4) is also the linearized form of the differential equation that governs the groundwater level in unconfined aquifers, but with S_s replaced by S_y/b where S_y is the specific yield and b the saturated thickness of the unconfined aquifer. Because these equations are linear, the head change due to the earthquake may be superimposed on the background hydraulic head.

For boundary conditions, we adopt a no-flow boundary condition at $x = 0$ (i.e., a local water divide) and $h = 0$ at $x = L$ (i.e., a local discharge to a stream) (Fig. 7.14b). Taking the background head as the reference value, we have the initial condition $h = 0$ at $t = 0$. The solution for Eq. (7.4) under these boundary conditions was derived

in Sect. 6.4.4 and is given below,

$$h(x, t) = \frac{1}{LS_s} \sum_{n=1}^{\infty} \cos \frac{n\pi x}{2L} \exp\left[-\frac{Dn^2\pi^2 t}{4L^2}\right] \times \int_{-L}^L Q_o(x') \cos \frac{n\pi x'}{2L} dx' \quad (6.13)$$

where $Q_o(x)$ is the coseismic vertical recharge distribution at $t = 0$. Differentiating (6.13) with respect to t we have

$$\frac{\partial h}{\partial t} = \frac{1}{LS_s} \sum_{n=1}^{\infty} \left(\cos \frac{n\pi x}{2L}\right) \left(-\frac{Dn^2\pi^2}{4L^2}\right) \exp\left(-\frac{Dn^2\pi^2}{4L^2}t\right) \times \int_{-L}^L Q_o(x') \cos \frac{n\pi x'}{2L} dx'. \quad (7.5)$$

For sufficiently long times after the earthquake, Eqs. (6.13) and (7.5) are dominated by the first term ($n = 1$) of the series expansion, i.e.,

$$h(x, t) \approx \frac{1}{LS_s} \cos \frac{\pi x}{2L} \exp\left[-\frac{D\pi^2}{4L^2}t\right] \int_{-L}^L Q_o(x') \cos \frac{\pi x'}{2L} dx' \quad (7.6)$$

and

$$\frac{\partial h}{\partial t} \approx \frac{1}{LS_s} \left(\cos \frac{\pi x}{2L}\right) \left(-\frac{D\pi^2}{4L^2}\right) \exp\left(-\frac{D\pi^2}{4L^2}t\right) \times \int_{-L}^L Q_o(x') \cos \frac{\pi x'}{2L} dx' = \left(-\frac{D\pi^2}{4L^2}\right) h \quad (7.7)$$

Dividing (7.7) by (7.6) we have Eq. (7.8), i.e.,

$$c \equiv \frac{\partial \ln h}{\partial t} \approx -\frac{D\pi^2}{4L^2}. \quad (7.8)$$

This model of coseismic recharge of streams by groundwater released from mountains has been used to simulate the increased stream discharge after the 1999 Chi-Chi earthquake in Taiwan (Fig. 7.15) and the 2014 South Napa earthquake in California (Fig. 7.3b, e).

The model also makes it possible to compute the amount of excess discharge in a stream after an earthquake. To make this estimate, Wang et al. (2004a) simplified the function $Q_o(x)$ further to that shown in Fig. 7.14d, i.e., $Q_o(x) = Q_o$ for $0 \leq x \leq L'$, otherwise $Q_o(x) = 0$. Equation (7.6) then reduces to

$$h(x, t) \approx \frac{Q_o}{LS_s} \cos \frac{\pi x}{2L} \left(\frac{2L}{\pi} \sin \frac{\pi L'}{2L} \right) \exp \left(-\frac{D\pi^2}{4L^2} t \right) \quad (7.9)$$

Differentiating (7.9) with respect to x and evaluating the derivative at the stream (i.e., $x = L$) we have the excess discharge

$$q_{ex} = -KA \left. \frac{\partial h}{\partial x} \right|_{x=L} \approx \frac{KAQ_o}{LS_s} \sin \frac{\pi L'}{2L} \exp \left(-\frac{D\pi^2}{4L^2} t \right), \quad (7.10)$$

where A is the cross-sectional area of the aquifer. Representing the amount of recharge to the aquifer by $Q_o V$ where $V = AL'$ and using $D = K/S_s$, we may rewrite (7.9) as

$$q_{ex} = \frac{DVQ_o}{L^2(L'/L)} \sin \frac{\pi L'}{2L} \exp \left(-\frac{D\pi^2}{4L^2} t \right) \quad (7.11)$$

Assuming that the coseismic recharge is eventually discharged as excess stream flow, the amount of excess discharge may then be obtained from the amount of coseismic recharge, i.e., VQ_o in (7.11). Notice that the parameter D/L^2 in the above equation may be calculated from the post-seismic baseflow recession constant listed in Table 7.1. We may then use Eq. (7.11) to fit the streamflow data, with VQ_o and the ratio L'/L being the unknown fitting parameters. Given $D/L^2 = 2.4 \times 10^{-7} s^{-1}$ (Table 7.1) for the post-seismic discharge at stream gauge H032 (see Fig. 7.13 for location), an excellent fit to the data is obtained with $VQ_o = 0.14 \text{ km}^3$ and $L'/L = 0.8$. The latter is consistent with the fact that the stream gauge H032 is located in the foothills where the flood plain is narrow and the station is close to the water divide (i.e., $x = 0$). Using the values of c or τ from Table 7.1 and fitting the stream flow data, Wang et al. (2004a) obtained the amount of excess flow at each stream gauge, as listed in Table 7.2. Summing the excess discharges in the two stream systems (H025 and H058), they estimated a total excess discharge of 0.7–0.8 km^3 from the west-central Taiwan foothills after the Chi-Chi earthquake.

Figure 7.16 shows another case where Sespe Creek, southern California, responded to the 1952 M7.5 Kern County earthquake located 63 km away from the center of the drainage basin. Again, the vertical recharge model Eq. (7.11) predicts an excess discharge that fits the observed postseismic discharge well (baseflow has been added back to the calculated excess discharge). Here the peak discharge occurs 9–10 days after the earthquake, even though the discharge began to increase coseismically. The difference in rise time from that in Fig. 7.15 (~2 days) reflects the differences in the distance between the stream gauge and the location of the coseismic recharge as well as the aquifer diffusivity.

Table 7.2 Estimated excess discharge in some streams after the Chi-Chi earthquake

Streams	Stream gauges	Total excess discharge (km ³)
<i>Wushi system</i>		
Wushi	H025	0.21
Baikang	H032	0.14
Nankang	H037	0.10
Wushi	H042	0.23
<i>Choshui system</i>		
Choshui	H057	0.56
Choshui	H058	0.55
Choshui	H063	0.44

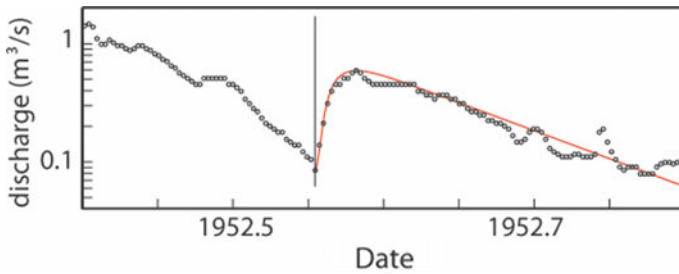


Fig. 7.16 Response of Sespe Creek, CA to the 1952 M7.5 Kern County earthquake. Daily discharge measurements collected and provided by the US Geological Survey are shown with circles. Curve is solution for the excess flow with $L'/L = 0.4$ added to the baseflow, to recover the entire hydrograph. Vertical line shows the time of the earthquake. There was no precipitation during the entire time interval shown in this graph (modified from Manga et al. 2003)

The 2010 M8.8 Maule earthquake in Chile triggered regional streamflow responses across Chile’s diverse topographic and hydro-climatic gradients. Mohr et al. (2017) analyzed the stream response and reported that out of 85 responding streams, 78 showed increased flow. Using the methods discussed in this section, they estimated the total amount of excess discharge to be $\sim 1.1 \text{ km}^3$, which is the largest reported to date. Other estimates include $0.7\text{--}0.8 \text{ km}^3$ after the 1999 M7.5 Chi-Chi earthquake (Wang et al. 2004a), 0.5 km^3 after the 1959 M7.5 Hebgen Lake earthquake (Muir-Wood and King 1993), 0.3 km^3 after the 1983 M7.3 Borah Peak earthquake (Muir-Wood and King 1993), 0.01 km^3 after the 1989 M6.9 Loma Prieta earthquake (Rojstaczer et al. 1995), and 10^6 m^3 after the 2014 M6.0 South Napa earthquake (Wang and Manga 2015).

7.4.3 Constraints From Multiple Stream Gauges

The extensive network of stream gauges near the epicenter of the Chi-Chi earthquake (Fig. 7.13) provides another constraint to test suggested hypotheses. Among the three gauged stream systems, two (Choshui Stream and the Wushi Stream) have many tributaries in the mountains, but the third (Peikang Stream) originates on the western edge of the frontal thrust (Fig. 7.13) and does not have any mountain tributaries.

After the Chi-Chi earthquake, all the tributaries in the mountains showed large postseismic streamflow increases (Table 7.2). On the alluvial fan, the Choshui Stream and the Wushi Stream, both with tributaries in the mountains, also showed large increases in streamflow, but comparison between the excess discharge documented at Gauge H057 and H058 (Table 7.2) shows that the discharge increase in the proximal area (H057) of the Choshui alluvial fan was the same as that in the distal area (H058) of the fan, suggesting that there was relatively little contribution of water from undrained consolidation or liquefaction of the sediments on the fan. In contrast, the Peikang Stream system, which does not have tributaries in the mountainous area, did not show any noticeable postseismic streamflow increases. We thus conclude that the excess discharge after the Chi-Chi earthquake originated mostly from the mountains where groundwater stored at high elevations was released by earthquake-enhanced vertical permeability, and any contribution from coseismic consolidation and liquefaction in the floodplain (alluvial fan) must have been volumetrically insignificant.

7.4.4 Constraints From the Threshold Seismic Energy

As for the case of coseismic change of groundwater level, most of the coseismic changes of stream discharge have been documented together with the earthquake magnitude and the epicentral distances. Figure 7.17 shows a compilation of the occurrences of coseismic change of stream discharge, plotted on a distance versus magnitude diagram. Also plotted as a metric are lines of constant seismic energy density (Eq. 6.10). Figure 7.17 shows that the seismic energy density of 0.1 J/m^3 , which concurs with the liquefaction limit (Chap. 8), also delimits the occurrence of coseismic changes of stream discharge.

Figure 7.17 shows the relationship between earthquake magnitude and distance between the epicenter and the center of the gauged basin for streams that responded to earthquakes. Also shown for reference is the liquefaction limit suggested by Papadopoulos and Lefkopoulos (1993), i.e., the maximum distance over which liquefaction was then reported. The coincidence of the liquefaction limit suggested by Papadopoulos and Lefkopoulos (1993) and the limit for the occurrence of coseismic streamflow increase (Fig. 7.17) is suggestive, though the empirical bound proposed by Papadopoulos and Lefkopoulos (1993) has been outdated by more recent compilation of liquefaction occurrences (Fig. 11.8). Furthermore, Montgomery et al. (2003)

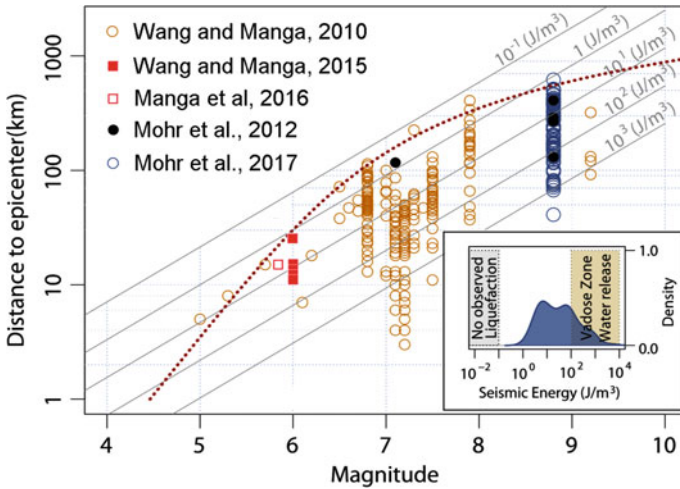


Fig. 7.17 Seismically triggered streamflow changes (circles and squares) as a function of earthquake magnitude and distance from epicenter, plotted together with contours of constant seismic energy density (grey lines; Eq. 6.10) (modified from Mohr et al. 2017). Brown circles are data from a compilation of global data (Wang and Manga 2010); solid red squares are data from the 2014 Mw6.0 South Napa earthquake; open red square is data for the Mw5.8 Pawnee earthquake in Oklahoma; black circles are data from the Maule earthquake, and the M7.1 2011 Araucania aftershock in Chilean headwater catchments; blue circles are data from Chile in response to the Maule earthquake. Brown dashed line is an empirical bound for observed liquefaction (Papadopoulos and Lefkopoulos 1993). Inset shows the histogram of responded streams plotted as a function of the estimated seismic energy density in the Chilean catchments after the Maule earthquake (Mohr et al. 2017) and the energy domains for liquefaction (Wang and Manga 2010) and for the release of vadose zone water in nearly saturated sandy soils (Mohr et al. 2015)

searched for a field association between liquefaction and increased streamflow after the 2001 M6.8 Nisqually, WA, earthquake, but found none.

7.4.5 Constraints from Laboratory Experiment

As discussed in Sect. 6.4.1, Breen et al. (2020) carried out laboratory experiments to test the models of consolidation and of water released from unsaturated soils for the coseismic increase in groundwater level and stream discharge. The result of the experiments showed that both mechanisms can explain the observation. These mechanisms are particularly useful to explain an increase in discharge in flat areas away from mountains, such as that after the 2016 Mw5.8 Pawnee earthquake, Oklahoma (Manga et al. 2016), where no other sources for the extra water are apparent. This point serves as a reminder that earthquakes may activate multiple mechanisms, but often only the dominant mechanism is revealed by observation and analysis. Thus, the mechanisms of undrained consolidation and releasing water from the vadose

zone may become important in flat areas like Oklahoma where other competing mechanisms are absent.

7.4.6 Constraints from Chemical Composition of the Excess Flow

Rojstaczer et al. (1995) argued that, for the elastic strain model of Muir-Wood and King (1993) to explain the increased discharge after earthquakes, a large portion of the deep crust needs to be involved in order to account for the extra water in the increased streamflow. The process would require not only a characteristic time far exceeding that observed in the earthquake-induced stream discharge but also would impart a distinct chemical signature in the discharged water from the deep crust. Following the 1989 Loma Prieta earthquake, Rojstaczer and Wolf (1992) collected water samples from streams near the epicenter and analyzed their chemical composition. They found that, while the stream chemistry showed a marked post-seismic increase in overall ionic strength, the overall proportions of the major ions were nearly the same as those before the earthquake; they argued that these changes were derived from groundwater released from the surrounding highlands instead of from the deep crust.

The hypothesis may also be constrained from the isotopic composition of the post-seismic increased flows. This is because the isotopic composition of rocks is significantly different from that of meteoric water; deep water–rock reactions would thus impart a distinct isotopic signature in the released groundwater. This prediction has been contradicted by several studies of the changes in groundwater composition after earthquakes (e.g., Claesson et al. 2004, 2007; Manga and Rowland 2009; Wang and Manga 2015; Hosono et al. 2020). Detailed discussion on this topic, however, is deferred to Chap. 9 where we focus on the earthquake-induced changes of groundwater composition.

7.5 Streamflow Changes in Hydrothermal Areas

Within 15 min. of the 22 December 2003 M6.5 San Simeon earthquake in central California, two stream gauges registered increased stream discharge, one along the Salinas River near the town of Paso Robles and the other along the Lopez Creek near the town of Arroyo Grande (Fig. 7.18), both known for their hot springs. As explained next, these streamflow increases can be explained by the coseismic recharge model introduced earlier, but apparently driven by the excess pore pressure in a geothermal reservoir, and are thus entirely different from those discussed earlier which were driven by gravitational potential.

Some background information about the local geology and climate may be required to better understand the different responses of these streams. Active tectonics

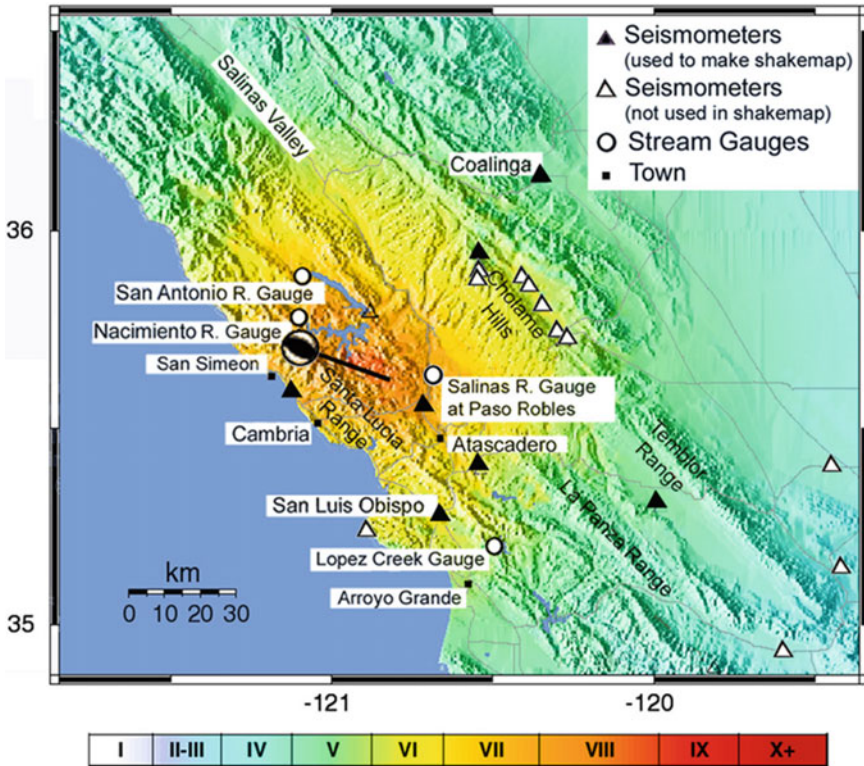


Fig. 7.18 Map showing the intensity of ground shaking in the 22 December 2003 M 6.5 San Simeon earthquake. Focal mechanism of the earthquake is taken from Harvard CMT Catalog. Circles show locations of stream gauges and triangles show locations of seismometers. Bold line shows the ruptured fault. The Salinas River flows NW through town of Paso Robles and the Salinas Valley (from USGS website)

since the late Tertiary has repeatedly faulted and uplifted the Coast Ranges of California. The climate of the area is semiarid, with most of the annual 250–330 mm precipitation occurring during the winter. A growing population and increased urbanization and agriculture has caused basin-wide decline of the groundwater level during the past several decades. As a result, the streambed of the Salinas River, with a flood plain ~100 m wide through the Paso Robles Basin, is usually dry except during rainy season, and was dry before the San Simeon earthquake. Drilling at Paso Robles encountered a hydrothermal reservoir at a depth of ~100 m. On the other hand, no hot springs are known in the nearby valleys of the San Antonio River or the Nacimiento River.

The epicenter of the San Simeon earthquake occurred 11 km NE of the town of San Simeon and 39 km WNW of Paso Robles. Rupture during the earthquake shows a strong ESE directivity (Fig. 7.18). Four new hot springs appeared after the earthquake on the two sides of the Salinas River (Fig. 7.19) near the town of Paso

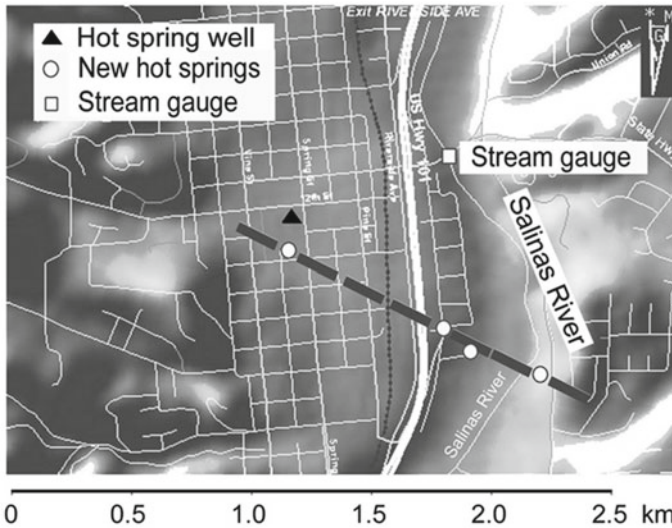


Fig. 7.19 Map of Paso Robles showing locations of the stream gauge and four new hot springs that formed after the earthquake. Note that the four new hot springs lie along a straight line that is parallel to the ruptured fault shown in Fig. 7.17. This line intersects Salinas River ~ 1 km upstream of the stream gauge. The location of a hot spring well, established long before the earthquake, is marked by a black triangle (from Wang et al. 2004b)

Robles. These new hot springs occurred along a straight line striking WNW, parallel to the earthquake rupture (Fig. 7.19) and crossing the Salinas River ~ 1 km upstream of the local stream gauge (Fig. 7.19). The well-head pressure at a hot spring well (Fig. 7.19) in Paso Robles was steady before the earthquake, but decreased from 0.33 to ~ 0.2 MPa within 2 days after the earthquake.

Recession analysis of the postseismic stream discharge in the Salinas River and Lopez Creek yields a characteristic time of ~ 40 min, suggesting that the sources of the extra water were close to the surface. However, there was no surface water source in the Paso Robles Basin and any surface water would have to be supplied from distant mountains, which is contradicted by the short characteristic time from the recession analysis. Thus, as suggested by the appearance of new hot springs in the area (Fig. 7.19), Wang et al. (2004b) proposed that the source for the coseismic increase of discharge in the two streams was a subsurface hydrothermal reservoir (Fig. 7.20b) that was sealed above by an impermeable layer (Fig. 7.20c). The seal was ruptured by the earthquake (Fig. 7.20d) and the hydrothermal water erupted to the surface to form the new hot springs and to recharge the stream. An ideal test of this hypothesis would have been a chemical analysis of the increased flow. Unfortunately, the duration of the extra discharge was short and precipitation in the area started one day after the earthquake, which made such analysis unattainable. Wang et al. (2004b) supported the conceptual model with a simulation. The excess discharge based on this model may be simulated using Eq. (7.11). The simulated result, shown with the curve

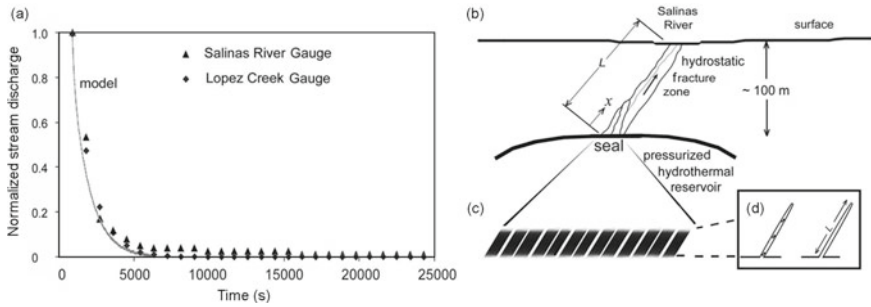


Fig. 7.20 **a** Normalized stream gauge data (triangles and diamonds) for the streamflow changes following the 2003 M 6.5 San Simeon earthquake, California. Curve shows the model simulation of the observed hydrographs. **b** Cartoon of the model proposed to explain the hour-long increase in streamflow. Rupturing of the seal of hydrothermal reservoir leads to expulsion of fluid into fracture zone. **c** Enlarged cartoon showing the seal with cracks over the geothermal reservoir. **d** Clogged crack and cleared crack; clearing of a clogged crack during the earthquake significantly increases its permeability and effective length (modified from Wang et al. 2004b)

in Fig. 7.20a, fits the observed postseismic discharge (triangles and diamonds). The estimated excess discharge after this earthquake ranged from 10^2 to 10^3 m^3 , orders of magnitude smaller than the examples mentioned in Sect. 7.4.2.

Abrupt increases in streamflow and hot spring discharge after earthquakes were also reported in other hydrothermal areas such as in the Long Valley, California (Sorey and Clark 1981), in the Napa Valley, California (Wang and Manga 2015), and in Japan (Mogi et al. 1989), suggesting that this type of hydrologic response may be common in hydrothermal areas. Such discharge may also cause changes in the temperature and the chemical composition of the streams and hot springs, as reported by Mogi et al. (1989) and Hosono et al. (2018), among others, and are discussed further in Chaps. 8 and 9.

In convergent tectonic regions, large volumes of pore water may be locked in the subducted sediments (Townend 1997) or beneath volcanic areas (Hartmann 2006). Sealing may be enacted partly by the presence of low-permeability mud, partly by precipitation of minerals in fractures and pores, and partly by the prevailing compressional stresses in such tectonic settings (Sibson and Rowland 2003). Earthquakes may rupture the seals and allow pressurized pore water to erupt to the surface and recharge streams. Husen and Kissling (2001) suggest that postseismic changes in the ratio of P- and S-wave velocities above the subducting Nazca Plate reflect fluid migration into the overlying plate following the rupture of permeability barriers. This process may explain the time variations in submarine fluid discharge at convergent margins (Carson and Sreaton 1998). Episodes of high discharge are correlated with seismic activity having features similar to tremor and are not correlated with large regional earthquakes (Brown et al. 2005).

7.6 Concluding Remarks

The different hypotheses discussed in this chapter imply different crustal processes and different water–rock interactions during an earthquake cycle. In most instances, these hypotheses are under-constrained. A reasonable approach is to test the different hypotheses against cases in which abundant and accurate data are documented such as the 1999 Chi-Chi earthquake in Taiwan and the 2016 Kumamoto earthquake in Japan. We may note that a single explanation need not apply to all cases of coseismic increased streamflow, and that multiple mechanisms may be activated by an earthquake.

References

- Angelier J, Chu HT, Lee JC et al (2000) Geologic knowledge and seismic risk mitigation: insight from the Chi-Chi earthquake. *Chi-Chi earthquake (1999) Taiwan*. In: Lo CH, Liao WI (eds) *Proceedings of international workshop on annual commemoration of Chi-Chi earthquake*, Science Aspect, pp 13–24
- Breen S, Zhang Z, Wang CY (2020) Shaking water out of sands: an experimental study. *Water Resour Res* 56: e2020WR028153
- Brodsky EE, Roeloffs E, Woodcock D et al (2003) A mechanism for sustained groundwater pressure changes induced by distant earthquakes. *J Geophys Res* 108(B8):2390. <https://doi.org/10.1029/2002JB002321>
- Brown KM, Tryon MD, DeShon HR (2005) Correlated transient fluid pulsing and seismic tremor in the Costa Rica subduction zone. *Earth Planet Sci Lett* 238:189–203
- Carson B, Sreaton EJ (1998) Fluid flow in accretionary prisms: evidence for focused, time-variable discharge. *Rev Geophys* 36:329–352
- Charmoille A, Fabbri O, Mudry J (2005) Post-seismic permeability change in a shallow fractured aquifer following a ML 5.1 earthquake (Fourbanne karst aquifer, Jura outermost thrust unit, eastern France). *Geophys Res Lett* 32:L18406. <https://doi.org/10.1029/2005GL023859>
- Claesson L, Skelton A, Graham C, Dietl C, Mörth M, Torssander P, Kockum I (2004) Hydrogeochemical changes before and after a major earthquake. *Geology* 32:641–644
- Claesson L, Skelton A, Graham C et al (2007) The timescale and mechanisms of fault sealing and water-rock interaction after an earthquake. *Geofluids* 7:427–440
- Elkhoury JE, Brodsky EE, Agnew DC (2006) Seismic waves increase permeability. *Nature* 411:1135–1138
- Fetter CW (2001) *Applied hydrogeology*, 4th edn. Prentice Hall, New Jersey
- Fleeger GM, Goode DJ, Buckwalter TF et al (1999) Hydrologic effects of the Pymatuning earthquake of September 25, 1998, in northwestern Pennsylvania, US Geological Survey Water-Resources Investigation Reports 99-4170
- Hartmann J (2006) Long-term seismotectonic influence on the hydrochemical composition of a spring located at Koryaksky-Volcano, Kamchatka: deduced from aggregated earthquake information. *Int J Earth Sci* 95:649–664. <https://doi.org/10.1007/s00531-005-0055-5>
- Hosono T, Hartmann J, Louvat P et al (2018) Earthquake-induced structural deformations enhance long-term solute fluxes from active volcanic systems. *Sci Rep* 8:14809. <https://doi.org/10.1038/s41598-018-32735-1>

- Hosono T, Yamada C, Shibata T et al (2019) Coseismic groundwater drawdown along crustal ruptures during the 2016 Mw 7.0 Kumamoto earthquake. *Water Resour Res* 55:5891–5903. <https://doi.org/10.1029/2019WR024871>
- Hosono T, Yamada C, Manga M, Wang CY, Tanimizu M (2020) Stable isotopes show that earthquakes enhance permeability and release water from mountains. *Nat Commun* 11:1–9
- Husen S, Kissling E (2001) Postseismic fluid flow after the large subduction earthquake of Antofagasta, Chile. *Geology* 29:847–850
- Ichiyanagi K, Imatsu M, Ide K et al (2020) Effects on fluvial discharges of the 2016 Kumamoto earthquakes, Japan. *J Hydrol* 583:124600. <https://doi.org/10.1016/j.jhydrol.2020.124600>
- Kagabu M, Ide K, Hosono T et al (2020) Describing coseismic groundwater level rise using tank model in volcanic aquifers, Kumamoto, southern Japan. *J Hydrol* 582:124464. <https://doi.org/10.1016/j.jhydrol.2019.124464>
- Koizumi N, Minote S, Tanaka T et al (2019) Hydrological changes after the 2016 Kumamoto earthquake, Japan. *Earth Planet Space* 71:128. <https://doi.org/10.1186/s40623-019-1110-y>
- Lee CT, Kelson KI, Kang KH (2000) Hanging wall deformation and its effect on buildings and structures as learned from the Chelungpu faulting in the 1999 Chi-Chi Taiwan earthquake. In: Liao WI (ed) Lo CH. Proceedings of international workshop on annual commemoration of Chi-Chi earthquake, Science Aspect, pp 93–104
- Lee JC, Chu HT, Angelier J et al (2002) Geometry and structure of northern rupture surface ruptures of the 1999 $M_w = 7.6$ Chi-Chi Taiwan earthquake: influence from inherited fold belt structures. *J Struct Geol* 24:173–192
- Lin WY (2000) Unstable groundwater supply after the big earthquake, Taiwan. *United Daily* (in Chinese)
- Manga M (2001) Origin of postseismic streamflow changes inferred from baseflow recession and magnitude-distance relation. *Geophys Res Lett* 28:2133–2136
- Manga M, Brodsky EE, Boone M (2003) Response of streamflow to multiple earthquakes and implications for the origin of postseismic discharge changes. *Geophys Res Lett* 30(5):1214. <https://doi.org/10.1029/2002GL016618>
- Manga M, Rowland JC (2009) Response of alum rock springs to the October 30, 2007 earthquake and implication for increased discharge after earthquakes. *Geofluids* 9:237–250
- Manga M, Wang CY, Shirzaei M (2016) Increased stream discharge after the 3 September 2016 Mw 5.8 Pawnee, Oklahoma earthquake. *Geophys Res Lett* 43:11588–11594. <https://doi.org/10.1002/2016GL071268>
- Mogi K, Mochizuki H, Kurokawa Y (1989) Temperature changes in an artesian spring at Usami in the Izu Peninsula (Japan) and their relation to earthquakes. *Tectonophysics* 159:95–108
- Mohr CH, Manga M, Wang CY, Kirchner JW, Bronstert A (2015) Shaking water out of soil. *Geology* 43:207–210. <https://doi.org/10.1130/G36261.1>
- Mohr CH, Manga M, Wang CY, Korup O (2017) Regional changes in streamflow after a megathrust earthquake. *Earth Planet Sci Lett* 458:418–428. <https://doi.org/10.1016/j.epsl.2016.11.013>
- Montgomery DR, Manga M (2003) Streamflow and water well responses to earthquakes. *Science* 300:2047–2049
- Montgomery DR, Greenberg HM, Smith DT (2003) Streamflow response to the Nisqually earthquake. *Earth Planet Sci Lett* 209:19–28
- Muir-Wood R, King GCP (1993) Hydrological signatures of earthquake strain. *J Geophys Res* 98:22035–22068
- Papadopoulos GA, Lefkopoulos G (1993) Magnitude–distance relations for liquefaction in soil from earthquakes. *Bull Seismol Soc Am* 83:925–938
- Roeloffs EA (1998) Persistent water level changes in a well near Parkfield, California, due to local and distant earthquakes. *J Geophys Res* 103:869–889
- Rojstaczer S, Wolf S (1992) Permeability changes associated with large earthquakes: an example from Loma Prieta, California, 10/17/89 earthquake. *Geology* 20:211–214
- Rojstaczer S, Wolf S, Michel R (1995) Permeability enhancement in the shallow crust as a cause of earthquake-induced hydrological changes. *Nature* 373:237–239

- Sato T, Sakai R, Furuya K et al (2000) Coseismic spring flow changes associated with the 1995 Kobe earthquake. *Geophys Res Lett* 27:1219–1222
- Sibson RH, Rowland JV (2003) Stress, fluid pressure and structural permeability in seismogenic crust, North Island, New Zealand. *Geophys J Int* 154:584–594
- Sorey ML, Clark MD (1981) Changes in the discharge characteristics of thermal springs and fumaroles in the Long Valley caldera, California, resulting from earthquakes on May 25–27, 1980. US Geological Survey Open-File Report 81–203
- Tokunaga T (1999) Modeling of earthquake induced hydrological changes and possible permeability enhancement due to the 17 January 1995 Kobe earthquake, Japan. *J Hydrol* 223:221–229
- Townend J (1997) Subducting a sponge; minimum estimates of the fluid budget of the Hikurangi Margin accretionary prism. *Geol Soc NZ Newslett* 112:14–16
- Wakita H (1975) Water wells as possible indicators of tectonic strain. *Science* 189:553–555
- Wang CY (2007) Liquefaction beyond the near field. *Seismo Res Lett* 78: 512–517
- Wang CY, Cheng LH, Chin CV et al (2001) Coseismic hydrologic response of an alluvial fan to the 1999 Chi-Chi earthquake (1999), Taiwan. *Geology* 29:831–834
- Wang CY, Wang CH, Manga M (2004a) Coseismic release of water from mountains: evidence from the 1999 ($M_w = 7.5$) Chi-Chi, Taiwan, earthquake. *Geology* 32:769–772
- Wang CY, Manga M, Dreger D (2004b) Streamflow increase due to rupturing of hydrothermal reservoirs: evidence from the 2003 San Simeon earthquake (2003), California, earthquake. *Geophys Res Lett* 31:L10502. <https://doi.org/10.1029/2004GL020124>
- Wang CY, Manga M (2010) Hydrologic responses to earthquakes and a general metric. *Geofluids* 10:206–216
- Wang CY, Liao X, Wang LP (2016) Large earthquakes create vertical permeability by breaching aquitards. *Water Resour Res* 52:5923–5937. <https://doi.org/10.1002/2016WR018893>
- Wang CY, Manga M (2015) New streams and springs after the 2014 Mw 6.0 South Napa earthquake. *Nature Communications* 6:7597. <https://doi.org/10.1038/ncomms8597>
- Water Resource Bureau (2000) Report and analysis of changes in surface and ground water due to the 9/21 Chi-Chi Earthquake: Taipei. Water Resource Bureau, Ministry of Economic Affairs, Taiwan (in Chinese), 37 p with 4 appendices
- Yan HR (2001) Water problems in the Yuanlin Mountains: Changes in groundwater after the Chi-Chi earthquake (1999), Taiwan. *Chinese Daily* (in Chinese)

Open Access This chapter is licensed under the terms of the Creative Commons Attribution 4.0 International License (<http://creativecommons.org/licenses/by/4.0/>), which permits use, sharing, adaptation, distribution and reproduction in any medium or format, as long as you give appropriate credit to the original author(s) and the source, provide a link to the Creative Commons license and indicate if changes were made.

The images or other third party material in this chapter are included in the chapter's Creative Commons license, unless indicated otherwise in a credit line to the material. If material is not included in the chapter's Creative Commons license and your intended use is not permitted by statutory regulation or exceeds the permitted use, you will need to obtain permission directly from the copyright holder.



Chapter 8

Groundwater Temperature



Abstract Changes of temperature in response to earthquakes have long been documented and, in the case where systematic patterns of change can be discerned, may reveal important hydrogeologic processes. Progress in our understanding of these processes, however, has been slow, largely because systematic measurements are relatively scarce. In this chapter we review some cases where earthquake-induced changes of groundwater temperature were documented and interpreted. More importantly, we show that most interpretations are under-constrained and accurate explanation of the measured changes is often difficult. In order to better constrain the interpretation, co-located measurement of groundwater flow from conductive fractures or formations intersecting the wells is needed to interpret temperature measurements. An often neglected mechanism is turbulent mixing of water in wells, which may occur frequently during earthquakes because the water column in a well at thermal equilibrium with the local geotherm is usually in a state of mechanical disequilibrium.

8.1 Introduction

Changes of temperature in response to earthquakes have been documented in many wells over the past several decades (e.g., Ma et al. 1990). Such changes may be expected, not only because earthquake-induced groundwater flow is effective in transporting heat, but because significant amounts of frictional heat could be generated along the ruptured fault, which may raise groundwater temperature. Progress in our understanding of these processes, however, has been slow, largely because relevant quantitative data are relatively scarce. Instrumental measurements of earthquake-induced temperature changes started in the late twentieth century and continuous recording of temperature has only become recently available. In the next section (Sect. 8.2), we review some recent studies of groundwater temperature responses to earthquakes, starting with the response to the 2008 Mw7.9 Wenchuan earthquake across the Chinese continent (He and Singh 2020), followed by the response to the 2016 Mw7.0 Kumamoto earthquake in central Kyushu, Japan (Miyakoshi et al.

2020), and ending with the response to the 2016 Mw5.8 Gyeongju earthquake in a well in SW South Korea (Lee et al. 2020).

While the earthquake-induced changes of groundwater temperature may be difficult to interpret in general, systematic patterns of the changes may be discerned and interpretation of the patterns may be made if the flow and the geometry of the drainage basin is relatively simple, the hydrogeology understood, and the data abundant. We devote Sect. 8.3 to discuss how regional patterns in these changes may be discerned and interpreted to better understand earthquake-related hydrogeological processes.

In Sect. 8.4 we review the studies of temperature changes in springs during earthquakes. One such study focuses on some cold springs in central Kyushu, Japan, before and after the 2016 Mw7.9 Kumamoto earthquake, Japan. The other case is a classic study of temperature changes in a hot springs in central Honshu in response to remote earthquakes (Mogi et al. 1989).

In Sect. 8.5 we review studies of temperature changes beneath the seafloor. One is the study of the temperature change on a ruptured fault beneath the Japan Trench, which ruptured during the 2011 Mw9.0 Tohoku-Oki earthquake off the Pacific coast of Japan (Fulton et al. 2013; Fulton and Brodsky 2016). The others are temperature measurements near the Juan de Fuca ridge off the Pacific coast of western US (Johnson et al. 2000; Davis et al. 2001; Dziak et al. 2003).

An important ambiguity in our understanding of earthquake-induced change of groundwater temperature originates from the uncertainty in the interpretation of the groundwater data. Most interpretations of such changes (e.g., He and Singh 2020; Miyakoshi et al. 2020; Lee et al. 2020) invoke the mechanism of enhanced permeability during earthquakes (e.g., Manga et al. 2012). A less well known, but potentially common, occurrence is the turbulent mixing of water in wellbores (Shi et al. 2007), which has become increasingly invoked in debates about the mechanisms of groundwater temperature change during earthquakes (e.g., Sections 8.2.3, 8.5.1, 8.5.2). We discuss this occurrence together with its observational and physical basis in Sect. 8.6. We also make recommendations in the concluding remarks for future research on earthquake-induced temperature changes.

8.2 Land Measurements

8.2.1 *China*

A comprehensive study was made of the response of groundwater temperature over the Chinese continent to the 2008 Mw7.9 Wenchuan earthquake, during which the groundwater temperature in numerous wells on the Chinese mainland showed changes (He and Singh 2020). Figure 8.1a shows that the spatial distribution of the coseismic change of groundwater temperature is random and does not correlate with the focal mechanism of the Wenchuan earthquake (shown by the beach-ball symbol) or the epicentral distance. Figure 8.1b shows that the response of water level to the

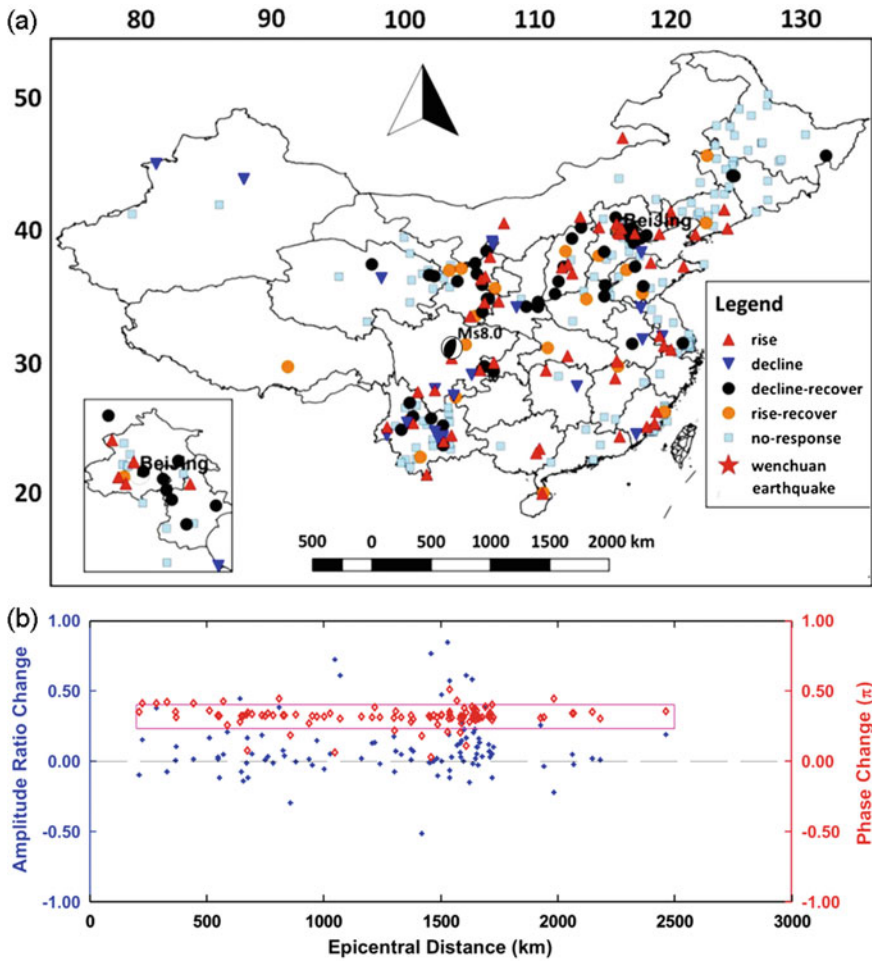


Fig. 8.1 **a** Spatial distribution of groundwater measurement wells in mainland China. Beach ball symbol shows the epicenter and the focal mechanism of the 2008 Wenchuan earthquake. The red triangles denote locations of coseismic rise of groundwater temperature, the inverted dark blue triangles denote coseismic decline of groundwater temperature, the black circles denote a coseismic decline followed by recovery, the yellow circles represent a coseismic rise followed by recovery, and the light blue squares indicate no change of the groundwater temperature. The inset window shows the spatial distribution of monitoring wells around Beijing. (from He and Singh 2020). **b** Changes of phase (red symbols, in unit of π) and amplitude ratio (blue symbols) of water level response to the M2 tide in the studied wells after the Wenchuan earthquake. Positive changes correspond to phase advance and amplitude increase, respectively (from He and Singh 2019)

M2 tide in these wells show a nearly uniform phase advance and a random change of amplitude ratio (He and Singh 2019). The phase advance of the tidal response of groundwater level after the Wenchuan earthquake (Fig. 8.1b) suggests a coseismic enhancement of the permeability in all the studied aquifers (see Chap. 5, Sect. 5.4), which in turn suggests an enhanced coseismic exchange of groundwater between the aquifer and the well. Because the relative location between the temperature gauge and the hydraulically conductive fractures/formations that intersect the well is unknown in most wells, and because the relative location may control the coseismic temperature change as explained later, the coseismic changes of groundwater temperature appear spatially random and disordered, as noted by the authors.

He and Singh (2020) identified four types of temperature changes (Fig. 8.2), i.e., sustained temperature rise after the earthquake, sustained temperature fall after the earthquake, transient coseismic fall that was followed shortly afterwards by recovery, and transient coseismic rise that was followed shortly afterwards by recovery. Here we group these responses into two categories: sustained temperature changes that continue for more than 10 days (Fig. 8.2a, b), and transient temperature changes (either transient rises or transient falls) that recover within a day (Fig. 8.2c, d). As we discuss later, these two categories of earthquake-induced changes may reflect two basically different causal mechanisms.

He and Singh (2020) also found a close association between the coseismic change of groundwater temperature and the coseismic change of groundwater level in some wells where both measurements are available (Fig. 8.3). Because temperature increases with depth, groundwater flows from a conductive fracture or aquifer into

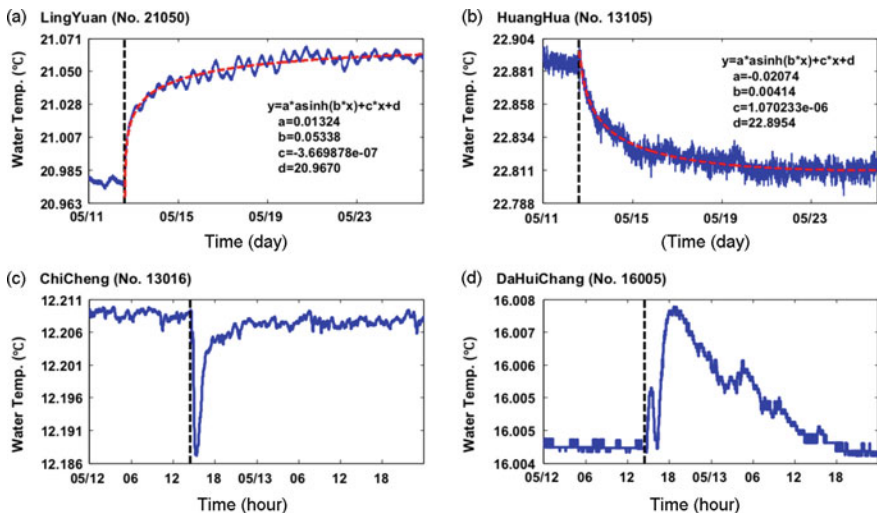


Fig. 8.2 Four types of coseismic groundwater temperature response to the Wenchuan earthquake. **a** Sustained temperature rise after the earthquake. **b** Sustained temperature fall after the earthquake. **c** Transient coseismic fall that recovers shortly afterwards. **d** Transient coseismic rise that recovers shortly afterwards (modified from He and Singh 2020)

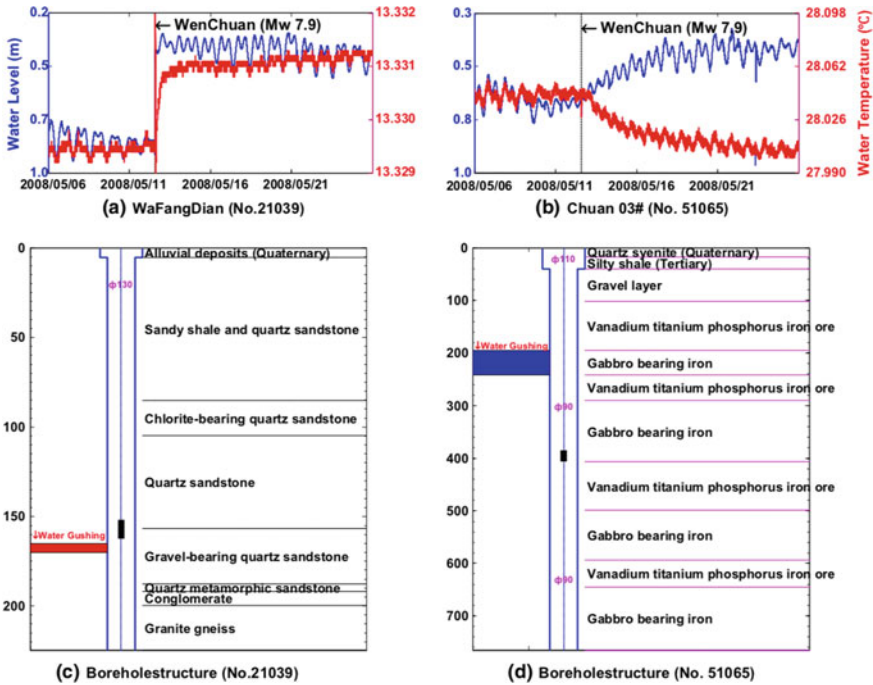


Fig. 8.3 **a** Sustained coseismic response of groundwater level and temperature in the same direction. **b** Sustained coseismic response of groundwater level and temperature in the opposite directions. **c** and **d** Lithology well logs of the two wells. Also shown are the relative positions of the temperature gauges (filled rectangles) and the conductive fractures (colored) in the wells (from He and Singh 2020)

the well will have a higher temperature than that at the temperature gauge if the hydraulically conductive fracture or aquifer is located deeper than the gauge, and vice versa. On the other hand, the relative locations of the temperature gauge in the well and the hydraulically conductive fracture or aquifer is unknown in most wells; thus either a temperature rise or a temperature fall is likely, which is consistent with the apparent random spatial distribution of the coseismic change of groundwater temperature after the Wenchuan earthquake (Fig. 8.1a).

While the hypothesis explains the sustained temperature changes (e.g., Fig. 8.2a, b), it may not be easily applied to explain the transient temperature changes (e.g., Fig. 8.2c, d); more discussion of the transient temperature changes is given in Sect. 8.6. Interpretation of these coseismic changes of groundwater temperature are made more challenging because of the lack of the lithology logs of the wells. Testing of different hypotheses on the causal mechanisms requires, in addition to accurate measurements of groundwater temperature and water level, accurate logs of the lithology and the locations of the conductive fractures and/or formations.

8.2.2 Japan

Miyakoshi et al. (2020) measured temperature–depth profiles in 10 wells distributed from the Aso Mountains to the lowlands after the 2016 Mw7.0 Kumamoto earthquake (Fig. 8.4), starting January 2017, nine months after the earthquake, until February 2018 when temperature stopped changing. Near the foot of the western Aso Mountain and the Takuma Plateau, groundwater temperature at depths >80 m first decreased and then increased (wells 1 and 3); at lower elevations, groundwater temperature generally showed a long-term warming. Also interesting to note is that this warming also occurs in the wells near the Suzenji fault zone (i.e., wells 6, 7 and 9) where significant groundwater drawdown over a 160 km² area was documented (Hosono et al. 2019).

The transient cooling in the well water at the foot of the Aso Caldera and the Takuma Plateau (Fig. 8.4a) was attributed to the post-seismic release of mountain groundwater (Miyakoshi et al. 2020), similar to the explanation of the post-seismic temperature decrease over the upper rim of an alluvial fan near the epicenter of the 1999 Chi-Chi earthquake (Sect. 8.3; Wang et al. 2012).

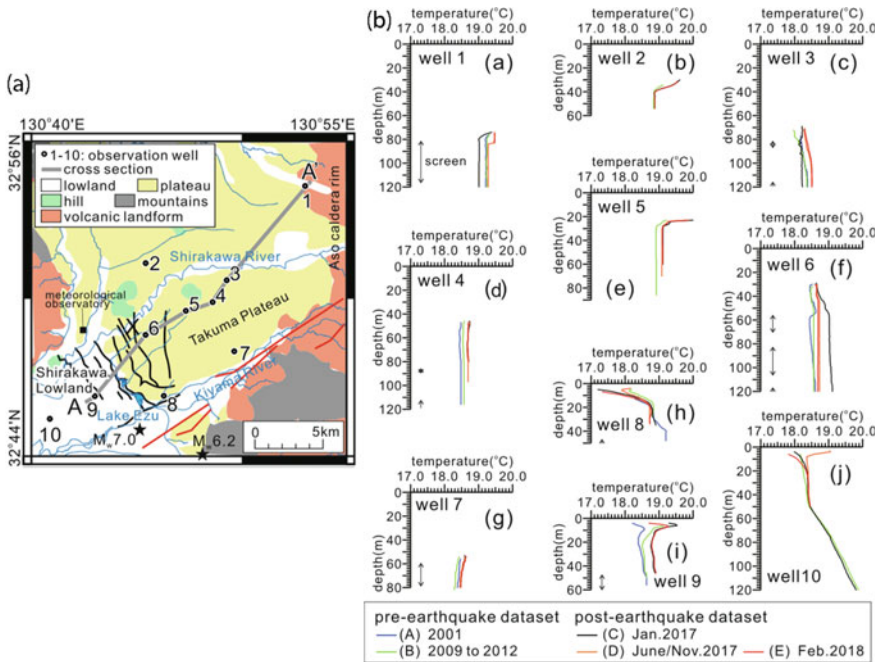


Fig. 8.4 a Map showing the study area and the distribution of wells from the western rim of the Aso Caldera (upper right) to the lowland (lower left). The NW-SE trending black lines show the location of the Suzenji fault zone. The well numbers correspond to those shown in (b). b Repeated temperature profiles in the wells shown in (a) before and after the 2016 Kumamoto earthquake (from Miyakoshi et al. 2020)

Miyakoshi et al. (2020) also proposed that the gradual warming of well water in the lowlands represents a long-term subsurface warming across the study area. An alternative interpretation of the gradual warming of groundwater in the lowland after the earthquake is enhanced basin-wide groundwater flow, as explained in Sect. 8.4, which has an upward component in the discharge area. This upward flow transports heat from greater depth, warming the groundwater at shallower depth, as explained in Sect. 8.3 (Wang et al. 2013).

8.2.3 Korea

A Mw5.8 earthquake occurred on 12 September 2016 near the city of Gyeongju, SE South Korea, the largest event in Korea recorded by modern instrumentation. Following the earthquake, changes of groundwater level, temperature and electrical conductivity were documented in a well 241 km to the west of the epicenter near the western coast of Korea (Lee et al. 2020). Temperature and electrical conductivity in this well were measured using an Eikelkamp diver (<https://diver-water-level-logger.com/diver-water-level-loggers/ctd-diver.html>) with an accuracy of ± 0.1 °C and a resolution of ± 0.01 °C; the sensor was sampled every second and was lowered into the borehole at a speed of ~ 20 cm/s (Kyoochui Ha, personal communication). Before the earthquake, the groundwater temperature above 50 m depth was sensitive to changes of surface temperature (Fig. 8.5), but below 50 m it became stable and showed a steady increase with depth, reflecting the local geothermal gradient. Following the earthquake, the groundwater temperature (red profile, Fig. 8.5) became evidently cooler below 50 m. The authors interpret this change to reflect an influx of cooler groundwater to the well through reactivated fracture paths; they also suggested that the influx of cooler groundwater was short lived because the temperature profile below 50 m recovered to the pre-earthquake profile about a month after the earthquake (black profile, Fig. 8.5).

An alternate explanation for the coseismic change of water temperature is that the water column in the well with the initial temperature is mechanically unstable and undergoes turbulent mixing when it is disturbed by the passing seismic waves, resulting in a water column more uniform in temperature (red curve in Fig. 8.5). Temperature recovered when the well water re-establishes thermal equilibrium with the wall rocks (blue curve in Fig. 8.5). Further discussion of this mechanism is given in Sect. 8.6.

8.3 Basin-Wide Changes

Groundwater flow has long been recognized as an effective means to promote heat transport across sedimentary basins (e.g., Forster and Smith 1989; Garven et al. 1993). As discussed in the last chapter, large earthquakes often release a large amount

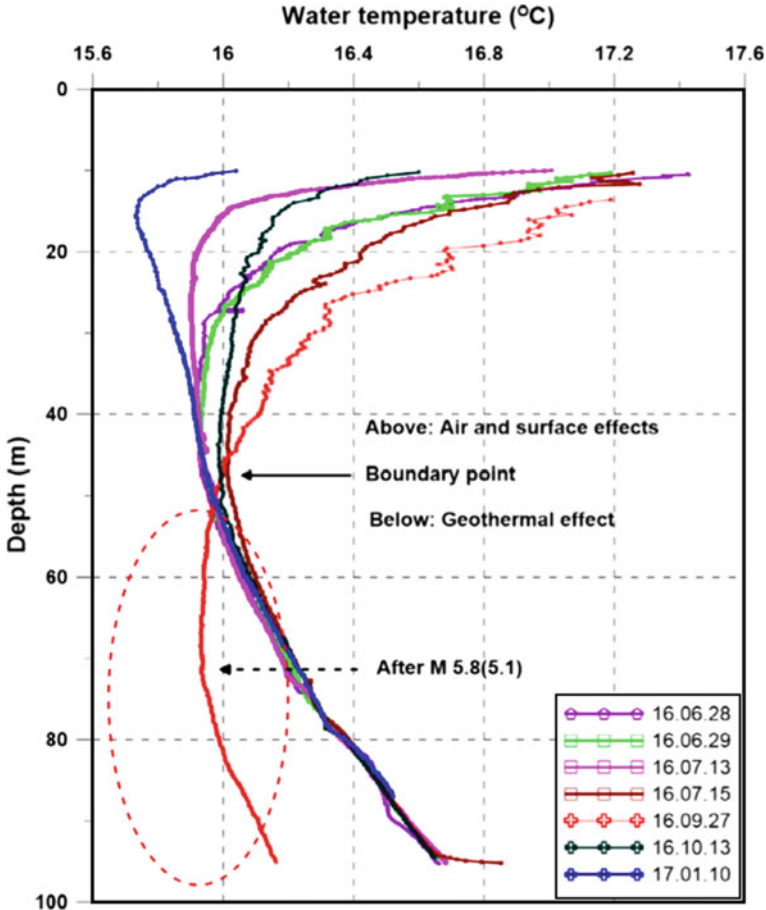


Fig. 8.5 Profiles of groundwater temperature in a well before and after the Mw5.8 Gyeongju earthquake. Dates for the profiles are shown in the legend. The dashed oval shows the lowering of the groundwater temperature after the earthquake (from Lee et al. 2020). The numbers in the legend show the time of measurement in year-month-date. For example: 16.09.27 means 2016, September 27.

of groundwater from mountains to nearby basins (e.g., Wang et al. 2004; Hosono et al. 2019). It should not be surprising that earthquakes might also cause basin wide change of groundwater temperature.

Figure 8.6 shows the epicenter of the Chi-Chi earthquake and a nearby alluvial fan on which groundwater temperature was measured in many wells before and after the earthquake. Because the geometry of this drainage basin is relatively simple and its hydrogeology is well understood through abundant borehole logging, the basin is ideal for revealing any regional pattern in the earthquake-induced temperature changes in groundwater and the causal hydrogeological processes.

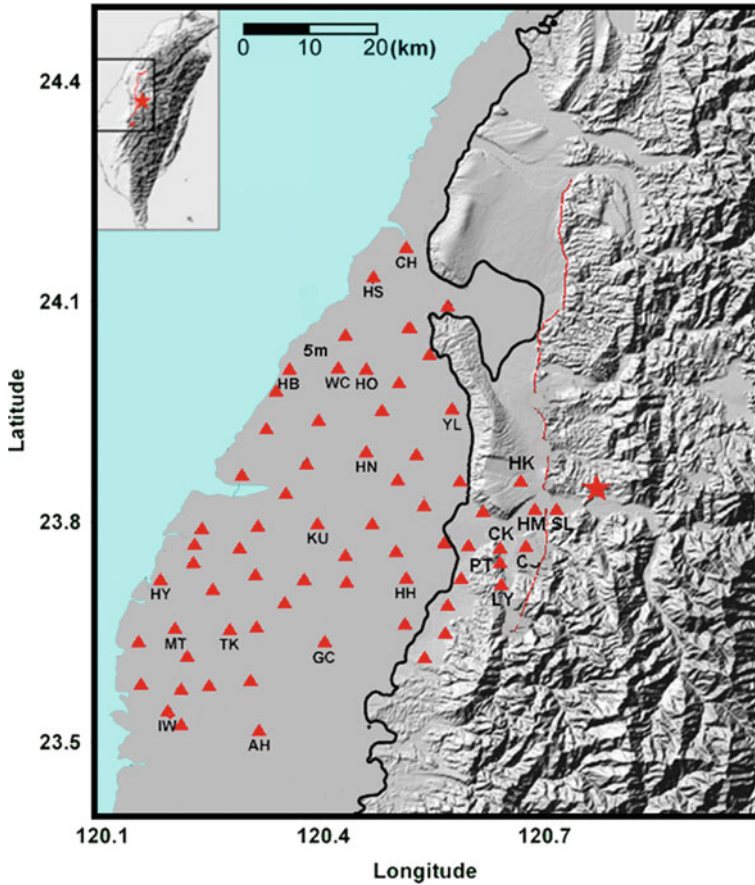


Fig. 8.6 Groundwater monitoring stations (red triangles) on an alluvial fan near the 1999 M7.6 Chi-Chi earthquake (red star) in Taiwan. Wells labeled with letters have temperature measurements before and after the 1999 Chi-Chi earthquake. Dashed curve shows the surface trace of the ruptured fault; solid black curve shows the thrust front of the Taiwan mountain belt; inset shows the location of the study area in Taiwan

Measurements were made in the wells during routine well maintenance, 7 months before and 2–3 months after the earthquake, using a temperature gauge with accuracy of ± 0.1 °C. The measured groundwater temperatures before the Chi-Chi earthquake are projected onto an east-to-west profile as a function of distance from the surface trace of the NS-trending, ruptured fault on the east of the profile to the coast on the west. Scatter in the data (Fig. 8.7a) is partly due to superposition of data from different latitudes onto a single profile. In spite of the scatter, the data show a clear trend of increasing temperature from the foothills on the east to the coast on the west, indicative of active heat transport by groundwater flow from the upper rim of the alluvial fan across the basin to the coast. Figure 8.7b shows groundwater temperatures

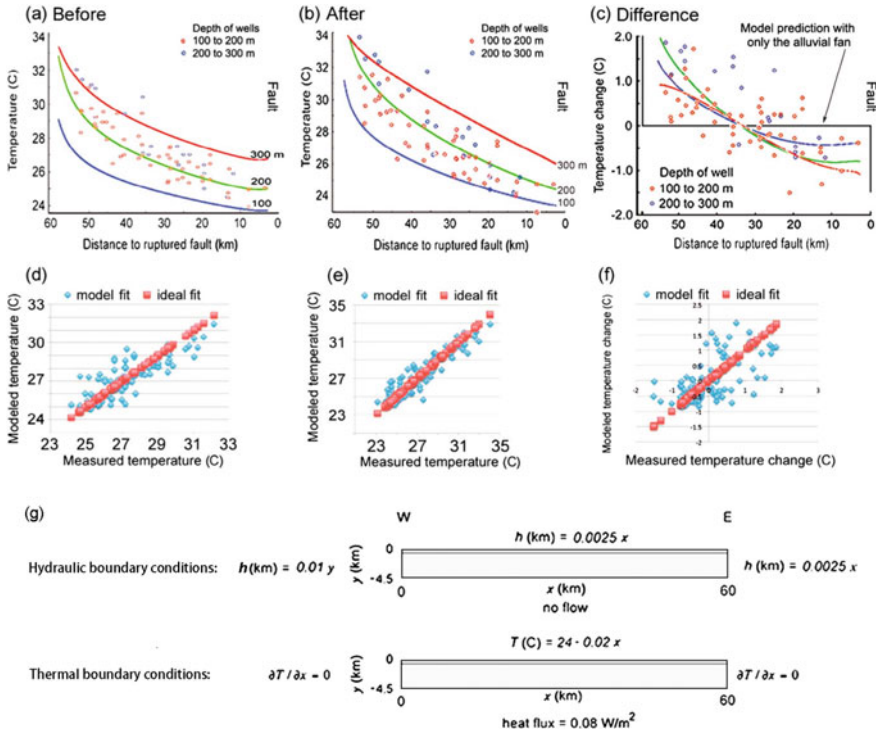


Fig. 8.7 **a** Groundwater temperature in wells on the Choshui alluvial fan ~7 months before the Chi-Chi earthquake. Circles are observed temperatures; different colors show measurements made at different depths. Note that numbering on the horizontal axis is from 60 km to 0 because distance is measured from the ruptured fault (indicated by the word “fault” on the right side of figure). **b** Groundwater temperature in the same wells 2–3 months after the earthquake. Circles are measured temperatures and curves are simulated temperatures 2–3 months after the earthquake. **c** Changes in groundwater temperature, i.e., difference between **(b)** and **(a)**. Curves of blue, green and red colors in each diagram show, respectively, simulated groundwater temperatures before the earthquake at 100, 200, and 300 m below the surface. **d** and **e** Simulated temperatures plotted against measured temperatures before and after the earthquake, respectively. **f** Differences between the simulated temperatures before and after the earthquake plotted against the differences between the measured temperatures. **g** Hydrogeology model and boundary conditions used in simulating the groundwater flow and temperatures in **(a)**, **(b)** and **(c)**. The heat flux boundary condition at the base of the model is based on measured heat flux from deep exploration wells in the same area (Hwang and Wang 1993) (from Wang et al. 2013)

in the same wells 2–3 months after the Chi-Chi earthquake. Here temperatures show the same trend as that before the earthquake but temperatures are slightly lowered near the ruptured fault and raised near the coast relative to those before the earthquake. Figure 8.7c shows the difference between Fig. 8.7a, b, i.e., the *change* of temperature after the earthquake. Despite of the scatter, the data show a clear trend from negative differences (temperature decreases) near the eastern rim of the fan near the ruptured fault to positive differences (temperature increases) near the coast on the west.

Wang et al. (2013) attributed the observed changes in groundwater temperature to a basin-wide increase of groundwater flux after the earthquake. To test this hypothesis, they used an idealized 2-dimensional model (Fig. 8.7g) that extends sub-horizontally from the ruptured fault on the east to the coast on the west, and vertically down from the surface to a depth of ~4.5 km. The model parameters are based on the existing well tests and known hydrogeology of the area. The upper 0.5 km of the model represents the Holocene alluvial deposits, and the lower 4 km represents the Plio-Pleistocene conglomerates, and the lower boundary represents the top of the impervious Miocene shale. Water properties are taken as functions of temperature to account for the temperature effects on water density and viscosity that, in turn, affect the velocity and direction of groundwater flow. As shown in Sect. 2.5.2, the differential equations that control groundwater flow and heat transport in such situation are coupled and nonlinear. Numerical procedures are required to obtain a solution. Together with reasonable material properties (e.g., Tyan et al. 1996) and boundary conditions (Fig. 8.7g), Wang et al. (2013) used a finite-element method to simulate the temperatures as shown in colored curves in Fig. 8.7a, b and c. The reasonable agreement between the simulated and measured temperatures (Fig. 8.7d, e and f) lends support to the interpretation.

Another interesting result is the simulated temperature change with the assumption that groundwater flow is restricted to the alluvial fan (black line in Fig. 8.7c). The model result is significantly different from the observation, which suggests that a substantial portion of the earthquake-induced groundwater flow occurs deep beneath the alluvial fan and that large earthquakes may enhance permeability and thus basin-wide groundwater flow to depths of several km.

8.4 Springs

8.4.1 Cold Springs

Koizumi et al. (2019) surveyed 11 springs in the region that experienced strong ground motion during the 2016 Kumamoto earthquake (Fig. 8.8a) and sampled at intervals of a few weeks to several months. Fortunately, 8 of the 11 springs were also surveyed 1 month to a few years before earthquake. The results show no clear evidence of earthquake-related change to the spring temperature (Fig. 8.8b), even though the flow rate did show coseismic changes (increases at three springs e, g and k, decreases at f and h, and no change at the rest). This led the authors to suggest that there was little contribution in the enhanced flow from hydrothermal fluids. The conclusion seems to be supported by their measurement of the chemistry of the spring water as discussed in the next chapter.

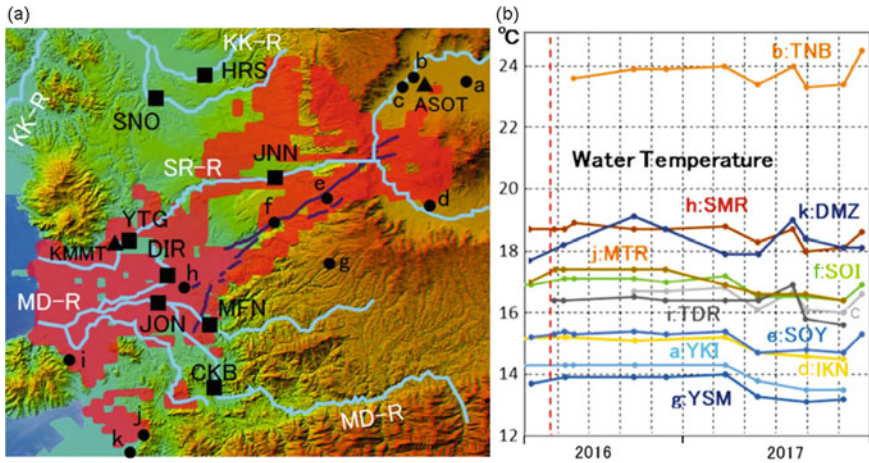


Fig. 8.8 Spring water temperature in central Kyushu. **a** Map showing the study area and the locations of the studied springs (black circles with labels). Area colored red experienced strong ground motion during the 2016 Kumamoto earthquake. **b** Time series of temperature of the studied springs in (a). No obvious change was recorded after the 2016 Kumamoto earthquake (marked by the red vertical dash line) (modified from Koizumi et al. 2019)

8.4.2 Hot Springs

One example of earthquake-induced change of hot spring temperature is from the Usami Hot Springs on the northeast coast of the Izu Peninsula in central Honshu, Japan. The term ‘hot spring’ is used following the preference by the authors (Mogi et al., 1989) even though measurements were made in a 600 m deep well installed in one of the springs. Accurate and continuous measurements of water temperature were made since 1982 (Mogi et al. 1989). Since 1985, however, the hot water in this well ceased to spout. Four temperature probes were installed in the well, but only the topmost probe’s data were reported (Mogi et al. 1989). Figure 8.9a shows that, when there are no earthquakes, the temperature of the well water falls gradually with time; at the time of earthquakes, on the other hand, temperature rises first rapidly but then gradually to reach a peak temperature. Mogi et al. (1989) interpreted the gradual decline of temperature during normal times to indicate a decrease in the amount of geothermal water in the hot spring as a result of ongoing precipitation of obstacles in underground passageways, slowly blocking the flow of the geothermal water. When a fairly strong earthquake occurs, the seismic waves dislodge the obstacles, and the flow of the geothermal water suddenly increases and temperature suddenly rises. This mechanism is similar to that suggested for the enhanced permeability model proposed to explain the earthquake-induced sustained changes in groundwater level (Chap. 6) and increases in stream flow (Chap. 7).

Another example is the temperature response of the Copland hot spring, New Zealand, to the 2009 Mw7.8 Dusky Sound earthquake (15 July 2009) and the 2010

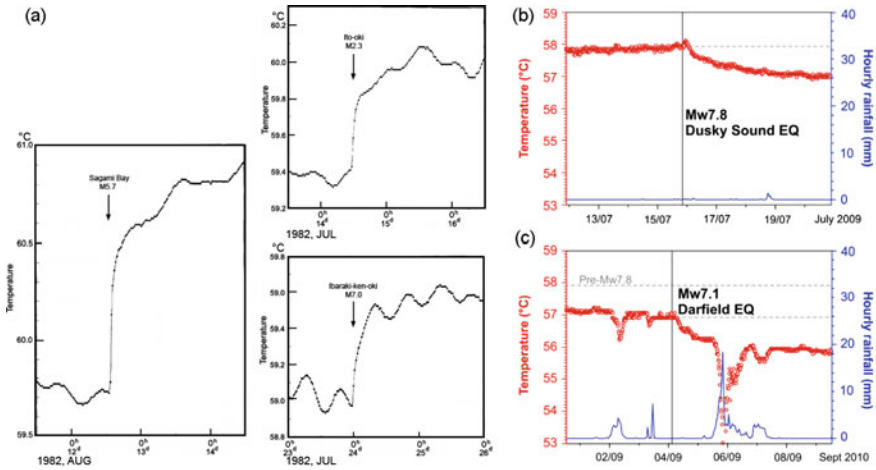


Fig. 8.9 a Examples of coseismic response of groundwater temperature in the Usami No. 24 well, Japan, to several earthquakes (from Mogi et al. 1989). Response of Copland spring temperatures (red) to the 2009 Mw7.8 Dusky Sound earthquake **b** and the 2010 Mw7.1 Darfield earthquake **c**; blue shows precipitation (from Cox et al. 2015)

Mw7.1 Darfield earthquake (Fig. 8.9b, c). The Copland hot spring is located in the foothills of the Southern Alp, about 12 km from the Alpine Fault. It has the strongest discharge among about forty thermal springs along the fault and emanates both water and gas at a temperature of ~57 °C through an alluvial fan deposit that overlies fractured metamorphic rocks (Cox et al. 2015). The earthquakes caused a ~1 °C delayed cooling over 5 days (Fig. 8.9b). The authors suggest that the delayed cooling was caused by an increased mixing of shallow-circulating meteoric water into the deep hot spring water after the earthquake, due perhaps to an increased infiltration of the shallow meteoric water through near-surface fractures generated by the earthquakes. The suggested mechanism seems to be consistent with the decreased concentrations of Cl, Li, B, Na, K, Sr and Ba and an increased SO₄ concentration in the spring water after the earthquakes.

Figure 8.10 plots the epicentral distance versus magnitude for earthquakes that caused water temperature changes in the Copland hot spring (Cox et al. 2015; red stars) and those within a radius of 600 km from the Usami No. 24 well that caused coseismic changes of water temperature in the thermal well (Mogi et al. 1989; red circles), together with those that caused other types of hydrological changes (King et al. 1994; Sato et al. 2000; Manga and Rowland 2009; Wang and Manga 2010a, b). Most responses of groundwater temperature occurred at an inferred seismic energy density between 10⁻² and 10⁻¹ J/m³. Two responses to small earthquakes (M2 to 3) occurred at an inferred seismic energy density between 10⁻⁴ and 10⁻³ J/m³. Mogi et al. (1989) interpreted the latter responses to represent a mix of foreshocks and earthquake swarms. Assuming that the data for hot springs in Fig. 8.10 are representative, the mechanism for changing hot spring and thermal well temperature

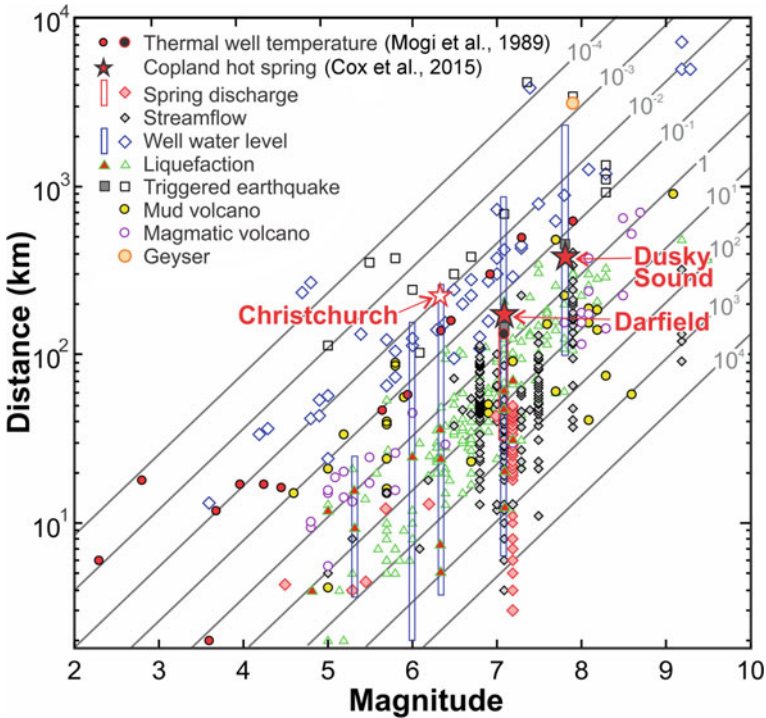


Fig. 8.10 Changes of temperature in some thermal wells in Japan in response to distant earthquakes (Mogi et al. 1989) and hot spring temperature change after the Mw7.8 Dusky Sound and Mw7.1 Darfield earthquakes at Copland hot spring (Cox et al. 2015), plotted on an earthquake magnitude versus distance diagram together with worldwide earthquake-triggered hydrological changes collated by Wang and Manga (2010a, b) with additions of spring discharge changes (King et al. 1994; Sato et al. 2000; Manga and Rowland 2009). The response of Copland spring following the Mw6.3 Christchurch earthquake is plotted for reference, although the response was not definitive (Cox et al. 2015). Contours of constant seismic energy density follow Wang and Manga (2010a, b) (modified from Cox et al. 2015)

requires a higher seismic energy density than that for changing groundwater level. The earthquakes for which changes were regarded as precursory (marked as ringed red circles; Mogi et al. 1989) will be discussed further in Chap. 13 on earthquake precursors.

8.5 Seafloor Measurements

8.5.1 Subduction Zones

Earthquake-induced temperature changes in subduction zones are important for understanding the mechanics of seismic hazards but are also difficult to measure. Part of the difficulty is the great depths of the seafloor in subduction zones. After the March 2011 Mw9.0 Tohoku-Oki earthquake off the Pacific coast of Japan, the Japan Trench Fast Drilling Project of the Integrated Ocean Drilling Program drilled a borehole (Fig. 8.11a) from the seafloor at a depth of 6.9 km below the mean sea level and reached the main plate boundary fault at a depth of ~820 m beneath the seafloor (mbsf). A string of 55 closely spaced temperature loggers with accuracy of 0.001 °C (Fig. 8.11b) was installed in the fully cased 20-cm borehole across the fault, and temperature measurements started 16 months after the earthquake (Fulton et al. 2013). The sensor string was recovered after 9-months of operation. The measurements captured a 0.31 °C temperature anomaly at the depth of the inferred plate boundary fault (Fig. 8.11b). At the same time, it also captured temperature increases at ~763 and 810 mbsf after a December 2012 Mw7.4 local earthquake but a temperature decrease at 784 mbsf (Fig. 8.11b). Fulton et al. (2013) interpreted the temperature anomaly at the depth of the inferred plate boundary fault to correspond to 27×10^6 J/m² of dissipated energy during the earthquake, implying a frictional coefficient of

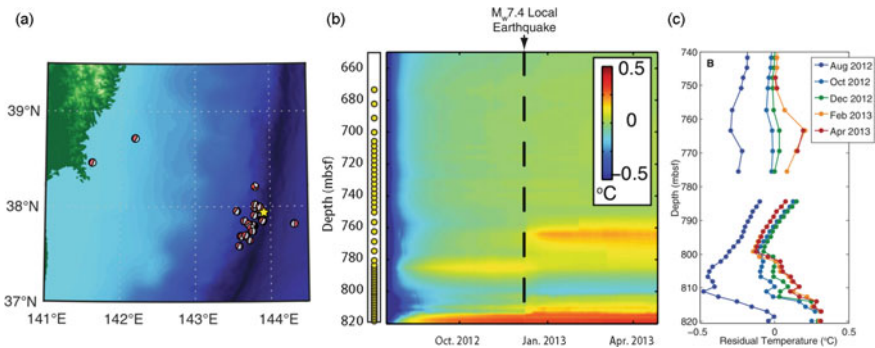


Fig. 8.11 **a** Map showing the site of the Japan Trench Fast (JFAST) Drilling Project (star). Focal mechanisms show regional earthquakes during the 9-month observation period (Fulton et al. 2013). **b** Residual daily average temperature after the background geotherm was removed. Yellow circles on the left edge of the diagram show sensor positions, and each row in the diagram represents the corresponding sensor's data. Each column is the daily average temperature after an average background geotherm is removed. The occurrence of a local Mw7.4 earthquake is shown by dashed line. Notice that after the earthquake, temperature increased at ~763 and ~810 mbsf but decreased at ~784 mbsf (Fulton and Brodsky 2016). **c** Depth profiles of residual temperature from five dates through the experiment separated by 2-month intervals (Fulton et al. 2013). Notice the different depth scales between (b) and (c). Relatively cool temperatures in August reflect the effects of drilling disturbance (modified from Fulton et al. 2013; Fulton and Brodsky 2016)

0.08, substantially smaller than the static friction for most rocks. This result implies a very low frictional resistance on the subduction fault, which is potentially important for understanding earthquake mechanics in subduction zones.

The interpretations by Fulton et al. (2013) and Fulton and Brodsky (2016) of the JFAST temperature measurement are interesting and provocative. Since pore pressure was not measured during the JFAST experiment, the interpretation of the temperature anomaly may be challenging. Fulton et al. (2013) interpreted the temperature anomaly at the inferred plate boundary fault (~820 mbsf) as the decaying signature of the frictional heat during the 2011 Tohoku-Oki earthquake and argued against the alternative interpretation of advection of heat by fluid flow up a permeable fault by stating that there was no indication of high permeability on the resistivity log at the depth of the inferred fault. On the other hand, they attributed the temperature increase at ~763 and 810 mbsf and the temperature decrease at 784 mbsf following the 2012 Mw7.4 local earthquake (Fig. 8.11b) to advection of heat by fluid flow.

Fulton and Brodsky (2016) further filtered out the long-wavelength signals in their record to highlight the remaining high-pass filtered fluctuations following the 2012 local earthquake in Fig. 8.12, which they attributed to fluid flow through the fault damage zone. The filtered temperature record at each depth is overlain on this diagram to highlight the patterns of temperature variation.

The changes on these temperature profiles were rapid, consistent with the hypothesis of advection of heat by flow. Fulton and Brodsky (2016) considered two candidates for the flow mechanism: coseismic influx of pore fluid from the formation to the borehole, and an internal flow entirely confined in the borehole, similar to that suggested by Shi et al. (2007). They favored the first mechanism and argued that these patterns are consistent with transient fluid flow from permeable pathways within the formation into the borehole annulus as illustrated by the schematic drawing on the

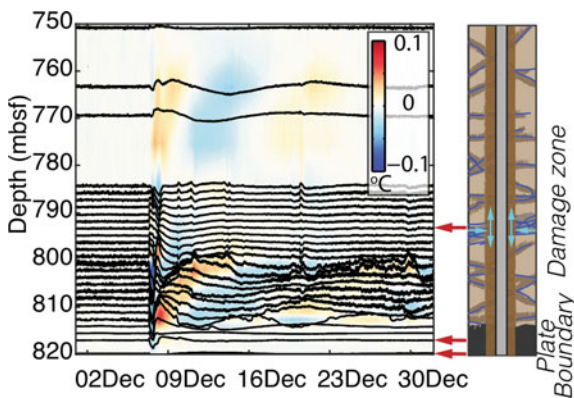


Fig. 8.12 High-pass filtered temperature data from depths 750–820 m below seafloor at the JFAST site during December 2012. Filtered temperature record at each depth is overlain to further highlight the temperature patterns. Cartoon illustrates how fluid flow out of a permeable zone results in flow up and down the borehole annulus (modified from Fulton and Brodsky 2016)

right of Fig. 8.12. Because the background geotherm increases with depth, this model predicts that fluids flowing into the borehole are warmer than the surroundings when they flow up the borehole and cooler than the surroundings when they flow down, resulting in the observed temperature pattern following the Mw7.4 event.

Fulton and Brodsky (2016) also cited several reasons to support their hypothesis that the variations on the high-pass filter profiles (Fig. 8.12) are caused by flows between some permeable formations and the well, rather than by flows confined in the borehole. They first argued that if fluid movement is internal to the borehole and independent of flows from the formation, then the effects should be observed at all depths, contradicted by signals that are repeatedly seen to center around the same depths over time. They then argued that, if a convection cell in the borehole was the cause, fluids would have to overturn over tens of meters within a borehole annulus with a radius of several centimeters, which is difficult. Finally, they argued that if water movement is confined solely within the borehole, the temperature change would have been greatest immediately after an earthquake, whereas the observed transient changes typically occurred over ~0.1 day.

These arguments can be contested. The first argument is based on the assumption of an initially uniform temperature gradient in the water column. The temperature gradient in the well is more likely to have perturbations due to fluid influxes through permeable fractures and formations. These perturbations may significantly influence the initiation of flow in different sections of the well. The second argument is based on the assumption that convection of well water occurs through laminar flow. Because the water column in wells with a geothermal temperature gradient is mechanically unstable (Sect. 8.6), it may undergo turbulent mixing when perturbed by passing seismic waves, as demonstrated by numerical simulations carried out by Shi et al. (2007); the results of the numerical simulations show that turbulent mixing easily occurs in a well with a geothermal gradient to quickly change the initial temperature. Their last argument was likely to be based on the theory of flow in a uniform borehole. Since the geometry of the real borehole is not uniform, water movement in the borehole and the associated temperature change may be complicated and require experimental or numerical evaluation. Observations in the Tangshan well (Sect. 8.6) show that the thermal effect of turbulent mixing in the well takes from 10 min to 2 h to reach the largest perturbations.

8.5.2 *Near Oceanic Ridge*

Several types of temperature changes near oceanic ridges have been documented. Some responded to earthquake swarms located directly below the vents (Sohn et al. 1998; Baker et al. 1999), some were responses to earthquakes along adjacent spreading centers (Dziak et al. 2003), and others were responses to ridge-flank earthquake swarms with epicenter distances up to 50 km away (Johnson et al. 2000, 2001).

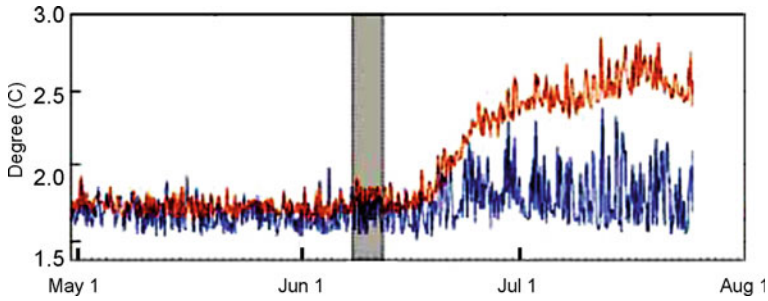


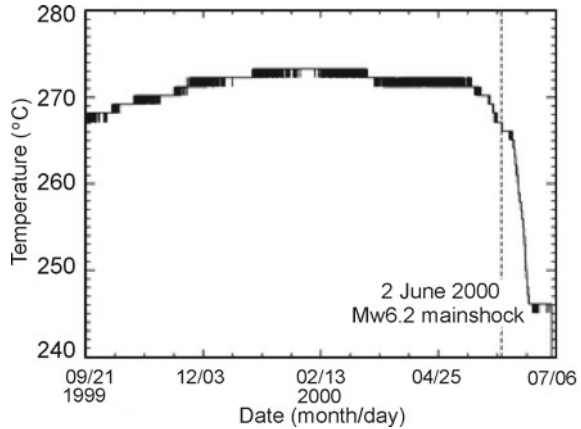
Fig. 8.13 Temperature records from a site on the Endeavour axial valley of the Juan de Fuca Ridge. The June 8–15, 1999, earthquake swarm is marked by the vertical shaded bar. Upper trace indicate data from thermistors located within the vents; blue trace indicate data from thermistors deployed in the adjacent (non-vent) bottom water (from Johnson et al. 2000)

Earthquake-induced changes of groundwater temperature near mid-oceanic ridges have been documented from hydrothermal veins and in ODP boreholes, which are discussed below in sequence. Temperature of hydrothermal vents along mid-oceanic ridges responded to local and distant earthquakes (Sohn et al. 1998, 1999; Johnson et al. 2000, 2001, 2006; Dziak et al. 2003). In the following we first discuss the results of some measurements in the vents along the Juan de Fuca Ridge in response to local and distant earthquake swarms.

On 8 June 1999, an earthquake swarm occurred beneath a segment of the ridge and lasted about a week (Johnson et al. 2001). A thermistor array, deployed before the earthquake swarm within a low temperature vent system on the Juan de Fuca Ridge, 7.5 km away from the earthquake swarm, recorded widespread increases of temperature. In Fig. 8.13 (Johnson et al. 2000), the gray band shows the occurrence of the earthquake swarm, the upper curve shows the temperature from a thermistor located directly in a vent, and the lower curve shows the temperature of the axial valley bottom water. The earthquake swarm produced a slow increase in vent temperature 8 days after the initiation of the swarm. All monitored vents within the axial valley responded similarly, with delayed responses varying from a few days to a month and the net heat flux increased by a factor of ten (Johnson et al. 2001).

Between 1–7 June 2000, another earthquake swarm, with 170 earthquakes and a mainshock of Mw6.2, occurred on the western Blanco Transform Fault. Two temperature probes, located in hydrothermal vents in an adjacent spreading center on the Juan de Fuca Ridge, ~39 km away from the earthquake swarm, registered temperature decreases, one occurring over days to weeks while the other changes were coseismic, as shown in the Fig. 8.14. The onset of the temperature decreases was gradual, but accelerated after the occurrence of the earthquake swarm, with a total decrease of more than 20 °C (Dziak et al. 2003). The fact that earthquakes can influence sub-surface hydrothermal fluids on the sea floor over significant distances from the epicenters, by either increasing or decreasing flow rates, implies that fluids in aquifers beneath the sea floor are frequently ‘stirred’ tectonically (Dziak et al. 2003).

Fig. 8.14 During June 1–7, 2000, an earthquake swarm, with 170 earthquakes and a mainshock of Mw6.2 occurred on the western Blanco Transform Fault. Two temperature probes, located in the hydrothermal vent of an adjacent spreading center, ~39 km away from the earthquake swarm, registered temperature decreases of more than 20 °C. One of the records is shown in this figure (from Dziak et al. 2003)

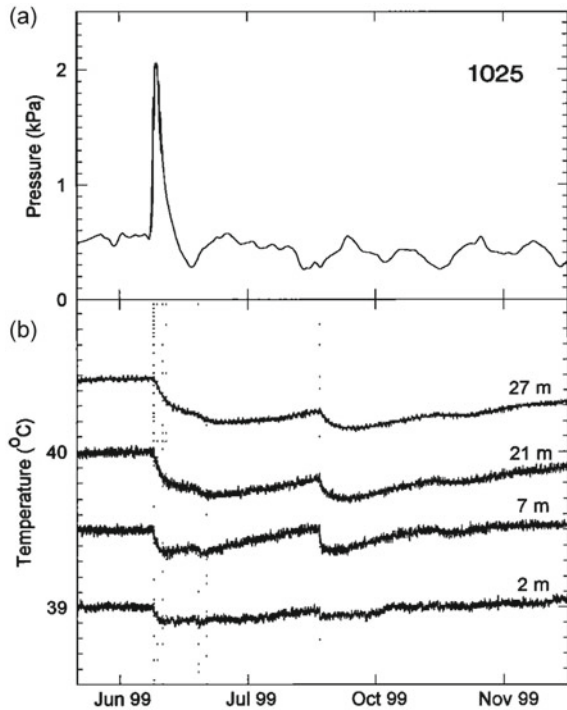


Temperature changes at hydrothermal vents after earthquake swarms are often interpreted to be the result of opening of clogged cracks and fractures that enhance permeability and flow between reservoirs of different temperatures (e.g., Johnson et al. 2000; Dziak et al. 2003). The substantial delay between the onset of the temperature response and the earthquake swarms may represent the time required for fluids of different temperatures to pass through the newly opened channels and to warm the pathways through which the fluid flows.

Temperature probes, as well as pore-pressure probes, in ODP boreholes on the eastern flank of the Juan de Fuca Ridge, responded to the June 8, 1999 earthquake swarm on the ridge (Fig. 8.15 from Davis et al. 2001). Noteworthy is that, while the temperature probe registered changes coinciding not only with the first earthquake, but also with the later earthquakes in the swarm (Fig. 8.15b), the pressure probe registered only a transient change coinciding with the first earthquake (Fig. 8.15a). The coseismic temperature changes were always negative and the amplitudes of the later temperature transients generally reflect the magnitude of the earthquakes, with the greatest change nearly as large as the initial one.

This observation by Davis et al. (2001) in the ODP boreholes is particularly interesting because both pore pressure and temperature were measured in the same boreholes, allowing a more constrained interpretation of the data. As noted earlier, while pore pressure responded only to the first earthquake in the swarm, temperature in the same boreholes responded to many later earthquakes, in addition to the first one. An explanation for why pore pressure responded only to the first earthquake (Fig. 8.15a) may be offered based on the hypothesis that the enhanced permeability occurs when clogged fractures are cleared. According to this hypothesis, the recovery of the enhanced permeability requires the fluid passageways to be resealed by precipitates, which may take much longer time than the time between successive earthquakes in the swarm, and thus the local pressure sources may not have time to re-pressurize between the successive earthquakes. An explanation for why temperature responded not only to the first but also to the later earthquakes (Fig. 8.15b) may

Fig. 8.15 Four-month record of **a** pore pressure and **b** temperatures in ODP borehole 1025C on the eastern flank of the Juan de Fuca Ridge. Times of the individual seismic events are indicated by dotted vertical lines. Depths of the temperature sensors are relative to the top of the basement. The uncased part of the hole extends a total of 47 m below the top of the basement. Temperature records are offset from the sensor at 21 m by 0.5 K for plotting convenience (from Davis et al. 2001)



be offered by using the model of turbulent mixing in wells (Shi et al. 2007; Sect. 8.6). After the water in the borehole becomes still, the water column readily re-establishes thermal equilibrium with the wall rocks, resetting the mechanical instability in the water column required for turbulent mixing before the next seismic event. Thus the water column may repeatedly undergo turbulent mixing when perturbed by earthquakes, causing recurrent temperature changes in the well water (see Sect. 8.6 for more detail).

8.6 Turbulent Mixing of Well Water

As shown in this chapter, most existing studies invoked an earthquake-enhanced permeability to interpret earthquake-induced changes of groundwater temperature. A less well known, but potentially common, process is a turbulent mixing of water in a well when the water column is disturbed by seismic waves (Shi et al. 2007). Since this mechanism has been invoked several times in this chapter to explain coseismic changes of groundwater temperature (e.g., Sections 8.2.3, 8.5.1, 8.5.2), we discuss this process here with its observational and physical basis.

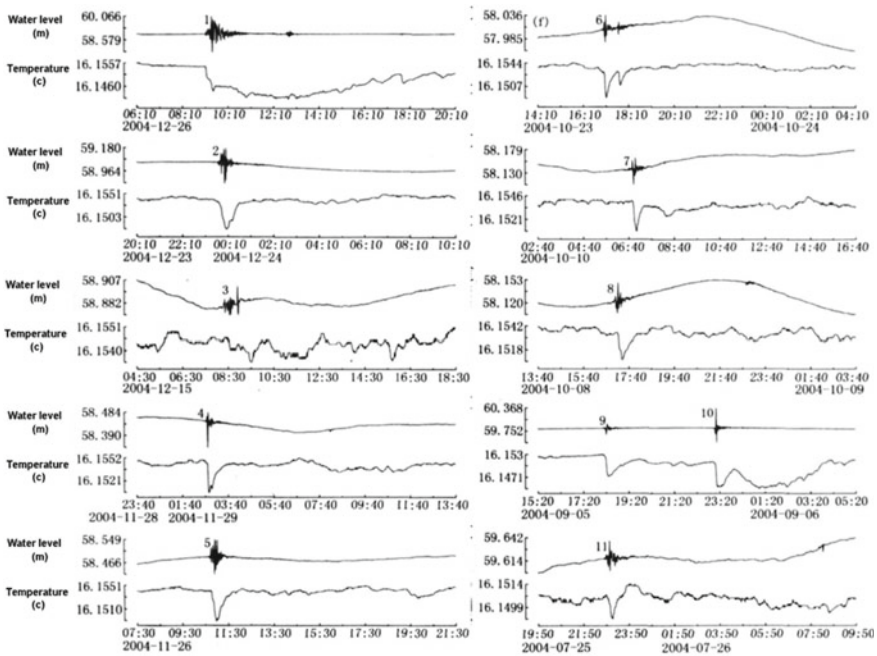


Fig. 8.16 Diagrams a–j show changes in temperature and groundwater level documented simultaneously in a well in the city of Tangshan, China, during 12 earthquakes. For each earthquake, the upper trace shows oscillations in groundwater level and the lower trace shows temperature changes. Note that some traces contain two earthquakes (from Shi et al. 2007)

Simultaneous and continuous measurements of temperature and groundwater level have been carried out in a well in the city of Tangshan, China, since 2001, together with the documentation of seismic waves by a seismometer installed near the well. Temperature was measured with a high-resolution (10^{-4} °C) probe 125 m beneath the wellhead. Figure 8.16 shows the hydroseismograms and concurrent temperature changes during 12 earthquakes (note that some traces contain two earthquakes). It is interesting that, in response to all the documented earthquakes, water level in this well oscillates (hydroseismogram; Fig. 8.16) and temperature always drops independent of the orientation of the causal fault, the distance from the hypocenter, and the magnitude of the seismic events. The rate of temperature drop is generally rapid: it begins when the seismic waves arrive, and the well-water oscillates with amplitudes ranging from several centimeters to ~1 m. Temperature decreases by 0.001 to 0.01 °C and generally takes 10–20 min to 2 h to reach the minimum. The recovery process takes 1 to ~10 h.

The observation that well water temperature always drops during the passage of the seismic waves from distant earthquakes with different mechanisms and fault orientations rules out static strain as a possible mechanism. Since the *average* velocity and displacement during the water-level oscillations are zero (Fig. 8.16), there is no

net transport of heat due to advection. Shi et al. (2007) suggested that the observed decrease of well water temperature was due to turbulent mixing of the water column in the well. Under static conditions, the temperature in the water column readily equilibrates with the local geotherm by conductive heat exchange with the wall rocks. Since the compressibility of water is relatively small, the change of density in static well water is controlled by thermal expansion. Density of the water column therefore decreases with depth, resulting in a state of mechanical disequilibrium. Hence, when the water column is disturbed by seismic waves, it may undergo turbulent mixing to reach a state of uniform temperature and density. To support the turbulent mixing model, Shi et al (2007) simulated the earthquake-induced turbulent heat transfer in the Tangshan well using finite element modeling, a formulation for turbulent heat flux according to a generalized Fick's law (Pinson et al. 2007), and a simplified differential equation for the statistically averaged temperature (Shi et al. 2007)

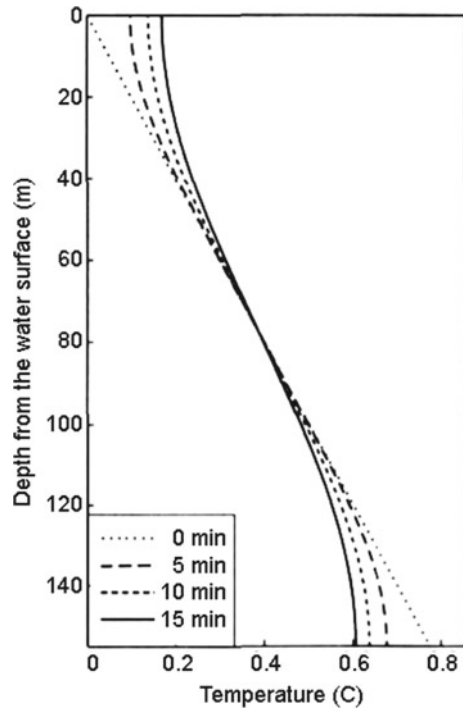
$$\frac{\partial T}{\partial t} = D \frac{\partial^2 T}{\partial z^2},$$

where D is a generalized thermal diffusivity and is the sum of a static thermal diffusivity and a turbulent thermal diffusivity. Solving the system of equations requires the knowledge of velocity and turbulent diffusivity profiles. Since neither of these are known, Shi et al (2007) greatly simplified the problem with assumed D values. They also used the local geotherm for the initial temperature and various boundary conditions to broadly cover the range of possibilities. Figure 8.17 shows one of the simulated temperature profiles in the well as a function of time; in this simulation, where the turbulent thermal diffusivity are assumed to be a constant of $1 \text{ m}^2/\text{s}$, and the top and the base of the water column is assumed to be thermally insulated. The latter assumption may be justified by the relatively short duration of the temperature change (Fig. 8.16), the relatively low thermal conductivity of rocks and air, and the small heat capacity of air.

Even though the simulation of the turbulent heat transfer process may be simplified, the results still provide a qualitative understanding of the process. It shows that turbulent mixing in the water column causes its temperature gradient and thus its mechanical instability to quickly decrease with time. After the water becomes still, however, thermal conduction between the water column and the wall rocks becomes the dominant heat exchange process, which readily re-establishes the geothermal gradient and re-instates the mechanical disequilibrium in the water column.

The mixing model may be further supported by a recent study of the temperature change in a well after the 2016 Mw5.8 Gyeongju earthquake in Korea (Sect. 8.2.3; Lee et al. 2020). As Fig. 8.5 shows, before the earthquake, temperature of the water column in this well at depths $>50 \text{ m}$ conformed to the local geothermal gradient. This is because that the skin depth of the annual surface fluctuation of temperature is $\sim 50 \text{ m}$ and the temperature at depths below 50 m usually has the geothermal gradient. As explained in Sect. 8.2.3, this temperature gradient implies a decrease

Fig. 8.17 Simulated temperature profiles with depth at four distinct times. The simulation assumed a constant turbulent thermal diffusivity of $1 \text{ m}^2/\text{s}$, an initial temperature equal to the local geotherm (adjusted to zero at the top), and thermal insulation at the top and the bottom of the water column (from Shi et al. 2007)



of density with depth and thus a state of mechanical disequilibrium in the water column. Soon after the earthquake, temperature in the well (red curve in Fig. 8.5) became nearly uniform with depth, reflecting a change of density distribution from a mechanically unstable state to a mechanically stable state, and this rapid change can only occur by turbulent mixing of the initially thermally stratified water column. After the earthquake, temperature in the well recovered to the geothermal gradient (black curve in Fig. 8.5), re-instating the mechanical disequilibrium.

Observations (Figs. 8.5, 8.15b and 8.16) thus suggest that turbulent mixing of well water may commonly occur when the water column is disturbed by seismic waves. Such temperature changes are relatively large and may last from an hour (Fig. 8.16) to a month (Figs. 8.5, 8.15b). Such changes may easily mask the more subtle changes due to geological processes such as frictional heat on ruptured faults during earthquakes and should be carefully removed in order to retrieve the signals produced by hydrogeological processes.

Since the temperature in the Tangshan well was measured at a single depth, it may not provide sufficient constraints on the model. Shi et al. (2007) proposed that the hypothesis could be tested by installing a string of high-resolution temperature probes at selected depths in the well to better constrain the model. Such measurements, though not done in this well, were realized in the borehole drilled to the ruptured fault after the 2011 Mw9.0 Tohoku-Oki earthquake off the Pacific coast of Japan, as discussed in Sect. 8.5.1.

8.7 Concluding Remarks

As noted, progress in understanding earthquake-induced changes of groundwater temperature has been slow, largely because relevant quantitative data are relatively scarce and instrumental measurements of earthquake-induced temperature changes started only in the last two decades. On the other hand, the available observations have provided highly valuable information for constraining models of earthquake-induced groundwater flow. Most changes of temperature in hot springs and submarine hydrothermal vents can be explained by a model of earthquake-enhanced permeability that is due to the dislodging of precipitates from clogged fluid channels, such as pre-existing fractures. Unclogged fractures act to breach hydrologic barriers (such as aquitards) and to connect otherwise isolated aquifers or other fluid sources.

Another complication for understanding the geological implications of the measured groundwater temperature is that the measured temperature may be strongly affected by local factors such as the coseismic influx of groundwater into the well through hydraulically conductive fractures and formations (He and Singh 2020). Since such local factors may strongly affect the measured temperature to mask the more subtle changes due to other physical processes such as rock friction, it can be challenging to interpret specific measurements without a priori knowledge about the locations of the conductive fractures in the well. Hence measurement of water flow and logging of conductive fractures/formations in the well may be important to constrain the interpretations of measured groundwater temperature.

Since the water column in thermal equilibrium with the local geothermal temperature is often in a state of mechanical disequilibrium, turbulent flow may occur in the well when the water column is disturbed by seismic waves. Such mixing of water may obscure the more subtle signals from geological processes. While the details of the model may require further quantification, it nonetheless shows that the effect of turbulent mixing of well water should be carefully considered when interpreting observed temperature changes to understand hydrogeological processes.

Earthquake-induced changes in temperature of groundwater contain rich information about the subsurface hydrogeological processes. This information has been relatively less developed and much remains to be explored and learned. With the advances in instrumental technology, data management, analysis and interpretation, it may be timely to measure groundwater temperature routinely in field programs.

References

- Baker ET, Fox CG, Cowen JP (1999) In situ observations of the onset of hydrothermal discharge during the 1998 submarine eruption of Axial volcano, Juan de Fuca Ridge. *Geophys Res Lett* 26:3445–3448
- Cox SC, Menzies CD, Sutherland R et al (2015) Changes in hot spring temperature and hydrogeology of the Alpine Fault hanging wall, New Zealand, induced by distal South Island earthquakes. *Geofluids* 15:216–239. <https://doi.org/10.1111/gfl.12093>

- Davis EE, Wang K, Thomson RE et al (2001) An episode of seafloor spreading and associated plate deformation inferred from crustal fluid pressure transients. *J Geophys Res* 106:21953–21963
- Dziak RP, Chadwick WW, Fox CG et al (2003) Hydrothermal temperature changes at the southern Juan de Fuca Ridge associated with M-w 6.2 Blanc transform earthquake. *Geology* 31:119–122
- Forster C, Smith L (1989) The influence of groundwater flow on thermal regime in mountainous terrain: a model study. *J Geophys Res* 97:9439–9451
- Fulton PM, Brodsky EE, Kano Y et al (2013) Low coseismic friction on the Tohoku-Oki fault determined from temperature measurements. *Science* 342:1214–1217. <https://doi.org/10.1126/science.1243641>
- Fulton PM, Brodsky EE (2016) In situ observations of earthquake-driven fluid pulses within the Japan Trench plate boundary fault zone. *Geology* 44:851–854
- Garven G, Ge S, Person MA et al (1993) Genesis of stratabound ore deposits in the midcontinent basins of North America. 1. The role of regional groundwater flow. *Am J Sci* 293:497–568
- He A, Singh RP (2019) Groundwater level response to the Wenchuan earthquake of May 2008, Geomatics. *Nat Hazards Risk* 10:336–352. <https://doi.org/10.1080/19475705.2018>
- He A, Singh RP (2020) Coseismic groundwater temperature response associated with the Wenchuan earthquake. *Pure Appl Geophys* 177:109–120
- Hosono T, Yamada C, Shibata T et al (2019) Coseismic groundwater drawdown along crustal ruptures during the 2016 Mw 7.0 Kumamoto earthquake. *Water Resour Res* 55:5891–5903. <https://doi.org/10.1029/2019WR024871>
- Hwang WT, Wang C-Y (1993) Sequential thrusting model for mountain building: constraints from geology and heat flow from Taiwan. *J Geophys Res* 98:9963–9973. <https://doi.org/10.1029/92JB02861>
- Johnson HP, Hutnak M, Dziak RP et al (2000) Earthquake-induced changes in a hydrothermal system on the Juan de Fuca mid-ocean ridge. *Nature* 407:174–177
- Johnson HP, Dziak RP, Fisher CR et al (2001) Impact of earthquakes on hydrothermal systems may be far reaching. *EOS Trans Am Geophys Union* 82:233–236
- Johnson HP, Baross JA, Bjorklund TA (2006) On sampling the upper crustal reservoir of the NE Pacific Ocean. *Geofluid* 6:251–271
- King CY, Basler D, Presser TS et al (1994) In search of earthquake-related chemical changes along the Hayward fault. *Appl Geochem* 9:83–91
- Koizumi N, Minote S, Tanaka T et al (2019) Hydrological changes after the 2016 Kumamoto earthquake, Japan. *Earth Planet Space* 71:128. <https://doi.org/10.1186/s40623-019-1110-y>
- Lee SH, Lee JM, Yoon H et al (2020) Groundwater impacts from the M5.8 earthquake in Korea as determined by integrated monitoring systems. *Groundwater*. <https://doi.org/10.1111/gwat.12993>
- Ma Z, Fu Z, Zhang Y et al (1990) Earthquake prediction: nine major earthquakes in China (1966–1976). Seismological Press, Beijing, p 332 (in Chinese)
- Manga M, Rowland JC (2009) Response of Alum Rock springs to the October 30, 2007 Alum Rock earthquake and implications for the origin of increased discharge after earthquakes. *Geofluids* 9:237–250
- Manga M, Beresnev I, Brodsky EE et al (2012) Changes in permeability caused by transient stresses: field observations, experiments, and mechanisms. *Rev Geophys* 50:RG2004
- Miyakoshi A, Taniguchi M, Ide K et al (2020) Identification of changes in subsurface temperature and groundwater flow after the 2016 Kumamoto earthquake using long-term well temperature-depth profiles. *J Hydrol* 582. <https://doi.org/10.1016/j.jhydrol.2019.124530>
- Mogi K, Mochizuki H, Kurokawa Y (1989) Temperature changes in an artesian spring at Usami in the Izu Peninsula (Japan) and their relation to earthquakes. *Tectonophysics* 159:95–108
- Pinson F, Gregoire O, Quintard M et al (2007) Modeling of turbulent heat transfer and thermal dispersion for flows in flat plate heat exchangers. *Int J Heat Mass Transf* 50:1500–1515
- Sato T, Sakai R, Furuya K et al (2000) Coseismic spring flow changes associated with the 1995 Kobe earthquake. *Geophys Res Lett* 27:1219–1222
- Shi Y, Cao J, Ma L et al (2007) Teleseismic coseismic well temperature changes and their interpretation. *Acta Seismol Sin* 29:265–273 (in Chinese with English abstract)

- Sohn RA, Fornari DJ, Von Damm KL et al (1998) Seismic and hydrothermal evidence of a cracking event on the East Pacific Rise near 98509N. *Nature* 396:159–161
- Sohn RA, Hildebrand JA, Webb SC (1999) A microearthquake survey of the high-temperature vent fields on the volcanically active East Pacific Rise (98 509 N). *J Geophys Res* 104:25367–25378
- Tyan CL, Chang YM, Lin WK et al (1996) The brief introduction to the groundwater hydrology of Choshui River Alluvial fan. In: Conference on groundwater and hydrology of the Choshui River Alluvial Fan, Taiwan. Water Resources Bureau 207–221 (in Chinese)
- Wang CY, Wang CH, Manga M (2004) Coseismic release of water from mountains: evidence from the 1999 ($M_w = 7.5$) Chi-Chi, Taiwan, earthquake. *Geology* 32:769–772
- Wang CY, Manga M (2010a) Earthquakes and water. *Lect Notes Earth Sci* 114:235
- Wang CY, Manga M (2010b) Hydrologic responses to earthquakes and a general metric. *Geofluids* 10:206–216
- Wang CY, Manga M, Wang CH, Chen CH (2012) Earthquakes and subsurface temperature changes near an active mountain front. *Geology* 40:119–122
- Wang CY, Wang LP, Manga M, Wang CH (2013) Basin-scale transport of heat and fluid induced by earthquakes. *Geophys Res Lett* 40:3893–3897. <https://doi.org/10.1002/grl.50738>

Open Access This chapter is licensed under the terms of the Creative Commons Attribution 4.0 International License (<http://creativecommons.org/licenses/by/4.0/>), which permits use, sharing, adaptation, distribution and reproduction in any medium or format, as long as you give appropriate credit to the original author(s) and the source, provide a link to the Creative Commons license and indicate if changes were made.

The images or other third party material in this chapter are included in the chapter's Creative Commons license, unless indicated otherwise in a credit line to the material. If material is not included in the chapter's Creative Commons license and your intended use is not permitted by statutory regulation or exceeds the permitted use, you will need to obtain permission directly from the copyright holder.



Chapter 9

Groundwater and Stream Composition



The water in wells is also more turbid than usual, and it emits a disagreeable odour. (Pliny the Elder, Natural History, Chapter 83).

Abstract Changes of groundwater chemistry have long been observed. We review some studies of the earthquake-induced changes of groundwater and streamflow composition. When data are relatively abundant and the hydrogeology is relatively simple, the observed changes may provide valuable insight into earthquake-induced changes of hydrogeological processes. Progress in this aspect, however, has been slow not only because systematic measurements are scarce but also because of the distribution of chemical sources and sinks in the crust are often complex and unknown. Most changes are consistent with the model of earthquake-enhanced groundwater transport through basin-wide or local enhanced permeability caused by earthquake-induced breaching of hydrologic barriers such as aquitards, connecting otherwise isolated aquifers or other fluid sources, leading to fluid source switching and/or mixing. Because the interpretation of earthquake-induced groundwater and stream compositions is often under-constrained, multi-disciplinary approaches may be needed to provide a better constrained interpretation of the observed changes.

9.1 Introduction

Changes in the turbidity, odor and taste of groundwater are probably among the earliest reported changes following earthquakes, as Pliny the Elder noted in his Natural History nearly two thousand years ago. Such changes and, more generally, the change of the chemical composition of groundwater, may be expected because earthquake-induced groundwater flow is effective in transporting solutes, and earthquake may open new passageways to connect fluids from different reservoirs to facilitate such exchange.

Progress in our understanding of these processes, however, has been slow partly because chemical measurements require discrete sampling of water and laboratory analyses are expensive and time-consuming. Hence quantitative data and systematic

measurements for groundwater composition are even less abundant than that for groundwater temperature. In addition, the distribution of chemical sources and sinks in the crust is complex and largely hidden from observation, making the interpretation of the measured changes challenging.

On the other hand, in the cases where the chemical signatures of earthquake-induced changes are clear and well documented, they may provide evidence for the origin of the extra water released by the earthquakes, as will be shown later in this chapter. Significant progress has been made in the last decade to expand the observational record. Interesting are some apparent contradictions between the observations from nearby wells. Understanding these differences and contradictions will require greater effort in data collection and analysis.

This chapter reviews some significant observations on earthquake-induced changes of groundwater composition, particularly those made in the past decade, and their interpretation. Most observations were made in groundwater wells and natural springs because their relatively confined environment minimizes the influence of surface waters. The presence of flowing waters in streams prior to earthquakes makes similar studies in streams more difficult. But in regions such as California with extended dry seasons, earthquakes may occur when many streams have little flow or are dry. Under these circumstances, studies of stream water composition before and after the earthquake may provide valuable information about the earthquake's effects on local hydrogeologic processes. For the convenience of discussion, we separate the discussion of the composition changes in stream water from those in groundwater wells and natural springs. When data are abundant and complex, we also categorize them into changes of the major elements, the trace elements, and the stable isotopes of oxygen and hydrogen. Many studies made measurements only after earthquakes; these are not reviewed here because the study of earthquake-induced changes requires measurements both before and after an earthquake.

Due to the scarcity of quantitative data and the complexity in the distribution of chemical reservoirs, interpretations of groundwater composition are often under-constrained. We end the chapter with a discussion on the need to integrate observational data for multiple types of groundwater responses in constraining the interpretation of the earthquake-induced chemical compositions.

9.2 Groundwater Composition

9.2.1 Major Elements

More than 90% of the dissolved solids in groundwater can be attributed to eight ions, Na^+ , Ca^{2+} , K^+ , Mg^{2+} , SO_4^{2-} , Cl^- , HCO_3^- , and CO_3^{2-} . Silica, SiO_2 , is also often present as a nonionic species. Variations among the relative proportions of these ions in the groundwaters of different regions reflect their different sources.

Most earthquake-related studies of groundwater composition have focused on the search for precursory changes, and we discuss these in more detail in Chap. 13. In a few cases, however, the composition of groundwater was systematically monitored before and after earthquakes. Such changes can provide useful constraints on models of earthquake-induced groundwater flow. In this section we discuss the results of recent studies on earthquake-induced changes of the major element concentration in water in some wells and natural springs.

9.2.1.1 Iceland

The Tjörnes Fracture Zone (TFZ) in northern Iceland (Fig. 9.1a) is a transform fault zone that offsets segments of the Mid-Atlantic Ridge and is seismically active. Borehole HU-01 (Fig. 9.1b) is 1500 m deep and is near one of the fault zones. In the upper 1150 m, the basalt horizons are intercalated with sediments; below 1150 m, basalt dominates. Water inflow in this borehole occurs at depths of 500 m, 700 m, 730 m (sandstones), and 1220 m (fractured basalt) below the surface. Borehole HA-01 (Fig. 9.1b) is 101 m deep and water inflow occurs at 65 m, 81.5 m, and 95.7 m. Weekly samples were collected from the HU-01 well starting July 2002 (Claesson et al. 2004, 2007) and from the HA-01 well starting 2008 (Skelton et al. 2014; Andrén et al. 2016).

A M5.8 earthquake occurred on 16 September 2002 off the northern coast of Iceland, with epicenter ~90 km north of Husavik (Fig. 9.1a, b). Two consecutive earthquakes occurred on 21 October 2012 (M 5.5) and 2 April 2013 (M 5.3) (Fig. 9.1a); both are ~76 km from Husavik.

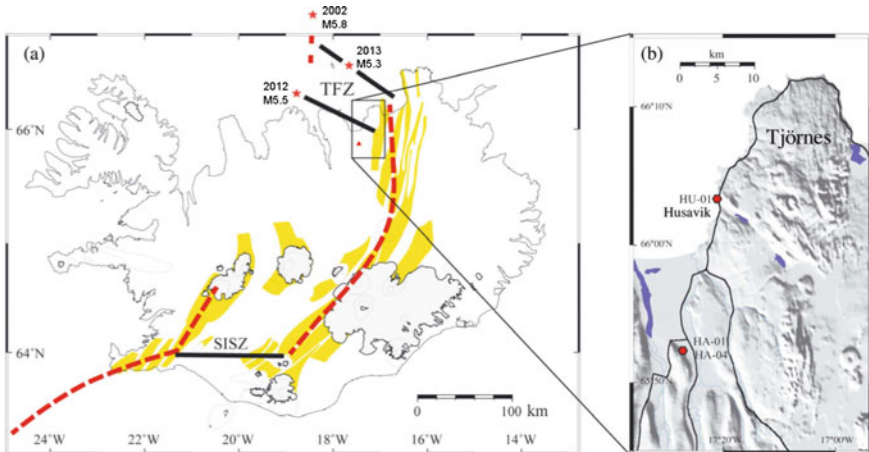


Fig. 9.1 a Map of Iceland showing the geographic locations of the epicenters of the studied earthquakes (red stars), the Mid-Atlantic Ridge (red dashed lines) and transform faults (black lines). Yellow areas mark the active volcanic systems. b Zoom in of the study area (Tjörnes peninsula) where the boreholes (red circles) are located (modified from Andrén et al. 2016)

Figure 9.2 shows the extended time series of the major element compositions in the HU-01 and HA-01 wells from 2002 to 2018 (Skelton et al. 2019). Much discussion on the changes of water composition in these wells has been focused on the premonitory changes, which we review in Chap. 13. Here we only discuss the changes of water chemistry after the earthquakes. Claesson et al. (2004) reported that after the 2002 M5.8 earthquake, groundwater in the HU-01 well showed increased concentrations of Na^+ , Ca^{2+} , K^+ , S, Si, Cl^- , and SO_4^{2-} by 12–19% in and decreased Na/Ca. Claesson et al. (2007) updated the earlier study and found that the chemical changes caused by the M5.8 earthquake recovered gradually over the subsequent two years before the trend was interrupted by a second rapid rise caused by other earthquakes near the end of 2004. The extended time series in Fig. 9.2 shows, however, that most of the

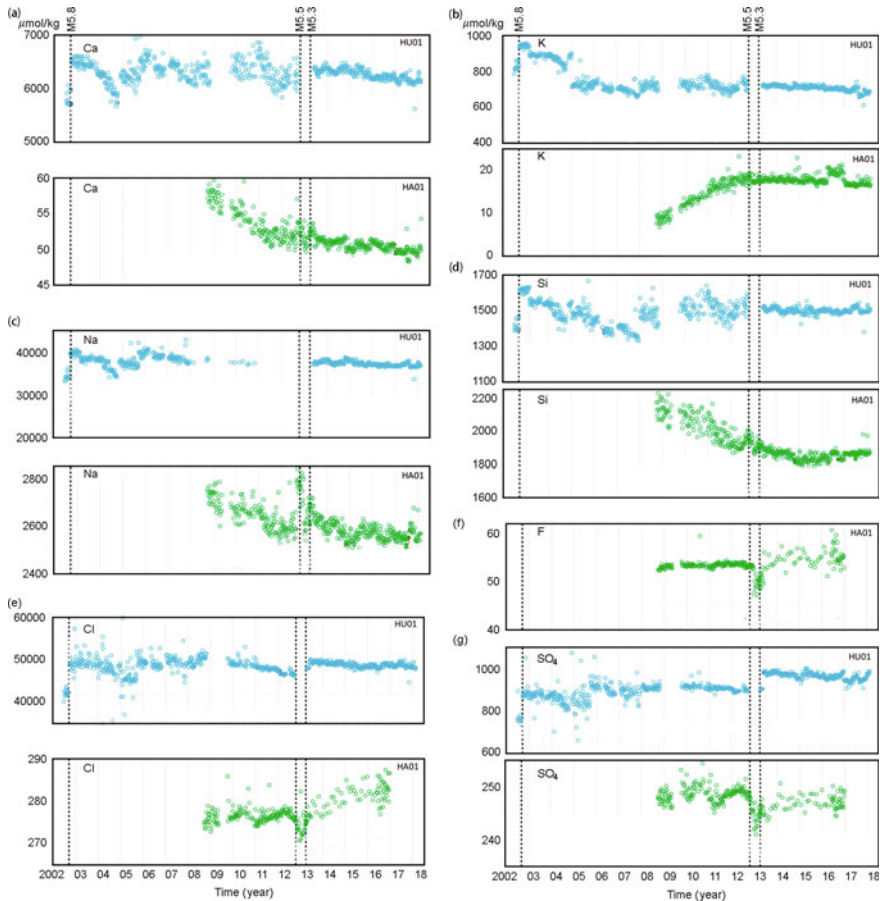


Fig. 9.2 Time series of weekly samples from 2002 to 2018, of **a** Ca^{2+} , **b** K^+ , **c** Na^+ , **d** Si, **e** Cl^- , **f** F^- , and **g** SO_4^{2-} at boreholes HU01 (blue circles) and HA01 (green circles). The 2002, 2012, and 2013 earthquakes are marked by vertical dashed lines. Analytical errors are $<2\%$ (modified from Skelton et al. 2019)

changes in well HU-01 before 2002 and 2004 earthquakes were not repeated during the 2012 M5.5 or the 2013 M5.3 earthquakes, except those of Cl^- and SO_4^{2-} . Also interesting are the differences between the chemical responses between the HU-01 well and the HA-01 well. The latter well shows no change in the concentration of K^+ and only small changes in Ca^{2+} and Si, even though it shows a sharp increase in the concentration of Na, similar to the HU-01 well after the 2002 M5.8 earthquake. The greatest contrast between the two wells occurred in the concentrations of Cl^- and SO_4^{2-} , which increased in the HU-01 well after the earthquakes but decreased in the HA-01 well. The reason for these differences is unknown, but is likely to be related to the different groundwater sources for the two wells, as revealed by the large differences between their background compositions (Fig. 9.2).

9.2.1.2 Japan

Groundwater chemistry has been continuously measured in central Kyushu long before the 2016 Mw7.0 Kumamoto earthquake, Japan. Before the earthquake, groundwater composition was relatively constant, but changed subtly afterwards (Fig. 9.3; e.g., Hosono et al. 2018; Hosono and Masaki 2020; Nakagawa et al. 2020). These authors found increased dissolved silica in many wells, similar to the findings in Iceland (Sect. 9.2.1.1). Contrary to the findings in Iceland, however, they found decreased concentrations of Cl^- , F^- , Na^+ , K^+ , Ca^{2+} . They interpret these decreases to be caused by dilution from groundwater released from the surrounding mountains. Increased concentrations of nitrates, SO_4^{2-} , and Mg^{2+} were interpreted to be due to leaching of contaminants and agricultural fertilizers from soils and sewage water pipe breaks. Finally, increases of Fe_{total} and Mn_{total} was interpreted to be due to leaching of marine clay by liquefaction in coastal areas.

Hosono et al. (2018) also reported that new spring water inside the Aso caldera after the 2016 Kumamoto earthquake (Fig. 9.4) was characterized by high sulfate content and low lithium and boron stable isotope ratios ($\delta^7\text{Li} = 2.6\text{‰}$ and $\delta^{11}\text{B} = 1.4$ to 2.6‰), consistent with meteorically-derived groundwater admixed with deeper fluids of hydrothermal origin. The occurrence of the new highly saline fluids in the northwestern plain where the earthquake caused major surface ruptures (Hosono et al. 2019) led the authors to suggest that these elevated hydrochemical fluxes migrated upward to the surface from greater depths along earthquake-generated fractures.

Koizumi et al. (2019) analyzed the composition of eleven springs in central Kyushu (see Fig. 9.5 for spring locations) after the 2016 Kumamoto earthquake and compared the results with the compositions before the earthquake. They found little change in the major element composition of the studied springs (Fig. 9.5); only the concentration of NO_3^- changed slightly just after the earthquake, which they attributed to leakage from surface sources.

Ide et al. (2020) also compared the concentrations of major elements in many springs in central Kyushu after the 2016 Kumamoto earthquake with those measured in the year of 2009. They also found no remarkable difference between the water compositions before and after the earthquake (Fig. 9.6).

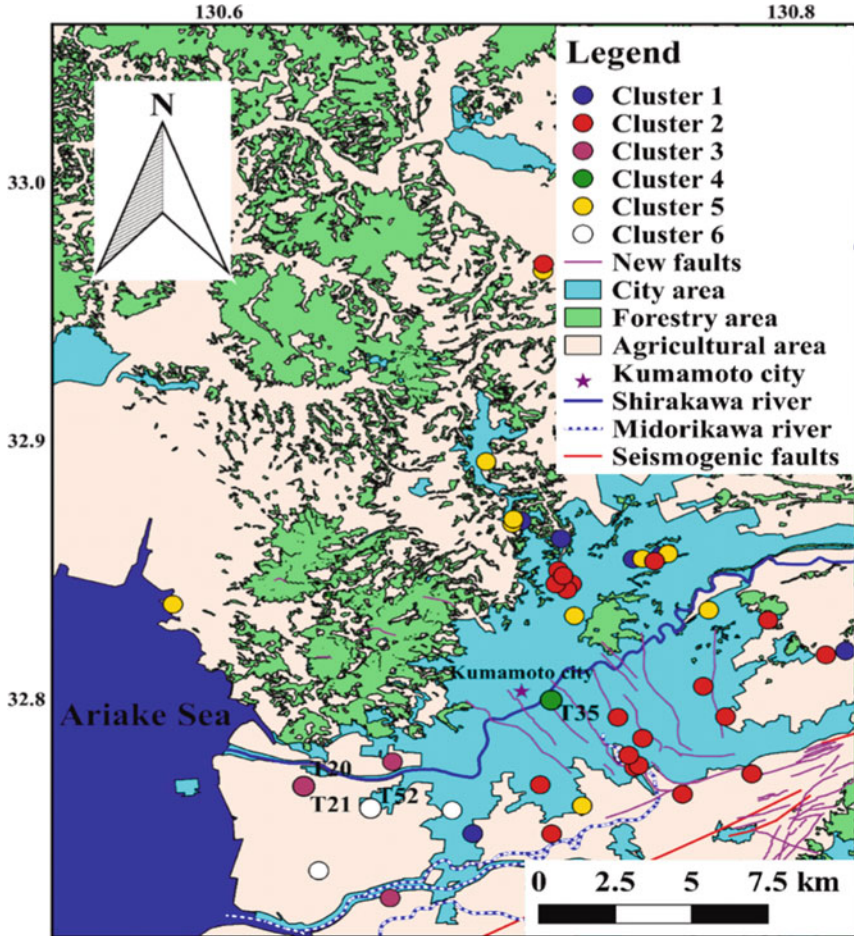


Fig. 9.3 Map showing the locations of wells sampled by Nakagawa et al. (2020) in the Kumamoto area after the 2016 earthquake. Different ‘clusters’ of wells showed distinct chemical changes. Cluster 1 wells showed increased SiO_2 and NO_3^- , but decreased F^- , Cl^- , Na^+ , K^+ , and Ca^{2+} concentrations. Cluster 2 wells showed increased SiO_2 , NO_3^- , Cl^- , SO_4^{2-} , and Mg^{2+} , but decreased F^- concentration. Cluster 3 wells displayed increasing Fe_{total} , Mn_{total} , and SiO_2 , but sharp decreases of Cl^- and Na^+ concentration. Cluster 3 wells showed increased Fe_{total} and Mn_{total} concentrations. Cluster 4 wells showed decreased Fe_{total} and Mg concentrations. Cluster 5 wells showed increased SiO_2 , SO_4^{2-} , and Mg^{2+} concentrations but decreased Cl^- concentration. Cluster 6 wells showed increased SO_4^{2-} , F^- , and Mg^{2+} ; other chemicals were basically unchanged (modified from Nakagawa et al. 2020)

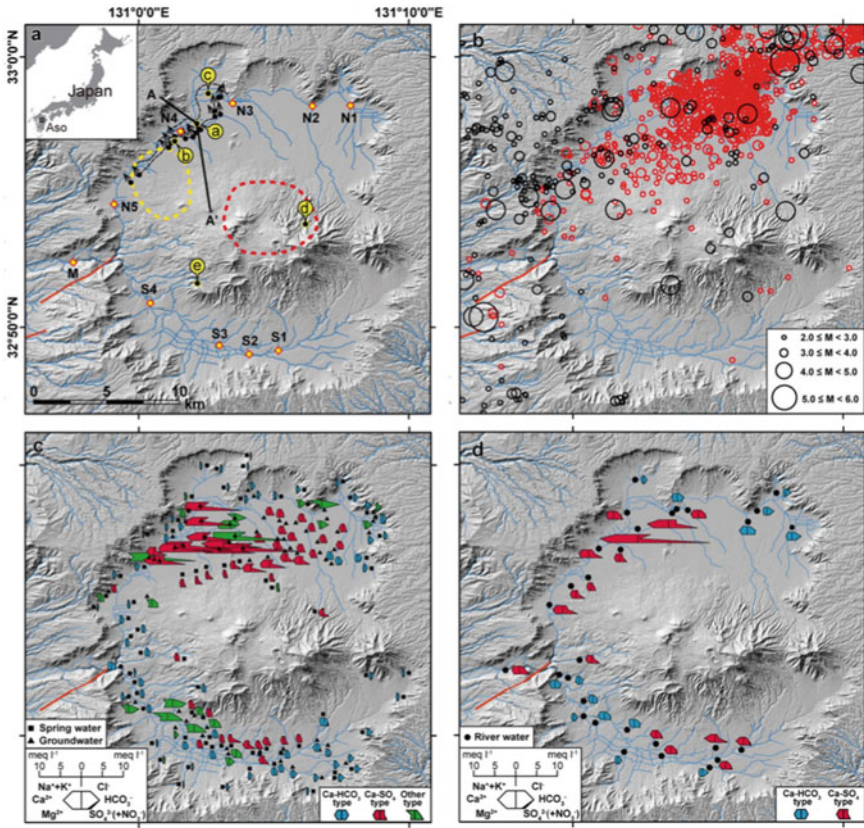


Fig. 9.4 **a** Maps showing the sampling sites in the Aso caldera watershed and dominant extensional fissures (black dots with arrows), and associated horizontal landsliding (area bounded by the black dashed curve) observed after the 2016 Kumamoto earthquake. **b** Map showing earthquake epicenters in the Aso caldera watershed before (1923–2016: black circles) and after the 2016 main shock (red circles). **c** Map showing spring and groundwater water chemistry from data from 1968–1995. Locations of reported low resistivity zone for hypothesized melt finger in the deep crust and magma chambers beneath central volcanoes are shown with a yellow dotted curve and red dotted curves, respectively (from Hosono et al. 2018)

The different conclusions by Hosono et al. (2018) and those by Koizumi et al. (2019) and Ide et al. (2020) may reflect the fact that the springs studied by Hosono et al. (2018) are inside the Aso Caldera, while most springs studied by Koizumi et al. (2019) and Ide et al. (2020) are outside the caldera and thus sample different groundwater sources.

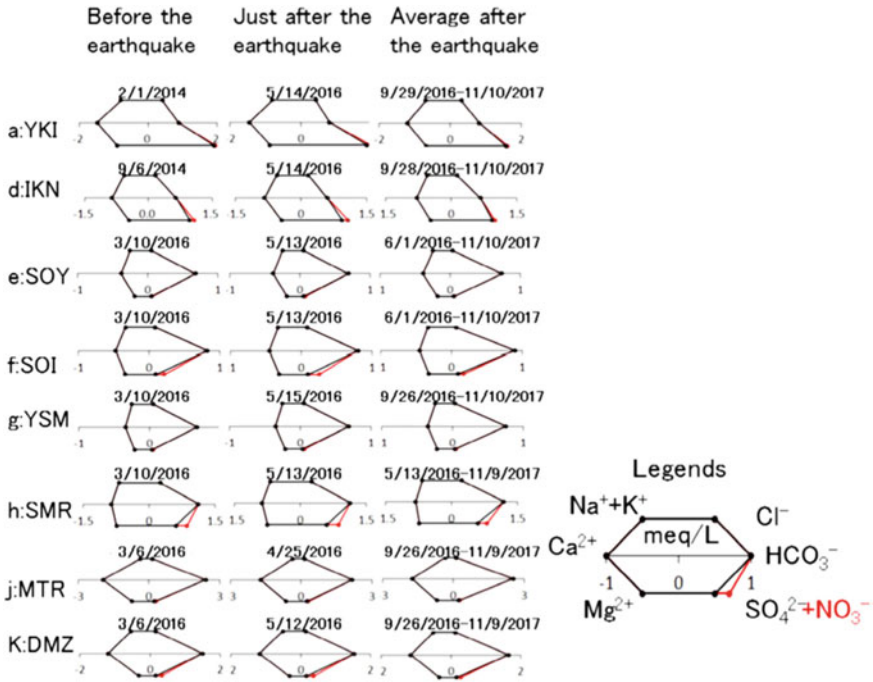


Fig. 9.5 Chemical composition at eight springs (see Fig. 7.5 for spring locations) before and after the 2016 Kumamoto earthquake. Sampling date is shown above each hexa diagram. The precision of measurements is from a few percent to 10% (from Koizumi et al. 2019)

9.2.1.3 Korea

Two consecutive earthquakes of M5.1 and M5.8, with strike-slip focal mechanisms and separated by less than an hour (Fig. 9.7), occurred on September 12, 2016, on the SE of the Korean peninsula. The second of these is the largest instrumentally recorded earthquake on the peninsula. Significant hydrological responses were reported (Kim et al. 2019; Kaown et al. 2020; Lee et al. 2020) and we discussed in Chap. 8 the response of the groundwater temperature to this earthquake. Here we discuss the response of the groundwater composition. Most measurements of groundwater composition took place after the earthquakes (Kim et al. 2019; Kaown et al. 2019). Fortunately, some wells (Fig. 9.7a) in the Korean national groundwater monitoring network measured the major element compositions both before and after the earthquake.

The hydrogeology of the studied area may be simply described as an alluvial sedimentary basin overlying a basement of Miocene to Cretaceous sedimentary formations and igneous rocks. At each of the groundwater stations (Fig. 9.7a) two wells are installed, one in the upper alluvial sediments, and the other in the deeper basement rocks. Figure 9.7b shows the composition of some major ions measured at different

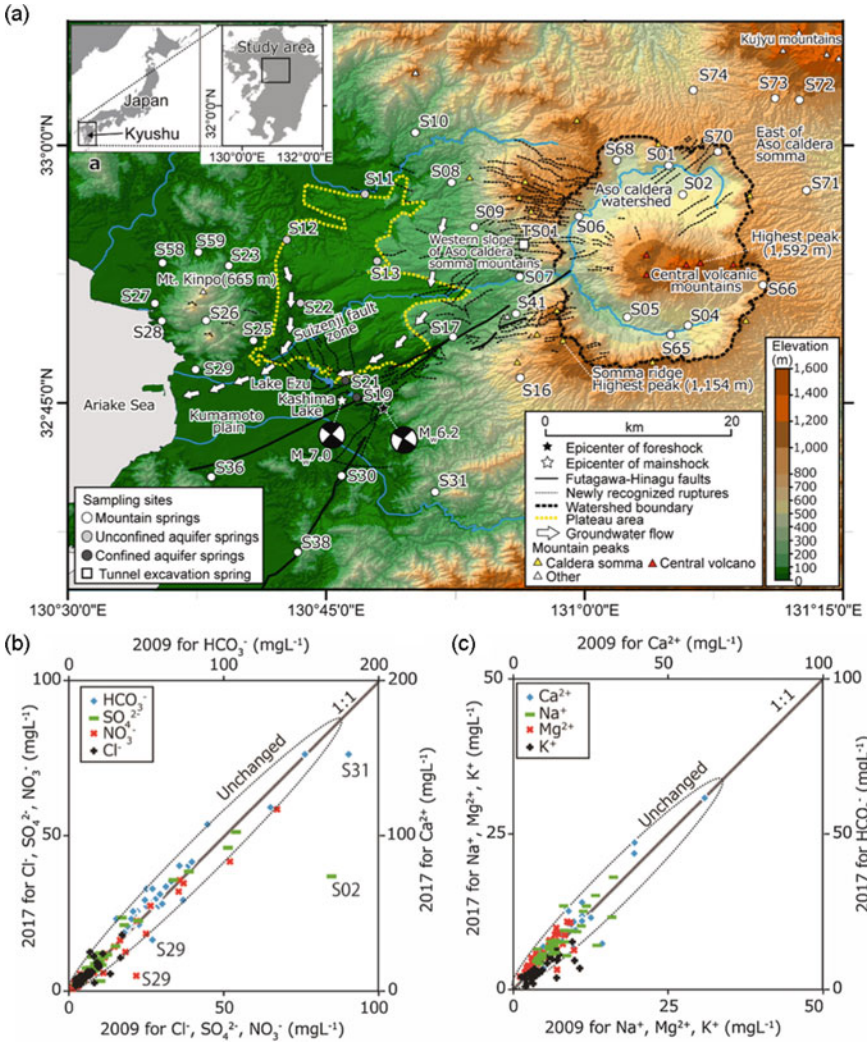


Fig. 9.6 a Map showing the locations of studied natural springs in central Kyushu by Ide et al. (2020). Comparison of b major anion concentrations and c major cation concentrations in springs between the 2009 and 2017 sampling campaigns, showing no remarkable change of the major dissolved ions (modified from Ide et al. 2020)

times. Measurements labeled 2014–2016 were made before the earthquake, while those labeled 2017 were measured after the earthquake. No clear changes of groundwater composition can be recognized in wells installed in the shallow sediments after the earthquake (left column of Fig. 9.7b). On the other hand, some clear changes of groundwater composition after the earthquakes were measured in wells installed in the basement rocks (right column of Fig. 9.7b). These include consistent post-seismic

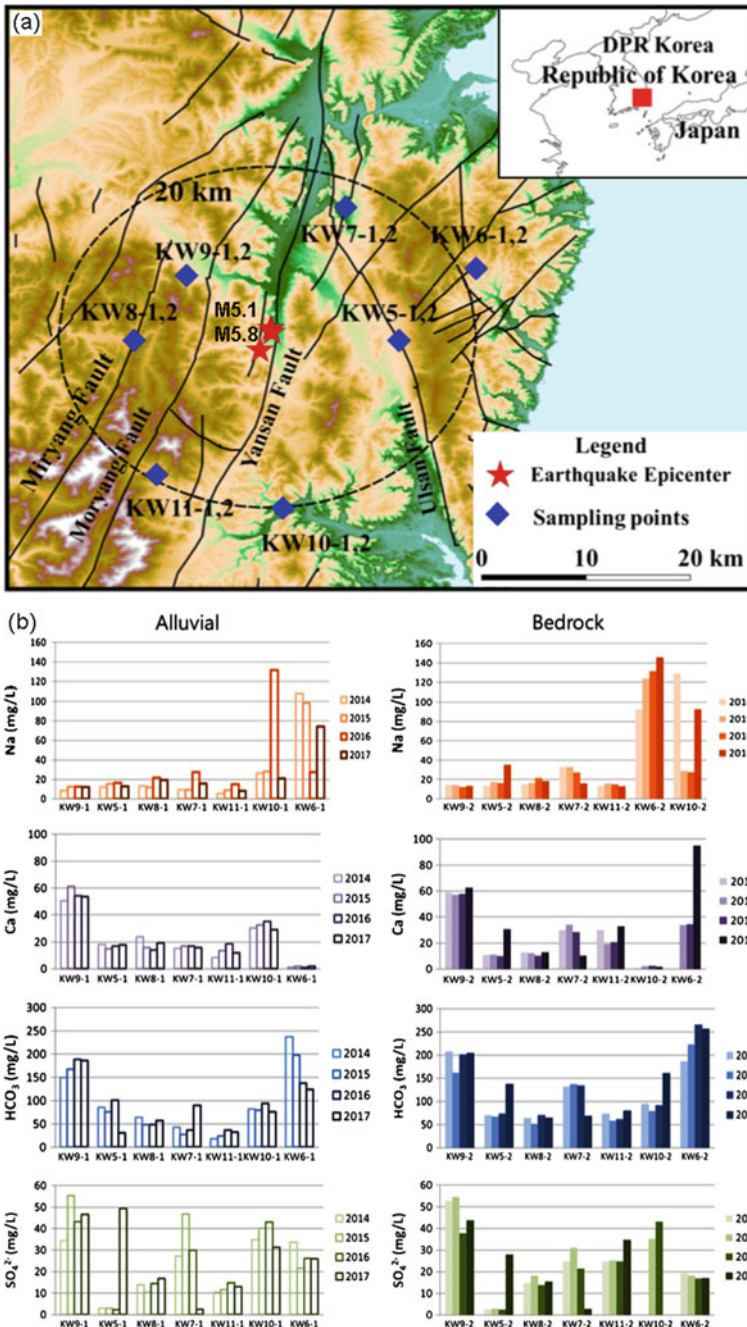


Fig. 9.7 a Locations of the studied area, the epicenter of the 2016 M5.8 earthquake, and the studied wells in SE Korea. b Concentrations of Na^+ , Ca^{+2} , HCO_3^- and SO_4^{2-} in the waters from the studied wells from 2014 to 2017. Measurements in the first three years were made before the earthquake; the one in 2017 was made after the earthquake (modified from Kaown et al. 2019)

increase of the concentrations of Na^+ , Ca^{+2} , HCO_3^- and SO_4^{2-} (well KW5-2), consistent post-seismic decrease in the concentrations of the four same ions (well KW7-2), and clear post-seismic increases in Na^+ and Ca^{+2} (well KW6-2), but no change in HCO_3^- or SO_4^{2-} . The inconsistent changes of groundwater composition after the earthquake among these wells suggest that the wells may be opened to different and isolated fractures in the basement rocks. They also illustrates the difficulty in understanding earthquake-induced composition changes.

9.2.2 Trace Elements

There is no universally agreed definition for ‘trace elements’ but the term is usually used for elements with concentrations below 0.1%. In this sense, whether an element may be a trace element or not depends on the lithology of the rock. For example, while Si is the most abundant element in beach sand, it may occur only in trace amounts in some carbonate aquifers.

9.2.2.1 Italy

Rosen et al. (2018) measured the chemical composition of four springs in the central Apennines of Italy before and after several earthquakes in 2016 to 2017. They found four springs at varying distances from the epicenters that all showed immediate post-mainshock increases in trace element concentrations but little change in major elements.

These springs are recharged by major aquifers hosted in Cenozoic to Mesozoic carbonate rocks that overly an evaporitic basal structure. The aquifers are characterized by two major flow paths: a shallower one with high flow rate and a deeper one with low to medium flow rates where seepage of deep mineralized fluid occurs along fractures. This dual-flow structure allows waters with different residence times to occur in the same aquifer.

The authors suggest that fluids enriched in trace elements may have been stored in fractures with slow flow and hence have long residence times. These fluids were expelled into the main flow paths after the earthquakes due to increased pore pressure and enhanced permeability. Rosen et al. (2018) also noticed that the response of the compositions of these trace elements to the later earthquakes is much weaker than that to the first (Fig. 9.8). They attributed the weaker response during the later earthquakes as the result of progressive depletion of the high solute fluids as the earlier shocks flushed such fluids stored in the fractures.

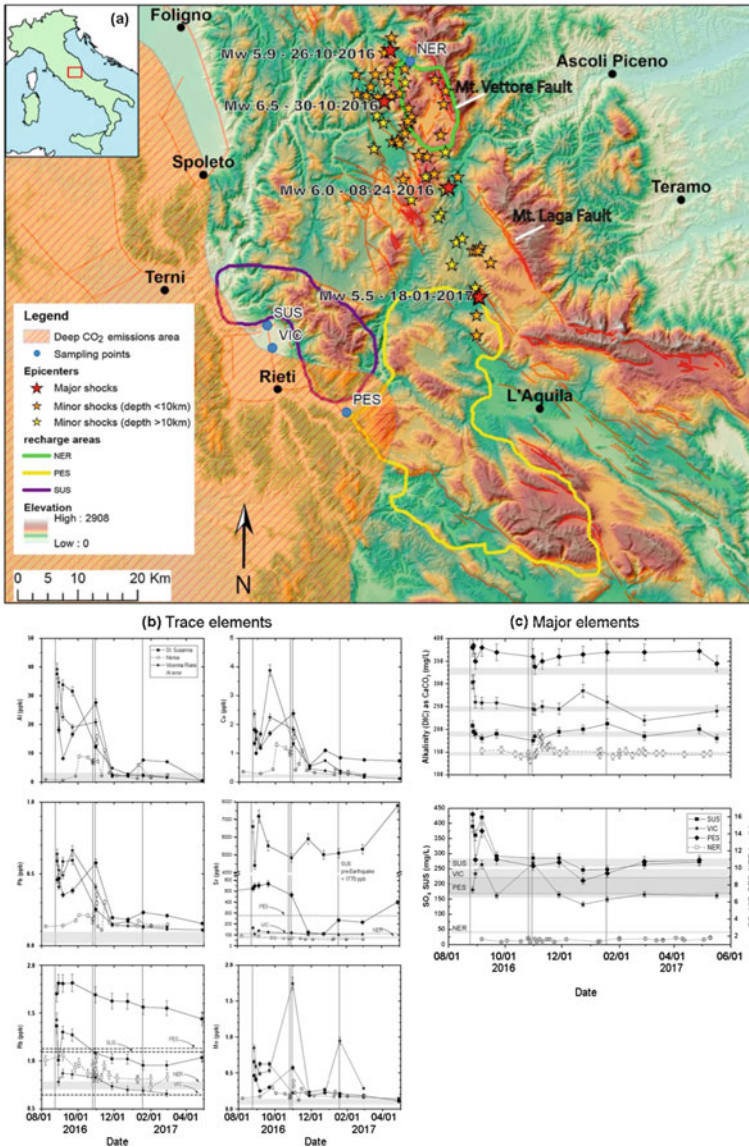


Fig. 9.8 a Location map of sampling sites of springs (blue circles) and epicenters of major earthquakes (stars). Colored contours show recharge areas for different springs. Red lines show surface traces of active faults. Time series of **b** trace metal concentrations and **c** major elements concentrations in four springs in central Apennines: Nerea spring (NER), Santa Susanna spring (SUS), Vicenna Riara spring (VIC), and Peschiera spring (PES). Vertical lines mark the times of the four major earthquakes; horizontal gray bands show pre-seismic values of Al, Cu, Pb, and Mn, where all springs had the same range. Dashed horizontal lines show the pre-seismic earthquake values of Sr and Rb at each individual spring (modified from Rosen et al. 2018)

9.2.2.2 China

For completeness we also include a study of the change of concentrations of the rare earth elements. Shi et al. (2020) studied the concentrations of both the major elements and the rare earth elements in a groundwater well in SW China before and after a nearby M5.0 earthquake (Fig. 9.9a). The well is located in a tectonic graben bounded by active strike-slip faults and opens to an aquifer hosted in a sequence of Sinian sandstones and shales, which is confined above by Quaternary lacustrine clay, sands and gravels. Shi et al. (2020) found that the concentrations of the rare earth elements in the groundwater increased sharply after the earthquake (Fig. 9.9b). On the other hand, the concentrations of the major elements (Fig. 9.9c) and the δD and $\delta^{18}O$ in this well showed no clear responses, similar to the findings of Rosen et al. (2018) in the central Apennines of Italy.

Shi et al. (2020) attributed the different responses of the rare earth elements and the major elements in the SW China well to the small background noise in the measurements of the rare earth elements and the large background noise in the measurements of the major ions. Here we suggest the model proposed by Rosen et al. (2018) of a multi-flow system as an alternative interpretation. Because the Jiangchuan well is located in a geothermal area and its water temperature is ~ 34 °C (Shi et al. 2020), the well water is likely to be a mixture of shallow groundwater and deep geothermal waters that flow into the well by seepage from conductive fractures. The nearby 2018 M5.0 earthquake may have enhanced the fracture permeability, leading to an increased geothermal flow that in turn may have transported rare earth elements into the well but insufficient fluid to affect water isotopes and major elements.

9.2.2.3 Iceland

Claesson et al. (2004, 2007) reported the changes of some trace element concentrations (B, Li, Sr, Rb, Mo; Fig. 9.10a) in the groundwater of borehole HU-01 of Iceland (see Fig. 9.1b for well location) following a 2002 M5.8 earthquake (see Fig. 9.1a for epicentral location) and other smaller earthquakes in 2004–2005. The trace element concentrations show coseismic increases with the same pattern as those for the major elements.

The observation by Claesson et al (2004) is in contrast with the observations in the central Italian Apennines (Rosen et al. 2018) and in SW China (Shi et al. 2020) where only the trace element concentrations increased but those for the major elements remained unchanged. This contradiction is another example that shows that the interpretation of groundwater composition changes is challenging. Different types of data, in addition to the chemical data, may be required to better constrain the problem.

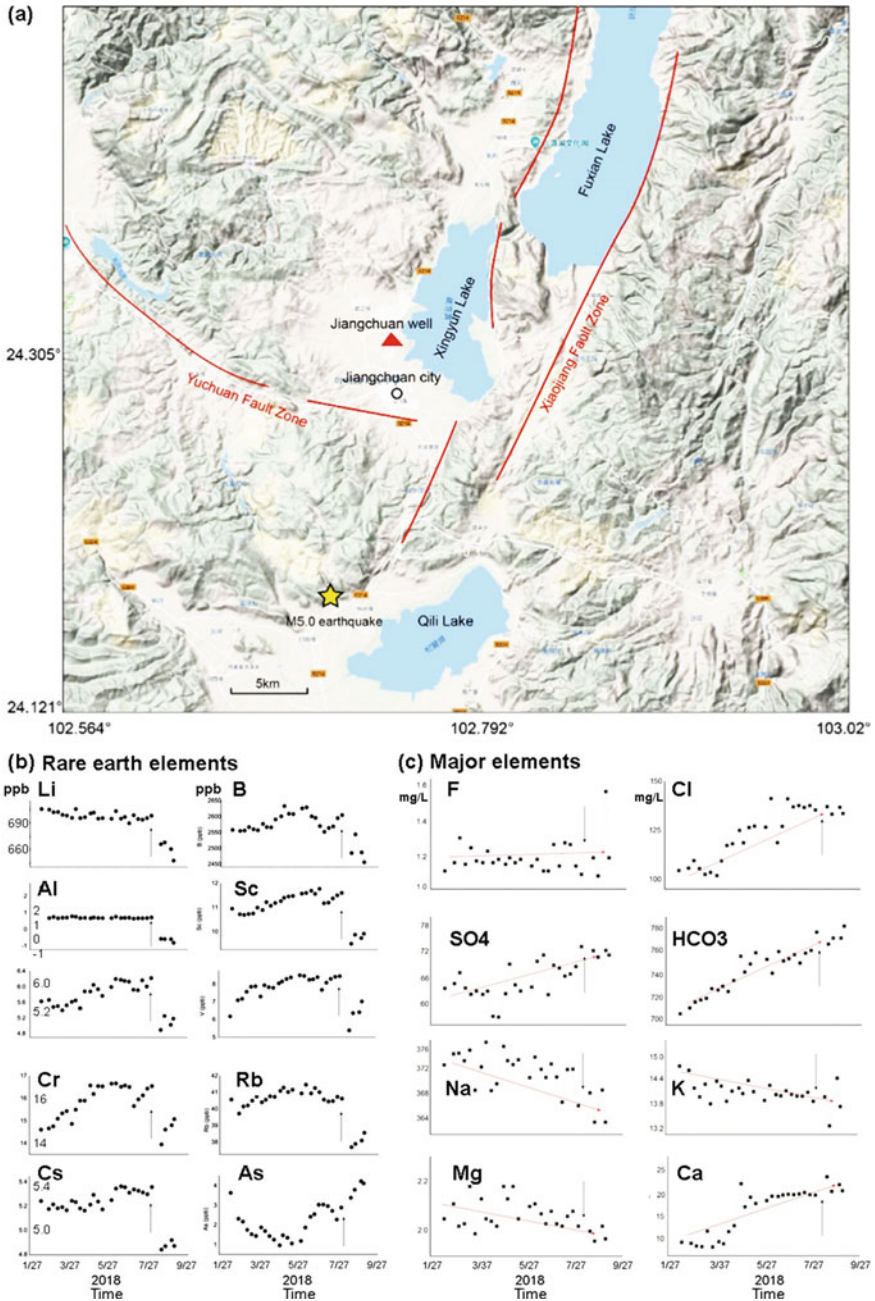


Fig. 9.9 a Location map of the Jiangchuan well and the epicenter of the 2018 M5.0 earthquake. Red lines show surface traces of active major fault zones. Time series of groundwater composition in the Jiangchuan well, SW China, of **b** the rare earth elements and **c** the major elements. The vertical arrows show the time of the 2018 M5.0 earthquake (from Shi et al. 2020)

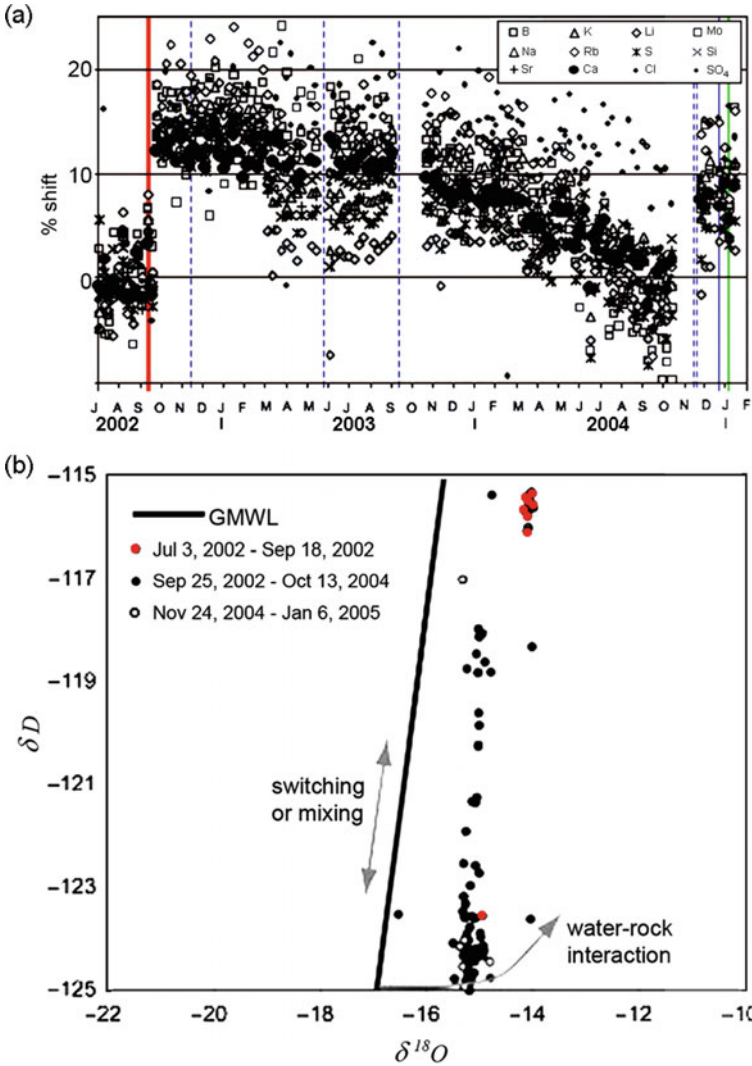


Fig. 9.10 **a** Plot of water chemistry over time for groundwater samples from borehole HU-01, showing the percentage shifts after earthquakes in the concentrations of B, K, Li, Mo, Na, Rb, S, Si, Sr, Ca, Cl and SO₄. The timing of M > 5, M > 4 and M > 3 earthquakes are marked by red, green and blue lines, respectively. **b** δD versus δ¹⁸O for groundwater samples from borehole HU-01 showing data from 3 July 2002 to 18 September 2002 (grey circles), 25 September 2002 to 13 October 2004 (black circles) and 24 November 2004 to 6 January 2005 (white circles). The abrupt hydrogeochemical shift, which occurred within 2–9 days after the M 5.8 earthquake on 16 September 2002, and its recovery during the subsequent two years indicate that switching between or mixing of aquifers is the primary hydrogeochemical control. GMWL is the Global Meteoric Water Line (from Claesson et al. 2007)

9.2.3 Stable Isotopes

Geologic processes often cause changes in the relative proportions of the stable isotopes of oxygen and hydrogen in groundwater. An important tracer to characterize the origin of the excess water is the isotopic composition of the post-seismic excess discharge. The differences in ^{18}O and D relative to VSMOW emerge from the fractionation processes during the transport and precipitation of water vapor. The combination of decreasing temperature and increasing rainout with elevation results in water that is isotopically lighter, i.e., depleted in the heavier isotope, and the rate of this decrease with elevation is reported as the $\delta^{18}\text{O}$ and δD lapse rates. Thus, water released from consolidation and from the pore waters in unsaturated soils would have a local isotopic signature, while water originating from high mountains would have a lighter isotopic signature, and water released from mid-crustal depths would have an isotopic signature with evidence of high temperature water-rock interaction (resulting in $\delta^{18}\text{O}$ isotopic shifts towards enriched compositions leaving δD unchanged). Thus, the change in the stable isotope composition after an earthquake may be used to infer for the source of the new groundwater. In this section we review examples in Iceland, Taiwan and Japan, where interesting findings and significant conclusions have been obtained.

9.2.3.1 Iceland

The 2002 M5.8 earthquake in Iceland (Fig. 9.1a) caused changes in the oxygen and hydrogen isotope ratios of groundwater in well HU-01 (see Fig. 9.1b for well location). Claesson et al. (2004, 2007) reported these changes (Fig. 9.10b) and differentiated between two models for the changes of $\delta^{18}\text{O}$ and δD in groundwater during and after earthquakes. In the first model, accelerated water-rock reactions are caused by an assumed increase in fresh mineral surfaces exposed to groundwater along newly formed cracks and fractures created by the earthquake, leading to rapid changes in groundwater composition. In the second model, rapid change in groundwater composition results from fluid-source switching or mixing of groundwater from a newly tapped aquifer containing chemically and isotopically distinct water, probably caused by unsealing of pre-existing faults and breaching of hydrologic barriers. The first model predicts that δD and $\delta^{18}\text{O}$ of groundwater after the earthquake would move away from the Global Meteoric Water Line (GMWL), i.e., along the single-arrow light-gray curve at the bottom of Fig. 9.10b. The second model, on the other hand, predicts that δD and $\delta^{18}\text{O}$ of the groundwater after the earthquake would change in a direction parallel to the Global Meteoric Water Line (GMWL), i.e., along the double-arrow path shown in Fig. 9.10b (Claesson et al. 2007).

The three sets of data for Iceland water samples, one collected shortly before and two after the M5.8 earthquake, show that the changes in δD and $\delta^{18}\text{O}$ of the groundwater after the earthquake are nearly parallel to the GMWL (Fig. 9.10). The

data are thus consistent with the model of source switching and/or mixing of groundwater with a newly tapped aquifer, but inconsistent with the model of accelerated water-rock reactions due to increased fresh mineral surfaces.

9.2.3.2 Taiwan

Groundwater samples were collected from a network of monitoring stations on the Choshui River fan for oxygen isotope analysis (small circles in Fig. 9.11) before and after the September 1999 Chi-Chi earthquake (Wang et al. 2005). At each station, two to five cluster wells were installed into different aquifers (Fig. 9.12) and the distribution of the isotopic composition of groundwater in each aquifer was determined independently. The upper five diagrams of this figure show the isotope compositions in the topmost aquifer (Aquifer I; see Fig. 9.12) before and after the Chi-Chi earthquake and their differences at several time intervals after the earthquake; the lower five diagrams of this figure show similar compositions in the third aquifer (Aquifer III; see Fig. 9.12). Before the Chi-Chi earthquake the distribution of $\delta^{18}\text{O}$ in Aquifer I (Fig. 9.11a) increased from $\sim -5\text{‰}$ near the coast to $\sim -8\text{‰}$ near the upper rim of the alluvial fan. Shortly after the earthquake (October to December 1999), $\delta^{18}\text{O}$ became more negative (Fig. 9.11b). The differences between Fig. 9.11a, b are given in Fig. 9.11c to show the earthquake-induced changes. Since the seasonal variation of $\delta^{18}\text{O}$ is less than 0.4‰ , all the changes more than 0.4‰ can be attributed to the earthquake; these areas are colored green to highlight the earthquake effect. The affected area covers a broad zone near the coast on both sides of the Chishui River, with a change up to 1‰ . Changes persisted to the end of this analysis, nearly two years after the earthquake, even though the area and magnitude of the increased depletion slightly diminished over time (Fig. 9.11d, e). Wang et al. (2005) attributed this depletion in Aquifer I to an increased contribution from the Choshui River that discharges depleted $\delta^{18}\text{O}$ water from the high mountains on the east.

However, Aquifers II and III showed areas of depleted $\delta^{18}\text{O}$ even before the earthquake; only the data from Aquifer III are shown here (Figs. 9.11a'–e'). Figure 9.11a' shows that before the earthquake, there was a large area of depleted $\delta^{18}\text{O}$ on the north-side of the Choshui River, probably due to recharge of groundwater from a higher elevation in the mountains to the east, transported to the aquifer through a subsurface abandoned river channel (Chang 1983). Shortly after the Chi-Chi earthquake (October–December 1999), the region of depleted $\delta^{18}\text{O}$ expanded (Fig. 9.11b'), and the earthquake-induced change (the difference between Fig. 9.11a, b) is given in Fig. 9.11c'. Comparing Fig. 9.11c and c' shows that the areas with a difference of $\delta^{18}\text{O}$ more than 0.4‰ are nearly identical in these two aquifers. The area of depletion in Aquifer III also slowly diminished over time and persisted for >2 years to the end of the study (Fig. 9.11e'), similar to Aquifer I.

The spatial coincidence of locations with more than 0.4‰ depletion of $\delta^{18}\text{O}$ in Aquifer I and Aquifer III led Wang et al. (2005) to suggest that there was vertical mixing of groundwater between different aquifers after the Chi-Chi earthquake. Figure 9.12 that shows the hydrogeological cross-section of the Choshui River fan,

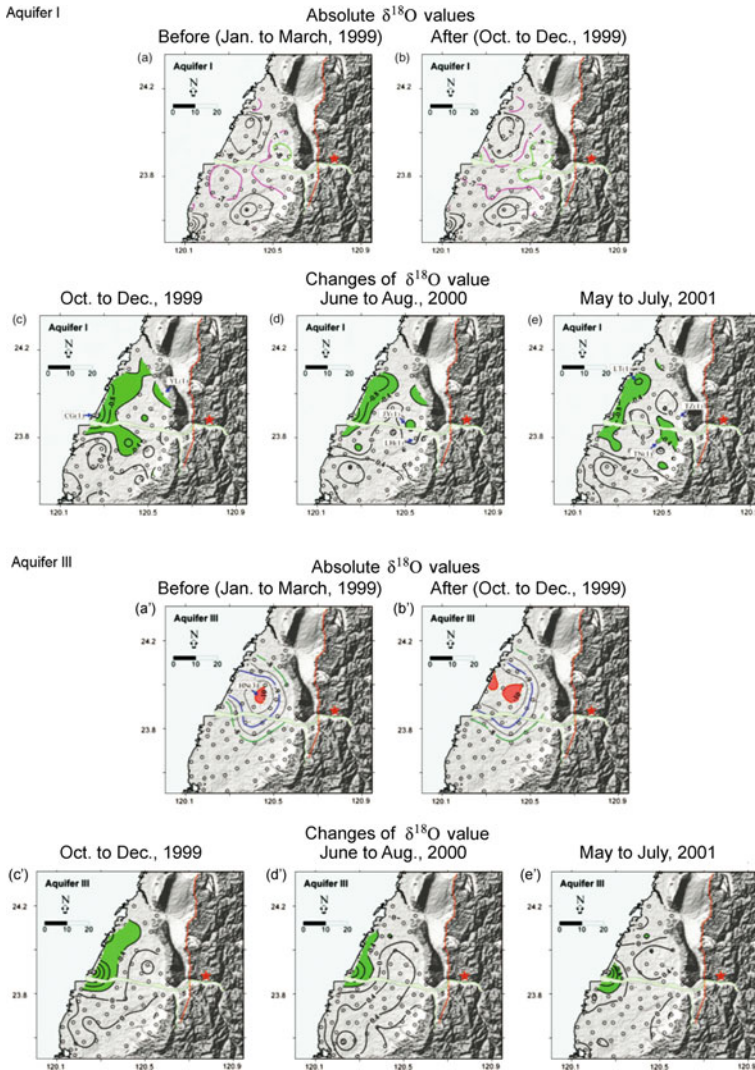


Fig. 9.11 Oxygen isotope contours for Aquifer I in the Choshui alluvial fan from 1999 to 2001. The open circles are the sampled groundwater stations. At each station, several wells were installed in different aquifers. Red color denotes areas where $\delta^{18}\text{O}$ values was below -10‰ ; green color denotes areas where $\delta^{18}\text{O}$ was depleted by more than 0.4‰ . **a** Absolute $\delta^{18}\text{O}$ values in January–March, 1999, before the Chi-Chi earthquake. **b** Absolute $\delta^{18}\text{O}$ values in October–December, 1999, shortly after the Chi-Chi earthquake. **c** Difference between **(b)** and **(a)**. **d** Difference between measurements made in January-to-August, 2000, and **(a)**. **e** Difference between measurements made in May–July 2001 and **(a)**. The scale bars are in km. **(a')** to **(e')**, similar to **(a)** to **(e)** but for Aquifer III (from Wang et al. 2005)

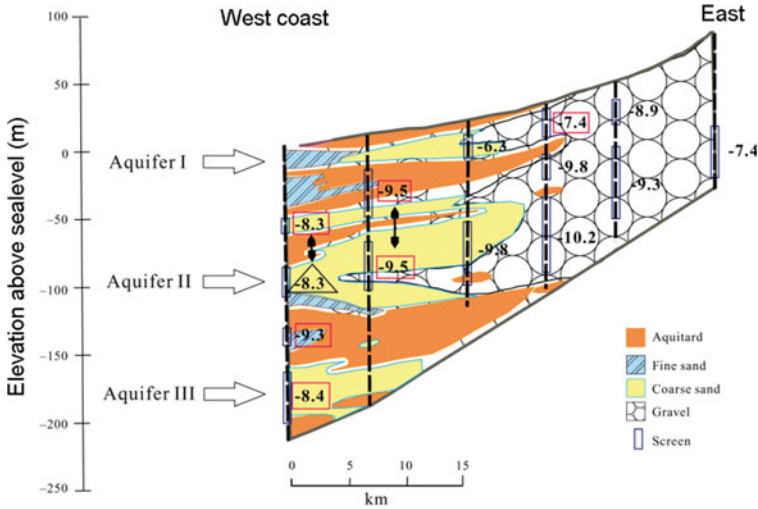


Fig. 9.12 Hydrogeologic cross-section of the Choshui River alluvial fan. The thick vertical dashed lines represent boreholes. The numbers represent the measured $\delta^{18}\text{O}$ in units of per mil for each sampling site after the Chi-Chi earthquake. The squares represent sites that had decreased oxygen isotope values after the earthquake, while the triangles represent sites that had increased oxygen isotope values. The double arrows indicate aquifers whose $\delta^{18}\text{O}$ values converged to the same value after the earthquake (modified from Wang et al. 2005)

in which aquifers with a convergence of the $\delta^{18}\text{O}$ values after the earthquake are connected with doubleheaded arrows. The suggestion of vertical mixing of groundwater between different aquifers is supported by subsequent studies that showed that the confinement between these aquifers was breached during the earthquake, which caused the initially different groundwater level in some aquifers to converge to the same level (Wang 2007) and their post-seismic tidal responses to become nearly identical after the Chi-Chi earthquake for an extended period (Wang et al. 2016).

The distribution of the change in $\delta^{18}\text{O}$ composition shortly after the Chi-Chi earthquake (Fig. 9.11c, c') shows entirely different patterns from that for the coseismic water-level change in the same aquifers (Fig. 6.4b, d). This difference suggests that that the change in isotope composition is unrelated to that that caused the coseismic water level change. This observation is consistent with the suggested mechanism of undrained consolidation for the groundwater level change (Wang et al. 2001) because undrained consolidation does not involve exchange of groundwater and thus is not expected to cause any change in groundwater composition. But it may be interesting to explain why an exchange of water source did not cause a change in water level. We consider the Peclet number for solute transport (Eq. 2.39), $Pe = \nu L/D$, where ν is the linear velocity of the groundwater flow, L is the characteristic distance between different aquifers and D is the hydrodynamic dispersion coefficient. Appreciable change in solute concentration by advective transport would occur if $Pe > 1$, that is, if $\nu \geq D/L$. A similar consideration shows that the effect of advective transport on

the hydraulic head occurs if $v \geq (K/S_s)/L$ (Phillips 1991), where K is the hydraulic conductivity and S_s is the specific storage of the aquifer. Given the order of magnitude estimate of longitudinal dispersivity $\alpha = 1$ to 10 m and a typical linear velocity of 10^{-8} m/s (Ingebritsen et al. 2006), $D \sim \alpha v$ is of the order of 10^{-8} – 10^{-7} m²/s, while K/S_s is of the order of 1 m²/s for the confined aquifers in the Choshui River fan (Tyan et al. 1996). Thus, the flow velocity required to significantly affect solute composition is 7–8 orders of magnitude smaller than that required to significantly affect the groundwater level. In other words, the amount of exchange of groundwater between Aquifers I and Aquifer III to cause the increased depletions of $\delta^{18}\text{O}$ near the coast may be too small to cause an observable change in the groundwater level.

Finally, while the similarity between Aquifer I and Aquifer III in the locations of the areas with more than 0.4‰ depletion of $\delta^{18}\text{O}$ suggests the occurrence of vertical mixing of groundwater after the Chi-Chi earthquake, it does not specify whether the groundwater flow was upward or downward, which may bear on the origin of the depleted water. An objective criterion comes from the study of groundwater temperature change beneath the Choshui River fan after the Chi-Chi earthquake. In Sect. 8.3 we showed that an appreciable increase of groundwater temperature occurred along a broad area along the western coast after the earthquake. This increase of groundwater temperature implies an upward flow of groundwater in the coastal area after the earthquake. Given the Peclet number for advective heat transport (Chap. 2, Eq. 2.2.9) $Pe = qL/D_h$, where q is Darcy velocity, $D_h = K_h/\rho_w c_w$ is the thermal diffusivity, K_h is the thermal conductivity, ρ_w and c_w , respectively, are the density and specific heat of water, advective heat transport becomes significant when $v\phi = q \geq D_h/L$, where ϕ is porosity. Since ϕ is of the order of 10^{-1} and D_h is of the order of 10^{-6} m²/s, appreciable advective transport of heat occurs if $v \sim 10^{-5} L^{-1}$ m/s, which is ~ 3 orders of magnitude greater than that required to cause appreciable advective transport of solute. Thus, the hypothesis that upward flow caused the vertical mixing of water between Aquifers I and Aquifer III after the Chi-Chi earthquake is consistent with both the post-seismic change of groundwater temperature and that of groundwater chemistry. Quantitative modeling is clearly necessary to test this hypothesis and to estimate the amount of flow involved in the exchange process.

9.2.3.3 Japan

There are several studies of the changes in the isotopic composition of groundwater after the 2016 Kumamoto earthquake. Hosono et al. (2020a) analyzed a comprehensive dataset for isotopic compositions of groundwater, spring water and river water in the affected region before and after the earthquake. They found that all waters changed their δD and $\delta^{18}\text{O}$ compositions towards more depleted values after the earthquake (Fig. 9.13). They also found that the composition of groundwater changed from resembling a mixture of multiple sources before the earthquake into a composition with a signature similar to the mountain foot spring waters after the earthquake (Fig. 9.13b–d), regardless of the sampling season, the aquifer types (confined

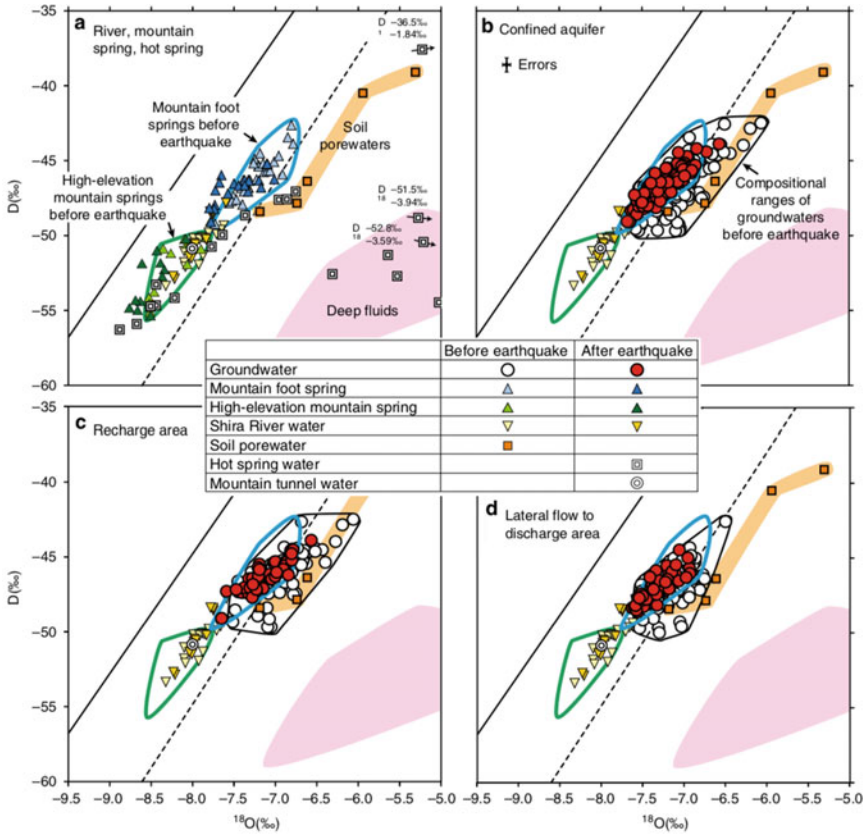


Fig. 9.13 Changes in δD and $\delta^{18}O$ compositions. **a** δD and $\delta^{18}O$ compositions of groundwater, spring water and river water both before (April 2011–July 2011) and after (August 2016–May 2017) the main shock for river and spring waters for samples collected in different seasons. The blue, green and black contours show, respectively, the composition ranges of the mountain-foot springs, the high-elevation springs and groundwaters before earthquake. Compositions of hot spring waters and mountain aquifer water from ongoing tunnel construction for the samples collected after the main shock are also plotted. Springs (blue and green triangles) and river (yellow triangle) water samples obtained after the earthquake are shown in darker colors than samples from before the earthquake. Samples collected in all seasons for both aquifers (unconfined and confined aquifers) are plotted together. **b** Compositional changes of groundwater from confined aquifers collected in various seasons before (November 2009–November 2011) and after (June 2016–December 2017) the earthquake. Samples after the earthquake are shown in red, while those before the earthquake are shown in white. Error bars show the sizes of measurement errors. **c** and **d**, respectively, changes of groundwater compositions from the recharge area and from the discharge area (from Hosono et al. 2020a)

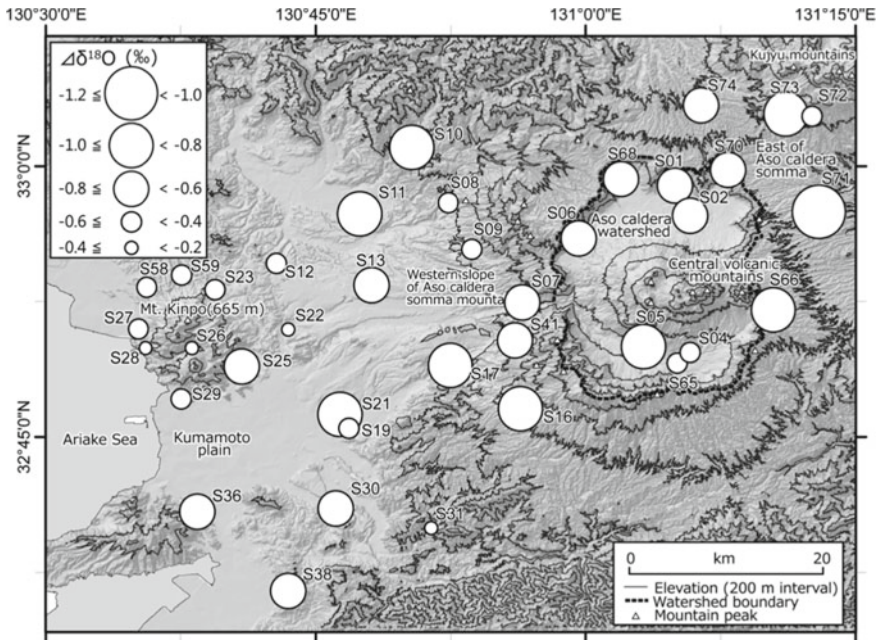


Fig. 9.14 Distribution of earthquake-induced changes in stable isotope ratio ($\delta^{18}\text{O}$) of spring water samples between 2009 and 2017 ($\Delta\delta^{18}\text{O} = \delta^{18}\text{O}_{2017} - \delta^{18}\text{O}_{2009}$). Circles show spring location and the circle sizes show the relative change magnitude (from Ide et al. 2020)

or unconfined) and the areas of the aquifers, implying an increased post-seismic contribution of water from mountain aquifers.

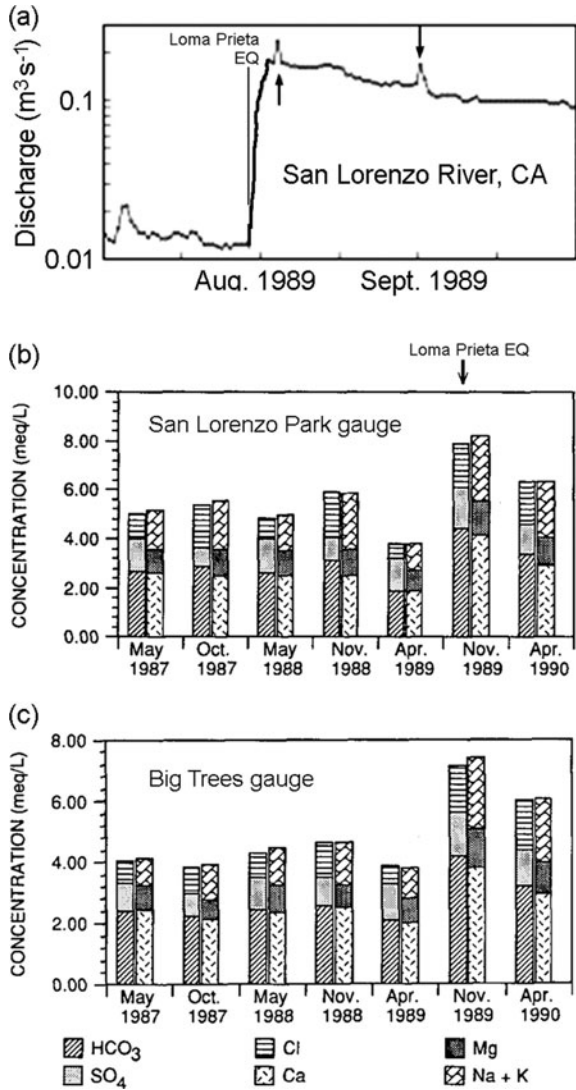
Ide et al. (2020) studied the change of water isotopes in many springs in central Kyushu after the 2016 Kumamoto earthquake. They also found a regional decrease of $\delta^{18}\text{O}$ of the spring waters (becoming more negative) after the earthquake (Fig. 9.14) by comparing their $\delta^{18}\text{O}$ after the earthquake with those measured in the year of 2009. These authors attributed this change to the mixing of water with lighter isotopic composition released from the Aso Caldera into the regional groundwater that supplies most springs in the study area. The observed $\delta^{18}\text{O}$ changes generally show greater absolute magnitudes closer to the Aso Caldera than those further away (Fig. 9.14), supporting their interpretations.

9.3 Stream Water Composition

As noted at the beginning of this chapter, the detection of earthquake-induced changes of water chemistry in streams may be challenging because the signals in the new water may be diluted by the existing water in the streams. Thus earthquake-induced changes of stream water chemistry are rarely studied unless the amount of water in

the streams before the earthquake is negligible. Such a situation, though unusual, occurred at least twice in central California in the past thirty years during the dry seasons when stream flow was either low or absent. Following the Loma Prieta earthquake, central California, on 17 October 1989, the discharge in some streams near the epicenter increased more than an order of magnitude over that before the earthquake (Fig. 9.15a). Rojstaczer and Wolf (1992) reported the stream discharge and the change of water chemistry at two gauging stations in the San Lorenzo drainage basin and compared these with earlier measurements (Fig. 9.15b, c) that had been

Fig. 9.15 **a** Discharge in the San Lorenzo River. Arrows show the occurrences of local precipitation. **b** Major ion chemistry in the stream water as a function of time at the San Lorenzo Park gauge, and **c** at the Big Trees gauge in the San Lorenzo drainage basin, central California (modified from Rojstaczer and Wolf 1992)



documented on a biannual basis. The stream chemistry showed a marked increase in overall ionic strength after the earthquake, but the proportions of the major ions were nearly the same as those before the earthquake. The increased ion concentration decreased significantly over a period of several months after the earthquake (Fig. 9.15) together with the decrease in the excess stream discharge. By April 1990, the stream water chemistry had begun to approach the pre-earthquake conditions at both stations. The change of stream chemistry, together with a general cooling of the stream water by several degrees, led Rojstaczer and Wolf (1992) and Rojstaczer et al. (1995) to suggest that the additional stream discharge following the Loma Prieta earthquake was derived from groundwater from the drainage basin instead of from mid-crustal depths. This is the main argument used by Rojstaczer et al. (1995) to argue against the static strain model of Muir-Wood and King (1993).

A second example is the South Napa earthquake in northern California (Fig. 7.3a), which occurred during a prolonged drought in California when many small creeks in the Coast Ranges were either dry or had little flow. These seasonal creeks (see Fig. 7.3a for locations) started to flow right after the earthquake (Figs. 7.3b, d and e). Since there was little or no water in the creeks before the earthquake, the new flows were not mixed with pre-existing waters and their composition represents the composition of the mobilized waters. For this reason, the composition of the new flows in the Napa and the Sonoma Valleys following the South Napa earthquake is particularly valuable.

Wang and Manga (2015) measured the $\delta^{18}\text{O}$ and δD in the new discharges following the South Napa earthquake. Figure 9.16a shows that the stable isotopes of hydrogen and oxygen of the new waters define a linear relation on a δD versus $\delta^{18}\text{O}$ plot, parallel to, but slightly shifted to the left of, the global meteoric water line (GMWL). Wang and Manga (2015) interpret the slight shift from GMWL to reflect differences in humidity and temperature that affect secondary evaporation as rain falls from clouds. The isotopic compositions of each flow, sampled at different times, cluster closely together, suggesting that each flow came from a distinct source of constant composition. Different flows, on the other hand, span a broad range of isotopic composition, suggesting that the different sources were recharged by meteoric water at different elevations. Also plotted are the isotopic compositions of the Napa River determined at various times of year from 1984 to 1987 (Coplen and Kendall 2000). From November to March, normally the rainy season, the isotopic composition of Napa River falls mostly close to the GMWL; during dry seasons, on the other hand, it becomes significantly heavier and falls to the right of the GMWL, reflecting the evaporation of river water and recharge from shallow groundwater or reservoirs in the valley during dry seasons.

Wang and Manga (2015) interpreted the isotopic signatures of the new flows (Fig. 9.16a) to suggest that the new flows originated from meteoric water that was stored as groundwater in the nearby mountains at different elevations, which was released by the South Napa earthquake through enhanced vertical permeability, like that suggested for the increased stream flows after the 1999 Chi-Chi earthquake.

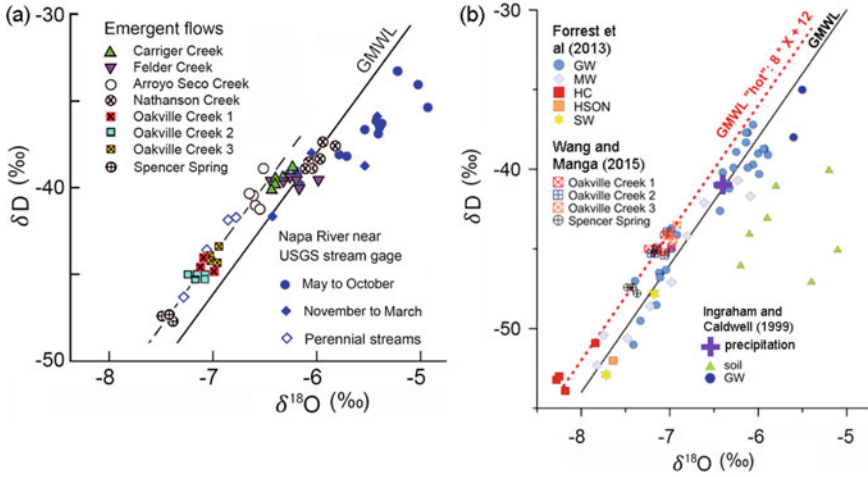


Fig. 9.16 **a** Stable isotope data for the studied streams and spring in Wang and Manga (2015). Shown are measurements of δD versus $\delta^{18}O$ for the new streams and Spencer Spring, the Napa River from 1984 to 1987, and three major perennial streams in foothills. Measurement errors are smaller than the size of symbols used. Solid line shows the GMWL. Data from this study define a local meteoric water line parallel to, but shifted slightly to the left of the GMWL. Notice that the isotopic compositions of each flow, sampled at different times, cluster together, while the isotopic compositions of different flows span a broad range along the local meteoric water line. During rainy seasons (normally November to March) the isotopic composition of the Napa River falls mostly close to the GMWL; during dry seasons, the Napa River composition becomes significantly heavier and falls to the right of the line due to evaporation and recharge by evaporated surface water. **b** Heiko Woith’s plot (personal communication) of stable isotope data from Wang and Manga (2015), Forrest et al. (2013) and Ingraham and Caldwell (1999). The label ‘GMWL hot’ on the dashed line suggests a mixing line between the meteoric water and geothermal water. GW: non-hydrothermal groundwater, MW: mixed hydrothermal/meteoric water, HC: hydrothermal groundwater from Calistoga; HSON: hydrothermal water from Sonoma; SW: saline water

It is also significant that the isotopic composition of some perennial streams in foothills falls along the same local meteoric water line defined by the new flows (Fig. 9.16a). Since these streams are recharged by baseflow in the mountains during the drought, the similarity between their isotopic composition and that of the new flows supports the suggestion that the new flows originated from the groundwater in the nearby mountains. Wang and Manga (2015) also compared the composition of the new waters with the average composition of the perennial Napa River, which represents an averaged stream water composition in the valley. The spread of $\delta^{18}O$ in the new waters is from -6 to -7.5‰ (Fig. 9.16a), while that of the Napa River water between May and October (before the rainy season) spreads from -5 to -6‰ . Thus, the earthquake may have caused an overall decrease of $\delta^{18}O$ by 1.5‰ (more negative) from that on the valley floor. Assuming a global lapse rate of 2.1‰ km^{-1} (Chamberlain and Poage 2000), Wang and Manga (2015) suggested that this difference in $\delta^{18}O$ corresponds to a difference in elevation of ~ 700 m, which may be compared with the difference in elevation between the valley floor (near sea level)

and some mountains in the studied area, such as Cobb Mountain at 1440 m above sea level, and Mount Saint Helena and Hood Mountain over 762 m above sea level, consistent with the hypothesis that the new waters were released from the nearby mountains.

After the South Napa earthquake, many springs also began to flow in the nearby mountains. According to the owner of a local ranch (John Tuteur, 9/13/2014), "... the (largest) spring is a major enhancement of what used to be a seep. The opening is approximately 20–25 cm wide and 5–6 cm deep. When I last visited the spring the water was coming out of the opening in a shape that matched the opening. The water flows down a flat channel into the creek approximately 8–10 m below the spring outlet. The other springs which are pretty difficult to reach on foot are more like seeps that are flowing in thin sheets down the face of a cliff side approximately 2–4 m above the stream channel. There are four or five of those seeps in close proximity to each other." Starting Sept. 14, 2014, Wang and Manga (2015) measured the discharge, temperature, isotopic and chemical composition of the largest hot spring (Spencer Spring, see Fig. 7.3a for location) at an elevation of ~200 m and away from any local water dams. Measurements continued until the end of July, 2020, with some interruptions in sampling caused by forest fires. Figure 9.17 shows that, while the discharge has decreased by more than an order of magnitude since the beginning of the measurements, temperature of the spring water has declined only slightly from 31 °C in the late 2014 to 30 °C in July, 2020, and the isotopic compositions has stayed nearly constant at -7.4‰ to -7.7‰ for $\delta^{18}\text{O}$, and at -46‰ to -48‰ for δD , suggesting that the spring water was supplied from a nearly constant source with little mixing of surface water, and that the decrease in discharge was probably due to a gradual clogging of the pathways connecting the source to the surface spring, which were opened by the earthquake. The nearly constant water temperature of the Spencer Spring is in contrast with the variable temperature of water in the streams, which ranges from 13 to 21 °C. The average surface temperature is ~15 °C and the regional average geothermal gradient is 46 °C/km; thus the new water may have come from depths greater than ~300 m beneath the surface assuming the average geothermal gradient at the spring site.

Curiously, the $\delta^{18}\text{O}$ and δD of the water in the Spencer Spring are the lightest among the new waters and plot on the extension of the dashed line in Fig. 9.15a. Forrest et al. (2013) also showed that fluids of inferred hydrothermal origin in the Napa and Sonoma Valleys are light in $\delta^{18}\text{O}$ and δD and remain close to the meteoric water line, suggesting that these hot springs are recharged by meteoric water. Heiko Woith (personal communication) plotted the data from Wang and Manga (2015), Forrest et al. (2013) and Ingrham and Caldwell (1999) together in Fig. 9.16b and labeled the dashed line that connects the new stream waters and the hydrothermal waters "GMWL hot", hypothesizing that the isotopic compositions of the new waters were due to the mixing of groundwater released from nearby mountains with increased hydrothermal water released from depth by the earthquake. More work is clearly needed to better understand the origin of the new waters.

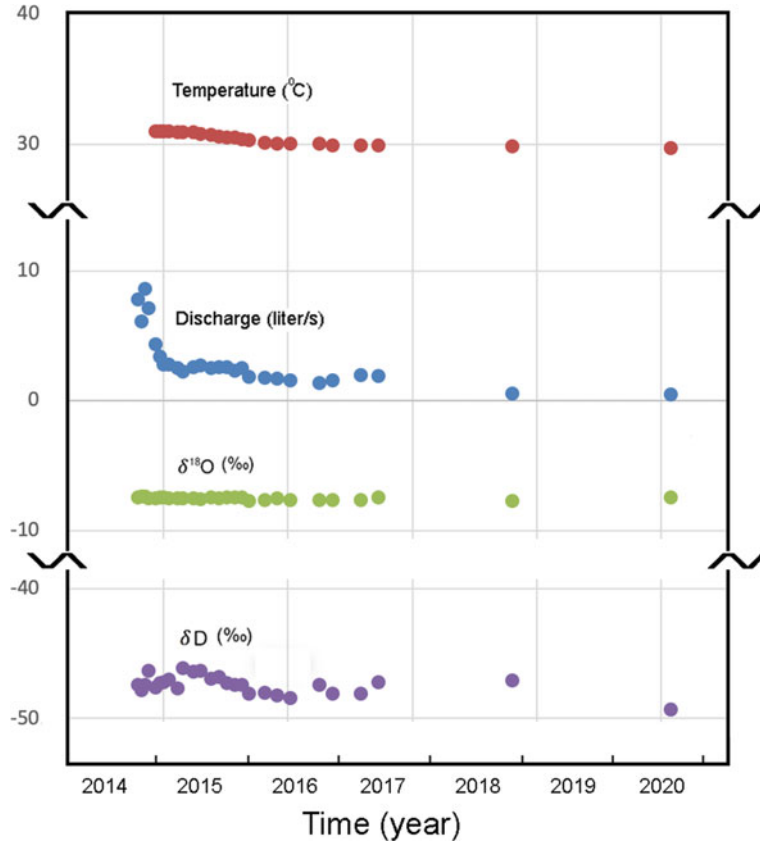


Fig. 9.17 Temperature, discharge, $\delta^{18}\text{O}$ and δD of water of the Spencer Spring of Napa Valley, California, following the 2014 South Napa earthquake to 2020 (diagram from the authors)

9.4 Need of Integrated Data to Interpret Composition Change

Discussions in the previous sections of this chapter have made clear that the interpretation of earthquake-induced changes in water composition is more challenging than that of other types of hydrological responses to earthquakes. Examples include the distinctly different responses of the concentrations of major elements in two geographically adjacent wells in Iceland (HA-01 and HU-01, see Fig. 9.1 for well locations) to the same earthquakes (Fig. 9.2; Skelton et al. 2019), the inconsistent responses in the groundwater compositions in the monitoring wells near the epicenter of the 2016 M5.8 earthquake in SE Korea, and the distinctly different responses between the concentrations of the major elements and trace elements in wells in the central Italian Apennines (Rosen et al. 2018) and in SW China (Shi et al. 2020),

but, at the same time, the similar responses between the major and the trace element concentrations to earthquakes in the HU-01 well in Iceland (Claesson et al. 2004).

Difficulties in explaining these conflicting observations may be expected because the earthquake-induced changes of groundwater compositions are likely to result from the exchanges of groundwater with unknown and isolated groundwater sources that may be affected by different factors such as source depth, elevation, temperature and water-rock reactions. Ideally, the interpretation of the earthquake-induced changes of groundwater composition requires not only measurement of the water composition before and after the earthquake, but also simultaneous measurements of groundwater level, groundwater temperature, the hydraulic properties of aquifers and aquitards, and a detailed knowledge of the local hydrogeology. A major challenge is that most studies of earthquake-induced changes of groundwater composition are made without such complementary information. Another challenge is the difficulty in obtaining continuous measurements of groundwater composition in most wells. Often measurements of groundwater composition are made following an earthquake, but the necessary reference of composition before the earthquake is missing; or the post-seismic measurements are made once without continuous measurements, resulting in an absence of information for understanding the time-dependent processes.

In the unusual case where several types of data are available and densely distributed in the earthquake-affected area, an integrated dataset may be used to better constrain our interpretation of the earthquake-induced processes. This situation, unfortunately, is rare. Largely through serendipity, however, the interpretation of the changes of isotopic composition of groundwater in western Taiwan following the Chi-Chi earthquake (Sect. 9.4.2) may serve as an illustration of what is meant here by using integrated data for interpreting composition change. In a nutshell, analysis earthquake-induced changes in the $\delta^{18}\text{O}$ composition from clustered wells on an alluvial fan near the earthquake epicenter (Figs. 9.11 and 9.12) revealed a striking similarity between the earthquake-induced changes in different aquifers separated by aquitards (Fig. 9.11c, c'), suggesting the occurrence of post-earthquake vertical mixing of initially isolated groundwaters among different aquifers (Wang et al. 2005). This same conclusion was drawn from the study of the post-seismic convergence of initially different groundwater level in different aquifers to the same level (Wang 2007) and the tidal analysis of groundwater level in the same area (Fig. 6.16; Wang et al. 2016), further demonstrating that the earthquake-breached confinement of the aquifers may have allowed vertical mixing of groundwater. Finally, the analysis of groundwater temperature in the same area demonstrated an enhanced basin-wide groundwater flow after the earthquake, with increased downward flow in the foothills and increased upward flow from depth near the coast (Fig. 7.3; Wang et al. 2013), which is also consistent with the suggestion of the post-earthquake basin-scaled mixing of groundwater. Hence, we may conclude that the earthquake-induced change of the $\delta^{18}\text{O}$ composition in western Taiwan was due to an increased basin-wide groundwater transport from the Taiwan western foothills to the coast following the Chi-Chi earthquake and a vertical mixing of groundwater between different depths.

Obviously, this hypothesis requires further field tests and coupled numerical simulations, but the fact that it is consistent with a variety of observations makes the hypothesis better constrained.

Following the 2016 Kumamoto earthquake, there has been a tremendous increase of high-quality data for water composition, groundwater level and groundwater temperature (e.g., Hosono et al. 2020b). It may be timely to integrate these data in a multidisciplinary interpretation to advance our understanding on earthquake-induced changes of groundwater temperature and composition.

9.5 Concluding Remarks

Groundwater chemistry has long been used as an important tracer for understanding hydrogeological processes in general, and their changes after earthquakes in particular. In this chapter we discussed some existing studies of the earthquake-induced changes of the groundwater composition and streamflow composition. Even though the data for these changes are much less abundant than those for the changes in groundwater level and stream discharge, they have provided valuable information to constrain models of earthquake-induced hydrogeological processes. Most changes are consistent with the model of earthquake-enhanced groundwater transport through basin-wide or local enhanced permeability. The enhanced permeability may breach hydrologic barriers such as aquitards, connecting otherwise isolated aquifers or other fluid sources, causing fluid source switching and/or mixing. Studies of these processes may be important not only for better understanding natural transport processes but also for better understanding earthquake-induced contamination of groundwater by surface water, as reported in central Kyushu, Japan, following the 2016 Kumamoto earthquake.

References

- Andrén M, Stockmann G, Skelton A (2016) Coupling between mineral reactions, chemical changes in groundwater and earthquakes in Iceland. *J Geophys Res Solid Earth* 121:2315–2337. <https://doi.org/10.1002/2015JB012614>
- Chamberlain CP, Poage MA (2000) Reconstructing the paleotopography of mountain belts from isotopic composition of authigenic minerals. *Geology* 28:115–118
- Chang JC (1983) A review of channel shift on Choshui alluvial fan. *Geographical Studies* (7), 85–100, Department of Geography, National Taiwan Normal University (in Chinese)
- Claesson L, Skelton A, Graham C et al (2004) Hydrogeochemical changes before and after a major earthquake. *Geology* 32:641–644
- Claesson L, Skelton A, Graham C et al (2007) The timescale and mechanisms of fault sealing and water-rock interaction after an earthquake. *Geofluids* 7:427–440
- Coplen TB, Kendall C (2000) Stable hydrogen and oxygen isotope ratios for selected sites of the U.S. Geological Survey's NASQAN and benchmark surface-water networks. USGS Open-file Report 00-160

- Forrest MJ et al (2013) Hydrothermal contamination of public supply wells in Napa and Sonoma Valleys, California. *Appl Geochem* 33:25–40
- Hosono T, Hartmann J, Louvat P (2018) Earthquake-induced structural deformations enhance long-term solute fluxes from active volcanic systems. *Sci Rep* 8:14809
- Hosono T, Yamada C, Shibata T et al (2019) Coseismic groundwater drawdown along crustal ruptures during the 2016 Mw 7.0 Kumamoto earthquake. *Water Resour Res* 55:5891–5903
- Hosono K, Masaki Y (2020) Post-seismic hydrochemical changes in regional groundwater flow systems in response to the 2016 Mw7.0 Kumamoto earthquake. *J Hydrol* 580. <https://doi.org/10.1016/j.jhydrol.2019.124340>
- Hosono K, Yamada C, Manga M et al (2020a) Stable isotopes show that earthquakes enhance permeability and release water from mountains. *Nat Commun* 11:1–9. <https://doi.org/10.1038/s41467-020-16604-y>
- Hosono K, Saltalippi C, Jean JS (2020b) Coseismic hydro-environmental changes: insights from recent earthquakes. *J Hydrol* 585. <https://doi.org/10.1016/j.jhydrol.2020.124799>
- Ide K, Hosono T, Kagabu M et al (2020) Changes of groundwater flow systems after the 2016 Mw7.0 Kumamoto earthquake deduced by stable isotopic and CFC-12 compositions of natural springs. *J Hydrol* 583. <https://doi.org/10.1016/j.jhydrol.2020.124551>
- Ingebritsen SE, Sanford WE, Neuzil CE (2006) *Groundwater in geologic processes*, 2nd edn. Cambridge University Press, New York
- Ingraham NL, Caldwell EA (1999) Influence of weather on the stable isotopic ratios of wines: tools for weather/climate reconstruction? *J Geophys Res* 104:2185–2194
- Kaown D, Koh DC, Kim H et al (2019) Evaluating the responses of alluvial and bedrock aquifers to earthquakes (M L 5.1 and M L 5.8) using hydrological and environmental tracer data. *Hydrol J* 27(6):2011–2025
- Kim J, Lee J, Petitta M et al (2019) Groundwater system responses to the 2016 ML 5.8 Gyeongju earthquake, South Korea. *J Hydrol* 576:150–163
- Koizumi N, Minote S, Tanaka T et al (2019) Hydrological changes after the 2016 Kumamoto earthquake, Japan. *Earth Planet Space* 71:128. <https://doi.org/10.1186/s40623-019-1110-y>
- Lee SH, Lee JM, Yoon H et al (2020) Groundwater impacts from the M5. 8 Earthquake in Korea as determined by integrated monitoring systems. *Ground Water*. <https://doi.org/10.1111/gwat.12993>
- Muir-Wood R, King GCP (1993) Hydrological signatures of earthquake strain. *J Geophys Res* 98:22035–22068
- Nakagawa K, Yu ZQ, Berndtsson R et al (2020) Temporal characteristics of groundwater chemistry affected by the 2016 Kumamoto earthquake using self-organizing maps. *J Hydrol* 582. <https://doi.org/10.1016/j.jhydrol.2019.124519>
- Phillips OM (1991) *Flow and reactions in permeable rocks*. Cambridge University Press, Cambridge
- Rojstaczer S, Wolf S (1992) Permeability changes associated with large earthquakes: an example from Loma Prieta, California, 10/17/89 earthquake. *Geology* 20:211–214
- Rojstaczer S, Wolf S, Michel R (1995) Permeability enhancement in the shallow crust as a cause of earthquake-induced hydrological changes. *Nature* 373:237–239
- Rosen MR, Binda G, Archer C et al (2018) Mechanisms of earthquake-induced chemical and fluid transport to carbonate groundwater springs after earthquakes. *Water Resour Res* 54:5225–5244. <https://doi.org/10.1029/2017WR022097>
- Shi Z, Zhang H, Wang G (2020) Groundwater trace elements change induced by M5.0 earthquake in Yunnan. *J Hydrol* 581. <https://doi.org/10.1016/j.jhydrol.2019.124424>
- Skelton A, Andrén M, Kristmannsdóttir H et al (2014) Changes in groundwater chemistry before two consecutive earthquakes in Iceland. *Nat Geosci* 7(10):752–756
- Skelton A, Liljedahl-Claesson L, Wästebý N et al (2019) Hydrochemical changes before and after earthquakes based on long-term measurements of multiple parameters at two sites in northern Iceland—a review. *J Geophys Res Solid Earth* 124:2702–2720. <https://doi.org/10.1029/2018jb016757>

- Tyan CL, Chang YM, Lin WK et al (1996) The brief introduction to the groundwater hydrology of Choshui River Alluvial fan. In: Conference on groundwater and hydrology of the Choshui River Alluvial Fan, Taiwan, Water Resources Bureau, pp 207–221 (in Chinese)
- Wang CH, Wang CY, Kuo CH et al (2005) Some isotopic and hydrological changes associated with the 1999 Chi-Chi earthquake, Taiwan. *Island Arc* 14:37–54
- Wang CY (2007) Liquefaction beyond the near field. *Seismol Res Lett* 78(5):512–517
- Wang CY, Manga M (2015) New streams and springs after the 2014 Mw 6.0 South Napa earthquake. *Nat Commun* 6:7597. <https://doi.org/10.1038/ncomms8597>
- Wang CY, Cheng LH, Chin CV et al (2001) Coseismic hydrologic response of an alluvial fan to the 1999 Chi-Chi earthquake, Taiwan. *Geology* 29:831–834
- Wang CY, Wang LP, Manga M et al (2013) Basin-scale transport of heat and fluid induced by earthquakes. *Geophys Res Lett* 40(15):3893–3897
- Wang CY, Liao X, Wang LP et al (2016) Large earthquakes create vertical permeability by breaching aquitards. *Water Resour Res* 52:5923–5937. <https://doi.org/10.1002/2016WR01889>

Open Access This chapter is licensed under the terms of the Creative Commons Attribution 4.0 International License (<http://creativecommons.org/licenses/by/4.0/>), which permits use, sharing, adaptation, distribution and reproduction in any medium or format, as long as you give appropriate credit to the original author(s) and the source, provide a link to the Creative Commons license and indicate if changes were made.

The images or other third party material in this chapter are included in the chapter's Creative Commons license, unless indicated otherwise in a credit line to the material. If material is not included in the chapter's Creative Commons license and your intended use is not permitted by statutory regulation or exceeds the permitted use, you will need to obtain permission directly from the copyright holder.



Chapter 10

Geysers



Abstract Geysers, springs that intermittently erupt boiling water, appear to be especially sensitive to earthquakes. As they are a surface manifestation of geothermal systems, their response to earthquakes provides a window into how earthquakes change hydrothermal systems and processes. The most common approach to document responses to earthquakes is to identify changes in the interval between eruptions. Sustained changes in eruption intervals may be caused by changes in permeability. Confirming what processes lead to changes at geysers is hampered by limited reliable, quantitative multi-parameter data sets.

10.1 Introduction

Geysers are springs that intermittently erupt mixtures of steam and liquid water (White 1967). They may be periodic or irregular, and their eruption behavior can change over time. A key outstanding question is “what processes, both internal and external to the geyser, influence the duration and volume of an eruption and the interval between eruptions” (Hurwitz and Manga 2017)? Earthquakes are one of those external influences.

Geysers are rare, with less than 1000 worldwide, and this number is decreasing owing to geothermal development of the hydrothermal systems they tap (Bryan 2005). Their rarity reflects the special conditions needed to create a geyser: a supply of heat that is large enough to boil water close to Earth’s surface, and a plumbing system that has the right geometry to permit episodic discharge. Other gases such as CO₂ may play a role in their eruption (Hurwitz et al. 2016; Ladd and Ryan 2016). Despite being rare, they are of interest for understanding the connection between earthquakes and water because they provide a window into how earthquakes affect hydrothermal systems. They may also serve as a model for understanding the processes that trigger the eruption of magmatic volcanoes and hydrothermal explosions. Figure 10.1 shows pictures of some geysers caught in the act of erupting, including some of those discussed in this chapter.



Fig. 10.1 Photos of geysers: **a** Lone Star geyser, Yellowstone National Park, **b** Great Geysir and Strokkur geysers, Iceland, and **c** Upper geyser basin, El Tatio, Chile. Photo **a** from S. Hurwitz USGS and **b** and **c** from the authors

Changes in the behavior of geysers are usually characterized by the interval between eruptions, hereafter abbreviated IBE, since this is the easiest attribute of eruptions to document. The volume erupted can be difficult to impossible to measure. The duration can also be tricky to define: some geyser eruptions begin with minor eruptions called preplay events (Kieffer 1989), and eruptions often taper off gradually. Geyser eruptions can be periodic (constant IBE), irregular, have a bimodal distribution of IBE, or exhibit chaotic features (Ingebritsen and Rojstaczer 1996).

10.1.1 *Response of Geysers to Earthquakes*

Geysers have long been known to be especially sensitive to earthquakes, as manifested by changes in the IBE. Examples include a geysiring well in California, USA (Silver and Vallette-Silver 1992) and natural geysers in Yellowstone National Park,

USA (e.g., Marler 1964; Rinehart and Murphy 1969; Hutchinson 1985; Husen et al. 2004; Hurwitz et al. 2014).

There is no systematic pattern to responses after earthquakes. Among the many Yellowstone geysers that have been documented to respond to earthquakes, the IBE decreases at some and increases at others (Husen et al. 2004; Hurwitz et al. 2014). Figure 10.2 shows the IBE at two Yellowstone geysers and how they responded

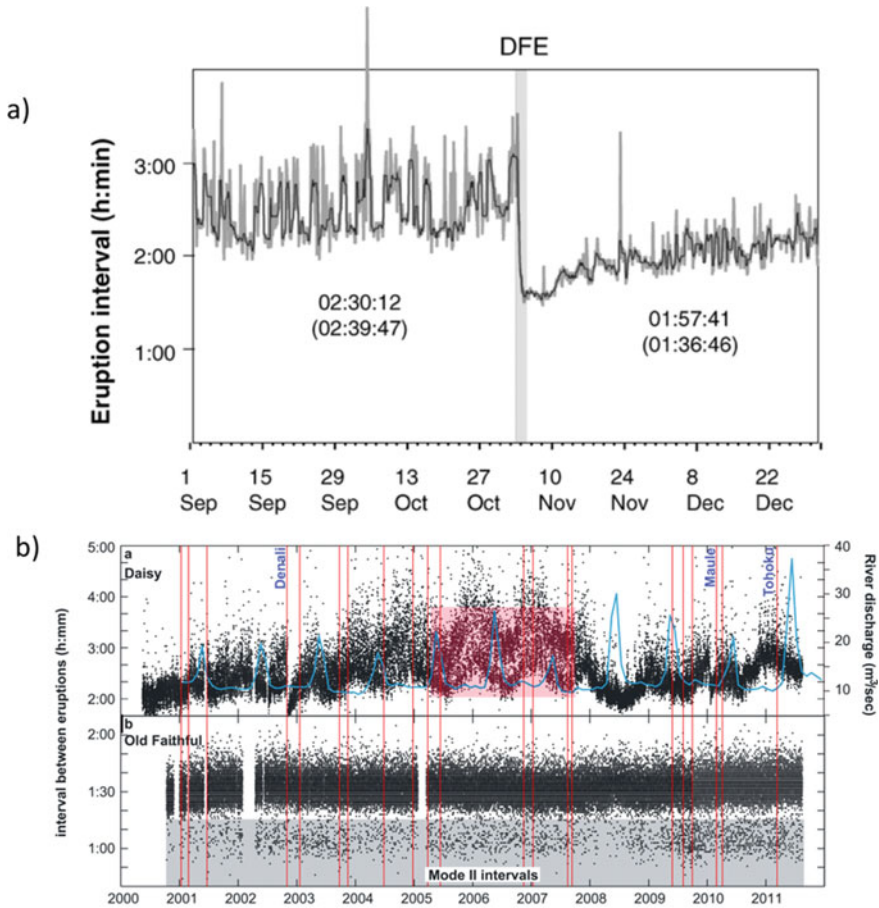
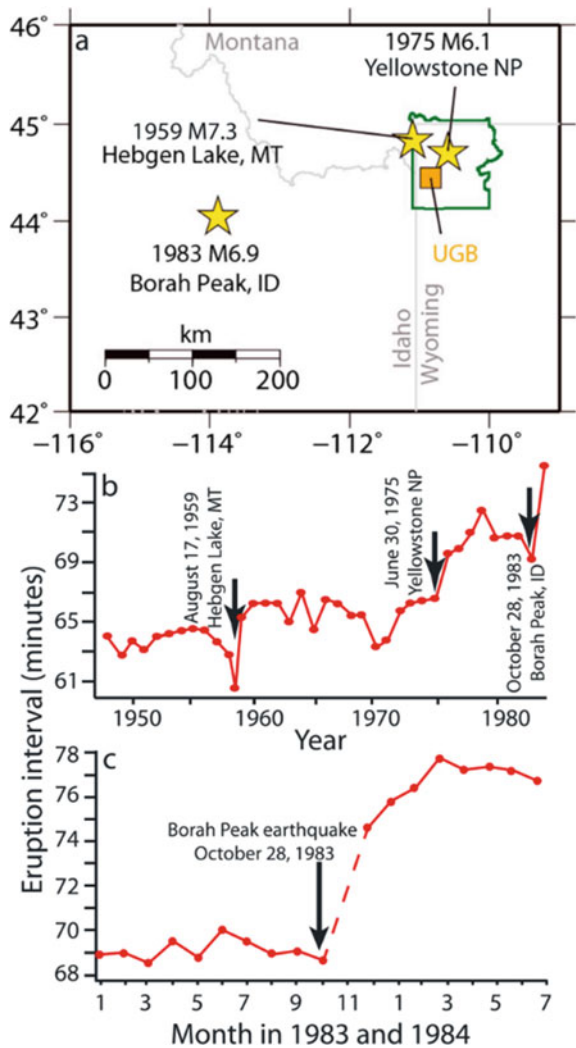


Fig. 10.2 a Response of Daisy Geyser in Yellowstone to the M 7.9 Denali earthquake located 3100 km from the geyser. DFE indicates the time of the Denali earthquake in Alaska, USA. The grey curve is raw data and the black curve is smoothed data. Times under the curves show median eruption intervals before and after the earthquake and are averaged over weeks or days (the latter in parentheses) (from Husen et al. 2004). b A longer time series for Daisy geyser and Old Faithful geyser showing that the pool geyser (Daisy) that responded to the 2002 Denali earthquake also varies seasonally, and that Old Faithful did not respond to either the earthquake or vary over the course of a year. The red lines show earthquakes with the largest ground motions in Yellowstone National Park (from Hurwitz et al. 2014)

to 2002 M7.9 Denali earthquake in Alaska, 3100 km away from the geysers. The IBE changed suddenly after the earthquake and then recovered to its pre-earthquake value over a time period of months. In other cases, the IBE appears to change more gradually (Fig. 10.3). Interestingly, some geysers that responded to large earthquakes in 1959 and 1983 did not respond to the 2002 Denali earthquake (Husen et al. 2004).

The vertical red lines in Fig. 10.2 show the time of other large teleseismic and regional events. None changed the eruptions of Daisy and Old Faithful geysers. The Denali earthquake produced the largest peak dynamic stresses during this time period, enhanced by directivity effects. Dynamic stresses less than 0.02 MPa have not changed the eruptions of any geysers in Yellowstone (Hurwitz et al. 2014).

Fig. 10.3 Response of Old Faithful geyser to regional earthquakes shown in panel (a). For all three earthquakes, panel (b), the eruption interval appears to increase. The change in eruption interval may be gradual, panel (c), unlike Daisy geyser (Fig. 10.2). The dashed curve indicates a time period without data (from Hurwitz et al. 2014)



The most remarkable feature of the response of geysers to earthquakes is the distance from the epicenter at which they show a sensitivity. They respond to earthquakes that produce static strains $<10^{-7}$ and dynamic strains $<10^{-6}$ (Hutchinson 1985; Silver and Vallette-Silver 1992). The Denali earthquake that changed the eruptions of Daisy geyser (Fig. 10.2) has a peak dynamic stress of 0.14 MPa and energy density of $10^{-3.5}$ J/m³ (Hurwitz et al. 2014). Some geysers thus respond to earthquakes at distances far greater than that for changes in stream discharge (Chap. 7) and the occurrence of liquefaction (Chap. 11), and distances similar to the most sensitive water wells (Chap. 6).

10.1.2 *Response of Geysers to Other Sources of Stress*

Geysers may respond to longer term changes in tectonic stress or regional deformation. For example, the reactivation of dormant Steamboat Geyser in Yellowstone in 2018, the tallest active geyser, has been attributed to regional uplift produced by fluid ascent and accumulation (Wicks et al. 2020), though this conclusion is contested (Reed et al. 2021).

The response of geysers to non-seismic and non-tectonic strains has been the subject of many studies, and conclusions are not consistent. Some of the inconsistencies may be the result of errors and gaps in eruption catalogs (Nicholl et al. 1994). Earth tides (Rinehart 1972a, b) and barometric pressure variations (White 1967) have been reported to influence geyser eruptions in Yellowstone. Rojstaczer et al. (2003), in contrast, found that Yellowstone geysers are not sensitive to Earth tides and barometric pressure variations—strains typically smaller than 10^{-7} . This is comparable to and larger than the static strains generated by earthquakes that changed eruption intervals.

Figure 10.2 has data for tens of thousands of eruptions providing an opportunity to identify responses. Old Faithful is not sensitive to barometric pressure changes or solid Earth tides, but the pool geyser, Daisy geyser, is sensitive to surface temperature and wind speed. Munoz-Saez et al. (2015a) recorded thousands of eruptions of a small geyser in El Tatio, Chile, and found no sensitivity to air temperature, atmospheric pressure, or tides. The sensitivity of pool geysers to environmental conditions makes sense: enhanced heat loss during winter or by wind increases the time needed for water to reach boiling conditions.

Geysers also respond to hydrological changes. Figure 10.2 shows seasonal variations of IBE for Daisy geyser. Hurwitz et al. (2008) document clear seasonal variations in IBE and a response to long term trends in precipitation. The latter observation indicates that recharge to the geyser plumbing system influences IBE.

10.2 Mechanisms

In order to understand how earthquakes can influence geysers it is first necessary to understand how and why geysers erupt. We thus first review published models for the processes that operate within geysers and then identify how earthquakes might influence these processes.

10.2.1 *How Do Geysers Work?*

The evolution of a geyser eruption provides insights and constraints into the processes that lead to their eruption. Geyser eruptions begin with the discharge of water at temperatures below the boiling point; this is followed by a fountain dominated by liquid which progressively becomes more steam-rich before ending with a quiet phase (White 1967; Karlstrom et al. 2013). Bubbles and steam play a central role in transferring heat to warm water in the conduit and in driving the eruption (Kieffer 1989; Adelstein et al. 2014).

Here we focus on intermittency as this is the property that is documented to change after earthquakes. Three different types of models have been proposed to explain why geysers are intermittent.

- (1) Ingebritsen and Rojstaczer (1993, 1996) develop a numerical model for ground-water flow and heat transport in an idealized geyser system that consists of a conduit and surrounding matrix. They show that the observed sequence of events at a geyser can occur periodically for specific combinations of heat flow, conduit and matrix permeabilities, and conduit length.
- (2) Steinberg et al. (1982a, b, c) present a model for geysers in which eruption is driven by the nucleation of steam bubbles in a superheated fluid. The IBE in this case is governed by the time it takes to achieve this degree of superheating. Hurwitz and Manga (2017) note that there is no strong evidence for superheating in natural geysers.
- (3) Many geysers appear to have cavities beneath the conduit feeding the eruption, observed directly with video cameras (e.g., Belousov et al. 2013), imaged seismically (e.g., Vandemeulebrouck et al. 2013; Wu et al., 2017) or inferred from ground deformation (e.g., Vandemeulebrouck et al. 2014; Ardid et al. 2019). These “bubble traps” can accumulate water at the boiling point and then initiate and sustain an eruption for an extended period of time. Geyser eruptions can influence nearby geysers indicating that the plumbing systems are not isolated to a single geyser (e.g., Munoz-Saez et al. 2015b) (Fig. 10.4).

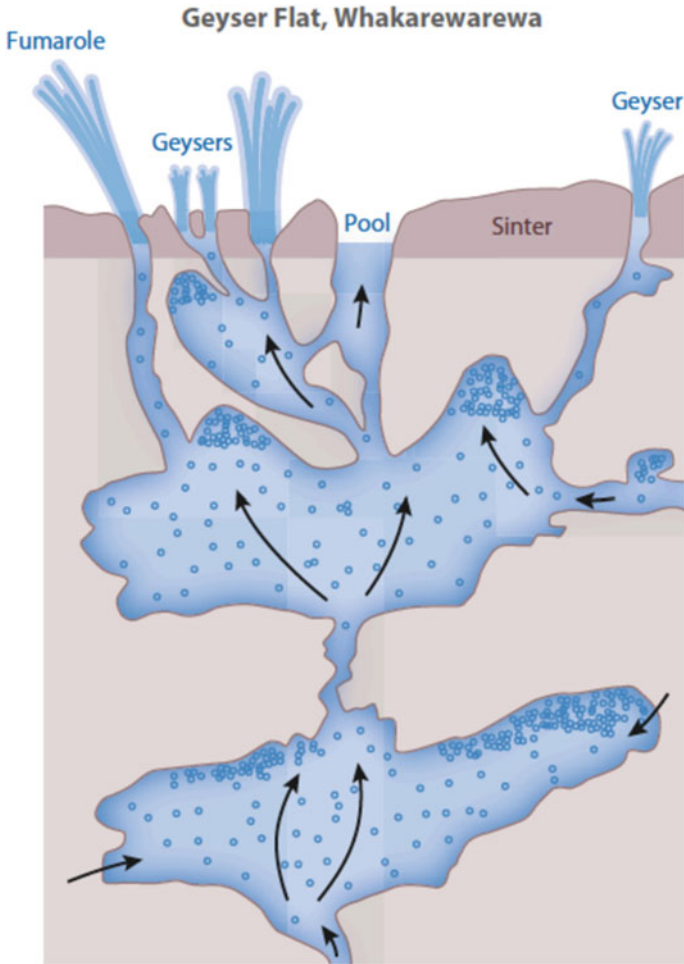


Fig. 10.4 Schematic illustration of a geyser illustrating the plumbing system below the surface. The surface manifestation of hydrothermal systems can include fumaroles (all vapor), hot springs (continuous discharge), and geysers (episodic eruption). Direct observations of Hutchinson et al. (1997) and Belousov et al. (2013) confirm that the main vent of geysers consists of a complex network of conduits with multiple constrictions. Bubble traps have been proposed to be required for geysers (Belousov et al. 2013) however geysering wells would appear to contradict this assertion (Rudolph et al. 2012) (from Hurwitz and Manga 2017 after Lloyd 1975)

10.2.2 Mechanisms for Altering Eruptions

Changes in eruption interval can be caused by changes in permeability of the conduit and/or surrounding matrix. As the permeability of the conduit is very high, changes in the matrix that governs conduit recharge are more likely (Ingebritsen and Rojstaczer 1993). That recharge influences IBE is highlighted by the climate sensitivity of

geysers (Hurwitz et al. 2008; Hurwitz et al. 2020). Changes in conduit length by reopening blocked and preexisting fractures is an alternative possibility (Ingebritsen et al. 2006). The mechanisms by which the permeability changes or fractures get unblocked remain unclear, but as with hydrological responses reviewed previously, it is likely that dynamic strains cause such changes. For example, the static stress changes from the Denali earthquake in Yellowstone were less than 10 Pa (Husen et al. 2004), far too small to have an impact, whereas the dynamic stresses were 4 orders of magnitude larger. The gradual post-earthquake changes in IBE can be explained by gradual fracture sealing and reduction of matrix permeability as has been documented at Yellowstone (e.g., Dobson et al. 2003).

Steinberg et al. (1982c) create a laboratory model of a geyser in which nucleation of bubbles in a superheated fluid drives periodic eruptions. They also show that vibrations can trigger eruptions, presumably by lowering the degree of superheating needed to initiate an eruption. This mechanism does not obviously explain why IBE sometimes increases, nor why changes are sustained over multiple eruptions.

Simultaneous measurements of discharge and eruption intervals may provide the key information to test models and identify the origin of seismic responses. It may be possible to distinguish between these two end members with additional measurements. In the first case, increased matrix permeability will lead to faster recharge and hence an increase in the mean discharge, though the magnitude of changes depends on details of the conduit and matrix properties (Ingebritsen and Rojstaczer 1996). Measuring discharge is not easy. The duration of eruption can be used as proxy for discharge, assuming choked flow conditions apply throughout the eruption (Kieffer 1989) but not all geysers reach those conditions nor are they sustained throughout an eruption (e.g., Karlstrom et al. 2013). Measurements at Old Faithful, Yellowstone (Kieffer 1989), the Calistoga geyser, California (Shteinberg 1999), Crystal Geyser, Utah (Gouveia and Friedman 2006) and lab models (Shteinberg 1999) are consistent with IBE scaling with the duration of the previous eruption for some geysers. Other geysers, however, have more complex relationships between eruption intervals: Eibl et al. (2020) found that Strokkur geyser, Iceland (Fig. 10.1) has a predictable waiting time for an eruption, but that the duration and pattern of subsequent eruptions are not predictable. Regardless of the regularity of eruptions, however, if the IBE is dominated by nucleation, then the mean discharge will be unaffected—changes in the IBE will be accompanied by equivalent changes in the amount of fluid erupted.

10.3 Conclusions About Geysers

Of the hydrological responses reviewed thus far, geysers stand out because some are extremely sensitive to seismic waves. The property of geysers used to document these changes is the interval between eruptions (IBE). With this one measure alone, it is challenging to distinguish between hypotheses about the origin of changes in the IBE.

If eruptions are controlled by properties of the geyser plumbing system, because changes in IBE are sustained over multiple eruptions, permanent changes must occur in this plumbing system. Ingebritsen and Rojstaczer (1996) argue changes most likely occur in the recharge to the geyser conduit which is governed by matrix permeability. If IBE is instead controlled by the ability of bubbles to nucleate in a supersaturated system, then it is possible that the earthquake created lower energy nucleation sites that permit eruption at smaller supersaturations.

One challenge in identifying the sensitivity of geysers to external forcing is a limited amount of reliable, quantitative data. Our present ability to monitor geysers with temperature loggers, video, and seismic instrumentation should allow the requisite data sets to be collected and expanded.

References

- Adelstein E, Tran A, Munoz-Saez C, Shteinberg A, Manga M (2014) Geyser preplay and eruption in a laboratory model with a bubble trap. *J Volcanol Geotherm Res* 285:129–135
- Ardid A, Vera E, Kelly C, Manga M, Munoz-Saez C, Maksymowicz A, Ortega-Culaciati F (2019) Geometry of geyser plumbing inferred from ground deformation. *J Geophys Res Solid Earth* 124:1072–1083. <https://doi.org/10.1029/2018JB016454>
- Belousov A, Belousova M, Nechayev A (2013) Video observations inside conduits of erupting geysers in Kamchatka, Russia, and their geological framework: implications for the geyser mechanism. *Geology* 41:387–390
- Bryan TS (2005) *Geysers: what they are and how they work*, 2nd edn. Mountain Press Publishing, Missoula, Montana, p 69
- Dobson PF, Kneafsey TJ, Hulen J, Simmons A (2003) Porosity, permeability, and fluid flow in the Yellowstone geothermal system, Wyoming. *J Volcanol Geotherm Res* 123:313–324
- Eibl EPS, Hainzl S, Vesely NIK et al (2020) Eruption interval monitoring at Strokkur Geyser, Iceland. *Geophys Res Lett* 47:e2019GL085266. <https://doi.org/10.1029/2019GL085266>
- Gouveia FJ, Friedmann SJ (2006) Timing and prediction of CO₂ eruptions from Crystal Geyser, Utah. <https://doi.org/10.2172/897988>
- Hurwitz S et al (2020) Yellowstone's Old Faithful Geyser shut down by a severe thirteenth century drought. *Geophys. Res. Lett.* 47, e2020GL089871.
- Hurwitz S, Kumar A, Taylor R, Heasler H (2008) Climate-induced variations of geyser periodicity in Yellowstone National Park, USA. *Geology* 36:451–454
- Hurwitz S, Sohn RA, Luttrell K, Manga M (2014) Triggering and modulation of geyser eruptions in Yellowstone National Park by earthquakes, earth tides, and weather. *J Geophys Res Solid Earth* 119:1718–1737
- Hurwitz S, Clor LE, McCleskey RB, Nordstrom DK, Hunt AG, Evans WC (2016) Dissolved gases in hydrothermal and geyser eruptions at Yellowstone. *Geology* 44:235–238
- Hurwitz S, Manga M (2017) The fascinating and complex dynamics of geyser eruptions. *Ann. Rev Earth Planet Sci* 45:31–59. <https://doi.org/10.1146/annurev-earth-063016-015605>
- Husen S, Taylor R, Smith RB, Heasler H (2004) Changes in geyser eruption behavior and remotely triggered seismicity in Yellowstone National Park induced by the 2002 M 7.9 Denali fault earthquake. *Geology* 32:537–540
- Hutchinson RA (1985) Hydrothermal changes in the upper Geyser Basin, Yellowstone National Park, after the 1983 Borah Peak, Idaho, earthquake. In Stein RS, Bucknam RC, USGS Open File Report 85-0290A:612–624

- Hutchinson RA, Westphal JA, Kieffer SW (1997) In situ observations of Old Faithful Geysers. *Geology* 25:875–878
- Ingebritsen SE, Rojstaczer S (1993) Controls of geyser periodicity. *Science* 262:889–892
- Ingebritsen SE, Rojstaczer S (1996) Geyser periodicity and the response of geysers to deformation. *J Geophys Res* 101:21891–21905
- Ingebritsen SE, Sanford WE, Neuzil C (2006) *Groundwater in geologic processes*, 2nd edn. Cambridge Univ Press, 341 pp
- Karlstrom L, Hurwitz S, Sohn R, Vandemeulebrouck J, Murphy F, Rudolph ML et al (2013) Eruptions at Lone Star Geysers, Yellowstone National Park, USA: 1. Energetics and eruption dynamics. *J Geophys Res Solid Earth* 118:4048–4062. <https://doi.org/10.1002/jgrb.50251>
- Kieffer SW (1989) Geologic nozzles. *Rev Geophys* 27:3–38
- Ladd B, Ryan MC (2016) Can CO₂ trigger a thermal geyser eruption? *Geology* 44:307–310
- Lloyd BF (1975) *Geology of Whakarewarewa hot springs*. Wellington NZ Government Printing
- Manga M, Brodsky EE (2006) Seismic triggering of eruptions in the far-field: volcanoes and geysers. *Ann Rev Earth Planet Sci* 34:263–291
- Marler GD (1964) Effects of the Hebgen Lake earthquake of August 27, 1959, on the hot spring of the Firehole Geysers basins, Yellowstone National Park. *US Geol Surv Prof Paper* 435-Q:185–197
- Munoz-Saez C, Manga M, Hurwitz S, Rudolph ML, Namiki A, Wang CY et al (2015a) Dynamics within geyser conduits, and sensitivity to environmental perturbations: insights from a periodic geyser in the El Tatio geyser field, Atacama Desert, Chile. *J Volcanol Geoth Res* 292:41–55. <https://doi.org/10.1016/j.jvolgeores.2015.01.002>
- Munoz-Saez C, Namiki A, Manga M (2015b) Geyser eruption intervals and interactions: examples from el Tatio, Atacama, Chile. *J Geophys Res Solid Earth* 120:7490–7507. <https://doi.org/10.1002/2015JB012364>
- Nicholl MW, Wheatcraft SW, Tyler SW (1994) Is old faithful a strange attractor? *J Geophys Res* 99:4495–4503
- Reed MH et al. (2021) The 2018 reawakening and eruption dynamics of Steamboat Geysers, the world's tallest active geyser. *Proc Nat Acad Sci* 118: e2020943118
- Rinehart JS (1972a) Fluctuations in geyser activity caused by variations in Earth tidal forces, barometric pressure, and tectonic stress. *J Geophys Res* 77:342–350
- Rinehart JS (1972b) 18.6 year tide regulates geyser activity. *Science* 177:346–347
- Rinehart JS, Murphy A (1969) Observations on pre- and post-earthquake performance of old faithful Geysers. *J Geophys Res* 74:574–575
- Rojstaczer S, Galloway DL, Ingebritsen SE, Rubin DM (2003) Variability in geyser eruptive timing and its causes: Yellowstone National Park. *Geophys Res Lett* 30:1953. <https://doi.org/10.1029/2003GL-17853>
- Rudolph ML, Manga M, Hurwitz S, Johnston M, Karlstrom L, Wang CY et al (2012) Mechanics of old faithful Geysers, Calistoga, California. *Geophys Res Lett* 39:L24308. <https://doi.org/10.1029/2012GL054012>
- Sin-Mei Wu, Kevin M. Ward, Jamie Farrell, Fan-Chi Lin, Marianne Karplus, Robert B. Smith (2017) Anatomy of Old Faithful From Subsurface Seismic Imaging of the Yellowstone Upper Geysers Basin. *Geophysical Research Letters* 44 (20):10,240-10,247
- Silver PG, Valette-Silver NJ (1992) Detection of hydrothermal precursors to large Northern California earthquakes. *Science* 257:1363–1368. <https://doi.org/10.1126/science.257.5075.1363>
- Steinberg GS, Merzhanov AG, Steinberg AS (1982a) Geyser process: theory, modeling and field experiment, Part 2. A laboratory models of a geyser. *Mod Geol* 8:61–74
- Steinberg GS, Merzhanov AG, Steinberg AS (1982b) Geyser process: theory, modeling and field experiment, Part 3. On metastability of water in geysers. *Mod Geol* 8:75–78
- Steinberg GS, Merzhanov AG, Steinberg AS (1982c) Geyser process: theory, modeling and field experiment, Part 4. On seismic influence on geyser regime. *Mod Geol* 8:79–86
- Shteinberg AS (1999) An experimental study of geyser eruption periodicity. *Doklady Phys* 44:305–308

- Vandemeulebrouck J, Roux P, Cros E (2013) The plumbing of old faithful Geyser revealed by hydrothermal tremor. *Geophys Res Lett* 40:1989–1993. <https://doi.org/10.1002/grl.50422>
- Vandemeulebrouck J, Sohn RA, Rudolph ML, Hurwitz S, Manga M, Johnston MJ et al (2014) Eruptions at Lone Star Geyser, Yellowstone National Park, USA: 2. Constraints on subsurface dynamics. *J Geophys Res Solid Earth* 119:8688–8707. <https://doi.org/10.1002/2014JB011526>
- White DE (1967) Some principles of geyser activity, mainly from Steamboat Springs, Nevada. *Am J Sci* 265:641–684
- Wicks CW, Dzurisin D, Lowenstern JB, Svarc J (2020) Magma intrusion and volatile ascent beneath Norris Geyser Basin, Yellowstone National Park. *J Geophys Res* 125:e2019JB018208. 10.1029/

Open Access This chapter is licensed under the terms of the Creative Commons Attribution 4.0 International License (<http://creativecommons.org/licenses/by/4.0/>), which permits use, sharing, adaptation, distribution and reproduction in any medium or format, as long as you give appropriate credit to the original author(s) and the source, provide a link to the Creative Commons license and indicate if changes were made.

The images or other third party material in this chapter are included in the chapter's Creative Commons license, unless indicated otherwise in a credit line to the material. If material is not included in the chapter's Creative Commons license and your intended use is not permitted by statutory regulation or exceeds the permitted use, you will need to obtain permission directly from the copyright holder.



Chapter 11

Liquefaction



Abstract Liquefaction of the ground during earthquakes has long been documented and has drawn much attention from earthquake engineers because of its devastation to engineered structures. In this chapter we review a few of the best studied field cases and summarize insights from extensive experimental data critical for understanding the interaction between earthquakes and liquefaction. Despite the progress made in the last few decades, several outstanding problems remain unanswered. One is the mechanism for liquefaction beyond the near field, which has been abundantly documented in the field. This is not well understood because, according to laboratory data, liquefaction should occur only in the near field where the seismic energy density is great enough to cause undrained consolidation leading up to liquefaction. Another outstanding question is the dependence of liquefaction on the frequency of the seismic waves, where the current results from the field and laboratory studies are in conflict. Finally, while in most cases the liquefied sediments are sand or silty sand, well-graded gravel has increasingly been witnessed to liquefy during earthquakes and is not simply the result of entrainment by liquified sand. It is challenging to explain how pore pressure could build up in gravelly soils and be maintained at a level high enough to cause liquefaction.

11.1 Introduction

In 373/2 BC, Helice, a coastal town in ancient Greece, disappeared entirely under the sea after being leveled by a great earthquake. In 1861, the same place was hit by another earthquake, though with less damage. Schmidt (1875) studied the affected area and documented the extensive lateral spreading and subsidence of land along the coast (Fig. 11.1).

One of the best studied regions for liquefaction features occurs in the New Madrid Seismic Zone of the central United States (Fig. 11.2), where widespread liquefaction was induced by nearby historic and prehistoric earthquakes. Liquefaction features, mapped over several thousand square kilometers (Obermeir 1989), are present in various shapes, sizes, and ages. Many surficial vented deposits, or sand blows, are

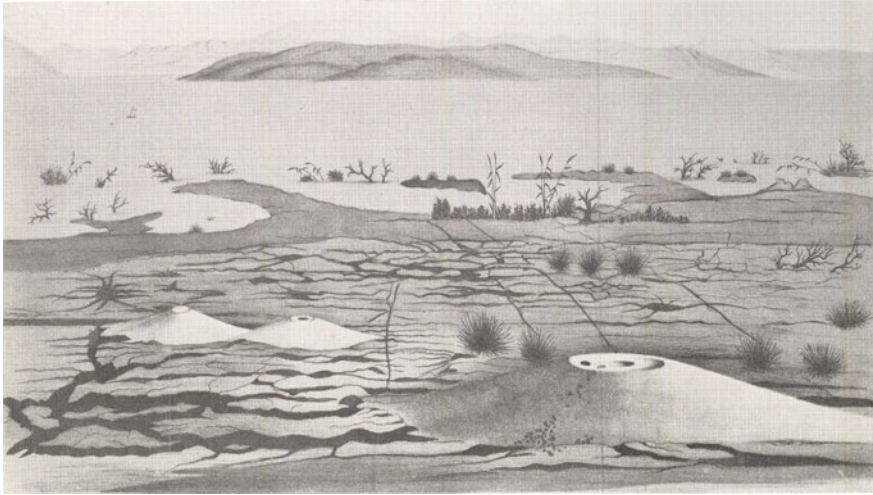
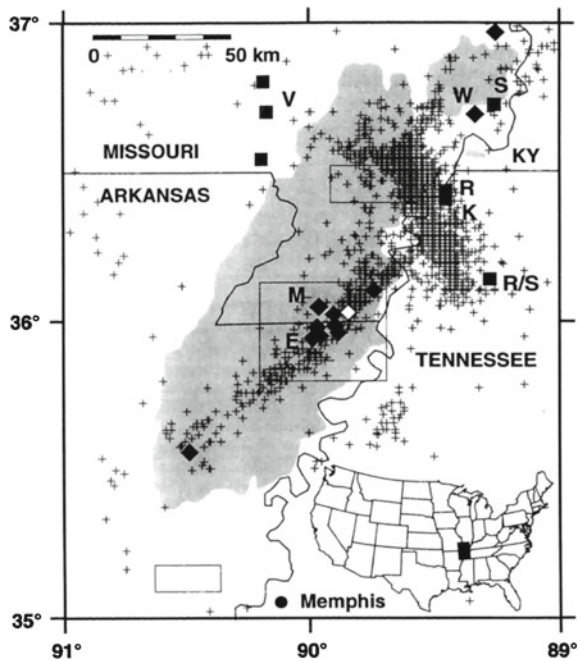


Fig. 11.1 Drawing shows the affected area of Helice after the earthquake of 1861. In the foreground, the remaining part of the land was broken into a collage of many irregular pieces separated by a patchwork of extensional fractures, covered sparingly by sand-craters. Off the coast in the Gulf of Corinth, tree tops mark part of the submerged coastal plain (from Marinatos 1960)

Fig. 11.2 Location map showing the liquefaction sites within the New Madrid seismic zone. Shaded area represents the area where >1% of the ground surface is covered by sand-blow deposits (Obermeir 1989). Seismicity (1974–1991), shown by crosses, defines the New Madrid Seismic Zone. Symbols and letters refer to sites of previous liquefaction and paleo-liquefaction studies (from Tuttle and Schweig 1996)



1.0–1.5 m in thickness and 10–30 m in diameter and are still easy to identify on the ground surface, on aerial photographs and even on satellite images, despite years of modification by active agricultural activities (Tuttle and Schweig 1996). Sand dikes, which represent the conduits for escaping pore water and sediments from the liquefied layers below the sand blows, are also abundant. Most of these features are thought to have formed during the 1810–1811 M8 New Madrid earthquakes, even though many may be prehistoric in age (Tuttle and Schweig 1996).

Two earthquakes in 1964 are particularly important in bringing liquefaction phenomena and their devastating effects to the attention of engineers and seismologists. These earthquakes inspired a great amount of research during the past 60 years in an effort to better understand liquefaction and to mitigate its damage.

The 1964 M9.2 Alaska earthquake occurred at a depth of approximately 30 km beneath Prince William Sound; the rupture extended laterally for 800 km parallel to the Aleutian trench and uplifted about 520,000 km² of the crust. Many landslides occurred; the most spectacular slide took place in the Turnagain Heights area of Anchorage, caused by liquefaction of the underlying soft clay and sands. The slide extended ~2800 m laterally along a bluff and continued inland for an average distance of ~300 m, resulting in 130 acres of land sliding toward the ocean (Seed 1968). Within the slide area the ground was broken into blocks that collapsed and tilted at all angles forming a chaotic collage of ridges and depressions. In the depressed areas, the ground dropped an average of 12 m during the sliding. Houses in the area, some of which moved laterally as much as 150 or 180 m, were completely destroyed.

During the 1964 M7.5 Nigata Earthquake, Japan, dramatic damage was caused by liquefaction of the sand deposits in the low-lying areas of Nigata City (Fig. 11.3). The soils in and around this city consist of recently reclaimed land and young sedimentary deposits having low density and a shallow ground water table. About 2000 houses in the City of Nigata were totally destroyed; more than 200 reinforced concrete buildings tilted rigidly without appreciable damage to the structure.

A more recent liquefaction event happened in New Zealand where widespread liquefaction occurred during both the 2010 Mw7.1 Darfield and the 2011 Mw6.2 Christchurch earthquakes. Greatest damage was induced by the second earthquake

Fig. 11.3 Tilted apartment buildings after the 1964 Nigata earthquake. Despite the extreme tilting, the building themselves suffered remarkably little structural damage (from the Earthquake Engineering Research Center Library, University of California at Berkeley)



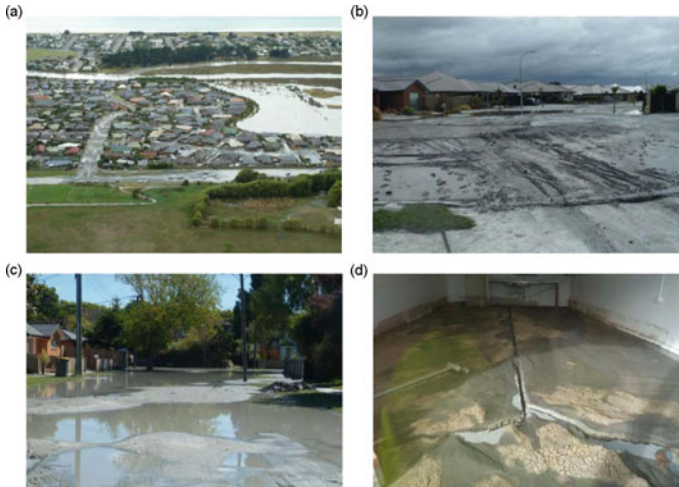


Fig. 11.4 Liquefaction-induced land damage and dwelling foundation damage due to Christchurch earthquakes: **a** extensive liquefaction in low-lying suburbs; **b** suburban Christchurch street covered with liquefaction ejecta; **c** pavement buried by liquefaction ejecta and ponded water after liquefaction; **d** Uplifted and cracked concrete floor inside house covered with liquefaction ejecta (modified from van Ballegooy et al. 2014)

because, while smaller, it occurred close to the population center of a major city. The majority of the ~3000 buildings in the central business district of the city and tens of thousands of residential buildings and properties were destroyed for all practical purposes (e.g., Fig. 11.4; van Ballegooy et al. 2014). Structures near river banks or the coast suffered the most liquefaction damage.

Another recent liquefaction event occurred in a densely populated area during the Mw7.9 Wenchuan earthquake, China. Various liquefaction-related processes were directly witnessed and left marks on structures. Based on a survey of observations, together with borehole investigation, Liu-Zeng et al. (2017) found that the liquefied layers are in general <8 m deep, where the lithology is dominated by coarse-grained alluvial gravel in a sandy matrix and capped by clayey to silty overbank deposits. They also found that anomalously high water ejections (>2.0 m; Fig. 11.5) and coarse ejected material are more common along the NE–SW trending surface projection of the Range Front blind thrust and its splay faults, suggesting that liquefaction intensity may have increased near these faults.

11.2 Sediment Consolidation and Liquefaction in Cyclic Loading

In addition to being a significant hydrogeologic process, liquefaction has drawn much attention from engineers because it can create great damage to engineered structures.

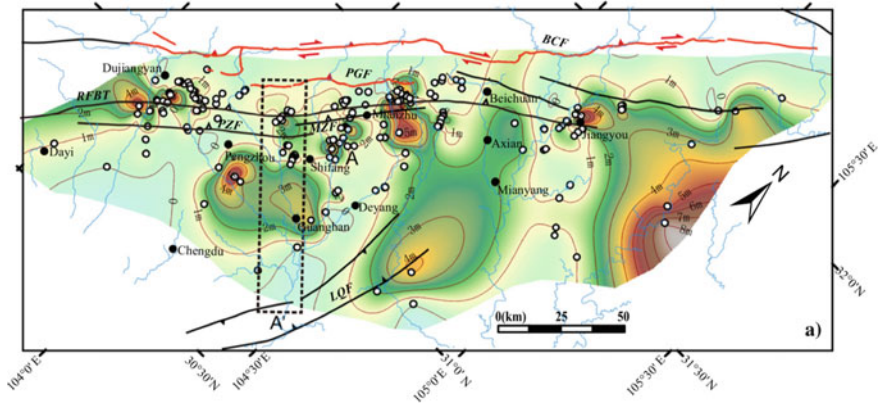


Fig. 11.5 Contour map showing variations in water ejection heights (m) following the 2008 Wenchuan earthquake. Circles show the locations of ejection height measurements. Red lines show the earthquake ruptured faults; black lines show the surface projections of known faults in the basin (from Liu-Zeng et al. 2017)

Since the 1960s, earthquake engineers have carried out a great amount of research to study liquefaction and to predict its occurrence. Their works are summarized in several special volumes (e.g., National Research Council 1985, 2016; Pitolakis 2007) and will not be repeated here. We thus summarize only some fundamental results critical to the understanding of the interaction between earthquakes and water.

Engineering practice has relied on two complementary approaches to study liquefaction. One approach is based on field data from various penetration tests (National Research Council 2016). Interpretations of these tests, however, are empirical and often do not offer physical insight. A second approach is based on controlled laboratory experiments. The results of the laboratory experiments have been variously applied to evaluate the liquefaction potential of field sites, either using a threshold stress (e.g., Seed and Idriss 1967; Youd 1972), strain (Fig. 3.9; Dobry et al. 1982; Vucetic 1994; Hsu and Vucetic 2004), or dissipated energy (Nemat-Nasser and Shokoh 1979; Berrill and Davis 1985; Law et al. 1990; Figueroa et al. 1994; Liang et al. 1995; Dief 2000; Green and Mitchell 2004) as criteria.

The effective stress principle (Sect. 3.2.2), first proposed in the early twentieth century (Terzaghi 1925), laid the foundation for soil mechanics and earthquake engineering. The mechanical integrity of sediments, which allows the sediments to carry weight, is mainly maintained through grain-to-grain contacts (Fig. 11.6a; see also Sect. 11.3). Seismic shaking may break the frictional contact and the load of the overburden is then transferred from the soil particles to the pore water (Fig. 11.6b). Since the duration of seismic shaking, normally tens of seconds, is short compared to the time required to dissipate pore pressure in the sediment, the process occurs in an ‘undrained’ state (Chap. 2), and pore pressure builds up. As a result, the ‘effective stress’ supported by the sediments decreases correspondingly. When pore pressure becomes high enough to support the overburden, the effective stress is reduced

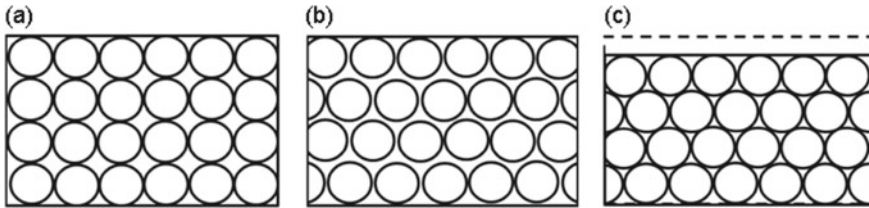


Fig. 11.6 Idealized schematic of pore-pressure change in soils during earthquakes. **a** Before an earthquake, individual soil grains are held in place by frictional or adhesive contact forces, creating a solid soil structure with water filling the spaces between the grains. Note the grain-to-grain contact. **b** After seismic shaking, particle rearrange with no change in volume (e.g., a lateral shift of a half diameter of every other row of particles in the figure), causing the particles to lose contact and go into suspension, and increased pore pressure as gravity load is transferred from the soil skeleton to the pore water. **c** As water flows out of the soil, pore pressure decreases, the soil particles settle into a denser configuration, and the soil skeleton once again carries the load (from National Research Council 2016)

to zero, and sediments become fluid-like, i.e., liquefy, which is often manifested on the surface by the ejection of sand-water mixtures to many meters high with the subsequent formation of sand-craters. Following the dissipation of pore pressure, sediments then settle under gravity into a more densely packed configuration (Fig. 11.6c), either by diffusion before liquefaction or by expulsion of pressurized water with liquefaction.

Different experimental designs have been used to document pore-pressure buildup during cyclic deformation in undrained conditions, e.g., cyclic torsional shearing of cylinders in a triaxial loading apparatus (e.g., Liang et al. 1995) and shake tables designed to operate in large centrifuge machines (e.g., Dief 2000). Some results were presented in Chap. 3 (Sect. 3.4) and are summarized in Fig. 11.7. Here the deformation behavior of a saturated soil under cyclic shear stress of constant amplitude is illustrated. Figure 11.7a shows the stress versus strain relation at increasing number of stress cycles. At relatively low number of stress cycles (below 15), the stress-strain relations are nearly linear; at higher numbers of stress cycles, however, the stress-strain relations become increasingly non-linear, with the shear strain increasing greatly at the same amplitude of cyclic stress, indicating the occurrence of liquefaction. Figure 11.7b shows that the normalized vertical effective stress decreases with increasing number of stress cycles at constant shear strain amplitude. Figure 11.7c and d are similar to Fig. 11.7a and b but show, instead, the increases of shear strain and decreases of the normalized effective normal stress, respectively, with increasing stress cycles.

The dissipated energy criterion is most useful in the study of the interaction between seismic waves and sediment response because seismic energy may be directly measured at the field site. Nemat-Nasser and Shokoh (1979) introduced the concept of dissipated energy for the analysis of densification and liquefaction of sediments. Berrill and Davis (1985), Law et al. (1990) and Figueroa et al. (1994) established relations between pore pressure development and the dissipated energy

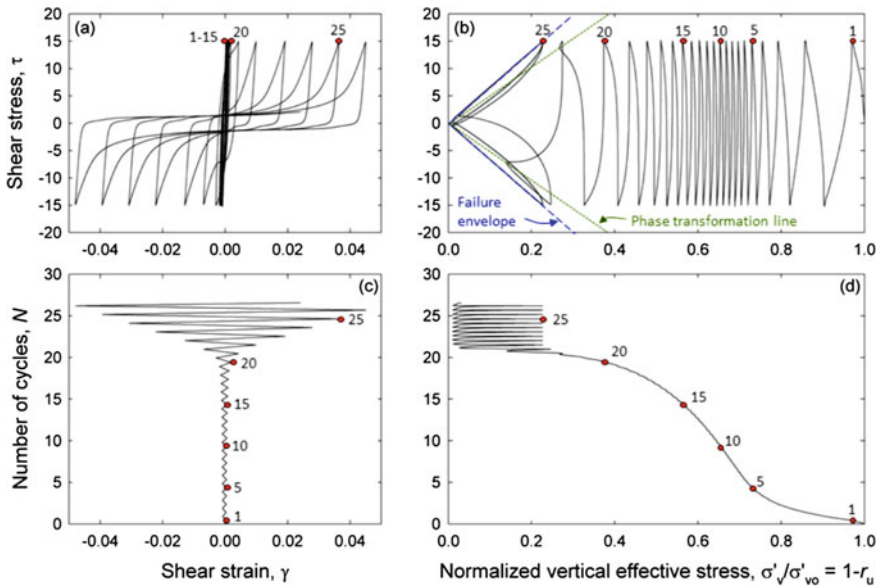


Fig. 11.7 Behavior of a saturated soil under cyclic shear stress of constant amplitude. Numbers shows the cycle number. **a** Stress-strain behavior of an initially stiff soil. Shear strain increases with more cycles. **b** Effective normal stress decreases with more cycles. **c** Shear strain increases with more cycles. **d** Effective normal stress decreases with more cycles (National Research Council 2016)

during cyclic loading to explore the use of energy density in the evaluation of the liquefaction potential of sediments. Liang et al. (1995) conducted torsional triaxial experiments on hollowed cylinders of sand to examine the effect of relative density, initial confining pressure and shear-strain magnitude and determined the energy per unit volume (i.e., dissipated energy density) accumulated up to liquefaction; they showed that the dissipated energy density required to induce liquefaction is a function of the relative density of the sediment and the confining pressure. Dief (2000) carried out shake table experiments in a centrifuge with scaled models under a wide range of physical conditions. Dief (2000) also determined the energy density accumulated up to the point of liquefaction.

Given the experimental time-histories of shear stress and strain (e.g., Figures 3.12 and 11.7a), the cumulative dissipated energy density required to initiate liquefaction by undrained consolidation may be determined by performing the following integral (Berrill and Davis 1985):

$$e = \int_0^t \tau(t)d\gamma \tag{11.1}$$

where τ is the shear stress, γ the shear strain, and the integration extends from the beginning of the cyclic loading to the onset of liquefaction (i.e., time = t). Since the stress-strain relation varies with each loading cycle when deformation is nonlinear, the integral can only be evaluated by numerical integration of the experimental stress and strain time histories.

Through such integration, Liang et al. (1995) estimated a dissipated energy density for liquefaction ranging from 290 to 2700 J/m³ for sediments with relative densities ranging from 51 to 71% subjected to confining pressures ranging from 41 to 124 kPa; Dief (2000) estimated a dissipated energy density ranging from 470 to 1700 J/m³ for relative densities ranging from 50 to 75% subjected to an equivalent confining pressures of ~ 30 kPa; and Green and Mitchell (2004) obtained a dissipated energy density ranging from 30 to 192 J/m³ for clean sand at an effective confining pressure of 100 kPa. Thus, there is a wide range in the dissipated energy density required to induce liquefaction for the studied ranges of sediment type, relative density and confining pressure. The large differences among the studies may be expected in view that sediments vary widely in their hydromechanical properties and the wide range of experimental conditions. Assuming that the sediment types, the relative density, and confining pressures in these studies are representative for the field conditions relevant to liquefaction, we may take the low value 30 J/m³, as determined by Green and Mitchell (2004) for clean sand, as the lower bound for the dissipated energy density required to induce liquefaction in the field. This lower bound imposes a threshold seismic energy density required to initiate consolidation-induced liquefaction in the field, which, in turn, sets a maximum distance from the earthquake source, beyond which consolidation-induced liquefaction may not be expected. The maximum distance so estimated may then be compared with the actual occurrence of liquefaction in the field to verify the hypothesis of undrained consolidation.

11.3 Liquefaction Beyond the Near Field

Figure 11.8 shows a plot of a global compilation of liquefaction data on a diagram of earthquake magnitude M versus the logarithm of the hypocentral distance of the documented liquefaction (Wang 2007) updated with data during the 2010–2011 Canterbury earthquake sequence (Simon Cox, personal communication). We use the earthquake magnitude M and the hypocentral distance r to characterize the liquefaction occurrence because the majority of reported (many historical) liquefactions are documented with these two parameters. The style of faulting, the directivity of fault rupture, and the distance to the ruptured fault are not available for most of these data, even though these factors may significantly affect liquefaction occurrence. Neither do most of the current data for liquefaction consider the difference between different magnitude scales. Refinement of the liquefaction data with these considerations is needed.

Several authors (Kuribayashi and Tatsuoka 1975; Ambraseys 1988; Papadopoulos and Lefkopulos 1993; Galli 2000; Wang et al. 2006; Wang 2007) showed that the

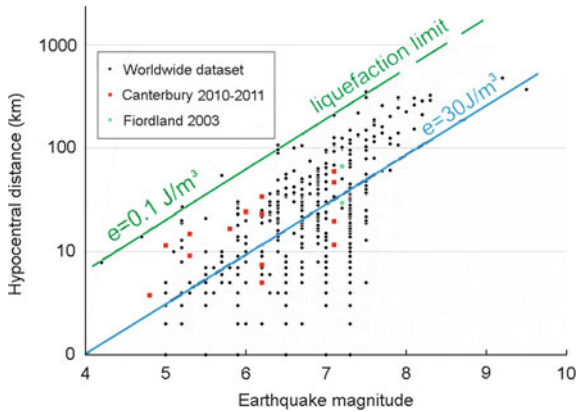


Fig. 11.8 Global data of documented liquefaction (black circles; Wang 2007) plotted on a diagram of earthquake magnitude versus the hypocentral distance, updated with data for the Canterbury earthquake sequence (2010–2011, red squares) and Fiordland (2003, green circle) compiled by Simon Cox (personal communication). Green line marks the liquefaction limit; blue line marks the contour for constant seismic energy density of 30 J/m^3 —the minimum dissipated energy density required to initiate consolidation in sensitive sediments (see text for explanation), which is approximately the boundary of the near field. Abundant liquefactions occurred at distances beyond the near field up to distances where the seismic energy density is $\sim 0.1 \text{ J/m}^3$

occurrence of liquefaction at a given M is delimited by a maximum distance—the liquefaction limit. Since the susceptibility of sediments to liquefaction varies significantly with sediment type and grain size (Seed and Lee 1966; National Research Council 1985, 2016; Dobry et al. 1982; Hsu and Vucetic 2004), sediments that liquefy at the liquefaction limit are likely those with the least resistance.

The threshold strain required to initiate undrained consolidation in the field may be the same as that in the laboratory (Hazirbaba and Rathje 2004). It may thus be justified to compare the seismic energy density in the field with the laboratory-based dissipated energy required to initiate liquefaction. Given the discussion in the last section on the laboratory-determined dissipated energy required to initiate liquefaction, we may associate the *maximum* distance of liquefaction occurrence due to undrained consolidation with the contour of $e = 30 \text{ J/m}^3$.

In Chap. 6 (Sect. 6.4.3) we derived an empirical relation among the epicentral distance (r), the earthquake magnitude (M) and the seismic energy density (e) of an idealized point-source earthquake (Eq. 6.23; Wang et al. 2006; Wang 2007)

$$\log_{10} e = -3 \log_{10} r + 1.44M - 4.62, \quad (11.2)$$

where r is in km. As noted in Chap. 6, this relation shows that contours of constant seismic energy density appear as straight lines on a diagram of \log versus M , such as the straight lines on Fig. 11.8. A seismic energy density of 30 J/m^3 is associated with the blue line in this diagram, which also marks approximately the epicentral distance equal to 1 ruptured fault length (Wells and Coppersmith 1994). The diagram shows

that a large number of liquefactions occurred beyond the near field at distances where the seismic energy density decreased to $\sim 0.1 \text{ J/m}^3$ (Wang 2007). Thus, undrained consolidation alone may not account for all occurrences of liquefaction.

The mechanism for liquefaction beyond the near field is not fully understood. We may invoke the hypothesis that, even though the seismic energy density in the intermediate field is not large enough to induce sediment liquefaction by undrained consolidation, the cyclic stresses from seismic waves nonetheless may move the mechanical state of the sediments towards a critical state so that they may liquefy if an additional increment of pore pressure becomes available to push the sediments over the liquefaction limit. Another viable mechanism is the spreading of pore pressure from a nearby high-pressure source that occurs when permeability is enhanced by earthquake (Roeloffs 1998; Brodsky et al. 2003; Wang 2007; Cox et al. 2021) which may push some critically stressed sediments over the critical state to become liquefied.

Finally, we note that the seismic energy density at the liquefaction limit is minute ($\sim 0.1 \text{ J/m}^3$). What are the micromechanisms that trigger liquefaction at such small seismic energies? More detailed laboratory and field studies are needed to resolve this problem.

11.4 Experiment at Wildlife Liquefaction Array, California

The Wildlife Liquefaction Array was a field experimental established in 1982 on a flood plain in southern California, about 10 km southeast of the Salton Sea (Fig. 11.9a), and designed specifically to study liquefaction processes. The array (Fig. 11.9b) consisted of two 3-component accelerometers, one placed on the surface and the other in a cased borehole at a depth of ~ 7 m, and six pore-pressure transducers placed around the accelerometers at various depths up to 12 m. Both the M6.2 Elmore earthquake and the M6.6 Superstition Hills earthquake triggered the accelerometers, but only the latter earthquake triggered liquefaction at the array, which caused sand boils with eruptions of water and sediments. Extensive ground cracking implied lateral spreading at the array (Holzer et al. 1989).

Many investigators have studied the Wildlife Liquefaction Array data (e.g., Zeghal and Elgamal 1994; Youd and Carter 2005; Holzer and Youd 2007). The in situ time histories of pore pressure and acceleration (Fig. 11.10) during and following the Superstition Hills earthquake reveal a complex interaction among ground shaking, pore pressure buildup and liquefaction. For the convenience of description, Zeghal and Elgamal (1994) divided the recorded time histories of ground shaking during the Superstition Hills earthquake into four stages: Stage 1 (0.0–13.7 s): Ground acceleration was below $\sim 0.1 \text{ g}$ and pore water pressure buildup was small. Stage 2 (13.7–20.6 s): Strongest shaking occurred, with peak accelerations of 0.21 and 0.17 g at the surface and downhole instruments, respectively. Pore-water pressure increased

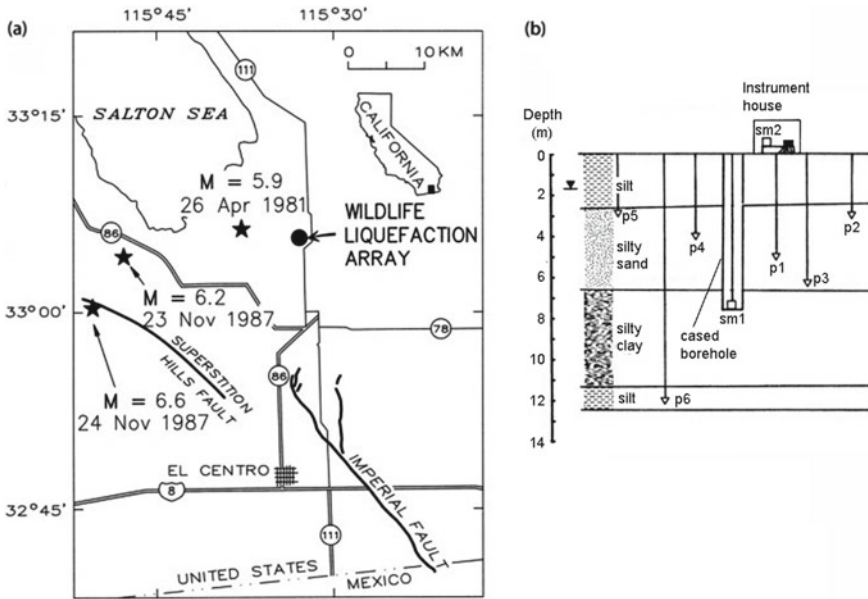
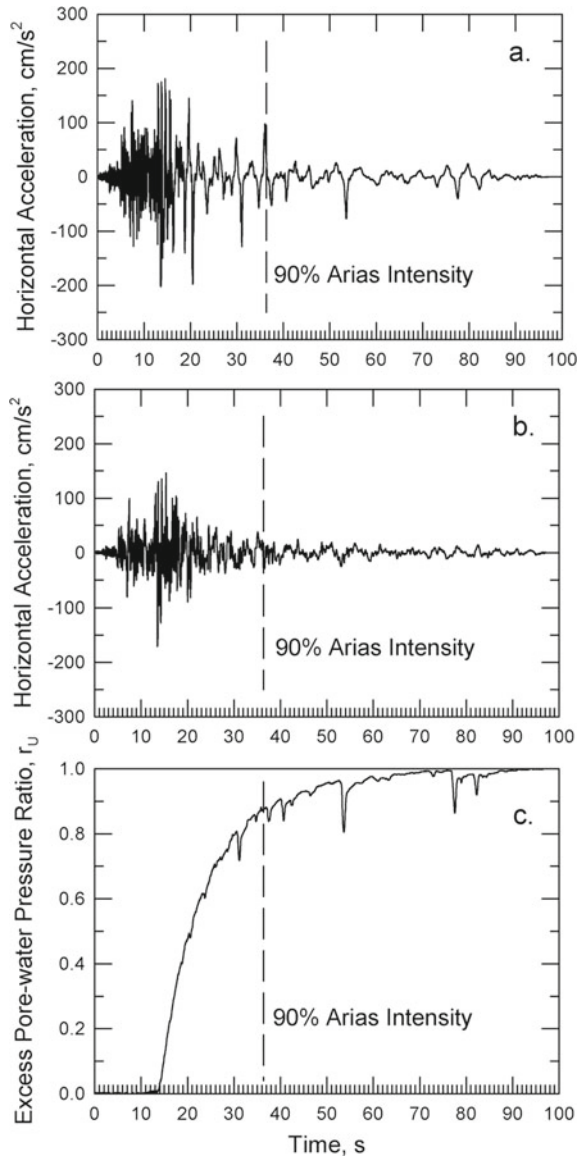


Fig. 11.9 **a** Location map of the Wildlife Liquefaction Array (filled circle) and earthquake epicenters (stars). M6.6 is the 1987 Superstition Hills earthquake, M6.2 is the 1987 Elmore Ranch earthquake, and M5.9 is the 1981 Westmorland earthquake. **b** Stratigraphic cross-section of array and schematic of instrument deployment. In plan view, pore-pressure transducers (denoted by p) are equally spaced on the perimeter of a circle with a diameter of 9.1 m. Accelerometers (sm1 and sm2) are near the center of the circle (modified from Holzer and Youd 2007)

rapidly, with small instantaneous drops. Stage 3 (20.6–40.0 s): Accelerations declined and stayed below 0.06 g. Pore-water pressure continued to increase at a high rate. Stage 4 (40.0–96.0 s): Ground acceleration was very low (~ 0.01 g), but excess pore pressure continued to rise, though at a slower rate, reaching the maximum pore pressure at 96 s.

Zeghal and Elgamal (1994) also demonstrated that the buildup of pore pressure was accompanied by a progressive softening of the sediments. Double-integrating the surface and downhole acceleration records leads to the time histories of displacements at the surface and downhole. The acceleration and displacement records may then be used to calculate the time histories of shear stress and the average shear strain (Zeghal and Elgamal 1994). Holzer and Youd (2007) recalculated the displacement history as displayed in Fig. 11.11. An interesting result is that large amplitude (up to $\sim 2\%$) long period (~ 5.5 s) cyclic shear strains continued to affect the sediments long after the high-frequency acceleration had abated. It shows that the sediments had softened so much that they underwent large shear deformations at very small shear stresses. Thus a large portion of the excess pore pressure at the Wildlife Reserve Array developed after the stronger high-frequency ground motion had abated, and liquefaction did not occur until the earthquake was almost over (Holzer et al. 1989).

Fig. 11.10 Time histories of **a** north-south surface accelerations, **b** north-south downhole accelerations, and **c** excess pore pressure ratio recorded by piezometer P5 during and following the Superstition Hills earthquake. The downward spikes show rapid and transient decreases in pore-pressure. Ratio was calculated by dividing recorded values by the value at 97 s (from Holzer and Youd 2007)



The progressive softening of sediments is best demonstrated by plotting the time history of shear stress against that of shear strain (Fig. 11.12), recalling that the slope of the stress-strain curve may be identified as the ‘rigidity’ of the sediments. At the onset of rapid pore-pressure increase, i.e., at 13.6 s (Fig. 11.10), the stress-strain curve shows steep slopes (Fig. 11.12), i.e., high rigidity. With increasing time, the slopes of the stress-strain curves decrease rapidly, showing that the sediments softened. Near

Fig. 11.11 Time histories of **a** north-south shear stress and **b** north-south shear strain at the Wildlife Reserve array during the Superstition Hills earthquake (from Holzer and Youd 2007)

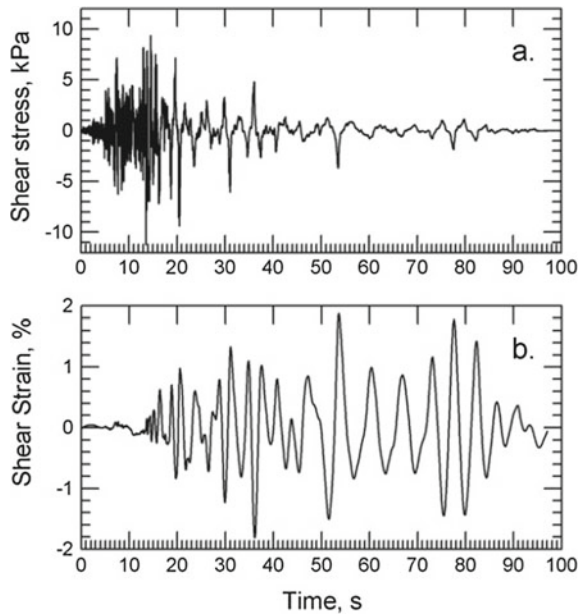
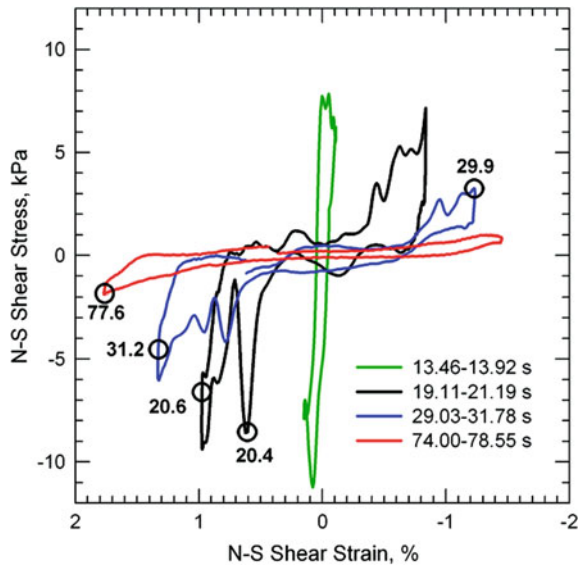


Fig. 11.12 Four hysteresis curves between shear stress and shear strain at different time segments. The times of instantaneous drop of pore pressure as recorded by piezometer P5 (Fig. 11.9) are labeled on the hysteresis curves (from Holzer and Youd 2007)



the strain extremes, however, the slopes increase suddenly, showing that the sediments stiffened once more. This latter stiffening was attributed to strain-hardening (Zeghal and Elgamal 1994) and may be related to the rapid and transient decreases in pore pressure as recorded by the piezometers (Fig. 11.10; some of the decreases

are labeled in Fig. 11.12), which, in turn, may be interpreted as a consequence of dilatancy in the strain-hardened sediments. With progressive softening, the activation of strain-hardening requires progressively greater shear strain. As a result, large deformation may be induced by very small disturbances and the sediments fluidize.

It has been a challenge to explain why pore pressure continued to increase long after the ground acceleration had abated (e.g., Holzer et al. 1989; Holzer and Youd 2007). One explanation is offered by the discussion in the last section of this chapter. We note first that the distance between the Wildlife Liquefaction Array and the epicenter of the M6.6 Superstition Hills earthquake (31 km, Holzer et al. 1989) is beyond the near field of the earthquake (<20 km); thus the seismic energy density at the Wildlife Reserve Array at the time of the earthquake may be too small to induce undrained consolidation, even in the most sensitive sediments. Second, we note that the rise in pore pressure (Fig. 11.9c) was gradual and sustained, distinct from that caused by undrained consolidation which would have appeared as a step-like increase coincident with the strongest ground shaking (Roeloffs 1998; Wang and Chia 2008). The gradual and sustained change of pore pressure, however, can be readily explained by the diffusion of pore pressure from a nearby high-pressure source that connected to the Wildlife Liquefaction Array through earthquake-enhanced permeability, as discussed in the previous section. Under such conditions, the duration of the pore-pressure increase does not depend upon the duration of ground shaking, but rather on the distance between the pore-pressure source and the Wildlife Liquefaction Array as well as the permeability between the two locations, thus explaining the continued pore-pressure buildup long after the ground acceleration had diminished. A different explanation offered by Holzer and Youd (2007) is that the strong ground shaking had initiated consolidation and thus pore-pressure increase in the sediments, and consolidation may have continued afterwards under the action of the long-period surface waves that arrived after the ground shaking had abated. If so, the sediments at the Wildlife Liquefaction Array would have to be more sensitive than the most sensitive sediments so far tested in the laboratory. An interesting point of this model is the positive feedback between pore-pressure buildup and sediment weakening, i.e., sediments which have been progressively weakened by rising pore pressure during seismic loading may continue to consolidate and generate pore pressure at progressively lower stresses, which further weakens the sediments.

In summary, the Wildlife Liquefaction Array experiment demonstrated that the occurrence of liquefaction is the culmination of a complex sequence of interactions among ground shaking, sediment deformation and pore-pressure redistribution and/or buildup. An increase in pore pressure weakens the sediment framework; this leads to greater deformation of the sediments. Continued increase in pore pressure may occur due to enhanced permeability connecting the sediments to a nearby source, or possibly by continued consolidation. This process continues at low frequency and very small shear stresses until the sediments liquefy.

11.5 Dependence of Liquefaction on Seismic Frequency

The period of seismic waves recorded near some liquefaction sites ranges from less than a second to many tens of seconds, as illustrated by the seismic records at the Wildlife Liquefaction Array discussed in the last section. It is thus important to investigate whether the initiation of liquefaction depends on the frequency of seismic waves and, if so, how does it depend on the seismic frequency.

Established engineering methods frequently use the peak ground acceleration (PGA) as an index to predict liquefaction risk (Seed and Idriss 1971). This is because PGA is proportional to the maximum shear stress induced in the sediment (Terzaghi et al. 1996). Midorikawa and Wakamatsu (1988) calculated PGA and PGV at ~ 130 liquefaction sites and found, however, that the occurrence of liquefaction is better correlated with the calculated PGV than with PGA. This result implies that liquefaction may be more sensitive to the low frequency components of the ground motion. This is because the integration of the acceleration records to calculate velocity ‘filters’ out higher frequencies, so PGV is more dominated by low frequencies than PGA. In the following we test these models by using the occurrence of liquefaction, groundwater-level changes, and strong-motion records from central Taiwan during the Chi-Chi earthquake (Wang et al. 2003; Wong and Wang 2007).

The 1999 $M_w 7.6$ Chi-Chi earthquake (Fig. 11.13) caused widespread liquefaction on the Choshui Alluvial Fan (Fig. 11.13b). An extensive network of strong-motion

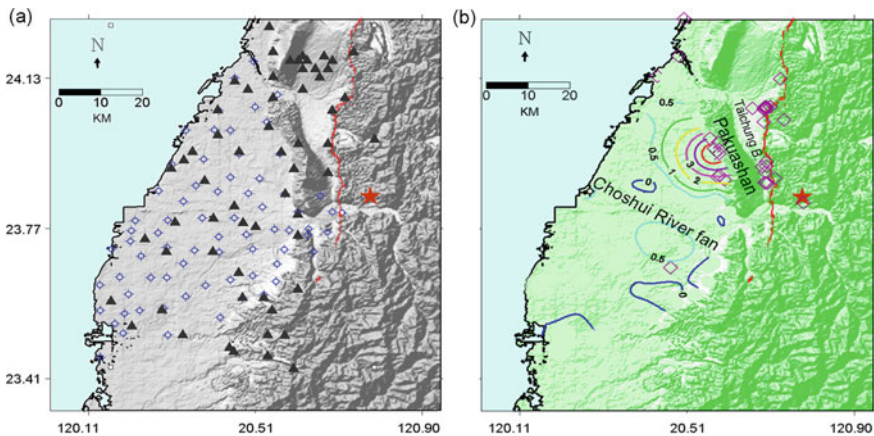


Fig. 11.13 **a** Distribution of strong-motion stations (solid triangles) and hydrologic stations (open circles) on the Choshui alluvial fan (i.e., the flat fan-shaped area to the west of the hilly area) and nearby areas in western Taiwan. At each of the stations, there are one to five monitoring wells drilled to different depths up to 300 m. Red star marks the epicenter of the Chi-Chi earthquake, and red curve shows the ruptured fault in the earthquake. **b** Contours (in m) of the coseismic changes in groundwater level in the topmost aquifer in the Choshui alluvial fan. Open diamonds show sites of liquefaction. Note that, on the Choshui alluvial fan, most liquefaction sites occurred in an area where the rise in groundwater level was above 2 m (modified from Wang et al. 2006)

seismographs and a similarly extensive network of clustered wells were installed on the fan (Fig. 11.13a) which captured both the ground motion and the concurrent groundwater level changes during and after the earthquake. These data provide a rare opportunity to investigate the field relationship among liquefaction, ground motion and groundwater level changes. Liquefaction sites on the Choshui River fan are closely associated with the largest coseismic rise of the groundwater level in the uppermost aquifer. At the same time, the distribution of liquefaction sites is entirely different from that of the highest pore pressure in the lower quifers (Fig. 6.4b and c), suggesting that liquefaction occurred only in the shallowest aquifer. No monitoring wells were installed in the basins east of the Choshui River fan; thus a similar comparison between pore pressure rise and the distribution of liquefaction cannot be made.

In order to test the frequency-dependence of pore-pressure development and liquefaction Wang et al. (2003) and Wong and Wang (2007) calculated the spectral acceleration, S_a , and spectral velocity, S_v , defined as the maximum response of a harmonic oscillator at 5% damping at each seismometer location. Contours for constant S_a and S_v were then interpolated from the calculated S_a and S_v values at the seismic stations (Fig. 11.14) using a kriging procedure. Visual inspection of the maps shows that there is a strong correlation between the liquefaction sites (filled diamonds) and S_a occurs at 0.7 and 1 Hz, but not at 2 Hz. A similar result occurs between the spatial distribution of S_v (not shown) and the liquefaction sites.

A statistical test of the correlation of liquefaction with seismic wave frequency may be provided by plotting the t -values for the correlations of water level increase (i.e., pore pressure increase) with S_a and S_v over a range of frequencies. Calculations were made from $\sim 10^{-3}$ to $\sim 10^2$ Hz, but only a section of this range is shown in Fig. 11.15 for clarity. In general, S_a and S_v below about 0.8 Hz are more strongly correlated with the water-level increase than those above 0.8 Hz. The strength of the

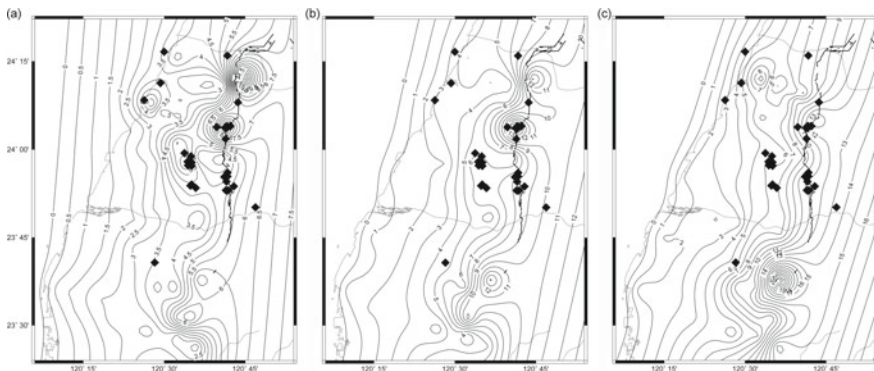


Fig. 11.14 Contours of spectral acceleration S_a at **a** 0.7 Hz, **b** 1 Hz, and **c** 2 Hz during the Chi-Chi earthquake, plotted together with the distribution of liquefaction sites in solid diamonds. Note the strong correlation between liquefaction sites and S_a at 0.7 Hz and the weak correlation at 2 Hz (from Wong and Wang 2007)

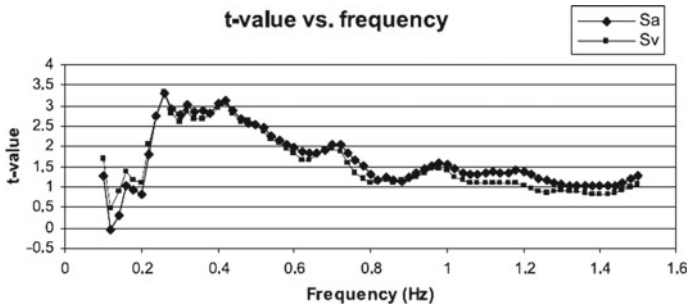


Fig. 11.15 t -values of the correlation of the water-level increase with S_a and S_v over a range of frequencies from 0.1 to 1.5 Hz, which pore pressure increases and liquefaction are typically attributed (from Wong and Wang 2007)

correlation peaks at 0.3–0.4 Hz, but declines rapidly at lower frequencies (Wong and Wang 2007).

Laboratory studies of the dependence of liquefaction on the frequency of the seismic loads are few. Yoshimi and Oh-Oka (1975) conducted a series of cyclic shear tests under undrained conditions to determine the conditions to induce liquefaction in saturated sands. Most specimens in their experiments had a relative density, i.e., the ratio of the density of a specimen to the average density of the solid grains, of approximately 40%, and the frequency of the cyclic shear stress ranged from 1 to 12 Hz. They found that liquefaction failure became imminent when the ratio of the peak shear stress to the vertical effective stress reached a certain critical value, but the condition to induce liquefaction was nearly independent of the frequency of the cyclic shear stress from 1 to 12 Hz.

Sumita and Manga (2008) measured the rheology of non-Brownian particle suspensions under oscillatory shear at frequencies ranging from 0.1 to 10 Hz. A rheological transition was found to occur at a shear strain threshold of 10^{-4} , whereby the shear modulus of the viscoelastic suspension reduces sharply. This transition is in excellent correspondence with the threshold shear strain determined in geotechnical engineering experiments where excess pore pressure begins to develop and the shear modulus of the sediments begins to decline (Dobry et al. 1982; Vucetic 1994; Hsu and Vucetic 2004, 2006). Sumita and Manga (2008) found no dependence of the threshold shear strain on the frequency of shearing from 0.1 to 10 Hz.

The field and laboratory results on the dependence of liquefaction on frequency thus appear to be in conflict. On the one hand, existing laboratory results show little frequency-dependence of liquefaction; on the other hand, in situ studies of seismically instrumented liquefaction sites show an association of liquefaction with low-frequency ground motions.

Using dynamic numerical models with nonlinear constitutive relations for sediments, Popescu (2002) and Ghosh and Madabhushi (2003) showed that the association of liquefaction and low-frequency ground motion may be due to sediment

softening induced by ground motions. They also suggest a spectra-dependent feedback loop for liquefying sediments: low frequency excitation causes ground softening and pore pressure increases more efficiently than for high frequency excitation. This softening in turn reduces the resonant frequency of the sediment column, amplifying low frequency motions and damping high frequency motions, leading to further softening and pore pressure increases, possibly leading to liquefaction.

Kostadinov and Towhata (2002) proposed a linearly elastic model of one dimensional wave propagation that suggests liquefaction may occur when the sediment column reaches a resonant state. Similarly, Bachrach et al. (2001) used a dynamic poroelastic model to simulate the effect of P-waves on pore-pressure buildup and liquefaction near the resonant frequency of sediment columns.

Further in situ, laboratory, and theoretical work are required to evaluate the dependence of pore-pressure buildup and liquefaction on the frequency of seismic waves. If the frequency dependence is due to resonance in the soil, as theoretical models suggest, local hydrologic and geologic conditions would affect ground motion frequencies.

Finally, to make predictions regarding liquefaction at particular sites, results must be integrated with site-specific geotechnical data. This requires the development of predictive theories of liquefaction that incorporate both the seismic spectral information of the ground motion, as well as geotechnical information such as SPT (Standard Penetration Test) and CPT (Cone Penetration Test). Such predictions should be verified with data from earthquake-affected sites where both geotechnical data and ground motion data are available. For more detailed discussions on the predictions of liquefaction at particular sites, the readers are referred to the volume of National Research Council (2016).

11.6 Concluding Remarks

Despite the tremendous progress made in the last ~60 years towards a better understanding of the processes of earthquake-induced liquefaction, several important problems remain not understood. Most of the past progress was made by earthquake engineers who based their approach on Terzaghi's theory that liquefaction is caused by pore pressure buildup due to undrained consolidation of saturated sediments. Thus, a pre-requisite for this mechanism is the undrained consolidation of sediments which can occur only when the seismic energy density exceeds a threshold that, in turn, imposes a limit of liquefaction in the near field of an earthquake. Field studies, however, have documented liquefaction at epicentral distances far beyond the near field (Fig. 11.8; Wang 2007) where the seismic energy density may be too low to cause sediments to consolidate. The mechanism for the liquefaction beyond the near field is not understood and requires further study.

Another outstanding question is the dependence of liquefaction on the frequency of the seismic waves. As discussed in Sect. 11.5, the current results from the field and laboratory studies are in conflict and more work is needed to resolve these conflicts.

In addition, the roles of different types of seismic waves in inducing liquefaction also needs to be better investigated.

Finally, while in most cases the liquefied sediments are sand or silty sand, well-graded gravel has increasingly been witnessed to liquefy during earthquakes. This occurred during the 1983 Borah Peak earthquake in Idaho (Youd et al. 1985), during the 1995 Hyogoken Nambu earthquake near Kobe, Japan (Kokusho 2007), and during the 2008 Wenchuan earthquake, China. With borehole investigations, Liu-Zeng et al. (2017) demonstrated that the ejected gravels during the Wenchuan earthquake were not simply the result of entrainment by liquified sand but was due to the liquefaction of gravelly layers themselves at depth. As these authors pointed out, because gravels typically have high permeability that allows for rapid dissipation of pore pressure, it is challenging to understand how pore pressure is built up in gravelly soils and maintained at a level high enough to cause liquefaction. Hence more investigation is required to understand the mechanism of the liquefaction of gravelly soils.

References

- Ambraseys NN (1988) Engineering seismology. *Earthq Eng Struct Dyn* 17:1–105
- Bachrach R, Nur A, Agnon A (2001) Liquefaction and dynamic poroelasticity in soft sediments. *J Geophys Res* 106:13515–13526
- Berrill JB, Davis RO (1985) Energy dissipation and seismic liquefaction in sands: revised model. *Soils Found* 25:106–118
- Brodsky EE, Roeloffs E, Woodcock D et al (2003) A mechanism for sustained water pressure changes induced by distant earthquakes. *J Geophys Res* 108(108):2390. <https://doi.org/10.1029/2002JB002321>
- Cox SC, van Ballegooy Sjoerd, Rutter HK, Harte DS, Holden C, Gulley AK, Lacrosse V, Manga M (2021) Can artesian groundwater and earthquake-induced aquifer leakage exacerbate the manifestation of liquefaction?. *Eng Geo* 281:105982
- Dief HM (2000) Evaluating the liquefaction potential of soils by the energy method in the centrifuge. PhD dissertation, Case Western Reserve University, Cleveland, OH
- Dobry R, Ladd RS, Yokel FY et al (1982) Prediction of pore water pressure buildup and liquefaction of sands during earthquakes by the cyclic strain method. National Bureau of Standards Building Science Series 138, National Bureau of Standards and Technology, Gaithersburg, MD, 150 pp
- Figueroa JL, Saada AS, Liang L, Dahisaria NM (1994) Evaluation of soil liquefaction by energy principles. *J Geotech Eng ASCE* 120:1554–1569
- Galli P (2000) New empirical relationships between magnitude and distance for liquefaction. *Tectonophysics* 324:169–187
- Ghosh B, Madabhushi SPG (2003) A numerical investigation into effects of single and multiple frequency earthquake motions. *Soil Dyn Earthq Eng* 23:691–704
- Green RA, Mitchell JK (2004) Energy-based evaluation and remediation of liquefiable soils. In: Yegian M, Kavazanjian E (eds) *Geotechnical engineering for transportation projects*. ASCE geotechnical special publication, no 126, vol 2, pp 1961–1970
- Hazirbaba K, Rathje EM (2004) A comparison between in situ and laboratory measurements of pore water pressure generation. In: 13th world conference on earthquake engineering, paper no 1220, Vancouver
- Holzer TL, Tinsley JC, Hank TC (1989) Dynamics of liquefaction during the 1987 Superstition Hills, California, earthquake. *Science* 244:56–59

- Holzer TL, Youd TL (2007) Liquefaction, ground oscillation, and soil deformation at the Wildlife Array, California. *Bull Seis Soc Am* 97:961–976
- Hsu CC, Vucetic M (2004) Volumetric threshold shear strain for cyclic settlement. *J Geotech Geoenviron Eng* 130:58–70
- Hsu CC, Vucetic M (2006) Threshold shear strain for cyclic pore-water pressure in cohesive soils. *J Geotech Geoenviron Eng* 132:1325–1335
- Kokusho T (2007) Liquefaction strengths of poorly-graded and well-graded granular soils investigated by lab tests. In: Pitolakis KD (ed) *Earthquake geotechnical engineering*. Springer, Dordrecht
- Kostadinov MV, Towhata I (2002) Assessment of liquefaction-inducing peak ground velocity and frequency of horizontal ground shaking at onset of phenomenon. *Soil Dyn Earthq Eng* 22:309–322
- Kuribayashi E, Tatsuoka F (1975) Brief review of liquefaction during earthquakes in Japan. *Soils Found* 15:81–92
- Law KT, Cao YL, He GN (1990) An energy approach for assessing seismic liquefaction potential. *Can Geotech J* 27:320–329
- Liang L, Figueroa JL, Saada AS (1995) Liquefaction under random loading: Unit energy approach. *J Geotech Eng* 121:776–781
- Liu-Zeng J, Wang P, Zhang Z et al (2017) Liquefaction in western Sichuan basin during the 2008 Mw7.9 Wenchuan earthquake, China. *Tectonophysics* 694:214–238. <https://doi.org/10.1016/j.tecto.2016.11.001>
- Marinatos SN (1960) Helice: A submerged town of classical Greece. *Archaeology* 13:186–193
- Midorikawa S, Wakamatsu K (1988) Intensity of earthquake ground motion at liquefied sites. *Soils Found* 28:73–84
- National Research Council (1985) *Liquefaction of soils during earthquakes*. National Academies Press, Washington, DC
- National Research Council (2016) *State of the art and practice in the assessment of earthquake-induced soil liquefaction and its consequences*. National Academies Press, Washington, DC. <https://doi.org/10.17226/23474>
- Nemat-Nasser S, Shokoh A (1979) A unified approach for densification and liquefaction of cohesionless sands in cyclic loading. *Can Geotech J* 16:659–678
- Obermeier SF (1989) The new Madrid earthquakes: an engineering-geologic interpretation of relic liquefaction features. *US Geol Surv Prof Pap* 1336-B, 114 pp
- Papadopoulos GA, Lefkopulos G (1993) Magnitude-distance relations for liquefaction in soil from earthquakes. *Bull Seism Soc Am* 83: 925–938
- Pitolakis KD (2007) *Earthquake geotechnical engineering*. Springer, Dordrecht
- Popescu R (2002) Finite element assessment of the effects of seismic loading rate on soil liquefaction. *Can Geotech J* 29:331–334
- Roeloffs EA (1998) Persistent water level changes in a well near Parkfield, California, due to local and distant earthquakes. *J Geophys Res* 103:869–889
- Schmidt FJ (1875) *Studien über Erdbeben*. Carl Scholtze, Leipzig, 360 pp
- Seed HB (1968) Landslides during earthquakes due to soil liquefaction. *J Soil Mech Found Div* 94:1055–1122
- Seed HB, Lee KL (1966) Liquefaction of saturated sands during cyclic loading. *J Soil Mech Found Div* 92:105–134
- Seed HB, Idriss IM (1967) Analysis of soil liquefaction: Niigata earthquake. *J Soil Mech Found Div* 93:83–108
- Seed HB, Idriss IM (1971) Simplified procedure for evaluating soil liquefaction potential. *J Soil Mech Found Div* 97:1249–1273
- Sumita I, Manga M (2008) Suspension rheology under oscillatory shear and its geophysical implications. *Earth Planet Sci Lett* 269:467–476
- Terzaghi K (1925) *Erdbaummechanik*. Franz Deuticke, Vienna
- Terzaghi K, Peck RB, Mesri G (1996) *Soil mechanics in engineering practice*. Wiley, New York

- Tuttle MP, Schweig ES (1996) Recognizing and dating prehistoric liquefaction features: lessons learned in the New Madrid seismic zone, central United States. *J Geophys Res* 101:6171–6178
- van Ballegooy S, Malan P, Lacrosse V et al (2014) Assessment of liquefaction-induced land damage for residential Christchurch. *Earthq Spectra* 30:31–55
- Vucetic M (1994) Cyclic threshold of shear strains in soils. *J Geotech Eng* 120:2208–2228
- Wang C-Y (2007) Liquefaction beyond the near field. *Seismo Res Lett* 78:512–517
- Wang C-Y, Chia Y (2008) Mechanism of water level changes during earthquakes: near field versus intermediate field. *Geophys Res Lett* 35:L12402. <https://doi.org/10.1029/2008GL034227>
- Wang C-Y, Dreger DS, Wang C-H et al (2003) Field relations among coseismic ground motion, water level change, and liquefaction for the 1999 Chi-Chi ($M_w = 7.5$) earthquake, Taiwan. *Geophys Res Lett* 30:1890. <https://doi.org/10.1029/2003gl017601>
- Wang C-Y, Wong A, Dreger DS, Manga M (2006) Liquefaction limit during earthquakes and underground explosions—implications on ground-motion attenuation. *Bull Seis Soc Am* 96:355–363
- Wells DL, Coppersmith KJ (1994) New empirical relationships among magnitude, rupture length, rupture width, rupture area, and surface displacement. *Bull Seis Soc Am* 84:974–1002
- Wong A, Wang C-Y (2007) Field relations between the spectral composition of ground motion and hydrological effects during the 1999 Chi-Chi (Taiwan) earthquake. *J Geophys Res* 112:B10305. <https://doi.org/10.1029/2006JB004516>
- Yoshimi Y, Oh-Oka H (1975) Influence of degree of shear stress reversal on the liquefaction potential of saturated sand. *Soils Found (Japan)* 15:27–40
- Youd TL (1972) Compaction of sands by repeated shear straining. *J Soil Mech Found Div Am Soc Civ Eng* 98:709–725
- Youd TL, Harp EL, Keefer DK, Wilson RC (1985) The Borah Peak, Idaho, earthquake of October 28, 1983—liquefaction. *Earthq Spectra* 2:71–89
- Youd TL, Carter BL (2005) Influence of soil softening and liquefaction on spectral acceleration. *J Geotech Geoenviron Eng* 131:811–825
- Zeghal M, Elgamal AW (1994) Analysis of site liquefaction using earthquake records. *J Geotech Eng* 120(6):996–1017

Open Access This chapter is licensed under the terms of the Creative Commons Attribution 4.0 International License (<http://creativecommons.org/licenses/by/4.0/>), which permits use, sharing, adaptation, distribution and reproduction in any medium or format, as long as you give appropriate credit to the original author(s) and the source, provide a link to the Creative Commons license and indicate if changes were made.

The images or other third party material in this chapter are included in the chapter's Creative Commons license, unless indicated otherwise in a credit line to the material. If material is not included in the chapter's Creative Commons license and your intended use is not permitted by statutory regulation or exceeds the permitted use, you will need to obtain permission directly from the copyright holder.



Chapter 12

Mud Volcanoes



Abstract The eruption of mud and magma can be influenced by earthquakes and reports date back more than 2000 years. Dozens of examples of eruptions have now been documented in response to both static and dynamic stresses from earthquakes. Already erupting systems are most sensitive to earthquakes compared to initiating new eruptions. Multiple plausible mechanisms have been proposed for triggering eruptions including disrupting particle-rich materials, mobilizing bubbles, or changing permeability—changes may occur both within and outside the reservoir hosting the materials that ultimately erupt. Using historical examples of triggered mud eruptions, we explain why it is unlikely that the Sidoarjo mud flow (sometimes nicknamed “Lusi”) was initiated by an earthquake. As multiparameter monitoring of volcanoes expands, it may eventually be possible to identify triggering mechanisms and how seismic waves influence magma and mud mobility in field settings.

12.1 Introduction

Mud volcanoes are surface structures formed by the eruption of mud and rock fragments from the subsurface. Colloquially, the term is used to describe a wide range of features, from decimeter-sized cones to features that are hundreds of meters high and create flows that extend laterally for a couple kilometers (Fig. 12.1). Submarine mud volcanoes, such as the serpentinite mud volcanoes in the Marianas forearc, can create edifices with diameters of 50 km that are 2.5 km high (e.g., Fryer 2012).

The term “mud volcano” is generally reserved for large structures made from the eruption of mud breccias driven to the surface by buoyancy and overpressure (e.g. Mazzini and Etiope 2017). As the erupting materials are fluid-rich, a number of types of fluid seepage features are associated with mud volcanoes. Gryphons are small mud cones (e.g., Fig. 12.1a), up to a few meters high, can be numerous, and often are aligned with tectonic structures. Pools discharging water and gas and minor amounts of sediment are also common. All features can have episodic discharge.

The erupted materials are three-phase: solids, water, and gases, the latter being dominantly methane and CO₂ (e.g., Kopf 2002). Fragments of country rock are also

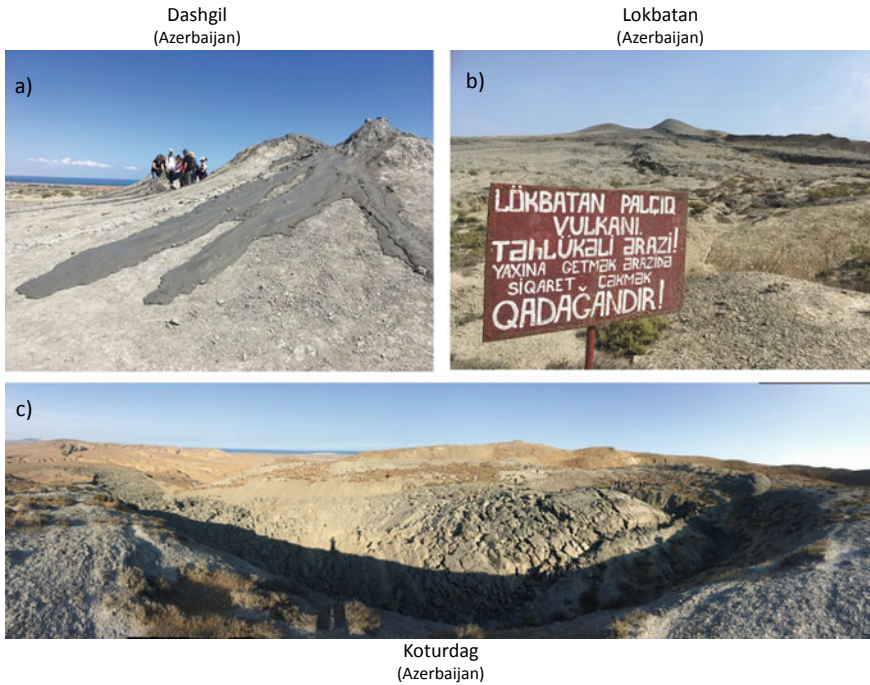


Fig. 12.1 Example mud volcanoes, all form Azerbaijan, with people for scale in all photos. Azerbaijan is famous for the number and diversity of mud volcanoes (Aliyev et al. 2002). **a** Gryphons and fresh flows at the Dashgil mud volcano; **b** large Lokbatan mud volcano with vent in the background; **c** very viscous Koturdag mud volcano showing the mud breccia emerging at the vent in the foreground and flowing downslope. Photos by the authors

sometimes entrained. Individual blocks in erupted breccias can be greater than 1 m in diameter. Large mud volcanoes can be rooted deeper than 10 km, such as those near the Black and Caspian Seas (e.g. Mazzini and Etiope 2017).

Mud volcanism requires thick layers of unconsolidated sediment or brecciated sedimentary rocks with high pore pressures. Figure 12.2 illustrates schematically the source of materials and subsurface piercement structures associated with mud volcanoes. They are thus most common in areas with high sedimentation rates such as sedimentary basins and accretionary prisms. There are perhaps about $\sim 10^3$ mud volcanoes on land (Etiope and Milkov 2004; Etiope 2015). The number offshore is poorly known and their locations not well mapped. Milkov (2000) extrapolated mapped regions to estimate that there may be thousands to hundreds of thousands of submarine mud volcanoes. Their eruption is favored by compressional settings which act to increase pore pressure and they often form along the tops of anticlines with feeder dike orientations controlled by the regional stress field (e.g., Bonini 2012). Faults and fault intersections often help create pathways for fluid ascent (Mazzini et al. 2009). They are frequently related to pressurized hydrocarbon reservoirs and hence are sometimes targeted for hydrocarbon exploration.

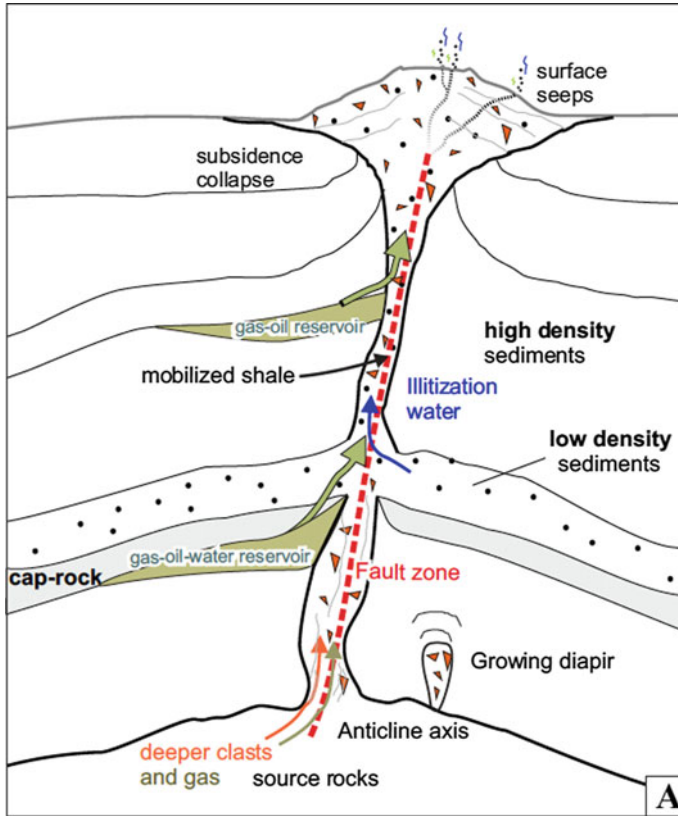


Fig. 12.2 Schematic illustration of a mud volcano’s subsurface “piercement” structure and source of solids, fluids and gas (from Mazzini and Etiope 2017)

12.2 Response of Mud Volcanoes to Earthquakes

A number of studies have documented eruptions of subaerial mud volcanoes within days of earthquakes (e.g., Snead 1964; Chigira and Tanaka 1997; Delisle 2005; Manga and Brodsky 2006; Mellors et al. 2007; Rukavickova and Hanzl 2008; Bonini 2009; Manga et al. 2009; Manga and Bonini 2012; Tsunogai et al. 2012; Bonini et al. 2016; Maestrelli et al. 2017). Tingay et al. (2018) provides a table summarizing the dates of the eruptions, and the earthquake magnitudes and their distance from the mud volcanoes. The number of documented triggered mud volcano eruptions is not large, 58 in this compilation. Of the total, 6 instances are triggered eruptions at the Niikappu mud volcano in Japan (Chigira and Tanaka 1997).

Figure 12.3 shows the relationship between earthquake magnitude and the distance between triggered eruptions of mud volcanoes and the earthquake epicenter. As with other hydrological responses to earthquakes, there appears to a clear upper bound on the distance over which eruptions might be triggered that increases as earthquake

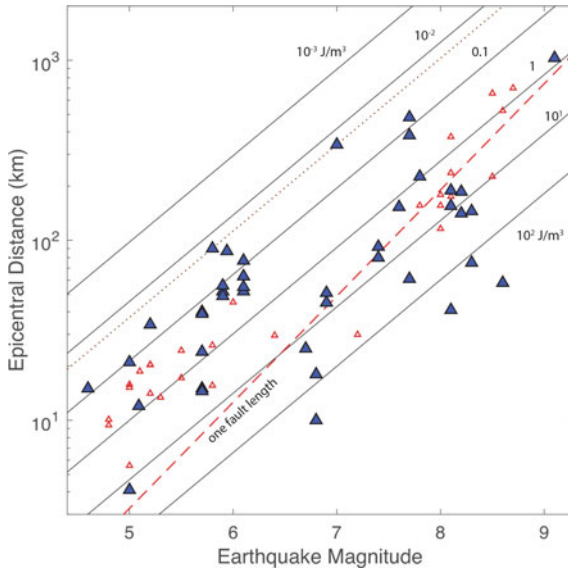


Fig. 12.3 Relationship between earthquake magnitude and distance of mud volcanoes that erupted within days of the earthquake (filled blue triangle). Data from the compilation in Tingay et al. (2018). The small open red triangles are magmatic volcanoes that erupted within days of earthquakes from the lists in Manga and Brodsky (2006) and Lemarchand and Grasso (2007). The sloping black lines and lines of constant seismic energy density, as estimated in Wang and Manga (2010). The sloping red dashed line is a line showing one fault length (delineating the near-field)

magnitude increases. This threshold is similar to that for streamflow responses and for the occurrence of liquefaction.

The repeated eruption of the Niikappu mud volcano, Japan, in response to earthquakes offers an excellent opportunity to better understand the conditions required for triggering. This is analogous to studying the response of a single water well to multiple earthquakes (Chaps. 66, 8) and response of a single stream to multiple earthquakes (Chap. 7). Manga et al. (2009) found that this mud volcano consistently obeyed the empirical threshold in Fig. 12.3 provided there was a repose time of at least 1–2 years between eruptions. Large, close earthquakes that occurred sooner did not trigger an eruption. This supports the arguments in Mellors et al. (2007) that a recharge period is needed before another eruption can be triggered.

Long-term triggering is more challenging to identify, but has been inferred for some mud volcanoes. Bonini et al. (2016) concluded that several mud eruptions were triggered in Azerbaijan within a year of earthquakes under conditions that the earthquakes were less than 10 fault length away and when coseismic static stress changes compressed the mud source and unclamped feeder dikes. Over longer time scales, Babyev et al. (2014) concluded that the Azerbaijan mud volcanoes have an increased eruption rate for several years after earthquakes and that dynamic rather than static strains play a dominant role in their delayed triggering.

12.3 Insights from Triggered Eruptions of Magmatic Volcanoes

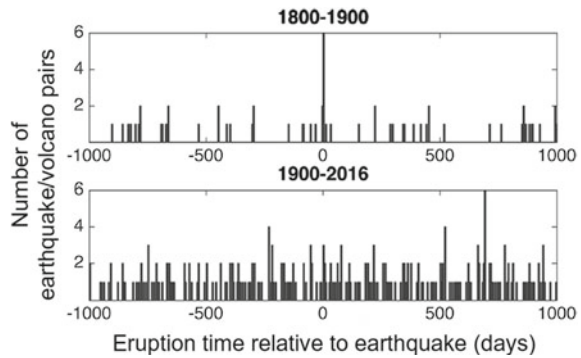
The modest number of well-documented eruptions of mud volcanoes limits our ability to perform a meaningful analysis of the probability that they are triggered by earthquakes. This is less problematic for earthquake-triggered eruptions of magmatic (“real”) volcanoes since accounts and catalogues of eruptions are more accessible and have more data. We thus provide a brief overview of what is known about the triggered eruptions of magmatic volcanoes and implications for mud volcanoes. Early reviews of this topic are published by Hill et al. (2002) and Manga and Brodsky (2006).

There is a long record of inferring that earthquakes trigger the eruption of magmatic volcanoes (e.g., Darwin 1840; Yokoyama 1971; Nakamura 1975). Since the initiation of an eruption requires rocks to break, pathways for fluid flow to open, or pressures in magma bodies to change, it is reasonable to expect that stress changes from earthquakes could initiate magma movement and then eruption.

The Smithsonian Institution maintains a catalog of volcanic eruptions that includes the date and magnitude of volcanic eruptions (Siebert and Simkin 2002; www.volcano.si.edu/world). This catalog is reasonably complete and meaningful for moderate to large explosive eruptions since about 1500 AD. It is thus possible to look for correlations between the occurrence of large (magnitude >8) earthquakes and volcanic eruptions over a period of at least 500 years, and with smaller earthquakes during the more recent past. In regions with a longer recorded history, e.g., Italy, a regional analysis may permit analysis of smaller earthquakes and eruptions extending further back in time.

Identifying a triggered eruption suffers from the complication that the surface manifestation of a triggered event may not occur for days to perhaps even years after the earthquake. The nature of any delay reflects the mechanism of triggering and the manner in which the magma erupts. The search for triggered eruptions is thus generally confined to a specific window in space and time. In a first global analysis, Linde and Sacks (1998) concluded that more eruptions occurred within a couple days of large earthquakes than could be expected by chance. Manga and Brodsky (2006) repeated the analysis and concluded that 0.4% of eruptions occur within 5 days of large earthquakes. This analysis (done with a more recent catalog of eruptions and earthquakes) is shown in Fig. 12.4 for eruptions with magnitude $VEI \geq 2$ and within 800 km the earthquake, and subdivided between the nineteenth century and more recent times. VEI is the Volcanic Explosive Index, and a value of 2 corresponds to moderate explosive eruptions (Newhall and Self 1982). The number of events that appear to be triggered within days during the nineteenth century is lower than previous analyses as eruption dates have been refined (Watt et al. 2009). Lemarchand and Grasso (2007) performed a similar analysis that included both smaller earthquakes and eruptions for the period 1973–2005 and similarly found that 0.3% of eruptions interacted with earthquakes (though for these smaller events, the occurrence of eruptions is distributed approximately symmetrically in time around

Fig. 12.4 Histogram showing the relationship between the time of volcanic eruptions relative to the time of large (magnitude >8) earthquakes within 800 km. Bin size is 5 days. This figure repeats an analysis first done by Linde and Sacks (1998), but with expanded and updated earthquake and eruption catalogues (from Sawi and Manga 2018)



the earthquake). Intriguingly, the same type of global analysis since 1900 suggests that there is no short-term triggering of earthquakes (Fig. 12.4b).

Figure 12.4 shows the relationship between earthquakes and eruptions within a few days of the earthquakes, plotting examples listed in Manga and Brodsky (2006) and Lemarchand and Grasso (2007). If there is a threshold ground motion or stress for short-term triggering of magmatic volcanoes, it is similar to that for mud volcanoes (though the latter seem to be more sensitive to earthquakes on these short time scales).

The aforementioned studies focused on eruptions within days for which a statistical analysis is easier to perform (Linde and Sacks 1998). Delayed triggering is more difficult to establish and several studies have examined the space-time connections between earthquakes and eruptions (e.g., Marzocchi 2002; Watt et al. 2009). Proposed examples of delayed triggering include an increase in eruptions in the Cascade arc, USA in the 1800s following a large subduction earthquake in 1700 (Hill et al. 2002); volcanic eruptions following the M9.3 December 2004 Sumatra earthquake, the 1952 M9.0 Kamchatka earthquake, and the 1964 M9.2 Alaska earthquake (Walter and Amelung 2007); increased eruption rates after Chilean earthquakes, 1906 M8 and 1964 M9.5 (Watt et al. 2009); the 1991 eruption of Pinatubo 11 months after a M7.7 event (Bautista et al. 1996); increases eruption rates in the Lesser Antilles arc between the mid nineteenth century and early twentieth century following megathrust earthquakes in 1839 and 1843 (Feuillet et al. 2011). Sawi and Manga (2018) performed a global analysis considering the time period since 1964 for which earthquake catalogs are complete to magnitude 6 and the eruption record should be most reliable. Short term triggering, within days, was not apparent, regardless of tectonic setting, magma type, or eruption style. They did find a 5–12% increase in the number of eruptions within 2 months to 2 years after earthquakes—evidence for a modest increase in delayed triggering. For larger earthquakes (M7.5 or greater) and closer distances (within 200 km), the probability of eruption increases to 50% during the 5 years after the earthquake (Nishimura 2017). These changing probabilities of eruption can inform risk assessment.

It is worth thinking about the possible biases that enter the catalogues of events used to search for correlations between earthquakes and eruptions. For example, the report by Darwin (1840) turns out to be unreliable (Watt et al. 2009; Lara et al. 2020).

There may be historical biases in recording events that are closely spaced in time. The analysis in Fig. 12.4 also only considers explosive eruptions with a VEI of 2 or greater. Smaller eruptions and effusive eruptions are more frequent. Yet, our record of VEI 2 eruptions is still probably only close to complete for about a century (with gaps during time periods of global disruption such as the world wars). Further, not all volcanoes are the same—some have open vents in which a persistently open path exists to the surface, and already-erupting systems do seem to be more sensitive to earthquakes than initiating new eruptions (Manga et al. 2009). Villarica, Chile, is one example, and it makes up 3 of the 11 triggered eruptions listed in Manga and Brodsky (2006).

12.4 Mechanisms

The mechanisms that trigger magmatic eruptions are likely to be more difficult to identify than the mechanisms that account for hydrological responses. This is because there are a greater number and complexity of processes that operate within magma reservoirs and that influence the ascent of magma. Here we review some of the mechanisms that have been proposed as triggers for both mud and magmatic volcanoes.

12.4.1 *Static or Dynamic Stresses?*

A central theme in studies of triggered eruptions is whether the triggering is controlled by static or dynamic stress changes. Manga and Brodsky (2006) argue that the static stress changes caused by earthquakes are in general too small to initiate eruption through any mechanism, and favor processes that are able to turn larger amplitude dynamic strains into some type of permanent or semi-permanent change. Bonini et al. (2016) analyzed the static stress changes on the feeder dikes beneath mud volcanoes from 9 settings on Earth. They identified a few settings where mud volcanoes erupted yet the static stress changes would have promoted clamping of dikes, thus favoring dynamic stresses for triggering the eruptions. In Azerbaijan, however, eruptions within a year of regional earthquakes are favored where dikes were unclamped—favoring a dominant role of static stress changes (Bonini et al. 2016). The strong tidal modulation of seismicity at Axial Volcano on the Juan de Fuca mid-ocean ridge provides important insights into the coupling of deformation and magma bodies. Scholz et al. (2019) show that magma bodies inflate and deflate in response to ocean tides, producing Coulomb stress changes larger than and opposite those from the tides themselves, thus controlling the seismicity. Scholz et al. (2019) further show that in this always seismically-active system, there is no stress triggering threshold.

The sequence of nine $M > 5$ events in central Italy from 2016–2017 triggered the eruption of 17 mud volcanoes and provides an excellent opportunity to assess the

roles of static and dynamic stresses. Maestrelli et al. (2017) found a correlation with the amplitude of dynamic stresses whereas static stress changes were negligible or would have clamped feeder dykes. At least in this setting, dynamic stresses appear to dominate.

In support of an important role of static stress changes, Bonali et al. (2013) find a correlation between earthquakes that unclamp feeder dikes and whether an eruption follows an earthquake for a number of volcanoes in Chile. Fault geometry near the volcano thus matters, and for some already-active volcanoes, activity may be suppressed (Farias and Basualto 2020). These effects may be important to distances as great as 600 km from the epicenter of M8+ earthquakes (Bonali et al. 2015; Farias and Basualto 2020). Lupi and Miller (2014) argued that a reduction of compressive stresses after megathrust earthquakes may lead to pulses of volcanism. Walter and Amelung (2007) also document a systematic pattern of coseismic volumetric expansion at triggered volcanoes. It is not intuitive that the pressure decrease in magma bodies that would accompany volumetric expansion would promote eruption: eruption should require an overpressure to force magma out of the chamber, or to create new dikes.

Mud volcanoes are most numerous on the sea floor in the accretionary prisms above the subduction interfaces that produce the largest earthquakes on Earth. In these settings the stress changes from megathrust ruptures can produce very large stress changes, as large as 2–10 MPa close to the epicenter, and may increase the permeability of fault-controlled pathways supplying fluids and solids to the mud volcanoes (Bonini 2019). Figure 12.5a shows unclamping stresses from the 2004 M7.2 and M7.4 earthquakes in the Nankai trough, Japan. The mud volcano labelled MV#5 enhanced its methane release for several years after the earthquakes (Tsunogai et al. 2012). Large earthquakes may thus control the location and timing of fluid, gas and mud discharge in the accretionary wedge (Fig. 12.5b). Instrumenting discharge features may thus provide insights into the permeability evolution of conduits and the controls on fluid transport in these submarine seepage systems.

12.4.2 Mechanisms for Initiating Eruptions

Magmatic and mud volcanoes share in common that gases play a role in providing buoyancy, they erupt materials that are liquefied or fluidized, and the source is usually over-pressured. Mechanisms through which dynamic strains influence the nucleation or growth of bubbles, or liquefy sediment or crystal mushes, are in principle possible in both systems.

12.4.2.1 Mechanisms Involving Bubbles

Given the importance of bubbles in driving magma to the surface and powering volcanic eruptions, several triggering mechanisms have been proposed that invoke

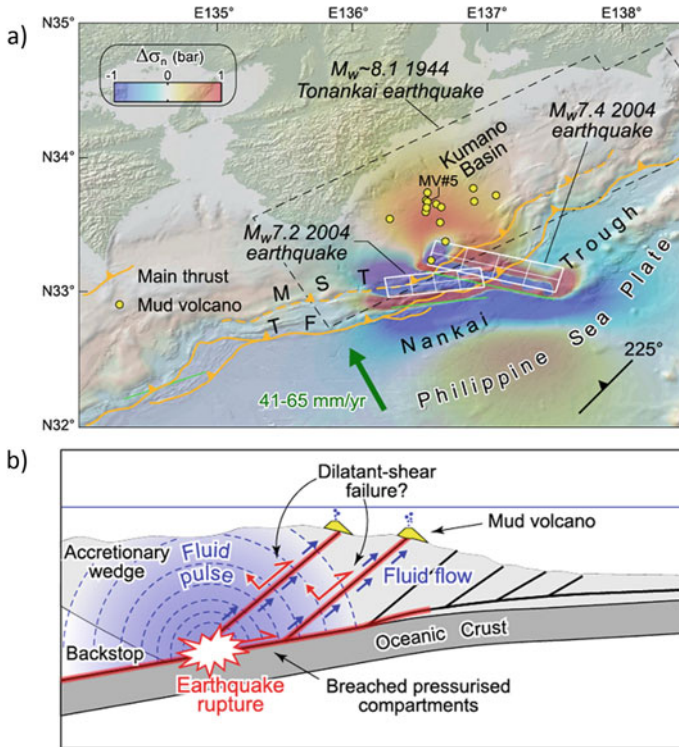


Fig. 12.5 **a** Unclamping stresses (changes in normal stress) on faults parallel to the subduction zone and at a depth of 7.5 km (colors). White rectangles outline the surfaces that slipped in 2004. Yellow circles show mud volcanoes and MV#5 responded to the earthquakes. **b** Schematic illustration processes that would enable fluids released from the subducted crust to move along faults and feed submarine mud volcanoes (adapted from in Bonini 2019)

bubbles. One possibility is the nucleation of new bubbles in a supersaturated liquid by the periodic changes in pressure generated by seismic waves (e.g., Manga and Brodsky 2006; Crews and Cooper 2014). A second possibility, is that diffusion of gas from a supersaturated liquid into preexisting bubbles is enhanced by dynamic strains. When bubbles experience oscillatory strain, there is an asymmetric diffusion of gas into and away from the bubble owing to the change in shape – this process is called rectified diffusion (e.g., Sturtevant et al. 1996). Ichihara and Brodsky (2006) have shown that this process results in insignificant growth of bubbles. A third possibility, is that pore pressures rise as bubbles carry high pressures to shallower depths as they rise (e.g., Steinberg et al. 1989; Sahagian and Proussevitch 1992; Linde et al. 1994), a process called advective overpressure. This mechanism requires that both the bubbles and surrounding matrix/liquid are incompressible, and several studies have shown that these assumptions are not satisfied (Bagdassarov 1994; Pyle and Pyle 1995). A fourth possibility is that gas hydrates dissociate. Submarine mud volcanoes are often associated with gas hydrates (Milkov 2004) and enhanced methane emission has

been attributed to earthquakes in both lakes (Rensbergen et al. 2002) and the ocean (Mau et al. 2007). However, triggered eruptions that have been identified so far are subaerial (this is very likely an observational bias), where gas hydrates should not exist. A final process is the mobilization of trapped bubbles by oscillating pressure gradients. Changing pressure gradients can dislodge bubbles trapped in pores (e.g., Beresnev et al. 2005; Deng and Cardenas 2013), increasing permeability and the ability of fluids to erupt. This process has been used to explain the triggered eruption of mud volcanoes (e.g., Rudolph and Manga 2012). At larger scales, sloshing of bubbly magma may cause magmatic foams to collapse, releasing gas and initiating eruptions (Namiki et al. 2016).

One intriguing possibility is that the volume expansion of a magma chamber can lead to a net increase in its overpressure owing to the growth of bubbles. Recall that Walter and Amelung (2007) found that triggered magmatic eruptions can occur in regions that experience volumetric expansion. Nishimura (2004) showed that the growth of bubbles that accompanies magma chamber expansion causes a decrease in the pressure difference between that inside and outside bubbles, and the surface tension energy liberated results in a net pressure increase in the magma. This effect is very small, except for very small bubbles (smaller than a few microns). Carr et al. (2018) suggested that the addition of CO₂ to a magma reservoir, mobilized for example by an earthquake, can lead to water exsolution and help create the overpressure needed to change eruption rates over the time scales and magnitudes seen at Merapi, Indonesia.

12.4.2.2 Liquefaction

As mud volcanoes erupt liquefied or fluidized sediment, mechanisms that invoke liquefaction by dynamic strain seem reasonable. However, liquefaction is generally viewed as a shallow phenomenon because overburden stresses at greater depths requires that pore pressure changes become unrealistically large (e.g., Youd et al. 2004; Chap. 11). This should not be a limitation in the settings where mud volcanism occurs as the erupted materials initially had high pore pressures, and only modest increases in pore pressure may be necessary even if the overburden stresses are high. Liquefaction by dynamic strain has been invoked to explain mud eruptions (e.g. Lupi et al. 2013).

Liquefaction or weakening of magmatic suspensions has also been invoked to explain the seismic triggering of magmatic volcanoes (Hill et al. 2002; Sumita and Manga 2008). A reduction in strength would be manifest as a decrease in seismic velocity. Battaglia et al. (2012) documented a reduction in seismic velocity beneath Yasur volcano, Vanuatu, followed by a partial recovery, following a M7.3 earthquake 80 km from the volcano summit; in this instance, however, no eruption occurred.

12.4.2.3 Breaching Reservoirs

Water level changes in wells, as discussed in Chap. 8, can be explained in many instances by changes in permeability or the breaching of hydrological barriers that allow fluids and pore pressure to be redistributed. This is a viable mechanism to fluidize or liquefy unconsolidated sediments if there are reservoirs below the source layer with high enough pore pressure (e.g., Wang 2007; Cox et al. 2021). In some settings, the gases and fluids that erupt at mud volcanoes may be sourced much deeper than the erupted mud (e.g., Cooper 2001; Mazzini et al. 2009; Shirzaei et al. 2015), supporting the idea that fluid and gas migration play a role in initiating eruptions. This process may lead to, however, a time lag in the manifestation of the triggered eruption governed by the time scale for fluids and/or gas to migrate (e.g., Husen and Kissling 2001). Stress transfer following regional tectonic earthquakes can lead to accelerated seismic energy release, as documented at Tungurahua, Ecuador and Popocateptl, Mexico volcanoes, and enhanced seismic energy release may be documenting the beginning of the material failure that leads to eruption (De la Cruz-Reyna et al. 2010).

12.5 The Sidoarjo (Lusi) Mud Flow

On the morning of 29 May 2006, mud began erupting in the Porong subdistrict, Sidoarjo in East Java, Indonesia. The eruption continues to present. The eruption rate was and remains large, about 100,000–200,000 m³/day during the first few years, and about 80,000 m³/day in recent years (Miller and Mazzini 2018). The duration and erupted volume are unprecedented for a mud eruption on land. Several studies have attempted to forecast its expected longevity and all expect the eruption to continue for many more years (e.g., Davies et al. 2011; Rudolph et al. 2011, 2013). The eruption has led to a disaster with extensive human and environmental impacts. Villages were buried and more than 40,000 people were displaced; environmental pollution and poor conditions for those relocated create chronic health problems (Drake 2016; Fig. 12.6).

From the very beginning, the reason the mud erupted was the source of scientific controversy connected to the theme of this book. Early reports in the news, and then in the scientific literature (e.g., Mazzini et al. 2007; Sawolo et al. 2009), argued that the eruption was triggered by the M6.3 Yogyakarta earthquake 254 km away. Manga (2007), in contrast, used a compilation of previous examples of triggered mud eruptions to argue that the earthquake was too far away to trigger a new eruption and, moreover, that there were earthquakes that caused stronger ground motion or were even larger and closer and none of these earthquakes triggered an eruption. Tingay et al. (2008) showed that static stress changes were vanishingly small and Davies et al. (2008) showed that dozens of earthquakes caused stronger ground motions without causing eruptions. Rather than an earthquake-trigger, others proposed that ongoing drilling of the Banjarpanji-1 gas exploration well by PT Lapindo Brantas, about 100 m away from the vent where mud first erupted, initiated the eruption as a

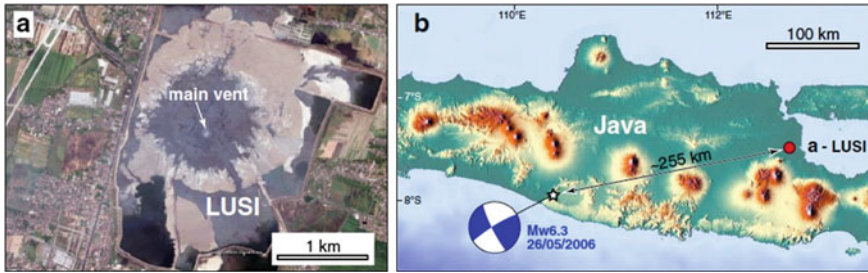


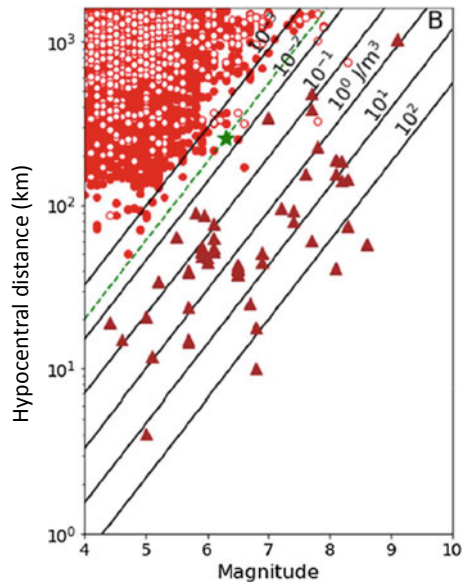
Fig. 12.6 **a** Satellite image of the Sidoarjo (Lusi) mud eruption from August 2012 (extracted from Google Earth) that began eruption on 29 May 2006. The eruption continues to present. **b** Location of the vent (red circle) and the location and focal mechanism of the M6.3 Yogyakarta earthquake on 26 May 2006 (from Bonini et al. 2016)

subsurface blowout (Davies et al. 2007, 2008; Tingay et al. 2008). These early studies initiated several more detailed analyses arguing for an earthquake trigger (e.g. Istadi et al. 2009; Lupi et al. 2013), against an earthquake trigger (Rudolph et al. 2015), or a drilling trigger (Tingay et al. 2015). A vigorous debate ensued in the scientific literature, including comments and replies (Davies et al. 2010; Sawolo et al. 2010). The debate continues to present, including two reviews (Miller and Mazzini 2018; Tingay et al. 2018).

For full disclosure, both authors of this book have written papers arguing why the earthquake did not cause the eruption and why drilling operations did. In brief, the strongest argument against an earthquake trigger is that there were other earthquakes that caused stronger ground motion but no eruption (Fig. 12.7). There is nothing special about the Yogyakarta earthquake. While it was a strike-slip event, and directivity effects can amplify ground motions and promote triggering (e.g., the Gwadar mud eruption in 2013 off the Makran coast responding to the M7.8 Balochistan earthquake with epicenter 383 km away), the orientation of the fault that slipped would not have enabled enhanced ground motion at the eruption site. The most compelling argument for a drilling trigger is the set of daily drilling reports themselves. Pressure data in the well record the birth of the eruption. Attempts to kill the eruption by pumping fluids into the well altered the eruption, providing evidence for a physical connection. The daily drilling reports are published in Tingay et al. (2018) and are annotated to help translate technical terms and to identify evidence and clarify what are interpretations and what are data.

In the scientific literature, the eruption is often called “Lusi”, a contraction for “Lumpur Sidoarjo” with “lumpur” the Indonesian word for mud. Locals call it the “Lapindo” mudflow after the drilling company (Drake 2020). The name for the eruption itself is controversial because of the connotations and social context. There is a political dimension to the eruption connected to providing compensation to victims. Regardless of the trigger, the eruption clearly has devastated environments and communities and recovery will be very slow (Drake 2016).

Fig. 12.7 A comparison of the Sidoarjo (Lusi) mud eruption and Yogyakarta earthquake (green star) with other examples of triggered mud volcanoes shown with filled triangles (the same set shown in Fig. 12.3). Also shown with circles are all the earthquakes that occurred between 1976 and the eruption initiation (28 May 2006). Filled symbols are events deeper than 30 km (from Tingay et al. 2018)



12.6 Effect of Earthquakes on Already-Erupting Mud Volcanoes

Given the strong sensitivity of geysers—also already-erupting systems—to earthquakes, we might reasonably expect already-erupting mud volcanoes to be more sensitive to earthquakes than the triggering of new eruptions. Observations of magmatic volcanoes support this contention. For example, Harris and Ripepe (2007) report changes in eruption rate at Semeru volcano, Indonesia, in response to the 2006 M6.3 Yogyakarta earthquake based on satellite thermal imaging. At Mt Merapi, Indonesia, Walter et al. (2007) report increases in extrusion rate or fumarole temperature after regional earthquakes. The open vent volcano Stromboli, Italy, also responds to earthquakes (Speranza and Carniel 2008). Satellite thermal data show that there may be global increases in volcanic unrest following the largest earthquakes, $M > 8.5$ (Delle Donne et al. 2010). A more recent analysis of 14 $M > 8$ events found that 3 led to short-lived global thermal emission increases, and 2 decreased thermal emissions (Hill-Butler et al. 2020). At persistently active (open vent) basaltic volcanoes, there is an increase in SO_2 emissions recorded by the Ozone Monitoring Instrument whereas decreases occur at andesitic volcanoes (Avouris et al. 2017).

The high level of earthquake activity in Indonesia and the longevity of the Sidoarjo eruption (Sect. 12.4) provide an opportunity to look for responses of the ongoing eruption to earthquakes. The main challenge is obtaining reliable quantitative information about the eruption. Responses to large distant and moderate regional earthquakes have been reported, though without data (Miller and Mazzini 2018). Figure 12.8 shows published eruptions rates and the magnitude of ground motion from earthquakes,

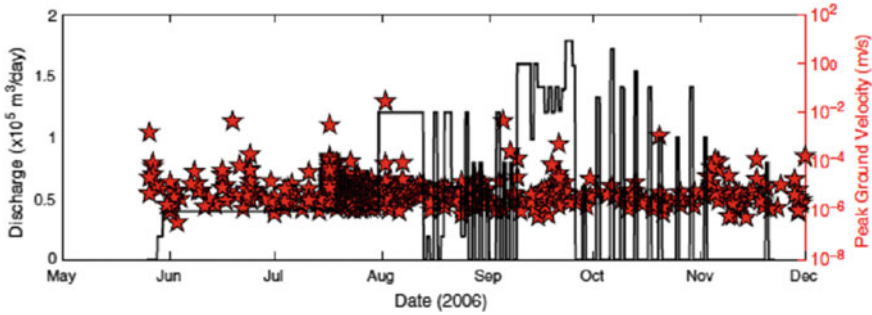


Fig. 12.8 Eruption rate at the Sidoarjo (Lusi) mud eruption. Black curve is discharge from Mazzini et al. (2007). Red stars are computed ground motion for earthquakes in the USGS catalog using the attenuation relationship for east Java in Davies et al. (2008). Data provided by A. Mazzini (from Bonini et al. 2016)

computed from source mechanisms and using a local attenuation model (Davies et al. 2008). Despite anecdotal reports of responses, there is no obvious signature of responses in the reported discharge.

The Salton Sea “mud volcanoes” in the Imperial Valley, California, technically gryphons and called hydrothermal features by Svensen et al. (2009), have responded multiple times to earthquakes and hence provide an opportunity to identify how frequency and amplitude of ground motion affect eruptions. Here, changes in eruptions are documented by increased gas flux and a greater number of fresh mud flows measured during discrete visits (Rudolph and Manga 2010). Using responses from 2 earthquakes and 4 no-responses, Rudolph and Manga (2012) conclude that for a given amplitude of ground motion, longer period waves are more effective at causing responses. The number of examples, however, is modest and a review of frequency-dependent triggering concluded that “the data supporting this conclusion are still extremely sparse” (Manga et al. 2012). This conclusion still holds several years later.

Menapace et al. (2017) installed pore pressure sensors near the conduit of a submarine volcano in the eastern Mediterranean Sea. They document pressure spikes after many earthquakes “but seemingly no triggered mud volcano eruptions”. They found that pressure changes are much more sensitive to earthquakes than are the eruptions of new mud volcanoes.

12.7 Concluding Remarks About Mud Volcanoes

It is important to recall that most eruptions at mud volcanoes and at magmatic volcanoes are not triggered by earthquakes. This implies that for triggered eruptions, the volcanic plumbing system must already be near failure, perhaps with stresses within less than a few percent of the failure stress (Manga et al. 2009). If we choose this

failure stress to be the tensile strength of rock, say 10 MPa, extra stresses of only 0.5 MPa are needed to overcome a 5% deficit, and can be provided by static stress changes in the near-field or dynamic stresses in the intermediate-field. Understanding the relationship between stress changes and eruptions is important for revealing which volcanoes are poised to erupt and the mechanisms that initiate eruptions (National Academies 2017).

It is clear that the number of triggered events is small, and the amount and quality of data from erupting mud volcanoes is too limited, to conclusively answer the most interesting questions about triggered eruptions: Is triggering from static or dynamic stress changes? What is the mechanism of triggering? Does earthquake sensitivity increase once the eruption begins? Key to addressing questions about triggering are more examples, accurate timing, and ideally nearly co-located eruptions and seismometers or strainmeters to characterize the ground motion. Volcanic eruptions begin in the subsurface, and seismic and deformation signals that accompany the initiation of unrest prior to the surface expression of eruption may be critical for identifying the mechanisms that lead to eruption. For already-erupting mud volcanoes, continuous gas flux, pressure and temperature measurements or continuous GPS are promising approaches that offer high temporal resolution.

References

- Aliyev AA, Guliyev IS, Belov IS (2002) Catalogue of recorded eruptions of mud volcanoes of Azerbaijan for a period of years 1810–2001. Nafta Press, Baku, Azerbaijan
- Avouris DM, Carn SA, Waite GP (2017) Triggering of volcanic degassing by large earthquakes. *Geology* 45:715–718
- Babaye G, Tibaldi A, Bonali F, Kadirov F (2014) Evaluation of earthquake-induced strain in promoting mud eruptions: the case of Shamakhi–Gobustan–Absheron areas, Azerbaijan. *Nat Hazards* 72:789–808
- Bagdassarov N (1994) Pressure and volume changes in magmatic systems due to the vertical displacement of compressible materials. *J Volcanol Geotherm Res* 63:95–100
- Battaglia J, Métaixian JP, Garaebiti E (2012) Earthquake-volcano interaction imaged by coda wave interferometry. *Geophys Res Lett* 39(11):L11309
- Bautista BC et al (1996) Relationship of regional and local structures to Mount Pinatubo activity. In: Newhall C, Punongbayan RS (eds) *Fire and mud*. Univ Washington Press, Seattle
- Beresnev IA, Vigil RD, Li W, Pennington WD, Turpening RM, Iassonov PP, Ewing RP (2005) Elastic waves push organic fluids from reservoir rock. *Geophys Res Lett* 32:L13303. <https://doi.org/10.1029/2005GL023123>
- Bonali FL, Tibaldi A, Corazzato C, Tormey DR, Lara LE (2013) Quantifying the effect of large earthquakes in promoting eruptions due to stress changes on magma pathway: the Chile case. *Tectonophysics* 583:54–67
- Bonali FL, Tibaldi A, Corazzato C (2015) Sensitivity analysis of earthquake-induced static stress changes on volcanoes: the 2010 Mw 8.8 Chile earthquake. *Geophys J Int* 201:1868–1890
- Bonini M (2009) Mud volcano eruptions and earthquakes in the Northern Apennines and Sicily, Italy. *Tectonophysics* 474:723–735
- Bonini M (2012) Mud volcanoes: indicators of stress orientation and tectonic controls. *Earth Sci Rev* 115:121–152

- Bonini M (2019) Seismic loading of fault-controlled fluid seepage systems by great subduction earthquakes. *Sci Rep* 9:1–12
- Bonini M, Rudolph ML, Manga M (2016) Long- and short-term triggering and modulation of mud volcano eruptions by earthquakes. *Tectonophysics* 672:190–211
- Carr BB, Clarke AB, Vitturi MDM (2018) Earthquake induced variations in extrusion rate: a numerical modeling approach to the 2006 eruption of Merapi Volcano (Indonesia). *Earth Planet Sci Lett* 482:377–387
- Chigira M, Tanaka K (1997) Structural features and the history of mud volcanoes in Southern Hokkaido, Northern Japan. *J Geol Soc Jpn* 103:781–791
- Cooper C (2001) Mud volcanoes of Azerbaijan visualized using 3D seismic depth cubes: the importance of overpressured fluid and gas instead of non-existent diapirs. In: Conference on Subsurface Sediment Mobilization. European Association of Geoscientists and Engineers, Ghent, Belgium
- Cox Simon C, Sjoerd van Ballegooy, Helen K. Rutter, David S. Harte, Caroline Holden, Anton K. Gulley, Virginie L, Michael M (2021) Can artesian groundwater and earthquake-induced aquifer leakage exacerbate the manifestation of liquefaction?. *Engineering Geology* 281:105982
- Crews JB, Cooper CA (2014) Experimental evidence for seismically initiated gas bubble nucleation and growth in groundwater as a mechanism for coseismic borehole water level rise and remotely triggered seismicity. *J Geophys Res Solid Earth* 119:7079–7091
- Darwin C (1840) XLII—On the connexion of certain volcanic phenomena in South America; and on the formation of mountain chains and volcanos, as the effect of the same power by which continents are elevated. *Trans Geol Soc Lond* 2:601–631
- Davies RJ, Swarbrick RE, Evans RJ, Huuse M (2007) Birth of a mud volcano: east Java, 29 May 2006. *GSA Today* 17:4–9
- Davies RJ, Brumm M, Manga M, Rubiandini R, Swarbrick R (2008) The east Java mud volcano (2006–present): an earthquake or drilling trigger? *Earth Planet Sci Lett* 272:627–638
- Davies RJ, Manga M, Tingay M, Lusianga S, Swarbrick R (2010) Discussion: Sawolo et al. (2009) the Lusi mud volcano controversy: was it caused by drilling? *Mar Pet Geol* 27:1651–1657
- Davies RJ, Mathias SA, Swarbrick R, Tingay MJ (2011) Probabilistic longevity estimate for the LUSI mud volcano, East Java. *J Geol Soc* 168:517–523
- De la Cruz-Reyna S, Tárrega M, Ortiz R, Martínez-Bringas A (2010) Tectonic earthquakes triggering volcanic seismicity and eruptions. Case studies at Tungurahua and Popocatepetl volcanoes. *J Volcanol Geotherm Res* 193:37–48
- Delisle G (2005) Mud volcanoes of Pakistan: an overview. In: Martinelli P (eds) *Mud volcanoes, geodynamics and seismicity*, pp 159–169
- Delle Donne D, Harris AJ, Ripepe M, Wright R (2010) Earthquake-induced thermal anomalies at active volcanoes. *Geology* 38:771–774
- Deng W, Cardenas MB (2013) Dynamics and dislodgment from pore constrictions of a trapped nonwetting droplet stimulated by seismic waves. *Water Resour Res* 49:4206–4218
- Drake P (2016) *Indonesia and the politics of disaster: power and representation in Indonesia's mud volcano*. Routledge
- Drake P (2020) Comment to “More than ten years of Lusi: a review of facts, coincidences, and past and future studies” by Miller and Mazzini (2018): taking the trigger debate above ground. *Mar Pet Geol* 113:104079
- Etiopé G (2015) Natural gas seepage. The Earth's hydrocarbon degassing. Springer. <https://doi.org/10.1007/978-3-319-14601-0>
- Etiopé G, Milkov AV (2004) A new estimate of global methane flux from onshore and shallow submarine mud volcanoes to the atmosphere. *Environ Geol* 46(8):997–1002
- Fariás C, Basualto D (2020) Reactivating and Calming Volcanoes: The 2015 MW 8.3 Illapel Megathrust Strike. *Geophysical Research Letters* 47(16): e2020GL087738.
- Feuillet N, Beauducel F, Tapponnier P (2011) Tectonic context of moderate to large historical earthquakes in the Lesser Antilles and mechanical coupling with volcanoes. *J Geophys Res Solid Earth* 116:B10308. <https://doi.org/10.1029/2001JB008443>

- Fryer P (2012) Serpentinite mud volcanism: observations, processes, and implications. *Annu Rev Mar Sci* 4:345–373
- Harris AJL, Ripepe M (2007) Regional earthquake as a trigger for enhanced volcanic activity: evidence from MODIS thermal data. *Geophys Res Lett* 34:L02304
- Hill DP, Pollitz F, Newhall C (2002) Earthquake-volcano interactions. *Phys Today* 55:41–47
- Hill-Butler C, Blackett M, Wright R, Trodd N (2020) The co-occurrence of earthquakes and volcanoes: assessing global volcanic radiant flux responses to earthquakes in the 21st century. *J Volcanol Geotherm Res.* <https://doi.org/10.1016/j.jvolgeores.2020.10.6770>
- Husen S, Kissling E (2001) Postseismic fluid flow after the large subduction earthquake of Antofagasta, Chile. *Geology* 29:847–850
- Ichihara M, Brodsky EE (2006) A limit on the effect of rectified diffusion in volcanic systems. *Geophys Res Lett* 33:L02316
- Istadi BP, Pramono GH, Sumtadireja P, Alam S (2009) Modeling study of growth and potential geohazard for LUSI mud volcano: East Java, Indonesia. *Mar Pet Geol* 26:1724–1739
- Kopf AJ (2002) Significance of mud volcanism. *Rev Geophys* 40:1005. <https://doi.org/10.1029/2000RG000093>
- Lara LE, Moreno R, Valdivia V et al (2020) The AD1835 eruption at Robinson Crusoe Island discredited: Geological and historical evidence. *Prog Phys Geogr: Earth Environ:* <https://doi.org/10.1177/0309133320937998>
- Lemarchand N, Grasso JR (2007) Interactions between earthquakes and volcano activity. *Geophys Res Lett* 34:L24303
- Linde AT, Sacks S (1978) Triggering of volcanic eruptions. *Nature* 395: 888-890
- Linde AT, Sacks IS (1998) Triggering of volcanic eruptions. *Nature* 395(6705): 888-890
- Linde AT, Sacks IS, Johnston MSJ, Hill DP, Bilham RG (1994) Increased pressure from rising bubbles as a mechanism for remotely triggered seismicity. *Nature* 371:408–410
- Lupi M, Saenger EH, Fuchs F, Miller SA (2013) Lusi mud eruption triggered by geometric focusing of seismic waves. *Nat Geosci* 6:642–646
- Lupi M, Miller SA (2014) Short-lived tectonic switch mechanism for long-term pulses of volcanic activity after mega-thrust earthquakes. *Solid Earth* 5:13–24
- Maestrelli D, Bonini M, Delle Donne D, Manga M, Piccardi L, Sani F (2017) Dynamic triggering of mud volcano eruptions during the 2016–2017 Central Italy seismic sequence. *J Geophys Res: Solid Earth* 122:9149–9165
- Manga M (2007) Did an earthquake trigger the May 2006 eruption of the Lusi mud volcano? *EOS* 88:201
- Manga M, Brodsky EE (2006) Seismic triggering of eruptions in the far field: volcanoes and geysers. *Annu Rev Earth Planet Sci* 34:263–291
- Manga M, Brumm M, Rudolph ML (2009) Earthquake triggering of mud volcanoes. *Mar Pet Geol* 26:1785–1798. <https://doi.org/10.1016/j.marpetgeo.2009.01.019>
- Manga M, Bonini M (2012) Large historical eruptions at subaerial mud volcanoes, Italy. *Nat Hazards Earth Syst Sci* 12:3377–3386
- Manga M, Beresnev I, Brodsky EE, Elkhoury JE, Elsworth D, Ingebritsen SE, May DC, Wang C-Y (2012) Changes in permeability caused by transient stresses: field observations, experiments, and mechanisms. *Rev Geophys* 50:RG2004
- Marzocchi W (2002) Remote seismic influence on large explosive eruptions. *J Geophys Res* 107:2018
- Mau S, Rehder G, Arroyo IG, Gossler J, Suess E (2007) Indications of a link between seismotectonics and CH₄ release from seeps off Costa Rica. *Geochem Geophys Geosys* 8:Q04003
- Mazzini A, Etiope G (2017) Mud volcanism: an updated review. *Earth Sci Rev* 168:81–112
- Mazzini A, Svensen H, Akhmanov G, Aloisi G, Planke S, Malthe-Sorensen A, Istadi B (2007) Triggering and dynamic evolution of Lusi mud volcano, Indonesia. *Earth Planet Sci Lett* 261:375–388

- Mazzini A, Neramoen A, Krotkiewski M, Podladchikov Y, Planke S, Svensen H (2009) Strike-slip faulting as a trigger mechanism for overpressure release through piercement structures. Implications for the Lusi mud volcano, Indonesia. *Mar Pet Geol* 26:1751–1765
- Mellors R, Kilb D, Aliyev A, Gasanov A, Yetirmishli G (2007) Correlations between earthquakes and large mud volcano eruptions. *J Geophys Res* 112:B04304
- Menapace W, Völker D, Sahling H, Zoellner C, dos Santos Ferreira C, Bohrmann G, Kopf A (2017) Long-term in situ observations at the Athina mud volcano, Eastern Mediterranean: taking the pulse of mud volcanism. *Tectonophysics* 721:12–27
- Milkov A (2000) Worldwide distribution of submarine mud volcanoes and associated gas hydrates. *Mar Geol* 167:29–42
- Milkov AV (2004) Global estimates of hydrate-bound gas in marine sediments: how much is really out there? *Earth-Sci Rev* 66:183–197
- Miller SA, Mazzini A (2018) More than ten years of Lusi: a review of facts, coincidences, and past and future studies. *Mar Pet Geol* 90:10–25
- Nakamura K (1975) Volcano structure and possible mechanical correlation between volcanic eruptions and earthquakes. *Bull Volcanol Soc Jpn* 20:229–240
- Namiki A, Rivalta E, Woith H, Walter TR (2016) Sloshing of a bubbly magma reservoir as a mechanism of triggered eruptions. *J Volcanol Geotherm Res* 320:156–171
- National Academies of Sciences, Engineering, and Medicine (2017) Volcanic eruptions and their repose, unrest, precursors, and timing. National Academies Press
- Newhall CG, Self S (1982) The volcanic explosivity index (VEI): an estimate of explosive magnitude for historical volcanism. *J Geophys Res* 87:1231–1238
- Nishimura T (2004) Pressure recovery in magma due to bubble growth. *Geophys Res Lett* 31:L12613. <https://doi.org/10.1029/2004GL019810>
- Nishimura T (2017) Triggering of volcanic eruptions by large earthquakes. *Geophys Res Lett* 44:7750–7756
- Pyle DM, Pyle DL (1995) Bubble migration and the initiation of volcanic eruptions. *J Volcanol Geotherm Res* 67:227–232
- Rensbergen PV, Batist MD, Klerkx J, Hus R, Poort J, Vanneste M, Granin N, Khlystov O, Krinitsky P (2002) Sublacustrine mud volcanoes and methane seeps caused by dissociation of gas hydrates in Lake Baikal. *Geology* 30:631–634
- Rudolph ML, Manga M (2010) Mud volcano response to the 4 April 2010 El Mayor-Cucapah earthquake. *J Geophys Res Solid Earth* 115:B12211. <https://doi.org/10.1029/2010JB007737>
- Rudolph ML, Karlstrom L, Manga M (2011) A prediction of the longevity of the Lusi mud eruption, Indonesia. *Earth Planet Sci Lett* 308:124–130
- Rudolph ML, Manga M (2012) Frequency dependence of mud volcano response to earthquakes. *Geophys Res Lett* 39:L14303. <https://doi.org/10.1029/2012GL052383>
- Rudolph ML, Shirzaei M, Manga M, Fukushima Y (2013) Evolution and future of the Lusi mud eruption inferred from ground deformation. *Geophys Res Lett* 40:1089–1092
- Rudolph ML, Manga M, Tingay M, Davies RJ (2015) Influence of seismicity on the Lusi mud eruption. *Geophys Res Lett* 42:7436–7443
- Rukavickova L, Hanzl P (2008) Mud volcanoes in the Khar Argalantyn Nuruu, NW Gobi Altay, Mongolia as manifestation of recent seismic activity. *J Geosci* 53:181–191
- Sahagian DL, Proussevitch AA (1992) Bubbles in volcanic systems. *Nature* 359(6395):485
- Sawi TM, Manga M (2018) Revisiting short-term earthquake triggered volcanism. *Bull Volcanol* 80:57. <https://doi.org/10.1007/s00445-018-1232-2>
- Sawolo N, Sutriano E, Istadi BP, Darmoyo AB (2009) The LUSI mud volcano triggering controversy: was it caused by drilling? *Mar Pet Geol* 26:1766–1784
- Sawolo N, Sutriano E, Istadi BP, Darmoyo AB (2010) Was LUSI caused by drilling?—Authors reply to discussion. *Mar Pet Geol* 27:1658–1675
- Scholz CH, Tan YJ, Albino F (2019) The mechanism of tidal triggering of earthquakes at midocean ridges. *Nat Commun* 10:2526

- Shirzaei M, Rudolph ML, Manga M (2015) Deep and shallow sources for the Lusi mud eruption revealed by surface deformation. *Geophys Res Lett* 42:5274–5281
- Siebert L, Simkin T (2002) *Volcanoes of the world: an illustrated catalog of holocene volcanoes and their eruptions*, Smithsonian Inst. Global Volcanism Digital Information Series, GVP-3. <http://www.volcano.si.edu/world>
- Snead RE (1964) Active mud volcanoes of Baluchistan, west Pakistan. *Geogr Rev* 54(4):546–560
- Speranza FF, Carniel R (2008) Structural changes of volcanic tremor at Stromboli volcano. *J Volcanol Geotherm Res* 171:103–117
- Steinberg GS, Steinberg AS, Merganov AG (1989) Fluid mechanism, of pressure growth in volcanic (magmatic) systems and seismic regime of the volcano prior to eruption. *Mod Geol* 13:267–274
- Sturtevant B, Kanamori H, Brodsky EE (1996) Seismic triggering by rectified diffusion in geothermal systems. *J Geophys Res* 101:25269–25282
- Sumita I, Manga M (2008) Suspension rheology under oscillatory shear and its geophysical implications. *Earth Planet Sci Lett* 269:467–476
- Svensen H, Hammer Ø, Mazzini A, Onderdonk N, Polteau S, Planke S, Podladchikov YY (2009) Dynamics of hydrothermal seeps from the Salton Sea geothermal system (California, USA) constrained by temperature monitoring and time series analysis. *J Geophys Res Solid Earth* 114:B09201. <https://doi.org/10.1029/2008JB006247>
- Tingay M, Heidbach O, Davies R, Swarbrick R (2008) Triggering of the Lusi mud eruption: earthquake versus drilling initiation. *Geology* 36:639–642
- Tingay MRP, Rudolph ML, Manga M, Davies RJ, Wang C-Y (2015) Initiation of the Lusi mudflow disaster. *Nat Geosci* 8:493
- Tingay M, Manga M, Rudolph ML, Davies R (2018) An alternative review of facts, coincidences and past and future studies of the Lusi eruption. *Mar Pet Geol* 95:345–361
- Tsunogai U, Maegawa K, Sato S et al (2012) Coseismic massive methane release from a submarine mud volcano. *Earth Planet Sci Lett* 341:79–85
- Walter TR, Amelung F (2007) Volcanic eruptions following $M \geq 9$ megathrust earthquakes: implications for the Sumatra-Andaman volcanoes. *Geology* 35:539–542
- Walter TR, Wang R, Zimmer M, Grosser H, Lühr B, Ratdomopurbo A (2007) Volcanic activity influenced by tectonic earthquakes: static and dynamic stress triggering at Mt. Merapi. *Geophys Res Lett* 34:L05304. <https://doi.org/10.1029/2006GL028710>
- Wang C-Y (2007) Liquefaction beyond the near field. *Seismol Res Lett* 78:512–517
- Wang C-Y, Manga M (2010) Hydrologic responses to earthquakes and a general metric. *Geofluids* 10(1–2):206–216
- Watt SFL, Pyle DM, Mather TA (2009) The influence of great earthquakes on volcanic eruption rate along the Chilean subduction zone. *Earth Planet Sci Lett* 277:399–407
- Yokoyama I (1971) Volcanic eruptions triggered by tectonic earthquakes. *Bull Geophys Inst Hokkaido Univ* 25:129–139
- Youd TL, Steidl JH, Nigbor RL (2004) Lessons learned and need for instrumented liquefaction sites. *Soil Dyn Earthq Eng* 24:639–646

Open Access This chapter is licensed under the terms of the Creative Commons Attribution 4.0 International License (<http://creativecommons.org/licenses/by/4.0/>), which permits use, sharing, adaptation, distribution and reproduction in any medium or format, as long as you give appropriate credit to the original author(s) and the source, provide a link to the Creative Commons license and indicate if changes were made.

The images or other third party material in this chapter are included in the chapter's Creative Commons license, unless indicated otherwise in a credit line to the material. If material is not included in the chapter's Creative Commons license and your intended use is not permitted by statutory regulation or exceeds the permitted use, you will need to obtain permission directly from the copyright holder.



Chapter 13

Hydrologic Precursors



Abstract Predicting earthquakes is a long-desired goal. The main challenge is to identify precursory signals that reliably predict the impending earthquake. Since hydrological and hydrogeochemical properties and processes can be very sensitive to minute strains, the hope is that measurements from hydrological systems might record precursory rock deformation that would otherwise be undetectable. Of the many hundreds of studies, we review a subset to illustrate how signals can be challenging to interpret and highlight questions raised by observations—examples come from China, Japan, Taiwan, India, the USA, Russia, France, Italy and Iceland. All are retrospective studies. Some signals seem to have no other explanation than being precursory, however, rarely is enough data available to undertake a thorough analysis. Some hydrological precursors might be recording deformation events that are slower than traditional earthquakes (and hence usually harder to detect). Long times series of data are critical for both identifying putative precursors and assessing their origin and reliability.

13.1 Introduction

Earthquake prediction is an enduring goal. The key challenge is to recognize precursory signals that would foretell the occurrence of earthquakes and hence allow a warning to be issued. For this reason, the search for precursors to earthquakes has a long history. Despite early optimism (Scholtz et al. 1973), we are not yet able to predict earthquakes—a successful prediction being defined here as some combination of time, location and magnitude within some stated and useful limits.

There are, however, mechanical reasons for anticipating precursors. Laboratory studies of rock deformation show that beyond the elastic limit, shearing of consolidated rock creates microcracks that open and hence increase the rock volume (e.g., Brace et al. 1966). At still higher deviatoric stresses, microcracks merge and localize to form a shear zone, leading to eventual large-scale rupture (e.g., Lockner and Beeler 2002). There are several ways in which the mechanical changes leading up to rupture can be manifest in hydrological measurements. First, the increase in surface

area produced by microcracks can release gases trapped in pores (e.g., radon) or change the ionic concentration and hence electrical conductivity of groundwater. Such possible changes provide the motivation for seeking and interpreting changes in gas concentration, hydrogeochemistry, or electrical conductivity. Second, microcracks can change hydrogeologic properties such as permeability as well as pore pressure. Such changes, in turn, can cause a redistribution of fluids and fluid pressure and hence may be detected from changes in water level in wells or changes in spring and stream discharge.

As reviewed in previous chapters, hydrogeologic systems can greatly magnify minute tectonic and seismic strains, as recorded by changes in pore pressure and water level in wells. For example, the change in pore pressure p under undrained conditions is given by (see also Eq. 3.25)

$$p = -K_u B \varepsilon_{kk} \quad (13.1)$$

where K_u is the undrained bulk modulus and B is Skempton's coefficient. A volumetric strain ε_{kk} as small as 10^{-8} can be expected to produce (detectable) water changes of 2 cm for reasonable choices of $B = 1$ and $K_u = 20$ GPa (Wang 2000). It is in part because of the potential sensitivity of hydrogeological systems that much of the search for precursors has focused on hydrological measurements. In addition, hydrological measurements can be made with relative ease (compared with electromagnetic and seismic surveys) and can be recorded continuously.

The hydrogeochemical basis for searching for precursors is similar. The gas composition of springs, for example, can respond to (small) tidal strains (e.g., Sugisaki 1981), hence any preseismic strain might be amplified in hydrogeochemical changes. Radon concentration changes are among the most commonly reported and discussed hydrogeochemical precursors (e.g., King 1980; Wakita et al. 1988; Virk and Singh 1993; Richon et al. 2003; Oh and Kim 2015; Fu et al. 2017; Papachristodoulou et al. 2020) and geochemical recorder of small strains (e.g., Trique et al. 1999; Kawabata et al. 2020)—this is not unreasonable given that radon accumulates over time in micropores, and can be released by small structural changes in rocks and pore connectivity. Small strains may also permit mixing between reservoirs by breaching barriers, or may expose fresh mineral surfaces which in turn permit water–rock interaction (e.g., Thomas 1988). In a manner similar to hydrological recovery after co-seismic hydrological changes (stream flow, water level in wells), water geochemistry also exhibits a postseismic recovery if disturbed by the earthquake (e.g., Claesson et al. 2007).

The elastic properties of rocks, and hence the velocities of seismic waves, are highly sensitive to the opening and closing of microcracks and to the changes in their degree of saturation (e.g., O'Connell and Budiansky 1974). Laboratory measurements confirm that precursory changes in wave speed occur for the full spectrum of fault failure, from slow events to normal earthquakes (Scuderi et al. 2016). Seismologists have carried out various experiments to test the microcrack hypothesis and produced a series of controversial results over the past 50 years. The first published

works of such tests were carried out by Kondratenko and Nersesov (1962) for earthquakes in the Tadjikistan region and by Semenov (1969) for earthquakes near Garm, both in the former Soviet Union. These reports were initially met with skepticism by seismologists in Japan and the United States (Bolt and Wang 1975). Nevertheless, the work was sufficiently suggestive to motivate other seismologists to set out independent experiments to examine the claims. The first U.S. experiments along these lines, using quite small earthquakes in the Adirondacks in New York, also detected reductions in the V_p/V_s ratio in three cases (Aggarwal et al. 1973). After the 1971 San Fernando earthquake (magnitude 6.5), Whitcomb et al. (1973) concluded that there had been a precursory decrease in the V_p/V_s ratio lasting about 30 months and a subsequent return to normal, which was followed quickly by the earthquake. On the other hand, McEvelly and Johnson (1974) used travel times between quarry blasts in central California along the San Andreas fault, with known position and origin time, and the University of California seismic network; their study indicated that the recorded fluctuations in travel times for the years 1961–1973 could be accounted for simply by reading errors and changes of shot location in the quarry. They concluded that there were no detectable premonitory travel-time changes prior to 17 earthquakes in the region with magnitudes between 4.5 and 5.4. Later work in the region (Robinson et al. 1974) showed, however, that positive P residuals were detectable before the 1972 M5.1 Bear Valley earthquake (magnitude 5.1). Wang (1974) interpreted these conflicting observations in terms of laboratory evidence that seismic velocities in stressed rocks are significantly affected by the relative orientation between seismic waves and microcracks; thus the conflicting observations in different field experiments may be partly explained by different relationships between the seismic ray path and the free surface in the source region, which controls the direction of stress-induced crustal microcracks. Niu et al. (2008) conducted an active source cross-well experiment at the San Andreas Fault Observatory at Depth (SAFOD) drill site and studied the shear wave travel time along a fixed pathway for three small earthquakes ($M \leq 3$) over a period of 2 months. They show excursions in the travel time before two of these earthquakes, but no excursion before the third. In summary, there is a physical basis for expecting precursors, precursors are seen in the lab, yet earthquake prediction outside the lab remains elusive.

13.2 What is a Precursor?

We begin by defining a “precursor” as a change in a measured quantity that occurs prior to an earthquake that does not originate from any process other than those that lead to the earthquake. Reported hydrological examples include changes in water pressure, streamflow, and water geochemistry and turbidity.

A useful precursor is one that also predicts the time, location and size of the forthcoming earthquake. To our knowledge, no paper has claimed to make these

three predictions based on reported hydrological anomalies, noting that the peer review process may be slow compared to the warning time offered by precursory signals.

13.3 Identifying Precursors

Definitive and consistent evidence for hydrological and hydrogeochemical precursors has remained elusive to the extent that there is no consensus on the significance and origin of reported precursors. Earthquake prediction is not currently operational. Difficulties include that, until recently, most reported changes were not corrected for the fluctuations in temperature, barometric pressure, earth tides, and other environmental factors, so that some changes taken to be earthquake-related may in fact be “noise” (e.g., Hartmann and Levy 2005). One common feature of reports is that changes are recorded at some sites but not at other nearby sites (e.g., Biagi et al. 2000). Moreover, instrument failures and personnel/program changes often do not allow persistent and consistent monitoring over long periods of time (King et al. 1994)—a necessary condition for obtaining reliable precursory data. Distinguishing a precursor from a response to a previous earthquake creates additional and unavoidable ambiguity.

Roeloffs (1988) lists the ideal, and arguably necessary, criteria and complementary data for establishing that some signal is in fact precursory. We reproduce (sometimes paraphrased or modified slightly) her list below and then comment of some of these criteria. As noted by Roeloffs (1988), poor documentation is the major impediment to using and interpreting water level data.

- (1) Depth of well
- (2) Rainfall over at least one year
- (3) Record of barometric pressure recorded at least once every three hours
- (4) Information about pumping and injection at wells in the vicinity
- (5) The entire observation record should be presented
- (6) Measurement technique (e.g., pressure transducer, float)
- (7) Sampling interval; this should be short enough to reliably distinguish between anomalies before and after the earthquake (Sugisaki 1978)
- (8) Response to earth tides
- (9) Co-seismic and post seismic response to the earthquake
- (10) Earthquake magnitude, azimuth, distance, depth and focal mechanism
- (11) Time, location and magnitude of any foreshocks
- (12) Raw water level data (unprocessed)
- (13) Description of other wells in the area that did not document the anomaly.

Roeloffs (1988) also points out that site geology, in particular the proximity to fault zones, and whether the aquifer is confined, are useful for interpreting any

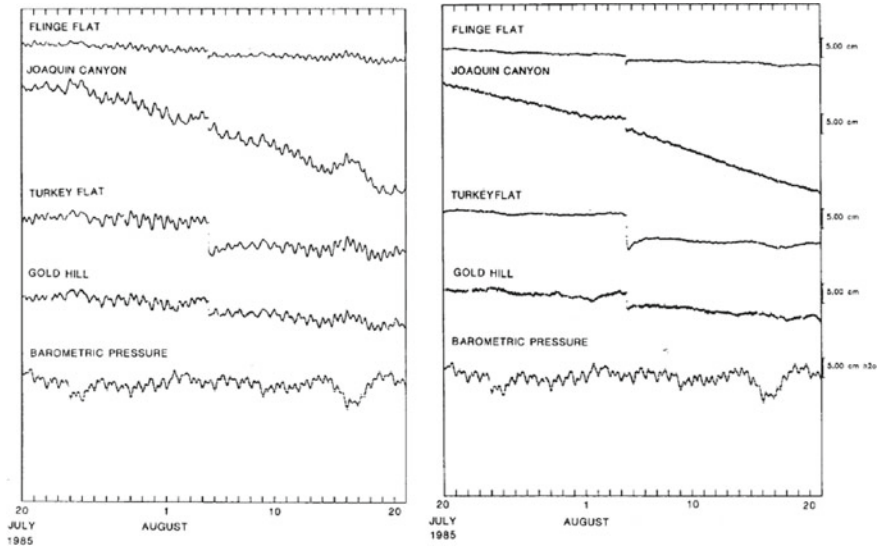


Fig. 13.1 Raw water level measurements (left) at 4 wells located near Parkfield, California. The coseismic response to the August 4 1985 M 6.1 Kettleman Hill, California earthquake can be clearly seen in the raw water level records. The earthquake was located 30–40 km from these wells. On the right is the same data with the effects of earth tides and barometric pressure removed. The coseismic response remains clear. Now, two proposed precursory signals can be seen, a gradual preseismic increase in Joaquin Canyon and Gold Hill (from Roeloffs and Quilty 1997)

signals. For gas or hydrogeochemical anomalies, multiple measurements of ions and gases are helpful in identifying the origin and reliability of the anomaly (Sugisaki and Sugiura 1985).

The importance of removing signals that arise from tides and barometric pressure variations is highlighted in Fig. 13.1 in which raw water level records are compared with records in which the effects of tides and barometric pressure changes are removed. The coseismic water level response becomes much clearer. In addition, two pre-seismic anomalous changes become apparent (discussed in more detail later).

Notwithstanding these difficulties, progress has been made in the past decade. For example, intensive and continued observations of various kinds of precursory hydrological and hydrogeochemical changes have been made in Japan during the past half century (Wakita 1996), providing a long time series of observations. Records are now routinely corrected to remove the noise introduced by fluctuations in temperature, barometric pressure, earth tides, and other factors (Igarashi and Wakita 1995). Tools are readily available to remove the effects of earth tides and barometric pressure variations (e.g., BAYTAP-G). The importance of these corrections should be clear from all the raw records presented in this chapter. Other signal processing techniques can be helpful. For example, high- and low-pass filtering has been applied to the time

series of raw hydrogeochemical data in Kamchatka, Russia, to remove long- and short-period changes unrelated to earthquake processes (Kingsley et al. 2001).

Effort has also been made to address the statistical significance of possible precursors. Statistical, rather than deterministic, procedures have been introduced (Maeda and Yoshida 1990) to assess the conditional probability of future seismic events. Multi-component, hydrochemistry analysis was applied to groundwater samples in Iceland before and after a major earthquake to enhance the possibility of detecting possible precursors (Claesson et al. 2004). Highlighting the importance of long time series, Claesson et al. (2007) extended the time series of geochemical measurements after this and subsequent earthquakes and found that the statistical significance of previously identified anomalies could not be verified.

13.4 Examples

There are hundreds of reports of possible earthquake precursors. Here we review and discuss only selected studies to (1) illustrate the range of types of measurements that have been made, (2) highlight the challenges with identifying precursors, and (3) identify some of the key questions raised by reported precursor identifications. In all but one of the examples that we discuss, the hydrological changes are identified retrospectively as being premonitory to the earthquake.

Reviews of reported hydrologic precursors include Roeloffs (1988) and Hartmann and Levy (2005). Hydrogeochemical precursor reviews include Hauksson (1981), Thomas (1988), Toutain and Baubron (1999), Woith (2015), and Martinelli and Dadomo (2018).

13.4.1 *China: Haicheng, 1975 and Tangshan, 1976*

The most celebrated and first (indeed only, as far as we know) prediction of a large earthquake was the 1975 magnitude 7.3 Haicheng earthquake in China. Based in part on hundreds of hydrological anomalies, a prediction of an imminent earthquake was made. Evacuations and preparations in Haicheng, with a population of about 1 million, contributed in part to the modest number of casualties, just over 2000. The prediction correctly identified the location, though not the precise time, of the event, and the magnitude was underestimated (Wang et al. 2006).

One and a half years later, the 1976 M 7.8 Tangshan earthquake occurred without the issuance of a prediction. Figure 13.2 shows the distribution of anomalies and time histories of radon concentration, groundwater level, land level and electrical resistivity in the region around Tangshan before and after the earthquake (Ma et al. 1990). The fact that no prediction was issued, despite the abundance of potentially precursory anomalies, highlights the difficulty in making predictions. Casualties from this earthquake exceeded 240,000.

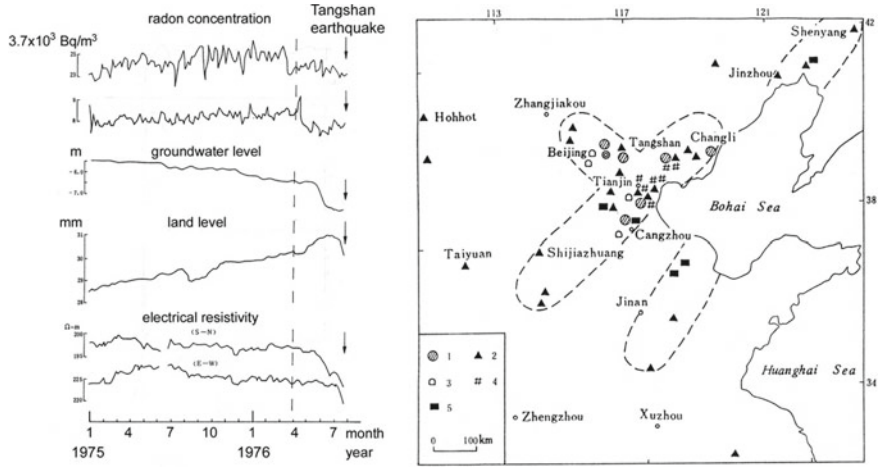


Fig. 13.2 Left: Some of the possibly precursory changes to the M7.8 Tangshan earthquake, China. The arrow shows the time of the earthquake. Right: Location of various precursory anomalies: resistivity (1), radon (2), land level (3), groundwater level (4), anomalies in oil wells (5) (from Ma et al. 1990)

13.4.2 Kobe, Japan, 1995

Following the 1995 M 7.2 Kobe earthquake several papers reported precursory changes in the concentrations of radon, chlorine, and sulfate ions in groundwater (e.g., Tsunogai and Wakita 1995; Igarashi et al. 1995) and in groundwater level (King et al. 1995). The hydrogeochemical changes could be identified by analyzing bottled spring water (Tsunogai and Wakita 1995). Figure 13.3 shows a gradual increase in chloride concentration that begins 7 months before the earthquake. The initiation of these changes coincides with a “drastic” increase in strain measured 5 km away from the well (Tsunogai and Wakita 1995). This coincidence supports a broader tectonic origin of the pre-earthquake changes. However, whether the deformation responsible for hydrogeochemical changes and strain is connected to the later Kobe earthquake is difficult to evaluate. Given the length of the proposed precursory signal, a longer time series of measurements would be useful for establishing the uniqueness of the recorded changes.

13.4.3 Nankaido, Japan, 1946

A few days prior to the 1946 M 8.3 Nankaido earthquake in Japan, water levels in some wells reportedly fell by more than 1 m and some wells went dry (Sato 1982). Linde and Sacks (2002) show that the pre-seismic deformation (observations reviewed in Roeloffs 2006) can be explained by aseismic slip along the subduction

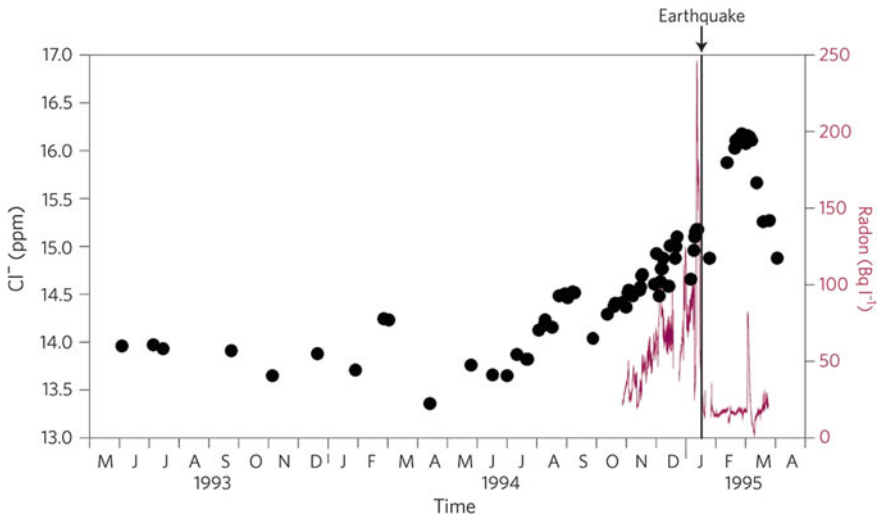


Fig. 13.3 Change in chloride and radon concentration in bottled groundwater 20 km from the epicenter of the 1995 M7.2 Kobe earthquake, Japan. Time of the earthquake is shown by the vertical line. Data from Tsunogai and Wakita (1995) and Igarashi et al. (1995) (from Ingebritsen and Manga 2014)

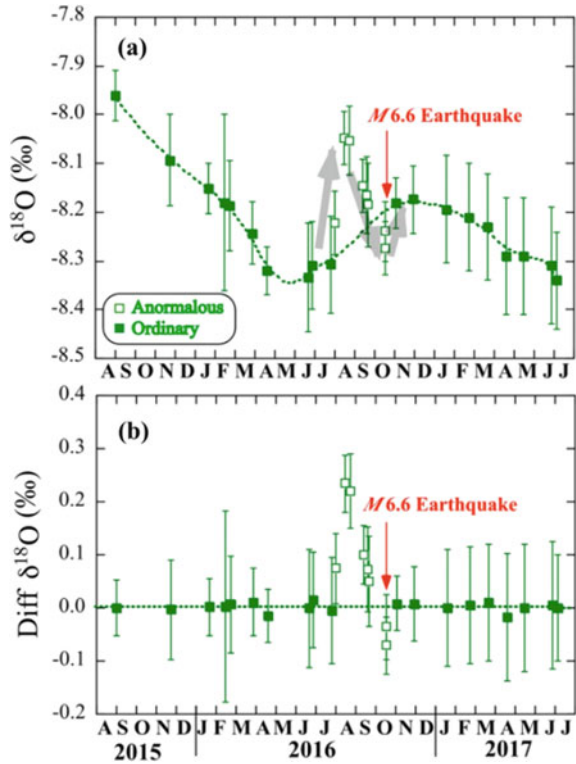
interface. This area is now intensively monitored with 1200 continuous GPS stations. This data (Ozawa et al. 2002) along with leveling and tide-gauge data document other aseismic slip events (importantly, not followed by large earthquakes) in the region. Multiple and large aseismic events highlight the caution that a correlation of strain and hydrologic changes does not necessarily reflect deformation leading directly to a major earthquake, but possibly document events that may remain purely aseismic.

The 1946 event was preceded by the 1944 M 8.2 Tonankai event, creating some ambiguity about whether the reported changes are responses or premonitory. Measured hydrological changes can lag behind tectonic strains (e.g., Ben-Zion et al. 1990) because of the time required for pore pressure diffusion.

13.4.4 Oxygen Isotope Precursors to the 2016 Tottori Earthquake, Japan

The magnitude 6.6 Tottori earthquake, Japan, occurred on October 21, 2016. It was a shallow strike-slip earthquake. Onda et al. (2018), following the analysis done after the Kobe earthquake (Sect. 13.4.2), analyzed commercially bottled water extracted from a 240 m deep aquifer. The well is only ~5 km from the fault that ruptured. Water isotopes show annual modulation. When this signal is removed (Fig. 13.4), Onda et al. (2018) identify an anomaly in oxygen isotopes prior to the earthquake that is not seen in hydrogen isotopes. Oxygen isotope changes not accompanied

Fig. 13.4 Variations on oxygen isotopes from bottled waters collected before and after the magnitude 6.6 Tottori earthquake in Japan. Panel a shows raw data and panel b removed the assumed seasonal variations. Open symbols show the inferred anomalous data. The red arrow shows the time of the earthquake (from Onda et al. 2018)



by changes in hydrogen isotopes are most easily explained by increasing water–rock interaction. Here this would be the release of water that experienced more extensive reaction with rocks than the bulk of the water in the sampled aquifer. Onda et al. (2018) performed rock crushing experiments to quantify the expected changes in water isotopes, and inferred a plausible 10^{-7} volumetric strain, though there is no geodetic data documenting that such strains did in fact occur. Missing in this analysis are complementary data of water pressure and temperature—if fluids are being released from precursory volumetric strains, pore pressure and temperature may increase (though in Chap. 9 we showed that the velocity required to affect solute composition is lower than that requires to change pore pressure and still lower than that required to change temperature). This study highlights the value of an archive of data from regular water sampling.

13.4.5 Kettleman Hills, California, 1985

Three days before the 1985 M 6.1 Kettleman Hill, California earthquake, Roeloffs and Quilty (1997) found a gradual, anomalous rise in water level of about 3 cm in

2 of 4 wells in the nearby Parkfield area. These changes are shown in Fig. 13.1. Barometric pressure changes and rainfall cannot explain these changes. One of these two wells exhibited several similar changes that were not followed by earthquakes. In the second, however, the documented increase was unique during the 5 year monitoring period. Figure 13.1 shows that the sign of these possible precursory changes is opposite to the coseismic change implying that they are not caused by accelerating pre-seismic slip.

This observation was included in the IASPEI Preliminary List of Significant Precursors (Wyss and Booth 1997). Nevertheless, important questions remain. What caused the anomalies? Why are they not recorded everywhere?

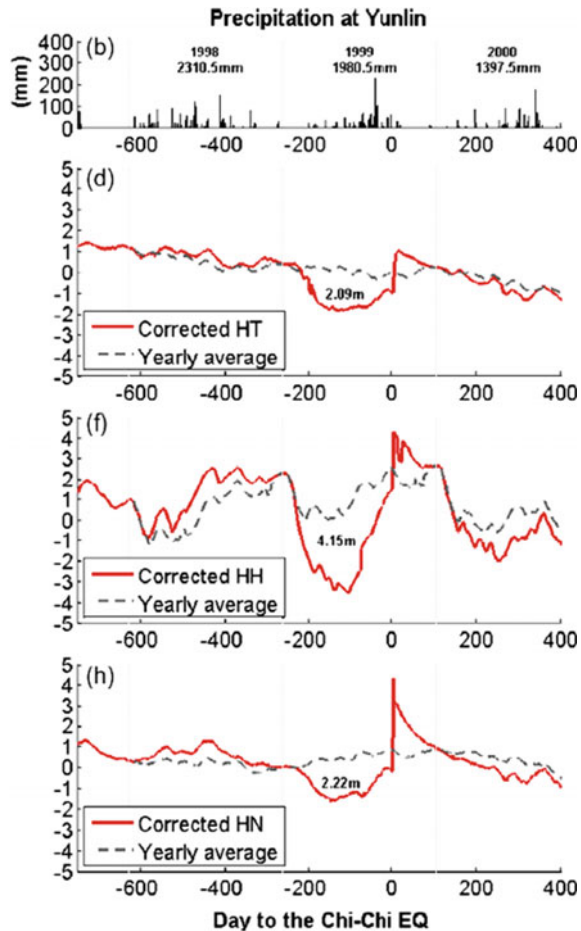
13.4.6 *Chi-Chi, Taiwan, 1999*

Abundant monitoring data in Taiwan provided a host of opportunities to look for precursors to the September 21, 2009 magnitude 7.7 Chi-Chi earthquake. Chen et al. (2015) report anomalous decreases in water level across the Choshuichi alluvial fan for approximately 100–200 days prior to the earthquake (Fig. 13.5). Using the network of monitoring wells, they show that this pattern is widespread and is at least qualitatively consistent with geodetic measurements of strain. It is not immediately clear that the anomalies are unique given that the time series is limited to only a few times longer than the duration of the anomaly. The time leading up to the earthquake was also marked by a late onset of the rainy season which would have contributed to lower water levels, though the magnitude of the changes seems too large to be due solely to a reduction in recharge.

Another reported possible precursor to the Chi-Chi earthquake is a change in the spectral characteristics of water level fluctuations in some wells in the month preceding the earthquake compared with those 2 and 3 months before the earthquake (Gau et al. 2007). This is not a compelling comparison as the amount and character of precipitation also changed (Fig. 13.5). As discussed in Sect. 9.3 and Roeloffs (1988), the full range of relevant environmental factors must be considered. Given the long-term memory and variability of hydrogeological systems, time series analysis should be undertaken for more than three months to assess the reliability of the analysis techniques in isolating seasonal effects, long term trends, and irregular variations. A longer analysis could also identify the uniqueness of the reported precursory change—an essential attribute of any precursor.

King and Chia (2018) report a large and rapid increase in streamflow 4 days before the earthquake. A nearby well showed an anomalous rise two days before the earthquake and a 4 cm drop three hours before the earthquake. They attribute these changes to pre-earthquake shallow slow slip events that created fractures enabling fluid migration. The authors do not report any independent geodetic data that confirm the inferred slow slip. The explanation does make a testable (in principle) prediction that there should be permeability changes.

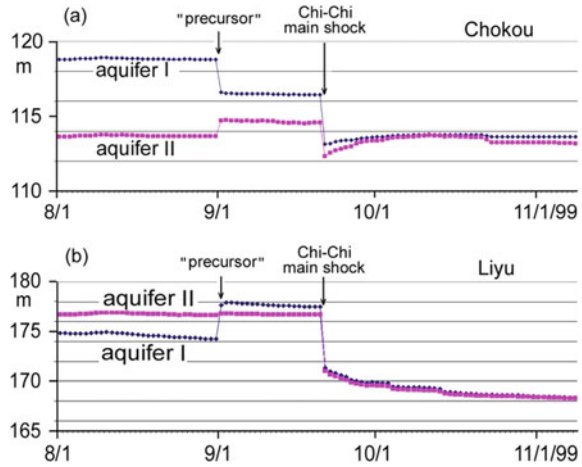
Fig. 13.5 Water level corrected for atmospheric pressure variations compared to the mean daily value where 0 is the day of the Chi-Chi earthquake. The yearly average is that from 1998 to 2000. It is not clear why those averages are not periodic (from Chen et al. 2015)



Song et al. (2006) analyzed the composition of water at hot and artesian springs in Taiwan. Large, reversible anomalies in Cl^- or SO_4^{2-} were identified over a few year period. At the hot springs, a couple anomalies precede earthquakes; however, anomalies do not exist before all earthquakes, and there is no correlation between the intensity of the shaking and the occurrence of precursory anomalies. Moreover, some anomalies are not followed by earthquakes. The artesian springs document postseismic changes, but these do not occur for all earthquakes and the occurrence of a response does not seem to be correlated with the intensity of shaking. Despite these severe limitations, Song et al. (2006) nevertheless claim that these springs are possibly ideal sites for recording precursors.

Some of the reported hydrologic “precursors” to the Chi-Chi earthquake are interesting as cautionary tales. One example of a “precursor” was claimed shortly after the earthquake. The earthquake occurred at 1:47 a.m., 21 September, local time. 59 of the 157 monitoring wells that showed stepwise changes in groundwater level reported

Fig. 13.6 Incorrectly identified groundwater level precursors to the 1999 M 7.3 Chi-Chi earthquake in Taiwan. The step a few weeks before the Chi-Chi earthquake is due to readjustment of the water level monitoring system



times of these change between the hour of 11 p.m., 20 September 20, and 1 a.m., 21 September. In other words, these records showed stepwise changes in groundwater level about 1 to 3 h before the earthquake. If true and repeated for other earthquakes, these would be ideal precursors. Careful examination and verification of the clock of the recording instruments in the field and inspection of the information management process (Chia et al. 2000), however, necessitated a readjustment of the time-axis of the entire groundwater-level records. After corrections were made, all the “precursors” turned out to be co-seismic responses. A second example of misidentified precursors is illustrated in Fig. 13.6. The stepwise changes in groundwater level in four wells two weeks before the Chi-Chi earthquake could be mistaken as “precursory”. These changes, however, turn out to be a result of readjustment of the recording instruments (Y. Chia, personal communication). Both examples highlight the importance of (1) using a common time-base for the hydrologic and seismic records, and (2) documenting all instrumental changes as part of the hydrologic records.

13.4.7 Kamchatka

Long term hydrogeochemical records are available in Kamchatka, an area with many large earthquakes. Biagi et al. (2006) illustrate a clear postseismic response in a spring following a M 7.1 earthquake about 100 km away—Fig. 13.7 shows this response. Biagi et al. (2006) also show that following this earthquake the spectral characteristics of the hydrogeochemical variations change, with an increase in short period variability. Biagi et al. (2006), expanding on Biagi et al. (2000), further claim that variations in other components, in particular H_2 and CO_2 , are precursory—their amplitude fluctuations decrease after the earthquake. We offer an alternative explanation for these changes and instead propose that they too are postseismic

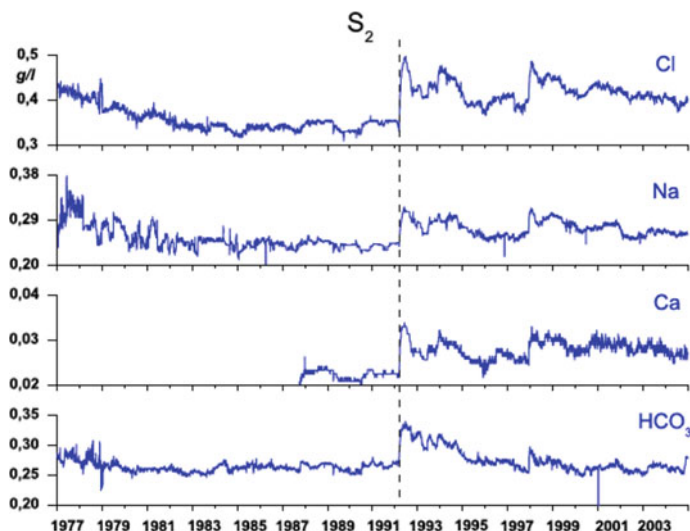


Fig. 13.7 Change in water composition at a spring in Kamchatka. Water is sampled every 3 days. The time of a M 7.1 earthquake about 100 km distant is shown by the vertical dashed line. There is a clear postseismic response (from Biagi et al. 2006)

changes—the earthquake-created changes in hydraulic connectivity that lead to the changes shown in Fig. 13.7 are also responsible for the character changes in H_2 and CO_2 .

With a long record of hydrogeochemical monitoring and many earthquakes, Kamchatka offers an opportunity to test approaches to identifying precursors. Kingsley et al. (2001) identified as precursory, any signals that exceed 3 standard deviations of the mean and that are seen at the same time (within 7 days) in at least 2 measurements. With this criterion, they identify 8 precursors (anomalies within 158 days of the earthquake) and 3 failures (anomalies not followed by earthquakes) for a time period with 5 large (magnitudes between 6.9 and 7.3) earthquakes. With a more restrictive criterion that anomalies are confined to ion data alone, Biagi et al. (2001) identify 3 anomalies, all of which are followed by earthquakes (the three closest large earthquakes to the wells). Examining their data (Fig. 2 in Biagi et al. 2001), however, shows that there are correlated anomalies slightly smaller than 3 standard deviations that are not followed by earthquakes. Moreover, as the 5 large earthquakes occurred within less than a 5 year period, and correlated anomalies (greater than 3 sigma) occur every year or so, we thus expect that roughly half of identified precursory anomalies would fall within the 158 day time window simply by chance. Once again, we are left with several questions: what caused these anomalies? why are some wells (apparently) more sensitive? What is the statistical significance of the anomalies?

13.4.8 Pyrenees, France, 1996

Toutain et al. (1997) analyzed the composition of bottled and dated spring water, as done following the 1995 Kobe earthquake (Tsunogai and Wakita 1996), to document the pre- and postseismic response of groundwater to a M 5.2 earthquake in the French Pyrenees. The spring is located 29 km from the epicenter. As shown in Fig. 13.8, about 5 days before the earthquake, the chloride concentration increased by about 40%, an increase much larger than the standard deviation of pre-seismic values (at least over the 200 days analyzed). The high chloride values persisted for about another 5 days

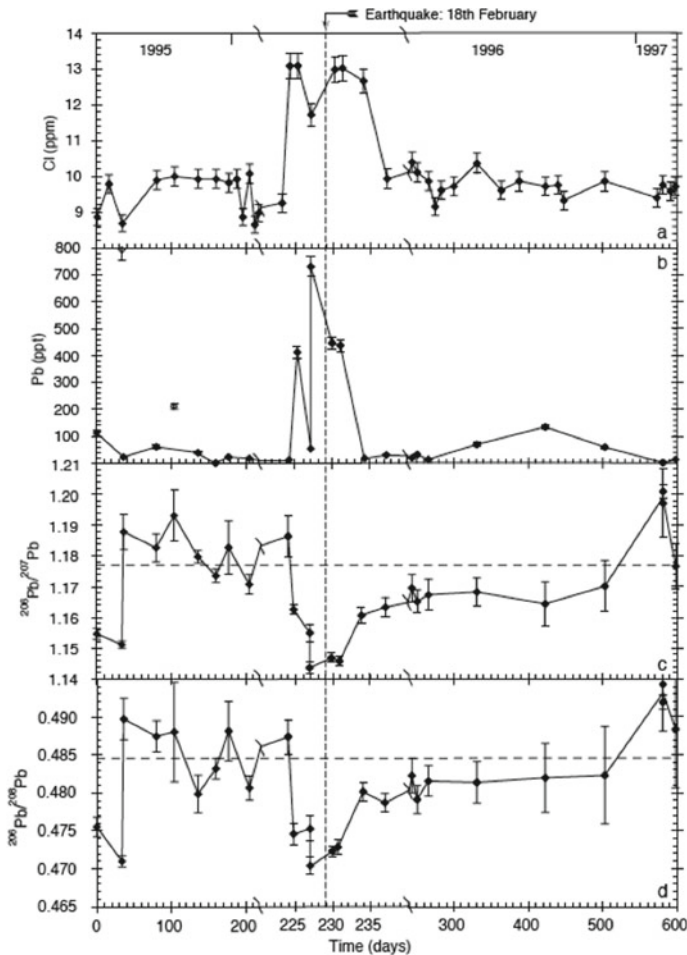


Fig. 13.8 Chloride and lead anomalies identified a posteriori from bottled waters. The time of a M 5.2 earthquake is shown by the vertical dashed line. The spring is located 29 km from the epicenter (from Poitrason et al. 1999)

and then returned to “normal”. Poitrasson et al. (1999) documented a lead anomaly in the same waters, also shown in Fig. 13.8. The lead anomaly has a shorter duration and is more than 10 times background values. The lead isotope changes suggest an anthropogenic source.

Toutain et al. (1997) propose that a small amount of chloride-rich water was injected into the aquifer feeding the springs—measured changes reflect mixing of previously isolated waters. The lead anomaly is not consistent with the possible sources for the chloride anomaly (Poitrasson et al. 1999), implying a third source of water. It is not clear why the start and end of the documented changes are so abrupt because dispersion should lead to more gradual changes, especially during the post-seismic period.

13.4.9 Reservoir Induced Seismicity, Koyna, India

Chadha et al. (2003) report on an experiment to search for precursors to the reservoir-induced earthquakes near the Koyna and Warna reservoirs, India. The project involved drilling 19 wells for monitoring purposes. In addition to coseismic water level changes, Chadha et al. (2003) identify small, centimeter-scale, changes in water levels over periods of days to many days before earthquakes with magnitudes between 4.3 and 5.2 and within distances of 24 km.

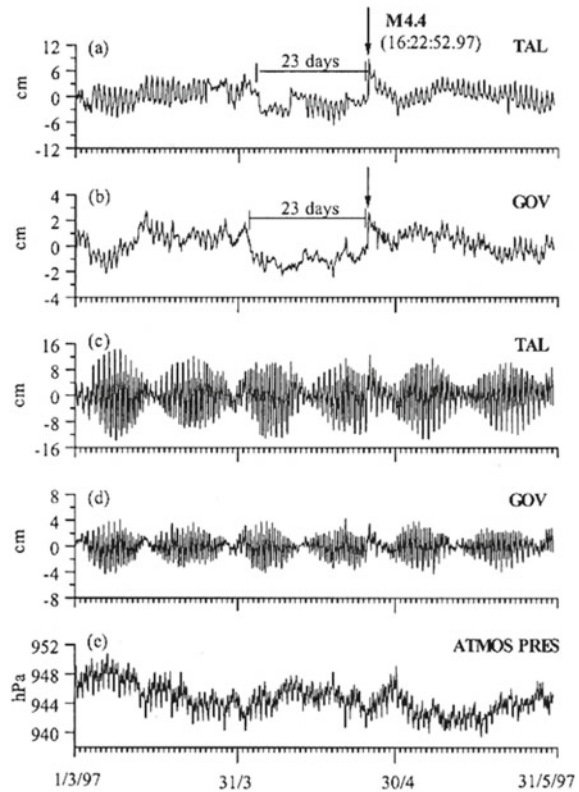
Figure 13.9 shows an example of two of the premonitory changes, including the raw data and barometric pressure. The coseismic signal and possible precursory anomalies are dwarfed by the response to tides and barometric pressure. After removing effects of tides and barometric pressure changes, a coseismic and post-seismic response become clear. This study does not address the uniqueness of the proposed precursor anomalies. Inspection of Fig. 13.9 and other figures in this paper shows that similar anomalies occur and are not followed by earthquakes. Other questions remain about these purported precursors: Why don't all wells record the same anomalies? Why is the time duration of the anomalies different from earthquake-to-earthquake?

Complementary hydrogeochemical and water level measurements have now been made at 15 wells for >12 years, beginning in 2005 (Reddy et al. 2017). No precursory signals are seen before earthquakes with magnitude <5. There are long term trends in water chemistry along with annual variations in water level—with no clear or repeatable patterns of changes before or after earthquakes.

13.4.10 Calistoga Geyser, California

As discussed in Chap. 11, geysers can be especially sensitive to small earthquake-generated strains. Silver and Vallette-Silver (1992) analyzed 18 years of eruptions at the Old Faithful, Calistoga, California geyser. During this period, they documented

Fig. 13.9 Water level in two wells (TAL and GOV) over a 5 months period. **a, b** Show water level after removing tides and barometric pressure effects (shown in e). **c, d** Show raw water level records. The time of a M 4.4 earthquake that occurred 3 km from the wells is shown with the arrow. Chadha et al. (2003) claim that the 23 day period before this event is a precursory anomaly (from Chadha et al. 2003)



three clear responses to regional earthquakes, as manifested in changes in the interval between eruption (IBE, the most common measure, as discussed in Chap. 11, of geyser response) or the distribution of IBE. Two earthquakes caused an increase in IBE. The third caused a change in the mode of eruption, from a single IBE to multiple IBEs. These three earthquakes are consistent with a magnitude-distance threshold similar to other hydrological responses (Fig. 14.4).

Silver and Vallette-Silver (1992) also propose that there are precursory changes in IBE that begin days before these three regional earthquakes. The data in this paper, however, clearly show many features similar to the proposed precursory changes that were not followed by earthquakes. We believe that the statistical analysis in this paper significantly underestimates the number of times the IBE changes character, by perhaps 1–2 orders of magnitude, over the monitored period.

13.4.11 Iceland, 2012–2013

Four to six months before a magnitude 5.6 earthquake in Iceland, there were hydrogen isotope and major ion changes (Fig. 13.10) in a 100 m deep artesian well (Skelton et al. 2014). Continued monitoring documented large hydrogeochemical responses to the earthquake (Fig. 9.2; Skelton et al. 2019). There are several abrupt changes in oxygen isotopes over the several year period with data (Fig. 13.10b), which suggests that permeable paths switch over time (Fig. 9.10). No water pressure data are available to quantify permeability changes. Statistical tests of the hydrogen isotope and Na concentration data show that excursions prior to the earthquake are not random, leading Skelton et al. (2014) to conclude that the changes are probable precursors. They, however, “make no claim of being able to predict earthquakes” and instead highlight that groundwater chemistry is a “promising target for future earthquake prediction studies”.

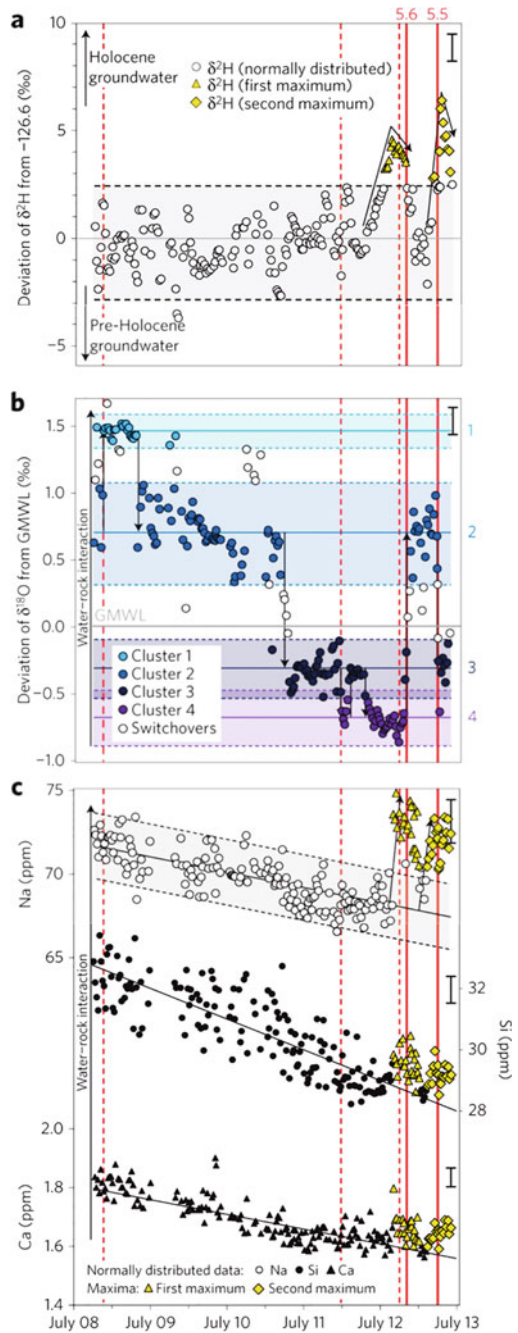
Iceland hosts abundant seismic and volcanic activity. Magma movement in the subsurface and volcanic eruptions create earthquakes, deform the crust and hence can change permeability, and discharge gases and aqueous fluids. In fact, eruption precursors at volcanoes are widespread and play a role in forecasting volcanic eruptions (National Academies of Sciences, Engineering, and Medicine 2017). An alternative interpretation of the hydrogeochemical data is thus that both the geochemical changes and the earthquakes are responses to magma movement (Ingebritsen and Manga 2014).

13.4.12 Central Italy Seismic Sequence, 2016

Several magnitude 6 earthquakes occurred in the central Apennines, Italy in 2016. A few months before the seismic swarm, there were anomalous changes in trace element concentrations, specifically As, V and Fe, in springs (Fig. 13.11). There were also large hydrogeochemical and water level responses to the earthquakes (and no unambiguous water level precursors). Barberio et al. (2017) attribute the geochemical changes to an influx of deep hydrothermal fluids or fluids mobilized from deep organic-rich units and hence that the changes are recording permeability changes. Those same permeability changes could redistribute pore pressure and hence promote seismicity. These inferences would certainly benefit from co-located pore pressure measurements at depth along with a longer time series to decipher annual variations and long-term trends. Since the earthquakes are between 57 and 96 km away from the springs, the inferred connections must reflect regional changes in strain.

Water pressure and electrical conductivity are also monitored at high frequency (50 Hz) in boreholes around the deep underground Gran Sasso laboratory in central Italy. Five days, and perhaps as long as 40 days, before the 24 August 2016 magnitude 6 Amatrice event, De Luca et al. (2018) document significant changes in the kurtosis and skewness of pressure fluctuations. They also document large pressure changes

Fig. 13.10 Changes in **a** hydrogen isotopes, **b** oxygen isotopes, **c** major ions in a 100 m deep artesian well in Iceland with the time of earthquakes shown with vertical lines (dashed lines are events with magnitudes less than 5). The water is hot (73–76 °C) and alkaline (from Skelton et al. 2019)



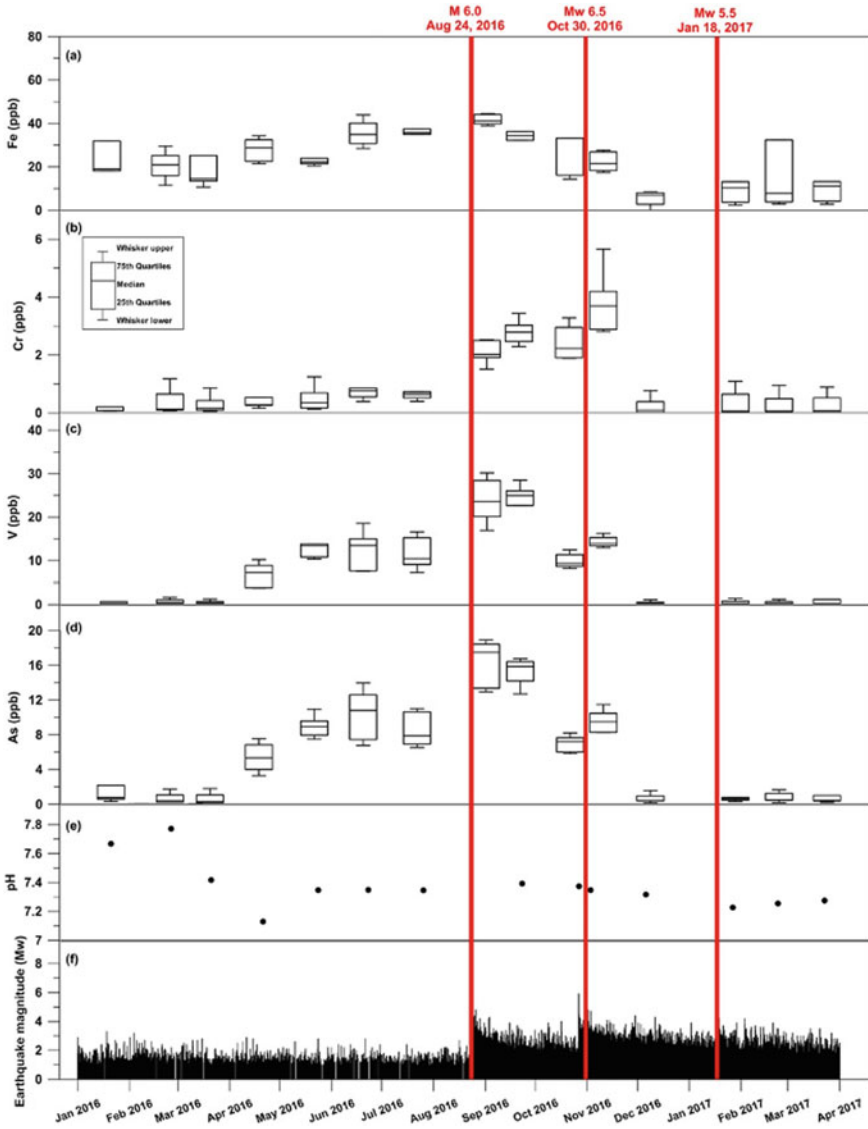


Fig. 13.11 Water chemistry at the Sulmona test site springs, Italy (panels a–e) and seismicity (panel f). Times of regional earthquakes are shown with vertical red lines. Panel b explains the meaning of the plotted symbols (from Barberio et al. (2017))

after the earthquake. They attribute precursory changes to microfracturing that leads to high frequency pressure changes and upflow of gases. If De Luca et al. (2018) have indeed documented a precursor, their results suggest that very high frequency sampling might be needed to identify the precursory signals.

13.4.13 Precursory Changes in Spring Temperature

In Chap. 8 we discussed the co- and post-seismic changes in temperature of a well on the Izu Peninsula, Japan (Mogi et al. 1989). At this well, rapid increases in temperature of 1–2 °C typically accompany regional earthquakes. Following earthquakes, temperature decreases approximately linearly. Also of note is a correlation of temperature changes with tides and barometric pressure, with magnitudes up to 0.5 °C. Mogi et al. (1989) attributed these trends to be the result of unblocking, followed by gradual resealing, of fractures.

For a small number of earthquakes, as many as 5, there are abnormal changes in temperature, defined as changes that are not coseismic, do not follow the linear trend of decreasing temperature, and do not appear to be related to tides or weather. Mogi et al. (1989) referred to such abnormal changes as precursory. The changes occur between 3 days and 10 months before regional earthquakes. In one case, the precursory changes are coincident with a regional earthquake swarm.

As with other claimed precursors, there is no obvious predictive feature—the abnormal signals differ in form, timing, and do not always occur. Figs. 7 and 9 in Mogi et al. (1989) also show abnormal changes not followed by earthquakes.

One possible explanation for the abnormal changes is that they are in fact responses to tectonic events—the “precursory” response coincident with a regional earthquake swarm being an example. There is a wide range of earthquake phenomena, particularly in subduction zone settings, in which slip does not only generate regular earthquakes (Beroza and Ide 2011). These events differ in the duration of the slip event, which can range from seconds for very-low frequency earthquakes (e.g., Ito et al. 2005), to hours for slow earthquakes (e.g., Linde et al. 1996) to days for slow-slip events (e.g., Hirose and Obara 2005) to many months for silent earthquakes (e.g., Dragert et al. 2001; Ozawa et al. 2002; Kostoglodov et al. 2003). Such events are common in Japan and other subduction zones (Ide et al. 2007), but also occur along strike-slip faults such as the San Andreas in California (e.g., Linde et al. 1996) and at volcanoes (e.g., Segall et al. 2006).

If the “precursory” changes reported by Mogi et al. (1989) are in fact responses to slower slip events than regular earthquakes, it suggests the changes are more sensitive to the magnitude of strain rather than dynamic strains. At the same time, this also implies that “precursors” are not useful for forecasting as not all slow earthquakes are followed by regular (and damaging) earthquakes.

13.5 Outlook

There are several retrospective reports of hydrological changes preceding earthquakes that appear to have no other obvious explanation. In few cases, however, do criteria meet those needed for critical evaluation—those listed in Sect. 13.2 and Roeloffs (1988). To identify these changes as precursory in a useful way also requires a criterion for distinguishing them from non-precursors before the actual earthquake occurs. Given the lack of success in using hydrological and hydrogeochemical anomalies to predict earthquakes (including all three desired features: size, location and date) it is not surprising that earthquake prediction is not the focus of modern seismology. Some readers may be surprised by our skepticism about some reported precursors and our critical assessment of the observations and data analysis. However, extraordinary claims require extraordinary proof (if not at least attention to, and documentation of, details); the ability to predict earthquakes certainly qualifies as an “extraordinary claim”.

Hydrological precursors to earthquakes, if they exist, can be thought of as being a subset of a broad range of transient phenomena that includes silent and slow earthquakes, transient creep, episodic tremor and slip, and seismic swarms. Such transient phenomena occur more often and provide more measurement opportunities. Consequently, their study may prove insightful about earthquake initiation and the types and origins of possible hydrological phenomena that can be mistaken as precursors to normal earthquakes.

Multiparametric monitoring is particularly important both for identifying spurious anomalies and understanding the origin of hydrological changes. Combined deformation and water level measurements have proven useful to understand the spatio-temporal relationship between transient hydrological changes and deformation (e.g., Ben-Zion et al. 1990) and to support the identification of hydrological precursors (Roeloffs and Quilty 1997). Long-term and multi-parameter monitoring requires investment and patience, but both are probably required to assess whether there are precursors and to establish the statistical significance of signals. Woith (2015) reviewed more than 100 studies that report radon precursors and found a negative correlation between the number of anomalies and the length of the time series analyzed. Woith (2015) concluded that tectonic anomalies probably exist but may be indistinguishable from non-tectonic anomalies. Advances in machine learning may help tease out signals that are otherwise challenging to recognize (e.g., Rouet-Leduc et al. 2017; Asim et al. 2018).

The now widespread use of ambient noise to monitor temporal changes in seismic velocity is opening up new opportunities for documenting changes in elastic properties, including responses to earthquakes (e.g., Brenguier et al. 2008; Nakata and Snieder 2011; Gassenmeier et al. 2016; Nimiya et al. 2017), creep (e.g., Hillers et al. 2019), healing of faults (e.g., Pei et al. 2019), and long term trends that may be recording an evolving stress state (e.g., Ikeda and Tsuji 2018; Taira et al.

2018). Connecting such monitoring to hydrological and hydrogeochemical data may prove especially useful for interpreting anomalies and identifying reliable precursory signals.

Although we may still be far from achieving a complete understanding of the underlying mechanisms of the various earthquake-related anomalies that are reported in the literature, there remain significant monitoring efforts. A negative result, such as the absence of clear precursory signals at the multiparametric and densely monitored Parkfield, California site (Bakun et al. 2005), may frustrate the effort to predict earthquakes, but provides important and useful constraints on models of rupture initiation and other tectonic processes that lead up to earthquakes. There still remains a physical basis for expecting precursory signals, and lab experiments confirm that that expectation holds in the lab.

References

- Aggarwal YP, Sykes LR, Armbruster J, Sbar ML (1973) Premonitory changes in seismic velocities and prediction of earthquakes. *Nature* 241:101–104
- Asim KM, Idris A, Iqbal T, Martinez-Alvarez F (2018) Seismic indicators based earthquake predictor system using Genetic Programming and AdaBoost classification. *Soil Dyn Earthq Eng* 111:1–7
- Bakun WH, Aagard B, Dost B et al (2005) Implications for prediction and hazard assessment from the 2005 Parkfield earthquake. *Nature* 437:969–974
- Barberio MD, Barbieri M, Billi A et al (2017) Hydrogeochemical changes before and during the 2016 Amatrice-Norcia seismic sequence (central Italy). *Sci Rep* 7(1):1–12
- Ben-Zion Y, Henyey TL, Leary PC, Lund SP (1990) Observations and implications of water level and creepmeter anomalies in the Mojave segment of the San Andreas fault. *Bull Seism Soc Am* 80:1661–1676
- Beroza GC, Ide S (2011) Slow earthquakes and nonvolcanic tremor. *Ann Rev Earth Planet Sci* 39:271–296
- Biagi PF, Picolo R, Ermini A et al (2001) Hydrogeochemical precursors of strin earthquakes in Kamchatka: further analysis. *Nat Hazards Earth Syst Sci* 1:9–14
- Biagi PF, Castellana L, Minafra A et al (2006) Groundwater chemical anomalies connected with the Kamchatka earthquake ($M=7.1$) on March 1992. *Nat Hazards Earth Syst Sci* 6:853–859
- Biagi PF, Ermini A, Kingsley SP et al (2000) Groundwater ion content precursors of strong earthquakes in Kamchatka (Russia). *PAGEOPH* 157:302–320
- Bolt BA, Wang CY (1975) The present status of earthquake prediction. *Crit Rev Solid State Mater Sci* 5:125–151
- Brace WF, Paulding J, Scholz C (1966) Dilatancy in the fracture of crystalline rocks. *J Geophys Res* 71:3939–3953
- Brenguier F, Shapiro NM, Campillo M et al (2008) Towards forecasting volcanic eruptions using seismic noise. *Nat Geosci* 1(2):126–130
- Chadha RK, Pandey AP, Kuempel HJ (2003) Search for earthquake precursors in well water levels in a localized seismically active area of reservoir triggered earthquakes in India. *Geophys Res Lett* 30:1416. <https://doi.org/10.1029/2002GL016694>
- Chen CH, Tang CC, Cheng KC et al (2015) Groundwater–strain coupling before the 1999 Mw 7.6 Taiwan Chi-Chi earthquake. *J Hydrol* 524:378–384

- Chia Y, Wang YS, Wu HP et al (2000) Changes of ground water level in response to the Chi-Chi earthquake. International workshop on annual commemoration of Chi-Chi earthquake. National Center for Research on Earthquake Engineering, Taipei, pp 317–328
- Claesson L, Skelton A, Graham C et al (2004) Hydrogeochemical changes before and after a major earthquake. *Geology* 32:641–644
- Claesson L, Skelton A, Graham C, Morth M (2007) The timescale and mechanisms of fault sealing and water-rock interaction after an earthquake. *Geofluids* 7:427–440
- De Luca G, Di Carlo G, Tallini M (2018) A record of changes in the Gran Sasso groundwater before, during and after the 2016 Amatrice earthquake, central Italy. *Sci Rep* 8(1):1–16
- Dragert H, Wang K, James TS (2001) A silent slip event on the deeper Cascadia subduction interface. *Science* 292:1525–1528
- Fu CC, Yang TF, Tsai MC et al (2017) Exploring the relationship between soil degassing and seismic activity by continuous radon monitoring in the Longitudinal Valley of eastern Taiwan. *Chem Geol* 469:163–175
- Gassenmeier M, Sens-Schönfelder C, Eulenfeld T et al (2016) Field observations of seismic velocity changes caused by shaking-induced damage and healing due to mesoscopic nonlinearity. *Geophys J Int* 204(3):1490–1502
- Gau HS, Chin T-C, Chen J-S, Liu, C.-W, (2007) Time series decomposition of groundwater level changes in wells due to the Chi-Chi earthquake in Taiwan: a possible hydrological precursor to earthquakes. *Hydrol Proc* 21:510–524
- Hartmann J, Levy JK (2005) Hydrogeological and gasgeochemical earthquake precursors—a review for application. *Nat. Hazards* 34:279–304
- Hauksson E (1981) Radon content of groundwater as an earthquake precursor: evaluation of worldwide data and physical basis. *J Geophys Res* 86:9397–9410
- Hillers G, Campillo M, Brenguier F et al (2019) Seismic velocity change patterns along the San Jacinto Fault Zone following the 2010 M 7.2 El Mayor-Cucapah and M 5.4 Collins Valley earthquakes. *J Geophys Res Solid Earth* 124(7):7171–7192
- Hirose H, Obara K (2005) Repeating short- and long-term slow slip events with deep tremor activity, around the Bungo channel region, southwest Japan. *Earth Planets Space* 57:961–972
- Ide S, Beroza GC, Shelly DR, Uchide T (2007) A scaling law for slow earthquakes. *Nature* 447:76–79
- Igarashi G, Wakita H (1995) Geochemical and hydrological observations for earthquake prediction in Japan. *J Phys Earth* 43:585–596
- Igarashi G, Saeki S, Takahata N et al (1995) Groundwater radon anomaly before the Kobe earthquake in Japan. *Science* 269:60–61
- Ikeda T, Tsuji T (2018) Temporal change in seismic velocity associated with an offshore MW 5.9 Off-Mie earthquake in the Nankai subduction zone from ambient noise cross-correlation. *Prog Earth Planet Sci* 5(1):1–12
- Ingebritsen SE, Manga M (2014) Earthquakes: hydrogeochemical precursors. *Nat Geosci* 7(10):697–698
- Ito Y, Obara K, Shiomi K, Sekine S, Hirose H (2005) Slow earthquakes coincident with episodic tremors and slow slip events. *Science* 296:503–506
- Kawabata K, Sato T, Takahashi HA et al (2020) Changes in groundwater radon concentrations caused by the 2016 Kumamoto earthquake. *J Hydrol* 584:124712
- King C-Y (1980) Episodic radon changes in subsurface soil gas along active faults and possible relation to earthquakes. *J Geophys Res* 85:3065–3078
- King C-Y, Chia Y (2018) Anomalous streamflow and groundwater-level changes before the 1999 M7. 6 Chi-Chi earthquake in Taiwan: possible mechanisms. *Pure Appl Geophys* 175(7):2435–2444
- King C-Y, Basler D, Presser TS et al (1994) In search of earthquake-related hydrologic and chemical changes along the Hayward fault. *Appl Geochem* 9:83–91
- King C-Y, Koizumi N, Kitigawa Y (1995) Hydrogeochemical anomalies and the 1995 Kobe earthquake. *Science* 269:38–39

- Kingsley SP, Biagi PF, Ermini A et al (2001) Hydrogeochemical precursors of strong earthquakes: a realistic possibility in Kamchatka. *Phys Chem Earth* 26:769–774
- Kondratenko AM, Nersesov IL (1962) Some results of the study of change in the velocity of longitudinal waves and relation between the velocities of longitudinal and transverse waves in a focal zone. *Trudy Insr Fizioli Zemli Acad Nauk USSR* 25:130–150
- Kostoglodov V, Singh SK, Santiago JA et al (2003) A large silent earthquake in the Guerrero seismic gap, Mexico. *Geophys Res Lett* 30:1807. <https://doi.org/10.1029/2003GL017219>
- Linde AT, Sacks IS (2002) Slow earthquakes and great earthquakes along the Nankai trough. *Earth Planet. Sci Lett* 203:265–275
- Linde AT, Gladwin MT, Johnston MSJ, Gwyther RL, Bilham RG (1996) A slow earthquake sequence on the San Andreas fault. *Nature* 383:65–67
- Lockner DA, Beeler NM (2002) Rock failure and earthquakes. In: Lee WHK et al (eds) *International handbook of earthquake and engineering seismology*. Academic, San Diego, pp 505–537
- Ma Z, Fu Z, Zhang Y et al (1990) Earthquake prediction: nine major earthquakes in China (1966–1976). Seismological Press, Beijing, p 332
- Maeda K, Yoshida A (1990) A probabilistic estimation of the appearance times of multiple precursory phenomena. *J Phys Earth* 38:431–444
- Martinelli G, Daddomo A (2018) Geochemical and fluid-related precursors of earthquakes: previous and ongoing research trends. In: *Pre-earthquake processes: a multidisciplinary approach to earthquake prediction studies*. *Geophys Monogr Ser* 234:219–228
- McEvilly TV, Johnson LR (1974) Stability of P and S velocities from central California quarry blasts. *Bull Seism Soc Am* 64:343–353
- Mogi K, Mochizuki H, Kurokawa Y (1989) Temperature changes in an artesian spring at Usami in the Izu Peninsula (Japan) and their relation to earthquakes. *Tectonophysics* 159:95–108
- Nakata N, Snieder R (2011) Near-surface weakening in Japan after the 2011 Tohoku-Oki earthquake. *Geophys Res Lett* 38(17):L17302. <https://doi.org/10.1029/2011GL048800>
- National Academies of Sciences, Engineering, and Medicine (2017) *Volcanic eruptions and their repose, unrest, precursors, and timing*. National Academies Press, Washington DC
- Nimiya H, Ikeda T, Tsuji T (2017) Spatial and temporal seismic velocity changes on Kyushu Island during the 2016 Kumamoto earthquake. *Sci Adv* 3(11):e1700813
- Niu F, Silver PG, Daley TM et al (2008) Preseismic velocity changes observed from active source monitoring at the Parkfield SAFOD drill site. *Nature* 454(7201):204–208
- O’Connell RJ, Budiansky B (1974) Seismic velocities in dry and saturated cracked solids. *J Geophys Res* 79:5412–5426
- Oh YH, Kim G (2015) A radon-thoron isotope pair as a reliable earthquake precursor. *Sci Rep* 5:13084
- Onda S, Sano Y, Takahata N et al (2018) Groundwater oxygen isotope anomaly before the M6. 6 Tottori earthquake in Southwest Japan. *Sci Rep* 8(1):1–7
- Ozawa S, Murakami M, Kaidzu M et al (2002) Detection and monitoring of ongoing aseismic slip in the Tokai region, central Japan. *Sci* 298:1009–1012
- Papachristodoulou C, Stamoulis K, Ioannides K (2020) Temporal variation of soil gas radon associated with seismic activity: a case study in NW Greece. *Pure Appl Geophys* 177(2):821–836
- Pei S, Niu F, Ben-Zion Y et al (2019) Seismic velocity reduction and accelerated recovery due to earthquakes on the Longmenshan fault. *Nature Geosci* 12(5):387–392
- Poitrasson F, Dundaas SH, Toutain J-P, Munoz M, Rigo A (1999) Earth-related elemental and isotopic lead anomaly in a springwater. *Earth Planet Sci Lett* 169:269–276
- Reddy DV, Kumar D, Rao NP (2017) Long-term hydrochemical earthquake precursor studies at the Koyna-Warna reservoir site in western India. *J Geol Soc India* 90(6):720–727
- Richon P, Sabroux JC, Halbwachs M et al. (2003) Radon anomaly in the soil of Taal volcano, the Philippines: a likely precursor of the M 7.1 Mindoro earthquake (1994). *Geophys Res Lett* 30(9):1481. doi:<https://doi.org/10.1029/2003GL016902>
- Robinson R, Wesson RL, Ellsworth WL (1974) Variation of P-wave velocity before the Bear Valley, California earthquake of 24 February, 1972. *Science* 184:12811283

- Roeloffs EA (1988) Hydrologic precursors to earthquakes: a review. *PAGEOPH* 126:177–209
- Roeloffs EA (2006) Evidence for aseismic deformation-rate changes prior to earthquakes. *Ann Rev Earth Planet Sci* 34:591–627
- Roeloffs E, Quilty E (1997) Water level and strain changes preceding and following the August 4, 1985 Kettleman Hills, California, earthquake. *PAGEOPH* 149:21–60
- Rouet-Leduc B, Hulbert C, Lubbers N et al (2017) Machine learning predicts laboratory earthquakes. *Geophys Res Lett* 44(18):9276–9282
- Sato H (1982) On the changes in the sea level at Tosashimuzu before the Nankaido earthquake of 1946. *J Seismo Soc Japan* 35:623–626
- Scholtz C, Sykes LR, Aggarwal YP (1973) Earthquake prediction: a physical basis. *Science* 181:803–810
- Scuderi MM, Marone C, Tinti E, Di Stefano G, Collettini C (2016) Precursory changes in seismic velocity for the spectrum of earthquake failure modes. *Nat Geosci* 9(9):695–700
- Segall P, Desmarais EK, Shelly D et al (2006) Earthquakes triggered by silent slip events on Kilauea volcano, Hawaii. *Nature* 442:71–74
- Semenov AN (1969) Variations in the travel-time of transverse and longitudinal waves before violent earthquakes. *Izv Acad Sci USSR Phys Solid Earth* 4 (English Trans.):245–248
- Skelton A, Andrén M, Kristmannsdóttir H et al (2014) Changes in groundwater chemistry before two consecutive earthquakes in Iceland. *Nat Geosci* 7(10):752–756
- Skelton A, Liljedahl-Claesson L, Wästebý N et al (2019) Hydrochemical changes before and after earthquakes based on long-term measurements of multiple parameters at two sites in Northern Iceland—a review. *J Geophys Res Solid Earth* 124(3):2702–2720
- Silver PG, Vallette-Silver NJ (1992) Detection of hydrothermal precursors to large northern California earthquakes. *Science* 257:1363–1368
- Song SR, Wu WY, Chen YL et al (2006) Hydrogeochemical anomalies in the springs of the Chiayi Area in west-central Taiwan as possible precursors to earthquakes. *PAGEOPH* 163:675–691
- Sugisaki R (1978) Changing He/Ar and N₂/Ar ratios of fault air may be earthquake precursors. *Nature* 275:209–211
- Sugisaki R (1981) Deep-seated gas emission induced by the earth tide: a basic observation for geochemical earthquake prediction. *Science* 212:1264–1266
- Sugisaki R, Sugiura T (1985) Geochemical indicator of tectonic stress resulting in an earthquake, central Japan, 1984. *Science* 229:1261–1262
- Taira TA, Nayak A, Brenguier F, Manga M (2018) Monitoring reservoir response to earthquakes and fluid extraction, Salton Sea geothermal field, California. *Science Advances* 4(1):e1701536
- Thomas D (1988) Geochemical Precursors to Seismic Activity. *PAGEOPH* 126:241–266
- Toutain JP, Munoz M, Poitrasson F, Lienard AC (1997) Springwater chloride ion anomaly prior to a M_L=5.2 Pyrenean earthquake. *Earth Planet Sci Lett* 149:113–119
- Toutain JP, Baubron J (1999) Gas geochemistry and seismotectonics: a review. *Tectonophysics* 304:1–27
- Trique N, Rochon P, Perrier F, Avouac JP, Sabroux JC (1999) Radon emanation and electric potential variations associated with transient deformation near reservoir lakes. *Nature* 399:137–141
- Tsunogai U, Wakita H (1995) Precursory chemical changes in groundwater: Kobe earthquake, Japan. *Science* 269:61–63
- Virk HS, Singh B (1993) Radon anomalies in soil-gas and groundwater as earthquake precursor phenomena. *Tectonophysics* 227:215–224
- Wakita H (1996) Geochemical challenge to earthquake prediction. *Proc Nat Acad Sci* 93:3781–3786
- Wakita H, Nakamura Y, Sano Y (1988) Short-Term and Intermediate-Term Geochemical Precursors. *PAGEOPH* 126:78–89
- Wang HF (2000) *Theory of linear poroelasticity*. Princeton University Press, New Jersey, 287pp
- Wang C-Y (1974) Earthquake prediction and oriented microcracks in rocks. *Nature* 251:405–408
- Wang K, Chen Q-F, Sun S, Wong A (2006) Predicting the 1975 Haicheng earthquake. *Bull Seism Soc Am* 96:757–795

- Whitcomb JH, Garmany JUD, Anderson DL (1973) Earthquake prediction: variation of seismic velocities before the San Fernando earthquake. *Science* 180:632–635
- Woith H (2015) Radon earthquake precursor: a short review. *Eur Phys J Spec Top* 224(4):611–627
- Wyss M, Booth DC (1997) The IASPEI procedure for the evaluation of earthquake precursors. *Geophys J Int* 131:423–424

Open Access This chapter is licensed under the terms of the Creative Commons Attribution 4.0 International License (<http://creativecommons.org/licenses/by/4.0/>), which permits use, sharing, adaptation, distribution and reproduction in any medium or format, as long as you give appropriate credit to the original author(s) and the source, provide a link to the Creative Commons license and indicate if changes were made.

The images or other third party material in this chapter are included in the chapter's Creative Commons license, unless indicated otherwise in a credit line to the material. If material is not included in the chapter's Creative Commons license and your intended use is not permitted by statutory regulation or exceeds the permitted use, you will need to obtain permission directly from the copyright holder.



Chapter 14

Epilogue



Abstract We identify some common threads and trends in the observations of hydrological responses to earthquakes. We suggest that seismic energy density is a useful metric for interpreting observations and relating different types of responses. We conclude with a summary of outstanding questions and new opportunities.

14.1 General Framework

The interaction between water and earthquakes vividly demonstrates the dynamic nature of the permeability of the uppermost crust, with implications for both earthquakes and groundwater transport. The processes of tectonic deformation and fluid movement are two-way coupled, as shown schematically in Fig. 14.1; i.e., changes in fluid pressure may alter stresses and hence can promote rock failure or accelerate slip on faults; at the same time, deformation and earthquakes may change pore pressure in the crust, causing changes of the water level in wells, discharge in streams, liquefaction of sediments, changes of groundwater temperature and chemical composition, and may even affect the eruptions of mud and magmatic volcanoes.

Figure 14.2 summarizes the magnitude of the reported permeability changes from lab experiments and field observations as a function of strain amplitude. It shows that, first, permeability usually increases after a disturbance, i.e., the ratio between the stimulated and the initial permeabilities is usually greater than 1; second, strain amplitudes as small as 10^{-6} can change permeability; third, permeability generally increases by less than a factor of ten unless new fractures form or their width increases significantly owing to pressurization of fractures; and fourth, there is no systematic dependence of the magnitude of the reported permeability changes on the strain amplitude, thus the change of permeability cannot be directly related to the applied strain. The results in Fig. 14.2 are also categorized by frequency, with filled boxes indicating frequencies greater than or equal to 10 Hz; everything else, except Faoro et al. (2012), has frequencies between 0.05 and 10 Hz, i.e., the range of seismic frequencies that cause the field responses. No obvious frequency-dependence is found either, but more experiments and observations are needed.

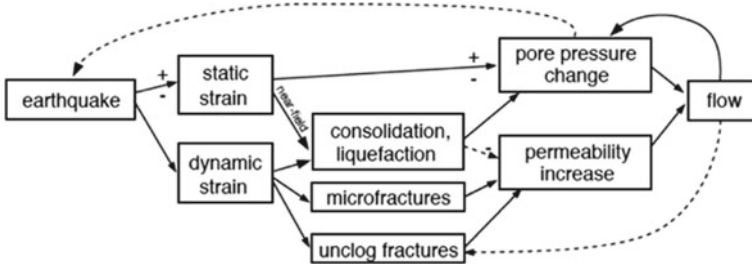


Fig. 14.1 Relationship between earthquakes and hydrology, and the processes through which interactions can occur. The + and - indicate the sign of the effect if it is known (from Manga and Wang 2007)

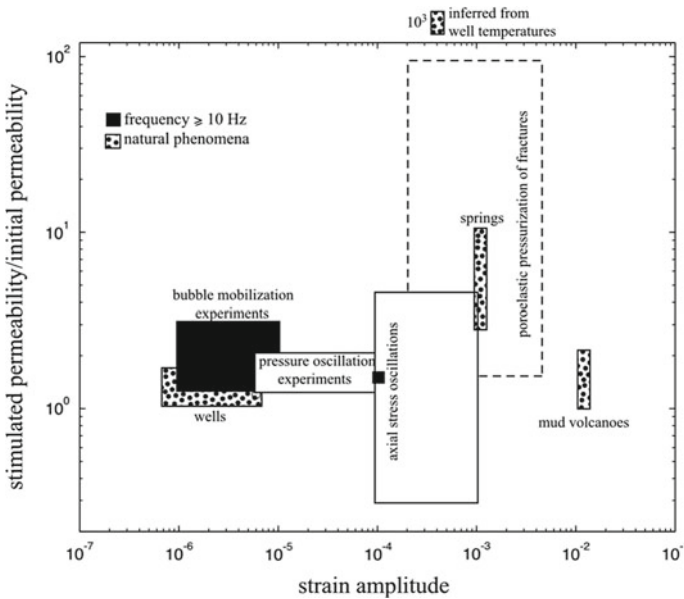
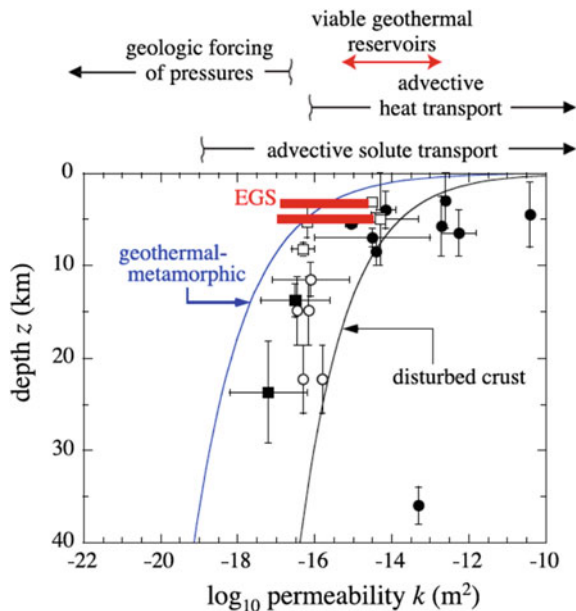


Fig. 14.2 Compilation of the permeability changes documented in the lab and field as a function of strain amplitude. Stippled boxes indicate field observations. Black filled boxes indicate experiments with frequencies ≥ 10 Hz. The dashed box indicates the strain amplitude and permeability changes for the pressurized fracture experiments presented in Faoro et al. (2012)—these are the only responses to non-oscillatory deformation shown in the compilation. Sources are as follows: bubble mobilization experiments (Li et al. 2005); pressure oscillation experiments (Elkhoury et al. 2011); axial stress oscillations in black (Roberts 2005) and in white (Liu and Manga 2009; Shmonov et al. 1999); well temperatures (Wang et al. 2012, 2013), with strain from Koizumi et al. (2004); springs (Manga and Rowland 2009); mud volcanoes (Rudolph and Manga 2010); wells (Elkhoury et al. 2006). For the bubble mobilization experiments of Beresnev et al. (2005), Li et al. (2005) we assumed a wave velocity of 3 km/s (from Manga et al. 2012)

The types of interactions shown in Figs. 14.1 and 14.2 may be extended to the evolution of permeability and groundwater flow in the deep crust. Rojstaczer et al. (2008) hypothesized that the permeability of the crust adjusts in a time-averaged sense so that it can accommodate recharge by precipitation and fluid released by internal forcing (metamorphism, tectonics, magmatism). If the pore pressure becomes large enough because the permeability is low, fracture may occur and will increase permeability. High permeability promotes groundwater flow, mineralization and ultimately permeability reduction. As a result, a balance is achieved in which the time-averaged permeability accommodates the transport of fluids provided to the crust, from below, within and above. Similar self-organizing feedbacks have been proposed for hydrothermal systems (e.g., Weis 2015) and deep fault zones (e.g., Lupi et al. 2011). Testing the Rojstaczer et al. (2008) hypothesis, however, is challenging because of the vast range of space and time scales involved in the processes that influence permeability and groundwater flow, even though the hypothesis is consistent with the mean permeability of the crust (Manning and Ingebritsen 1999). Other observational evidence supporting this idea includes mineral deposits that record transient, high permeability flow paths (e.g., Micklethwaite and Cox 2004) and short-lived high temperatures caused by transient flow in the lower crust (e.g., Camacho et al. 2005). Indeed, the permeability of disturbed crust, whether disturbed by tectonic events or manipulating the subsurface, can increase by a couple orders of magnitude highlighting that permeability is a dynamic physical property (Fig. 14.3).

We have also seen that the various hydrologic responses are, to a first degree of approximation, scaled by earthquake magnitude M and hypocenter distance r

Fig. 14.3 Permeability as a function of depth. Curve for geothermal-metamorphic is based on the compilation of data in Manning and Ingebritsen (1999), Ingebritsen and Manning (2002). The disturbed crust curve is from Ingebritsen and Manning (2010). The arrows above the plot show the processes that dominate at different permeabilities (from Manga et al. 2012)



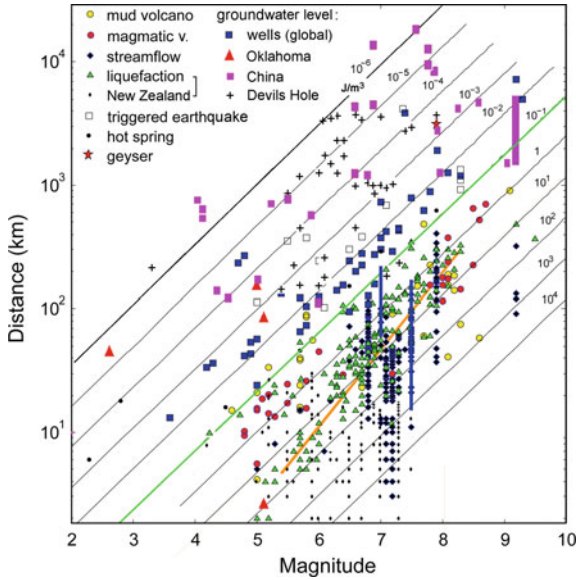


Fig. 14.4 Distribution of earthquake-induced hydrologic changes as functions of earthquake magnitude and epicentral distance. Data include an earlier global dataset from Wang and Manga (2010), water level data for Devils Hole from Weingarten and Ge (2014) and for China from Sun et al. (2018) and Zhang et al. (2019a), and liquefaction data for New Zealand from Simon Cox (personal communication). Also plotted are the contours of constant seismic energy density e (Eq. 6.10; Wang 2007). Note that the new data for liquefaction from New Zealand provides further support to the liquefaction limit (highlighted green line), especially at small earthquakes from $M = 4$ to 5. The orange line shows typical fault length as a function of magnitude. Note also that new water-level data from Devils Hole and China significantly extend the threshold of seismic energy density for water-level response from 10^{-4} J/m^3 (Wang and Manga 2010) to $< 10^{-6} \text{ J/m}^3$

and may thus be plotted together, as in Fig. 14.4. The data are compiled from an earlier global dataset (Wang and Manga 2010), new water-level data from Devil Hole, Nevada (Weingarten and Ge 2014) and China (Yan et al. 2014; Sun et al. 2018; Zhang et al. 2019a), and new liquefaction data from New Zealand (Simon Cox, personal communication).

We have also used an empirical relation among the seismic energy density e , the earthquake magnitude M , and the epicentral distance r (Eq. 6.10) as a reference to compare the different hydrologic responses:

$$\log_{10} e = -3 \log_{10} r + 1.44M - 4.62, \tag{14.1}$$

where r is in km and e in J/m^3 . We stress that this relation was constructed on the basis of ground motion data for southern California (Wang 2007) and is thus region-specific and may not apply to other areas such as New Zealand (Weaver et al. 2020).

It is not made for other regions only because there is a lack of available strong motion data for other specific regions.

Despite of the uncertainty in this relation, we use it here as a common reference to the global hydrological responses (Fig. 14.4). The figure shows that some hydrologic responses require much greater seismic energy density (e.g., liquefaction, mud volcanoes) than others (e.g., water level changes in wells, earthquake triggering). Part of the difference may be due to differences in the regional geology. Part of the difference may be a result of incomplete data. On the other hand, most other data summarized in Fig. 14.4 are abundant, come from a wide range of geological settings, and thus the differences in the threshold energy among the different hydrologic responses may be significant. Scatter in the hydrologic responses is expected for two reasons. First, if triggering of a particular hydrological response is a threshold process, then we might expect triggering to be possible for all distances up to the threshold. Second, because the hydro-mechanical properties of rocks and sediments are highly variable, less seismic energy density is required for a specific response at sites underlain by sediments or rocks more sensitive to seismic disturbances than at sites underlain by less sensitive rocks or sediments.

The new water-level data from Devils Hole, Nevada (Weingarten and Ge 2014) and China (Sun et al. 2018; Zhang et al. 2019a) significantly extend the threshold of seismic energy density for water-level response from 10^{-4} J/m³ (Wang and Manga 2010) to 10^{-6} J/m³ or lower. It is likely that this boundary may even be further extended when more data becomes available. On the other hand, the liquefaction limit proposed by Wang (2007; highlighted in green in Fig. 14.4) is supported by the new liquefaction data from New Zealand (Simon Cox, personal communication, 2020), especially at small earthquake magnitudes of $M = 4$ to 5.

Without a priori knowledge of the seismic sensitivity of the rocks and sediments at most of the documented sites, we simplify the comparison by focusing on the threshold seismic energy density, i.e., the lower bound of the seismic energy density required to initiate a specific type of hydrological response in the most sensitive sediments or rocks. Thus liquefaction, some mud volcanoes and streamflow increases are bounded by the contour with $e \sim 10^{-1}$ J/m³, while groundwater level may respond to $e < 10^{-6}$ J/m³. It is important to note that the examples for mud volcano eruptions shown in Fig. 14.4 include only clearly identified triggered eruptions. Geysers have long been known to be sensitive to earthquakes, as manifested by changes in the time interval between eruptions (Ingebritsen and Rojstaczer 1993), and some geysers in the Yellowstone National Park have responded to $e \sim 10^{-3}$ J/m³ from the Denali earthquake (Fig. 14.4; Husen et al. 2004). Given the limited number of data, however, we are unable to confirm whether this may be representative for other geysers and it is worth highlighting that most Yellowstone geysers did not obviously respond to the Denali earthquake. Triggered seismicity also appears to be especially sensitive to seismic disturbances and may respond to e as small as 10^{-4} J/m³ (Fig. 14.4; Brodsky and Prejean 2005; Hill and Prejean 2007). It is, however, important to highlight that the question whether triggered seismicity is a hydrological phenomenon is a matter of active debate (e.g., Hill 2008) and it is likely that some triggered earthquakes are not caused by earthquake-induced re-distribution of pore pressure. Regardless of a

clear hydrologic connection, triggered earthquakes by large ($M > 9$) earthquakes may be global (e.g., West et al. 2005; Velasco et al. 2008)—consistent with the threshold limit for triggered earthquakes shown in Fig. 14.4.

Beyond the near field, dynamic strain must be invoked because the static poroelastic strain is either too small or has the wrong sign to account for the coseismic changes in groundwater systems. Dynamic strain by itself cannot lead to sustained hydrologic changes, but it can dislodge blockage from fractures to enhance permeability (Mogi et al. 1989; Roeloffs 1998; Brodsky et al. 2003; Wang and Chia 2008). Roeloffs (1998) noticed that, at a given well, the amplitude of the sustained groundwater-level change increases in proportion to the increased peak ground velocity (PGV), which is directly related to the seismic energy density. Based on the analysis of groundwater response to Earth tides, Elkhoury et al. (2006) first showed that seismic waves enhance the permeability of shallow crust and the magnitude of this enhancement increases with increased peak ground velocity, and thus with increased seismic energy density. Wong and Wang (2007) found that PGV is a much better predictor for water level changes and liquefaction than peak ground acceleration (PGA). Mohr et al. (2017) also found that PGV was the best ground motion predictor of streamflow changes. Weaver et al. (2020) further found that PGV is better correlated with water level changes in wells than other measures of ground motion. Taken together, it appears that earthquake-enhanced permeability in the shallow crust may be closely related to the seismic energy density and may explain a broad spectrum of hydrologic responses that occur in the intermediate and far fields.

14.2 Future Research

An important theme throughout this book is that much remains to be learned about the interactions between water and earthquakes. We highlight below several unsolved problems that we consider important, and may be fruitful for future research to advance our understanding of the interaction between water and earthquakes.

1. Recent advances in space technology such as InSAR have allowed continuous monitoring of ground deformation, which opens the door to investigate the interactions among groundwater processes, crustal deformation and earthquakes. While studies in this direction are still in their initial stage (e.g., Shirzaei et al. 2016; Johnson et al. 2017; Shi et al. 2020), the combination of space-monitoring of ground deformation and groundwater processes has the potential to provide insight to the interaction between water and earthquake processes, and its promise for future research cannot be over-emphasized.
2. Estimates of the hydraulic parameters have been increasingly made using the water-level response to the oscillatory changes of the crustal strain in response to the tidal, barometric and seismic wave forcing. But the transmissivity estimated

from the different kinds of forcing can be different by several orders of magnitude (Sun et al. 2020). These authors attributed such differences to the different frequencies among the different kinds of forcing. But how transmissivity may depend on the forcing frequency and what are the mechanisms that may produce such dependence are largely unknown. Recent advances in instrumentation and data storage have allowed the documentation of water level data from yearly to seismic frequencies (Shih 2009; Sun et al. 2018; Zhang et al. 2019b), and thus have greatly extended the time scale for quantitative analysis. This opens the door for investigating the frequency dependence of aquitard impedance.

3. Tidal analysis has increasingly been used in studies of the water-level response to earthquakes. However, due to the absence of strain measurements near most wells, tidal analyses have largely relied on theoretical tides for the analysis of the water-level response. Such simplification may lead to errors in the inferred phase shift (Harrison 1974; Beaumont and Berger 1975) and thus in the inferred response to earthquakes. This uncertainty needs to be corrected, if possible, or at least considered and discussed in order to avoid drawing misleading conclusions.
4. Mohr et al. (2015) proposed that pore water was released from the unsaturated zone during the 2010 M8.8 Maule earthquake to explain the increased discharge of some streams in the Chilean coast ranges. This mechanism may also explain the rapid responses of stream flow (Manga et al. 2016) and water level (Wang et al. 2017) to the induced earthquakes in the flat mid-continental USA, such as Oklahoma, where no immediate sources of extra water are evident on Earth's surface. Breen et al. (2020) used a laboratory experiment to verify this hypothesis; but more experiments and field data are needed to better understand the effects of earthquakes on the unsaturated zone.
5. Field observation that liquefaction occurs at distances far beyond the near field and is bounded by the liquefaction limit on a magnitude versus hypocenter distance diagram (green contour in Figs. 11.8 and 14.3; Wang 2007) is inconsistent with the notion of most earthquake engineers that liquefaction occurs only in the near field (blue contour in Fig. 11.8). Nor is it consistent with the results of laboratory studies that show that liquefaction is preceded by undrained consolidation. This inconsistency is curious but not understood. It is thus important, particularly for the mitigation of liquefaction damage, to understand why the threshold seismic energy for triggering liquefaction by earthquakes is so much lower than that in the near field and in laboratory studies.
6. The mechanism leading to enhanced permeability is not entirely clear. Brodsky et al. (2003) suggested that seismic vibrations may unclog fractures by mobilizing colloidal particles in the fracture. Others have suggested that seismic vibrations may dislodge gas bubbles from the throats that connect pores (e.g., Beresnev and Johnson 1994; Beresnev et al. 2005; Deng and Cardenas 2013). At low flow velocity, clay particles suspended in water may form flocculated deposits which may effectively fill fractures, blocking flow, and such fluids are non-Newtonian and have a yield strength equivalent to a threshold energy density of 10^{-3} J/m³ at a few percent solid fraction for different clays (Coussot 1995). The 2002 M7.9 Denali earthquake enhanced groundwater flow in Iowa,

some 5000 km away, to such an extent that clay particles flushed from local aquifers discolored well waters. More experimental studies seem justified to test which of the suggested mechanisms actually occur in field settings and to identify telltale signatures of the process.

7. The empirical relation developed among seismic energy, earthquake magnitude and epicentral distance (Chap. 6; Wang 2007) is sometimes applied to different parts of the world to study the earthquake-induced hydrologic responses. As emphasized previously, this relation was developed specifically from the seismic data for southern California and its application to other regions, if not verified, may lead to error, such as in New Zealand (Weaver et al. 2020). Given the current availability of dense seismic networks in many parts of the world, the development of region-specific empirical relations between seismic energy density and responses may be worthwhile.
8. As more data for the hydrologic responses to earthquakes are collected and the analysis of data becomes more refined, an important consideration in the interpretation of these responses is the effect of geology and rock properties on the measured seismic response. Earthquake engineers have long emphasized the importance of site geology on the distribution of seismic hazards. Similar considerations should be included in the interpretation of hydrologic responses to earthquakes.
9. Identifying and understanding the interactions between earthquakes and water require data. Instruments, data storage, and data transmission are now much less expensive than ever before. Whereas sampling water level daily to hourly may have been standard practice, it is becoming feasible to sample every second, allowing wells to record hydroseismograms and enabling tidal and barometric analysis. High frequency data enables frequency-dependence of responses to be identified and used to monitor the evolution of properties (see item 1). Obtaining more data is not sufficient—ideally this data is made available so that researchers can test new models, look for correlations, and revisit past studies with new understanding. We applaud those nations, agencies, or individuals who share their data!

References

- Beaumont C, Berger J (1975) An analysis of tidal strain observations from the United States of America: I. The laterally homogeneous tide. *Bull Seismol Soc Am* 65(6):1613–1629
- Beresnev IA, Johnson PA (1994) Elastic wave stimulation of oil production: a review of methods and results. *Geophysics* 59:1000–1017
- Beresnev IA, Vigil RD, Li W et al (2005) Elastic waves push organic fluids from reservoir rock. *Geophys Res Letters* 32:L13303. <https://doi.org/10.1029/2005GL023123>
- Breen S, Zhang Z, Wang CY (2020) Shaking water out of sands: an experimental study. *Water Resour Res* 56: e2020WR028153. <https://doi.org/10.1029/2020WR028153>

- Brodsky EE, Roeloffs E, Woodcock D et al (2003) A mechanism for sustained water pressure changes induced by distant earthquakes. *J Geophys Res* 108:2390. <https://doi.org/10.1029/2002JB002321>
- Brodsky EE, Prejean SG (2005) New constraints on mechanisms of remotely triggered seismicity at Long Valley Caldera. *J Geophys Res* 110:B04302. <https://doi.org/10.1029/2004JB003211>
- Camacho A, Lee JK, Hensen BJ, Braun J (2005) Short-lived orogenic cycles and the eclogitization of cold crust by spasmodic hot fluids. *Nature* 435(7046):1191–1196
- Coussot P (1995) Structural similarity and transition from Newtonian to non-Newtonian behavior for clay-water suspensions. *Phys Rev Lett* 74:3971–3974
- Deng W, Cardenas MB (2013) Dynamics and dislodgment from pore constrictions of a trapped nonwetting droplet stimulated by seismic waves. *Water Resour Res* 49(7):4206–4218
- Elkhoury JE, Brodsky EE, Agnew DC (2006) Seismic waves increase permeability. *Nature* 441:1135–1138
- Elkhoury JE, Niemeijer A, Brodsky EE et al (2011) Laboratory observations of permeability enhancement by fluid pressure oscillation of in-situ fractured rock. *J Geophys Res* 116:B02311. <https://doi.org/10.1029/2010JB007759>
- Faoro I, Elsworth D, Marone C (2012) Permeability evolution during dynamic stressing of dual permeability media. *J Geophys Res* 117:B01310. <https://doi.org/10.1029/2011JB008635>
- Harrison JC (1974) Cavity and topography effects on the measurement of tilt and strain. *EOS Trans Am Geophys Union* 56:1151
- Hill DP (2008) Dynamic stresses, coulomb failure, and remote triggering. *Bull Seism Soc Am* 98:66–92
- Hill DP, Prejean SG (2007) Dynamic triggering. In: Schubert G (ed) *Treatise on geophysics*, vol 4, pp 293–320
- Husen S, Taylor R, Smith RB et al (2004) Changes in geyser eruption behavior and remotely triggered seismicity in Yellowstone. National park produced by the 2002 M 7.9 Denali fault earthquake Alaska. *Geology* 32:537–540
- Ingebritsen SE, Rojstaczer SA (1993) Controls on geyser periodicity. *Science* 262:889–892
- Ingebritsen SE, Manning CE (2002) Diffuse fluid flux through orogenic belts: implications for the world ocean. *Proc Natl Acad Sci USA* 99:9113–9116. <https://doi.org/10.1073/pnas.132275699>
- Ingebritsen SE, Manning CE (2010) Permeability of the continental crust: dynamic variations inferred from seismicity and metamorphism. *Geofluids* 10:193–205
- Johnson CW, Fu Y, Bürgmann R (2017) Seasonal water storage, stress modulation, and California seismicity. *Science* 356(6343):1161–1164
- Koizumi N, Lai WC, Kitagawa Y (2004) Comment on “Coseismic hydrological changes associated with dislocation of the September 21, 1999 Chichi earthquake, Taiwan” by Min Lee et al. *Geophys Res Lett* 31:L13603. <https://doi.org/10.1029/2004GL019897>
- Li W, Vigil RD, Beresnev IA et al (2005) Vibration-induced mobilization of trapped oil ganglia in porous media: experimental validation of a capillary-physics mechanism. *J Colloid Interface Sci* 289:193–199
- Liu W, Manga M (2009) Changes in permeability caused by dynamic stresses in fractured sandstone. *Geophys Res Lett* 36:L20307
- Lupi M, Geiger S, Graham CM (2011) Numerical simulations of seismicity-induced fluid flow in the Tjörnes Fracture Zone, Iceland. *J Geophys Res Solid Earth* 116(B7):B07101
- Manga M, Wang CY (2007) Earthquake hydrology. In: Schubert G (ed) *Treatise on geophysics*, vol 4, pp 293–320
- Manga M, Rowland JC (2009) Response of Alum Rock springs to the October 30, 2007 earthquake and implications for the origin of increased discharge after earthquakes. *Geofluids* 9:237–250
- Manga M, Beresnev I, Brodsky EE et al (2012) Changes in permeability caused by transient stresses: field observations, experiments, and mechanics. *Rev Geophys* 50:RG2004. <https://doi.org/10.1029/2011RG000382>

- Manga M, Wang CY, Shirzaei M (2016) Increased stream discharge after the 3 September 2016 Mw 5.8 Pawnee. *Okla Earthq Geophys Res Lett* 43:11588–11594. <https://doi.org/10.1002/2016GL071268>
- Manning CE, Ingebritsen SE (1999) Permeability of the continental crust: the implications of geothermal data and metamorphic system. *Rev Geophys* 37:127–150
- Micklethwaite S, Cox SF (2004) Fault-segment rupture, aftershock-zone fluid flow, and mineralization. *Geology* 32(9):813–816
- Mohr CH, Manga M, Wang CY et al (2015) Shaking water out of soil. *Geology* 43(3):207–210
- Mohr CH, Manga M, Wang CY, et al, (2017) Regional changes in streamflow after a megathrust earthquake. *Earth Planet Sci Lett* 458:418–428
- Mogi K, Mochizuki H, Kurokawa Y (1989) Temperature changes in an artesian spring at Usami in the Izu Peninsula (Japan) and their relation to earthquakes. *Tectonophysics* 159:95–108
- Roberts PM (2005) Laboratory observations of altered porous fluid flow behavior in Berea sandstone induced by low-frequency dynamic stress stimulation. *Accoustical Phys* 51:S140–S148
- Roeloffs EA (1998) Persistent water level changes in a well near Parkfield, California, due to local and distant earthquakes. *J Geophys Res* 103:869–889
- Rojstaczer SA, Ingebritsen SE, Hayba DO (2008) Permeability of continental crust influenced by internal and external forcing. *Geofluids* 8:128–139
- Rudolph ML, Manga M (2010) Mud volcano response to the April 4, 2010 El Mayor-Cucapah earthquake. *J Geophys Res* 115:B12211. <https://doi.org/10.1029/2010JB007737>
- Shirzaei M, Ellsworth WL, Tiampo KF, González PJ, Manga M (2016) Surface uplift and time-dependent seismic hazard due to fluid injection in eastern Texas. *Science* 353:1416–1419
- Shi Z, Hu X, Wang CY (2020) Hydro-mechanical coupling in the shallow crust—insight from groundwater level and satellite radar imagery in a mining area (in review)
- Shih DCF (2009) Storage in confined aquifer: spectral analysis of ground-water responses to seismic Rayleigh waves. *J Hydrology* 374:83–91
- Shmonov VM, Vitovtova VM, Zharikov AV (1999) Experimental study of seismic oscillation effect on rock permeability under high temperature and pressure. *Int J Rock Mech Mining Sci* 36:405–412
- Sun X, Xiang Y, Shi Z (2018) Estimating the hydraulic parameters of a confined aquifer based on the response of groundwater levels to seismic Rayleigh waves. *Geophys J Int* 213:919–930
- Sun X, Shi Z, Xiang Y (2020) Frequency dependence of in-situ transmissivity estimation of well-aquifer systems from periodic loadings, *Water Resources Research* (in press)
- Velasco AA, Hernandez S, Parsons T et al (2008) Global ubiquity of dynamic earthquake triggering. *Nature Geosci* 1:375–379
- Wang CY (2007) Liquefaction beyond the near field. *Seismo Res Lett* 78:512–517
- Wang CY, Chia Y (2008) Mechanism of water-level changes during earthquakes: near field versus intermediate field. *Geophys Res Lett* 35:L12402. <https://doi.org/10.1029/2008GL034227>
- Wang CY and Manga M (2010) *Earthquakes and water*. Springer, Lecture notes in earth sciences, vol 114, 249pp
- Wang CY, Manga M, Wang CH et al (2012) Earthquakes and subsurface temperature changes near an active mountain front. *Geology* 40:119–122
- Wang CY, Wang LP, Manga M et al (2013) Basin-scale transport of heat and fluid induced by earthquakes. *Geophys Res Lett* 40:3893–3897
- Wang CY, Manga M, Shirzaei M et al (2017) Induced seismicity in Oklahoma affects shallow groundwater. *Seismol Res Lett* 88:956–962
- Weaver KC, Arnold R, Holden C et al (2020) A probabilistic model of aquifer susceptibility to earthquake-induced groundwater-level changes. *Bull Seismol Soc Am* 110:1046–1063
- Weingarten M, Ge S (2014) Insights into water level response to seismic waves: a 24 year high-fidelity record of global seismicity at Devils Hole. *Geophys Res Lett* 41:74–80. <https://doi.org/10.1002/2013GL058418>
- Weis P (2015) The dynamic interplay between saline fluid flow and rock permeability in magmatic-hydrothermal systems. *Geofluids* 15(1–2):350–371

- West M, Sanchez JJ, McNutt SR (2005) Periodically triggered seismicity at Mount Wrangell, Alaska, after the Sumatra earthquake. *Science* 308:1144–1146
- Wong A, Wang CY (2007) Field relations between the spectral composition of ground motion and hydrological effects during the 1999 Chi-Chi (Taiwan) earthquake. *J Geophys Res* 112:B10305. <https://doi.org/10.1029/2006JB004516>
- Yan R, Woith H, Wang R (2014) Groundwater level changes induced by the 2011 Tohoku earthquake in China mainland. *Geophys J Int* 199:533–548
- Zhang H, Shi Z, Wang G et al (2019a) Large earthquake reshapes the groundwater flow system: Insight from the water-level response to Earth tides and atmospheric pressure in a deep well. *Water Resour Res* 55:4207–4219. <https://doi.org/10.1029/2018WR024608>
- Zhang Y, Wang CY, Fu LY et al (2019b) Unexpected far-field hydrological response to a great earthquake. *Earth Planet Sci Lett* 519:202–212

Open Access This chapter is licensed under the terms of the Creative Commons Attribution 4.0 International License (<http://creativecommons.org/licenses/by/4.0/>), which permits use, sharing, adaptation, distribution and reproduction in any medium or format, as long as you give appropriate credit to the original author(s) and the source, provide a link to the Creative Commons license and indicate if changes were made.

The images or other third party material in this chapter are included in the chapter's Creative Commons license, unless indicated otherwise in a credit line to the material. If material is not included in the chapter's Creative Commons license and your intended use is not permitted by statutory regulation or exceeds the permitted use, you will need to obtain permission directly from the copyright holder.



Index

A

Accretionary prism, 188, 191, 324, 330
Active fault zone, 155, 185, 194
Advective transport, 18, 19, 21, 275, 276
Alaska earthquake (1964), 136, 303, 328
Amplitude ratio, 91, 95, 96, 103, 104, 107–110, 119, 120, 122, 131, 133, 138, 233, 234
Anisotropic permeability, 13
Anisotropic stress, 31
Anthropogenic process, 10
Aquifer, 9–11, 14, 15, 18, 24, 25, 38–40, 56, 67, 76, 83, 84, 91, 93–108, 110–124, 126, 128–132, 135, 138–144, 146, 147, 150, 155, 157, 158, 160, 161, 163–165, 167, 168, 174–176, 181–185, 188, 194, 206, 210, 212–214, 216–218, 220, 234, 235, 248, 254, 257, 267, 269, 271–278, 284, 285, 315, 316, 350, 351, 357, 376
Aquitard, 9, 84, 93, 101, 103, 106–111, 113–116, 122–131, 141, 142, 145, 146, 164, 254, 257, 284, 285, 375
Arbuckle aquifer, 110–115, 150, 164, 175
Athy's law, 43
Azerbaijan mud volcano, 326

B

Barometric efficiency, 122, 126, 127, 129, 131–133
Barometric pressure, 10, 31, 39, 83–85, 91, 92, 94, 121–125, 127, 129–131, 134, 140, 155, 182, 293, 346, 347, 352, 357, 358, 362

Barometric response, 5, 84, 113, 121–123, 128–134, 136, 140, 145, 147, 157, 194
Barometric response function, 39, 135
Baseflow, 212, 213, 214, 216, 217, 220, 221, 281
Basement, 67, 105–107, 110–112, 115, 163, 193, 250, 264, 265, 267
Basement leakage, 105–107, 110, 115
Basin-wide enhanced groundwater flow, 237, 284
Basin-wide groundwater transport, 284
Biot-Willis coefficient, 28, 31, 45, 62
Borah Peak earthquake (1983), 209, 319
Breaching of aquifer confinement, 91, 101, 275, 284
Bubble, 74, 167, 168, 294–297, 323, 330–332, 371, 375
Bubble trap, 294, 295
Bulk modulus, 24, 27, 29, 33, 94, 101, 107, 139, 344

C

Calistoga geyser, 296, 357
Canterbury earthquake (2010), 308, 309
Capillary effect, 98, 99, 114, 116, 120, 171, 175
Capillary fringe, 11, 116, 118, 120
Capillary tension, 11, 95, 114, 116, 155, 171, 194
Capillary zone, 11, 91, 114, 116, 120
Change in groundwater composition, 272, 275

- Change in stream discharge, 201, 202, 204, 206, 207, 210–212, 214, 222, 223, 293, 344
- Change in stream water composition, 258, 281
- Characteristic slip distance, 55
- Characteristic time, 182, 183, 213, 217, 224, 226
- Chelungpu fault, 161, 183, 185, 186, 188
- Chemical reservoir, 258
- Chi-Chi earthquake (1999), 156, 159–161, 163–165, 167, 171–175, 177, 183, 184, 186, 188, 210, 214, 216–222, 228, 236, 238–240, 273–276, 280, 284, 315, 316, 352–354
- Choshui alluvial fan, 216, 222, 240, 274, 315
- Christchurch earthquake (2011), 244, 303, 304
- Clogging, 168, 173, 282
- Clustered wells, 163, 164, 214, 284, 316
- Coefficient of molecular diffusion, 20
- Coherence, 132, 134
- Cohesion strength, 51, 63
- Compressive strain, 330
- Concentration, 19, 243, 259–262, 265–269, 271, 275, 280, 283, 284, 344, 348–350, 356, 359
- Conduit permeability, 294
- Confined aquifer, 9, 10, 14, 24, 39, 84, 91, 93, 95–98, 101–103, 121, 123, 132, 140, 143, 157, 158, 160, 161, 174–176, 184, 218, 276, 277
- Consolidated sediment, 10, 163, 333
- Consolidation, 23, 42, 43, 46, 48, 155, 157, 165, 167, 170, 171, 173, 177, 178, 180, 181, 193, 206, 209, 210, 212, 222, 223, 272, 275, 301, 304, 307–310, 314, 318, 375
- Constrained specific storage, 35
- Coseismic responses
 - consolidation, 157, 165, 209
 - elastic strain, 74, 166, 206
 - groundwater composition, 155, 157, 191, 193
 - groundwater temperature, 232–235, 243, 250
 - liquefaction, 157, 165, 206
 - mud volcano eruption, 373
 - streamflow increase, 222–224
 - water-level decrease, 156
 - water-level increase, 156
- Coulomb failure stress, 2
- Coulomb's failure law, 51, 62
- Coulomb stress change, 2, 3, 329
- Critical state, 47, 310
- Crustal rupture, 157, 161
- Cyclic loading, 46, 47, 177, 178, 304, 307, 308
- D**
- Damage zone, 184–187, 246
- Darcy's law, 9, 12, 13, 15, 16, 39
- Denali earthquake (2002), 136, 291–293, 296, 373, 375
- Depleted $\delta^{18}\text{O}$, 272–274, 276
- Diffusion coefficient, 20
- Dilatancy, 47, 314
- Dilatational strain, 98
- Discharge area, 237, 277
- Dispersivity, 21, 276
- Disruption of capillary tension, 171
- Dissipated energy, 177, 178, 245, 305–309
- Diurnal tide, 86, 103, 149
- Drainage basin, 212, 220, 232, 238, 279, 280
- Drained bulk modulus, 33
- Drained pore modulus, 33, 34
- Dynamic strain, 5, 74, 156, 293, 296, 329, 330–332, 362, 374
- Dynamic stress, 2, 3, 73–75, 292, 293, 296, 323, 329, 330, 337
- E**
- Earthquake hydrology, 4, 9, 84, 85, 131, 157
- Earthquake prediction, 343, 345, 346, 359, 363
- Earthquake swarm, 191, 193, 243, 247–249, 362
- Earthquake-triggered eruption, 327
- Earth tide, 11, 24, 83, 84, 86–91, 106, 110, 114, 116, 155, 187, 293, 346, 347, 374
- Edifice, 323
- Effective porosity, 10, 20, 209
- Effective stress, 27, 28, 32, 43, 64, 67, 167, 176, 184, 305, 306, 317
- Ejection
 - height, 305
 - material, 304
- Electrical conductivity, 212, 237, 344, 359
- El Mayor-Cucapah earthquake (2010), 24, 25
- Enhanced Geothermal System (EGS), 11, 67
- Enhanced permeability, 155, 157, 165, 167, 171, 173, 192, 193, 212, 232, 242,

249, 250, 254, 257, 267, 285, 314, 374, 375

Episodic discharge, 289, 323

Eruption, 4, 5, 289–297, 310, 323–330, 332–337, 357–359, 369, 373

Excess discharge, 218, 220–222, 226, 227, 272

Excess pore pressure, 125, 224, 311, 312, 317

F

Failure criterion, 51–54, 62

Far field, 3, 4, 74, 75, 123, 124, 155, 159, 173, 185, 193, 374

Fault permeability, 187

Fault zone, 67, 155, 159, 184, 185, 187–190, 194, 206, 236, 259, 270, 346, 370

Fick's law, 20, 252

Fluid extraction, 67, 69

Fluid injection, 62, 64, 66

Fluid source mixing, 272, 285

Fluid source switching, 257, 272, 285

Fourier's law, 17, 18

Fracking, 67

Fracture

- aperture, 167
- compliance, 148

Frequency dependence, 316–318, 370, 375, 376

Friction, 3, 23, 49–53, 55, 62, 64, 71, 72, 74, 246, 254

Frictional criterion, 55

Frictional heat, 231, 246, 253

Frictional instability, 23, 50

Friction coefficient, 50, 51, 53, 62

G

Gain, 29, 129, 130, 134, 135

Gas hydrate, 331, 332

Geertsma uniaxial expansion coefficient, 37

Geotherm, 231, 245, 247, 252, 253

Geyser

- eruption mechanism, 294, 295
- interval between eruption (IBE), 289–297
- seismic response, 296

Global Meteoric Water Line, 271, 272, 280–282

Gravitational potential, 86, 224

Groundwater composition change, 269

Groundwater flow equation, 9, 10, 12, 15, 17–21, 40, 93, 107, 126, 217

Groundwater level change

- coseismic static strain, 165, 174
- earthquake-enhanced permeability, 173
- far field, 155, 159, 173, 185, 193
- near field, 155, 156, 159, 160, 162, 173, 180, 181, 193
- oscillation, 159, 168, 169, 187, 193
- recession, 180–183, 195
- undrained consolidation, 155, 157, 165, 167, 170, 171, 173, 177, 178, 180, 193

Groundwater oscillation, 136, 193

Groundwater temperature change, 232, 276

Groundwater transport, 18, 257, 284, 285, 369

Gryphon, 323, 324, 336

Gutenberg-Richter scaling, 65

H

Haicheng earthquake (1975), 348

Heat transport, 15, 17–19, 21, 237, 239, 241, 276, 294

Hebgen Lake earthquake (1959), 209, 221

Helice, 301, 302

Horizontal permeability, 132, 134, 207, 214

Hot spring, 224–227, 232, 242–244, 254, 277, 282, 295, 353

Hutubi earthquake (2016), 139

Hydraulic conductivity, 12, 16, 17, 101, 105–107, 112–114, 116, 117, 121, 123, 126, 128, 139, 141, 146, 181, 206, 207, 210, 217, 276

Hydraulic diffusivity, 43, 67, 95, 119, 123, 125, 129, 130, 166, 183, 188, 212, 213

Hydraulic fracture, 67

Hydraulic gradient, 101, 156, 167, 206

Hydraulic head, 9, 12, 14, 16, 25, 36, 93, 94, 101, 102, 105, 106, 119, 143, 181, 183, 212, 218, 276

Hydrochemical flux, 261

Hydrodynamic dispersion, 21, 275

Hydrologic precursor, 5, 343, 348

Hydro-mechanical coupling, 5

Hydroseismogram, 136, 251, 376

Hydrothermal area, 224, 227

Hydrothermal vent, 248, 249, 254

I

Induced seismicity, 5, 11, 59, 62, 64, 65, 67, 69–71, 76, 110, 112, 157, 357

Injection induced seismicity, 67

Instability, 23, 49–51, 53–57, 250, 252

Intermediate field, 4, 73, 159, 162, 173, 310, 337
 Isotopic composition, 224, 272, 273, 276, 278, 280–282, 284

J

Jiuzhaigou earthquake (2017), 202
 Juan de Fuca Ridge, 232, 248–250

K

Kern County earthquake (1952), 220, 221
 Kettleman Hill earthquake (1985), 347, 351
 Kobe earthquake (1995), 173, 212, 349, 350, 356
 Kumamoto earthquake (2016), 157–160, 165, 204, 207, 208, 210, 228, 231, 232, 236, 241, 242, 261, 263, 264, 276, 278, 285

L

Leakage factor, 101, 107–110, 112, 115
 Leaky aquifer, 9, 39, 91, 98, 100, 101, 103–105, 107, 135, 144, 148

Liquefaction

coseismic consolidation, 315
 cyclic loading, 304, 307, 308
 dissipated energy, 305–309
 intensity, 304
 mud volcanoes, 326, 332
 potential, 305, 307
 seismic energy, 301, 306, 308–310, 314, 318
 Loading efficiency, 43, 125, 126, 188–191
 Local meteoric water line, 281
 Loma Prieta earthquake (1989), 173, 212, 213, 221, 224, 279, 280

M

Magmatic eruption, 329, 332
 Major elements, 258–261, 264, 267–270, 283
 Matrix permeability, 294, 296, 297
 Maule earthquake (2010), 11, 165, 210, 211, 214, 215, 221, 223, 375
 Mechanical instability, 250, 252
 Microcrack, 167, 343–345
 Mid-ocean ridge, 329
 Migration rate of seismicity, 66
 Mohr circle, 52, 53

Mohr-Coulomb failure criterion, *see* Coulomb's failure law
 Mud volcano
 Sidoarjo, 335
 triggering mechanism, 323, 330

N

Nankaido earthquake (1946), 349
 Near field, 3, 73, 155, 156, 159, 160, 162, 173, 180, 181, 193, 212, 301, 308–310, 314, 318, 326, 337, 374, 375
 New Madrid Seismic Zone, 302
 Nigata earthquake (1964), 303
 Niikappu mud volcano, 325, 326
 Non-oscillatory response, 156
 Noodbergum effect, 66
 Nusselt number, 19

O

Ocean floor, 188
 ODP borehole, 248–250
 Old Faithful geyser, 291, 292
 Oscillatory response, 136, 156
 Overpressure, 74, 323, 330–332

P

Peak ground acceleration, 315, 374
 Peak ground velocity, 174, 175, 178, 179, 374
 Peclet number, 19, 21, 275, 276
 Permeability, 4, 9, 10, 12–14, 16, 30, 39, 49, 67, 74, 100, 112, 114, 116, 125, 132, 134, 135, 139, 140, 142, 155–157, 165, 167–169, 171, 173, 174, 176, 184–188, 192–194, 207, 210, 212, 214, 217, 222, 227, 232, 234, 241, 242, 246, 249, 250, 254, 257, 267, 269, 280, 285, 289, 294–297, 310, 314, 319, 323, 330, 332, 333, 344, 352, 359, 369–372, 374, 375
 Phase shift, 91, 92, 95, 96, 98–100, 102–105, 108–114, 115, 119, 120, 122, 126–128, 131–135, 138, 149, 150, 174, 175, 185, 212, 375
 Plate Boundary Observatory, 24, 25, 31
 Plumbing system, 184, 289, 293–295, 297, 336
 Poisson's ratio, 32, 33, 37, 136
 Pore-pressure changes, 42, 160, 191, 192, 306
 Pore-pressure heterogeneity, 167

Pore-pressure spreading, 191
 Poroelastic constant, 28, 33–35, 38
 Poroelastic deformation, 23, 43, 68, 83
 Poroelastic expansion coefficient, 36, 37
 Poroelasticity, 23, 24, 40, 76, 160
 Porosity, 10, 13, 14, 18, 20, 39, 43, 130, 181, 209, 276
 Porous flow, 19, 20, 23
 Postseismic recession, 181, 182, 195, 217
 Precipitate, 49, 249, 254
 Precursors
 hydrological, 343, 363
 geochemical, 344, 346, 348
 Precursory change, 259, 344, 349, 352, 358, 362
 Prediction, 58, 59, 105, 129, 130, 140, 165, 181, 183, 224, 318, 343, 345, 346, 348, 352, 359, 363
 Premonitory, 260, 345, 348, 350, 357
 Pressure gauge, 112
 Principle stresses, 52–54
 Progressive softening, 311, 314

R

Radon, 344, 348–350, 363
 Rare earth elements, 269, 270
 Rate-and-state friction, 64, 71, 72, 74
 Rayleigh number, 19
 Rayleigh wave, 74, 136, 138–140, 168
 Recession analysis, 183, 216, 217, 226
 Recession constant, 182, 183, 213–215, 217, 220
 Recharge area, 181, 268, 277
 Rectified diffusion, 331
 Relative conductivity, 16, 117, 118
 Representative Elementary Volume (REV), 10, 16, 33, 35, 36
 Reservoir-induced seismicity, 69, 72
 Residual water content, 11
 Reynolds number, 13
 Ridge flank, 247
 Rift valley, 162
 Rise time, 156, 171, 220
 Rock friction, 23, 49, 51
 Rocky Mountain Arsenal, 64, 65

S

San Andreas fault, 142, 185, 187, 345
 Sand blow, 301–303
 Sand dike, 303
 San Simeon earthquake (2003), 224, 225, 227

Saturated flow, 14–17, 117
 Saturated water content, 11, 117
 Sea floor pore-pressure, 249
 Seasonal variations of seismicity, 72
 Seismic energy density, 5, 140, 163, 178–180, 190, 191, 194, 212, 222, 223, 243, 244, 301, 308–310, 314, 318, 326, 369, 371–374, 376
 Seismic energy density relation, 190
 Seismic frequency, 314, 315, 375
 Semidiurnal tide, 103, 149, 150
 Shear modulus, 32, 177, 178, 317
 Sidoarjo (Lusi) mud eruption, 334–336
 Skempton's coefficient, 24, 28, 31, 37, 94, 101, 107, 117, 344
 Slow seismic events, 191
 Solid tide, 83, 84, 93
 Solomon Island earthquake (2016), 139
 Solute transport, 9, 19, 20, 21, 275
 South Napa earthquake (2014), 206s, 219, 221, 223, 280, 282, 283
 Specific discharge, 12, 13, 18, 39, 116
 Specific heat, 18, 19, 276
 Specific storage
 constrained (constant strain), 29
 hydrogeological, 36
 unconstrained (constant stress), 35
 uniaxial, 36
 unjacketed, 35
 Specific water capacity, 17
 Specific yield, 14, 114, 218
 Stable isotopes, 258, 261, 272, 278, 280, 281
 State variable, 55, 56
 Static strain, 156, 165, 166, 174, 215, 251, 280, 293, 326
 Static stress, 2, 73, 74, 296, 326, 329, 330, 333, 337
 Step-like decrease, 156
 Step-like increase, 155, 159, 170, 173, 193, 314
 Stick-slip, 51, 54, 64
 Storativity, 14, 93, 101, 103, 106, 107–109, 111, 114, 115, 126, 135, 139, 142, 184
 Stream discharge
 anisotropic permeability, 13, 187
 baseflow change, 213
 consolidation hypothesis, 171
 enhanced permeability hypothesis, 155, 157, 165–167, 171, 173, 192, 193, 212, 232, 242, 250, 254, 257, 267, 285, 314, 374, 375

Stream gauge, 202, 203, 204, 206, 207, 213, 214, 216–218, 220–222, 224–227
 Submarine geothermal vents, 254
 Subsidence, 301
 Sumatra earthquake (2004), 2, 74, 75, 166, 328
 Supersaturated liquid, 331
 Superstition Hills earthquake (1987), 310–314
 Sustained change, 155, 156, 162, 166, 173, 193, 242, 289, 314

T

Tangshan earthquake (1976), 348, 349
 Temperature change
 hot spring, 232, 244, 254
 marine hydrothermal system, 254
 well, 243, 250, 371
 Tectonic stress, 70, 293
 Tensional fracture, 162, 302
 Terzaghi theory of consolidation, 43
 Thermal conductivity, 17–19, 127, 252, 276
 Threshold distance, 162
 Threshold seismic energy density, 180, 212, 308, 372
 Threshold strain, 48, 180, 309
 Tidal efficiency, 38
 Tidal potential, 85–88, 148–150
 Tidal strain, 87–89, 91, 94, 98, 101, 104, 132, 148, 174, 212, 344
 Tide, 10, 11, 24, 25, 31, 83–95, 99, 100, 102, 103, 106, 108–111, 114–116, 119, 122, 124, 134, 135, 137, 140, 148–150, 155, 174–176, 182, 187, 193, 233, 234, 293, 329, 346, 347, 350, 357, 358, 362, 374, 375
 Tohoku earthquake (2011), 26, 131–134, 136, 159, 166, 172, 176, 191
 Tortuosity, 20
 Trace elements, 258, 267, 269, 283, 284, 359
 Tracer, 272, 285
 Transmissivity, 93, 95, 101, 105, 106, 108, 110, 114, 115, 122, 123, 126, 132, 135, 139, 140, 142, 184, 185, 187, 374, 375
 Triggered eruption, 325, 327, 329, 332, 333, 336, 337, 373
 Triggered seismicity, 74, 373
 Turbulent mixing, 231, 232, 237, 247, 250, 252–254

U

Unclogging, 168

Unconfined aquifer, 9, 10, 14, 91, 95, 97, 98, 100, 103, 104, 105, 106, 114, 116–118, 120, 157, 175, 218
 Unconsolidated sediment, 10, 42, 111, 157, 163, 170, 173, 184, 324, 333
 Unconstrained specific storage, 35
 Undrained bulk modulus, 24, 29, 94, 101, 107, 139, 344
 Undrained consolidation, 155, 157, 165, 167, 170, 171, 173, 177, 178, 180, 193, 210, 212, 222, 223, 275, 301, 307–310, 314, 318, 375
 Undrained Poisson ratio, 33
 Uniaxial specific storage, 36
 Unjacketed bulk modulus, 33
 Unjacketed pore modulus, 33
 Unsaturated flow, 9, 16, 17
 Unsaturated zone, 10, 11, 91, 114, 116, 117, 119, 123, 128, 155, 165, 169, 170, 171, 173, 181, 194, 212, 375
 USGS Oklahoma Deep Well, 111–114

V

van Genuchten-Mualem relation, 118
 Vertical incompressibility, 37–39
 Vertical permeability, 16, 107, 116, 132, 135, 207, 210, 212, 214, 217, 222, 280
 Volcanic Explosive Index (VEI), 327, 329
 Volumetric strain, 24–26, 28, 30, 31, 37, 40, 47, 73, 92–94, 101, 104, 106, 111, 134, 136, 138, 159, 160, 161, 165–167, 344, 351

W

Wastewater injection, 67
 Water content, 10, 11, 16, 17, 24, 116, 117, 121
 Water table, 9, 10, 11, 14, 91, 95–98, 114, 116–125, 170, 171, 209, 303
 Wellbore storage, 102, 143
 Wenchuan earthquake (2008), 71, 175, 185, 186, 231–235, 304, 305, 319
 Western Foothills, Taiwan, 160, 162, 163, 284
 Wildlife Liquefaction Array, 310, 311, 314, 315
 Wildlife Reserve experiment, 313

Y

Yellowstone geyser, 291, 293, 373
 Young's modulus, 32

Open Access This book is licensed under the terms of the Creative Commons Attribution 4.0 International License (<http://creativecommons.org/licenses/by/4.0/>), which permits use, sharing, adaptation, distribution and reproduction in any medium or format, as long as you give appropriate credit to the original author(s) and the source, provide a link to the Creative Commons license and indicate if changes were made.

The images or other third party material in this book are included in the book’s Creative Commons license, unless indicated otherwise in a credit line to the material. If material is not included in the book’s Creative Commons license and your intended use is not permitted by statutory regulation or exceeds the permitted use, you will need to obtain permission directly from the copyright holder.

